

UC Berkeley

UC Berkeley Electronic Theses and Dissertations

Title

Bioorthogonal Chemical Tools Toward the Study of Bacterial Pathogens

Permalink

<https://escholarship.org/uc/item/7xh9q4m8>

Author

Shieh, Peyton

Publication Date

2015

Peer reviewed|Thesis/dissertation

Bioorthogonal Chemical Tools Toward the Study of Bacterial Pathogens

by

Peyton Shieh

A dissertation submitted in partial satisfaction of the

requirements for the degree of

Doctor of Philosophy

in

Chemistry

in the

Graduate Division

of the

University of California, Berkeley

Committee in Charge:

Professor Carolyn R. Bertozzi, Chair

Professor Ming C. Hammond

Professor Gerard Marriott

Fall 2015

Abstract

Bioorthogonal Chemical Tools Toward the Study of Bacterial Pathogens

by

Peyton Shieh

Doctor of Philosophy in Chemistry

University of California, Berkeley

Professor Carolyn R. Bertozzi, Chair

In this dissertation, I describe the development of bioorthogonal chemical tools toward the study of bacterial pathogens during infection. Bioorthogonal chemistry has enabled the visualization of biomolecules not amenable to fluorescent protein fusion. By feeding an organism an unnatural metabolite bearing a bioorthogonal chemical reporter, the reporter is incorporated into the cellular biopolymer of interest and can be detected by bioorthogonal reaction with an imaging agent. To adapt this approach towards visualizing pathogenic bacteria in an infection setting, my dissertation research focused on two main areas. First, I developed a family of fluorogenic azide probes activated by bioorthogonal click reactions with alkynes. These probes offer significant advantages in imaging studies where it is challenging to wash away unreacted probe, such as within live cells or in live organisms, the settings in which bacterial pathogens reside. Secondly, I developed a family of unnatural D-alanine analogues bearing cyclooctynes, which are incorporated into nascent peptidoglycan in a wide variety of bacterial species and undergo bioorthogonal reactions with azides. In conjunction with the fluorogenic azide probes I developed, these analogues enabled the visualization of cell wall synthesis in an intracellular bacterial pathogen during infection.

In Chapter 1, I review the field of bioorthogonal smart probes, which become fluorescent or release molecular cargo upon bioorthogonal reaction. I focus on the molecular design strategies used by others to endow these probes with such a property. The diversity of approaches used to develop bioorthogonal smart probes sets the stage for my own work on fluorogenic azide probes across the visible spectrum.

In Chapter 2, I describe the development of the first fluorogenic azide probes with visible light excitation/emission in aqueous solvent. To design such probes, we opted to take advantage of photoinduced electron transfer (PeT), a mechanism of fluorescence quenching that was thoroughly characterized for fluorescein derivatives. At the time, it was unclear whether PeT from pendant aryl azide-functionalized fluorescein derivatives would efficiently switch fluorescence upon click reaction with alkynes. Using computational methods, we screened a panel of aryl azides derived from commercially available bromoanilines. The best hits from this computational screen were taken on for experimental validation using a highly modular synthetic route. From this screen, we identified our first-generation compound, an azidonaphthyl substituted fluorescein, which underwent an up to 34-fold enhancement in fluorescence upon click reactions and was suitable for labeling of linear alkynes on proteins and fixed cells.

In Chapter 3, I discuss an extension of this strategy to develop longer wavelength fluorogenic azide probes with emission approaching the near-infrared, an important wavelength for *in vivo* imaging due to high tissue penetrance and minimized background autofluorescence. To push emission wavelengths into the near-infrared, I opted to use Si-rhodamine based fluorophores, which are switched by PeT in an analogous manner to fluoresceins. From this work, I identified a novel motif, the 2,4-dialkoxy-5-azido pendant aryl ring, that was able to efficiently switch the fluorescence of this near-infrared emitting scaffold. Water-soluble derivatives of these probes enabled the robust no-wash live-cell imaging of linear and strained alkynes.

In Chapter 4, I demonstrate that the 2,4-dialkoxy-5-azido pendant aryl ring identified in the previous chapter is capable of switching fluorescence across multiple fluorophore types. Installation of this motif into a panel of four xanthene fluorophores resulted in dramatic fluorescence enhancements upon click reaction, among the highest reported for azide probes of any emission wavelength. Computational and electrochemical studies were performed to elucidate the origins of the superior performance of this motif versus other aryl azide moieties. In addition, I explored different choices of solubilizing groups and showed that zwitterionic moieties, common in materials science but scarcely used in chemical biology, potentially inhibit non-specific binding of these fluorophores. Finally, I showcase the utility of these probes for visualizing a large panel of linear alkynes in fixed and living cells, in tissue and *in vivo*.

In Chapter 5, I discuss the development of a novel metabolic labeling strategy for bacterial peptidoglycan. Our efforts focused on the incorporation of unnatural D-alanine derivatives, which are incorporated into the stem peptides of newly synthesized peptidoglycan. As D-amino acids are rarely utilized in mammalian systems, these metabolites are selective for the bacterial peptidoglycan biopolymer and enable its visualization in an infection setting. I describe the development of cyclooctyne-functionalized D-alanine analogues, which enable the catalyst-free visualization of nascent peptidoglycan in a variety of bacterial species upon bioorthogonal reaction with azide probes. Using this approach, we were able to visualize, within live mammalian cells, peptidoglycan synthesis of the intracellular pathogen *Mycobacterium marinum*.

In Chapter 6, I review recent developments on novel cyclooctyne reaction partners. Since our first disclosure of catalyst-free click reactions between azides and strained alkynes, various groups have systematically investigated alternative reaction partners for cyclooctynes, including other 1,3-dipoles, dienes, and sulfur species. Not only do these novel reaction partners enable more rapid bioconjugation, but they also give the cyclooctyne new roles as a platform for multifunctional probe design and as a chemical tool to understand redox signaling in biological systems. Ultimately, these developments, in conjunction with my work incorporating cyclooctynes into peptidoglycan, will open the door to many exciting future directions on the study of the bacterial cell wall.

Chair _____

This dissertation is dedicated to my parents.

Thanks for everything.

Bioorthogonal Chemical Tools Toward the Study of Bacterial Pathogens

Table of Contents

Acknowledgements	xi
Chapter 1: Design Strategies for Bioorthogonal Smart Probes	1
Introduction.....	1
Aldehyde/Ketone-Nucleophile Condensations.....	2
The Staudinger Ligation.....	5
Azide-Alkyne Click Cycloadditions.....	8
Nitrile Imine-Alkene Cycloadditions.....	13
The Tetrazine Ligation.....	15
Selected Applications of Bioorthogonal Smart Probes.....	20
Conclusion and Dissertation Overview	22
Notes and References.....	24
Chapter 2: A PeT-Based Approach Toward Fluorogenic Azide Probes	29
Introduction.....	29
Results and Discussion.....	29
Conclusion.....	44
Experimental Procedures	45
References.....	59
Chapter 3: Development of a Highly Fluorogenic Azide Probe with Near-Infrared Emission	61
Introduction.....	61
Results and Discussion.....	61
Conclusion.....	78
Experimental Procedures	79
References.....	105
Chapter 4: A Universal Motif for Fluorogenic Azide Probes Across the Visible Spectrum	107
Introduction.....	107
Results and Discussion.....	107
Conclusion.....	143
Experimental Procedures	144
References.....	172
Chapter 5: Metabolic Incorporation of Cyclooctynes into Bacterial Peptidoglycan	175
Introduction.....	175
Results and Discussion.....	176
Conclusion.....	195
Experimental Procedures	196
References.....	202

Chapter 6: New Tricks for Old Cyclooctynes.	204
Introduction	204
Reactions with Modified Azides	206
Reactions with Nitrones	208
Reactions with Nitrile Oxides	210
Reactions with Diazos	211
Reactions with Quinones	214
Reactions with Sydnones	215
Reactions with Tetrazines	215
Reactions with Thiols and Higher-Order Sulfur Compounds	219
Conclusion	222
References	223
Appendix	226

List of Figures

Figure 1-1. General classes of bioorthogonal smart probes.....	2
Figure 1-2. Aldehyde-ketone-nucleophile condensations.....	3
Figure 1-3. Smart hydrazine probes.....	4
Figure 1-4. Aldehyde detection via oxime bond fragmentation	4
Figure 1-5. The archetypical Staudinger ligation.....	5
Figure 1-6. A smart Staudinger probe activated by phosphine oxidation.....	6
Figure 1-7. Phosphine probes activated by ester cleavage in the Staudinger ligation	7
Figure 1-8. Copper-catalyzed and copper-free click reactions between alkynes and azides to form triazoles	8
Figure 1-9. Various smart azide probes quenched by ICT	9
Figure 1-10. Smart azide probes utilizing PeT	11
Figure 1-11. Smart alkyne and cyclooctyne probes activated by reactions with azides.....	12
Figure 1-12. The nitrile imine-alkene cycloaddition reaction.....	14
Figure 1-13. The tetrazine ligation.....	15
Figure 1-14. Smart tetrazine conjugates containing flexible linkers and well-suited for imaging alkenes in biological systems.....	16
Figure 1-15. Rigidly linked smart tetrazine probes.....	18
Figure 1-16. A smart <i>trans</i> -cyclooctene probe for drug delivery	20
Figure 1-17. DNA template-accelerated bioorthogonal reactions of smart probes for sequence-specific detection of DNA	22
Figure 1-18. A rapidly photoactivatable tetrazole probe	22
Figure 2-1. Truncated structures used for modeling.....	31
Figure 2-2. Computation-aided design of fluorogenic azidofluorescein analogs	33
Figure 2-3. Alkynes used for triazolylfluorescein synthesis.....	35
Figure 2-4. Relationship between calculated pendant aryl E_{HOMO} and fluorescence quantum yield of azidofluoresceins and triazolylfluoresceins.....	37
Figure 2-5. Absorption and fluorescence spectra of equimolar concentrations of azido- and triazolylfluoresceins.....	38
Figure 2-6. Alkyne- and ligand-dependent fluorescence turn-on by 2.1	38
Figure 2-7. Protein labeling by 2.1 is alkyne- and copper-dependent	39
Figure 2-8. Cell-surface labeling by 2.1	40
Figure 2-9. Cell-surface labeling by 5-azidofluorescein.....	41
Figure 2-10. No-wash cell labeling with azidofluorescein probes.....	42
Figure 2-11. Consequences of aryl azide reduction	43
Figure 3-1. Design of a PeT-based fluorogenic azido Si-rhodamine.....	62
Figure 3-2. Structures of azido S-rhodamines synthesized and studied	64
Figure 3-3. Fluorescence enhancement of 3.9 during copper-catalyzed click reaction <i>in situ</i>	68
Figure 3-4. Absorbance spectra of 3.9 under the copper-catalyzed reaction conditions described above.....	68
Figure 3-5. Fluorescence quantum yield vs. calculated E_{HOMO}	69
Figure 3-6. Emission spectra of 3.11 under the copper-catalyzed reaction conditions described above.....	71
Figure 3-7. No-wash CHO cell labeling with 3.11	72
Figure 3-8. Real-time CHO K1 cell surface labeling.....	72

Figure 3-9. Fluorescence image of Ac ₄ ManNAI-treated HEK 293T cells labeled with 3.11	73
Figure 3-10. Mitochondrial staining by 3.11 in HEK 293T cells	73
Figure 3-11. Eliminating mitochondrial staining by 3.11 in HEK 293T cells using tributylphosphine	74
Figure 3-12. Fluorescence enhancement of 3.15 under the copper-catalyzed click conditions described above	76
Figure 3-13. High contrast image of Ac ₄ ManNAc-treated cells, demonstrating that 3.15 is not cell permeable	76
Figure 3-14. No-wash mammalian cell surface labeling with bis-sulfated probe 3.15	77
Figure 3-15. Fluorescence enhancement upon reaction with <i>endo</i> -bicyclononyl	78
Figure 4-1. Cyclic voltammetry analysis of substituted aryl systems	108
Figure 4-2. Role of azide and triazole conformation in aryl HOMO energies	109
Figure 4-3. Plot of oxidation potential of aryl rings vs. calculated E _{HOMO}	110
Figure 4-4. Structures of dimethoxy-substituted fluorophores 4.6 to 4.8	111
Figure 4-5. Fluorescence enhancement of dimethoxy azide probes	113
Figure 4-6. Fluorescence enhancement of bis-oligoethylene glycol azide probes 4.13a , 4.16a , and 4.17a	115
Figure 4-7. Fluorescence spectra of equimolar concentrations of probes in various environments.	116
Figure 4-8. CalFluors and their fluorescence enhancements	118
Figure 4-9. Fluorescence spectra of CalFluors in the presence of various additives	119
Figure 4-10. Fluorescence of CalFluor 647 in the presence of various detergents	119
Figure 4-11. No-wash labeling of cell-surface glycoproteins on HEK 293T cells	120
Figure 4-12. Higher-contrast images of cells labeled with Ac ₄ ManNAc control and treated with CalFluors	121
Figure 4-13. No-wash labeling of cell surface glycans on CHO K1 cells with CalFluors.	121
Figure 4-14. Real-time imaging of glycans on live cell surfaces.	122
Figure 4-15. Labeling cell surface glycoproteins on live CHO K1 cells using 3-azido-7-hydroxycoumarin for BTAA-catalyzed click reactions.	122
Figure 4-16. Fluorescence enhancement of 3-azido-7-hydroxycoumarin	123
Figure 4-17. No-wash labeling of glycoproteins on fixed CHO K1 cells with CalFluors	124
Figure 4-18. Labeling fixed HEK 293T cells with CalFluor 555	125
Figure 4-19. Labeling fixed CHO K1 cells with CalFluor 555	125
Figure 4-20. No-wash labeling of fixed CHO K1 cells with 3-azido-7-hydroxycoumarin	126
Figure 4-21. No-wash labeling of fixed CHO K1 cells with bis-oligoethylene glycol functionalized azidofluorescein 4.13a	126
Figure 4-22. No-wash labeling of fixed CHO K1 cells with Si-rhodamine probe 3.15 under TBTA-catalyzed click conditions	127
Figure 4-23. Labeling fixed CHO K1 cells with CalFluor 647 or AlexaFluor 647 azide	127
Figure 4-24. Visualizing sialic acids on live developing zebrafish with CalFluors	129
Figure 4-25. Visualizing EdU-labeled DNA in fixed and permeabilized samples using fluorogenic azide probes	131
Figure 4-26. Comparing no-wash labeling of newly synthesized DNA by CalFluor 555 and 3-azido-7-hydroxycoumarin in HEK 293T cells.	132
Figure 4-27. Comparison of no-wash EdU labeling using CalFluor 647 or AlexaFluor 647 azide in HEK 293T cells	132

Figure 4-28. No-wash labeling newly of synthesized RNA using EU and CalFluors	133
Figure 4-29. Labeling newly synthesized RNA using EU	133
Figure 4-30. Comparing EU labeling in HEK 293T cells between CalFluor 555 and 3-azido-7-hydroxycoumarin under TBTA-catalyzed click conditions.	134
Figure 4-31. pH sensitivity of the fluorescein-based CalFluor 488 and CalFluor 580-derived triazole products.	135
Figure 4-32. pH sensitivity of CalFluor 488 and CalFluor 580-oligonucleotide conjugates in fixed and permeabilized cells	136
Figure 4-33. No-wash labeling of EdU in fixed and permeabilized CHO K1 cells with CalFluors.	138
Figure 4-34. No-wash labeling of EU in fixed and permeabilized CHO K1 cells with CalFluors.	139
Figure 4-35. Labeling of EU in fixed and permeabilized CHO K1 cells with CalFluors	140
Figure 4-36. Labeling EdU-containing DNA in fixed and permeabilized <i>E. coli</i>	141
Figure 4-37. No-wash labeling newly synthesized proteins in fixed and permeabilized in HEK 293T cells with CalFluors.	142
Figure 5-1. Structure of un-crosslinked peptidoglycan	176
Figure 5-2. Biosynthesis of peptidoglycan	177
Figure 5-3. Incorporation of unnatural D-amino acids into peptidoglycan.	179
Figure 5-4. Labeling of wild-type <i>L. monocytogenes</i> with azido-PEG ₃ -carboxyrhodamine 110	181
Figure 5-5. Competition experiment using wild-type <i>L. monocytogenes</i>	182
Figure 5-6. Competition experiment using the D-alanine auxotroph <i>L. monocytogenes dal⁻ dal⁻</i>	183
Figure 5-7. Labeling of <i>L. monocytogenes pbp5::tn</i> with azido-PEG ₃ -carboxyrhodamine 110.	184
Figure 5-8. Optical density of wild-type <i>L. monocytogenes</i> grown in the presence of D-alanine or cyclooctyne D-alanine derivatives 5.3 to 5.5	184
Figure 5-9. Labeling of <i>M. smegmatis</i> with azido-PEG ₃ -carboxyrhodamine 110.....	185
Figure 5-10. Labeling of <i>C. glutamicum</i> with azido-PEG ₃ -carboxyrhodamine 110	185
Figure 5-11. Labeling <i>E. coli</i> with azido-carboxyrhodamine 110	186
Figure 5-12. A comparison of two-step versus one-step labeling approaches for peptidoglycan imaging.	188
Figure 5-13. Bacterial peptidoglycan labeling with fluorogenic azide probes	191
Figure 5-14. No-wash peptidoglycan labeling of <i>C. glutamicum</i> with reduced amino acid loading.	191
Figure 5-15. No-wash peptidoglycan labeling of the Gram-negative <i>E. coli</i>	192
Figure 5-16. Labeling <i>M. marinum</i> with cyclooctyne D-alanine 5.5 and fluorogenic azide probes.	193
Figure 5-17. Labeling <i>M. marinum</i> within J774 murine macrophages using fluorogenic azide probes.	194
Figure 6-1. Various strained alkynes and their second-order rate constants for cycloaddition with benzyl azide	204
Figure 6-2. Various cyclooctyne derivatives that can be biosynthetically incorporated	205
Figure 6-3. Non-azide reaction partners for bioconjugation with cyclooctynes.....	206
Figure 6-4. Cyclooctyne reactivity with modified azides.....	207

Figure 6-5. Alkyne-nitrone cycloadditions	209
Figure 6-6. Alkyne-diazo cycloadditions.....	211
Figure 6-7. Diazo-functionalized monosaccharides enable robust two-color glycan imaging...213	
Figure 6-8. Oxidation of catechols to 1,2-quinones and their inverse electron-demand Diels-Alder reaction with cyclooctynes.....	214
Figure 6-9. Alkyne-tetrazine cycloadditions.	216
Figure 6-10. Biomolecule labeling through the reaction of a genetically encoded cyclooctyne 6.10 with a tetrazine-fluorophore conjugate.	217
Figure 6-11. Generation of bispecific antibodies using bioorthogonal chemistry	219
Figure 6-12. Reactions of cyclooctynes with oxidized sulfur species.	221

List of Schemes

Scheme 2-1. Synthesis of azidofluorescein 2.1	34
Scheme 2-2. Synthesis of azidofluorescein 2.4	34
Scheme 3-1. General procedure for the synthesis of azido Si-rhodamines from bromoanilines and the conversion of azido Si-rhodamines to triazolyl Si-rhodamines.	63
Scheme 3-2. Synthesis of probe 3.11	70
Scheme 3-3. Synthesis of probe 3.15	75
Scheme 4-1. Synthesis of dimethoxy-substituted azide fluorophores 4.6a-4.8a and their corresponding triazole products 4.6b-4.8b	111
Scheme 4-2. Synthesis of oligoethylene-glycol substituted probe 4.13a and its corresponding triazole product 4.13b	114
Scheme 4-3. Synthesis of CalFluors and their corresponding triazole products.	117
Scheme 5-1. Synthesis of cyclooctyne-functionalized D-alanine analogs 5.3 to 5.5	180
Scheme 6-1. Protein N-terminus labeling using alkyne-nitrone cycloaddition.....	209
Scheme 6-2. Selective cycloadditions on a bifunctional linker in the absence of presence or BAIB.	211
Scheme 6-3. [3+2] cycloaddition/retro-Diels-Alder reaction of sydnones and cyclooctynes.....	215
Scheme 6-4. Addition of thiols into bicyclononyne 6.3 enables the facile generation of multifunctional probes.	220

List of Tables

Table 2-1. Calculated HOMO Energies (Hartrees) of candidate azidofluoresceins and their products.....	32
Table 2-2. Fluorescence properties of azido- and triazolylfluoresceins in pH 7.4 PBS..	36
Table 3-1. Photophysical properties of Si-rhodamines 3.1-3.9 and their amino and triazolyl counterparts in PBS pH 7.4.....	65
Table 3-2. Structures and calculated aryl E_{HOMOS} in Hartrees of the pendant aryl rings of evaluated probes 3.1 to 3.9 ..	67
Table 4-1. Photophysical properties of all fluorophores	112

Acknowledgements

Whenever I open up someone else's thesis, I always flip to the acknowledgements first. To all the wonderful people I've encountered on the road towards my Ph.D., I hope that this section will do right by you.

After meeting with Carolyn during visiting weekend, I knew that I needed to attend UC Berkeley and join her lab. Her enthusiasm for science is contagious, and, as I first experienced that weekend, it is hard to leave a meeting without catching some of that excitement. In addition, the environment she has fostered within her research group is truly unique. The amount of freedom I was given to work on such diverse projects, along with her generosity in supporting my pursuits, has allowed me to develop as a scientist.

I would also like to thank Professor Ned Jackson, who took me into his lab at Michigan State University the summer after junior year in high school. Seeing how chemists could build such beautiful structures out of such simple starting materials was nothing short of breathtaking. I enrolled in an organic chemistry class the next semester, and it's led me down the path I've taken.

At Harvard, I must thank Professor Evans for giving me the opportunity to work in his laboratory. I learned an extraordinary amount of organic chemistry under his tutelage. My mentors Arthur Catino and Yimon Aye were tremendously helpful and supportive as well. In addition, I am incredibly grateful to Dr. Ahamindra Jain for putting me in touch with Professor David Evans regarding research. Thank you for making the effort to help me out. I hope you know how much of an impact this had on my career in science.

During my time in Carolyn's lab, I've had the opportunity to work directly with some fantastic colleagues. First, I thank my undergraduates Andrew Cullen, Vivian Dien, and Arjun Aditham. I really could not have asked for a better bunch of students, and I wish you all the best of luck in the future. My rotons, Allegra Aron and Sam Keyser, were great as well. I'm extremely grateful to Sloan Siegrist for her patience training me in microbiology. Thank you for showing me how enjoyable collaborative science can be. I would also like to thank Frances Rodriguez-Rivera, Ioannis Mountziaris, and Mireille Kamariza for being fantastic collaborators during my last few months in the lab. Brendan Beahm first introduced me to zebrafish work, Elena Dubikovskaya and Allison Cohen were my mentors during my Bertozzi lab rotation, and Matthew Hangauer, although we never worked together directly, deserves credit for what turned out to be an extremely fruitful area of research. Finally, I thank Asia, Olga, and Sia for keeping the lab running so smoothly.

I'd like to thank the members of Latimer 802, who have made my time in lab so enjoyable. First, I thank Jason Hudak and Brian Belardi for welcoming me to the room and for being great mentors early on in graduate school. I'm lucky to have received so much guidance from two of the best scientists I know. In addition, Jason's penchant for pushing the limits both in and out of lab is something I will always aspire to. Lauren Wagner, although our time together in 802 was short, has always been a friendly face within the lab. David Spiciarich has been a great colleague and an even better listener – thanks for all the conversations. Christina Woo has been an excellent addition to the room, and I know that she'll go off to do amazing things in her independent career.

Thanks to my classmates, Douglas Fox and Peter Robinson, for their patience during qualifying exam season. The members of Vanity Journal Club are acknowledged for their attendance and participation. Chelsea Gordon was incredibly helpful with my initial move to Berkeley as well as my post-graduation plans. Yisu has been a good friend, and it was always fun to kick it. I thank Mason Appel for being an excellent friend and making those late nights in lab that much more entertaining. Your flatulence will not be missed. Finally, I thank everyone else in the group for making the lab such a pleasant place to work.

Outside of the Bertozzi lab, I have to thank Professor Robert Bergman for the opportunity to teach physical organic chemistry. Professor Luke Lee has also been a great source of advice over the past year.

Most importantly, I thank my parents for their unwavering support. It means so much to have that anchor in life.

Chapter 1: Design Strategies for Bioorthogonal Smart Probes

Note: Portions of this chapter were published in *Org. Biomol. Chem.* **2014**, *12*, 9307-9320.

Introduction

Bioorthogonal reactions proceed readily and selectively in biological systems. By tagging a biomolecule of interest with one of the two reaction partners (the chemical reporter group), the biomolecule can be selectively labelled by bioorthogonal reaction with a secondary reagent bearing a fluorescent probe or affinity handle (Figure 1-1A). The small size of chemical reporter groups allows for their efficient incorporation into biomolecules by hijacking native biosynthetic pathways. This has facilitated the visualization and study of biomolecules not directly encoded by the genome. The topic of bioorthogonal reactions has been extensively reviewed, with recent reviews providing detailed discussions on the suitability of individual reactions for different applications.¹⁻⁵

The ability of bioorthogonal chemistry to selectively label biomolecules has often been paired with fluorescence microscopy, where the spatiotemporal dynamics of these labeled biomolecules can be monitored. In bioorthogonal labeling reactions, an excess of fluorescent secondary reagent is typically required to maximize labeling efficiency of the reporter-tagged biomolecule. This excess reagent will have to be carefully removed through a series of washing steps to guarantee that only covalently attached probe remains. Otherwise, fluorescence from unreacted probe may obscure any signal from the labeled biomolecule of interest. As overall reaction rate is directly proportional to both rate constant and reagent concentration, a higher rate constant means less secondary reagent is needed. This minimizes the amount of unreacted probe present at the end of the reaction, reducing overall background signal. A major motivation in the field of bioorthogonal chemistry has therefore been to improve reaction kinetics.

A complementary approach to minimize background fluorescence from unreacted probe is through the development of bioorthogonal smart probes, which are activated by bioorthogonal reaction. Fluorescent probes (also known as fluorogenic or turn-on probes), for example, undergo an enhancement in fluorescence upon bioorthogonal reaction (Figure 1-1B). By using these probes, fluorescence is only observed where the bioorthogonal reaction occurs. For imaging applications, bioorthogonal smart probes can prove crucial in situations where it is difficult to remove excess probe, such as for labeling reactions performed intracellularly or *in vivo*. In addition, there are instances where washing steps are undesirable, such as the real-time visualization of dynamic biological processes.

Bioorthogonal smart probes also include compounds that release drugs or imaging agents only upon bioorthogonal reaction (Figure 1-1C). These caged compounds enable targeted delivery if a certain cell type preferentially incorporates a reporter group-tagged molecule. Selectivity is achieved if the caging process dramatically alters the activity or properties of the drug or imaging agent.

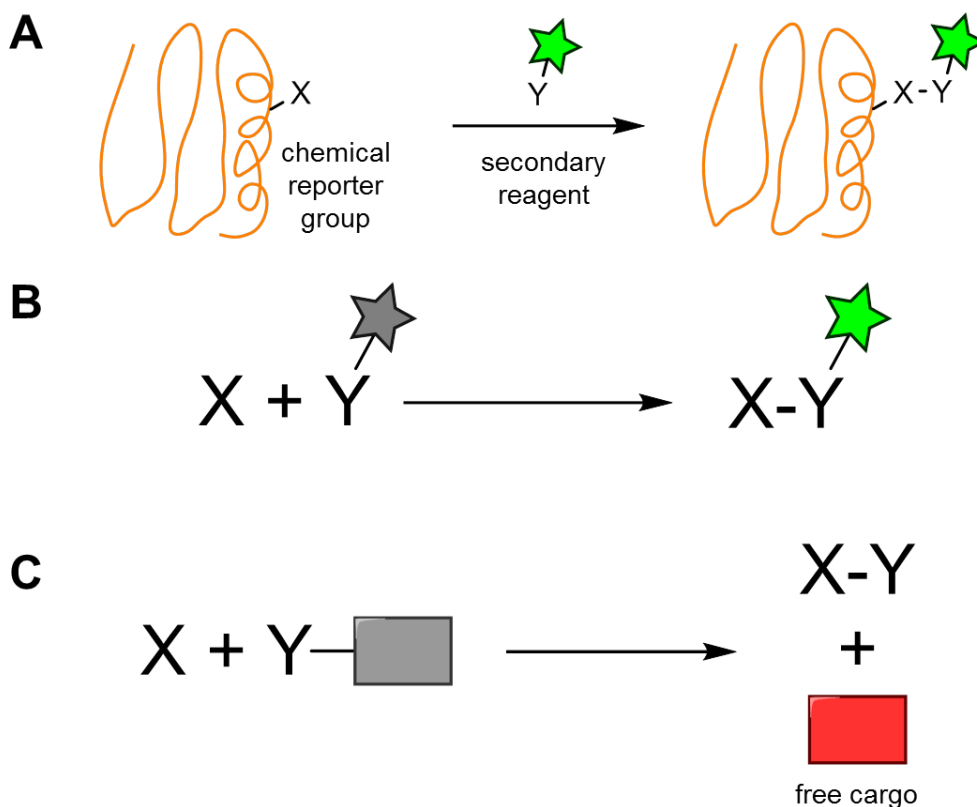


Figure 1-1. (A) Bioorthogonal reactions enable the selective modification of biomolecules. (B) Fluorescent smart probes undergo an enhancement in fluorescence upon bioorthogonal reaction. (C) Caged compounds deliver their cargo only after bioorthogonal reaction.

Here, I discuss design strategies used for the development of bioorthogonal smart probes, with particular emphasis on fluorescent probes. Considerations when evaluating these smart probes include the level of signal enhancement that occurs upon bioorthogonal reaction; probes with higher turn-on enable more sensitive detection. Additionally, for fluorescent probes, longer wavelength excitation and emission are beneficial as complications from phototoxicity, background autofluorescence, or poor tissue penetrance are minimized. This chapter is organized by bioorthogonal reaction type, with each section beginning with a brief introduction of the reaction. The final section highlights selected applications of bioorthogonal smart probes, such as their use in monitoring bioorthogonal reaction progress and sequence-specific oligonucleotide detection.

Aldehyde/Ketone-Nucleophile Condensations

The condensation of aldehydes with α -effect amine nucleophiles, such as alkoxyamines or hydrazines to form oxime or hydrazone linkages, respectively, was one of the first commonly used chemoselective ligation reactions in biological systems (Figure 1-2). An obvious limitation to the bioorthogonality of this reaction is the presence of aldehydes and ketones in intracellular

metabolites. Yet, aldehydes and ketones are absent on the exterior of the cell, making this approach effectively bioorthogonal for reactions performed on the cell surface.

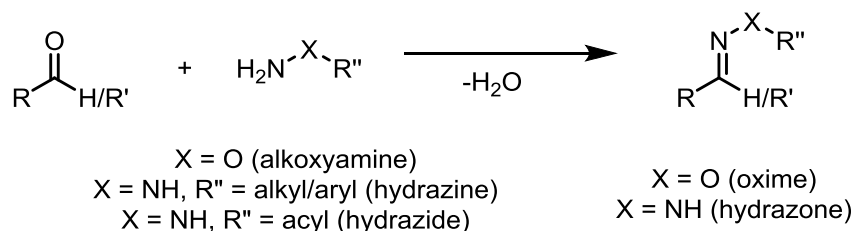


Figure 1-2. The condensation of carbonyls with alkoxyamines or hydrazines/hydrazides to form oximes or hydrazones, respectively.

Aldehydes and ketones have been introduced onto cell surfaces via the biosynthetic incorporation of unnatural substrates, the periodate oxidation of cell surface glycans, and the enzymatic oxidation of alcohols or thiols in endogenous biomolecules.⁶⁻¹² The condensation of α -effect amine nucleophiles occurs rapidly under acidic conditions, but the presence of additives can enable efficient labeling at neutral pH.^{10,13} Alkoxyamines and hydrazines condense with aldehydes with second-order rate constants of 1 to 10 M⁻¹s⁻¹ in pH 4.5 to 6.5 aqueous buffer, whereas hydrazides react orders of magnitude more slowly. The resulting adducts are prone to hydrolysis in aqueous environments, since the forward reaction involves a release of an equivalent of water. Oxime linkages, however, are significantly more stable than hydrazones,¹⁴ and the stability of these adducts can be further increased through the use of modified alkoxyamine or hydrazine reagents.^{15,16}

Aryl hydrazines undergo significant changes in their electronic properties upon condensation with carbonyl functionalities. The color change observed when staining ketones and aldehydes during thin layer chromatography with 2,4-dinitrophenylhydrazine is one manifestation of this phenomenon. Thus, hydrazine-functionalized fluorophores may be expected to show fluorescence modulation upon reaction with ketones or aldehydes. As well, the lone pair of the distal hydrazine nitrogen may quench fluorescence through internal charge transfer (ICT) processes.¹⁷ Hydrazine-functionalized nitrobenzoxadiazoles, BODIPYs, and coumarins have been developed whose fluorescence is activated by reaction with ketones or aldehydes (**1.1-1.3**, Figure 1-3).¹⁸⁻²⁴ It should be noted that fluorescence enhancements of these compounds are highest in less polar solvents, and it has been reported that the hydrazone adducts of compound **1.1** are virtually non-fluorescent in neutral aqueous solutions. Additionally, aryl hydrazines and their adducts are prone to oxidation, which can complicate handling and storage.

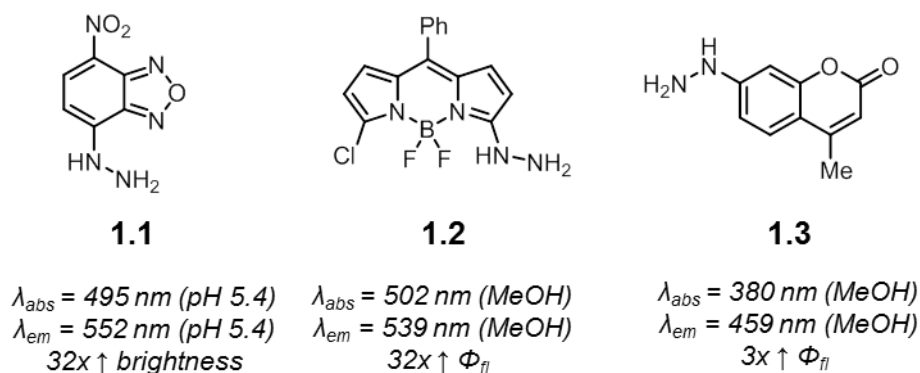


Figure 1-3. Smart hydrazine probes. Hydrazine-functionalized nitrobenzoxadiazole (**1.1**), BODIPY (**1.2**), and coumarin (**1.3**). Spectroscopic properties correspond to the hydrazone products derived from these probes (benzaldehyde adduct for **1.1**, propionaldehyde adduct for **1.2**, and salicylaldehyde adduct for **1.3**).

Approaches that utilize alkoxyamines offer the benefits of ease of handling and the formation of a significantly more stable adduct in biological systems. Unfortunately, the fluorescence properties of alkoxyamine-functionalized fluorophores, in contrast to hydrazines, do not appear to be significantly perturbed by reaction with ketones or aldehydes.²⁵ In another approach, Raymond and coworkers prepared weakly fluorescent alkoxyamine-substituted coumarin **1.4** (Figure 1-4).²⁶ After oxime formation (**1.5**), elimination yields nitrile and the highly fluorescent coumarin phenolate product **1.6**. This elimination can be promoted through the use of higher pH or bovine serum albumin additive. The authors used these probes to detect biologically relevant aldehydes *in vitro*. While this strategy does not generate stable adducts, a reinvestigation of this approach in the context of bioorthogonal chemistry may be worth pursuing.

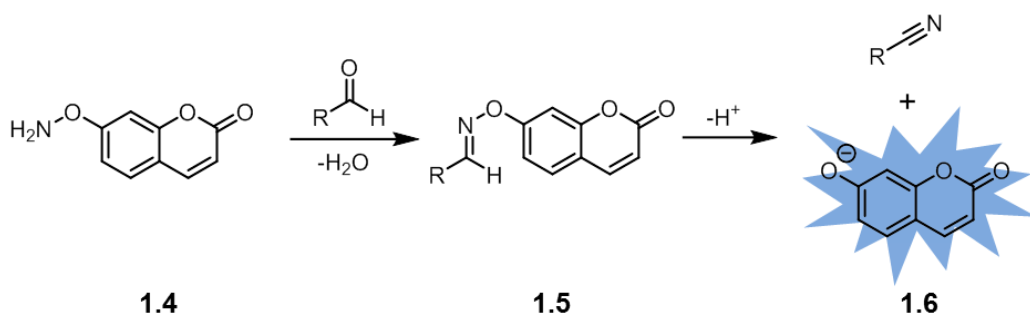


Figure 1-4. Aldehyde detection via oxime bond fragmentation. After formation of oxime **1.5**, fragmentation produces a nitrile and the free phenolate **1.6**.

Progress has been made in the development of smart probes suitable for the detection of aldehyde-functionalized biomolecules, yet the design of new probes, especially those based off

alkoxyamines, is an important future direction. Likewise, the identification of alternative reagents that rapidly form stable adducts with ketones or aldehydes under aqueous conditions will provide new avenues for the visualization of these functional groups in biological systems.^{27,28}

The Staudinger Ligation

The Staudinger ligation is a modification of the original Staudinger reduction of an azide by phosphines. Diverging from the Staudinger reduction, the intermediate aza-ylide is intercepted by a nearby ester, resulting in the formation of a phosphorane, which collapses to form a phosphine oxide and a stable amide linkage (Figure 1-5).²⁹ As the two reaction partners are completely abiotic, selective ligation can occur in all biological compartments, in contrast to aldehyde or ketone condensation reactions. The second-order rate constant of the reaction is $\sim 10^{-3} \text{ M}^{-1}\text{s}^{-1}$ in acetonitrile. Over the course of the reaction, the phosphine is oxidized to a phosphine oxide while the ester is cleaved to release methanol.³⁰ These two processes have been exploited for the development of smart phosphine probes activated by the Staudinger ligation.

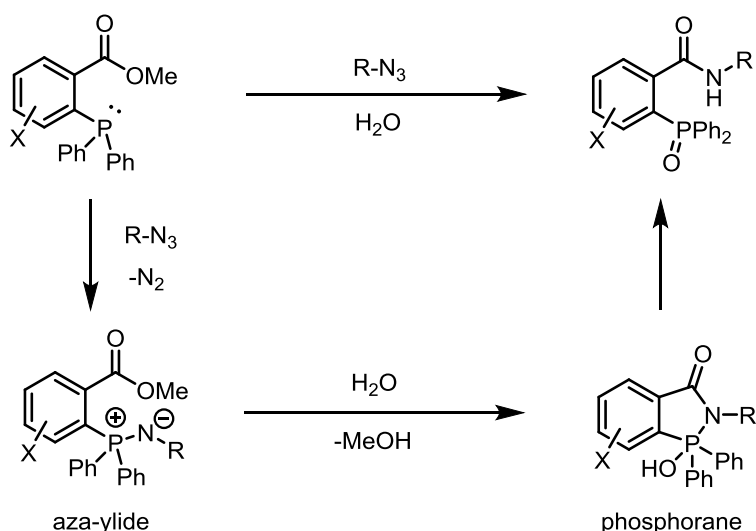


Figure 1-5. The archetypical Staudinger ligation. The phosphine reacts with an azide to generate a stable amide linkage and phosphine oxide with concomitant release of methanol.

In the phosphine oxidation approach, Bäuerle and coworkers have demonstrated that the fluorescence of coumarins is sensitive to the nature of the substituent at the 3-position.³¹ Thus, a coumarin functionalized with a phosphine at the 3-position was prepared by Bertozzi and coworkers (**7**, Figure 1-6).³² The phosphorus lone pair may quench fluorescence due to ICT processes, and oxidation of the phosphine during the Staudinger ligation to form **1.8** will activate fluorescence. Compound **7** showed comparable kinetics to traditional Staudinger probes ($k = 1.5 \times 10^{-3} \text{ M}^{-1}\text{s}^{-1}$ in 1:1 acetonitrile/water). It underwent a 60-fold enhancement in fluorescence quantum yield upon Staudinger ligation, to a final quantum yield of 0.65, suggesting that quenching was fully relieved by phosphine oxidation. Unfortunately, phosphine oxidation can

occur in the absence of azide due to ambient oxygen, and the attachment of phosphines onto fluorophores can accelerate this reaction, likely due to the generation of high-energy intermediates. This liability of non-specific phosphine oxidation may also limit other strategies beyond ICT for developing smart phosphine probes activated by the Staudinger ligation.

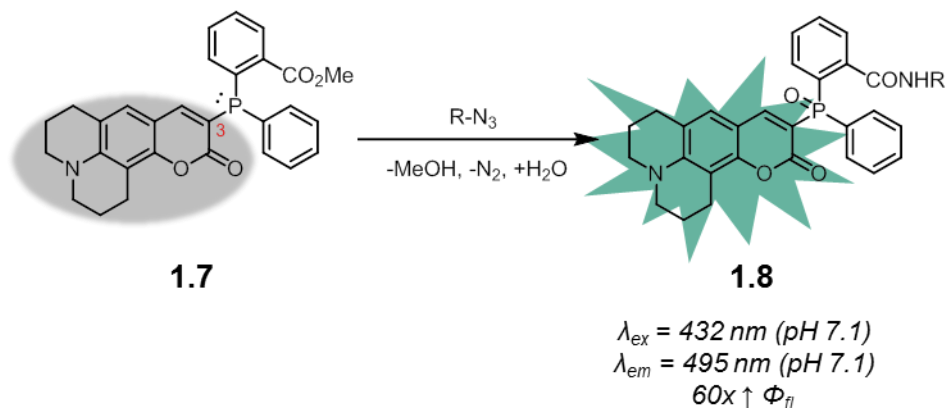


Figure 1-6. A smart phosphine probe activated by phosphine oxidation during the Staudinger ligation. Spectroscopic properties correspond to the product derived from reaction of **1.7** with an aliphatic azide.

To avoid this issue, a different strategy that relied on ester cleavage over the course of the reaction was pursued. In Förster resonance energy transfer (FRET)-based smart phosphine probes, a FRET quencher is attached to the alkoxide substituent of the ester while a fluorophore is conjugated directly to the triarylphosphine (**1.9**, Figure 1-7A).³³ After Staudinger ligation, the FRET quencher is released, revealing the fluorescence of the original fluorophore. This strategy was implemented by Bertozzi and coworkers using a fluorescein-derivative conjugated to the phosphine and Disperse Red 1 as the quencher. This compound had similar reaction kinetics to other Staudinger ligation probes [$\sim 4 \times 10^{-3} \text{ M}^{-1}\text{s}^{-1}$ in 1:1 acetonitrile/phosphate buffered saline (PBS)], consistent with studies demonstrating that aza-ylide formation is rate determining.³⁰

Unlike coumarin-phosphine **7**, the phosphine-oxide product derived from non-specific oxidation of **1.9** remained quenched. In contrast, compound **1.9** underwent a 170-fold enhancement in fluorescence quantum yield upon Staudinger ligation to form **1.10**, reaching a final quantum yield of 0.64 in pH 7.0 PBS. This FRET-based smart phosphine probe was suitable for the detection of azide-functionalized glycoproteins on living cells. Importantly, direct visualization of these glycoproteins on live cells using traditional fluorophore phosphine conjugates resulted in high non-specific background staining unless highly charged fluorophores were used, demonstrating the advantages of smart probes.³⁴ The limited cell permeability of **1.9** has precluded its use for the visualization of intracellular targets. In principle, this strategy is generalizable to longer wavelength fluorophores by changing both the fluorophore and the quencher. Finally, as FRET efficiency varies as a function of $1/r^6$, (r = distance from donor to acceptor), versions of this probe with more tightly-linked fluorophore and quencher should show even higher enhancement upon ligation.

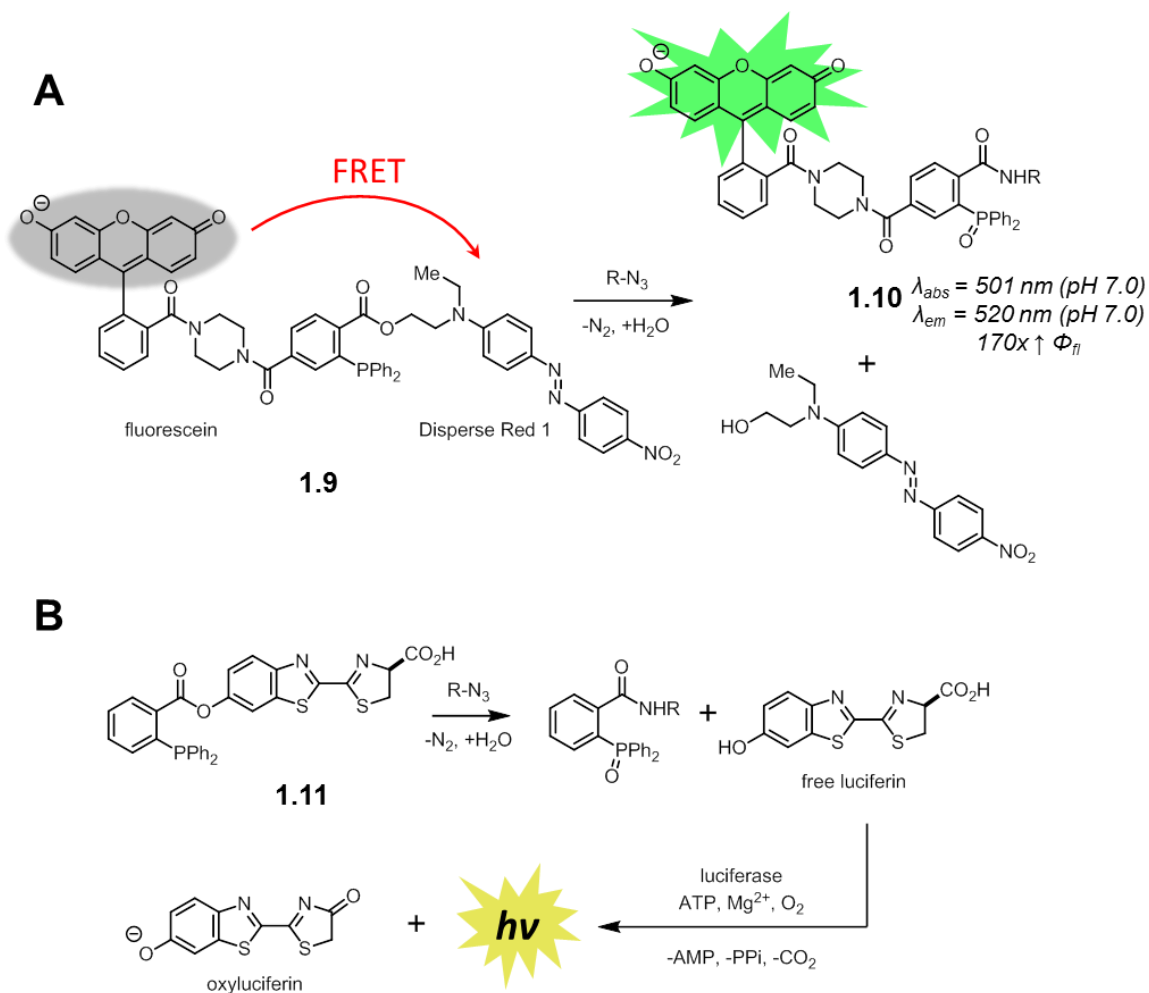


Figure 1-7. Phosphine probes activated by ester cleavage in the Staudinger ligation. (A) A FRET-based smart phosphine probe (**1.9**) where a quencher is released upon Staudinger ligation. Spectroscopic properties correspond to the product derived from reaction of **1.9** with benzyl azide. (B) A caged luciferin-phosphine conjugate (**1.11**) that releases free luciferin upon Staudinger ligation.

This strategy was also used by Bertozzi and coworkers to develop a smart probe for bioluminescence imaging through the use of a caged luciferin (**1.11**, Figure 1-7B).³⁵ Acylation of luciferin blocks processing by luciferase to generate light.³⁶ Only upon release of free luciferin after Staudinger ligation is a suitable substrate for luciferase available and bioluminescence observed. The selectivity of this probe was demonstrated by bioluminescence signal in cultured cells only in the presence of azide-functionalized glycoproteins. The inherent sensitivity of bioluminescence imaging allowed for azide detection using nanomolar concentrations of probe, orders of magnitude lower than required for fluorescence-based methods. In principle, this caging strategy can be used with any fluorophore in which acylation or alkylation results in a significant reduction in fluorescence. A limitation, however, of this strategy is that it would not yield a covalently-attached fluorescent adduct, reducing spatial resolution.

Finally, phosphines containing other electrophilic traps have also been developed, most notably in the context of the “traceless” Staudinger ligation for native amide bond formation in peptide synthesis.^{37,38} For bioorthogonal labeling applications, this may be advantageous when the bulky triarylphosphine oxide adduct is not desirable. These phosphines have been used as a platform for bioorthogonal smart probes in the context of drug delivery, where active drug is released upon reaction.³⁹ While the Staudinger ligation has been supplanted by newer bioorthogonal reactions with more rapid kinetics, its exquisite selectivity, especially in the context of *in vivo* applications, provide motivation for further advances in smart probe design.⁴⁰

Azide-Alkyne Click Cycloadditions

The azide-alkyne “click” cycloaddition is one of the most widely used bioorthogonal reactions. The reaction occurs in the presence of Cu(I) catalyst or in the absence of copper through the use of strained cyclooctynes to form stable triazole linkages (Figure 1-8).⁴¹⁻⁴³ The second-order rate constant of the copper-free cycloaddition with the parent cyclooctyne is $\sim 10^{-3} \text{ M}^{-1}\text{s}^{-1}$ in acetonitrile. Modifying the electronics of the cyclooctyne or increasing ring strain via aryl/cyclopropane ring fusions and heteroatom incorporation have increased the rate constants to over $1 \text{ M}^{-1}\text{s}^{-1}$ in acetonitrile.⁴³⁻⁴⁹ The most efficient ligands for copper-catalyzed click reactions produce reaction rates greater than $10^4 \text{ M}^{-1}\text{s}^{-1}$ with respect to concentration of copper catalyst.⁵⁰⁻⁵³ Earlier contributions to this area of fluorogenic click probes, through 2010, have been reviewed by Wang and coworkers.⁵⁴ Unlike the Staudinger ligation, where ester cleavage provided a general approach for the design of activatable probes, such strategies are not readily apparent in azide-alkyne click cycloadditions. Triazoles are components of many fluorophores, but these examples are highly dependent on the substitution pattern of both the alkyne and azide reaction partner. As a result, regenerating triazole-containing fluorophores by click reaction will not be a broadly applicable strategy for the visualization and detection of tagged biomolecules.⁵⁵⁻⁵⁹

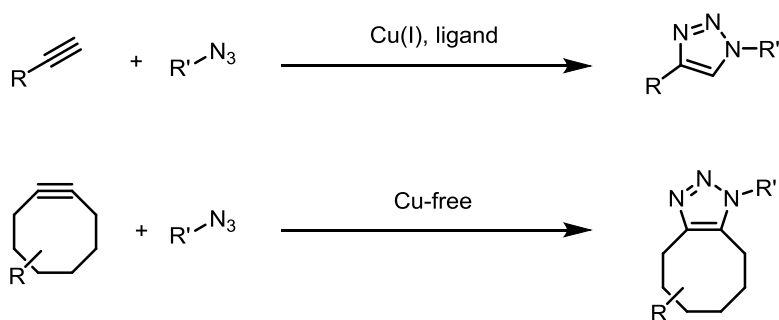


Figure 1-8. Copper-catalyzed and copper-free click reactions between alkynes and azides to form triazoles.

Significant progress has been made in the development of smart azide probes activated by cycloaddition with alkynes. These probes commonly take advantage of the fact that the lone pair of the proximal azide nitrogen is delocalized into the triazole after click reaction, and thus cannot participate in fluorescence quenching. A significant advantage of preparing azide probes is their

ease of synthesis, as the azide can be readily prepared from amines and is tolerant of a variety of synthetic operations, making the preparation of large fluorophore libraries fairly straightforward.

The first smart azide probes were the azidocoumarins reported by Wang and coworkers.⁶⁰ Similar to the previously described smart coumarin-phosphine probe **1.7**, introduction of an azide into the 3-position of coumarins also significantly quenches fluorescence via ICT. Upon reaction with alkynes, the lone pair of the azide is delocalized into the triazole and fluorescence is enhanced. Wang and coworkers prepared a panel of azidocoumarins via an efficient and modular route. Of these compounds, 3-azido-7-hydroxycoumarin (**1.12**, Figure 1-9) showed the most impressive fluorescence enhancement upon click reaction, around several hundred-fold in pH 7.4 PBS, to yield a highly fluorescent triazole product. The robust enhancement in fluorescence of this probe and its decent water solubility and cell permeability have made this probe a popular choice for the detection of alkynes on intracellular and extracellular targets in biological systems.^{61,62} By replacing the hydroxyl group with other electron donating groups such as amines, excitation and emission maxima of these azidocoumarins is shifted to longer wavelengths, but fluorescence enhancement is also diminished.

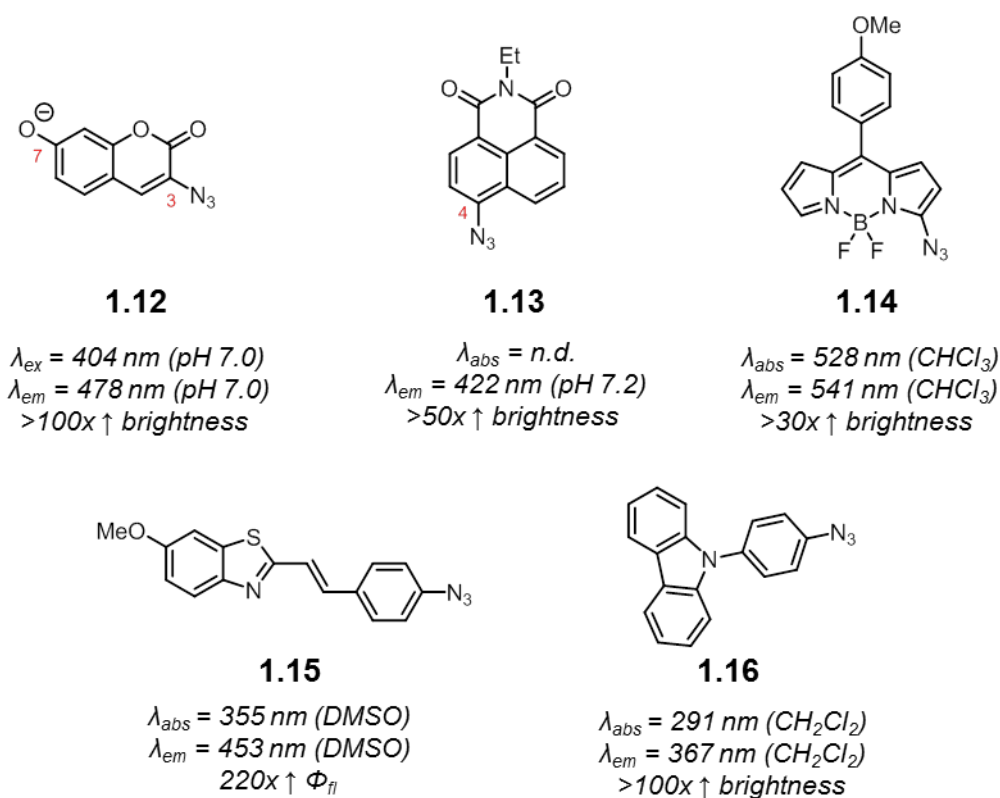


Figure 1-9. Various smart azide probes quenched by ICT: 3-azido-7-hydroxycoumarin (**1.12**) and azide-functionalized 1,8-naphthalimide (**1.13**), BODIPY (**1.14**), benzothiazole (**1.15**), and carbazole (**1.16**). Spectroscopic properties correspond to representative triazole products derived from these azide probes.

The 1,8-naphthalimide system has also been used for developing smart azide probes.⁶³ Again, the presence of an azide in 4-position of naphthalimide (**1.13**) quenches fluorescence via ICT. After triazole formation, quenching is relieved and fluorescence is enhanced. Quenching via ICT may also be operant in other scaffolds, such as in azide-functionalized BODIPY, benzothiazole, and carbazoles (**1.14-1.16**), although other factors may be at play.⁶⁴⁻⁶⁷

The lone pair of azides can also quench fluorescence via photoinduced electron transfer (PeT), which differs from ICT in that the azide is electronically decoupled from the fluorophore in the ground state.⁶⁸ Wang and coworkers showed that azide-functionalized anthracene compounds undergo an up to 75-fold increase in fluorescence upon triazole formation (**1.17**, Figure 1-10).⁶⁹ The absorption of these compounds remained constant during the click reaction, consistent with a PeT mechanism.

As described in this dissertation, I took advantage of PeT from the pendant aryl ring of xanthene fluorophores to develop smart azide probes.⁷⁰ Xanthene fluorophores exhibit visible light excitation and emission, minimizing complications from background autofluorescence in biological samples. Nagano and coworkers have elegantly demonstrated that PeT efficiency in fluoresceins can be predicted using computational chemistry.⁷¹ The change in electron density of the pendant aryl azide to an aryl triazole would result in significant fluorescence enhancement if the proper substituents on the pendant aryl ring were present. After screening for these proper substituents using computational methods, they identified an azidonaphthyl-substituted fluorescein, **1.18**, which underwent a 34-fold enhancement in fluorescence quantum yield upon triazole formation in pH 7.4 PBS and was suitable for the visualization of terminal alkyl-functionalized glycoproteins in fixed mammalian cells.

Given the generality of PeT, I next developed smart azide probes with near-infrared emission were next developed. At these wavelengths, background fluorescence from endogenous biomolecules is minimal and tissue penetrance highest. These probes were designed around the Si-rhodamine scaffold developed by Nagano and coworkers, and were identified using the same strategy as for the fluorogenic azidofluoresceins.^{72,73} One azido-Si-rhodamine, **1.19**, underwent a 48-fold enhancement in fluorescence quantum yield upon triazole formation in pH 7.4 PBS. Water-soluble versions of **1.19** were well-suited for the visualization of linear alkyl-functionalized glycoproteins on the surface of live mammalian cells and cyclooctyne-functionalized peptidoglycan in the Gram-positive bacteria. The fluorescence quantum yields of the triazole products, derived from **1.18** and **1.19**, 0.8 and 0.2, respectively, suggest that PeT quenching is fully relieved following click reaction. Finally, this PeT strategy should be generalizable to other fluorophore scaffolds beyond xanthenes.⁷⁴

An interesting property of these two probes is that the reduction of aryl azides, a potential degradation pathway in biological systems by endogenous thiols, results in a further reduction in fluorescence.⁷⁵ This may be advantageous for the labeling of intracellular targets, as fluorescence from unreacted probe is minimized over time. In contrast, this degradation pathway can be problematic if azide reduction results in a dramatic enhancement in fluorescence.⁶³

A limitation of azide-functionalized probes is that they require either the incorporation of relatively bulky cyclooctynes or the use of a copper catalyst. Recent progress in increasing the biocompatibility of copper-click reactions have utilized copper-chelating groups on azide probes, which minimizes the amount of copper necessary for the reaction and enables labeling of

intracellular linear alkynes.^{76,77} Further advances in this area may further expand the scope of biomolecules that can be visualized by azide-functionalized smart probes.

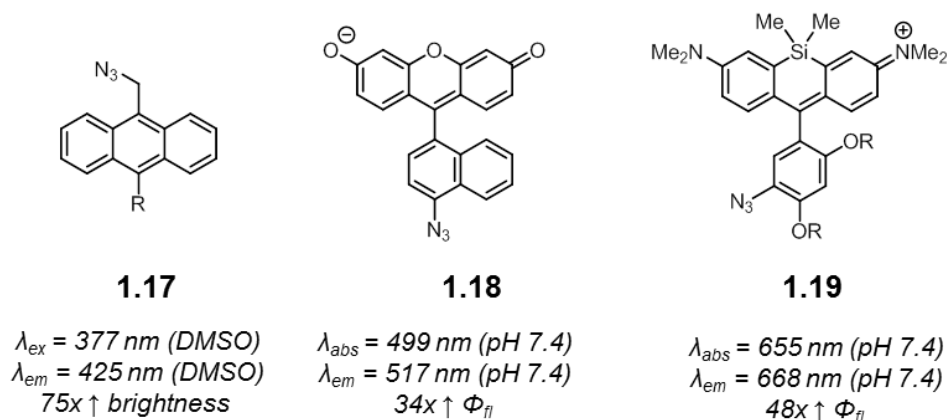


Figure 1-10. Smart azide probes utilizing PeT: azide-functionalized anthracene (**1.17**), fluorescein (**1.18**), and Si-rhodamine (**1.19**, R = oligoethylene glycol groups). Spectroscopic properties correspond to representative triazole products derived from these azide probes.

Unlike azides, alkynes do not have a lone pair to inherently quench fluorescence via charge transfer pathways. Smart alkyne probes are therefore more challenging to design and the mechanisms by which these probes operate may be difficult to rationalize. In seminal work by Fahrni and coworkers, they discovered that coumarins containing an alkyne at the 7-position undergo an enhancement in fluorescence upon triazole formation (**1.20**, Figure 1-11).^{78,79} The more electron-donating character of the triazole relative to the alkyne lowers the energy of the (π, π^*) state well below the (n, π^*) state. This prevents fluorescence quenching via (π, π^*)¹-(n, π^*)³ intersystem crossing, and results in a 18-fold enhancement in fluorescence quantum yield upon click reaction.

Other smart alkyne probes have also been identified by rapid access to libraries of probes via Sonogashira coupling. For example, a panel of six alkynyl xanthene compounds were prepared and reacted with a set of 17 azide probes – this combinatorial approach led to the identification of a combination of alkyne probe, azide, and solvent which resulted in a 9-fold enhancement in brightness upon triazole formation (**1.21**).⁸⁰ In addition, smart alkynyl naphthalimides, benzothiazoles, and benzoxadiazoles are known (**1.22-1.24**).^{63,81-83} Of these probes, alkynyl coumarins, naphthalimides, and benzothiazoles have been shown to be suitable for the detection of azide-functionalized biomolecules in biological systems.^{63,82,84}

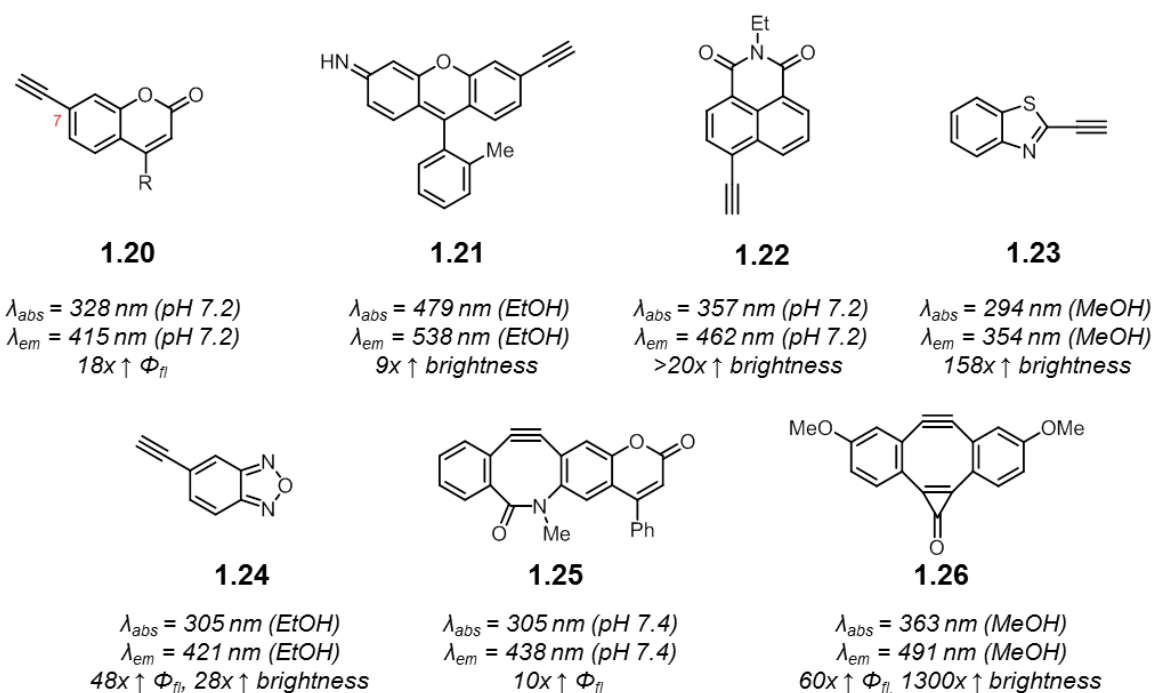


Figure 1-11. Smart alkyne and cyclooctyne probes activated by reactions with azides: linear alkynes include 7-alkynyl coumarin (**1.20**, R = methyl or alkoxyethyl) and alkyne-functionalized xanthene (**1.21**), 1,8-naphthalimide (**1.22**), benzothiazole (**1.23**), and benzoxadiazole (**1.24**), while cyclooctynes include coumBARAC (**1.25**) and FI-DIBO (**1.26**). Spectroscopic properties correspond to representative triazole products derived from these alkyne probes.

Smart cyclooctynes combine the advantages of the azide as a reporter group, such as small size and good stability, with the ability to react in the absence of potentially cytotoxic copper catalyst. The difficulty in synthesizing cyclooctynes, however, has hampered the preparation of fluorescent cyclooctynes for evaluation. Still, several pioneering examples exist of such smart cyclooctyne probes.

The alkynyl coumarin identified by Fahrni and coworkers has been adapted for copper-free click chemistry by incorporating the alkyne as part of a cyclooctyne (**1.25**, coumBARAC). Upon reaction with azides, the compound showed a 10-fold enhancement in fluorescence quantum yield.⁸⁵ More recently, Boons and coworkers reported a cyclooctyne (**1.26**, FI-DIBO) which undergoes an impressive 1300-fold enhancement in brightness upon reaction with azides.⁸⁶ Computational studies suggested that fluorescent activation of this probe was due to an enhancement in oscillator strength of the $S_0 - S_1$ transition upon triazole formation. Cyclooctynes may suffer from background labeling of proteins due to reactions with thiols.⁸⁷ For a typical cyclooctyne fluorophore conjugate, this will result in fluorescence background. On the other hand, FI-DIBO did not exhibit fluorescence turn-on due to this side reaction. Importantly, both coumBARAC and FI-DIBO showed reactivity with azides comparable to their parent cyclooctynes.

Nitrile Imine-Alkene Cycloadditions

Nitrile imines react readily with alkenes under physiological conditions to form pyrazolines (Figure 1-12A). These nitrile imines can be generated by photolysis of tetrazoles (“photo-click” chemistry), with the expulsion of nitrogen gas.^{88,89} The initial photolysis occurs with good efficiency, but a drawback is the requirement of UV activation (originally 302 nm for **1.27**), which leads to phototoxicity after prolonged exposure. Modifications of the structure of these tetrazoles allow for longer wavelength activation, such as at 365 or 405 nm (**1.28**, Figure 1-12B).⁹⁰ Tetrazole **1.29**, which can be activated using two-photon excitation with a 700 nm laser, further minimizes this limitation.⁹¹ Alternatively, the intermediate nitrile imines can also be generated spontaneously by decomposition of hydrazoneyl chlorides such as **1.30** at neutral pH.⁹²⁻⁹⁴ This is advantageous in situations where photolysis of the tetrazole may result in damage to biological samples, although the benefits of photoactivation, such as spatial and temporal control, are lost.

Increasing the electron density of the nitrile imine, decreasing the electron density of the alkene, or increasing the strain of the alkene all result in an enhancement in the rate of cycloaddition. Recent reports have shown that by increasing the strain of the alkene, through the use of cyclopropenes or spirohexenes, the rate of the cycloaddition can increase dramatically, greater than $10^4 \text{ M}^{-1}\text{s}^{-1}$ for spirohexenes in 1:1 acetonitrile/chloride-free phosphate buffer (Figure 1-12C).^{95,96}

A notable feature of this reaction is that, unlike the starting tetrazole or hydrazoneyl chlorides, the product pyrazolines are highly fluorescent, which makes these probes inherently fluorogenic. The resulting fluorophores typically have excitation maxima in the ultraviolet and emit cyan to green fluorescence. While the intermediate nitrile imine is unstable and can form byproducts from hydrolysis or dimerization, these compounds are not fluorescent, providing an excellent strategy to visualize alkene-tagged molecules, including intracellular targets, in living systems. Some fluorescence background, however, may result from weakly fluorescent nitrile imine intermediates.⁹⁷

To shift the emission wavelengths of the resulting pyrazoline fluorophores to the red or near infrared, Lin and coworkers conjugated the tetrazole to heteroaromatic systems such as thiophenes. These oligothiophene-conjugated tetrazoles, such as **1.31**, form pyrazoline products with emission wavelengths greater than 600 nm.⁹⁸

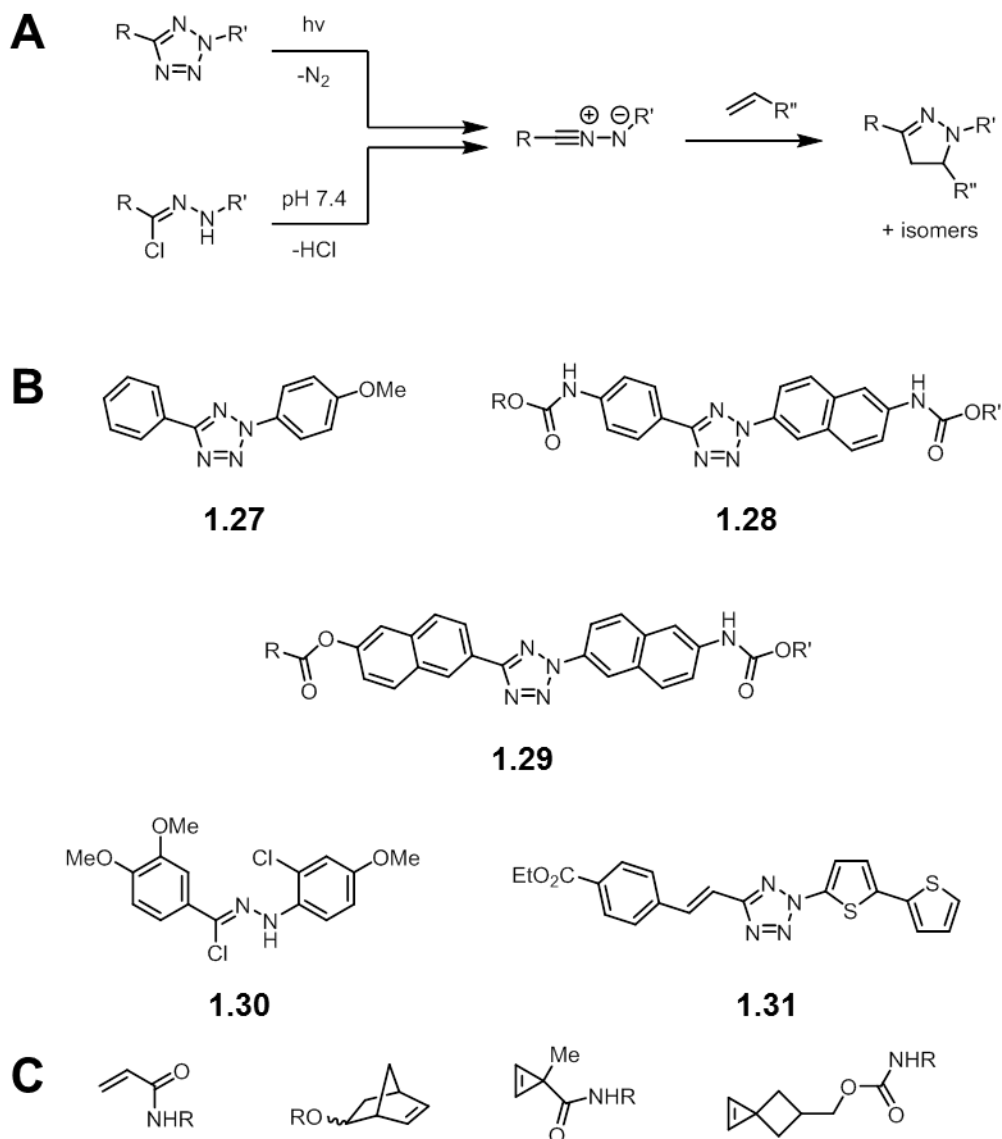


Figure 1-12. The nitrile imine-alkene cycloaddition reaction. (A) The intermediate nitrile imine can be generated by photolysis of a tetrazole or by spontaneous decomposition from hydrazonoyl chlorides. The nitrile imine can then undergo cycloaddition with alkenes to form a stable pyrazoline product. (B) Structures of selected tetrazoles and hydrazonoyl chlorides that produce fluorescent pyrazolines upon nitrile imine formation and alkene cycloaddition: an electron rich tetrazole (**1.27**), a 365 nm activatable tetrazole (**1.28**), a two-photon activatable tetrazole (**1.29**), a hydrazonoyl chloride (**1.30**), and a tetrazole that produces long-wavelength emitting pyrazolines (**1.31**). R, R' = solubilizing groups. (C) Various alkene reaction partners that undergo rapid cycloadditions with nitrile imines: acrylamides, norbornenes, cyclopropenes, and spirohexenes.

The Tetrazine Ligation

Tetrazines are electron deficient heterocycles that undergo rapid inverse electron-demand Diels-Alder reactions with strained alkenes and alkynes (Figure 1-13).^{99,100} After cycloaddition with alkenes, nitrogen is extruded via a retro Diels-Alder reaction to yield a stable dihydropyridazine adduct. These reactions can have second-order rate constants greater than $10^4 \text{ M}^{-1}\text{s}^{-1}$ in organic solvents, depending on the tetrazine and alkene/alkyne reaction partners used, permitting efficient and quantitative conversion to product with low concentrations of reagents. In general, monosubstituted tetrazines ($R = \text{aryl}$, $R' = \text{H}$) show the highest reactivity, but also suffer from stability issues in the presence of water or biologically relevant nucleophiles. Tetrazine stability is dramatically enhanced by changing the substituents, for example, to $R' = \text{Me}$ or $R, R' = 2\text{-pyridyl}$ groups.^{99,101} In terms of dienophile reaction partner, *trans*-cyclooctenes afford the highest kinetics, which can be further enhanced by cyclopropane ring fusion (Figure 1-13A).¹⁰² A potential limitation of these highly reactive *trans*-cyclooctenes is isomerization to the more stable but less reactive *cis* isomer in the presence of thiols.¹⁰² More recently, cyclopropenes have been described that combine small size and stability with good kinetics, greater than $10 \text{ M}^{-1}\text{s}^{-1}$ in 7:1 $\text{H}_2\text{O}/\text{DMSO}$ (Figure 1-13B).^{103,104} Finally, tetrazines also undergo cycloadditions with sterically unhindered cyclooctynes to form pyridazine adducts (Figure 1-13C).¹⁰⁵

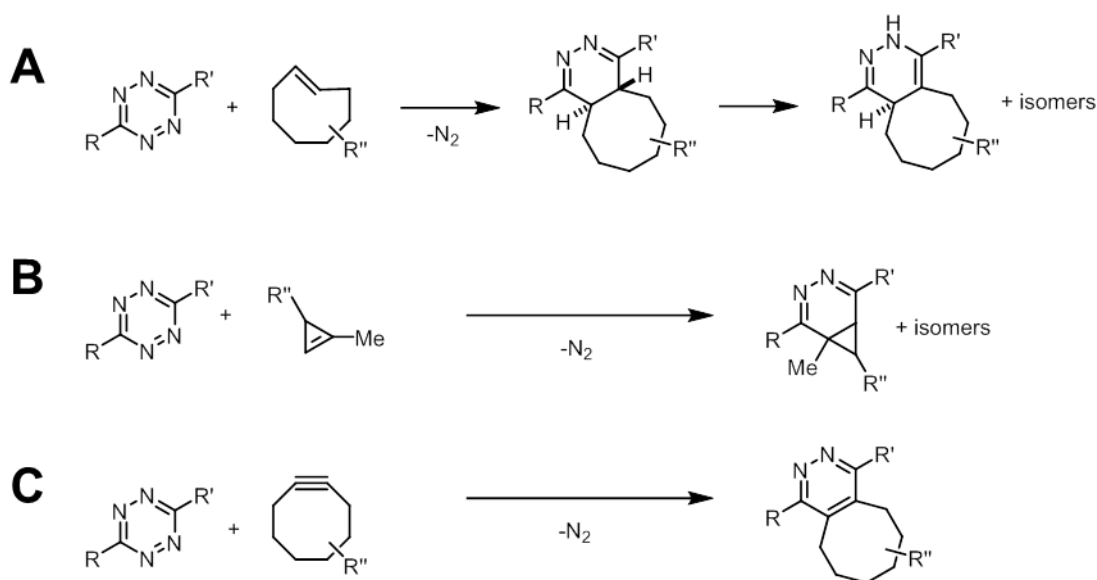


Figure 1-13. The tetrazine ligation. Tetrazines react rapidly with (A) strained *trans*-cyclooctenes (B) cyclopropenes, or (C) cyclooctynes to yield stable adducts.

Tetrazines absorb visible light, with an absorption maximum of around 520 nm. Weissleder and coworkers showed that a series of green-to-red fluorophores are efficiently quenched by tetrazines via FRET, with up to a 20-fold enhancement in fluorescence after destruction of the tetrazine upon Diels-Alder cycloaddition (**1.32** to **1.33**, Figure 1-14A).¹⁰⁶ In separate work, Chin and coworkers demonstrated that tetrazines can also quench longer wavelength fluorophores

such as tetramethylrhodamine (**1.34**), although the fluorescence enhancement was less pronounced, possibly due to increased tetrazine-fluorophore separation (Figure 1-14B).¹⁰⁷

Weissleder and coworkers next evaluated a panel of these tetrazine-fluorophore conjugates for live cell imaging.¹⁰⁸ While these conjugates demonstrated good fluorogenic properties *in vitro*, their performance in the context of visualizing *trans*-cyclooctene-functionalized small molecules bound to intracellular protein targets varied. They found that carboxyfluorescein diacetate (CFDA) tetrazine conjugate **1.35** performed best for intracellular imaging in live cells (Figure 1-

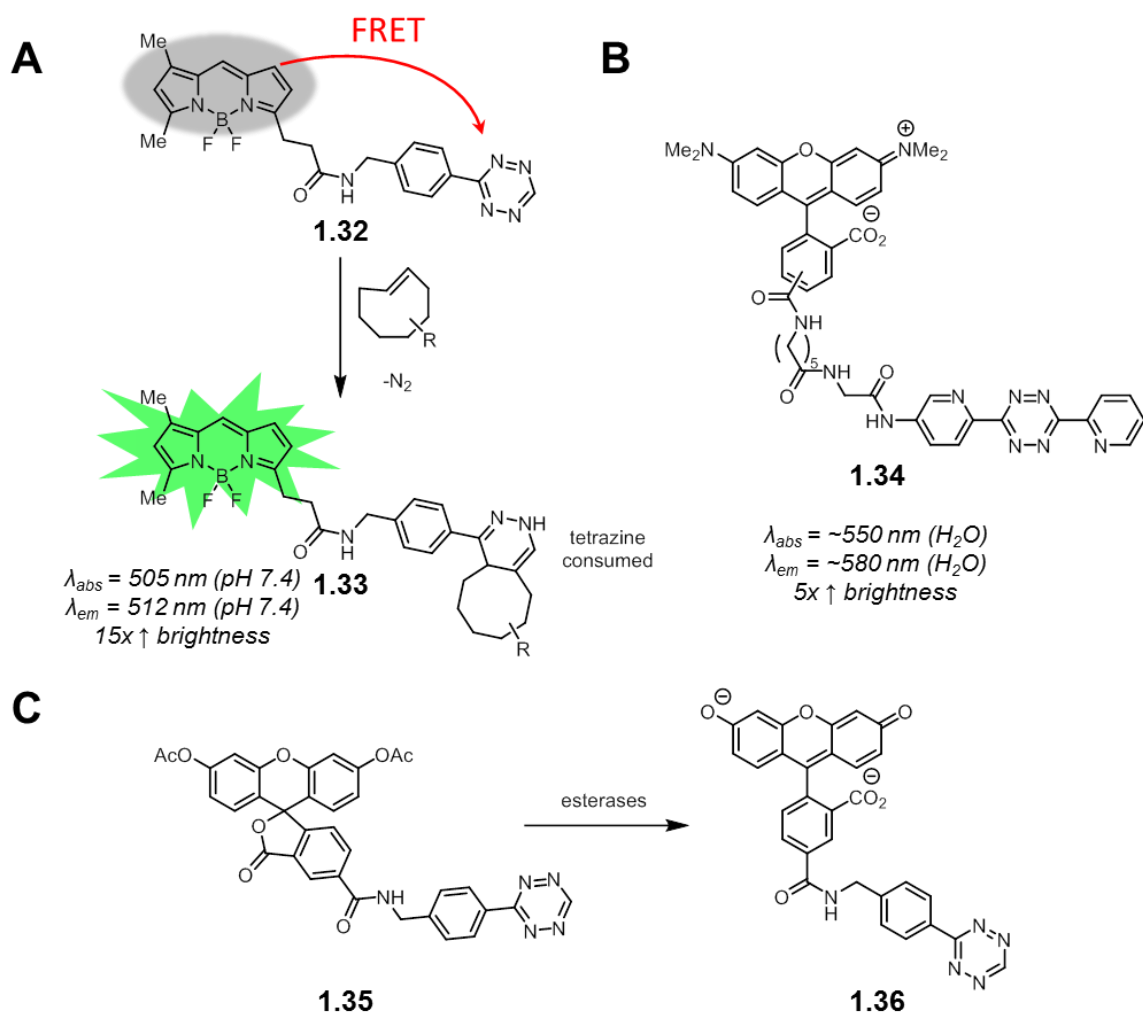


Figure 1-14. Smart tetrazine conjugates containing flexible linkers and well-suited for imaging alkenes in biological systems. (A) BODIPY-tetrazine conjugate **1.32**. As the tetrazine is consumed by cycloaddition to form **1.33**, FRET quenching is relieved and fluorescence is restored. (B) A tetramethylrhodamine-tetrazine conjugate. (C) Carboxyfluorescein diacetate-tetrazine conjugate **1.35**. The acetates are cleaved by intracellular esterases to reveal the free fluorescein **1.36**. Spectroscopic properties correspond to cycloaddition products of the corresponding tetrazine probes.

14C). This compound is virtually non-fluorescent, as acetylation causes the fluorophore to exist in a spirolactonized form. The acetates are cleaved by intracellular esterases, revealing free fluorescein **1.36** (which remains quenched by tetrazine until cycloaddition). Other groups have also had success in applying this CFDA-tetrazine probe for intracellular labeling of *trans*-cyclooctene and cyclooctyne functionalized proteins in living cells.^{109,110}

By decreasing the distance of the tetrazine to the fluorophore, FRET efficiency can increase dramatically. The close proximity of the tetrazine may allow for other quenching pathways, such as through bond energy transfer (TBET), which may not be possible if the tetrazine is connected to the fluorophore via a flexible linker.¹¹¹⁻¹¹² The first realization of this strategy was a series of BODIPY-tetrazine conjugates where the tetrazine was directly attached off the BODIPY core with a rigid phenyl linker (**1.36-1.38**, Figure 1-15A).¹¹³ Notably, compound **1.37**, the best of the three, underwent a 1600-fold enhancement in brightness upon reaction with *trans*-cyclooctene. To demonstrate that TBET was operative, BODIPY-tetrazine **1.38** was synthesized. This compound arranges the BODIPY and tetrazine groups such that their transition dipoles are nearly perpendicular. While this alignment should prevent efficient FRET, a 120-fold enhancement in fluorescence was still observed upon reaction with *trans*-cyclooctenes, suggesting that other quenching pathways were at play. Finally, minimal influence of solvent polarity on fluorescence ruled out PeT. After cycloaddition, the fluorescence quantum yields of these compounds reached up to 0.8, indicating that quenching was fully relieved upon tetrazine ligation. The suitability of this fluorophore for biological applications was demonstrated by imaging *trans*-cyclooctene-functionalized antibodies on both fixed and live cells.

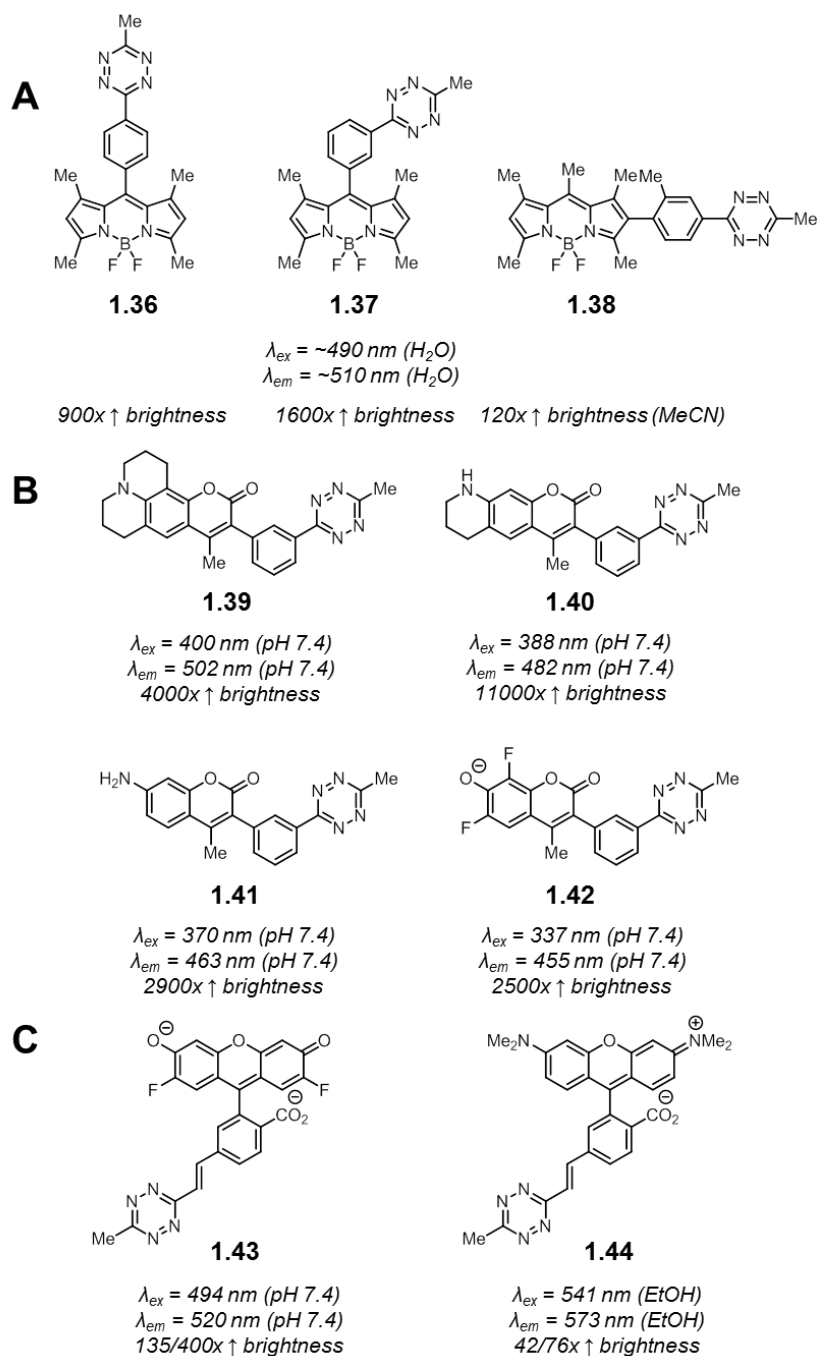


Figure 1-15. Rigidly linked smart tetrazine probes: tetrazine-functionalized (A) BODIPYs (**1.36-1.38**), (B) coumarins (**1.39-1.42**), and (C) xanthenes (**1.43-1.44**). Spectroscopic properties of compounds **1.36** to **1.42** correspond to the products derived from cycloaddition with *trans*-cyclooctene. For compounds **1.43** and **1.44**, spectroscopic properties correspond to products derived from cycloaddition with cyclopropene or with *trans*-cyclooctene (and subsequent oxidation), respectively.

To expand on this approach in the context of multicolor imaging, Weissleder and coworkers synthesized a panel of rigidly-linked coumarin-tetrazine conjugates (**1.39-1.42**, Figure 1-15B).¹¹⁴ Since TBET permits donors to excite significantly red-shifted acceptors, tetrazines may efficiently quench shorter-wavelength emitting fluorophores such as the blue-emitting coumarins. The coumarin-tetrazine conjugates were designed such that transition dipoles of the coumarin fluorophore and the tetrazine aligned significantly to maximize contributions from FRET in addition to TBET. This resulted in extremely efficient fluorescent quenching which was relieved upon tetrazine ligation, resulting in an up to an impressive 11,000-fold enhancement in fluorescence to final quantum yields of 0.3-0.5. These compounds, named HELIOS probes, were suitable for the detection of a variety of *trans*-cyclooctene-functionalized molecules in fixed and live cells virtually immediately after incubation.

In another implementation of this strategy, Devaraj and coworkers developed a surrogate for vinyl-tetrazines, which could be attached to iodine-functionalized xanthene fluorophores via Heck coupling reactions.¹¹⁵ Using this strategy, they prepared Oregon Green and tetramethyl rhodamine fluorophores conjugated to tetrazines via a rigid styrenyl linker (**1.43-1.44**, Figure 1-15C). The Oregon Green probe **1.43** underwent a 135-fold fluorescence enhancement in pH 7.4 PBS upon reaction with cyclopropenes. Notably, the red-emitting tetramethylrhodamine was also efficiently quenched; a 42-fold enhancement in fluorescence was observed for **1.44** upon reaction with cyclopropene in ethanol. Importantly, these styrenyl tetrazines remained highly reactive, with rate constants of over $100 \text{ M}^{-1}\text{s}^{-1}$ in 1:1 DMF/pH 7.4 PBS for reactions with *trans*-cyclooctene. Rigid xanthene-tetrazine conjugates can also be prepared using other synthetic strategies, although increased donor-acceptor distance decreases the efficiency of fluorescence quenching.¹¹⁶

Interestingly, the dihydropyridazine adduct from reaction of **1.43** or **1.44** with *trans*-cyclooctene was partially oxidized to the pyridazine. Devaraj and coworkers completed this oxidation by treatment with 2,3-dichloro-5,6-dicyano-1,4-benzoquinone (DDQ) before performing fluorescence measurements. This DDQ oxidized product was more fluorescent than the cycloadducts with cyclopropene – a 400-fold enhancement in fluorescence was observed for **1.43** while a 76-fold enhancement in fluorescence was observed for **1.44**. In principle, these products can also arise from reaction with cyclooctynes instead of *trans*-cyclooctenes. The superior fluorescence enhancement upon alkyne-tetrazine vs. alkene-tetrazine cycloaddition was also recapitulated in a separate study of NIR-fluorophore tetrazine conjugates.¹¹⁷ Although the product from tetrazine-cyclooctene cycloaddition resulted in no fluorescence enhancement, consistent with previous observations, the product from the tetrazine-cyclooctyne cycloaddition resulted in a 1.6-fold enhancement in fluorescence. The origin of these differences may be worthy of further investigation.

One potential limitation of these probes is that tetrazines may degrade by other pathways besides the bioorthogonal reaction, which will also relieve FRET quenching. Methyl tetrazines, in contrast to monosubstituted tetrazines, have been shown to be highly stable in serum.¹⁰⁰ In addition, Devaraj and coworkers showed that their xanthene-tetrazine conjugates were stable in both aqueous buffer and in the presence of a large excess of cysteine, demonstrating that these degradation pathways should not contribute to background fluorescence for their fluorogenic tetrazine probes.¹¹⁵

The scope of smart tetrazine fluorophores utilizing FRET or TBET is inherently limited by the absorption wavelengths of tetrazines. This may be addressed through modification of the tetrazine to change its absorption properties, which will expand the scope of fluorophores that can be efficiently quenched via these strategies.

A recent report from Robillard and coworkers described a *trans*-cyclooctene that releases amine-functionalized cargo upon reaction with tetrazine (**1.45**, Figure 1-16). After cycloaddition with tetrazine, the dihydropyridazine product **1.46** undergoes a β -elimination of carbamate, which liberates the free amine after decarboxylation.¹¹⁸ The cycloaddition rate of **1.45** was diminished 20-fold compared to the parent *trans*-cyclooctene due to the steric hindrance from the carbamate. Still, both cycloaddition and elimination steps were sufficiently rapid such that a majority of the cargo was released within minutes after the addition of sub-millimolar concentrations of tetrazine. While this strategy was used for drug delivery, attachment of a fluorescent probe and a quencher or simply a caged fluorophore will produce a smart *trans*-cyclooctene imaging probe, similar to the smart Staudinger ligation probes. One caveat, however, is that this strategy requires the use of a tetrazine as a reporter group, which has not been as widely used as strained alkenes.¹¹⁹

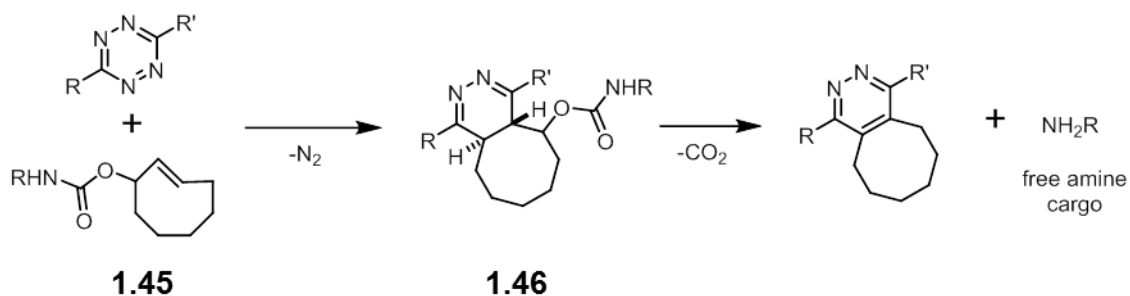


Figure 1-16. A smart *trans*-cyclooctene probe (**1.45**) for drug delivery. Cycloaddition with tetrazines to form dihydropyridazine **1.46** results in elimination of the carbamate group to release its amine-functionalized cargo.

Selected Applications of Bioorthogonal Smart Probes

As bioorthogonal smart probes are activated only when they encounter their reaction partner, the signal from these probes can be used as a proxy for reaction progress. Thus, these probes, particularly fluorophores, have been useful tools for monitoring and optimizing bioorthogonal reactions. For example, smart probes have been used to track the progress of small-molecule conjugation reactions onto biomolecules and glass surfaces.^{120,121} Additionally, smart azide and alkyne-functionalized fluorophores have been used in the evaluation of new ligands and reaction partners for the copper-catalyzed azide-alkyne click reaction.^{52,53,63,76,77} Reaction partners with higher rate constants activate smart probes more rapidly. The signal from these probes can therefore be used to identify the fastest reagent combinations, particularly in a high-throughput fashion.

The rate of activation of bioorthogonal smart probes not only depends on reaction rate constant but also on reagent concentration. The signal from these probes can consequently be used to determine the concentration of its reaction partner in solution. This enables, for example, the rapid determination of concentrations of tagged metabolites retrieved from biological systems.

More interestingly, reaction rate also depends on the *effective* concentration of the two reagents. If the two bioorthogonal reaction partners are held in close proximity, their effective concentration and thus reaction rate can increase dramatically.¹²² Ligand-receptor and protein-protein binding interactions, among others, are mediators of signaling processes in biology. Our understanding of these processes can be greatly augmented by technologies that enable the visualization or detection of these interactions in living systems. A bioorthogonal smart probe and its reaction partner conjugated onto the two different binding partners will more rapidly produce signal if binding occurs. Care must be taken, however, in choosing the attachment sites of the bioorthogonal reagents to minimally perturb binding.

Aside from detecting binding interactions, bioorthogonal smart probes can be used to sense specific isoforms and post-translational-modification states of proteins or specific sequences of oligonucleotides. In this approach, effectively a bioorthogonal “AND” switch, the smart probe and its reaction partner are conjugated onto two groups targeted to different sites of a specific biomolecule. If the two targeting groups can bind the same molecule, the bioorthogonal reagents will be held in close proximity and reaction is accelerated.

One implementation of this strategy is the sequence-specific detection of DNA in living systems (Figure 1-17).¹²³ The two bioorthogonal reaction partners are conjugated to two different oligonucleotides. Only in the presence of a template strand of DNA that can hybridize with both oligonucleotides will the rapid fluorescence activation of the smart probe occur. Examples of this approach use the Staudinger ligation or azide-alkyne/tetrazine-cyclopropene cycloadditions.¹²⁴⁻¹²⁶ Of these examples, only tetrazine- and cyclopropene-functionalized oligonucleotides have been shown to capably detect template DNA inside of living mammalian cells. Importantly, mismatches in the hybridized DNA significantly reduce reaction rate, resulting in sequence-specific detection.

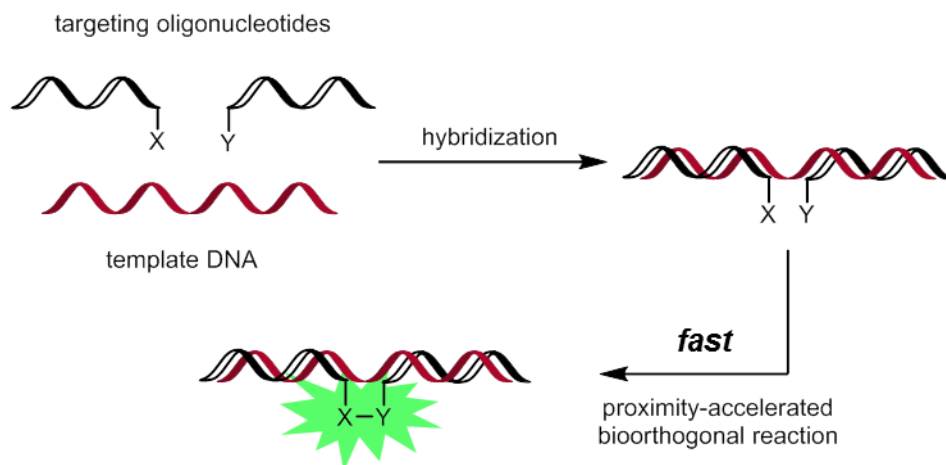


Figure 1-17. DNA template-accelerated bioorthogonal reactions of smart probes for sequence-specific detection of DNA.

Finally, the nitrile imine-alkene cycloaddition has been used by Lin and coworkers as a platform to develop photoactivatable probes that are suitable for visualizing trafficking processes or for superresolution imaging (**1.47**, Figure 1-18).¹²⁷ While the kinetics of the cycloaddition with unfunctionalized terminal alkenes are modest, the reaction rate can be enhanced dramatically by using an intramolecular variant of the reaction. Indeed, these probes were fully converted to fluorescent pyrazoline product **1.48** within minutes of irradiation with a handheld 302 nm UV lamp. By attaching these probes to a Taxol derivative, Lin and coworkers were able to visualize microtubules in live cells, albeit using conventional microscopy techniques. In principle, other bioorthogonal reactions may use this same strategy for the development of photoactivatable fluorescent probes.¹²⁸

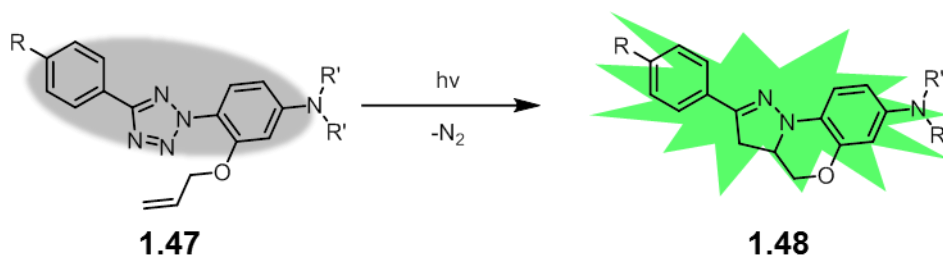


Figure 1-18. A rapidly photoactivatable tetrazole probe.

Conclusion and Dissertation Overview

While significant progress has been made in the development of new bioorthogonal chemistries, these efforts are aided by the development of better, smarter probes for these reactions. The fluorescent probes described here have enabled the visualization and detection of tagged biomolecules with ever higher sensitivity, while the caged probes hold promise for the selective delivery of drugs or imaging agents. Further advances in probe development, such as probes

based off other imaging modalities, and novel applications of these probes will expand the versatility of bioorthogonal chemistry to aid our understanding of biological systems.

In this dissertation, I outline my own efforts towards the development of a general strategy to access fluorogenic azide probes across the visible spectrum. This family of fluorophores addresses one of the major limitations common to many of the bioorthogonal smart probes described in this chapter: short wavelength excitation and emission. These probes enable the detection of linear and strained alkynes with improved levels of sensitivity over traditional “always-on” fluorophores. In conjunction with a platform for the metabolic incorporation of cyclooctynes into bacterial peptidoglycan, these fluorophores enabled the visualization of cell wall synthesis of a bacterial pathogen during infection and may be an enabling tool for studying these pathogens *in vivo*.

Notes and References

1. Patterson, D. M.; Nazarova, L. A.; Prescher, J. A. *ACS Chem. Biol.* **2014**, *9*, 592-605.
2. Lang, K.; Chin, J. W. *ACS Chem. Biol.* **2014**, *9*, 16-20.
3. Lang, K.; Chin, J. W. *Chem. Rev.* **2014**, *114*, 4764-4806.
4. Ramil, C. P.; Lin, Q. *Chem. Commun.* **2013**, *49*, 11007-11022.
5. Debets, M. F.; van Hest, J. C. M.; Rutjes, F. P. J. T. *Org. Biomol. Chem.* **2013**, *11*, 6439-6455.
6. Mahal, L. K.; Yarema, K. J.; Bertozzi, C. R. *Science* **1997**, *276*, 1125-1128.
7. Chen, I.; Howarth, M.; Lin, W.; Ting, A. Y. *Nat. Methods* **2005**, *2*, 99-104.
8. Wang, L.; Zhang, Z.; Brock, A.; Schultz, P. G. *Proc. Natl. Acad. Sci.* **2002**, *100*, 56-51.
9. Tuley, A.; Lee, Y.-J.; Wu, B.; Wang, Z. U.; Liu, W. R. *Chem. Commun.* **2014**, *50*, 7424-7426.
10. Zeng, Y.; Ramya, T. N. C.; Dirksen, A.; Dawson, P. E.; Paulson, J. C. *Nat. Methods* **2009**, *6*, 207-209.
11. Rannes, J. B.; Ioannou, A.; Willies, S. C.; Grogan, G.; Behrens, C.; Flitsch, S. L.; Turner, N. J. *J. Am. Chem. Soc.* **2011**, *133*, 8436-8439.
12. Carrico, I. S.; Carlson, B. L.; Bertozzi, C. R. *Nat. Chem. Biol.* **2007**, *3*, 321-322.
13. Crisalli, P.; Kool, E. T. *J. Org. Chem.* **2013**, *78*, 1184-1189.
14. Kalia, J.; Raines, R. T. *Angew. Chem. Int. Ed.* **2008**, *47*, 7523-7526.
15. Agarwal, P.; van der Weijden, J.; Sletten, E. M.; Rabuka, D.; Bertozzi, C. R. *Proc. Natl. Acad. Sci.* **2013**, *110*, 46-51.
16. Agarwal, P.; Kudirka, R.; Albers, A. E.; Barfield, R. M.; de Hart, G. W.; Drake, P. M.; Jones, L. C.; Rabuka, D. *Bioconjug. Chem.* **2013**, *24*, 846-851.
17. In quenching via ICT, the excited singlet state of the fluorophore may quickly convert into a twisted charge transfer state where electron density is transferred from donor to acceptor moiety. This state rapidly returns to the ground state via non-radiative decay pathways, quenching fluorescence. Smart probes based off ICT processes typically show changes in absorption or emission wavelengths after bioorthogonal reaction. See also: de Silva, A. P.; Gunaratne, H. Q. N.; Gunnlaugsson, T.; Huxley, A. J. M.; McCoy, C. P.; Rademacher, J. T.; Rice, T. E. *Chem. Rev.* **1997**, *97*, 1515-1566.
18. Gubitz, G.; Wintersteiger, R.; Frei, R. W. *J. Liq. Chromatogr.* **1984**, *7*, 839-854.
19. Koizumi, H.; Suzuki, Y. *J. Chromatogr.* **1988**, *457*, 299-307.
20. Uzu, S.; Kanda, S.; Nakashima, K.; Akiyama, S. *Analyst* **1990**, *115*, 1477-1482.
21. Konarzycka-Bessler, M.; Bornscheuer, U. T. *Angew. Chem. Int. Ed.* **2003**, *42*, 1418-1420.
22. Dilek, O.; Bane, S. L. *Tet. Lett.* **2007**, *49*, 1413-1416.
23. Dilek, O.; Bane, S. L. *J. Fluoresc.* **2011**, *21*, 347-354.
24. Banerjee, A.; Panosian, T. D.; Mukherjee, K.; Ravindra, R.; Gal, S.; Sackett, D. L.; Bane, S. *ACS Chem. Biol.* **2010**, *5*, 777-785.
25. Key, J. A.; Li, C.; Cairo, C. W. *Bioconjug. Chem.* **2012**, *23*, 363-371.
26. Salahuddin, S.; Renaudet, O.; Reymond, J.-L. *Org. Biomol. Chem.* **2004**, *2*, 1471-1475.
27. Kitov, P. I.; Vinals, D. F.; Ng, S.; Tjhung, K. F.; Derda, R. *J. Am. Chem. Soc.* **2014**, *136*, 8149-8152.
28. Ji, A.; Ren, W.; Ai, H. *Chem. Commun.* **2014**, *50*, 7469-7472.
29. Saxon, E.; Bertozzi, C. R. *Science* **2000**, *287*, 2007-2010.

30. Lin, F. L.; Hoyt, H. M.; van Halbeek, H.; Bergman, R. G.; Bertozzi, C. R. *J. Am. Chem. Soc.* **2005**, *127*, 2686.
31. Schiedel, M. S.; Briehn, C. A.; Bauerle, P. *Angew. Chem. Int. Ed.* **2001**, *40*, 4677-4680.
32. Lemieux, G. A.; de Graffenried, C. L.; Bertozzi, C. R. *J. Am. Chem. Soc.* **2003**, *125*, 4708-4709.
33. Hangauer, M. J.; Bertozzi, C. R. *Angew. Chem. Int. Ed.* **2008**, *47*, 2394-2397.
34. Chang, P. V.; Prescher, J. A.; Hangauer, M. J.; Bertozzi, C. R. *J. Am. Chem. Soc.* **2007**, *129*, 8400-8401.
35. Cohen, A. S.; Dubikovskaya, E. A.; Rush, J. S.; Bertozzi, C. R. *J. Am. Chem. Soc.* **2010**, *132*, 8563-8565.
36. Denburg, J. L.; Lee, R. T.; McElroy, W. D. *Arch. Biochem. Biophys.* **1969**, *134*, 381-394.
37. Saxon, E.; Armstrong, J. I.; Bertozzi, C. R. *Org. Lett.* **2000**, *2*, 2141-2143.
38. Nilsson, B. L.; Kiessling, L. L.; Raines, R. T. *Org. Lett.* **2000**, *2*, 1939-1941.
39. Azoulay, M.; Tuffin, G.; Sallem, W.; Florent, J.-C. *Bioorg. Med. Chem. Lett.* **2006**, *16*, 3147-3149.
40. Prescher, J. A.; Dube, D. H.; Bertozzi, C. R. *Nature* **2004**, *430*, 873-877.
41. Rostovtsev, V. V.; Green, L. G.; Fokin, V. V.; Sharpless, K. B. *Angew. Chem. Int. Ed.* **2002**, *41*, 2596-2599.
42. Tornøe, C. W.; Christensen, C.; Meldal, M. *J. Org. Chem.* **2002**, *67*, 3057-3064.
43. Agard, N. J.; Prescher, J. A.; Bertozzi, C. R. *J. Am. Chem. Soc.* **2004**, *126*, 15046-15047.
44. Baskin, J. M.; Prescher, J. A.; Laughlin, S. T.; Agard, N. J.; Chang, P. V.; Miller, I. A.; Lo, A.; Codelli, J. A.; Bertozzi, C. R. *Proc. Natl. Acad. Sci.* **2007**, *104*, 16793-16797.
45. Ning, X.; Guo, J.; Wolfert, M. A.; Boons, G.-J. *Angew. Chem. Int. Ed.* **2008**, *47*, 2253-2255.
46. Jewett, J. C.; Sletten, E. M.; Bertozzi, C. R. *J. Am. Chem. Soc.* **2010**, *132*, 3688-3690.
47. Debets, M. F.; van Berkel, S. S.; Schoffelen, S.; Rutjes, F. P.; van Hest, J. C.; van Delft, F. L. *Chem. Commun.* **2010**, *46*, 97-99.
48. Dommerholt, J.; Schmidt, S.; Temming, R.; Hendriks, L. J. A.; Rutjes, F. P. J. T.; van Hest, J. C. M.; Lefeber, D. J.; Friedl, P.; van Delft, F. L. *Angew. Chem. Int. Ed.* **2010**, *49*, 9422-9425.
49. de Almeida, G.; Sletten, E. M.; Nakamura, H.; Palaniappan, K. K.; Bertozzi, C. R. *Angew. Chem. Int. Ed.* **2012**, *51*, 2443-2447.
50. Hong, V.; Steinmetz, N. F.; Manchester, M.; Finn, M. G. *Bioconjug. Chem.* **2010**, *21*, 1912-1916.
51. Presolski, S. I.; Hong, V.; Cho, S.-H.; Finn, M. G. *J. Am. Chem. Soc.* **2010**, *132*, 14570-14576.
52. Soriano Del Amo, D.; Wang, W.; Jiang, H.; Besanceney, C.; Yan, A. C.; Levy, M.; Liu, Y.; Marlow, F. L.; Wu, P. *J. Am. Chem. Soc.* **2010**, *132*, 16893-16899.
53. Besanceney-Webler, C.; Jiang, H.; Zheng, T.; Feng, L.; Soriano del Amo, D.; Wang, W.; Klivansky, L. M.; Marlow, F. L.; Liu, Y.; Wu, P. *Angew. Chem. Int. Ed.* **2011**, *50*, 8051-8056.
54. Le Droumaguet, C.; Wang, C.; Wang, Q. *Chem. Soc. Rev.* **2010**, *39*, 1233-1239.
55. Jarowski, P. D.; Wu, Y.-L.; Schweizer, W. B.; Diederich, F. *Org. Lett.* **2008**, *10*, 3347-3350.
56. Scrafton, D. K.; Taylor, J. E.; Mahon, M. F.; Fossey, J. S.; James, T. D. *J. Org. Chem.* **2008**, *73*, 2871-2874.

57. Schweinfurth, D.; Hardcastle, K. I.; Bunz, U. H. F. *Chem. Commun.* **2008**, 2008, 2203-2205.
58. Bag, S. S.; Kundu, R. *J. Org. Chem.* **2011**, 76, 3348-3356.
59. Er, J. C.; Tang, M. K.; Chia, C. G.; Liew, H.; Vendrell, M.; Chang, Y.-T. *Chem. Sci.* **2013**, 4, 2168-2176.
60. Sivakumar, K.; Xie, F.; Cash, B. M.; Long, S.; Barnhill, H. N.; Wang, Q. *Org. Lett.* **2004**, 6, 4603-4606.
61. Beatty, K. E.; Xie, F.; Wang, Q.; Tirrell, D. A. *J. Am. Chem. Soc.* **2005**, 127, 14150-14151.
62. Beatty, K. E.; Liu, J. C.; Xie, F.; Dieterich, D. C.; Schuman, E. M.; Wang, Q.; Tirrell, D. A. *Angew. Chem. Int. Ed.* **2006**, 45, 7364-7367.
63. Sawa, M.; Hsu, T.-L.; Itoh, T.; Sugiyama, M.; Hanson, S. R.; Vogt, P. K.; Wong, C.-H. *Proc. Natl. Acad. Sci.* **2006**, 103, 12371-12376.
64. Wang, C.; Xie, F.; Suthiwangcharoen, N.; Sun, J.; Wang, Q. *Sci. China Chem.* **2012**, 55, 125-130.
65. Herner, A.; Nikic, I.; Kallay, M.; Lemke, E. A.; Kele, P. *Org. Biomol. Chem.* **2013**, 11, 3297-3306.
66. Herner, A.; Girona, G. E.; Nikic, I.; Kallay, M.; Lemke, E. A.; Kele, P. *Bioconjug. Chem.* **2014**, 25, 1370-1374.
67. Horner, A.; Volz, D.; Hagendorf, T.; Furniss, D.; Greb, L.; Ronicke, F.; Nieger, M.; Schepers, U.; Brase, S. *RSC Adv.* **2014**, 4, 11528-11534.
68. In quenching via PeT for the probes described here, the excited singlet state of the fluorophore moiety accepts an electron from a nearby electron donor. The diradical intermediate relaxes back down to the ground state via back electron transfer. Fluorescence is activated when the donor is no longer capable of transferring electrons to the acceptor fluorophore. As the fluorophore moiety remains untouched upon activation of PeT probes, absorption and emission wavelengths should remain unchanged. See also Ref. 17.
69. Xie, F.; Sivakumar, K.; Zeng, Q.; Bruckman, M. A.; Hodges, B.; Wang, Q. *Tetrahedron* **2008**, 64, 2906-2914.
70. Shieh, P.; Hangauer, M. J.; Bertozzi, C. R. *J. Am. Chem. Soc.* **2012**, 134, 17428-17431.
71. Urano, Y.; Kamiya, M.; Kanda, K.; Ueno, T.; Hirose, K.; Nagano, T. *J. Am. Chem. Soc.* **2005**, 127, 4888-4894.
72. Shieh, P.; Siegrist, M. S.; Cullen, A. J.; Bertozzi, C. R. *Proc. Natl. Acad. Sci.* **2014**, 111, 5456-5461.
73. Koide, Y.; Urano, Y.; Hanaoka, K.; Terai, T.; Nagano, T. *ACS Chem. Biol.* **2011**, 6, 600-608.
74. Shie, J.-J.; Liu, Y.-C.; Lee, Y.-M.; Lim, C.; Fang, J.-M.; Wong, C.-H. *J. Am. Chem. Soc.* **2014**, 136, 9953-9961.
75. Staros, J. V.; Bayley, H.; Standring, D. N.; Knowles, J. R. *Biophys. Res. Commun.* **1978**, 80, 568-572.
76. Uttamapinant, C.; Tangpeerachaikul, A.; Grecian, S.; Clarke, S.; Singh, U.; Slade, P.; Gee, K. R.; Ting, A. Y. *Angew. Chem. Int. Ed.* **2012**, 51, 5852-5856.
77. Bevilacqua, V.; King, M.; Chaumontet, M.; Nothisen, M.; Gabillet, S.; Buisson, D.; Puente, C.; Wagner, A.; Taran, F. *Angew. Chem. Int. Ed.* **2014**, 53, 5872-5876.
78. Zhou, Z.; Fahrni, C. J. *J. Am. Chem. Soc.* **2004**, 126, 8862-8863.

79. Key, J. A.; Koh, S.; Timerghazin, Q. K.; Brown, A.; Cairo, C. W. *Dyes and Pigments* **2009**, *82*, 192-203.
80. Li, J.; Hu, M.; Yao, S. Q. *Org. Lett.* **2009**, *11*, 3008-3011.
81. Qi, J.; Tung, C.-H. *Bioorg. Med. Chem. Lett.* **2011**, *21*, 320-323.
82. Qi, J.; Han, M.-S.; Chang, Y.-C.; Tung, C.-H. *Bioconjug. Chem.* **2011**, *22*, 1758-1762.
83. Key, J. A.; Cairo, C. W. *Dyes and Pigments* **2011**, *88*, 95-102.
84. Rong, L.; Liu, L.-H.; Chen, S.; Cheng, H.; Chen, C.-S.; Li, Z.-Y.; Qin, S.-Y.; Zhang, X.-Z. *Chem. Commun.* **2013**, *50*, 667-669.
85. Jewett, J. C.; Bertozzi, C. R., *Org. Lett.*, **2011**, *13*, 5937-5939.
86. Friscourt, F.; Fahrni, C. J.; Boons, G.-J. *J. Am. Chem. Soc.* **2012**, *134*, 18809-18815.
87. van Geel, R.; Prujin, G. J. M.; van Delft, F. L.; Boelens, W. C. *Bioconjug. Chem.* **2012**, *23*, 392-398.
88. Song, W.; Wang, Y.; Qu, J.; Madden, M. M.; Lin, Q. *Angew. Chem. Int. Ed.* **2008**, *47*, 2832-3824.
89. Song, W.; Wang, Y.; Qu, J.; Lin, Q. *J. Am. Chem. Soc.* **2008**, *130*, 9654-9655.
90. Wang, Y.; Hu, W. J.; Song, W.; Lim, R. K. V.; Lin, Q. *Org. Lett.*, **2008**, *10*, 3725-3738.
91. Yu, Z.; Ohulchansky, T. Y.; An, P.; Prasad, P. N.; Lin, Q. *J. Am. Chem. Soc.* **2013**, *135*, 16766-16769.
92. Kaya, E.; Vrabel, M.; Deiml, C.; Prill, S.; Fluxa, V. S.; Carrell, T. *Angew. Chem. Int. Ed.* **2012**, *51*, 4466-4469.
93. Lee, Y.-J.; Wu, B.; Raymond, J. E.; Zeng, Y.; Fang, X.; Wooley, K. R.; Liu, W. R. *ACS Chem. Biol.* **2013**, *8*, 1664-1670.
94. Wang, X. S.; Lee, Y.-J.; Liu, W. R. *Chem. Commun.* **2014**, *50*, 3176-3179.
95. Yu, Z.; Pan, Y.; Wang, Z.; Wang, J.; Lin, Q. *Angew. Chem. Int. Ed.* **2012**, *51*, 10600-10604.
96. Yu, Z.; Lin, Q. *J. Am. Chem. Soc.* **2014**, *136*, 4153-4156.
97. Song, W.; Wang, Y.; Yu, Z.; Vera, C. I. R.; Qu, J.; Lin, Q. *ACS Chem. Biol.* **2010**, *5*, 875-887.
98. An, P.; Yu, Z.; Lin, Q. *Org. Lett.* **2013**, *15*, 5496-5499.
99. Blackman, M. L.; Royzen, M.; Fox, J. M. *J. Am. Chem. Soc.* **2008**, *130*, 13518-13519.
100. Devaraj, N. K.; Weissleder, R.; Hilderbrand, S. A. *Bioconjug. Chem.* **2008**, *19*, 2297-2299.
101. Karver, M. R.; Weissleder, R.; Hilderbrand, S. A. *Bioconjug. Chem.*, **2011**, *22*, 2283-2270.
102. Taylor, M. T.; Blackman, M. L.; Dmitrenko, O.; Fox, J. M. *J. Am. Chem. Soc.* **2011**, *133*, 9646-9649.
103. Yang, J.; Seckute, J.; Cole, C. M.; Devaraj, N. K. *Angew. Chem. Int. Ed.* **2012**, *51*, 7476-7479.
104. Patterson, D. M.; Nazarova, L. A.; Xie, B.; Kamber, D. N.; Prescher, J. A. *J. Am. Chem. Soc.* **2012**, *134*, 18638-16843.
105. Chen, W.; Wang, D.; Dai, C.; Hamelberg, D.; Wang, B. *Chem. Commun.* **2012**, *48*, 1736-1738.
106. Devaraj, N. K.; Hilderbrand, S.; Upadhyay, R.; Mazitschek, R.; Weissleder, R. *Angew. Chem. Int. Ed.* **2010**, *49*, 2869-2872.
107. Lang, K.; Davis, L.; Torres-Kolbus, J.; Chou, C.; Deiters, A.; Chin, J. W. *Nat. Chem.* **2012**, *4*, 298-304.

108. Yang, K. S.; Budin, G.; Reiner, T.; Vinegoni, C.; Weissleder, R. *Angew. Chem. Int. Ed.* **2012**, *51*, 6598-6603.
109. Liu, D. S.; Tangpeerachaikul, A.; Selvaraj, R.; Taylor, M. T.; Fox, J. M.; Ting, A. Y. *J. Am. Chem. Soc.* **2012**, *134*, 792-795.
110. Lang, K.; Davis, L.; Wallace, S.; Mahesh, M.; Cox, D. J.; Blackman, M. L.; Fox, J. M.; Chin, J. W. *J. Am. Chem. Soc.* **2012**, *134*, 10317-10320.
111. Dumas-Verdes, C.; Miomandre, F.; Lepicier, E.; Galangau, O.; Vu, T. T.; Clavier, G.; Meallet-Renault, R.; Audebert, P. *Eur. J. Org. Chem.* **2010**, *2010*, 2525-2535.
112. In through-bond energy transfer, the donor transfers energy via twisted π -bonds to an acceptor. Unlike FRET, minimal spectral overlap between the donor and acceptor is required, although the acceptor should still absorb light at a longer wavelength than the donor emits. See also: Jiao, G.-S.; Thoresen, L. H.; Burgess, K. *J. Am. Chem. Soc.* **2003**, *125*, 14668-14669.
113. Carlson, J. C. T.; Meimetis, L. G.; Hilderbrand, S. A.; Weissleder, R. *Angew. Chem. Int. Ed.* **2013**, *52*, 6917-6920.
114. Meimetis, L. G.; Carlson, J. C. T.; Giedt, R. J.; Kohler, R. H.; Weissleder, R. *Angew. Chem. Int. Ed.* **2014**, *53*, 7531-7534.
115. Xu, H.; Yang, J.; Seckute, J.; Devaraj, N. K. *Angew. Chem. Int. Ed.* **2014**, *53*, 5805-5809.
116. Wiczorek, A.; Buckup, T.; Wombacher, R. *Org. Biomol. Chem.* **2014**, *12*, 4177-4185.
117. Neves, A. A.; Stockmann, H.; Wainman, Y. A.; Kuo, S. J. C.-H.; Fawcett, S.; Leeper, F. J.; Brindle, K. M. *Bioconjug. Chem.* **2013**, *24*, 934-941.
118. Versteegen, R. M.; Rossin, R.; Hoeve, W. T.; Janssen, H. M.; Robillard, M. S. *Angew. Chem. Int. Ed.* **2013**, *52*, 14112-14116.
119. Seitchik, J. L.; Peeler, J. C.; Taylor, M. T.; Blackman, M. L.; Rhoads, T. W.; Cooley, R. B.; Refakis, C.; Fox, J. M.; Mehl, R. M. *J. Am. Chem. Soc.* **2012**, *134*, 2898-2901.
120. Dirks, A. J.; Cornelissen, J. J. L. M.; Nolte, R. J. M. *Bioconjug. Chem.* **2009**, *20*, 1129-1138.
121. Wijdeven, M. A.; Nicosia, C.; Borrmann, A.; Huskens, J.; van Delft, F. L. *RSC Adv.* **2014**, *4*, 10549-10552.
122. Lewis, W. G.; Green, L. G.; Grynszpan, F.; Radic, Z.; Carlier, P. R.; Taylor, P.; Finn, M. G.; Sharpless, K. B. *Angew. Chem. Int. Ed.* **2002**, *41*, 1053-1057.
123. Other examples of fluorogenic DNA-templated reactions for oligonucleotide detection are discussed in this review: Michaelis, J.; Roloff, A.; Seitz, O. *Org. Biomol. Chem.* **2014**, *12*, 2821-2833.
124. Cai, J.; Li, X.; Yue, X.; Taylor, J. S. *J. Am. Chem. Soc.* **2004**, *126*, 16324-16325.
125. Sun, H.; Peng, X. *Bioconjug. Chem.* **2013**, *24*, 1226-1234.
126. Seckute, J.; Yang, J.; Devaraj, N. K. *Nucl. Acids Res.* **2013**, *41*, e148.
127. Yu, Z.; Ho, L. Y.; Lin, Q. *J. Am. Chem. Soc.* **2011**, *133*, 11912-11915.
128. Poloukhine, A. A.; Mbua, N. E.; Wolfert, M. A.; Boons, G.-J.; Popik, V. V. *J. Am. Chem. Soc.* **2009**, *131*, 15769-15776.

Chapter 2: A PeT-Based Approach Toward Fluorogenic Azide Probes

Note: Portions of this chapter were published in *J. Am. Chem. Soc.* **2012**, *134*, 17428-17431.

Introduction

Bioorthogonal chemistry has enabled the visualization and study of biomolecules that cannot be tagged with genetically encoded fluorescent proteins.¹ Much work has been devoted to expanding the toolbox of bioorthogonal reactions, and these efforts can be complemented by the development of fluorogenic probes.² Such probes are typically endowed with a functionality that suppresses fluorescence. Its transformation during the reaction creates a new functionality that no longer quenches fluorescence of the underlying system, resulting in a fluorescence enhancement. These probes offer significant advantages for imaging studies where it is not possible to wash away unreacted probe, such as real-time imaging of dynamic processes in cells or visualization of molecules in live organisms. To identify new therapeutic strategies for bacterial pathogens, we aimed to develop chemical tools that would enable the visualization of pathogen-associated biomolecules in an infection setting. As a result, we hoped that the development of novel fluorogenic probes for imaging inside living cells and *in vivo* would be enabling technologies.

One of the most widely used bioorthogonal reactions is the azide-alkyne [3+2] cycloaddition to form a triazole. This reaction has enabled the selective visualization of azide- or alkyne-labeled proteins, glycans, nucleic acids, and lipids.³ Several azide-⁴⁻⁷ and alkyne⁷⁻¹¹-functionalized fluorogenic probes have been reported, largely based on coumarins^{4,8}, naphthalimides⁷ and other systems that require UV excitation and emit blue light.^{5,10,11} Such wavelengths are not ideal for biological imaging due to high levels of autofluorescence and poor tissue penetrance.¹³

An obvious improvement upon these designs would be the development of azido or alkynyl fluorogenic probes with longer excitation and emission wavelengths. Some attempts at achieving this goal have been made. Recently, an azido BODIPY probe was reported, but the compound was unstable and unable to specifically react with alkynes on cellular biomolecules.⁶ An alkynyl benzothiazole analog that emits at ~500 nm has been reported but its fluorescence enhancement upon reaction with azides was a modest 3.5-fold in aqueous buffer.¹¹ A screen of 200 combinations of various alkynyl xanthenes and organic azides produced two reagent pairs that reacted to give a fluorescence enhancement of 10-fold in organic solvent.¹² The utility of these alkyne/azide pairs in biological settings remains unclear. Thus, fluorogenic azido or alkynyl probes that perform well as cell imaging reagents remain an important goal. In this chapter, I describe our initial work showing rational design and experimental validation of azide-functionalized fluorogenic probes based on the widely-used blue-excitation green-emission fluorescein scaffold.

Results and Discussion

Our design capitalized on a theoretical model developed by Nagano and coworkers that enables prediction of fluorescence quantum yield based on density functional theory calculations.¹⁴ Nagano demonstrated that the pendant aryl ring of fluorescein can quench fluorescence via photoinduced electron transfer.¹⁵ This quenching can be increased or decreased in a predictable manner by altering the electron density of the aryl ring using various substituents. More

importantly, Nagano and coworkers also demonstrated a direct relationship between experimentally determined fluorescence quantum yield and the calculated HOMO energy (E_{HOMO}) of the pendant aryl ring at the B3LYP/6-31G(d) level of theory. Thus, in principle, by calculating the E_{HOMO} values of the aryl ring, one can predict the fluorescence quantum yield of the corresponding fluorescein and identify suitable targets for experimental evaluation. This insight has guided the design of other activatable fluorescein-based probes.^{16,17}

Applying this concept to the development of a fluorogenic azidofluorescein, we performed computational analyses of a panel of fluorescein analogs in which the azide group was directly appended to a variety of aryl substituents (Figure 2-1, Table 2-1). We anticipated that triazole formation would lower the aryl E_{HOMO} value relative to that of the azide-functionalized substrate, reducing photoinduced electron transfer and resulting in fluorescence turn-on (Figure 2-2). We focused our analysis on targets that could be readily synthesized from commercially available bromo- or iodoaryl starting materials with a substituent ortho to the halogen. In particular, we focused on aryl rings that contained a substituent ortho to the halogen. This ortho substituent restricts rotation around the $C_{\text{aryl}}-C_{\text{xanthene}}$ bond and is necessary for maintaining predictable fluorescence quantum yields.¹⁴ Table 2-1 shows the 15 analogs chosen for computational studies as well as the E_{HOMO} values of the aryl azides and corresponding triazoles calculated at the B3LYP 6-31G(d) level of theory. Triazole products were truncated to include only proximal substituents, avoiding complications arising from mixtures of similar-energy conformers.

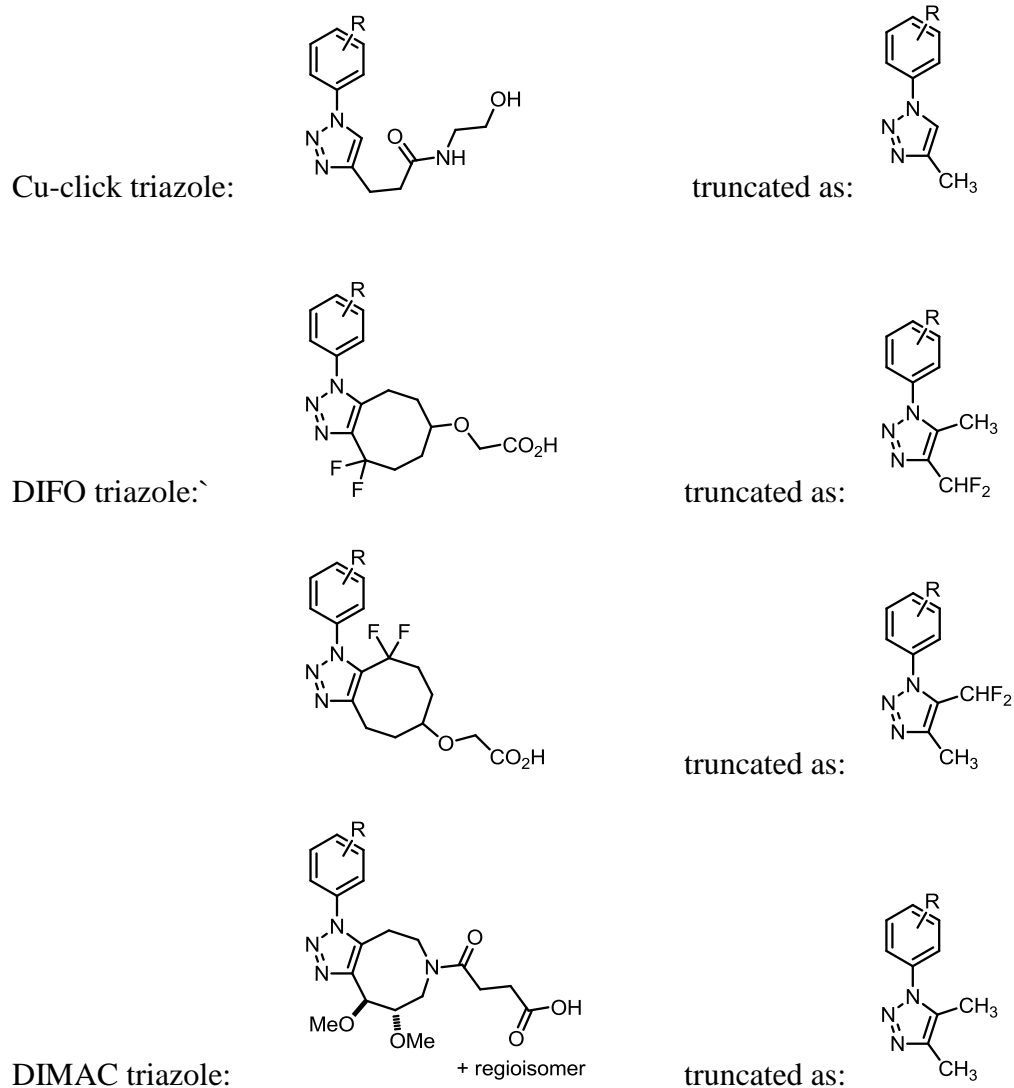


Figure 2-1. Truncated structures used for modeling. Only the substituents directly attached to the triazole were included in calculations.

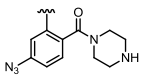
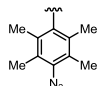
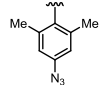
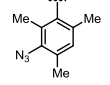
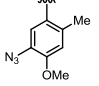
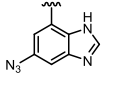
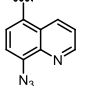
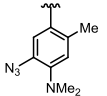
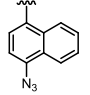
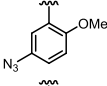
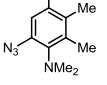
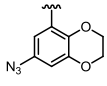
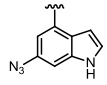
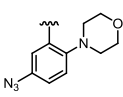
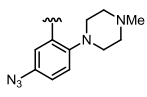
Azidofluorescein	Azide	Cu-triazole	DIFO-triazole	DIMAC-triazole
	-0.223	-0.225	-0.224/-0.230	-0.225
	-0.224	-0.232	-0.231/-0.238	-0.231
	-0.222	-0.231	-0.240/-0.248	-0.229
	-0.219	-0.240	-0.243/-0.249	-0.232
	-0.219	-0.238	-0.243/-0.250	-0.225
	-0.215	-0.238	-0.232/-0.240	-0.225
	-0.214	-0.224	-0.238/-0.245	-0.215
	-0.210	-0.212	-0.209/-0.218	-0.211
	-0.210	-0.220	-0.223/-0.234	-0.221
	-0.208	-0.218	-0.223/-0.231	-0.220
	-0.207	-0.207	-0.201/-0.210	-0.204
	-0.205	-0.214	-0.218/-0.226	-0.216
	-0.198	-0.208	-0.210/-0.218	-0.210
	-0.196	-0.203	-0.205/-0.213	-0.204
	-0.193	-0.196	-0.197/-0.203	-0.197

Table 2-1. Calculated HOMO Energies (Hartrees) of candidate azidofluoresceins and their products.

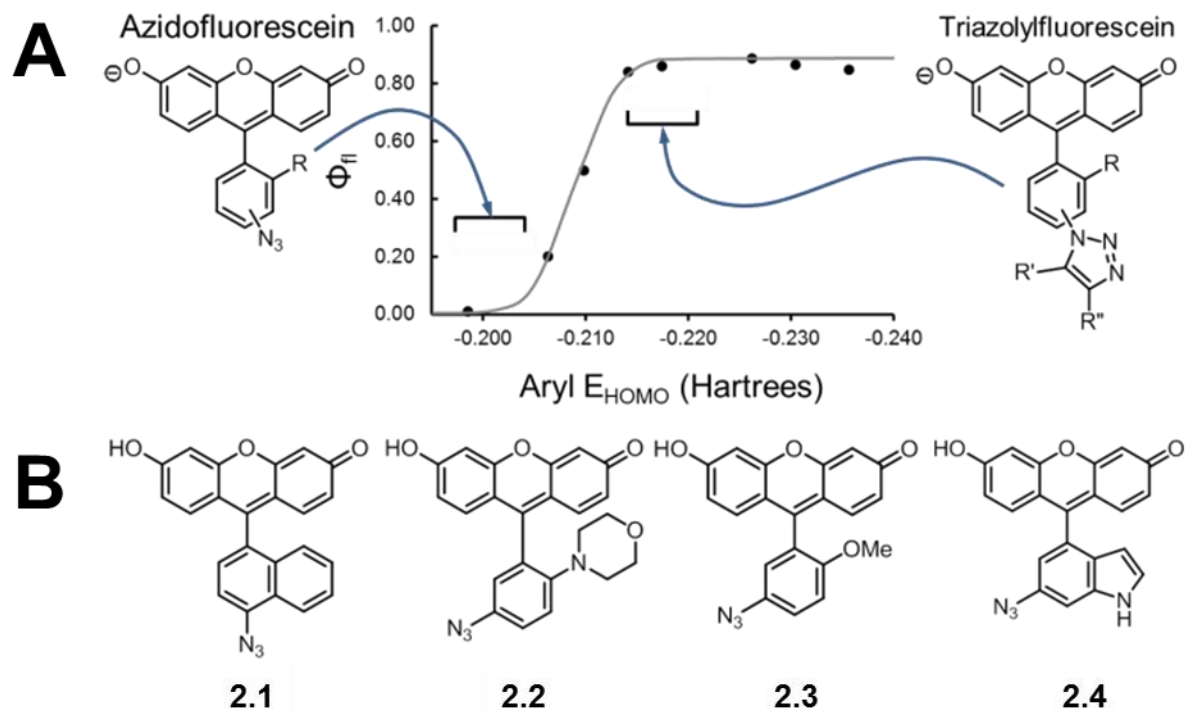
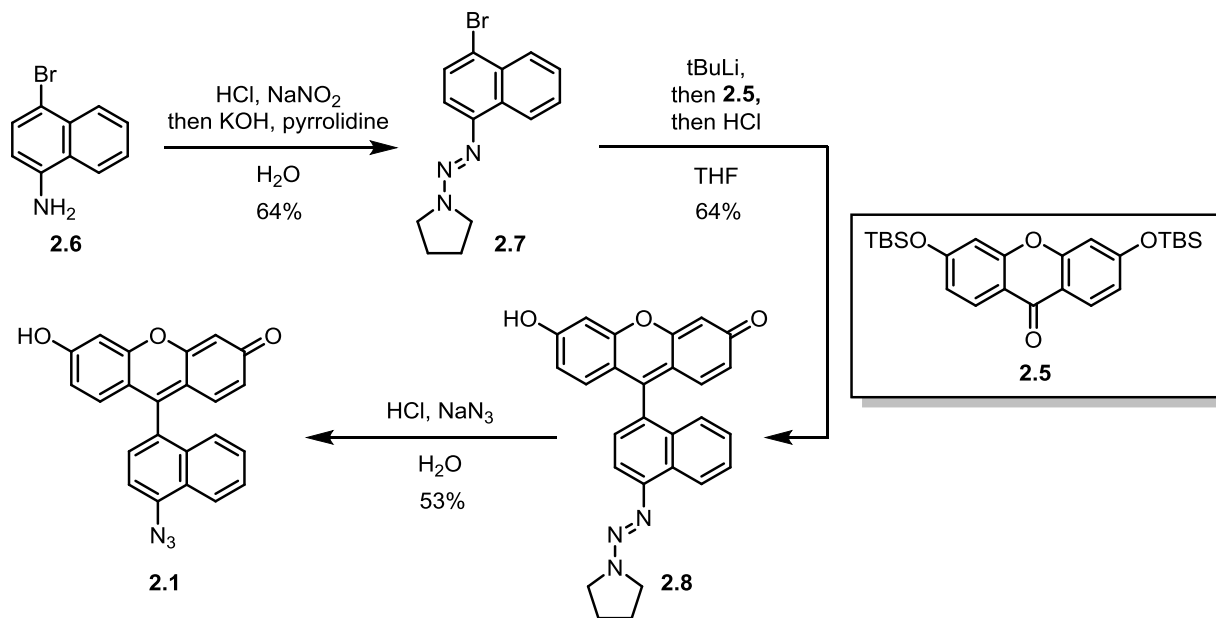


Figure 2-2. Computation-aided design of fluorogenic azidofluorescein analogs. (A) Relationship between pendant aryl E_{HOMO} and fluorescence quantum yield. The ideal E_{HOMO} values of the azido and triazolylfluorescein analogs (left and right, respectively) are indicated with brackets.¹⁴ (B) Structures of target azidofluoresceins **2.1-2.4**.

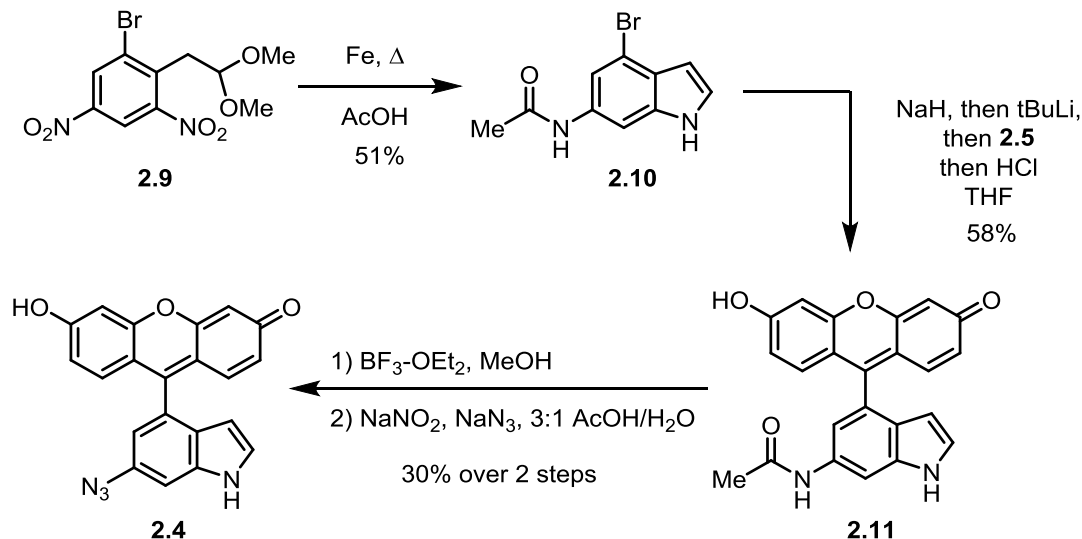
Calculations indicated that all compounds, with one exception, undergo the expected decrease in aryl E_{HOMO} value upon triazole formation. From these compounds, four (**2.1-2.4**, Figure 2-2B) were chosen as targets for synthesis and further evaluation. These candidates possessed azide E_{HOMO} values of -0.196 to -0.210 Hartrees and triazole E_{HOMO} values of -0.203 to -0.220 Hartrees. Given the relationship between fluorescence quantum yield and E_{HOMO} value, we anticipated that compounds **2.1-2.4** would undergo an increase in fluorescence quantum yield at pH 7.4 upon triazole formation.

Compounds **2.1**, **2.2** and **2.3** were prepared by addition of the corresponding aryl organolithium compound to a protected xanthone derivative, an approach reported previously by Tsien and coworkers (Scheme 2-1).²⁰ To generate compound **2.1**, we subjected commercially available bromoaniline **2.6** to diazotization and then protected the diazonium group by reaction with pyrrolidine,^{18,19} affording aryl triazene **2.7**. The aryl triazene underwent lithium halogen exchange and addition to bis-TBS-protected xanthone **2.5**²⁰ to afford fluorescein derivative **2.8**. We developed a novel purification strategy for **2.5** – trituration of the crude reaction mixture with pentane efficiently removed the silanol byproducts to yield pure material. Treatment of this compound with acid unmasked the diazonium group, which was displaced by azide anion to afford azido-fluorescein **2.1**. Using this same strategy, azidofluoresceins **2.2** and **2.3** were prepared. Attempts to convert 4-bromo-6-aminoindole, the starting material for compound **2.4**, to

the corresponding triazene were unsuccessful.²¹ Instead, we opted to start from acetylated indole **2.10**, prepared from known compound **2.9** by iron reduction and acetylation in acetic acid (Scheme 2-2). In one pot, we treated **2.10** with two equivalents of sodium hydride, then with tert-butyllithium to effect lithium halogen exchange; coupling with **2.5**, afforded, after acid workup, compound **2.11**. Deacetylation using $\text{BF}_3\text{-OEt}_2$ in MeOH ,²² diazotization, and azide displacement afforded the desired azidofluorescein **2.4**. Note that other protecting groups, including 2,5-dimethylpyrroles and phthalimides, were evaluated with limited success.



Scheme 2-1. Synthesis of azidofluorescein **2.1**.



Scheme 2-2. Synthesis of azidofluorescein **2.4**.

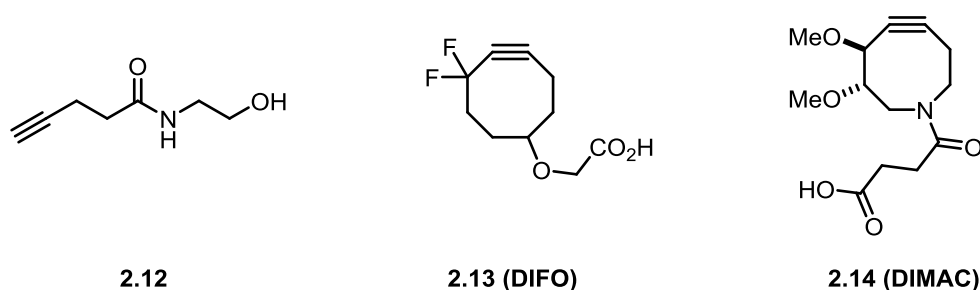


Figure 2-3. Alkynes used for triazolylfluorescein synthesis.

To synthesize the triazole products for photophysical measurements, azidofluoresceins **2.1-2.4** were further reacted with model alkynes **2.12-2.14** (Figure 2-3) under Cu-catalyzed (for compound **2.12**) or Cu-free (**2.13** [also abbreviated DIFO] and **2.14** [DIMAC]) conditions.^{23,24} The fluorescence quantum yields of all compounds were then measured in pH 7.4 phosphate-buffered saline (PBS) (Table 1). Each triazolylfluorescein showed an increase in fluorescence quantum yield compared to the parent azidofluorescein. The relationship between fluorescence quantum yield and calculated E_{HOMO} followed a trend similar to that observed by Nagano (Figure 2-4). As a point of comparison, we analyzed known 5-azidofluorescein (N₃-fluor, Table 2-2), which is currently used as an alkyne-specific probe but is not reported to be fluorogenic.^{25,26} To access this molecule, we developed a new synthetic route that obviates the need for chromatographic purification. The calculated E_{HOMO} values of 5-azidofluorescein and its corresponding triazole product with **2.12** were -0.242 and -0.246 Hartrees, respectively, suggesting that both compounds should be highly fluorescent. Consistent with prediction, we found the two compounds to have fluorescent quantum yields of 0.75 and 0.59, respectively.

Interestingly, the fluorescence enhancement of **2.1-2.4** upon triazole formation was dependent on the structure of the alkyne substrate, but not in a systematic way. Presumably, structure-dependent pathways for nonradiative decay contribute to the observed fluorescence of the triazole products. One potential explanation – differences in pK_as of the fluorescein derivatives – was considered by remeasuring various quantum yields at pH 13. This may be problematic, as protonation of the fluorescein xanthene results in a 3-fold decrease in fluorescence quantum yield. At pH 7.4, subtle changes in fluorescein pK_a will result in significant changes in the concentration of protonated xanthene. At pH 13, however, the population of protonated xanthene will be negligible, regardless of subtle changes in pK_a. Fluorescence quantum yields were comparable at these two different pHs, ruling out this potential source of variability in fluorescence quantum yields. Nonetheless, half of the azidofluorescein-alkyne pairs gave a fluorescence turn-on of >10-fold, indicating that rational design principles can more efficiently identify fluorogenic reagent pairs than undirected screening approaches.

Compound	λ_{ex}	λ_{em}	Φ_{500}	Φ_{500} (pH 13)	Increase
fluorescein	490	510	--	0.85	--
2.1	497	513	0.024	0.014	--
2.1-2.12	495	518	0.70	0.59	29x
2.1-DIFO	499	517	0.81	--	34x
2.1-DIMAC	499	517	0.72	--	30x
reduced-2.1	495	514	0.0067	--	0.25x
2.2	501	521	0.00056	0.0012	--
2.2-2.12	506	517	0.0018	0.0072	3.2x
2.2-DIFO	507	522	0.0018	--	3.2x
2.2-DIMAC	507	521	0.00076	--	1.4x
2.3	496	516	0.057	0.046	--
2.3-2.12	499	520	0.72	--	13x
2.3-DIFO	499	519	0.49	--	8.6x
2.3-DIMAC	499	518	0.72	--	13x
2.4	497	518	0.0052	0.0061	--
2.4-2.12	499	519	0.13	--	25x
2.4-DIFO	497	520	0.019	--	3.7x
2.4-DIMAC	497	516	0.020	--	3.8x
N₃-fluor	492	511	0.75	0.80	--
N₃-fluor-2.12	494	516	0.59	--	0.79x

Table 2-2. Fluorescence properties of azido- and triazolylfluoresceins in pH 7.4 PBS. “**2.1-2.12**” denotes the triazolylfluorescein product from reaction of **2.1** and **2.12**. Other triazolylfluoresceins are named analogously.

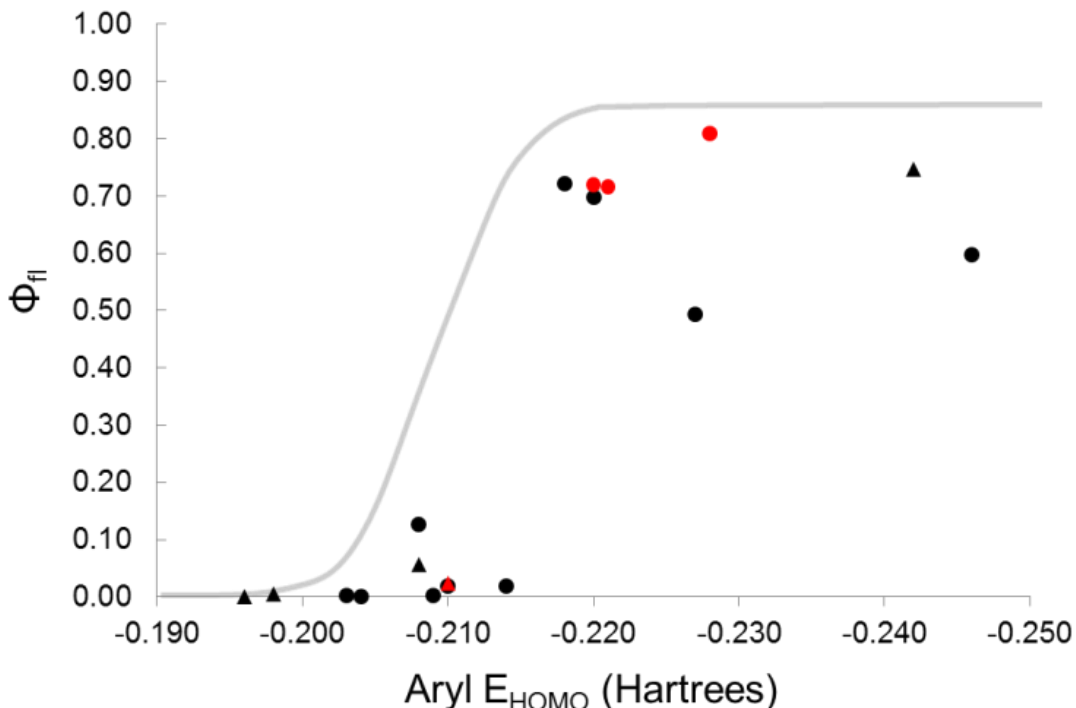


Figure 2-4. Relationship between calculated pendant aryl E_{HOMO} and fluorescence quantum yield of azidofluoresceins and triazolyfluoresceins. The grey line denotes the relationship between aryl E_{HOMO} and fluorescence quantum yield determined in Ref. 14. Points represent experimental data from individual azidofluoresceins (triangles) and triazolyfluoresceins (circles). The points corresponding to compound **2.1** and its triazole products are highlighted in red.

Of the reagents tested, azidofluorescein **2.1** gave the highest and most alkyne-independent increase in fluorescence quantum yield at pH 7.4. A comparison of equimolar amounts of **2.1** and the triazole product derivated from reaction with DIFO showed that the absorption spectra of the two compounds were very similar, consistent with the xanthene moiety remaining unchanged between the two reactions. Subtle changes in the absorption spectra may be due to subtle shifts in xanthene pKa between the two compounds. Importantly, while the absorption spectra of the two solutions were very similar, the triazole solution was significantly more fluorescent. We next chose to further evaluate the use of **2.1** in biological labeling. First, we performed a model reaction with alkyne **2.12** under standard biological labeling conditions (CuSO_4 , ligand,^{27,28} and sodium ascorbate). The expected fluorescence increase was observed and the reaction was complete within 1 h (Figure 2-6). The alkyne-dependent fluorescence enhancement demonstrates the potential utility of these probes to rapidly assay the concentration of alkyne-tagged metabolites. We next demonstrated that azidofluorescein **2.1** can selectively label alkyne-tagged proteins. Bovine serum albumin (BSA) was functionalized with alkynes by modification of its lysine side chains with 4-pentynoyl-NHS-ester. An alkene-modified control sample was produced by reaction of BSA with 4-pentenoyl-NHS ester. Alkyne- or alkene-modified BSA, as well as unmodified BSA, were incubated with **2.1**, CuSO_4 , TBTA, and sodium ascorbate in 95:5 pH 7.4 PBS/tert-butanol, and the samples were analyzed by SDS-PAGE. Fluorescence scanning

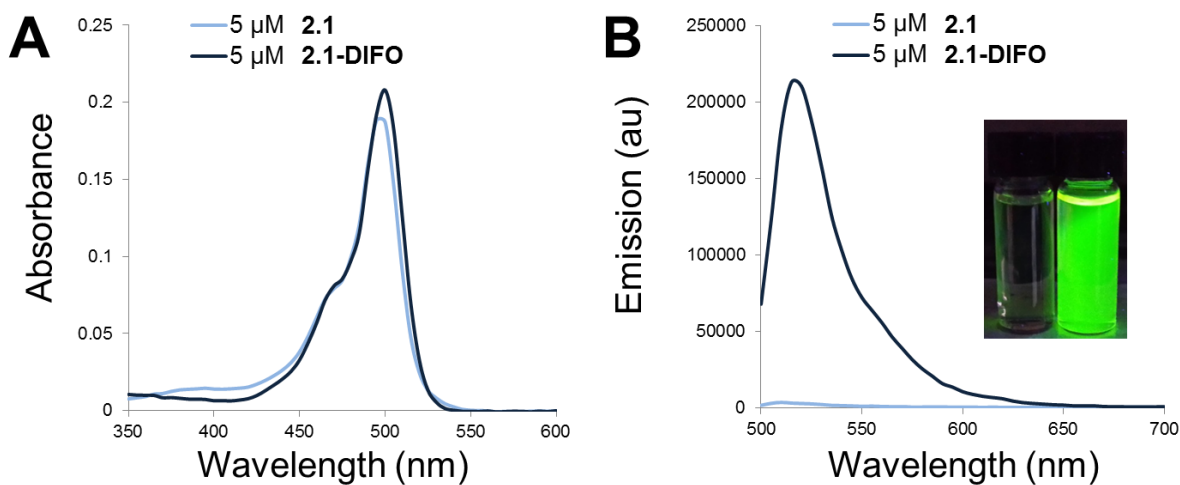


Figure 2-5. (A) Absorption and (B) fluorescence spectra of equimolar concentrations of **2.1** and **2.1-DIFO** triazole.

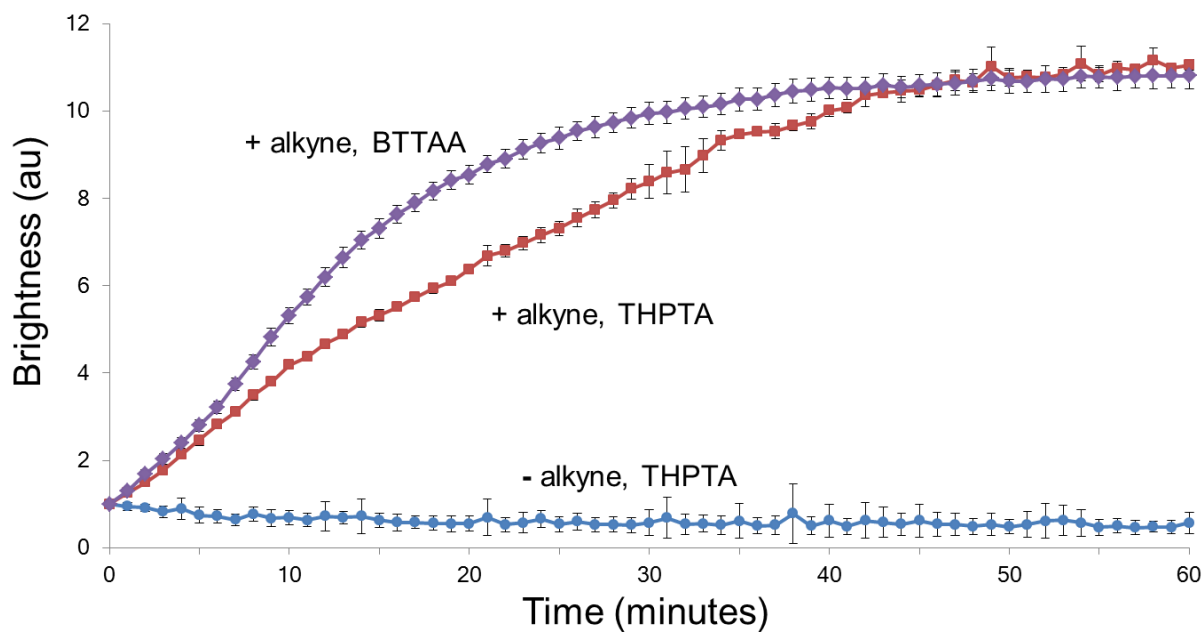


Figure 2-6. Alkyne- and ligand-dependent fluorescence turn-on by **2.1**. A significant increase in fluorescence is observed only in the presence of alkyne **2.12**.

showed that only alkyne-modified BSA was chemically labeled, and in a Cu-dependent manner (Figure 2-7). Very faint copper-dependent fluorescence background in unmodified or alkene-modified BSA was observed, which we attribute to copper-catalyzed decomposition of the aryl azide to the nitrene, although further studies are needed to verify the nature of the reactive species.

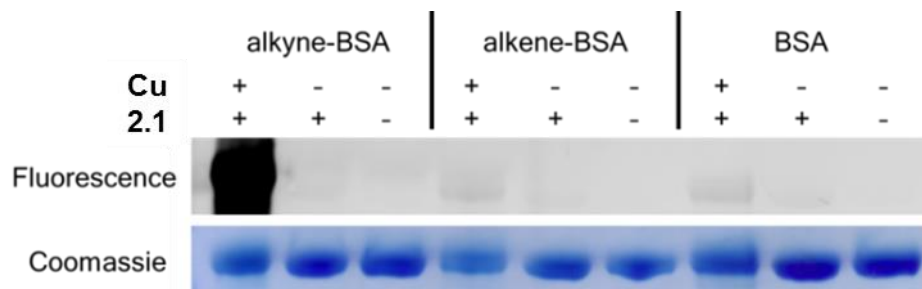


Figure 2-7. Protein labeling by **2.1** is alkyne- and copper-dependent. Significant protein labeling by **2.1** is only observed for alkyne-modified BSA in the presence of CuSO₄.

To evaluate azidofluorescein **2.1** as a biological imaging reagent, Chinese Hamster Ovary (CHO) cells were metabolically labeled with peracetylated *N*-(4-pentynoyl)mannosamine (Ac₄ManNAI) (50 μM for 3 days) as previously described.^{29,30} These cells convert Ac₄ManNAI to the corresponding alkynyl-sialic acid, which is then incorporated into cell-surface glycoproteins. Control cells were incubated with peracetylated *N*-acetylmannosamine (Ac₄ManNAc). The cells were then fixed with paraformaldehyde and incubated with compound **2.1**, CuSO₄, sodium ascorbate, and TBTA for 1 h. After washing, the cells showed robust alkyne-dependent labeling with **2.1** (Figure 2-8). Similar results were obtained with the always fluorescent 5-azidofluorescein (Figure 2-9). The experiment was then repeated, but without the washing step after reaction with **2.1**. As shown in Figure 2-10, bright cell-surface fluorescence was observed for alkyne-labeled cells (Figure 2-10B) compared to the background observed with control (Ac₄ManNAc-labeled) cells (Figure 2-10D). By contrast, the strong fluorescence signal from the always fluorescent 5-azidofluorescein gave high background under no-wash conditions (Figure 2-10F), thereby obscuring cell-surface labeling of alkynyl sugars.

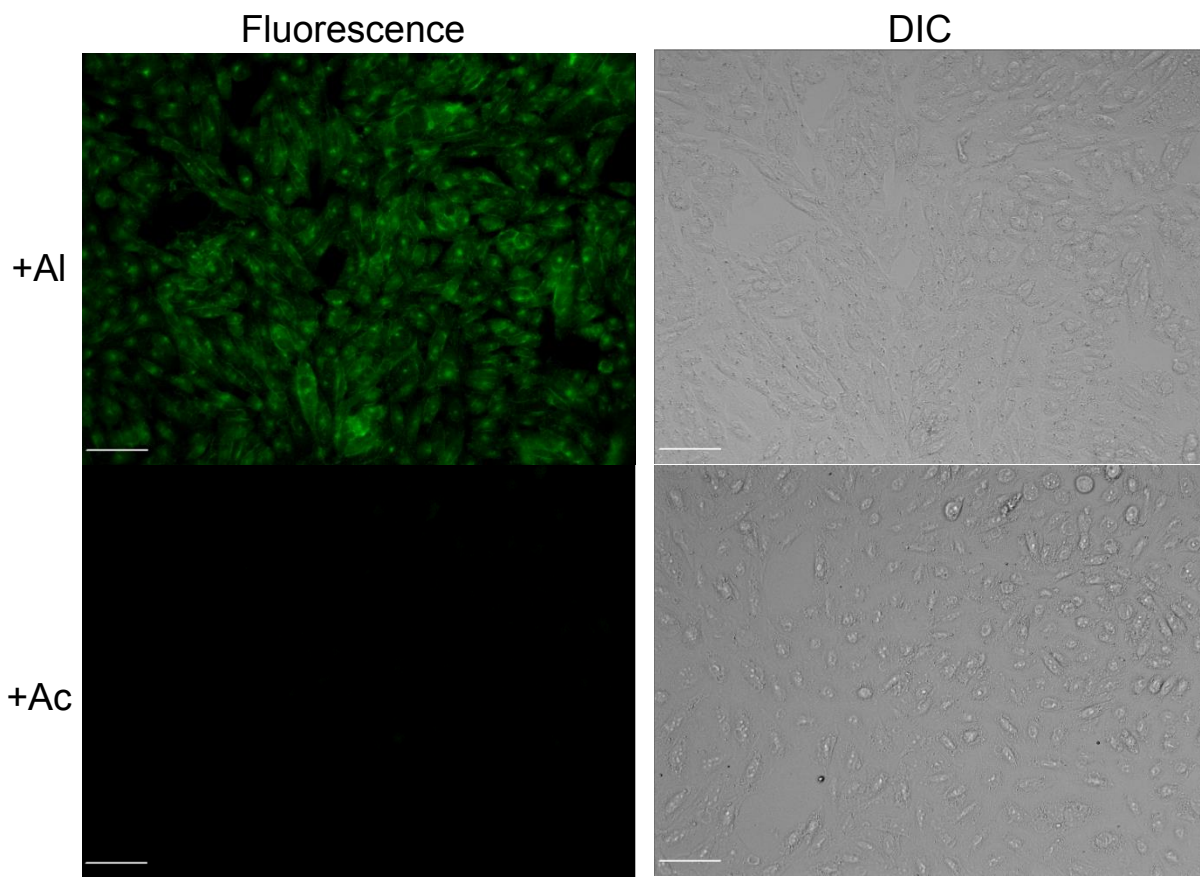


Figure 2-8. Cell-surface labeling by **2.1** (25 μ M from a 5 mM stock in tBuOH) is alkyne-dependent. Scale bar = 50 μ m. FITC filter, fluorescence cut-off at 210 to 600.

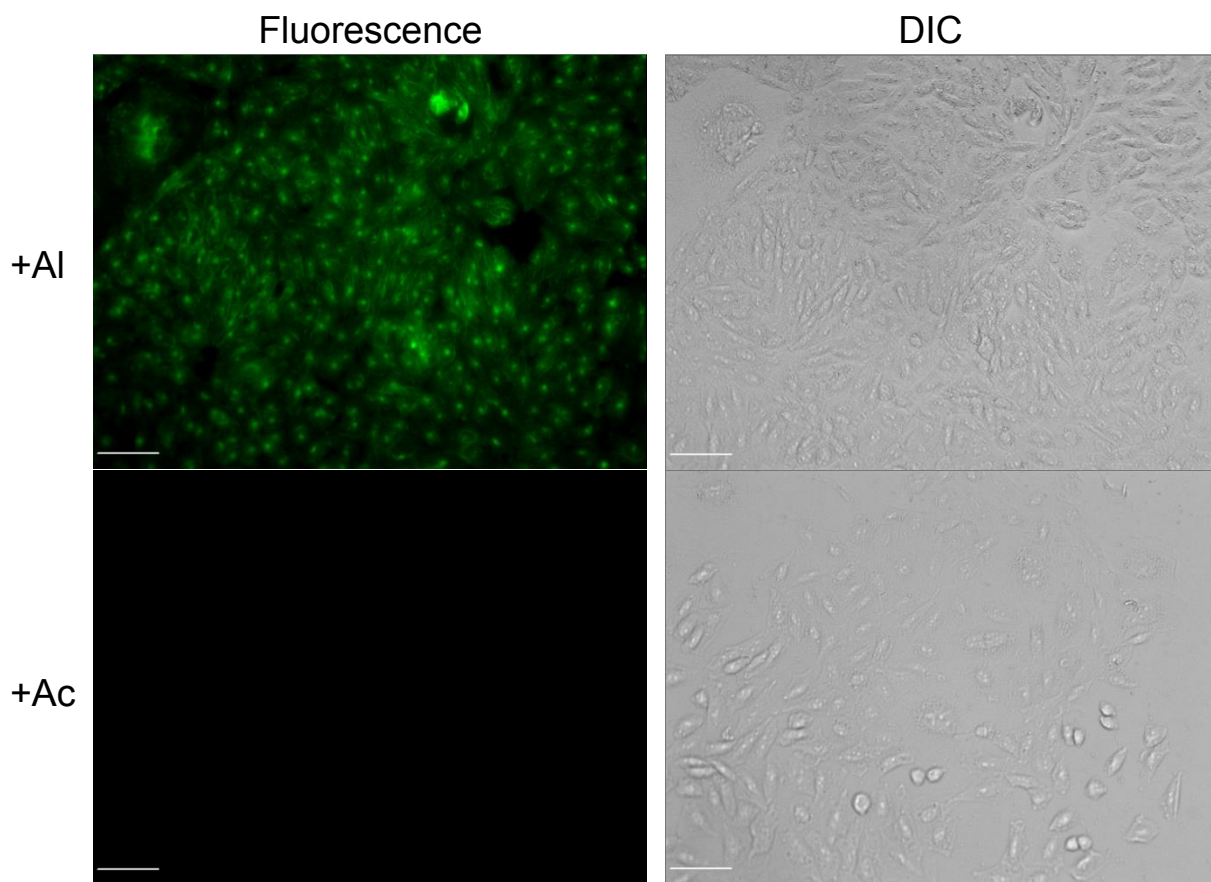


Figure 2-9. Cell-surface labeling by 5-azidofluorescein (25 μM from a 5 mM stock in DMSO) is alkyne-dependent. Scale bar = 50 μm . FITC filter, with fluorescence cut-off at 250 to 1500.

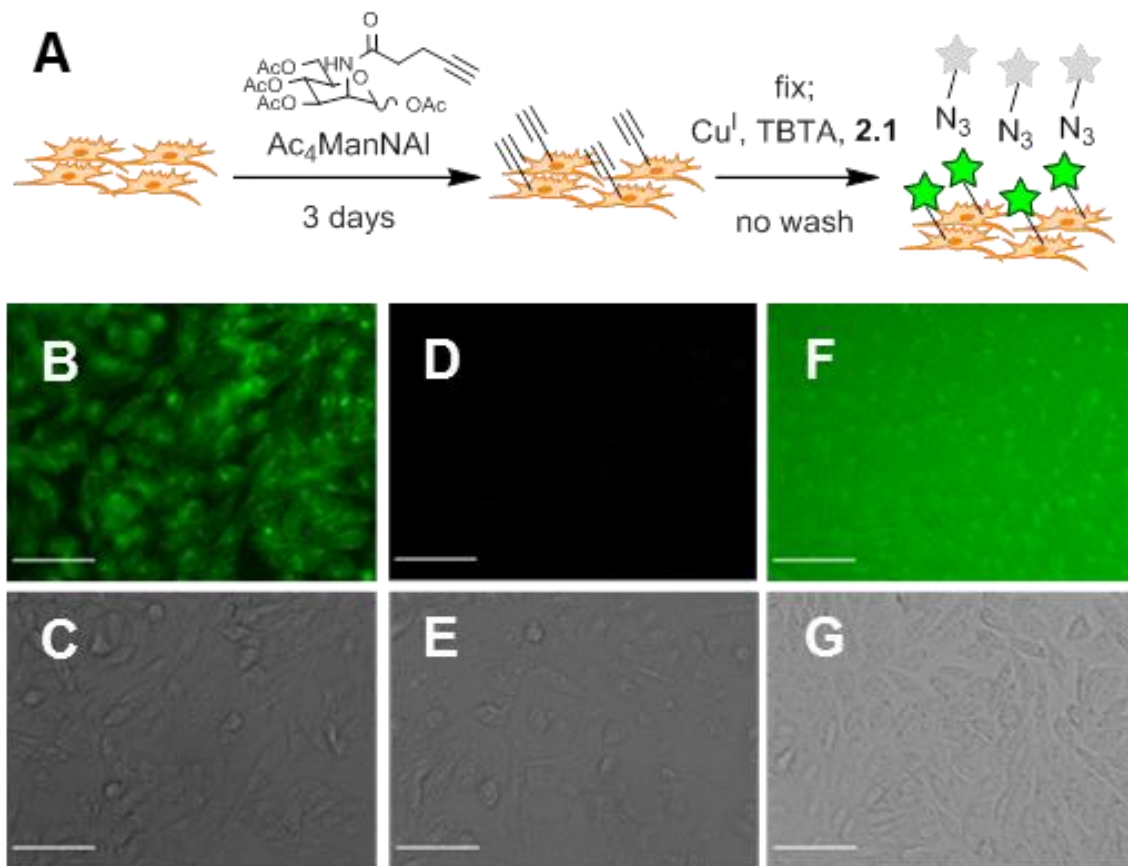


Figure 2-10. No-wash cell labeling with azidofluorescein probes. (A) Outline of the no-wash labeling experiment using Ac₄ManNAI and **2.1**. CHO cells were metabolically labeled with Ac₄ManNAI or Ac₄ManNAc for 3 d. The cells were then then reacted with 25 μM probe as well as the other reagents for Cu-catalyzed click chemistry for 1 h. (B)-(G). Top row: fluorescence images; Bottom row: corresponding DIC images. (B),(C) Ac₄ManNAI-treated cells reacted with **2.1** (inset shows a 3-fold magnification to highlight cell-surface labeling). (D),(E), Ac₄ManNAc-treated cells reacted with **2.1**. (F),(G), Ac₄ManNAI-treated cells reacted with 5-azidofluorescein. Scale bar = 50 μm. Exposure time/fluorescence cutoffs were 150 ms/150-400 for (B), (D) and 10 ms/500-900 for (F).

A potential problematic side reaction of aryl azides is their reduction to the corresponding anilines by endogenous thiols. This reaction has been demonstrated to proceed under physiological conditions,³¹ and indeed it undermined the use of azidonaphthalimide **2.15** as biological imaging reagents.⁷ While **2.15** was reported to undergo a significant fluorescence increase upon click reaction to form a triazole, reduction also resulted in a 60-fold enhancement in fluorescence (Figure 2-11A). Aryl azide reduction has also been used to detect intracellular hydrogen sulfide, and **2.15** was shown to be an efficient sensor of hydrogen sulfide inside living cells.^{32,33} Calculations indicate that this reduction pathway would not be an issue for **2.1**, as the predicted aryl E_{HOMO} value of the aniline reduction product is higher than that of the starting aryl azide (-0.189 Hartrees vs. -0.210 Hartrees). To demonstrate this experimentally, we reduced **2.1** with dithiothreitol and measured the fluorescence quantum yield of the arylamine product

reduced 2.1. As expected, reduction resulted in a four-fold decrease in fluorescent quantum yield at pH 7.4 from 0.024 to 0.0067, indicating that, if this side reaction occurs *in vivo*, it would not contribute significantly to background fluorescence (Figure 2-11B, Table 2-2).

Beyond thiols, azide reduction may also occur via photolysis, forming a transient nitrene that can be converted to the amine via sigma bond insertion. Photolysis of aryl azides is a commonly used strategy for photocrosslinking endogenous biomolecules, although UV light is typically required. Such photolysis was problematic for previously described azide probes, including azidonaphthalimide **2.15**, because of direct conjugation of the azide with the chromophore. As the chromophore is more effective at capturing ambient light as compared to simple aryl rings, **2.15** suffers from poor photostability, often decomposing to highly fluorescent byproducts. For our PeT-based fluorogenic azide probes, as the azide is not directly conjugated to the xanthene, visible-light mediated azide photolysis occurs with low efficiency. As described above, since reduction results in a decrease in fluorescence for probe **2.1**, this side-reaction can actually improve signal over background. While transient nitrenes can also rearrange to form a didehydroazepine, this pathway is disfavored in fused aryl systems such as naphthalenes due to higher ring strain of the azepine intermediate.³⁵ We have found that some photolysis can still occur using the azidonaphthyl switch of **2.1**. Fluorophores with improved photostability can be developed by moving to other aryl azide switches with less conjugated pi-systems, as described later in this dissertation.

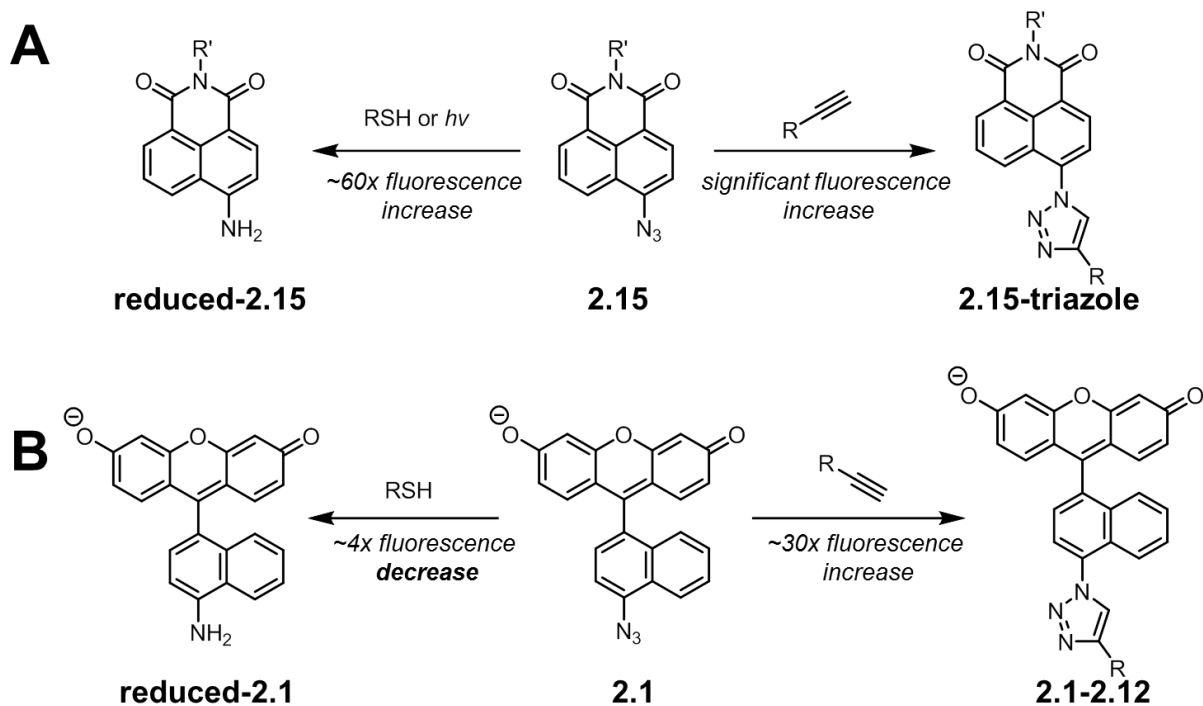


Figure 2-11. Consequences of aryl azide reduction. (A) Azidonaphthalimide probe **2.15** undergoes significant fluorescence enhancement upon reduction by reaction with thiols or light. (B) **2.1** undergoes a reduction in fluorescence upon conversion to the amine under similar conditions.

Conclusion

In summary, by taking advantage of the observed relationship between E_{HOMO} of a pendant aryl substituent and fluorescence quantum yield, we were able to identify potential fluorogenic azidofluoresceins, and demonstrated the suitability of azidofluorescein **2.1** for no-wash imaging of cells. We anticipate that this general strategy will be useful for the development of fluorogenic alkynyl fluorescein analogs as well. Indeed, calculations indicate that conversion of aryl alkynes to the corresponding triazoles results in a significant increase in E_{LUMO} . In principle, alkynyl fluoresceins that are internally quenched by PeT, in this case from the xanthene to the aryl ring, should undergo fluorescence enhancement upon triazole formation.³⁶ In addition, the extension of the design principle to red-shifted fluorophores seemed reasonable given the generality of PeT, which we pursued in work discussed in the next chapter.

Experimental Procedures

Density functional theory (DFT) calculations

Geometries were optimized and HOMO energy levels were calculated using the Gaussian 09 software package at the B3LYP/6-31G(d) level of theory, as reported previously.¹⁴ Calculations were performed at the UC Berkeley College of Chemistry Molecular Graphics and Computation Facility. Structures were truncated to simplify calculations. Azidofluoresceins were predicted to exist primarily in the anionic form at pH 7.4, so the trend derived at pH 13 was used to identify target compounds for synthesis.

Measuring fluorescence quantum yield

Fluorescence quantum yield measurements were performed following literature procedure.³⁷ 2 mM solutions of the compounds in MeOH were diluted in phosphate buffered saline (PBS) for measurements at pH 7.4 or 0.1 M NaOH (aq) for measurements at pH 13. Similar measurements were made for a standard of known fluorescence quantum yield (fluorescein in 0.1 M NaOH, $\Phi = 0.85$). The reported quantum yields are the average of three measurements. Absorbance spectra were recorded on a Varian Cary 50 UV-Visible spectrophotometer. Fluorescence spectra were recorded on a Photon Technology International Quanta Master 4 L-format scanning spectrofluorometer equipped with an LPS-220B 75-W xenon lamp and power supply, A-1010B lamp housing with an integrated igniter, switchable 814 photon counting/analog photomultiplier detection unit, and MD5020 motor driver. Measurements were made in 1 cm x 0.2 cm quartz cuvettes with a total sample volume of 1 mL.

Plate-reader fluorescence measurements

Reactions were run in a 96-well black-bottom plate, and measurements were made using a Molecular Devices SpectraMax M3 Multi-mode Microplate Reader. Each well contained 200 μ L of sample containing 1.5 μ M **2.1**, 5 mM sodium ascorbate, 50 μ M CuSO₄, 100 μ M ligand, and 100 μ M alkyne **2.12** in 95:5 0.1 M pH 7.4 potassium phosphate buffer (KPi)/DMSO. The ligands, THPTA²⁷ and BTAA²⁸, have been shown to efficiently catalyze the azide-alkyne [3+2] cycloaddition in the presence of micromolar concentrations of copper, and their relative efficiencies have been evaluated using a similar plate-reader assay.²⁸ To make these solutions, to each well was added 160.4 μ L pH 7.4 KPi, 6 μ L DMSO, 0.2 μ L of 50 mM CuSO₄ in H₂O, 10 μ L of freshly-prepared 100 mM sodium ascorbate in pH 7.4 KPi, and 0.4 μ L of 50 mM ligand in H₂O. Immediately before measurements were made, 3 μ L of 50 μ M **2.1** in DMSO and 20 μ L 1 mM alkyne in 95:5 pH 7.4 KPi/DMSO were added. For measurements without alkyne, 20 μ L 95:5 pH 7.4 KPi/DMSO was added instead. The plate was shaken for 8 seconds, then fluorescence measurements (excitation/emission at 500/515 nm) were taken every minute for 1 h. Runs were performed in triplicate.

Protein labeling with 2.1

Bovine serum albumin (BSA) was incubated with either 4-pentynoyl or 4-pentenoyl NHS ester to generate the corresponding alkyne- and alkene- labeled BSA. 5 mg BSA was incubated with

450 μ L pH 8.4 0.1 M potassium phosphate buffer and 50 μ L 12 mM NHS-ester in DMSO at 4 $^{\circ}$ C overnight (18 h). The reaction was diluted w/ 10 mL pH 7.4 phosphate-buffered saline (PBS), then concentrated using Amicon Ultra-15 centrifugal filter unit with a 30K MWCO at 3750 x g for 10 minutes at 4 $^{\circ}$ C to remove any remaining NHS-ester. The dilution and filtration were repeated two more times. ESI analysis of the collected protein indicated an average of 3 modifications for 4-pentynoyl NHS ester and 10 modifications for 4-pentenoyl NHS ester. 0.5 mg/mL stocks of protein in pH 7.4 PBS were prepared based off A_{280} . For the labeling experiment, 0.44 mg/mL protein in 95:5 pH 7.4 PBS/tBuOH was incubated with 100 μ M TBTA, 2 mM sodium ascorbate, 0 or 1 mM CuSO_4 , and 0 or 50 μ M **2.1** at rt for 1 h in the dark. Specifically, to 88.5 μ L of 0.5 mg/mL protein in PBS was added 2.5 μ L of 4 mM TBTA in DMSO, 2 μ L of 100 mM freshly-prepared sodium ascorbate in PBS, 2 μ L of 50 mM CuSO_4 in H_2O or 2 μ L pH 7.4 PBS, and 5 μ L 1 mM **2.1** in tBuOH or just tBuOH. 30 μ L of each mixture was mixed with 10 μ L 4x SDS loading dye lacking β -mercaptoethanol, and 25 μ L of each was loaded onto a 10% Bis-Tris gel. The gel was run for 90 min at 180 V. The gel was imaged using the Typhoon 9410 Variable Mode Imager (excitation/emission at 488/520 nm) and stained with Coomassie.

Fixed cell labeling experiments

CHO K1 cells were grown in 8-well Lab-Tek Chambered Coverglass systems. Each well contained cells in 300 μ L F12 media containing fetal bovine serum, penicillin/streptomycin, and either 50 μ M Ac_4ManNAI or Ac_4ManNAc for 3 d at 37 $^{\circ}$ C, as described previously.^{29,30} The cells were then gently washed with 3 x 300 μ L pH 7.4 PBS, then fixed with 200 μ L chilled 3% w/v paraformaldehyde in pH 7.4 PBS for 20 min at 4 $^{\circ}$ C. The fixed cells were washed with 3 x 300 μ L PBS, then incubated with 200 μ L PBS containing 25 μ M dye, 10.0 μ M TBTA, 1 mM CuSO_4 , 2 mM sodium ascorbate, and 0.1 mg/mL BSA in the dark at rt for 1 h. BSA was found to help keep the reagents in solution during the labeling period. Specifically, to each well was added 195 μ L of solution containing 146 μ L PBS, 40 μ L 0.5 mg/mL BSA in PBS, 5 μ L of 4 mM TBTA in DMSO, and 4 μ L of 100 mM freshly prepared sodium ascorbate in PBS. 1 μ L of 5 mM dye in tBuOH or DMSO, then 4 μ L of 50 mM CuSO_4 in H_2O were added to initiate the reaction. The cells were then taken directly on for imaging for no-wash labeling experiments. For labeling experiments with washing, the cells were first washed with 3 x 300 μ L PBS, then covered in 200 μ L PBS before imaging. Microscopy was performed using a Zeiss AxioVert 200M inverted microscope using a Plan-Neofluar 20x/0.75 objective. A 175W xenon lamp housed in a Sutter DG4 illuminator linked to the microscope by an optical fiber assured shuttering and illumination. Exposure time was 150 ms for all images except for no-wash imaging with 5-azidofluorescein, which required an exposure time of 10 ms to prevent saturation of the detector. Images were acquired and processed using SlideBook 5.0, and are shown as a single z-plane.

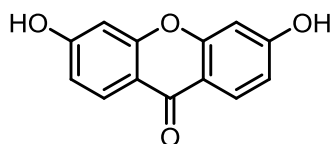
Synthetic procedures

All chemical reagents obtained from commercial suppliers were used without further purification. All reactions were performed in oven- or flame-dried glassware under an inert atmosphere, unless otherwise noted. Anhydrous dichloromethane, tetrahydrofuran and acetonitrile were either dried over CaH_2 and freshly distilled or passed through an activated alumina column prior to use. Anhydrous DMF was used as purchased. Water was either double

distilled or passed through a Milli-Q filtration system prior to use. Tris-(benzyltriazolymethyl)amine (TBTA)³⁸, DIFO³⁹, DIMAC²⁴, BTTAA²⁸, and Ac₄ManNAI³⁰ were prepared according to literature procedures. THPTA was generously provided by the M.G. Finn group (Georgia Institute of Technology).

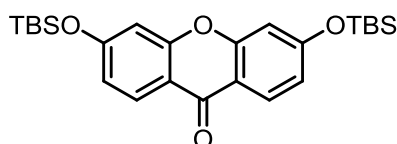
Flash chromatography was performed using Merck 60 Å 230-400 mesh silica gel or Silicycle SiliaFlash P60 silica gel. Analytical thin layer chromatography was performed using glass-backed Analtech Uniplate silica gel plates containing a fluorescent indicator. Reversed-phase HPLC was performed on a Varian Pro Star system with a Varian UV-Vis detector model 345 (210, 254 nm) on a Dynamax Microsorb C-18 preparative column (21.4 x 250 mm) at a flow rate of 20 mL/min or on a Dynamax Microsorb C-18 semi-preparative column (10.0 x 250 mm) at a flow rate of 3 mL/min.

NMR spectra were obtained on Bruker AVQ-400, AVB-400 or DRX-500 spectrometers at ambient temperature at the UC Berkeley College of Chemistry NMR Facility. ¹³C resonances are unassigned and reported as observed. ¹H NMR shifts are calibrated to residual undeuterated solvent: δ 7.26 for CHCl₃, 2.50 for d₅-DMSO, and 3.31 for CHD₂OD. ¹³C NMR shifts are calibrated to solvent peaks: δ 77.16 for CDCl₃, 39.52 for d₆-DMSO, and 49.00 for CD₃OD. Low resolution mass spectrometry was performed using an Agilent 6120 Single Quad mass spectrometer. High resolution mass spectrometry was performed at the UC Berkeley Mass Spectrometry Laboratory. Uncorrected melting points were determined using a Thomas Hoover capillary melting point apparatus.



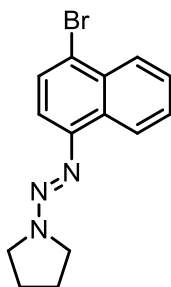
Known **2.16**⁴⁰ was prepared according to literature procedure with minor modifications.⁴⁰ In brief, bis(2,4-dihydroxyphenyl)methanone (4.92 g, 20 mmol), a bright yellow solid, was suspended in 40 mL H₂O in a pressure tube behind a blast shield. The sealed pressure tube was heated to 180 °C for 72 h, during which the solid dissolved and a salmon-colored precipitate gradually began to form. The vessel was then allowed to cool to 80 °C, upon which the tube was opened and the contents immediately poured out and filtered. The solids were further washed with water, yielding analytically pure **2.16** (4.49 g, 98%) as a salmon colored solid that was carried directly onto the next step.

R_f = 0.30 (10:1 CHCl₃/MeOH); ¹H NMR (400 MHz, d₆-DMSO): δ 6.81, (d, 2H, *J* = 2.2 Hz), 6.85 (dd, 2H, *J* = 8.8 Hz, 2.2 Hz), 7.98 (d, 2H, *J* = 8.8 Hz), 10.82 (s, 2H); ¹³C NMR (100 MHz, d₆-DMSO): δ 102.15, 113.69, 114.18, 127.89, 157.64, 163.37, 174.13. HRMS (ESI): Calculated for C₁₃H₉O₄ [M+H]⁺: 229.0495, found 229.0497.



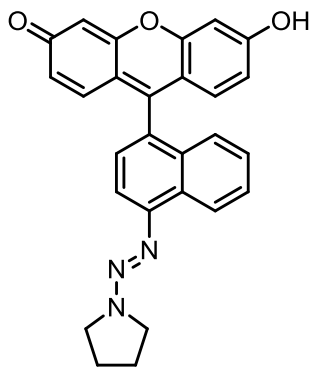
Known **2.5**²⁰ was prepared according to literature procedure with minor modifications.²⁰ In brief, **2.16** (5.67 g, 24.85 mmol) was dissolved in 50 mL anhydrous DMF. The salmon colored solution was cooled to 0 °C in an ice bath, then *tert*-butyldimethylsilyl chloride (22.47 g, 149.1 mmol) and imidazole (16.92 g, 248.5 mmol) were added. Upon addition of the imidazole, the salmon colored solution into a thick white slurry. The slurry was allowed to warm to rt and stirred for 4 h. Then, the reaction was diluted with 300 mL toluene and the reaction washed with 5 x 200 mL H₂O, dried over MgSO₄, and concentrated *in vacuo*, yielding an off-white wet solid. The solid was taken up in 100 mL pentane and the undissolved solid was collected by filtration. The filtrate was concentrated *in vacuo* and this procedure was repeated twice more with 50 mL pentane to collect more product. The collected solids were combined and further dried *in vacuo* to yield **2.5** (8.05 g, 71%) as a free-flowing white powder.

R_f = 0.70 (4:1 hexanes/EtOAc); ¹H NMR (400 MHz, CDCl₃): δ 0.24 (12H, s), 0.98 (18H, s), 6.80 (2H, s), 6.81, (d, 2H, *J* = 8.6 Hz), 8.16 (d, 2H, *J* = 8.6Hz); ¹³C NMR (100 MHz, CDCl₃): δ -4.08, 25.83, 107.62, 116.72, 117.84, 128.47, 158.02, 161.63, 175.99. HRMS (ESI): Calculated for C₂₅H₃₇O₄Si₂ [M+H]⁺ 457.2225, found 457.2233.



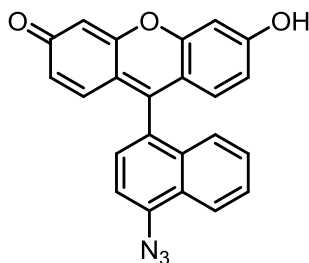
1-amino-4-bromonaphthalene (4.50 g, 20.3 mmol), a grey powder, was suspended in 34 mL concentrated HCl and cooled to 0 °C. A solution of NaNO₂ (1.398 g, 20.3 mmol) in 2.25 mL ice cold water was added dropwise, turning the grey suspension a greenish color. The resulting solution of diazonium salt was stirred for 10 min at 0 °C, then poured into a chilled solution of pyrrolidine (1.60 g, 1.85 mL, 22.5 mmol) in 67.5 mL 1 M KOH, resulting in a considerable warming and formation of a brown solution. The reaction mixture was stirred for 1 h at 0 °C, brought to pH 12 with the careful addition of 10 M KOH, extracted with 2 x 150 mL CH₂Cl₂, dried over MgSO₄, and concentrated *in vacuo* to yield a red solid. The solid was purified by flash chromatography on silica gel (hexanes to 10:1 hexanes/EtOAc) to yield **2.7** (3.93 g, 64%) as a dark red solid.

R_f = 0.20 (10:1 hexanes/EtOAc); m.p. 74-75 °C (decomp); ¹H NMR (400 MHz, CDCl₃): δ 1.95 (m, 4H), 3.85 (m, 4H), 7.46 (d, 1H, *J* = 8.4 Hz), 7.66 (m, 2H), 7.84 (d, 1H, *J* = 8.0 Hz), 8.33 (m, 1H), 8.81 (m, 1H); ¹³C NMR (100 MHz, CDCl₃): δ 23.64, 23.89, 46.78, 51.13, 111.92, 118.53, 124.42, 125.90, 126.81, 127.31, 130.15, 130.59, 132.41, 146.67; HRMS (ESI): Calculated for C₁₄H₁₅N₃Br [M+H]⁺ 304.0449, found 304.0454.



2.7 (0.912 g, 3.00 mmol), a deep red solid, was dissolved in 12 mL anhydrous THF. The deep red solution was cooled to $-78\text{ }^{\circ}\text{C}$. Then, *tert*-butyllithium (1.31 M in pentanes, 4.58 mL, 6.00 mmol) was slowly added down the side of the flask. The now red-brown solution was stirred at $-78\text{ }^{\circ}\text{C}$ for 30 min. Then, **2.5** (1.50 g, 3.30 mmol), dissolved in 2 mL anhydrous THF, was slowly added. The reaction was stirred at $-78\text{ }^{\circ}\text{C}$ for 2 h, then warmed to rt and quenched with 2 mL 2 M HCl. After stirring for 15 minutes, the reaction was neutralized with 1 mL 1 M NaOH. The solvent was removed *in vacuo* and the remaining red residue was purified by flash chromatography on silica gel (CHCl_3 to 10:1 CHCl_3), yielding **2.8** (0.839 g, 64%) as a red-orange solid.

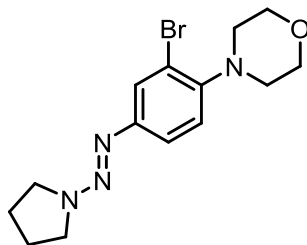
$R_f = 0.40$ (10:1 $\text{CHCl}_3/\text{MeOH}$); m.p. $283\text{--}285\text{ }^{\circ}\text{C}$; $^1\text{H NMR}$ (400 MHz, d_6 -DMSO): δ 3.76 (m, 4H), 3.98 (m, 4H), 6.45 (m, 2H), 6.55 (m, 2H), 6.76 (m, 2H), 7.45 (m, 5H), 8.65 (m, 1H); $^{13}\text{C NMR}$ (100 MHz, d_6 -DMSO): δ 23.46, 23.89, 47.33, 51.49, 102.49, 103.77, 110.88, 115.90, 122.06, 124.33, 125.49, 126.21, 126.60, 127.57, 128.36, 128.77, 130.70, 132.46, 147.72, 149.38, 156.77; HRMS (ESI): Calculated for $\text{C}_{27}\text{H}_{22}\text{N}_3\text{O}_3$ $[\text{M}+\text{H}]^+$ 436.1661, found 436.1653.



2.8 (0.218 g, 0.50 mmol), a red-orange powder, was suspended in 50 mL water and cooled to $0\text{ }^{\circ}\text{C}$. NaN_3 (3.25 g, 50.00 mmol) was then added. After the NaN_3 had dissolved, 25 mL concentrated HCl was carefully added, turning the suspension a greenish-blue color. **[Caution: Addition of NaN_3 to acid results in formation of hydrazoic acid, which is hazardous. Therefore, perform this addition in a well-ventilated hood with proper protection.]** The solution was stirred at $0\text{ }^{\circ}\text{C}$ for 90 min, upon which the red-orange color had returned. The reaction was neutralized with the slow addition of 40 mL 10M NaOH, then the ice bath removed and the reaction stirred at rt for 10 min. Then, 2M HCl was added dropwise until the pH reached $\sim 5\text{--}6$ and a red precipitate had formed. The solid was collected by filtration, washed with 2 x 30 mL H_2O , then taken up in MeOH and concentrated to yield crude product as a red-orange solid. The solid was taken up in MeOH and 0.05 mL 10M NaOH was added, turning the solution a deep red color.

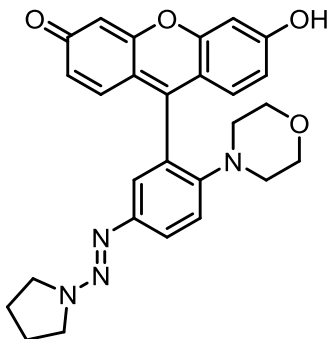
The solvent was removed *in vacuo* to yield the sodium salt of **2.1**, which as purified in batches by preparative reversed-phase HPLC with a 30 min gradient from 40% to 100% MeCN in H₂O to yield analytically pure **2.1** (100 mg, 50% for sodium salt) as a red solid.

R_f = 0.45 (10:1 CHCl₃/MeOH); ¹H NMR (500 MHz, d₆-DMSO): δ 6.09 (dd, 2H, *J* = 9.3 Hz, 2.1 Hz), 6.13 (d, 2H, *J* = 2.0 Hz), 6.48 (d, *J* = 9.3 Hz, 2H), 7.50 (d, 8.4 Hz, 1H), 7.55 (t, 1H, *J* = 7.5 Hz), 7.59 (d, 1H, *J* = 7.7 Hz), 7.64 (t, 1H, *J* = 7.3 Hz), 7.66 (d, 1H, *J* = 7.5 Hz), 8.19 (d, 1H, *J* = 8.6 Hz), ¹³C NMR (125 MHz, d₆-DMSO): δ 103.37, 110.17, 114.36, 122.56, 123.53, 125.52, 125.72, 126.96, 127.56, 128.13, 128.40, 129.65, 132.31, 136.78, 148.02, 157.49, 179.90; HRMS (ESI): Calculated for C₂₃H₁₂N₃O₃ [M-H]⁻ 378.0884, found 378.0889.



3-bromo-4-(4-morpholinyl)benzenamine (500 mg, 1.95 mmol) was dissolved in 0.4 mL concentrated HCl and cooled to 0 °C. A solution of NaNO₂ (134 mg, 1.95 mmol) in 0.2 mL cold H₂O was added dropwise. The resulting solution of diazonium salt was stirred for 10 min and then added all at once to a chilled solution of pyrrolidine (0.18 mL, 2.1 mmol) in 1.67 mL 1 M KOH. The reaction mixture was stirred for 30 min at 0 °C, then diluted with 5 mL H₂O, extracted with CH₂Cl₂ and dried over MgSO₄. The crude product was concentrated *in vacuo* and purified by flash chromatography on silica gel (CH₂Cl₂ to 20:1 CH₂Cl₂/MeOH) to yield **2.17** (456.2 mg, 69%) as dark red crystals.

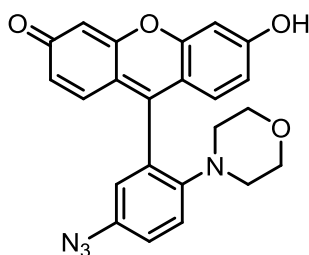
m.p. 131-132 °C (decomp); ¹H NMR (400 MHz, CDCl₃): δ 2.01 (m, 4H), 3.02 (m, 4H), 3.76 (m, 4H), 3.87 (m, 4H), 7.00 (d, 1H, *J* = 8.4 Hz), 7.32 (dd, 1H, *J* = 8.4, 2.0 Hz), 7.68 (d, 1H, *J* = 2.0 Hz); ¹³C NMR (100 MHz, CDCl₃): δ 18.42, 18.42, 52.29, 67.21, 120.15, 120.62, 120.63, 124.84, 147.20, 148.12; HRMS (ESI): Calculated for C₁₄H₂₀N₄OBr [M+H]⁺ 339.0820, found 339.0829.



2.17 (218 mg, 0.644 mmol) was dissolved in 4 mL anhydrous THF and the solution was cooled to -78 °C. *tert*-butyllithium (0.42 mL of 1.7 M solution in pentane, 0.708 mmol) was added dropwise. The resulting solution was stirred for 10 min at -78 °C and then **2.5** (323 mg, 0.708

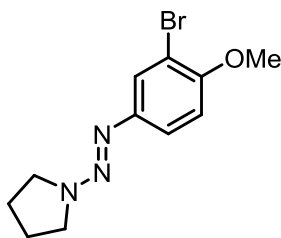
mmol) predissolved in 2 mL anhydrous THF cooled to $-78\text{ }^{\circ}\text{C}$ was added dropwise. The solution was stirred for 1 h at $-78\text{ }^{\circ}\text{C}$, then diluted with 2 mL H_2O by dropwise addition and adjusted to pH 1 with concentrated HCl. The solution was warmed to rt and stirred overnight, then neutralized with KOH. The crude product was concentrated *in vacuo* and purified by flash chromatography on silica gel (CH_2Cl_2 to 10:1 $\text{CH}_2\text{Cl}_2/\text{MeOH}$) to yield **2.18** (155 mg, 51%) as a dark red solid.

m.p. $249\text{--}250\text{ }^{\circ}\text{C}$; ^1H NMR (400 MHz, CDCl_3): δ 1.99 (m, 4H), 2.76 (m, 4H), 3.28 (m, 4H), 3.74 (m, 4H), 6.88 (m, 4H), 7.20 (m, 1H), 7.30 (m, 3H), 7.56 (d, 1H, $J = 8.8\text{ Hz}$), 8.49 (br s, 1H); ^{13}C NMR (100 MHz, CDCl_3): δ 23.74, 23.74, 52.05, 66.82, 103.53, 114.24, 120.45, 121.78, 122.72, 123.17, 127.62, 131.88, 147.06, 147.97, 155.35, 158.20, 175.60; HRMS (ESI): Calculated for $\text{C}_{27}\text{H}_{27}\text{N}_4\text{O}_4$ $[\text{M}+\text{H}]^+$ 471.2032, found 471.2025.



2.18 (117 mg, 0.248 mmol) was dissolved in 15 mL 2:1 $\text{H}_2\text{O}/\text{MeOH}$ and cooled to $0\text{ }^{\circ}\text{C}$. NaN_3 (1.61 g, 24.8 mmol) was added, followed by 5 mL concentrated HCl. **[Caution: Addition of NaN_3 to acid results in formation of hydrazoic acid, which is hazardous. Therefore, perform this addition in a well-ventilated hood with proper protection.]** The solution was stirred at $0\text{ }^{\circ}\text{C}$ for 3 h, then the MeOH was removed *in vacuo*. The remaining solution was neutralized with sat. NaHCO_3 and extracted with CH_2Cl_2 . The organic layer was then removed and concentrated *in vacuo* to yield **2.2** (87 mg, 85%) as an orange solid. For analytical experiments, a small quantity of **2.2** was further purified by semi-preparative reversed-phase HPLC.

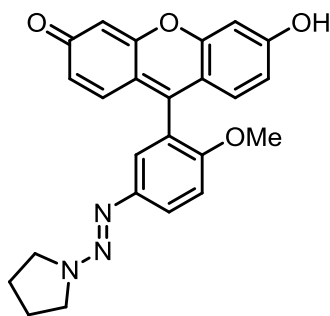
m.p. $252\text{--}253\text{ }^{\circ}\text{C}$; ^1H NMR (400 MHz, CD_3OD): δ 2.77 (m, 4H), 3.26 (m, 4H), 6.71 (m, 3H), 6.74 (m, 1H), 6.98 (m, 1H), 7.25 (m, 2H), 7.32 (m, 1H), 7.40 (m, 1H); ^{13}C NMR (100 MHz, CD_3OD): δ 50.20, 64.88, 101.32, 112.36, 113.64, 119.68, 119.81, 120.27, 127.41, 129.72, 130.05, 134.01, 146.54, 150.96, 156.41; HRMS (ESI): Calculated for $\text{C}_{23}\text{H}_{19}\text{N}_4\text{O}_4$ $[\text{M}+\text{H}]^+$ 415.1406, found 415.1412.



3-bromo-4-methoxyaniline (985 mg, 4.87 mmol) was suspended in 20 mL concentrated HCl and cooled to $0\text{ }^{\circ}\text{C}$. A solution of NaNO_2 (342 mg, 4.95 mmol) in 2 mL cold H_2O was added

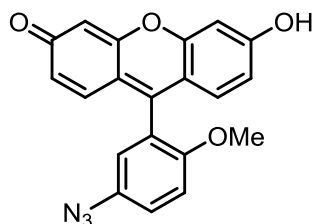
dropwise. The resulting solution of diazonium salt was stirred for 10 min and then added all at once to a chilled solution of pyrrolidine (0.45 mL, 5.5 mmol) in 12 mL 1 M KOH. The reaction mixture was stirred for 30 min at 0 °C and then diluted with 50 mL H₂O, brought to pH 12 with KOH, extracted with CH₂Cl₂ and dried over Na₂SO₄. The solution was filtered and concentrated *in vacuo* to yield **2.19** (1.34 g, 97%) as a dark red solid.

m.p. 79-81 °C (decomp); ¹H NMR (400 MHz, CDCl₃): δ 1.88 (m, 4H), 3.65 (m, 4H), 3.77 (s, 3H), 6.78 (d, 1H, *J* = 8.8 Hz), 7.27 (dd, 1H, *J* = 8.4, 2.4 Hz), 7.64 (d, 1H, *J* = 2.4 Hz); ¹³C NMR (100 MHz, CDCl₃): δ 23.73, 23.73, 46.67, 50.61, 56.35, 111.73, 111.83, 120.95, 124.12, 145.89, 153.23; HRMS (ESI): Calculated for C₁₁H₁₅N₃OBr [M+H]⁺ 284.0398, found 284.0393.



2.19 (750 mg, 2.61 mmol) was dissolved in 7.5 mL anhydrous THF and cooled to -78 °C. *tert*-butyllithium (1.54 mL of 1.7 M solution in pentane, 2.61 mmol) was added dropwise. The resulting solution was stirred for 30 min at -78 °C and then **2.5** (1.31 g, 2.87 mmol) predissolved in 10 mL THF cooled to -78 °C was added dropwise. The solution was stirred for 2 h at -78 °C, then diluted with 50 mL water by dropwise addition and adjusted to pH 1 with concentrated HCl. The solution was warmed to rt and stirred for 10 min, then neutralized with sat. NaHCO₃. The crude product was concentrated *in vacuo* and purified by flash chromatography on silica gel (CH₂Cl₂ to 10:1 CH₂Cl₂/MeOH) to yield **2.20** (497 mg, 46%) as an orange solid.

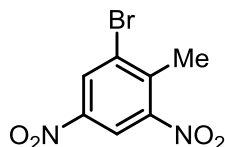
m.p. 270-272 °C; ¹H NMR (400 MHz, d₆-DMSO): δ 3.48 (m, 8H), 3.66 (s, 3H), 6.52 (m, 4H), 6.93 (d, 2H, *J* = 9.6 Hz), 7.20 (m, 2H), 7.48 (d, 1H, *J* = 8.0); ¹³C NMR (100 MHz, d₆-DMSO): δ 23.66, 23.66, 56.29, 103.64, 112.73, 114.72, 121.42, 121.76, 123.29, 130.74, 144.86, 147.91, 153.19, 154.31, 156.22, 156.68; HRMS (FAB): Calculated for C₂₄H₂₂N₃O₄ [M+H]⁺ 416.1610, found 416.1612.



2.20 (251 mg, 0.604 mmol) was suspended in 56 mL water and cooled to 0 °C. NaN₃ (3.93 g, 40 mmol) was added, followed by 28 mL concentrated HCl. **[Caution: Addition of NaN₃ to acid results in formation of hydrazoic acid, which is hazardous. Therefore, perform this addition in a well-ventilated hood with proper protection.]** The solution was stirred at 0 °C for 2 h and as

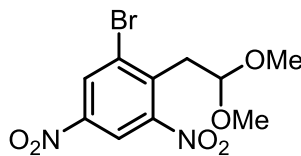
neutralized with sat. NaHCO_3 and extracted with CH_2Cl_2 . The organic layer was dried over Na_2SO_4 , filtered, and concentrated *in vacuo* to yield **2.3** (215 mg, 99%) as an orange solid. For analytical experiments, a small quantity of **2.3** was further purified by semi-preparative reversed-phase HPLC.

m.p. 254-255 °C; ^1H NMR (400 MHz, d_6 -DMSO): δ 3.65 (s, 3H), 6.10 (m, 2H), 6.20 (m, 2H), 6.65 (m, 2H), 6.97 (m, 1H), 7.19 (m, 2H); ^{13}C NMR (100 MHz, d_6 -DMSO): δ 56.42, 103.49, 109.99, 113.66, 121.40, 121.44, 123.63, 124.12, 129.94, 132.15, 146.97, 154.34, 157.66, 179.76; HRMS (FAB): Calculated for $\text{C}_{20}\text{H}_{14}\text{N}_3\text{O}_4$ $[\text{M}+\text{H}]^+$ 360.0984, found 360.0985.



Known **2.21**^{41,42} was synthesized based off of literature procedure.⁴³ 1-methyl-2,4-dinitrobenzene (10.93 g, 66.0 mmol), an off-white crystalline solid, was added to a flask containing 30 mL H_2SO_4 . The suspension was heated to 60 °C, upon which the solid had dissolved. To this clear solution was added N-bromosuccinimide (14.13 g, 79.0 mmol) in three portions over 20 min. After the first addition, the solution warmed significantly and began to take on a reddish color. Once all the N-bromosuccinimide had been added, the flask was gently capped with a Teflon cap and the reaction was stirred for 2.5 h at 60 °C. The now pink reaction mixture was cooled to ~40 °C, then poured into a beaker containing 100 g ice. The mixture immediately turned a cloudy white, with a red-orange liquid remaining at the bottom. This liquid solidified over the course of 15 min of standing at room temperature. The supernatant was poured out and this red-orange solid dissolved in 250 mL Et_2O . To this solution was added 200 mL 50% saturated $\text{Na}_2\text{S}_2\text{O}_3$, and turning the red solution a light yellow color. The aqueous layer was removed, and the organic layer was washed with 3 x 150 mL sat. NaHCO_3 (caution: gas evolution!), dried over MgSO_4 , and then concentrated *in vacuo* to yield **2.21** (13.71 g, 80%) as a white solid.

R_f = 0.60 (4:1 hexanes/ EtOAc); ^1H NMR (400 MHz, CDCl_3): δ 2.68 (s, 3H), 8.59 (d, 1H, J = 2.3 Hz), 8.65 (d, 1H, J = 2.3 Hz); ^{13}C NMR (125 MHz, CDCl_3): δ 20.13, 118.45, 120.08, 130.71, 139.78, 145.91, 150.89.

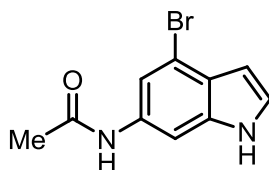


Known **2.9** was synthesized based off modifications of literature procedure.^{42,43} **2.21** (13.71 g, 52.5 mmol), an off-white solid, was dissolved in 40 mL anhydrous N,N-dimethylformamide. Then, to this pale yellow solution was added N,N-dimethylformamide dimethyl acetal (7.51 g, 8.37 mL, 63.02 mmol) was added, immediately turning the solution a dark blue color. The reaction was stirred for 18 h at rt, during which it turned a deep red color. The solvent was removed *in vacuo* to yield crude enamine as a deep red solid, which was carried directly onto the next step without further purification.

$R_f = 0.25$ (4:1 hexanes/EtOAc); $^1\text{H NMR}$ (400 MHz, CDCl_3): δ 2.96 (s, 6H), 5.26 (d, 1H, $J = 13.4$ Hz), 6.98 (d, 1H, $J = 13.4$ Hz), 8.29 (d, 1H, $J = 3.4$ Hz), 8.45 (d, 1H, $J = 3.4$ Hz).

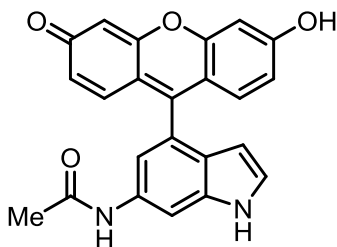
The enamine was dissolved in 105 mL MeOH. Then, 8.7 mL concentrated HCl was slowly added to the deep red solution. The reaction allowed to reflux for 5 h, during which its appearance changed to a cloudy brown. The reaction was cooled and diluted with 100 mL H_2O and 100 mL EtOAc. The organic layer was collected and the product was further extracted with 2 x 150 mL EtOAc. The combined organic layers were washed with saturated NH_4Cl , dried over MgSO_4 , and concentrated, yielding a deep brown oil. The compound was purified by flash chromatography on silica gel (hexanes to 10:1 hexanes/EtOAc) to yield **9** (11.10 g, 63%) as a red-orange solid.

$R_f = 0.20$ (10:1 hexanes/EtOAc); $^1\text{H NMR}$ (400 MHz, CDCl_3): δ 3.30 (s, 6H), 3.66 (d, 2H, $J = 5.3$ Hz), 4.48 (t, 1H, $J = 5.3$ Hz), 8.54 (d, 1H, $J = 2.4$ Hz), 8.64 (d, 1H, $J = 2.4$ Hz); $^{13}\text{C NMR}$ (125 MHz, CDCl_3) δ 35.50, 54.46, 103.03, 118.91, 128.18, 130.81, 138.10, 146.29, 152.08.



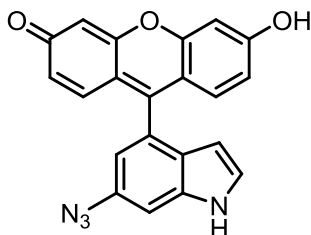
2.9 (8.07 g, 24.08 mmol) was dissolved in 200 mL glacial acetic acid. Then, iron powder (26.90 g, 481.6 mmol) was added. A bubbler was attached, and the reaction was heated to 85 °C for 1 h, turning the grey suspension to a thick yellow slurry. Then, the reaction was heated to 100 °C and stirred for 16 h. The reaction was cooled to rt and the acetic acid removed *in vacuo*. The remaining light brown residue was diluted with 200 mL 1 M KOH and 200 mL EtOAc and the organic layer collected. The aqueous layer was extracted with another 200 mL EtOAc. The organic layer was washed with 5 x 200 mL sat. NaHCO_3 (caution: vigorous gas evolution!). The organic layer was dried with MgSO_4 and concentrated *in vacuo*, yielding a brown residue. The compound was partially purified by flash chromatography on silica gel (4:1 to 1:1 to 1:2 hexanes/EtOAc), to yield a mixture of desired product and unacetylated indole as a viscous brown oil. The solid was taken up in 30 mL Et_2O and filtered to yield product as a light brown solid. The solid was further washed with another 50 mL Et_2O . This was repeated once more to yield another crop of product, yielding **2.10** (3.13 g, 51%) as a light brown solid.

$R_f = 0.20$ (1:1 hexanes/EtOAc); $^1\text{H NMR}$ (500 MHz, CD_3OD): δ 2.14 (s, 3H), 6.40 (d, 1H, $J = 3.2$ Hz), 7.26 (d, 1H, $J = 3.2$ Hz) 7.28 (d, 1H, $J = 1.7$ Hz) 7.82 (s, 1H) $^{13}\text{C NMR}$ (125 MHz, CD_3OD): δ 23.73, 102.32, 103.67, 114.43, 116.69, 126.53, 126.97, 134.61, 137.57, 171.47. HRMS (ESI): Calculated for $\text{C}_{10}\text{H}_{10}\text{O}_1\text{N}_2\text{Br}$ $[\text{M}+\text{H}]^+$ 252.9974, 254.9953, found 252.9971, 254.9951.



2.10 (0.506 g, 2.00 mmol) was dissolved in 20 mL anhydrous THF and cooled to 0 °C. Then, sodium hydride (40% dispersion in mineral oil, 0.160 g, 4.00 mmol) was added. Bubbling was observed and the clear solution turned a green color. After stirring for 15 min, the solution was cooled to -78 °C. Then, *tert*-butyllithium (1.41 M in pentanes, 2.83 mL, 4.00 mmol) was added dropwise down the side of the flask, immediately turning the solution into a viscous yellow slurry. After stirring for 30 min, a solution of **2.5** (1.04 g, 2.20 mmol) in 6 mL anhydrous THF was slowly added down the side of the flask, turning the reaction mixture a deep red color. After stirring for 2 h at -78 °C, the reaction was allowed to warm to room temperature over 15 min. The reaction was quenched with the careful addition of 4 mL 2 M HCl (caution: gas evolution!), upon which the deep red color of the reaction mixture changed to a light red-orange partway through addition. As more of the HCl was added, the deep red color reappeared. After stirring for another 15 min, the solvent was removed *in vacuo* and the remaining deep red solid was purified by flash chromatography on silica gel (CHCl₃ to 10:1 CHCl₃/MeOH to 7:1 CHCl₃/MeOH), yielding **2.11** (0.442 g, 58%) as a red solid.

R_f = 0.05 (10:1 CHCl₃/MeOH); ¹H NMR (400 MHz, CD₃OD): δ 2.18 (s, 3H), 6.01 (s, 1H), 7.08 (d, 2H, *J* = 9.5 Hz), 7.25 (s, 1H), 7.29 – 7.36 (m, 2H), 7.72 (d, 2H, *J* = 9.4 Hz), 8.09 (s, 1H), 11.14 (s, 1H); ¹³C NMR (100 MHz, d₆-DMSO): δ 24.18, 92.58, 99.94, 103.18, 103.67, 113.57, 114.92, 116.78, 121.23, 123.15, 123.41, 126.65, 131.64, 133.86, 136.16, 157.28, 168.51. HRMS (ESI): Calculated for C₂₃H₁₅N₂O₄ [M-H]⁻ 383.1026, found 383.1037.

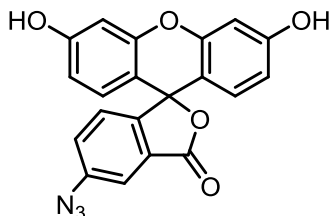


2.11 (81.0 mg, 0.211 mmol), a red solid, was dissolved in 6 mL anhydrous MeOH. Then, boron trifluoride diethyl etherate, (0.180 g, 0.160 mL, 1.27 mmol) was added. The deep red solution was allowed to reflux for 6 h. After cooling to rt, 0.600 mL triethylamine was added dropwise to quench the reaction and the solution was concentrated *in vacuo* to yield a deep red solid. The solid was taken up in 10 mL H₂O and filtered. The solid was washed with another 10 mL H₂O, dissolved in MeOH and concentrated *in vacuo* to yield crude aminoindole as a red-brown solid, which was carried directly onto the next step without further purification.

$R_f = 0.05$ (10:1 $\text{CHCl}_3/\text{MeOH}$); $^1\text{H NMR}$ (400 MHz, CD_3OD): δ 5.86 (d, 1H, $J = 3.3$ Hz), 7.01 (s, 1H), 7.06 (d, 1H, $J = 3.2$ Hz), 7.11 (s, 1H), 7.32 (d, 2H, $J = 9.4$ Hz). LRMS (ESI): Calculated for $\text{C}_{21}\text{H}_{15}\text{N}_2\text{O}_3$ $[\text{M}+\text{H}]^+$ 343.1, found 343.4.

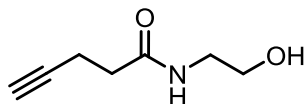
The crude aminoindole was dissolved in 6 mL 2:1 $\text{AcOH}/\text{H}_2\text{O}$. The deep red solution was cooled to 0°C . Then, NaNO_2 (16.1 mg, 0.232 mmol) was slowly added and the reaction stirred for 10 min at 0°C . Then, NaN_3 (15.1 mg, 0.232 mmol) was carefully added (caution: gas evolution!). The resulting red solution was stirred for 30 min at 0°C , then warmed to rt and stirred for 14 h. The solution was concentrated *in vacuo* to yield a red-brown residue. The residue was purified by preparative reversed-phase HPLC with a 25 min gradient from 25% to 100% MeCN in H_2O to yield **2.4** (23.0 mg, 30%) as a red-brown solid.

$R_f = 0.2$ (10:1 $\text{CHCl}_3/\text{MeOH}$); $^1\text{H NMR}$ (400 MHz, d_6 -DMSO): δ 6.02 (s, 1H), 6.46-6.50 (m, 4H), 6.86-6.92 (m, 3H), 7.33 (s, 1H), 7.39 (s, 1H), 8.31 (s, 1H), 11.44 (s, 1H); ^{13}C (125 MHz, d_6 -DMSO): δ 100.92, 102.81, 103.69, 125.63, 126.64, 127.79, 130.59, 133.21, 136.81, 148.78, 157.44, 157.47, 159.11. HRMS (ESI): Calculated for $\text{C}_{21}\text{H}_{13}\text{O}_3\text{N}_4$ $[\text{M}+\text{H}]^+$ 369.0982, found 369.0989.



5-aminofluorescein (0.174 g, 0.500 mmol), a deep-red solid, was dissolved in 10 mL 2:1 $\text{AcOH}/\text{H}_2\text{O}$ and cooled to 0°C . To this deep red solution was added NaNO_2 , a white powder (52 mg, 0.75 mmol). After stirring for 15 minutes, the solution had turned to a light red color. NaN_3 (66 mg, 1.00 mmol) was then carefully added (caution: gas evolution!), turning the solution to a yellow slurry. The reaction was stirred for 1 hr at 0°C and 1 h at room temperature. The slurry was filtered over vacuum and the solid washed with 20 mL 2M HCl and 100 mL H_2O , yielding **5-azidofluorescein**²⁶ (0.156 g, 84%) as a yellow solid after further drying *in vacuo*.

$R_f = 0.40$ (10:1 $\text{CHCl}_3/\text{MeOH}$); $^1\text{H NMR}$ (400 MHz, d_6 -DMSO): δ 6.51-6.63 (m, 4H), 6.67 (d, 2H, $J = 2.3$ Hz), 7.30 (d, 1H, $J = 8.2$ Hz), 7.51 (dd, 1H, $J = 8.2$ Hz, $J = 2.3$ Hz), 7.64 (d, 1H, $J = 2.2$ Hz), 10.13 (s, 2H); ^{13}C NMR (100 MHz, d_6 -DMSO): δ 83.27, 102.23, 109.28, 112.60, 114.35, 125.61, 126.75, 127.97, 129.03, 141.74, 148.72, 151.85, 159.54, 167.75. HRMS (ESI): Calculated for $\text{C}_{20}\text{H}_{12}\text{O}_5\text{N}_3$ $[\text{M}+\text{H}]^+$ 374.0771, found 374.0773.



4-pentynoic acid (0.196 g, 2.00 mmol), a white crystalline solid, and N-hydroxysuccinimide (0.230 g, 2.00 mmol), a white solid, were dissolved in 10 mL anhydrous THF. The clear solution was cooled to 0°C . Then, N,N'-dicyclohexylcarbodiimide (0.454 g, 2.20 mmol), a waxy white solid, was added. The reaction was stirred at 0°C for 5 minutes, then allowed to stir at rt for 6 h,

during which it turned a cloudy white. The reaction was then filtered and the filtrate concentrated *in vacuo* to yield crude NHS ester as a pale yellow oil. This crude product was dissolved in 10 mL anhydrous THF and cooled to 0 °C. Then, 2-aminoethanol (0.122 g, 0.121 mL, 2.00 mmol), a clear liquid, was added and the reaction was stirred at rt for 16 h, then concentrated *in vacuo*, yielding a white residue. The residue was purified by flash chromatography on silica gel (CHCl₃ to 10:1 CHCl₃/MeOH), yielding known **2.12**⁴⁴ (0.140 g, 49%) as a pale yellow oil that solidified upon storage at 4 °C to a white solid.

R_f = 0.35 (10:1 CHCl₃/MeOH); ¹H NMR (400 MHz, CDCl₃): δ 2.05 (s, 1H), 2.36 (s, 1H), 2.46 (t, 2H, *J* = 7.0 Hz), 2.56 (t, 2H, *J* = 7.0 Hz) 3.49 (dd, 2H, *J* = 6.2 Hz, *J* = 5.2 Hz) 3.77 (2H, s) 6.07, (1H, s) ¹³C NMR (100 MHz, CDCl₃): 14.89, 35.24, 42.41, 62.16, 69.41, 82.83, 172.09. HRMS (ESI): Calculated for C₇H₁₂O₂N₁ [M+H]⁺ 142.0863, found 142.0865.

General procedure for azidofluorescein-alkyne cycloaddition product. Azidofluorescein (0.010 mmol) was dissolved in 1 mL MeOH and the solution degassed under vacuum and backfilled with N₂. The reaction was stirred with Cu(MeCN)₄PF₆ (1.8 mg, 0.0050 mmol), tris-(benzyltriazolylmethyl)amine (2.7 mg, 0.0050 mmol), and alkyne **2.12** (7.0 mg, 0.050 mmol). The mixture was stirred in the dark under N₂ for 2 days, then concentrated. The residue then purified by semi-preparative reversed-phase HPLC to yield the adduct.

2.1-2.12. Purified by a 30 minute gradient from 10% to 95% MeCN in H₂O. HRMS (ESI): Calculated for C₃₀H₂₅N₄O₅ [M+H]⁺ 521.1819, found 521.1829.

2.2-2.12. Purified by a 25 minute gradient from 10% to 30% MeCN in H₂O. HRMS (ESI): Calculated for C₃₀H₃₀N₅O₆ [M+H]⁺ 556.2191, found 556.2204.

2.3-2.12. Purified by a 25 minute gradient from 10% to 30% MeCN in H₂O. HRMS (ESI): Calculated for C₂₇H₂₅N₄O₆ [M+H]⁺ 501.1769, found 501.1779.

2.4-2.12. Purified by a 25 minute gradient from 10% to 30% MeCN in H₂O. HRMS (ESI): Calculated for C₂₈H₂₄N₅O₅ [M+H]⁺ 510.1772, found 510.1788.

N₃-fluor-2.12. Purified by a 30 minute gradient from 0% to 40% MeCN in H₂O. HRMS (ESI): Calculated for C₂₇H₂₃N₄O₇ [M+H]⁺ 515.1561, found 515.1580.

General procedure for DIFO cycloaddition products. Azidofluorescein (0.010 mmol) and DIFO (2.2 mg, 0.010 mmol) were dissolved in 1 mL 1:1 MeCN/H₂O with 5% MeOH cosolvent. The solution as stirred for 1 h at rt in the dark. The crude product was concentrated *in vacuo* and purified by semi-preparative reversed-phase HPLC. No attempt was made to separate the roughly 1:1 mixture of regioisomeric cycloaddition products.

2.1-DIFO. Purified by a 25 minute gradient from 20% to 60% MeCN in H₂O. LRMS (ESI): Calculated for C₃₃H₂₆F₂N₃O₆ [M+H]⁺ 598.2, found 598.9.

2.2-DIFO. Purified by a 25 minute gradient from 20% to 60% MeCN in H₂O. HRMS (ESI): Calculated for C₃₃H₃₁F₂N₄O₇ [M+H]⁺ 633.2155, found 633.2172.

2.3-DIFO. Purified by a 25 minute gradient from 20% to 60% MeCN in H₂O. HRMS (ESI): Calculated for C₃₀H₂₆F₂N₃O₇ [M+H]⁺ 578.1733, found 578.1748.

2.4-DIFO. Purified by a 25 minute gradient from 0% to 40% MeCN in H₂O. HRMS (ESI): Calculated for C₃₁H₂₅F₂N₄O₆ [M+H]⁺ 587.1737, found 587.1750.

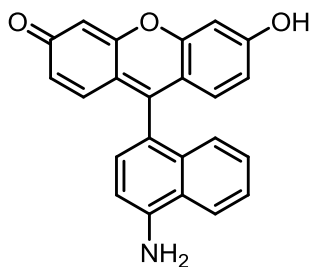
General procedure for DIMAC cycloaddition products. Azidofluorescein (0.010 mmol) and DIMAC (2.9 mg, 0.010 mmol) were dissolved in 1 mL 1:1 MeCN/H₂O. The solution as stirred for 16 h at rt in the dark. The crude product was concentrated *in vacuo* and purified by semi-preparative reversed-phase HPLC. No attempt was made to separate the regioisomeric cycloaddition products.

2.1-DIMAC. Purified by a 25 minute gradient from 10% to 60% MeCN in H₂O. HRMS (ESI): Calculated for C₃₆H₃₃N₄O₈ [M+H]⁺: 649.2293, found 649.2308.

2.2-DIMAC. Purified by a 25 minute gradient from 0% to 60% MeCN in H₂O. HRMS (ESI): Calculated for C₃₆H₃₈N₅O₉ [M+H]⁺ 684.2664, found 684.2688.

2.3-DIMAC. Purified by a 25 minute gradient from 0% to 60% MeCN in H₂O. HRMS (ESI): Calculated for C₃₃H₃₃N₄O₉ [M+H]⁺ 629.2242, found 629.2251.

2.4-DIMAC. Purified by a 25 minute gradient from 0% to 40% MeCN in H₂O. LRMS (ESI): Calculated for C₃₄H₃₂N₅O₈ [M+H]⁺: 638.2, found 638.3.



2.1 (3.8 mg, 0.010 mmol), a red solid, was dissolved in 5 mL 1:1 0.1 M pH 7.4 KP_i buffer/MeOH. Then, dithiothreitol (15.4 mg, 0.100 mmol), a white solid, was added. Bubbling was observed upon addition. The reaction was stirred at rt for 1 h, then concentrated. The red residue was purified by semi-preparative reversed-phase HPLC using a 25 minute gradient from 20 to 60% MeCN in H₂O to yield **reduced-2.1** as a red-orange solid.

HRMS (ESI): Calculated for C₂₃H₁₆NO₃ [M+H]⁺: 354.1125, found 354.1131.

References

1. For a general review of bioorthogonal chemistry, see: Sletten, E. M.; Bertozzi, C. R. *Angew. Chem. Int. Ed.* **2009**, *48*, 6974-6998.
2. For a review on fluorogenic click probes, see: Le Droumaguet, C.; Wang, C.; Wang, Q. *Chem. Soc. Rev.* **2010**, *39*, 1233-1239.
3. For reviews on applications of the azide-alkyne [3+2] cycloaddition in chemical biology, see: Best, M. D. *Biochemistry* **2009**, *48*, 6571-6584. Jewett, J. C.; Bertozzi, C. R. *Chem. Soc. Rev.* **2010**, *39*, 1272-1279.
4. Sivakumar, K.; Xie, F.; Cash, B. M.; Long, S.; Barnhill, H. N.; Wang, Q. *Org. Lett.* **2004**, *6*, 4603-4606.
5. Xie, F.; Sivakumar, K.; Zeng, Q. B.; Bruckman, M. A.; Hodges, B.; Wang, Q. *Tetrahedron* **2008**, *64*, 2906-2914.
6. Wang, C.; Xie, F.; Suthiwangcharoen, N.; Sun, J.; Wang, Q. *Sci. China Chem.* **2012**, *55*, 125-130.
7. Sawa, M.; Hsu, T. L.; Itoh, T.; Sugiyama, M.; Hanson, S. R.; Vogt, P. K.; Wong, C. H. *Proc. Natl. Acad. Sci.* **2006**, *103*, 12371-12376.
8. Zhou, Z.; Fahrni, C. J. *J. Am. Chem. Soc.* **2004**, *126*, 8862-8863.
9. Jewett, J. C.; Bertozzi, C. R. *Org. Lett.* **2011**, *13*, 5937-5939.
10. Key, J. A.; Cairo, C. W. *Dyes and Pigments* **2010**, *88*, 95-102.
11. Qi, J.; Han, M.-S.; Chang, Y.-C.; Tung, C.-H. *Bioconjug. Chem.* **2011**, *22*, 1758-1762.
12. Li, J.; Hu, M.; Yao, S. Q. *Org. Lett.* **2009**, *11*, 3008-3011.
13. Weissleder, R.; Ntziachristos, V. *Nature Medicine* **2003**, *9*, 123-128.
14. Urano, Y.; Kamiya, M.; Kanda, K.; Ueno, T.; Hirose, K.; Nagano, T. *J. Am. Chem. Soc.* **2005**, *127*, 4888-4894.
15. Miura, T.; Urano, Y.; Tanaka, K.; Nagano, T.; Ohkubo, K.; Fukuzumi, S. *J. Am. Chem. Soc.* **2003**, *125*, 8666-8671.
16. Kamiya, M.; Kobayashi, H.; Hama, Y.; Bernardo, M.; Nagano, T.; Choyke, P. L.; Urano, Y. *J. Am. Chem. Soc.* **2007**, *129*, 3918-3929.
17. Kobayashi, T.; Urano, Y.; Kamiya, M.; Ueno, T.; Kojima, H.; Nagano, T. *J. Am. Chem. Soc.* **2007**, *129*, 6696-6697.
18. Gross, M. L.; Blank, D. H.; Welch, W. M. *J. Org. Chem.* **1993**, *58*, 2104-2109.
19. Liu, C. Y.; Knochel, P. *J. Org. Chem.* **2007**, *72*, 7106-7115.
20. Mintaz, A. K.; Kao, J. P. Y.; Tsien, R. Y. *J. Biol. Chem.* **1989**, *265*, 8171-8178.
21. For another example of an unsuccessful attempt at triazene formation from aminoindoles, see: Cirrincione, G.; Almerico, A. M.; Dattolo, G.; Aiello, E.; Diana, P.; Grimaudo, S.; Barraja, P.; Mingoia, F.; Gancitano, R. A. *Eur. J. Med. Chem.* **1994**, *29*, 889-891..
22. Miltsov, S.; Rivera, L.; Encinas, C.; Alonso, J. *Tetrahedron Lett.* **2003**, *44*, 2301-2303.
23. Baskin, J. M.; Prescher, J. A.; Laughlin, S. T.; Agard, N. J.; Chang, P. V.; Miller, I. A.; Lo, A.; Codelli, J. A. Bertozzi, C. R. *Proc. Natl. Acad. Sci.* **2007**, *104*, 16793-16797.
24. Sletten, E.; Bertozzi, C. R. *Org. Lett.* **2008**, *10*, 3097-3099.
25. Rotman, A.; Heldman, J. *Biochemistry* **1981**, *20*, 5995-5999.
26. Salic, A.; Mitchison, T. J. *Proc. Natl. Acad. Sci.* **2008**, *105*, 2415-2420
27. Hong, V.; Steinmetz, N. F.; Manchester, M.; Finn, M. G. *Bioconjug. Chem.* **2010**, *21*, 1912-1916.

28. Besanceney-Webler, C.; Jiang, H.; Zheng, T.; Feng, L.; Soriano del Amo, D.; Wang, W.; Klivansky, L. M.; Marlow, F. L.; Liu, Y.; Wu, P. *Angew. Chem. Int. Ed.* **2011**, *50*, 8051-8056.
29. Hsu, T.-L.; Hanson, S. R.; Kishikawa, K.; Wang, S.-K.; Sawa, M.; Wong, C.-H. *Proc. Natl. Acad. Sci.* **2007**, *104*, 2614-2619.
30. Chang, P. V.; Chen, X.; Smyrniotis, C.; Xenakis, A.; Hu, T. S.; Bertozzi, C. R.; Wu, P. *Angew. Chem. Int. Ed.* **2009**, *48*, 4030-4033.
31. Staros, J. V.; Bayley, H.; Standring, D. N.; Knowles, J. R. *Biochem. Biophys. Res. Commun.* **1978**, *80*, 568-572.
32. Lippert, A. R.; New, E. J.; Chang, C. J. *J. Am. Chem. Soc.* **2011**, *133*, 10078-100800.
33. Peng, H.; Chen, S.; Chen, Z.; Ren, W.; Ai, H. *J. Am. Chem. Soc.* **2012**, *134*, 9589-9592.
34. Montoya, L. A.; Pluth, M. D. *Chem. Commun.* **2012**, *48*, 4767-4769.
35. Iddon, B.; Meth-Cohn, O.; Scriven, E. F. V.; Suschitzky, H.; Gallagher, P. T. *Angew. Chem. Int. Ed.* **1979**, *18*, 900-917.
36. Mineno, T.; Ueno, T.; Urano, Y.; Kojima, H.; Nagano, T. *Org. Lett.* **2006**, *8*, 5963-5966
37. Williams, A. T. R.; Winfield, S. A.; Miller, J. N. *Analyst* **1983**, *108*, 1067.
38. Hein, J. E.; Krasnova, L. B.; Iwasaki, M.; Fokin, V. V. *Org. Synth.* **2011**, *88*, 238.
39. Codelli, J. A.; Baskin, J. M.; Agard, N. J.; Bertozzi, C. R. *J. Am. Chem. Soc.* **2008**, *130*, 11486-11493.
40. Grover, P. K.; Shah, G. D.; Shah, R. C. *J. Chem. Soc. (Lond.)* **1955**, 3892-3895
41. Melhuish, M. W.; Moodie, R. B. *J. Chem. Soc. Perkin Trans. 2: Phys. Org. Chem. (1972-1999)*, **1989**, *6*, 667-673.
42. McCormick, K. D.; Boyce, C. W.; Shih, N.-Y.; Aslanian, R. G.; Chao, J.; Fevrier, S.; Mangiaracina, P.; Yu, Y.; Huang, C.-Y.; Liang, B.; Lu, H.; Liu, R.-Q. *PCT Int. Appl.* **2008**, WO 2008100457 A2 20080821.
43. Rajesh, K.; Somasundaram, M.; Saiganesh, R.; Balasubramanian, K. K. *J. Org. Chem.* **2007**, *72*, 5867-5869.
44. Tokunaga, T.; Umezome, T.; Hume, W. E.; Nagata, R.; Okazaki, K.; Ueki, Y.; Kumagai, K. *PCT Int. Appl.* **2000**, WO 2000010975 A1 20000302.

Chapter 3: Development of a Highly Fluorogenic Azide Probe with Near-Infrared Emission

Note: Portions of this chapter were published in *Proc. Natl. Acad. Sci.* **2014**, *111*, 5456-5461.

Introduction

In the previous chapter, I described our initial demonstration of utilizing rational design to develop fluorogenic azide probes switched by photoinduced electron transfer. More broadly, within the field of bioorthogonal chemistry, significant effort have been made toward the discovery of fluorogenic probes activated by various bioorthogonal reactions, including the Staudinger ligation^{2,3} as well as azide-alkyne,⁴⁻¹⁵ tetrazine-alkene,¹⁶⁻¹⁸ tetrazine-alkyne,¹⁹ and photoactivated tetrazole-alkene cycloadditions.²⁰⁻²¹ However, the dyes employed have emission maxima below 600 nm. The identification of activatable near-infrared (NIR) fluorogenic probes, with emission maxima approaching 700 nm, has proven much more challenging. These longer wavelengths are ideal for interrogating biological systems, as background autofluorescence is minimized and tissue penetrance is highest. There have been a few reports of such long-wavelength fluorogenic probes activated by bioorthogonal chemistry. For example, the reaction of tetrazine-conjugated DyLight650 with a cyclooctyne analog formed a product that was 1.6-fold brighter than the starting material.²² Likewise, weakly fluorescent long-wavelength pyrazolines can be generated by the photoactivated tetrazole-alkene cycloaddition of non-fluorescent substrates.²³ Brighter NIR dyes with more dramatic fluorescence enhancements are desirable for applications of bioorthogonal chemistry to biological imaging.

In this chapter, I describe a series of fluorogenic azido Si-rhodamine probes with emission maxima near 670 nm and up to 48-fold enhancement in fluorescence quantum yield upon triazole formation. Further optimization of these probes yielded compounds that were very well-suited for the detection of terminal alkynes on live mammalian cell surfaces without the need to remove excess probe i.e. “no-wash” labeling.

Results and Discussion

Recently, Xiao, Nagano and their respective coworkers found that replacement of the oxygen atom in the xanthene moiety of tetramethylrhodamine with a silicon atom (Si-rhodamine) induces a dramatic red-shift in emission of nearly 100 nm into the NIR region.^{24,25} Importantly, the fluorescence quantum yields of these probes could be modulated by over 100-fold through photoinduced electron transfer (PeT), rendering Si-rhodamine a promising scaffold for sensor development.²⁶⁻²⁸ Additionally, carboxy-substituted Si-rhodamines are well-suited for cell labeling due to spirolactonization and loss of fluorescence during non-specific binding events.²⁹

I sought to identify azide-functionalized Si-rhodamines that would undergo a significant enhancement in fluorescence quantum yield upon triazole formation. Since Nagano and coworkers have shown that Si-rhodamines are amenable to the same kinds of computational predictions, I reasoned that these NIR dyes might be engineered to respond to bioorthogonal chemistries (Figure 3-1).

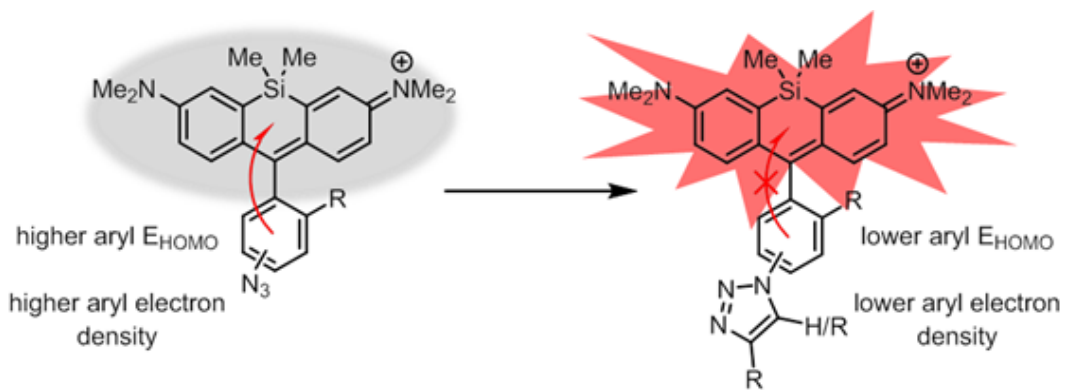
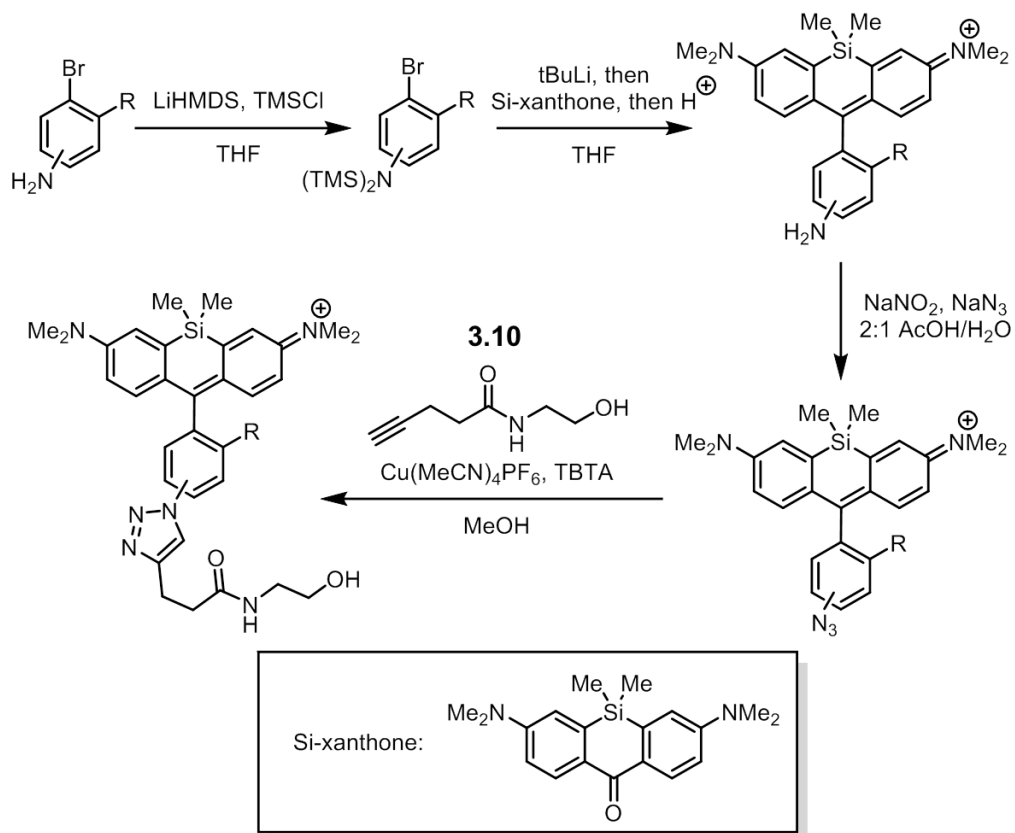


Figure 3-1. Design of a PeT-based fluorogenic azido Si-rhodamine.

I developed an efficient and modular synthesis to access azide-functionalized Si-rhodamines from various bromoanilines (Scheme 3-1). The bromoanilines were first protected as the bis-trimethylsilyl (TMS) derivatives by deprotonation with lithium hexamethyldisilazide (LiHMDS) and reaction with trimethylsilyl chloride (TMSCl). This protection procedure was extremely robust, reliably yielding the bis-trimethylsilyl protected anilines after simple filtration to remove lithium salts and unreacted starting material. Next, the protected bromoanilines were subjected to lithium-halogen exchange and added into Si-xanthone, which afforded the amino Si-rhodamines after acidic workup. As described later, the photophysical properties of these intermediates were measured in comparison to their azido and triazolyl counterparts. The amino Si-rhodamines were finally subjected to diazotization with sodium nitrite and displacement by azide ion to yield the desired azido Si-rhodamines. Through this route, I generated compounds **3.1-3.9** (Figure 3-2). To evaluate fluorescence enhancement upon triazole formation, I also synthesized the corresponding triazolyl Si-rhodamines by copper-catalyzed click chemistry with 4-pentynoyl ethanolamine amide (compound **3.10**, Scheme 3-1).

The bis-trimethylsilyl protecting group offers many advantages over the triazene functionality used in our synthesis of azidofluoresceins. First, I found that triazenyl bromoarenes added into Si-xanthone in poor yields. The enhanced reactivity of the bis-trimethylsilyl anilines may be due to the electron-withdrawing character of the triazene group. Additionally, the sluggish reactivity of Si-xanthone compared to the fluorescein xanthone may be attributed to the two electron donating dimethylamino groups and the dimethylsilicon substituents blocking the Burgi-Dunitz trajectory for incoming nucleophiles. Beyond reactivity issues, the triazene deprotection and azide displacement step to prepare azidofluoresceins often resulted in the formation of small quantities of reduced arene product, likely due to hydride transfer from the released pyrrolidine. This contaminant, while separable for fluoresceins, was impossible to remove in the context of Si-rhodamines. Finally, using the bis-trimethylsilyl protecting group enabled access to the corresponding amino fluorophore en route to the azido and triazolyl fluorophores, facilitating their photophysical characterization.



Scheme 3-1. General procedure for the synthesis of azido Si-rhodamines from bromoanilines and the conversion of azido Si-rhodamines to triazolyl Si-rhodamines.

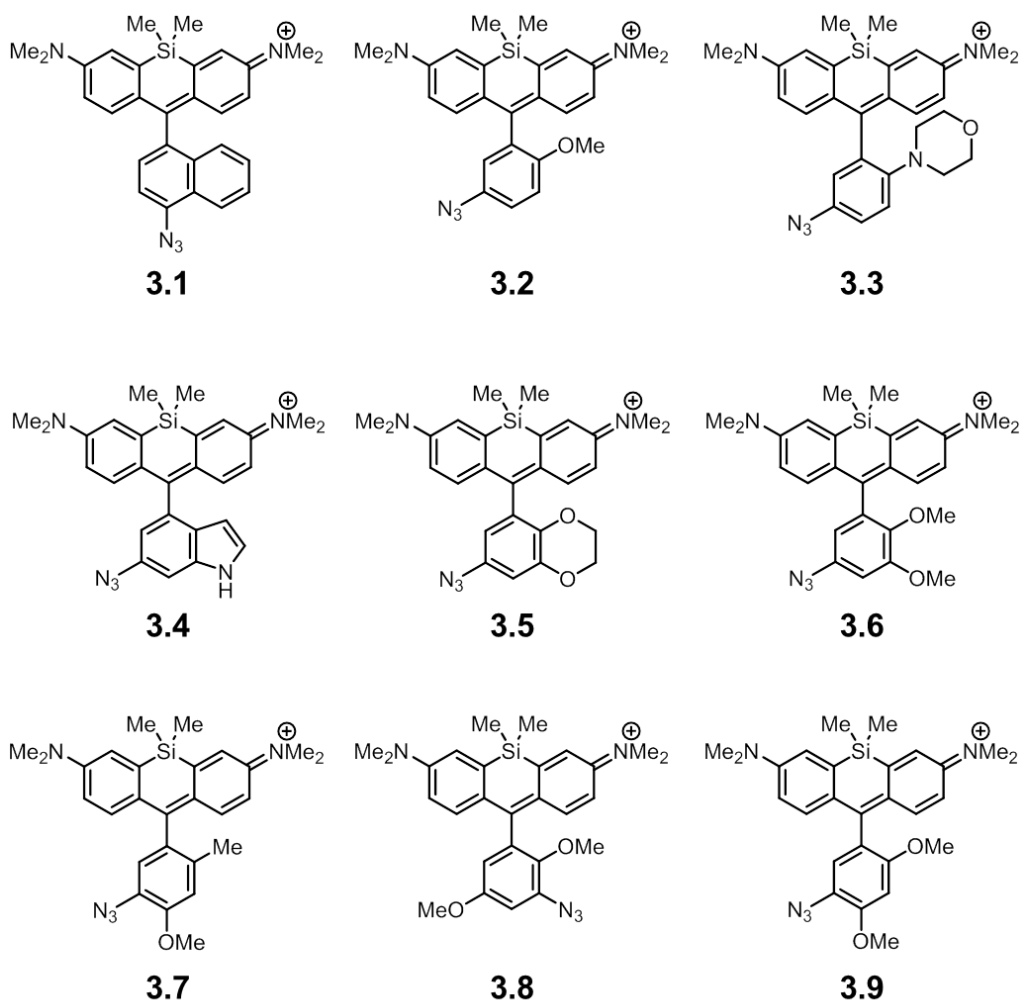


Figure 3-2. Structures of azido Si-rhodamines synthesized and studied.

The fluorescence quantum yields of the purified amino, azido, and triazolyl Si-rhodamines were measured in pH 7.4 PBS using cresyl violet in methanol ($\Phi_{fl} = 0.54$) as a standard (Table 3-1). The four analogs containing the same pendant aryl rings from the last chapter³⁰ (**3.1** to **3.4**, Figure 3-3) did not display significant fluorescence enhancement upon triazole formation. The best candidate of the four, 8-azidonaphthyl-substituted Si-rhodamine **3.1**, afforded only a 5-fold increase in fluorescence quantum yield as compared with the 29-fold enhancement we observed with the corresponding fluorescein.³⁰ This result was not unexpected given the difference in electronics between the two systems and Nagano and coworkers' previous observation that more electron-rich pendant aryl rings are needed to quench fluorescence via PeT in Si-rhodamines.²⁷ While disappointing, I chose to expand my search of candidate pendant aryl azides beyond those derived from commercially available bromo- or iodoanilines.

Compound	λ_{abs} (nm)	λ_{em} (nm)	Φ_{fl}	Change in Φ_{fl}
3.1-NH₂	653	669	0.0016	24-fold ↓
3.1-N₃	654	666	0.038	--
3.1-triazole	656	670	0.19	5.0-fold ↑
3.2-NH₂	650	669	0.0025	32-fold ↓
3.2-N₃	653	667	0.081	--
3.2-triazole	655	669	0.19	2.3-fold ↑
3.3-NH₂	650	672	0.00096	1.4-fold ↓
3.3-N₃	656	667	0.0014	--
3.3-triazole	663	676	0.0015	1.1-fold ↑
3.4-NH₂	650	673	0.00088	5.5-fold ↓
3.4-N₃	660	669	0.0048	--
3.4-triazole	654	668	0.0088	1.8-fold ↑
3.5-NH₂	653	667	0.00093	21-fold ↓
3.5-N₃	655	668	0.019	--
3.5-triazole	656	668	0.18	9.5-fold ↑
3.6-NH₂	652	665	0.00067	58-fold ↓
3.6-N₃	654	669	0.039	--
3.6-triazole	656	670	0.18	4.6-fold ↑
3.7-NH₂	648	669	0.0015	45-fold ↓
3.7-N₃	650	666	0.066	--
3.7-triazole	652	666	0.25	3.7-fold ↑
3.8-NH₂	654	672	0.0012	41-fold ↓
3.8-N₃	655	669	0.051	--
3.8-triazole	657	671	0.16	3.2-fold ↑
3.9-NH₂	650	664	0.0014	3.0-fold ↓
3.9-N₃	654	666	0.0042	--
3.9-triazole	655	668	0.20	48-fold ↑

Table 3-1. Photophysical properties of Si-rhodamines **3.1-3.9** and their amino and triazolyl counterparts in PBS pH 7.4.

Computational results suggested that the pendant aryl rings of compounds **3.5-3.9** possess higher electron density than that of compound **3.1** (Table 3-2). I therefore synthesized these compounds and characterized their photophysical properties experimentally (Table 3-1). 3-Azido-4,6-dimethoxy-Si-rhodamine **3.9** (Figure 3-2), the most promising of this group, displayed a 48-fold increase in fluorescence quantum yield upon triazole formation. This fluorescence enhancement was recapitulated *in situ* by monitoring fluorescence immediately after addition of alkyne **3.10** to a solution of CuSO₄, the ligand BTAA³¹, sodium ascorbate and compound **3.9** (Figure 3-3). Under these conditions, the absorption of the compound did not change significantly (Figure 3-4), indicating that the observed change in fluorescence intensity arises solely from an increase in fluorescence quantum yield.

An interesting feature of compounds **3.1-3.9** is that their fluorescence quantum yields, which are already lower than those of the corresponding triazoles, are even further reduced by conversion to the corresponding amines (Table 3-1), a potential route of biological degradation.³² Thus, azide reduction, if it occurs, will suppress rather than enhance background fluorescence for this set of azido Si-rhodamine probes. This property stands in contrast to probes where azide reduction is a key part of sensor design.³³⁻³⁵ While a trend exists between calculated E_{HOMO} and fluorescence quantum yield for compounds **3.1-3.9** (Figure 3-5), the observed differences in quantum yields for some compounds with similar E_{HOMO} s (for example, compare the data for compounds **3.8** and **3.9** in Table 3-1) suggests that other factors might influence PeT efficiency, or that other fluorescence quenching mechanisms are at play.

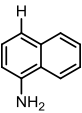
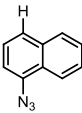
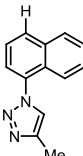
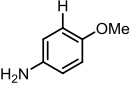
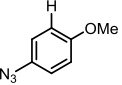
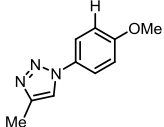
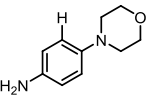
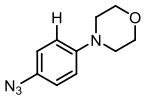
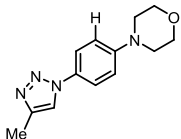
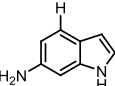
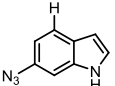
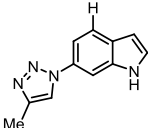
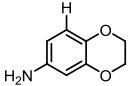
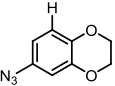
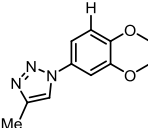
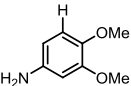
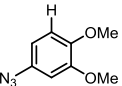
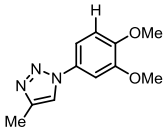
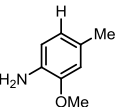
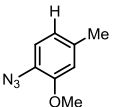
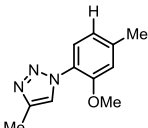
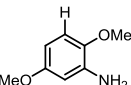
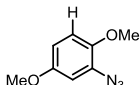
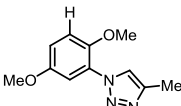
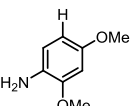
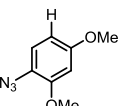
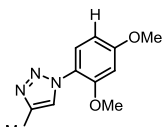
	NH₂		N₃		triazole	
3.1		-0.189		-0.210		-0.219
3.2		-0.182		-0.208		-0.218
3.3		-0.167		-0.188		-0.194
3.4		-0.174		-0.198		-0.208
3.5		-0.181		-0.206		-0.214
3.6		-0.174		-0.198		-0.206
3.7		-0.181		-0.207		-0.224
3.8		-0.180		-0.200		-0.209
3.9		-0.174		-0.199		-0.211

Table 3-2. Structures and calculated aryl E_{HOMOS} in Hartrees of the pendant aryl rings of evaluated probes **3.1** to **3.9**. The H represents the attachment point onto the xanthene moiety. The triazole was truncated as a methyl group to simplify calculations.

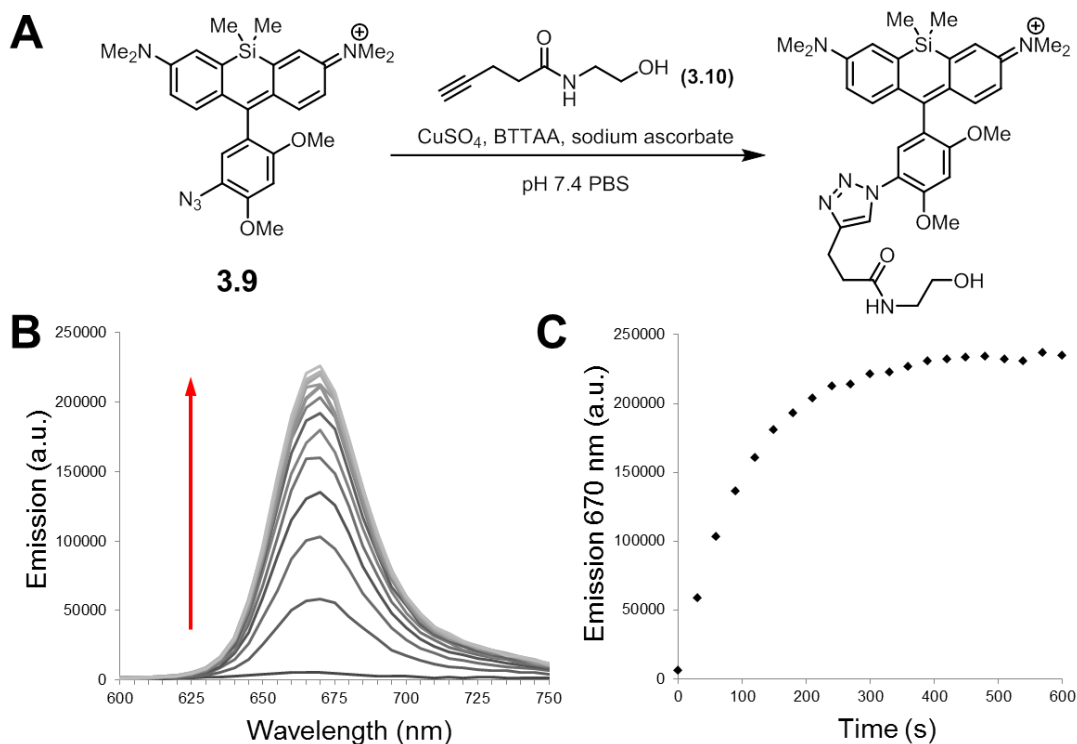


Figure 3-3. Fluorescence enhancement of **3.9** during copper-catalyzed click reaction *in situ*. (A) The reaction between fluorogenic Si-rhodamine **3.9** and alkyne. (B) Emission spectra taken during the reaction. Scans were taken every 30 seconds, with the first scan taken immediately before addition of alkyne. $\lambda_{\text{ex}} = 600 \text{ nm}$. (C) Plot of emission at 670 nm vs. time for this reaction.

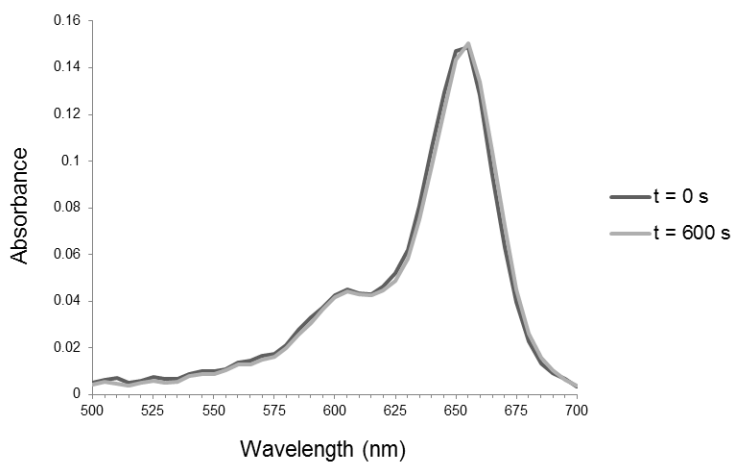


Figure 3-4. Absorbance spectra of **3.9** under the copper-catalyzed reaction conditions described above.

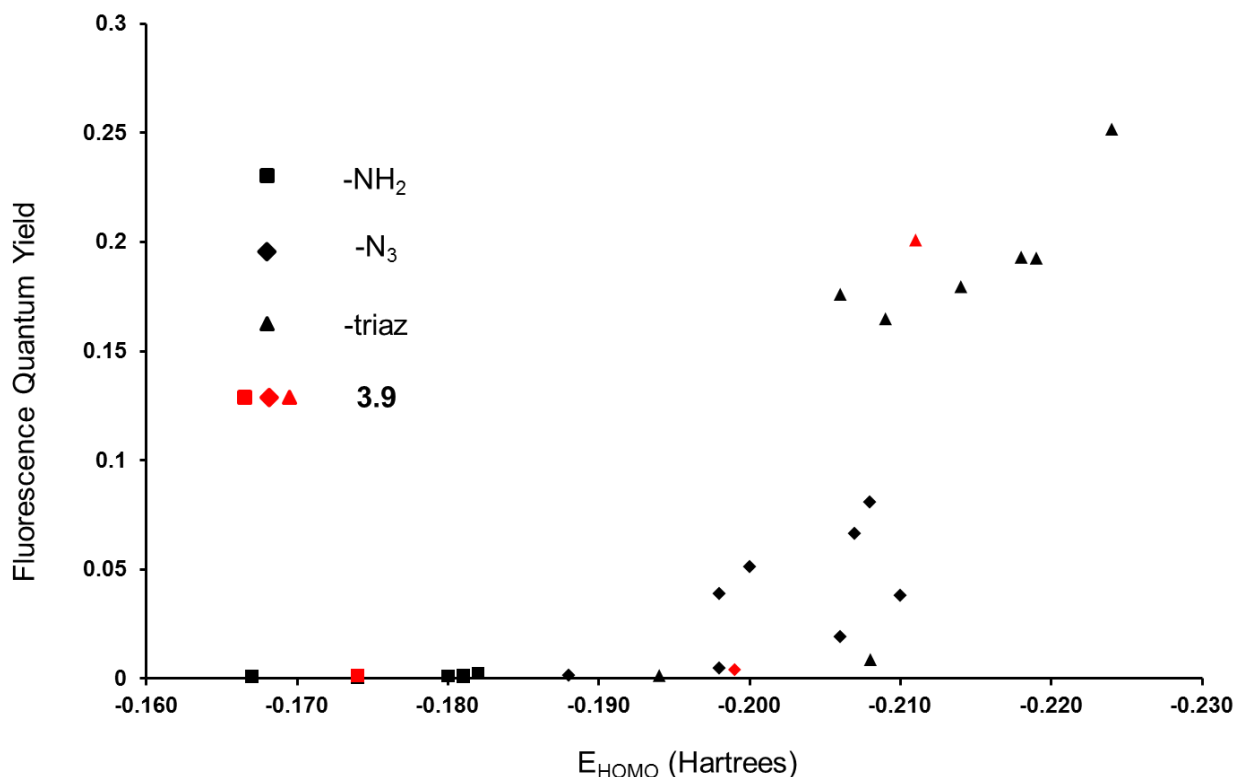


Figure 3-5. Fluorescence quantum yield vs. calculated E_{HOMO} s. The points highlighted in red correspond to derivatives of **3.9**.

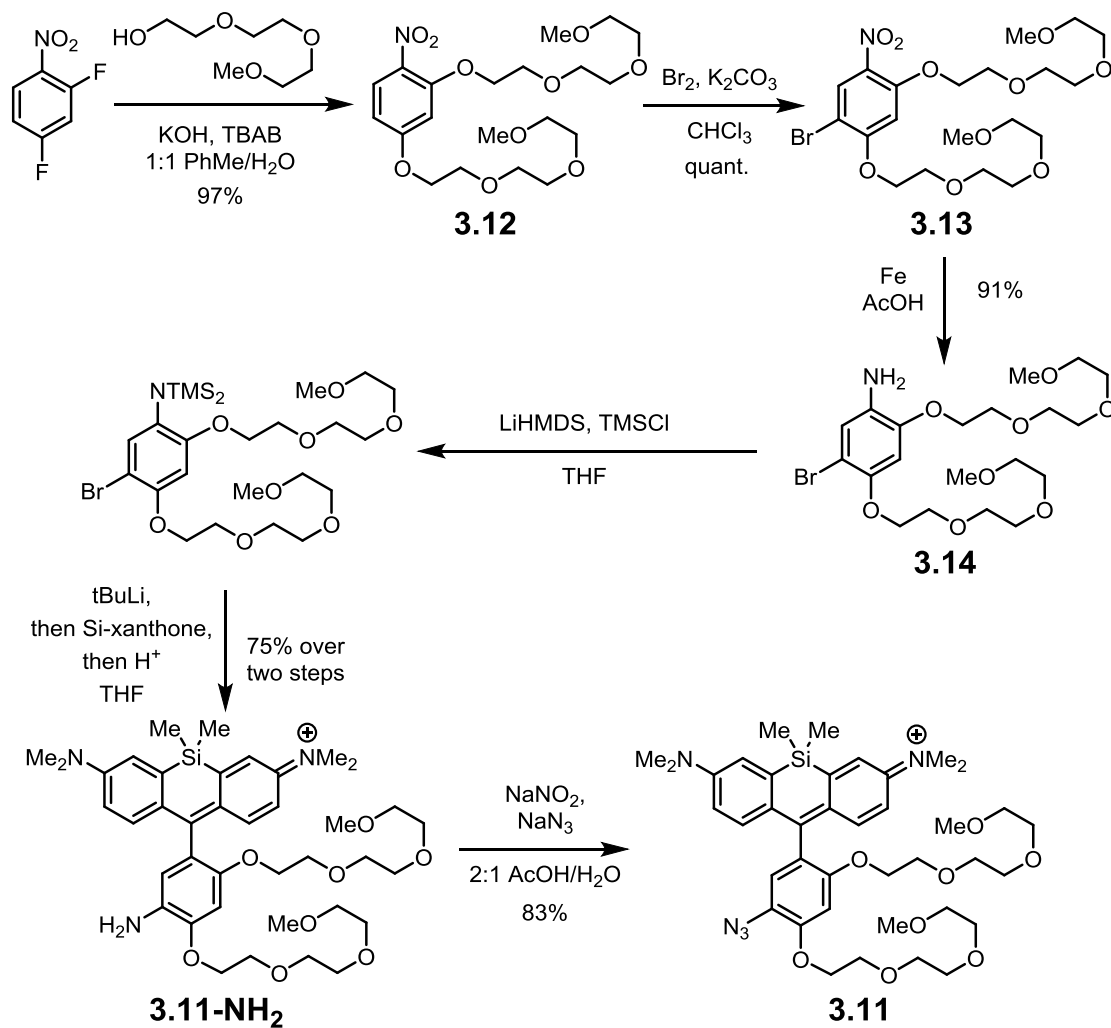
Optimization of azido Si-rhodamine 3.9 for mammalian cell surface labeling

I tested compound **3.9** as a biological imaging reagent using mammalian cells that had been metabolically labeled with peracetylated *N*-pentynoylmannosamine (Ac₄ManNAI), which is metabolized to *N*-pentynoyl sialic acid (SiaNAI) and presented on cell-surface glycoconjugates.^{36,37} However, compound **3.9** showed significant alkyne-independent background labeling even after repeated washing steps, most likely due to its substantial hydrophobic character. This non-specific binding was more problematic for Si-rhodamines as compared to fluoresceins owing to their higher hydrophobicity. While these probes are fluorogenic, non-specific binding via hydrophobic interactions can diminish the fluorescent turn-on response, as discussed in the next chapter. Additionally, sequestration of the probe leads to poorer labeling efficiency by decreasing effective probe concentration.

I hypothesized that replacing the methoxy groups with more water soluble alkoxy substituents would maintain the electronic balance between the pendant aryl and the Si-xanthene moieties while enhancing hydrophilicity. In particular, I first chose to introduce oligoethylene glycol side chains to increase the aqueous solubility of the resulting probe while maintaining cell permeability. To this end, I synthesized compound **3.11** in six steps from 2,4-difluoronitrobenzene (Scheme 3-2). I began with a double nucleophilic aromatic substitution of difluoronitrobenzene under phase transfer conditions by triethylene glycol monomethyl ether, generating compound **3.12**. Bromination using bromine and potassium carbonate in chloroform, then reduction using iron in acetic acid afforded bromoaniline **3.14**. Using this bromoaniline, I

synthesized the corresponding azido Si-rhodamine **3.11** in three steps following the general procedure outlined in Scheme 3-1.

Consistent with my hypothesis, compound **3.11** underwent a significant fluorescence enhancement upon copper-catalyzed click reaction with alkyne **3.10** (Figure 3-6). The ability to modify this switch without changing its electronic character represents a significant advantage over the azidonaphthyl switch identified in the previous chapter. Additionally, I noticed that the rate of reaction was higher for **3.11** as compared to **3.9**. This rate enhancement may be due to chelation of the copper catalyst, increasing its effective concentration.



Scheme 3-2. Synthesis of probe **3.11**. TBAB = tetrabutylammonium bromide.

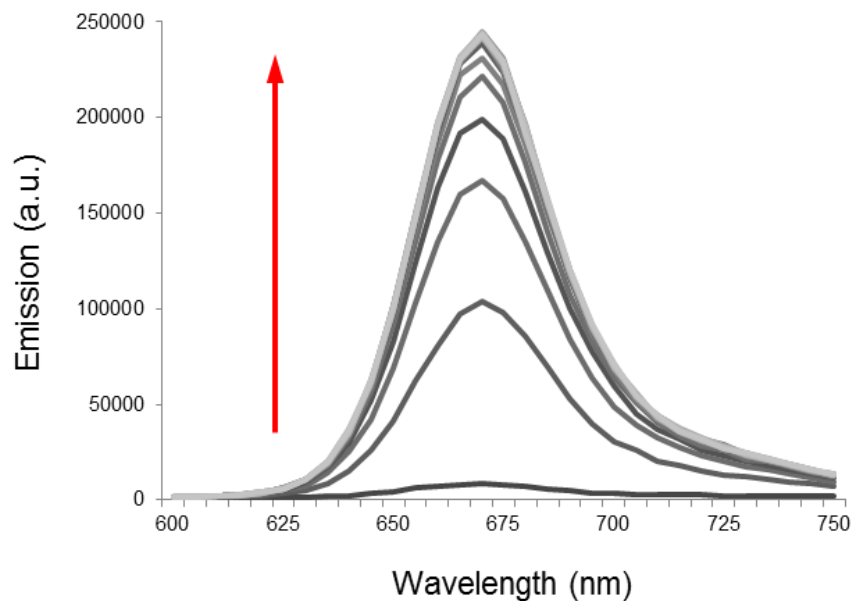


Figure 3-6. Emission spectra of **3.11** under the copper-catalyzed reaction conditions described above. Emission scans were taken every 30 seconds, with excitation at 600 nm.

I next evaluated Si-rhodamine **3.11** as a reagent for imaging SiaNAI residues on live cell surfaces. CHO K1 cells were incubated with 50 μM Ac₄ManNAI for 3 days, washed, and then incubated with 5 μM **3.11**, 50 μM CuSO₄, 300 μM BTAA (2-[4-{(bis[(1-tert-butyl-1H-1,2,3-triazol-4-yl)methyl]amino)methyl}-1H-1,2,3-triazol-1-yl]acetic acid), and 1 mM sodium ascorbate. After 15 minutes, without washing away excess probe, I observed robust cell-surface labeling (Figure 3-7). I was also able to visualize cell-surface glycan labeling as it occurred in real time (Figure 3-8). Gratifyingly, background labeling was minimal on control cells treated with *N*-acetylmannosamine (Ac₄ManNAc) (Figure 3-7).

When I performed a similar experiment using HEK 293T cells, punctate fluorescence appeared within the cells almost immediately after exposure compound **3.11** (Figure 3-9). It has been previously demonstrated that Si-rhodamines, as lipophilic cations, can localize to the mitochondria.²⁵ Indeed, such localization of this probe was confirmed by co-staining with Mitotracker Green (Figure 3-10). This observation suggests that, while probe **3.11** has the potentially beneficial property of cell permeability, it may be compromised by unwanted mitochondrial labeling in some eukaryotic cell types.

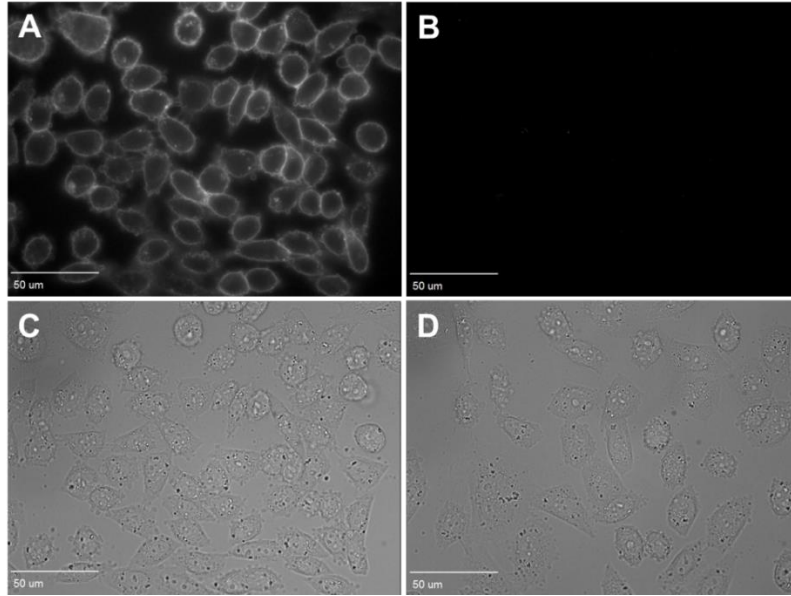


Figure 3-7. No-wash CHO cell labeling with **3.11**. Labeling was performed for 15 min and quenched with BCS following the above procedure. Scale bar = 50 μm .

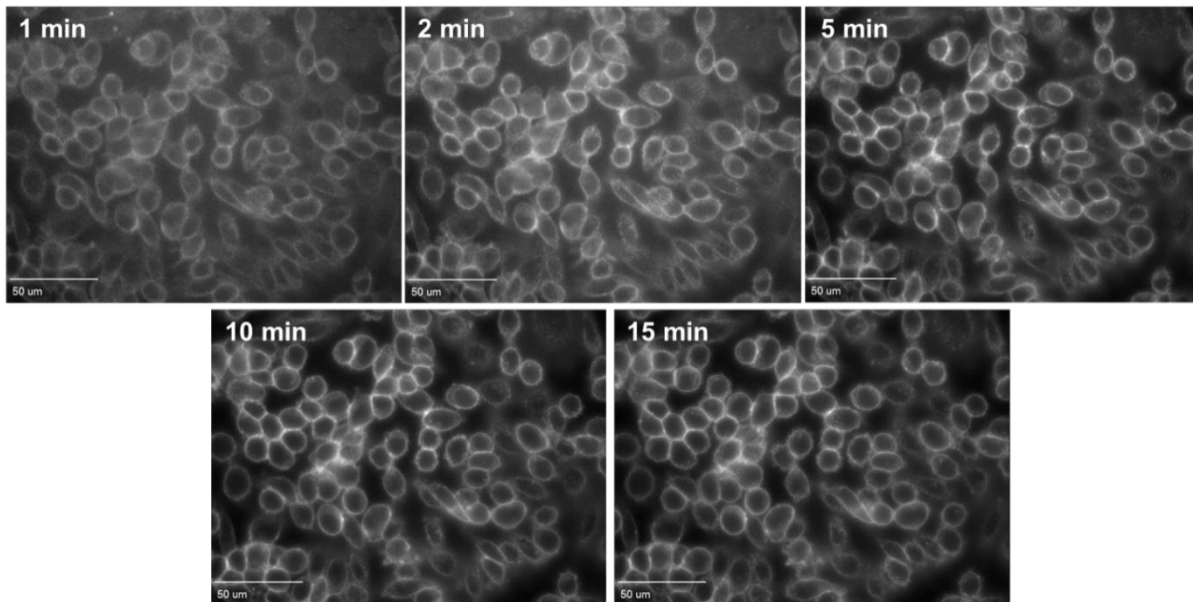


Figure 3-8. Real-time CHO K1 cell surface labeling. CHO K1 cells were labeled with **3.11** following the previously described procedure, then immediately taken on for imaging. Contrast is enhanced at early time points to show cell-surface labeling. Scale bar = 50 μm .

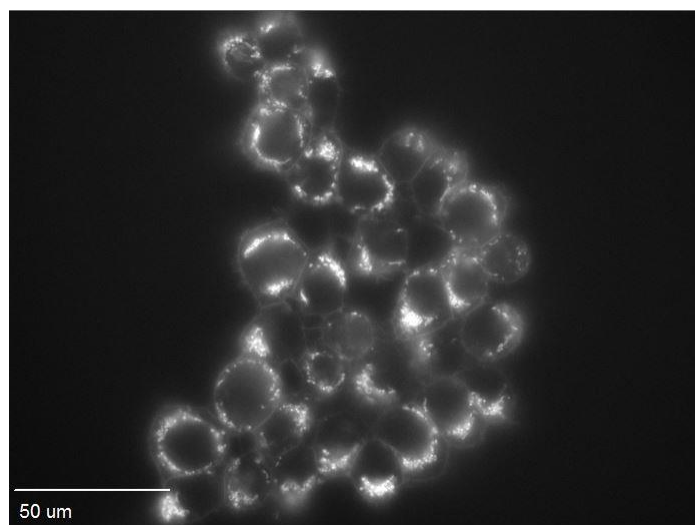


Figure 3-9. Fluorescence image of Ac₄ManNAI-treated HEK 293T cells labeled with **3.11**. Labeling was performed for 15 min and quenched with BCS following the above procedure. Scale bar = 50 μm.

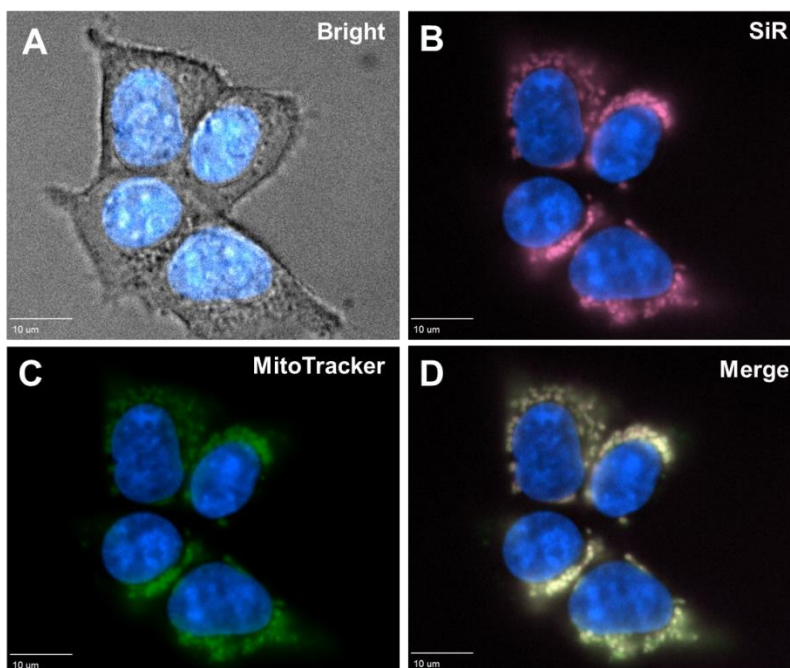


Figure 3-10. Mitochondrial staining by **3.11** in HEK 293T cells. (A) Brightfield image (B) Cy5 channel showing fluorescence from **3.11** (C) FITC channel showing mitochondrial staining by MitoTracker Green FM. (D) Overlay of Cy5 and FITC channels Scale bar = 10 μm.

I explored an approach to eliminate this background from unreacted probe by intentionally reducing any excess azide to the amine. As discussed earlier, reduction to the amine reliably results in a decrease in fluorescence (Table 3-1). Therefore, identification of a suitable reducing

agent may minimize background fluorescence during imaging applications. Tsien and coworkers identified a cell permeable reducing agent for imaging tetracysteine motifs in live cells using FAsH (fluorescein arsenical hairpin binder). They found that tributylphosphine was an effective reducing agent for intracellular disulfide bonds with no apparent toxicity at early time points.^{38,39} Therefore, I took cells labeled with the probe as in Figure 3-9 and treated the cells with tributylphosphine following their protocol. Strikingly, I found that mitochondrial fluorescence decreased upon tributylphosphine treatment (Figure 3-11). Given the likelihood of toxicity at later time points, however, I chose not to pursue this strategy further.

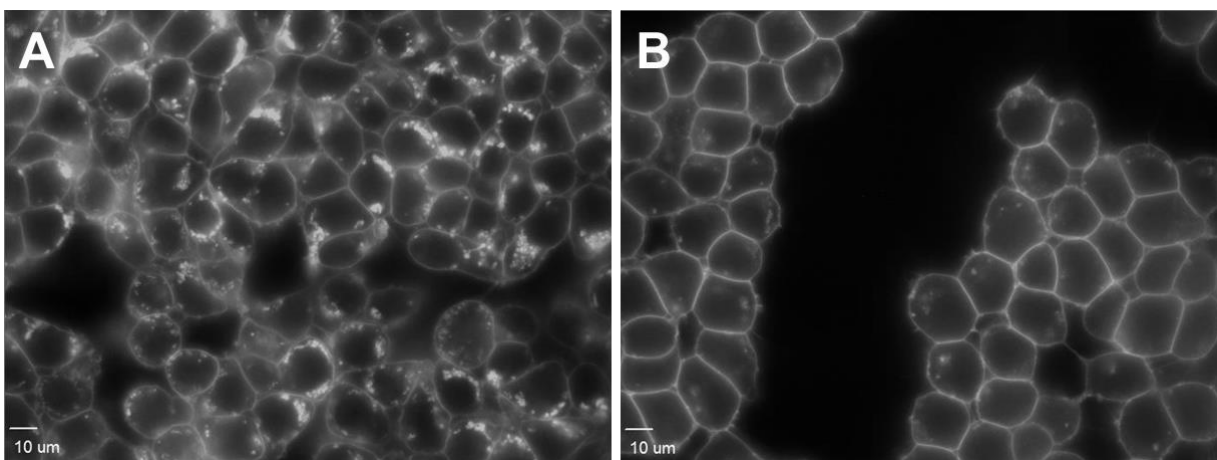
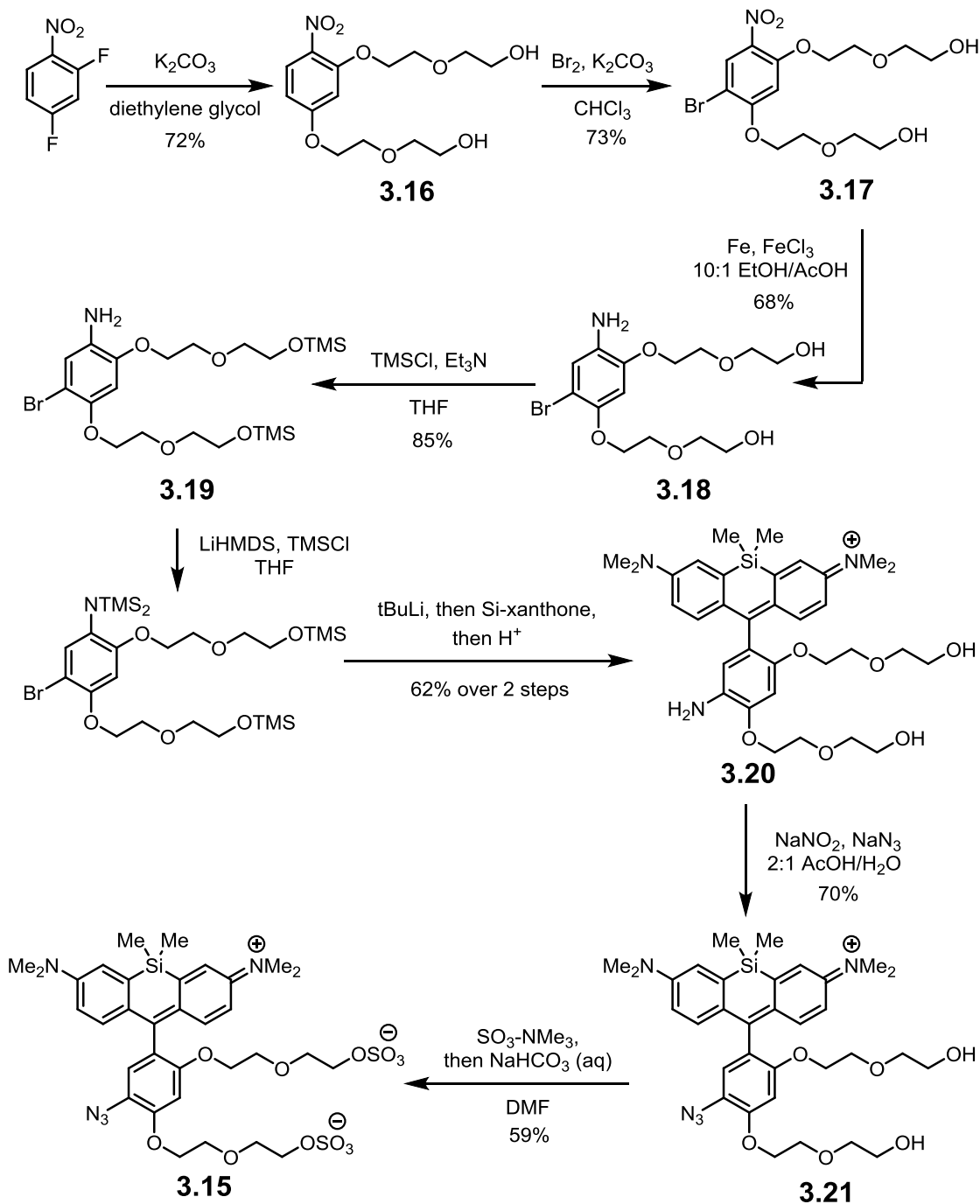


Figure 3-11. Eliminating mitochondrial staining by **3.11** in HEK 293T cells using tributylphosphine. Cy5 channel showing fluorescence from **3.11** (A) before or (B) after tributylphosphine treatment. Scale bar = 10 μ m.

Ultimately, to eliminate mitochondrial labeling, I synthesized bis-sulfated probe **3.15**, anticipating that the negative charges would limit cell permeability as well as mitochondrial localization (Scheme 3-3). I again began with a double nucleophilic aromatic substitution reaction by heating difluoronitrobenzene with potassium carbonate in diethylene glycol to produce **3.16**. The product was then brominated using bromine and potassium carbonate in chloroform, then reduced with iron and ferric chloride in a mixture of ethanol and acetic acid to furnish bromoaniline **3.18**. The alcohols were protected as trimethylsilyl ethers, then bis-O-protected bromoaniline **3.19** was carried forward to azido-Si rhodamine **3.21** using the three-step general procedure. Finally, the alcohols of **3.21** were sulfated using sulfur trioxide pyridine complex in N,N-dimethylformamide followed by sodium bicarbonate workup to yield sulfated azido Si-rhodamine **3.15**.

Like its predecessors, compound **3.15** displayed significant fluorescence enhancement upon triazole formation (Figure 3-12). In contrast to compound **3.11**, this bis-sulfated probe gave robust cell-surface labeling under no-wash conditions for both CHO K1 and HEK 293T cells, with no unwanted background or mitochondrial labeling (Figures 3-13, 3-14). This demonstrated the effectiveness of sulfation to eliminate all unwanted background towards the imaging of cell-surface biomolecules. Finally, both **3.11** and **3.15** underwent similar enhancements in

fluorescence upon catalyst free reaction with bicyclononyne⁴⁰ (Figure 3-15), showing that fluorescence enhancement is largely independent of alkyne structure and opening the door to catalyst-free bioorthogonal labeling applications *in vivo*.



Scheme 3-3. Synthesis of probe **3.15**.

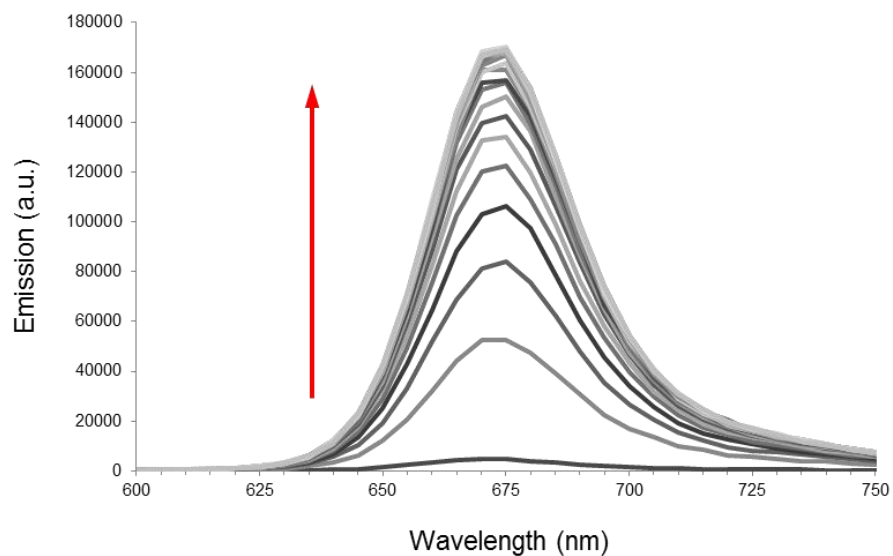


Figure 3-12. Fluorescence enhancement of **3.15** under the copper-catalyzed click conditions described above. Emission scans were taken every 30 seconds, with excitation at 600 nm.

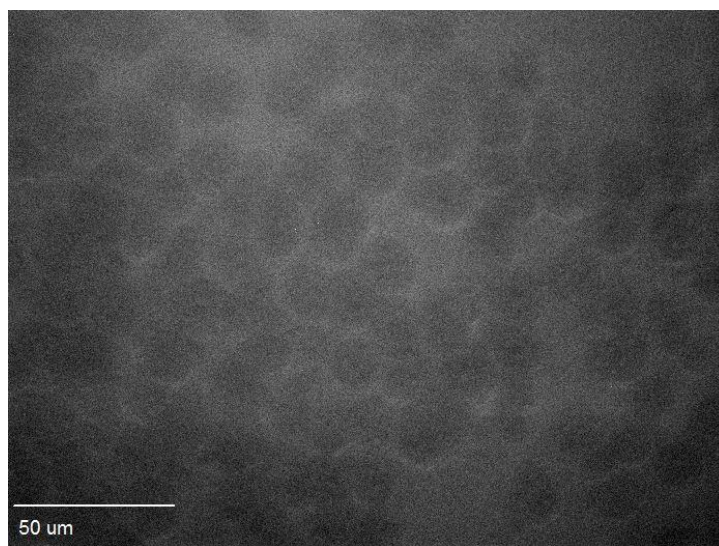


Figure 3-13. High contrast image of Ac_4ManNAc -treated cells, demonstrating that **3.15** is not cell permeable. Scale bar = 50 μm .

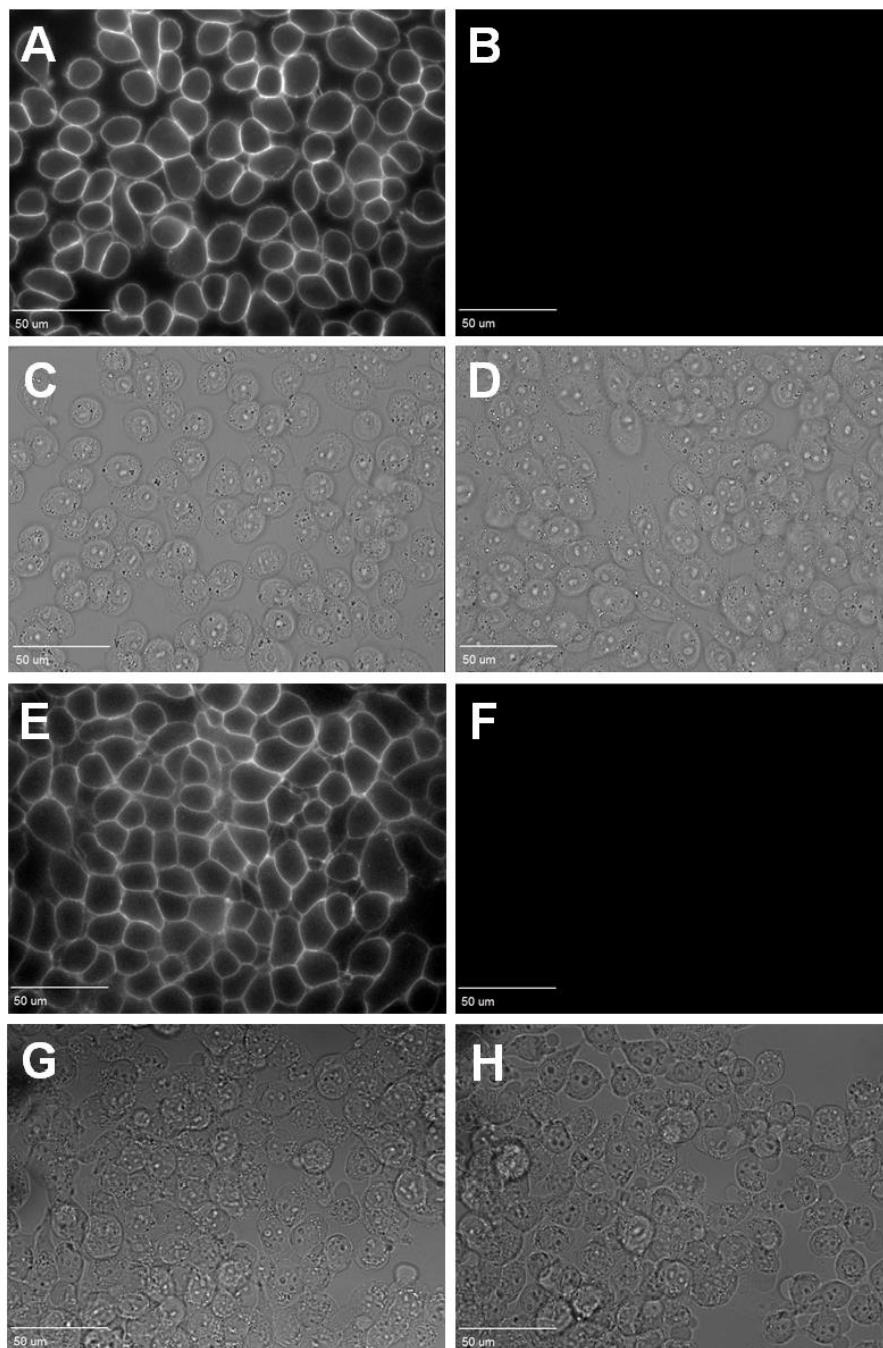


Figure 3-14. No-wash mammalian cell surface labeling with bis-sulfated probe **3.15**. (A),(C) Fluorescence and brightfield images of CHO K1 cells treated with Ac₄ManNAI and labeled with **3.15**. (B),(D) Fluorescence and brightfield images of CHO K1 cells treated with Ac₄ManNAc and labeled with **3.15**. (E),(G) Fluorescence and brightfield images of HEK 293T cells treated with Ac₄ManNAI and labeled with **3.15**. (F),(H) Fluorescence and brightfield images of HEK 293T cells treated with Ac₄ManNAc and labeled with **3.15**. Scale bar = 50 μm.

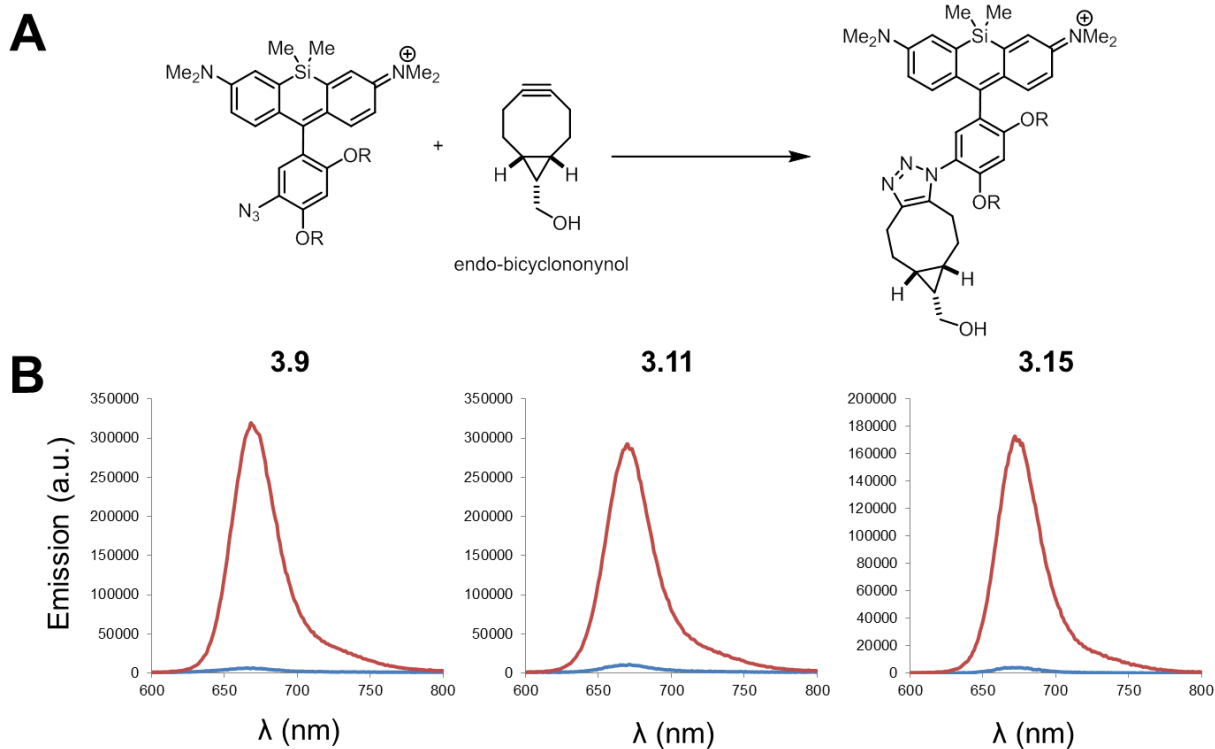


Figure 3-15. Fluorescence enhancement upon reaction with endo-bicyclononynol. (A) Reaction of azido Si-rhodamines **3.9**, **3.11**, and **3.15** with endobicyclononynol to form a triazole. (B) Fluorescence spectra of 2 μ M azide probe incubated with either 2 eq. endo-bicyclononynol in DMSO (red) or only DMSO (blue) for 18 h. Excitation at 600 nm.

Conclusion

In this chapter, I discuss my work on the development of fluorogenic NIR azide probes with up to 48-fold enhancement in fluorescence upon triazole formation. Derivatives with improved water solubility enabled no-wash NIR imaging of glycoconjugates on live mammalian cells. This modular synthesis of Si-rhodamine analogs with variously substituted pendant aryl rings allows facile modification of their physical and biochemical properties while maintaining a significant fluorescence enhancement. This modular route would ultimately enable the development of a universal platform for fluorogenic azide probes, as discussed in the next chapter.

Experimental Procedures

DFT Calculations

Aryl E_{HOMOS} were calculated by first performing a conformational search in MacroModel. Low energy conformers were further optimized using Jaguar at the B3LYP/6-31G(d) level of theory. The reported E_{HOMO} corresponds to the lowest energy conformer after DFT calculations. No significant differences in energies were observed by considering sets of conformers or by optimizing the geometry with the xanthene moiety present. Calculations were performed at the UC Berkeley College of Chemistry Molecular Graphics and Computation Facility.

Measuring fluorescence quantum yields

Fluorescence quantum yields were measured by creating 2 mM stocks of dyes in MeOH. The dyes were then diluted to 20 μM in PBS, which was further diluted in PBS to various final concentrations. The absorbance and emission spectra of five different concentrations of dye were measured while keeping maximum absorbance under 0.2. Solutions of probe were excited at 600 nm, and emission was integrated from 600 to 800 nm. Plotting integrated emission vs. absorbance at 600 nm yielded a line, whose slope corresponds to the fluorescence quantum yield. Absolute quantum yields were determined by comparison with the slope of the line measured for cresyl violet in MeOH ($\Phi_{\text{fl}} = 0.54$). The reported quantum yields are the average of three sets of measurements. Absorbance spectra were recorded on a Varian Cary 50 UV-Visible spectrophotometer. Fluorescence spectra were recorded on a Photon Technology International Quanta Master 4 L-format scanning spectrofluorometer equipped with an LPS-220B 75-W xenon lamp and power supply, A-1010B lamp housing with an integrated igniter, switchable 814 photon counting/analog photomultiplier detection unit, and MD5020 motor driver. Measurements were made in 1 cm x 0.4 cm quartz cuvettes with a total sample volume of 1 mL.

Monitoring absorbance/fluorescence during copper-catalyzed click reactions

To a 1 cm x 0.2 cm quartz cuvette was added 944 μL PBS. Next, 2 μL 50 mM BTAA in PBS and 1 μL 50 mM CuSO_4 in H_2O were added to a 1 cm x 0.4 cm quartz cuvette and the solution mixed with a pipette. Next, 50 μL freshly prepared 100 mM sodium ascorbate in PBS was added and the solution mixed again. Then, 2 μL 1 mM azido Si-rhodamine in 4:1 PBS/MeOH was added and the solution mixed. The emission spectra were recorded at this time ($t = 0$ s). Finally, 1 μL 100 mM alkyne in DMSO was added and the solution vigorously mixed and monitored every 30 s for 10 min. Final concentrations for all reagents are 2 μM azido Si-rhodamine, 100 μM alkyne, 100 μM BTAA, 50 μM CuSO_4 , and 5 mM sodium ascorbate with a total volume of 1 mL. Fluorescence spectra were recorded on a Photon Technology International Quanta Master 4 L-format scanning spectrofluorometer equipped with an LPS-220B 75-W xenon lamp and power supply, A-1010B lamp housing with an integrated igniter, switchable 814 photon counting/analog photomultiplier detection unit, and MD5020 motor driver. Absorbance spectra were recorded on a Varian Cary 50 UV-Visible spectrophotometer.

Fluorescence microscopy

For mammalian cells, microscopy was performed using a Zeiss AxioVert 200M inverted microscope using a Plan-Neofluar 40x/0.75 or 63x/0.75 objective. For bacterial cells, microscopy was performed using a 100x/1.3 objective. A 175W xenon lamp housed in a Sutter DG4 illuminator linked to the microscope by an optical fiber assured shuttering and illumination. Exposure time was 1000 ms using the Cy5 filter for labeling with azido Si-rhodamines and 1000 ms using the FITC filter for labeling with azido-PEG₃-carboxyrhodamine 110. Images were acquired and processed using SlideBook 5.0, and are shown as a single z-plane.

No-wash mammalian cell labeling

Cells were grown in 8-well Lab-Tek Chambered Coverglass systems in media (HAM-F12 for CHO K1 cells, DMEM for HEK 293T cells) containing fetal bovine serum, penicillin/streptomycin, and either 50 μ M Ac₄ManNAI or Ac₄ManNAc for 3 d at 37 °C, as described previously.¹ The cells were then washed with 3 x 300 μ L PBS, then incubated with 100 μ L freshly prepared click solution. Click solution comprised of 50 μ M CuSO₄, 300 μ M BTAA, 2.5 mM sodium ascorbate, and 5 μ M azido Si-rhodamine. After 15 min, the reactions were quenched with the addition of 1 μ L of 100 mM BCS (final concentration 1 mM). No changes in fluorescence were observed before or after the addition of BCS. For real-time imaging, images were acquired as the labeling progressed without quenching the reaction.

Mitochondrial co-staining experiments

HEK 293T cells were grown in a LabTek 8-well chambered glass slide in DMEM containing fetal bovine serum, penicillin/streptomycin for 3 d at 37 °C. The cells were then incubated with 100 nM MitoTracker Green FM and 1 μ g/mL Hoechst 33342 in fresh media for 30 min at 37 °C, then media removed and the cells incubated with 100 μ L PBS containing 5 μ M **3.11**. The cells were then directly imaged.

Tributylphosphine treatment on HEK 293T cells

HEK 293T cells were grown in a LabTek 8-well chambered glass slide in the presence of 50 μ M Ac₄ManNAI for 3 d at 37 °C. The cells were then washed with 3 x 300 μ L PBS, then incubated with 100 μ L freshly prepared click solution. Click solution comprised of 50 μ M CuSO₄, 300 μ M BTAA, 2.5 mM sodium ascorbate, and 5 μ M azido Si-rhodamine. After 15 min, the reactions were quenched with the addition of 1 μ L of 100 mM BCS (final concentration 1 mM). The reaction mixture was then removed, replaced with 300 μ L PBS, and imaged. Finally, 0.3 μ L 1 M tributylphosphine in ethanol was added and the cells imaged after 10 minutes.

Reaction of azido Si-rhodamines with endo-bicyclononyl

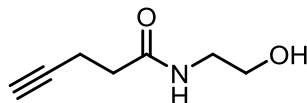
25 μ L of 1 mM azido Si-rhodamine in 4:1 PBS/MeOH was mixed with 0.5 μ L of DMSO or 0.5 μ L 100 mM endo-bicyclononyl (2 equiv.) in DMSO. The solutions were covered with foil and gently shaken overnight (18 h). 2.04 μ L of each solution was diluted to a final volume of 1 mL in PBS for fluorescence measurements.

Synthetic procedures

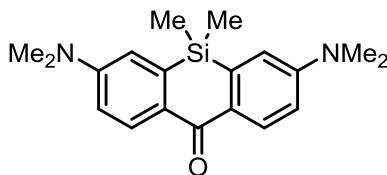
All chemical reagents obtained from commercial suppliers were used without further purification. Anhydrous dichloromethane, tetrahydrofuran and acetonitrile were passed through an activated alumina column prior to use. Anhydrous DMF was used as purchased. Water was double distilled prior to use. Ac_4ManNAI ³⁷ and BTTAA ³¹ were prepared according to literature procedures.

Flash chromatography was performed using Silicycle SiliaFlash P60 silica gel. Analytical thin layer chromatography was performed using glass-backed Analtech Uniplate silica gel plates containing a fluorescent indicator. Reversed-phase HPLC was performed on a Varian Pro Star system with a Varian UV-Vis detector model 345 (210, 254 nm) on a Dynamax Microsorb C-18 preparative column (21.4 x 250 mm) at a flow rate of 20 mL/min or on a Dynamax Microsorb C-18 semi-preparative column (10.0 x 250 mm) at a flow rate of 4 mL/min.

NMR spectra were obtained on Bruker AVQ-400, AVB-400, DRX-500, AV-500, or AV-600 spectrometers at ambient temperature at the UC Berkeley College of Chemistry NMR Facility. ¹H NMR shifts are calibrated to residual undeuterated solvent: δ 7.26 for CHCl_3 , 2.50 for d_5 -DMSO, 4.79 for HDO, and 3.31 for CHD_2OD . ¹³C NMR shifts are calibrated to solvent peaks: δ 77.16 for CDCl_3 , 39.52 for d_6 -DMSO, and 49.00 for CD_3OD . High resolution mass spectrometry was performed at the UC Berkeley Mass Spectrometry Laboratory.



0.245 g (2.50 mmol) 4-pentynoic acid, a white crystalline solid, was dissolved in 25 mL dry CH_2Cl_2 in a flame-dried flask. Then, 0.382 g HOBt hydrate (2.50 mmol, 1 equiv.), an off white powder, was added. The cloudy white suspension was cooled to 0 °C, then 0.387 mL (0.316 g, 2.50 mmol, 1 equiv.) diisopropylcarbodiimide, a clear liquid, was added. The solution was warmed to rt and stirred vigorously for 10 min, then 0.21 mL (0.214 g, 3.50 mmol, 1.4 equiv.) ethanolamine, a viscous yellow liquid, was added, immediately turning the slightly cloudy white solution to a thick white slurry. The reaction was stirred at rt for 8 h, then filtered to remove the HOBt. The clear filtrate was concentrated to yield an off-white residue. The residue was purified by flash chromatography using 20:1 to 10:1 $\text{CHCl}_3/\text{MeOH}$, yielding alkyne **3.10** (0.323 g, 2.29 mmol, 92%) as a clear oil that solidified to a white solid upon storage at -20 °C. Spectral data were identical to reported values.³



2.02 g (4.90 mmol) 4,4'-methylenebis(3-bromo-N,N-dimethylaniline)²⁵, a light pink solid, was added to a flame-dried flask and azeotropically dried with benzene. The solid was dissolved in

48 mL dry THF in a flame-dried flask. The clear solution was cooled to $-78\text{ }^{\circ}\text{C}$. Next, 10.7 mL *sec*-butyllithium (0.96 M in cyclohexane, 10.3 mmol, 2.1 equiv.), was added slowly directly into the solution. The now yellow solution was stirred at $-78\text{ }^{\circ}\text{C}$ for 30 min. Next, 0.71 mL (0.759 g, 5.88 mmol, 1.2 equiv.) dimethyldichlorosilane, a clear liquid, in 24 mL dry THF was added dropwise down the side of the flask. Upon completion of addition, the solution was warmed to rt and stirred for 3 h under N_2 . The solution was quenched by the addition of 6 mL 2M HCl, and the cloudy solution then poured into 100 mL sat. NaHCO_3 and extracted with 3 x 150 mL CH_2Cl_2 . The combined organic layers were dried over MgSO_4 and concentrated, yielding intermediate N3,N3,N7,N7,5,5-hexamethyl-5,10-dihydrodibenzo[b,e]silole-3,7-diamine as an air-sensitive light blue-green oil. $R_f = 0.3$ (10:1 hex/EtOAc, UV/ I_2).

The light blue-green oil was dissolved in 35 mL CH_2Cl_2 and cooled to $0\text{ }^{\circ}\text{C}$. Next, 2.32 g (10.86 mmol, 3 equiv.) potassium permanganate, a grey solid, was dissolved in ~ 20 mL hot water and 4.9 mL 1M KOH (4.90 mmol, 1 equiv.), 0.333 g (0.980 mmol, 0.2 equiv.) tetrabutylammonium bisulfate, a white solid, and cold water were added to give a final volume of 30 mL. The purple solution was added to the reaction flask, turning the solution to a muddy brown. The flask containing the reagents was washed with another 20 mL CH_2Cl_2 and 20 mL H_2O . The cloudy brown solution was stirred for 30 min, after which TLC indicated consumption of starting material, then the reaction was quenched by the addition of 10 mL AcOH. (Letting the reaction go for too long results in the formation of significant amounts of a difficult-to-separate byproduct with a slightly lower R_f than the desired Si-xanthone). The solution was cooled to $0\text{ }^{\circ}\text{C}$, then 3.8 g Na_2SO_3 was carefully added, turning the brown solution an olive-green. The reaction was diluted with 150 mL 50% brine and extracted with 5 x 100 mL CH_2Cl_2 , dried over MgSO_4 , and concentrated, yielding a blue-green solid. The solid was purified by flash chromatography with 7:1 hexanes/EtOAc to yield **Si-xanthone** (0.706 g, 2.18 mmol, 44%) as a golden yellow solid. Spectral data were identical to reported values.²⁵

General procedure for the synthesis of bis-trimethylsilyl-protected bromoanilines:

Bromoaniline was dissolved in dry THF (concentration of 0.30 M) in a flame-dried flask and cooled to $-78\text{ }^{\circ}\text{C}$. To the solution was added 2.1 equiv. freshly prepared 0.60 M LiHMDS in THF, also cooled to $-78\text{ }^{\circ}\text{C}$, dropwise via cannula. After addition, the solution was stirred for 10 min at $-78\text{ }^{\circ}\text{C}$, warmed to rt for 5 min, then cooled back to $-78\text{ }^{\circ}\text{C}$. Finally, 2.1 equiv. trimethylsilyl chloride was added dropwise and the solution warmed to rt and stirred overnight (16 h). The now cloudy solution was concentrated and taken up in hexanes and filtered. The filtrate was concentrated to afford bis-TMS-protected aniline, generally contaminated with small amounts of tris-trimethylsilylamine, which was used directly in the next step without further purification.

General procedure for the synthesis of amino Si-rhodamines

Bis-TMS-protected aniline was dissolved in dry THF in a flame-dried flask to a final concentration of 0.2 M. The solution was cooled to $-78\text{ }^{\circ}\text{C}$. To the solution was then added dropwise 2 equiv. *t*BuLi (freshly titrated, from a ~ 1.6 M solution in pentanes). After 30 minutes, 0.48 equiv. Si-xanthone, a yellow solid, was suspended in 3 mL dry THF (concentration of 0.1 M) and added in one portion. The solution was immediately warmed to rt and stirred for 1 h. The reaction was then quenched by the slow addition of 3 equiv. HCl (from a 2 M aqueous solution), turning the solution a deep blue color. The blue solution was quickly poured into 10% sat.

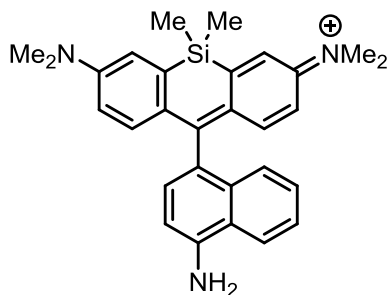
NaHCO₃ and extracted 5 times with CH₂Cl₂, dried over MgSO₄, and concentrated to yield a blue solid. The solid was purified by flash chromatography with CHCl₃ to 20:1 CHCl₃/MeOH to 7:1 CHCl₃/MeOH to yield the product as a blue solid. For photophysical measurements, the solid was further purified by reverse-phase HPLC using a 20-100% MeCN/H₂O + 0.1% TFA gradient.

General procedure for the synthesis of azido Si-rhodamines

Amino Si-rhodamine, a blue solid, was dissolved in a 2:1 AcOH/H₂O mixture to a final concentration of 0.025 M. The blue solution was cooled to 0 °C. Next, 1.5 eq. sodium nitrite, a white powder, was added. The solution was stirred for 5 min at 0 °C, during which the color lightened slightly. Next, 2 eq. sodium azide, a white solid, was added. Bubbling was observed. The solution was stirred for 1 h at 0 °C and 1 h at rt, then concentrated *in vacuo*. The remaining blue residue was purified with flash chromatography using CHCl₃ to 20:1 CHCl₃/MeOH to 7:1 CHCl₃/MeOH to yield the product as a blue solid. The product was further taken up in CHCl₃ and washed 3 times with 0.1% TFA in H₂O to yield the product as the TFA salt. For photophysical measurements and biological experiments, the solid was further purified by reverse-phase HPLC using a 20-100% MeCN/H₂O + 0.1% TFA gradient.

General procedure for the synthesis of triazolyl Si-rhodamines

Azido Si-rhodamine, a blue solid, was dissolved in MeOH to a final concentration of 0.02 M. The blue solution was placed under a N₂ atmosphere, then 5 equiv. alkyne **3.10**, a white solid, was added. Next, 0.5 equiv. Cu(MeCN)₄PF₆, a white powder, was added, followed by 0.01 equiv. TBTA (added from a 10 mM solution in MeOH). The blue solution was stirred for 15 h, after which consumption of starting material was confirmed by LC-MS. The solution was concentrated and the blue residue purified by reverse-phase HPLC using a 20-100% MeCN/H₂O + 0.1% TFA gradient to yield the product as a blue solid.

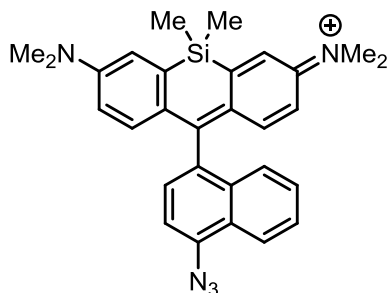


0.111 g (0.500 mmol) of 1-amino-4-bromonaphthalene was converted to the bis-trimethylsilyl-protected-aminobromonaphthalene (0.173 g, 0.472 mmol, 94%), a wet pink-grey solid, via the general procedure.

0.120 g (0.328 mmol) of this intermediate was converted to **3.1-NH₂** (64.2 mg, 0.132 mmol, 80% based off Si-xanthone), a blue solid, via the general procedure.

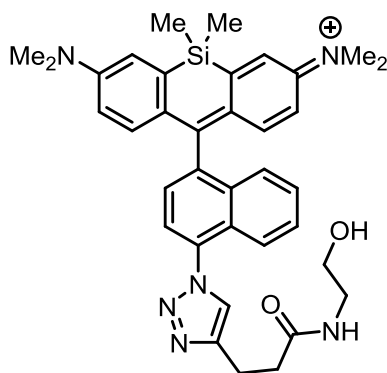
¹H NMR (500 MHz, CDCl₃): δ 0.04 (s, 3H), 0.06 (s, 3H), 3.36 (s, 12H), 4.72 (brs, 2H), 6.48 (dd, 2H, *J* = 9.6 Hz, 2.9 Hz), 6.97 (d, 1H, *J* = 7.6 Hz), 7.09 (d, 1H, *J* = 7.7 Hz), 7.14 (d, 2H, *J* = 9.6 Hz), 7.20 (d, 2H, *J* = 2.9 Hz), 7.27-7.35 (m, 2H), 7.41-7.49 (m, 1H), 7.97 (d, 1H, *J* = 8.5 Hz);
¹³C NMR (151 MHz, CDCl₃): δ -0.64, -0.53, 41.12, 108.26, 113.70, 120.38, 1212.84, 122.76,

125.10, 125.49, 126.50, 126.98, 128.41, 129.18, 133.26, 142.80, 144.50, 148.14, 153.98, 171.50; HRMS (ESI): Calculated for $C_{29}H_{32}N_3Si$ [M-Cl]⁺ 450.2360, found 450.2352.



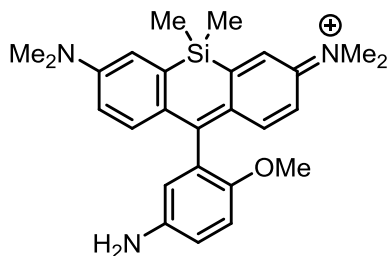
47.1 mg (0.0971 mmol) **3.1-NH₂** was converted to **3.1-N₃** (34.5 mg, 0.0585 mmol, 60%), a blue solid, via the general procedure.

¹H NMR (600 MHz, CDCl₃): δ 0.63 (s, 3H), 0.66 (s, 3H), 3.32 (s, 12H), 6.47 (dd, 2H, *J* = 9.6 Hz, 2.6 Hz), 6.98 (d, 2H, *J* = 9.6 Hz), 7.18 (d, 2H, *J* = 2.7 Hz), 7.47-7.30 (m, 4H), 7.52 (ddd, 1H, *J* = 8.3 Hz, 6.6 Hz, 1.3 Hz), 8.22 (d, 1H, *J* = 8.5 Hz); ¹³C NMR (100 MHz, CDCl₃): δ -0.82, -0.80, 40.97, 113.08, 114.03, 120.90, 123.14, 126.07, 126.10, 126.99, 127.05, 128.48, 128.58, 133.03, 133.36, 137.93, 142.19, 148.50, 154.22, 168.31; HRMS (ESI): Calculated for $C_{29}H_{30}N_5Si$ [M-TFA]⁺ 476.2265, found 476.2256.



5.9 mg (0.010 mmol) of **3.1-N₃** was converted to **3.1-triazole** (6.3 mg, 0.0086 mmol, 86%), a blue solid, via the general procedure.

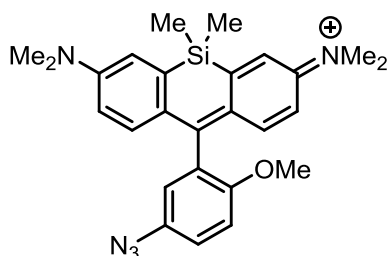
HRMS (ESI): Calculated for $C_{36}H_{41}N_6O_2Si$ [M-TFA]⁺ 617.3055, found 617.3048.



0.202 g (1.00 mmol) 3-bromo-4-methoxyaniline was converted to bis-trimethylsilyl-protected bromoaniline (0.340 g, 0.985 mmol, 98%), a brown oil, via the general procedure.

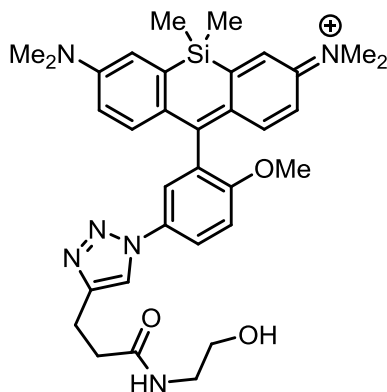
69.1 mg (0.200 mmol) of this intermediate was converted to **3.2-NH₂** (26.0 mg, 0.056 mmol, 56% based off Si-xanthone), a blue solid, via the general procedure.

¹H NMR (400 MHz, CD₃OD): δ 0.58 (s, 3H), 0.62 (s, 3H), 3.35 (s, 12H), 3.76 (s, 3H), 6.78 (dd, 2H, *J* = 9.6 Hz, 2.8 Hz), 7.12 (d, 2H, *J* = 9.6 Hz), 7.16 (d, 1H, *J* = 2.7 Hz), 7.32-7.40 (m, 3H), 7.60 (dd, 1H, *J* = 8.9 Hz, 2.8 Hz); ¹³C NMR (125 MHz, CDCl₃): δ -0.81, -0.64, 41.11, 56.53, 112.82, 113.82, 117.08, 117.49, 120.32, 128.11, 128.15, 140.34, 142.31, 148.23, 149.39, 154.12, 169.17; HRMS (ESI): Calculated for C₂₆H₃₂N₃OSi [M-Cl]⁺ 430.23092, found 430.23010.



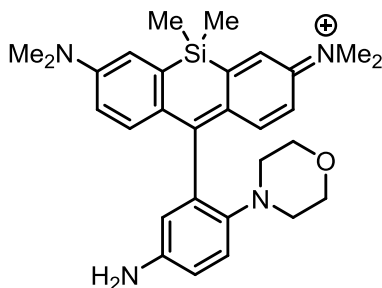
42.3 mg (0.0908 mmol) of **3.2-NH₂** was converted to **3.2-N₃** (30.7 mg, 0.0539 mmol, 59%), a blue solid, via the general procedure.

¹H NMR (400 MHz, CDCl₃): δ 0.57 (s, 3H), 0.59 (s, 3H), 3.35 (s, 12H), 3.69 (s, 3H), 6.65 (dd, 2H, *J* = 9.6 Hz, 2.8 Hz); 6.74 (d, 1H, *J* = 2.8 Hz); 7.06 (d, 1H, *J* = 8.9 Hz); 7.14 (d, 2H, *J* = 9.6 Hz); 7.14 (d, 2H, *J* = 2.8 Hz), 7.17 (dd, 1H, *J* = 2.8 Hz, 8.9 Hz); ¹³C NMR (125 MHz, CDCl₃): δ -0.98, -0.72, 40.98, 56.36, 112.65, 114.11, 120.73, 120.88, 120.93, 127.83, 129.06, 132.69, 141.65, 148.45, 154.06, 154.26, 166.39; HRMS (ESI): Calculated for C₂₆H₃₀N₅OSi [M-TFA]⁺ 456.2214, found 456.2211.



5.7 mg (0.010 mmol) of **3.2-N₃** was converted to **3.2-triazole** (2.5 mg, 0.0035 mmol, 35%), a blue solid, via the general procedure.

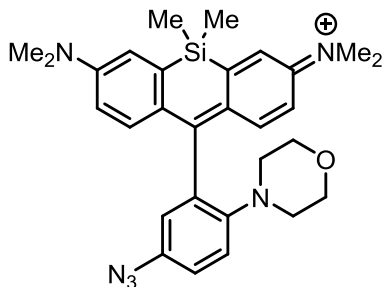
HRMS (ESI): Calculated for C₃₃H₄₁N₆O₃Si [M-TFA]⁺ 597.3004, found 597.2991.



0.386 g (1.50 mmol) 3-bromo-4-morpholinoaniline, a light yellow solid, was converted to bis-trimethylsilyl-protected bromoaniline (0.625 g, 1.50 mmol, quant.), a golden yellow solid, via the general procedure.

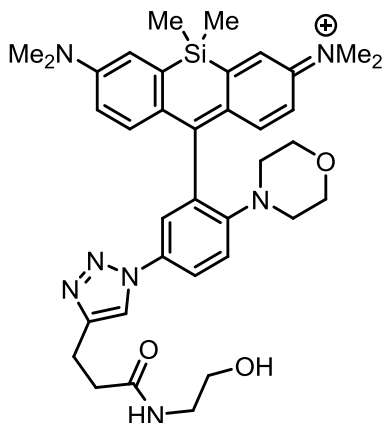
0.263 g (0.655 mmol) of the above intermediate was converted to **3.3-NH₂** (0.123 g, 0.236 mmol, 76% based off Si-xanthone) via the general procedure.

¹H NMR (400 MHz, CDCl₃): δ 0.53 (s, 3H), 0.68 (s, 3H), 2.62 (t, 4H, *J* = 4.4 Hz), 3.31 (t, 4H, *J* = 4.4 Hz), 3.39 (s, 12H), 6.58 (d, 1H, *J* = 2.7 Hz), 6.65 (dd, 2H, *J* = 9.6 Hz, 2.8 Hz), 6.86 (dd, 1H, *J* = 8.6 Hz, 2.7 Hz), 7.10 (d, 1H, *J* = 8.6 Hz), 7.13 (d, 2H, *J* = 2.8 Hz), 7.35 (d, 2H, *J* = 9.6 Hz); ¹³C NMR (100 MHz, CDCl₃): δ -1.88, -0.24, 41.08, 52.74, 67.37, 113.61, 117.11, 117.37, 120.09, 122.99, 128.00, 136.46, 142.14, 142.19, 143.06, 147.95, 153.93, 171.69; HRMS (ESI): Calculated for C₂₉H₃₇N₄OSi [M-Cl]⁺ 485.2731, found 485.2731.



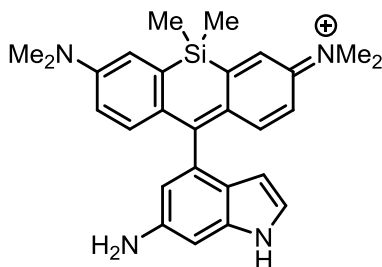
55.6 mg (0.107 mmol) **3.3-NH₂** was converted to **3.3-N₃** (42.1 mg, 0.0674 mmol, 63%) via the general procedure.

¹H NMR (500 MHz, CDCl₃): δ 0.52 (s, 3H), 0.65 (s, 3H), 2.75 (t, 4H, *J* = 4.6 Hz), 3.35 (t, 4H, *J* = 4.6 Hz), 3.38 (s, 12H), 6.67 (dd, 2H, *J* = 9.6 Hz, 2.9 Hz), 6.76 (d, 1H, *J* = 2.6 Hz), 7.19 (m, 6H); ¹³C NMR (125 MHz, CDCl₃): δ -1.83, 0.06, 31.01, 52.12, 67.11, 114.03, 120.68, 121.02, 121.46, 122.52, 127.40, 135.51, 135.85, 141.70, 147.92, 148.25, 154.10, 168.03; HRMS (ESI): Calculated for C₂₉H₃₅N₆OSi [M-TFA]⁺ 511.2636, found 511.2636.



6.3 mg (0.010 mmol) **3.3-N₃** was converted to **3.3-triazole** (6.17 mg, 0.0081 mmol, 81%) via the general procedure.

HRMS (ESI): Calculated for C₃₆H₄₆N₇O₃Si [M-TFA]⁺ 652.3426, found 652.3425

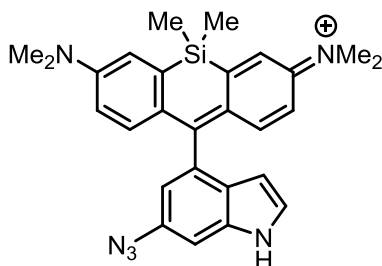


0.363 g (1.72 mmol) 4-bromo-6-amino indole, a brown solid, was dissolved in 5.1 mL dry THF and the light brown solution cooled to -78 °C. Next, 3.1 mL (1.72 mmol) of freshly prepared 0.6 M LiHMDS solution, also cooled to -78 °C, was added dropwise via cannula, turning the solution of indole a deep red brown. The solution was stirred at -78 °C for 10 min, warmed to rt for 5 min, then cooled to -78 °C again, during which it turned a cloudy brown. Finally, 0.218 mL (0.187 g, 1.72 mmol, 1 equiv.) trimethylsilyl chloride was added dropwise. The solution was warmed to rt and stirred for 4 h. The solution was cooled to -78 °C and another 6.2 mL (3.61 mmol) of 0.6 M LiHMDS solution was added via cannula at -78 °C. The solution was stirred at -78 °C for 10 min, then warmed to rt for 5 min and cooled back to -78 °C. 0.42 mL TMSCl was added. The reaction was warmed to rt and stirred overnight (16 h). The solution was concentrated, taken up in 50 mL hexanes and filtered, yielding tris-TMS-protected bromoindole (0.697 g, 0.796 mmol, 46%) contaminated with significant amounts of tris-trimethylsilyl amine (~1.9 equiv. by NMR) as a brown oil.

0.570 g (0.655 mmol) of the tris-protected bromoindole was converted to a 1:1 mix of **3.4-NH₂** and TMS-protected-**3.4-NH₂** (53 mg, 0.111 mmol, 36% based off Si-xanthone) as a blue solid. Analytically pure material could be obtained by HPLC purification using 20-100% MeCN/H₂O + 0.1% TFA.

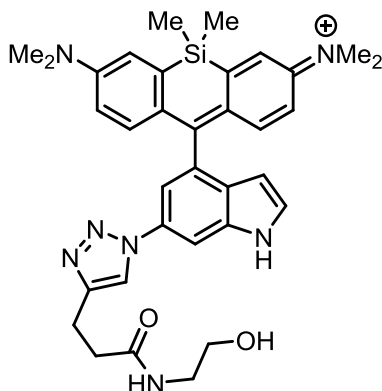
¹H NMR (500 MHz, CD₃OD): δ 0.62 (s, 3H), 0.66 (s, 3H), 3.33 (s, 12H), 6.06 (d, 1H, *J* = 3.2 Hz), 6.67 (dd, 2H, *J* = 9.7 Hz, 2.9 Hz), 6.93 (d, 1H, *J* = 1.8 Hz), 7.10 (d, 2H, *J* = 9.7 Hz), 7.37 (app. d, 3H, *J* = 2.8 Hz), 7.60 (d, 1H, *J* = 1.8 Hz); ¹³C NMR (100 MHz, CD₃OD): δ -1.15, -1.07,

40.87, 101.74, 106.67, 114.94, 115.61, 122.15, 128.63, 129.03, 129.12, 133.62, 137.08, 142.96, 149.50, 155.74, 168.65; HRMS (ESI): Calculated for $C_{27}H_{31}N_4Si$ $[M-Cl]^+$ 439.2313, found 439.2309.



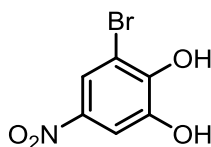
23.7 mg (0.050 mmol) **3.4-NH₂** was converted to **3.4-N₃** (9.6 mg, 0.016 mmol, 34%), a blue solid, via the general procedure.

¹H NMR (500 MHz, CDCl₃): δ 0.61 (s, 3H), 0.61 (s, 3H), 3.29 (s, 12H), 5.89 (s, 1H), 6.43 (dd, 2H, *J* = 9.6 Hz, 2.8 Hz), 6.55 (d, 1H, *J* = 1.8 Hz), 7.10 (d, 2H, *J* = 2.8 Hz), 7.18 (d, 2H, *J* = 9.6 Hz), 7.26 (s, 1H), 7.44 (s, 1H), 12.06 (brs, 1H); ¹³C NMR (125 MHz, CDCl₃): δ -0.76, -0.68, 40.88, 99.82, 103.58, 112.08, 113.77, 120.35, 126.39, 128.10, 128.18, 130.93, 133.08, 136.88, 143.12, 148.47, 154.21, 170.78; HRMS (ESI): Calculated for $C_{27}H_{29}N_6Si$ $[M-TFA]^+$ 465.2218, found 465.2214.



2.9 mg (0.0050 mmol) of **3.4-N₃** was converted to **3.4-triazole** (2.9 mg, 0.0040 mmol, 80%), a blue solid, via the general procedure.

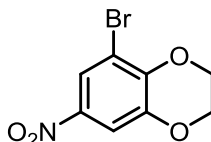
HRMS (ESI): Calculated for $C_{34}H_{40}N_7O_2Si$ $[M-TFA]^+$ 606.3007, found 606.2998.



The starting material 2-bromo-6-methoxy-4-nitrophenol was prepared according to literature procedure.⁴¹ 1.24 g (5.00 mmol) 2-bromo-6-methoxy-4-nitrophenol, a yellow powder, was suspended in 10 mL AcOH and 10 mL 48% HBr. The suspension refluxed overnight under N₂. After 20 h, the solution was cooled to rt, diluted with 100 mL 50% brine, extracted with 5 x 150

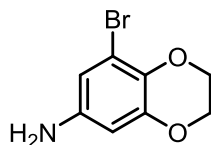
mL CH₂Cl₂, dried over MgSO₄, and concentrated to yield **3.22** (1.12 g, 4.78 mmol, 96%) as a yellow-brown solid.

R_f = 0.55 (1:1 hex/EtOAc, UV/I₂); ¹H NMR (500 MHz, d₆-DMSO): δ 7.61 (d, 1H, *J* = 2.7 Hz), 7.88 (d, 1H, *J* = 2.7 Hz), 10.95 (brs, 2H); ¹³C NMR (125 MHz, d₆-DMSO): δ 108.74, 109.21, 119.28, 139.34, 145.79, 150.22; HRMS (ESI): Calculated for C₆H₃BrNO₄ [M-H]⁻ 231.9251, found 231.9251.



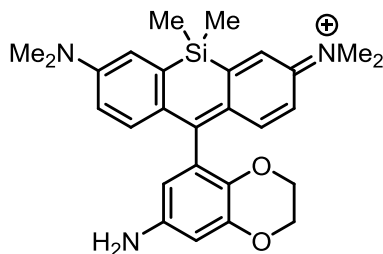
1.17 g (5.00 mmol) **3.22**, a yellow-brown solid, was dissolved in 7.5 mL ethylene glycol. 1.42 g (10.25 mmol, 2.05 equiv.) potassium carbonate, a white powder, was added, turning the light yellow solution a deep red. Next, 0.86 mL 1,2-dibromoethane, a clear liquid, (1.88 g, 10.00 mmol, 2 equiv.), was added and the solution heated to 120 °C under N₂ for 12 h. Another 0.21 mL 1,2-dibromoethane, a clear liquid, was added, and the solution heated to 120 °C for another 4 h. The cloudy red solution was cooled to rt, diluted with 100 mL H₂O, extracted with 5 x 100 mL CH₂Cl₂, dried over MgSO₄, and concentrated, yielding a light brown solid. The solid was purified by flash chromatography with hexanes to 7:1 hexanes/EtOAc to yield **3.23** (0.752 g, 2.89 mmol, 58%) as a white solid.

R_f = 0.15 (10:1 hex/EtOAc, UV); ¹H NMR (500 MHz, CDCl₃): δ 4.34 (m, 2H), 4.47 (m, 2H), 7.76 (d, 1H, *J* = 2.6 Hz), 8.07 (d, 1H, *J* = 2.6 Hz); ¹³C NMR (100 MHz, CDCl₃): δ 64.15, 65.57, 110.86, 112.78, 121.26, 141.58, 143.87, 146.69; HRMS (EI): Calculated for C₈H₆BrNO₄ [M⁺] 258.9480, found 258.9475.



0.724 g (2.78 mmol) **3.23**, a white solid, was covered with 10 mL AcOH. Next, 0.466 g iron, a grey powder, (8.35 mmol, 3 equiv.), was added. The suspension was vigorously stirred at 100 °C under N₂ for 1 h, turning to a cloudy yellow-grey slurry. The solution was cooled to rt and diluted with 80 mL 50% brine and extracted with 3 x 80 mL CH₂Cl₂, dried over MgSO₄, and concentrated, yielding a pale pink oil. The oil was purified by flash chromatography with 3:1 to 1:1 hexanes/EtOAc to yield **3.24** (0.309 g, 1.34 mmol, 48%) as a light pink oil.

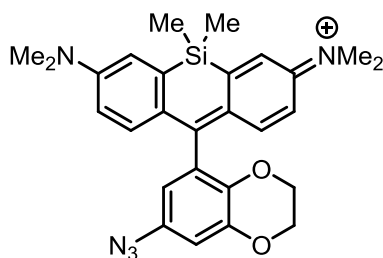
R_f = 0.45 (4:1 hex/EtOAc, UV/I₂); ¹H NMR (600 MHz, CDCl₃): δ 3.53 (brs, 2H), 4.22 (m, 2H), 4.27 (m, 2H), 6.20 (d, 2H, *J* = 2.7 Hz), 6.48 (d, 2H, *J* = 2.7 Hz); ¹³C NMR (125 MHz, CDCl₃): δ 64.42, 64.59, 103.50, 110.58, 111.96, 133.55, 140.87, 144.58; HRMS (ESI): Calculated for C₈H₉BrNO₂ [M+H]⁺ 229.9811, found 229.9812.



0.309 g (1.50 mmol) **3.24** was converted to bis-trimethylsilyl-protected bromoaniline (0.625 g, 1.50 mmol, quant.), a red-brown oil, via the general procedure.

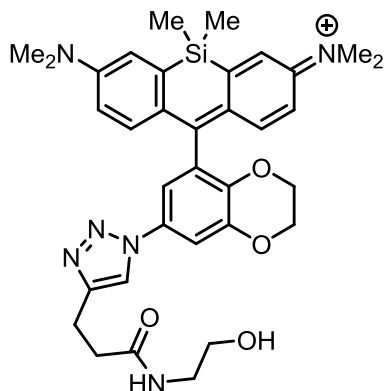
0.245 g (0.655 mmol) of the above intermediate was converted to **3.5-NH₂** (0.106 g, 0.214 mmol, 69% based off Si-xanthone), a blue solid, via the general procedure.

¹H NMR (600 MHz, CDCl₃): δ 0.54 (s, 3H), 0.55 (s, 3H), 3.36 (s, 12H), 3.98 (t, 2H, *J* = 3.9 Hz), 4.16 (t, 2H, *J* = 3.8 Hz), 6.07 (d, 1H, *J* = 2.7 Hz), 6.35 (d, 1H, *J* = 2.7 Hz), 6.64 (dd, 2H, *J* = 9.6 Hz, 2.9 Hz), 7.08 (d, 2H, *J* = 2.9 Hz), 7.37 (d, 2H, *J* = 9.6 Hz); ¹³C NMR (151 MHz, CDCl₃): δ -0.77, -0.62, 41.15, 64.37, 64.78, 104.72, 109.92, 114.00, 120.48, 127.74, 127.97, 133.89, 140.81, 142.24, 144.05, 148.24, 154.24, 167.85; HRMS (ESI): Calculated for C₂₇H₃₂N₃O₂Si [M-Cl]⁺ 458.2258, found 458.2252.



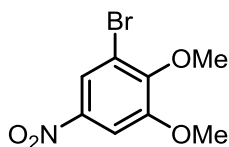
71.2 mg **3.5-NH₂** (0.144 mmol) was converted to **3.5-N₃** (33.7 mg, 0.056 mmol, 39%), a blue solid, via the general procedure.

¹H NMR (400 MHz, CDCl₃): δ 0.56 (s, 3H), 0.58 (s, 3H), 3.37 (s, 12H), 4.11 (m, 2H), 4.26 (m, 2H), 6.35 (d, 1H, *J* = 2.6 Hz), 6.68 (dd, 2H, *J* = 2.6 Hz, 9.6 Hz), 6.71 (d, 1H, *J* = 2.6 Hz), 7.13 (d, 2H, *J* = 2.7 Hz), 7.23 (d, 2H, *J* = 9.5 Hz); ¹³C NMR (151 MHz, CDCl₃): δ -0.94, -0.76, 41.04, 64.57, 64.68, 108.79, 112.94, 114.21, 120.89, 127.71, 128.69, 133.33, 138.77, 141.58, 144.71, 148.49, 154.33, 165.23; HRMS (ESI): Calculated for C₂₇H₃₀N₅O₂Si [M-TFA]⁺ 484.2163, found 484.2158.



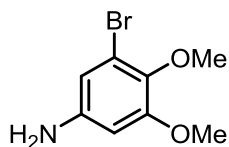
6.0 mg **3.5-N₃** (0.010 mmol) was converted to **3.5-triazole** (5.3 mg, 0.0072 mmol, 72%), a blue solid, via the general procedure.

HRMS (ESI): Calculated for C₃₄H₄₁N₆O₄Si [M-TFA]⁺ 625.2953, found 625.2939.



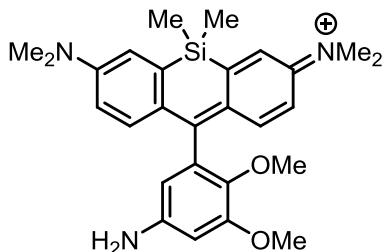
0.992 g (4.00 mmol) 2-bromo-6-methoxy-4-nitrophenol, a pale-yellow solid, was suspended in 5.6 mL dry DMF in a flame-dried flask. Next, 1.10 g (8.00 mmol, 2 equiv.) potassium carbonate, a white powder and 0.320 mL (0.738 g, 5.20 mmol, 1.3 equiv.) methyl iodide, a clear liquid, were added. A reflux condenser was attached and the reaction mixture heated to 40 °C under N₂ for 6 h. The now orange-brown suspension was cooled to rt, then diluted with 25 mL H₂O, turning the solution a cloudy yellow. The product was extracted with 3 x 25 mL Et₂O and the combined ether layers washed with 25 mL H₂O and 2 x 25 mL brine, dried over MgSO₄, and concentrated, yielding **3.25** (0.938 g, 3.58 mmol, 89%) as a light brown solid.

R_f = 0.40 (10:1 hexanes/EtOAc, UV); ¹H NMR (600 MHz, CDCl₃): δ 3.97 (s, 3H), 3.97 (s, 3H), 7.75 (d, 1H, *J* = 2.6 Hz), 8.10 (d, 1H, *J* = 2.6 Hz); ¹³C NMR (151 MHz, CDCl₃): δ 56.49, 60.93, 106.91, 117.31, 120.72, 143.76, 151.98, 153.21; HRMS (EI): Calculated for C₈H₈BrNO₄ [M⁺] 260.9637 found 260.9637.



0.852 g (3.25 mmol) **3.25**, a light brown solid, was suspended in 12 mL AcOH. 0.544 g (9.75 mmol, 3 equiv.) iron, a grey powder, was added and the grey suspension heated to 100 °C for 1 h. The now light brown slurry was cooled to rt and diluted with 80 mL 50% brine and extracted with 3 x 80 mL CH₂Cl₂. The organic layers were dried over MgSO₄ and concentrated, yielding a pink oil. The oil was purified by flash chromatography with 3:1 to 1:1 hexanes/EtOAc, yielding **3.26** (0.469 g, 2.02 mmol, 62%) as an off-white solid.

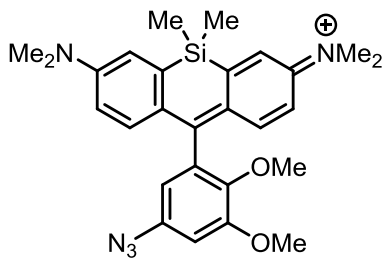
$R_f = 0.40$ (1:1 hexanes/EtOAc, UV/I₂); $^1\text{H NMR}$ (500 MHz, CDCl_3): δ 3.57 (brs, 2H), 3.76 (s, 3H), 3.81 (s, 3H), 6.20 (d, 1H, $J = 2.4$ Hz), 6.45 (d, 1H, $J = 2.4$ Hz); $^{13}\text{C NMR}$ (151 MHz, CDCl_3): δ 55.94, 60.81, 99.60, 110.24, 138.83, 143.93, 154.12; HRMS (ESI): Calculated for $\text{C}_8\text{H}_{11}\text{BrNO}_2$ $[\text{M}+\text{H}]^+$ 231.9968, found 231.9969.



0.464 g (2.00 mmol) **3.26** was converted to bis-trimethylsilyl-protected bromoaniline (0.766 g, 2.00 mmol, quant.), a red-brown oil, via the general procedure.

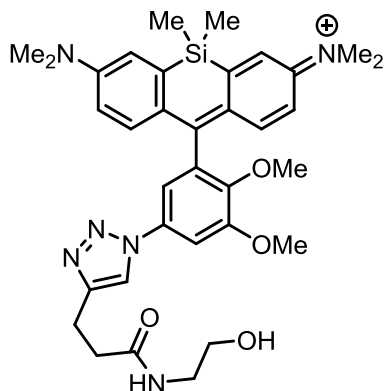
0.245 g (0.655 mmol) of the above intermediate was converted to **3.6-NH₂** (0.106 g, 0.214 mmol, 69% based off Si-xanthone), a blue solid, via the general procedure.

$^1\text{H NMR}$ (400 MHz, CDCl_3): δ 0.55 (s, 3H), 0.57 (s, 3H), 3.32 (s, 12H), 3.52 (s, 3H), 3.93 (s, 3H), 6.58 (s, 1H), 6.63 (dd, 2H, $J = 9.6$ Hz, 2.8 Hz), 7.08 (d, 2H, $J = 2.8$ Hz), 7.10 (s, 1H), 7.28 (d, 2H, $J = 9.6$ Hz), 8.45 (brs, 2H); $^{13}\text{C NMR}$ (151 MHz, CD_3OD): δ -1.37, -0.95, 40.91, 56.19, 61.20, 101.84, 108.79, 114.79, 121.76, 128.86, 134.63, 139.44, 143.12, 145.77, 149.30, 154.61, 155.3, 169.42; HRMS (ESI): Calculated for $\text{C}_{27}\text{H}_{34}\text{N}_3\text{O}_2\text{Si}$ $[\text{M}-\text{Cl}]^+$ 460.2415, found 460.2411.



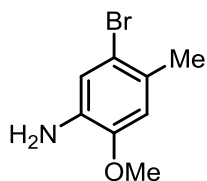
51.8 mg (0.104 mmol) **3.6-NH₂** was converted to **3.6-N₃** (32.3 mg, 0.054 mmol, 52%), a blue solid, via the general procedure.

$^1\text{H NMR}$ (500 MHz, CDCl_3): δ 0.59 (s, 3H), 0.59 (s, 3H), 3.36 (s, 12H), 3.56 (s, 3H), 3.95 (s, 3H), 6.40 (d, 1H, $J = 2.5$ Hz), 6.66 (dd, 2H, $J = 9.6$ Hz, 2.4 Hz), 6.68 (d, 1H, $J = 2.5$ Hz), 7.16 (d, 2H, $J = 2.6$ Hz), 7.23 (d, 2H, $J = 9.5$ Hz); $^{13}\text{C NMR}$ (100 MHz, CDCl_3): δ -0.98, -0.81, 41.05, 56.17, 61.17, 104.40, 111.57, 114.04, 120.86, 127.65, 134.00, 136.21, 141.70, 143.55, 148.46, 153.90, 154.29, 165.79; Calculated for $\text{C}_{27}\text{H}_{32}\text{N}_5\text{O}_2\text{Si}$ $[\text{M}-\text{TFA}]^+$ 486.2320, found 486.2316.



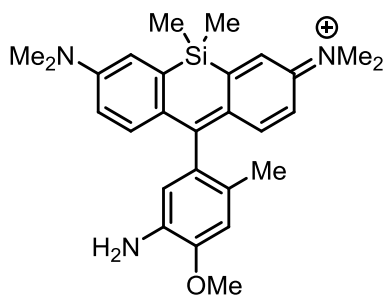
3.0 mg (0.0050 mmol) **3.6-N₃** was converted to **3.6-triazole** (3.1 mg, 0.0042 mmol, 84%), a blue solid, via the general procedure.

HRMS (ESI): Calculated for C₃₄H₄₃N₆O₄Si [M-TFA]⁺ 627.3110, found 627.3107.



The starting material 1-bromo-4-methoxy-2-methyl-5-nitrobenzene was prepared according to literature procedure.⁴² 0.505 g (2.05 mmol) 1-bromo-4-methoxy-2-methyl-5-nitrobenzene, a yellow solid, was dissolved in 8.8 mL AcOH. Next, 0.344 g (6.14 mmol, 3 equiv.) iron, a grey powder, was added and the grey suspension heated to 100 °C under N₂ for 1 h. The now greenish-grey slurry was cooled to rt and diluted with 50 mL H₂O, extracted with 3 x 30 mL ethyl acetate, dried over MgSO₄, and concentrated. The crude product was then purified with flash chromatography using hexanes to 10:1 hexanes/EtOAc to yield **3.27** (0.364 g, 1.69 mmol, 82%) as a clear oil.

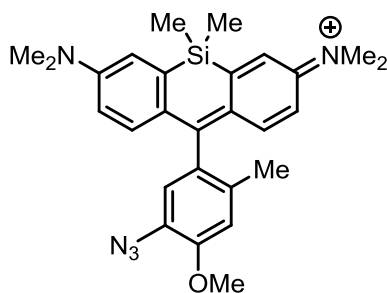
R_f = 0.25 (10:1 hexanes/EtOAc, UV/I₂); ¹H NMR (500 MHz, CDCl₃): δ 2.29 (s, 3H), 3.70 (brs, 2H), 3.82 (s, 3H), 6.63 (s, 1H), 6.87 (s, 1H); ¹³C NMR (151 MHz, CDCl₃): δ 22.37, 55.80, 112.88, 115.22, 118.32, 135.37, 146.77; HRMS (ESI): Calculated for C₈H₁₁BrNO [M+H]⁺ 216.0019, found 216.0019.



0.323 g (1.49 mmol) **3.27** was converted to bis-trimethylsilyl-protected bromoaniline (0.549 g, 1.49 mmol, quant.), an orange oil, via the general procedure.

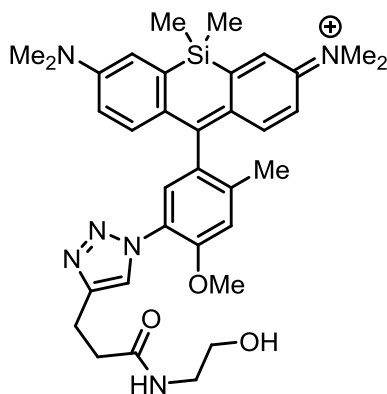
0.236 g (0.655 mmol) of the above intermediate was converted to **3.7-NH₂** (0.153 g, 0.312 mmol, quant. based off Si-xanthone), a blue solid, via the general procedure.

¹H NMR (600 MHz, CDCl₃): δ 0.59 (s, 3H), 0.62 (s, 3H), 1.90 (s, 3H), 3.39 (s, 12H), 3.93 (s, 3H), 6.51 (s, 1H), 6.63 (dd, 2H, *J* = 9.7 Hz, 2.6 Hz), 6.70 (s, 1H), 7.16 (d, 2H, *J* = 2.6 Hz), 7.25 (d, 2H, *J* = 9.7 Hz); ¹³C NMR (151 MHz, CDCl₃): δ -1.01, -0.66, 18.91, 41.09, 55.64, 111.84, 113.85, 115.73, 120.33, 125.21, 127.98, 130.29, 133.80, 142.19, 147.55, 148.19, 154.02, 171.52; HRMS (ESI): Calculated for C₂₇H₃₄N₃OSi [M-Cl]⁺ 444.2466, found 444.2461.



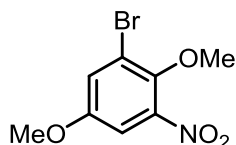
20.0 mg (0.045 mmol) **3.7-NH₂** was converted to **3.7-N₃** (17.5 mg, 0.037 mmol, 83%), a blue solid, via the general procedure.

¹H NMR (600 MHz, CDCl₃): δ 0.58 (s, 3H), 0.59 (s, 3H), 1.99 (s, 3H), 3.37 (s, 12H), 3.97 (s, 3H), 6.65 (dd, 2H, *J* = 9.6 Hz, 2.8 Hz), 6.70 (s, 1H), 6.86 (s, 1H), 7.11 (d, 2H, *J* = 9.6 Hz), 7.16 (d, 2H, *J* = 2.9 Hz); ¹³C NMR (151 MHz, CDCl₃): δ -1.09, -0.85, 19.41, 40.92, 56.23, 113.95, 114.17, 120.74, 120.77, 126.07, 127.71, 130.98, 133.74, 141.56, 148.40, 152.11, 154.18, 168.60; HRMS (ESI): Calculated for C₂₇H₃₂NOSi [M-TFA]⁺ 470.2371, found 470.2367.



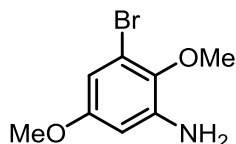
3.0 mg (0.0051 mmol) **3.7-N₃** was converted to **3.7-triazole** (2.4 mg, 0.0034 mmol, 67%), a blue solid, via the general procedure.

HRMS (ESI): Calculated for C₃₄H₄₃O₃N₆Si [M-TFA]⁺ 611.3160, found 611.3160.



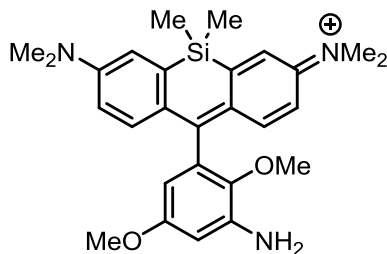
1.24 g (5.00 mmol) 2-bromo-4-methoxy-6-nitrophenol, a bright orange crystalline solid, was dissolved in 7 mL dry DMF in a flame-dried flask. Next, 1.38 g (10.0 mmol, 2 equiv.) potassium carbonate, a white powder, was added, turning the solution a deep red color. Finally, 0.40 mL (0.923 g, 6.50 mmol, 1.3 equiv.) methyl iodide, a clear liquid, was added, a reflux condenser attached, and the solution heated to 40 °C overnight (10 h). The now cloudy light brown solution was cooled and diluted with 30 mL H₂O, causing a white precipitate to form. The product was extracted with 3 x 30 mL Et₂O and the organic layers washed with 30 mL H₂O and 2 x 30 mL brine, dried over MgSO₄, and concentrated, yielding **3.28** (1.28 g, 4.88 mmol, 98%) as an off-white solid.

R_f = 0.45 (10:1 hex/EtOAc, UV); ¹H NMR (500 MHz, CDCl₃): δ 3.83 (s, 3H), 3.96 (s, 3H), 7.28 (d, 1H, *J* = 3.1 Hz), 7.35 (d, 1H, *J* = 3.5 Hz); ¹³C NMR (151 MHz, CDCl₃): δ 55.72, 59.97, 101.34, 107.17, 117.09, 138.78, 141.60, 154.70, 156.94; HRMS (EI): Calculated for C₈H₈BrNO₄ [M⁺] 260.9637, found 260.9644.



1.07 g (4.06 mmol) **3.28**, an off-white powder, was dissolved in 15 mL AcOH. Next, 0.681 g (12.19 mmol, 3 equiv.) iron, a grey powder, was added and the grey suspension heated to 100 °C under N₂ for 1 h. The now brown slurry was cooled to rt, diluted with 50 mL 50% brine and extracted with 3 x 50 mL CH₂Cl₂. The organic layers were dried over MgSO₄ and concentrated, yielding a brown oil. The oil was purified with flash chromatography using 4:1 to 2:1 hexanes/EtOAc to yield **3.29** (0.747 g, 3.22 mmol, 79%) as a pale-yellow oil.

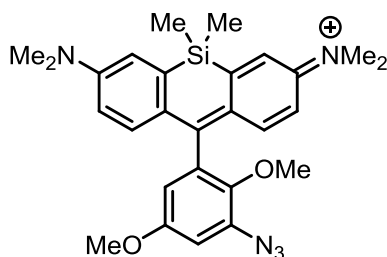
R_f = 0.55 (1:1 hex/EtOAc, UV); ¹H NMR (500 MHz, CDCl₃): δ 3.71 (s, 3H), 3.78 (s, 3H), 3.94 (brs, 2H), 6.24 (d, 1H, *J* = 2.9 Hz), 6.46 (d, 1H, *J* = 2.9 Hz); ¹³C NMR (151 MHz, CDCl₃): δ 56.41, 62.85, 109.36, 120.30, 124.01, 144.68, 145.23, 155.69; HRMS (ESI): Calculated for C₈H₁₁BrNO₂ [M+H]⁺ 231.9968, found 231.9969.



0.580 g (2.50 mmol) **3.29** was converted to bis-trimethylsilyl-protected bromoaniline (0.891 g, 2.37 mmol, 95%), a golden-yellow oil, via the general procedure.

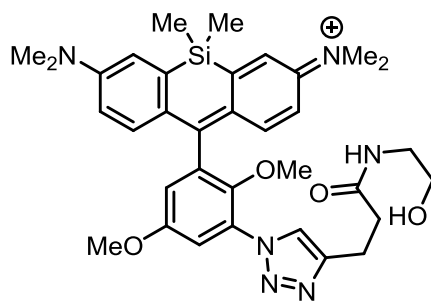
0.247 g (0.655 mmol) of the above intermediate was converted to **3.8-NH₂** (0.121 g, 0.244 mmol, 78% based off Si-xanthone), a blue solid, via the general procedure.

¹H NMR (400 MHz, CDCl₃): δ 0.59 (s, 3H), 0.63 (s, 3H), 3.41 (s, 12H), 3.75 (s, 3H), 6.02 (d, 1H, *J* = 2.9 Hz), 6.55 (d, 1H, *J* = 2.9 Hz), 6.68 (dd, 2H, *J* = 9.6 Hz, 2.8 Hz), 7.18 (d, 2H, *J* = 2.8 Hz), 7.42 (d, 2H, *J* = 9.6 Hz); ¹³C NMR (125 MHz, CDCl₃): δ -1.31, -0.56, 41.00, 55.52, 60.15, 101.97, 104.66, 113.71, 120.35, 127.56, 132.36, 138.42, 141.37, 142.16, 147.98, 153.95, 155.75, 167.63; HRMS (ESI): Calculated for C₂₇H₃₄N₃O₂Si [M-Cl]⁺ 460.2415, found 460.2412.



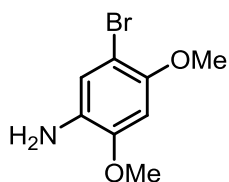
54.4 mg (0.110 mmol) **3.8-NH₂** was converted to **3.8-N₃** (66.3 mg, 0.110 mmol, quant.), a blue solid, via the general procedure.

¹H NMR (600 MHz, CDCl₃): δ 0.57 (s, 3H), 0.60 (s, 3H), 3.37 (s, 12H), 3.48 (s, 3H), 3.80 (s, 3H), 6.43 (d, 1H, *J* = 2.8 Hz), 6.67 (dd, 2H, *J* = 9.6 Hz, 2.7 Hz), 6.75 (d, 1H, *J* = 2.8 Hz), 7.16 (d, 2H, *J* = 2.8 Hz), 7.24 (d, 2H, *J* = 9.5 Hz); ¹³C NMR (125 MHz, CDCl₃): δ -1.21, -0.56, 41.04, 56.05, 62.12, 107.03, 111.83, 114.15, 120.90, 127.63, 134.52, 134.56, 141.72, 143.06, 148.40, 154.30, 155.95, 165.44; HRMS (ESI): Calculated for C₂₇H₃₂N₅O₂Si [M-TFA]⁺ 486.2320, found 486.2317.



6.0 mg (0.010 mmol) **3.8-N₃** was converted to **3.8-triazole** (3.4 mg, 0.0046 mmol, 46%), a blue solid, via the general procedure.

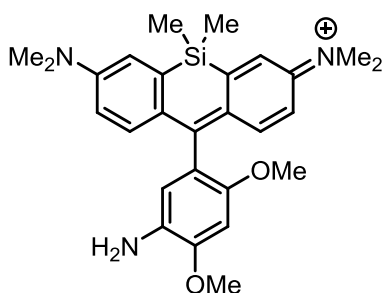
HRMS (ESI): Calculated for C₃₄H₄₃N₆O₄Si [M-TFA]⁺ 627.3110, found 627.3106.



The starting material 1-bromo-2,4-dimethoxy-5-nitrobenzene was prepared according to literature procedure.⁴³ 1.30 g (5.00 mmol) 1-bromo-2,4-dimethoxy-5-nitrobenzene, an off-white

solid, was suspended in 15 mL AcOH. To the light yellow suspension was added 0.837 g (15.0 mmol, 3 equiv.) iron, a grey powder. The now grey suspension was heated to 100 °C under N₂ for 1 h. The cloudy grey slurry was cooled to rt, diluted with 100 mL 50% brine, and extracted with 3 x 60 mL CH₂Cl₂. The combined organic layers were carefully washed with 50 mL NaHCO₃ (caution: gas evolution!), dried over MgSO₄, and concentrated, yielding a yellow-orange solid. The solid was purified with flash chromatography with 3:1 hexanes/EtOAc to yield **3.30** (0.956 g, 4.12 mmol, 82%) as an off-white solid.

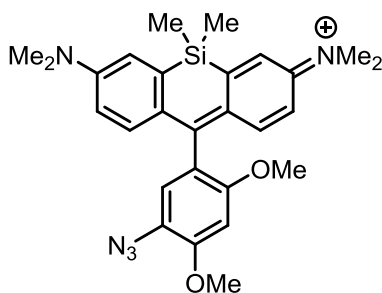
R_f = 0.70 (1:1 hex/EtOAc, UV/I₂); ¹H NMR (500 MHz, CDCl₃): δ 3.56 (brs, 2H), 3.83 (s, 3H), 3.85 (s, 3H), 6.49 (s, 1H), 6.89 (s, 1H); ¹³C NMR (151 MHz, CDCl₃): δ 55.97, 57.68, 98.81, 102.43, 119.09, 131.19, 147.46, 149.00; HRMS (ESI): Calculated for C₈H₁₁BrNO₂ [M+H]⁺ 231.9968, found 231.9968.



0.464 g **3.30** (2.00 mmol) was converted to the bis-trimethylsilyl protected bromoaniline (0.709 g, 1.90 mmol, 95%), a red-brown solid, via the general procedure.

0.245 g (0.655 mmol) of this intermediate was then converted to **3.9-NH₂** (0.141 g, 0.284 mmol, 91% based off Si-xanthone), a blue solid, via the general procedure.

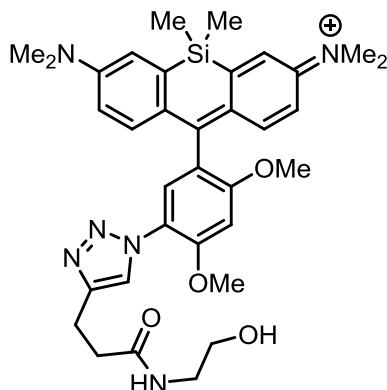
¹H NMR (500 MHz, CDCl₃): δ 0.54 (s, 3H), 0.56 (s, 3H), 3.35 (s, 12H), 3.60 (s, 3H), 3.95 (s, 3H), 6.47 (s, 1H), 6.56 (s, 1H), 6.62 (dd, 2H, *J* = 9.6 Hz, 2.8 Hz), 7.08 (d, 2H, *J* = 2.8 Hz), 7.31 (d, 2H, *J* = 9.5 Hz); ¹³C NMR (125 MHz, CDCl₃): δ -0.76, -0.60, 41.15, 55.98, 56.99, 96.78, 113.80, 116.86, 119.35, 120.25, 128.61, 129.74, 142.52, 148.20, 148.85, 149.61, 154.08, 169.56; HRMS (ESI): Calculated for C₂₇H₃₄N₃O₂Si [M-Cl]⁺ 460.2420, found 460.2408.



76.6 mg (0.155 mmol) **3.9-NH₂** was converted to **3.9-N₃** (63.4 mg, 0.105 mmol, 68%), a blue solid, via the general procedure.

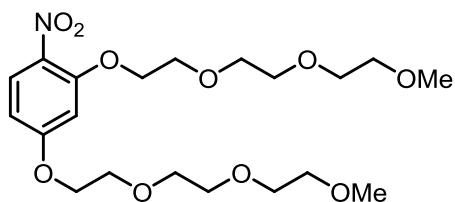
¹H NMR (600 MHz, CDCl₃): δ 0.60 (s, 3H), 0.63 (s, 3H), 3.40 (s, 12H), 3.76 (s, 3H), 4.07 (s, 3H), 6.71 (dd, 2H, *J* = 2.8 Hz, 9.6 Hz), 6.72 (s, 1H), 6.72 (s, 1H), 7.15 (d, 2H, *J* = 2.8 Hz), 7.25 (d, 2H, *J* = 9.6 Hz); ¹³C NMR (125 MHz, CDCl₃): δ -1.04, -0.76, 40.88, 56.41, 56.46, 96.91,

113.95, 119.65, 120.46, 120.69, 121.77, 128.24, 141.88, 148.27, 153.60, 154.12, 154.73, 166.98; HRMS (ESI): Calculated for $C_{27}H_{32}N_5O_2Si$ [M-TFA]⁺ 486.2320, found 486.2314.



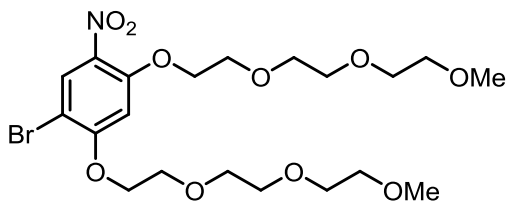
6.0 mg (0.010 mmol) **3.9-N₃** was converted to **3.9-triazole** (1.85 mg, 0.0025 mmol, 25%), a blue solid, via the general procedure.

HRMS (ESI): Calculated for $C_{34}H_{43}N_6O_4Si$ [M-TFA]⁺ 627.3110, found 627.3100.



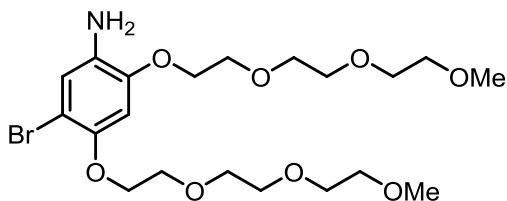
1.31 mL (1.91 g, 12.0 mmol) 2,4-difluoronitrobenzene, a pale yellow liquid, was dissolved in 10 mL toluene. Next, 7.52 mL (7.88 g, 48.0 mmol, 4 equiv.) triethylene glycol monomethyl ether, a clear liquid, was added. 10 mL 50% KOH was then added, immediately warming the solution and turning it a golden yellow color. Finally, 387 mg (1.20 mmol, 0.1 equiv.) tetrabutylammonium bromide, a white solid, was added and the solution vigorously stirred at 60 °C overnight (16 h). The solution was cooled to rt and diluted with 80 mL cold brine. The product was then extracted with 3 x 80 mL ethyl acetate, the organic layer washed with 3 x 120 mL sat. NaHCO₃, dried over MgSO₄, and concentrated, yielding **3.12** (5.19 g, 11.6 mmol, 97%) as a yellow oil.

R_f = 0.70 (10:1 CHCl₃/MeOH, UV); ¹H NMR (400 MHz, CDCl₃): δ 3.37 (s, 3H), 3.38 (s, 3H), 3.55 (m, 4H), 3.67 (m, 8H), 3.73 (m, 2H), 3.78 (m, 2H), 3.87 (t, 2H, J = 4.8 Hz), 3.92 (t, 2H, J = 4.8 Hz), 6.51 (dd, 1H, J = 9.1 Hz, 2.5 Hz), 6.59 (d, 1H, J = 2.5 Hz), 7.96 (d, 1H, J = 9.1 Hz); ¹³C NMR (100 MHz, CDCl₃): δ 59.06, 59.10, 68.18, 69.25, 69.44, 69.66, 70.54, 70.64, 70.70, 70.72, 70.93, 70.97, 71.17, 71.96, 101.47, 105.78, 128.25, 133.32, 154.92, 163.90; HRMS (ESI): Calculated for $C_{20}H_{33}NNaO_{10}$ [M+Na]⁺ 470.1997, found 470.2005.



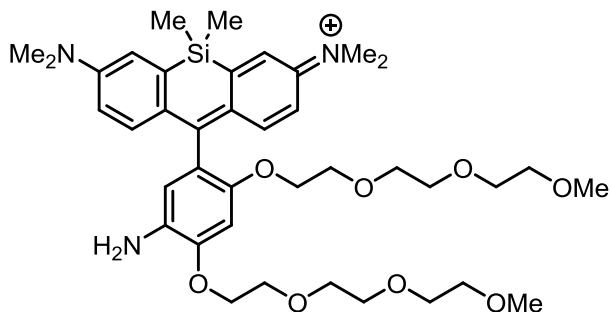
4.37 g (9.76 mmol) **3.12**, a yellow oil, was dissolved in 20 mL CHCl₃. Next, 1.42 g (10.25 mmol, 1.05 equiv.) potassium carbonate, a white solid, was added. Finally, 0.526 mL (1.64 g, 10.25 mmol, 1.05 equiv.) bromine, a red liquid, was added dropwise to the vigorously stirring solution. Bubbling was observed. The red solution was stirred for 2 h in the dark. Another 0.1 mL bromine was added and the reaction stirred for 1 h, then quenched with 50 mL sat. Na₂S₂O₃, extracted with 3 x 50 mL CHCl₃, washed with 50 mL sat. Na₂S₂O₃, 3 x 50 mL sat. NaHCO₃, dried over MgSO₄ and concentrated to yield **3.13** (5.14 g, 9.76 mmol, quant.) as a pale brown oil.

R_f = 0.75 (10:1 CHCl₃/MeOH, UV); ¹H NMR (400 MHz, CDCl₃): δ 3.35 (s, 3H), 3.36 (s, 3H), 3.53 (m, 4H), 3.65 (m, 8H), 3.77 (m, 4H), 3.92 (m, 4H), 4.24 (t, 2H, *J* = 4.4 Hz), 4.26 (t, 2H, *J* = 4.4 Hz), 6.68 (s, 1H), 8.20 (s, 1H); ¹³C NMR (151 MHz, CDCl₃): δ 59.12, 59.15, 69.41, 69.48, 69.89, 70.39, 70.59, 70.67, 70.76, 70.81, 71.19, 71.30, 72.02, 72.04, 100.12, 102.48, 130.72, 133.23, 154.47, 160.21; HRMS (ESI): Calculated for C₂₀H₃₂BrNNaO₁₀ [M+Na]⁺ 548.1102, found 548.1103.



2.63 g (5.00 mmol) **3.13**, a pale brown oil, was dissolved in 15 mL AcOH. Next, 0.838 g (15.0 mmol, 3 equiv.) iron, a grey powder, was added and the grey suspension stirred at 100 °C for 1 h. The grey slurry was cooled to rt, diluted with 50 mL 50% brine, and extracted with 3 x 30 mL CH₂Cl₂. The combined organic layers were carefully washed with 3 x 30 mL sat. NaHCO₃ (caution: gas evolution!), dried over MgSO₄, and concentrated, yielding a yellow oil. The oil was purified by flash chromatography using CHCl₃ to 20:1 CHCl₃/MeOH to 10:1 CHCl₃/MeOH to yield **3.14** (2.26 g, 4.55 mmol, 91%) as a brown oil.

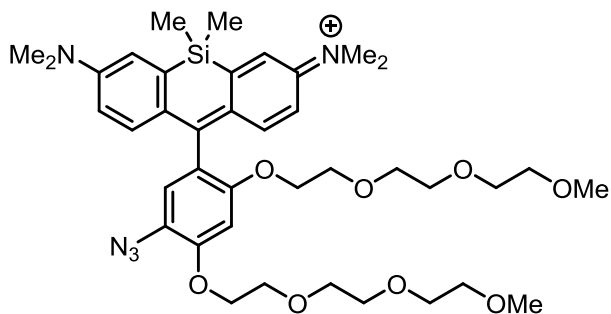
R_f = 0.50 (10:1 CHCl₃/MeOH, UV/I₂); ¹H NMR (500 MHz, CDCl₃): δ 3.37 (s, 3H), 3.38 (s, 3H), 3.55 (m, 4H), 3.67 (m, 10H), 3.77 (m, 2H), 3.83 (m, 6H), 4.08 (t, 2H, *J* = 5.0 Hz), 4.11 (t, 2H, *J* = 5.0 Hz), 6.57 (s, 1H), 6.87 (s, 1H); ¹³C NMR (151 MHz, CDCl₃): δ 59.06, 59.06, 68.99, 69.64, 69.83, 70.56, 70.58, 70.65, 70.72, 70.77, 70.83, 70.97, 71.96, 71.96, 103.58, 104.56, 118.85, 132.83, 146.14, 147.80; HRMS (ESI): Calculated for C₂₀H₃₅BrNO₈ [M+H]⁺ 496.1541, found 496.1542.



0.993 g (2.00 mmol) **3.14** was converted to the bis-trimethylsilyl-protected bromoaniline (1.28 g, 2.00 mmol, quant.), a red-brown oil, via the general procedure with one modification. Due to the poor solubility of the product in hexanes, the product was taken up and filtered in toluene instead.

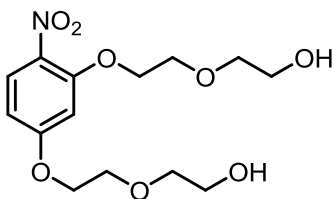
0.420 g (0.655 mmol) of this intermediate was converted to **3.11-NH₂** (0.178 g, 0.234 mmol, 75% based off Si-xanthone), a blue solid, via the general procedure.

¹H NMR (500 MHz, CDCl₃): δ 0.55 (s, 3H), 0.60 (s, 3H), 3.33 (s, 3H), 3.39 (s, 19H), 3.47 (m, 4H), 3.51 (m, 2H), 3.57 (m, 2H), 3.67 (m, 2H), 3.61 (m, 2H), 3.72 (m, 2H), 3.90 (t, 2H, *J* = 5.1 Hz), 3.93 (t, 2H, *J* = 5.1 Hz), 6.49 (s, 1H), 6.64 (s, 1H), 6.64 (dd, 2H, *J* = 9.6 Hz, 2.8 Hz), 7.13 (d, 2H, *J* = 2.9 Hz), 7.34 (dd, 2H, *J* = 9.6 Hz, 2.5 Hz); ¹³C NMR (151 MHz, CDCl₃): δ -1.11, -0.54, 41.03, 58.98, 59.02, 68.80, 69.68, 69.69, 69.94, 70.42, 70.49, 70.55, 70.62, 70.66, 70.79, 71.86, 71.95, 100.81, 113.70, 116.75, 120.19, 120.86, 128.53, 131.15, 142.54, 147.72, 148.11, 148.52, 154.04, 169.37; HRMS (ESI): Calculated for C₃₉H₅₈N₃O₈Si [M-Cl]⁺ 724.3988, found 724.3983.



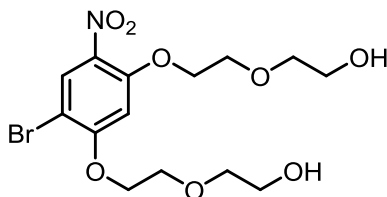
67.0 mg (0.0881 mmol) **3.11-NH₂** was converted to **3.11** (63.2 mg, 0.0783 mmol, 83%), a blue solid, via the general procedure.

¹H NMR (500 MHz, CDCl₃): δ 0.55 (s, 3H), 0.58 (s, 3H), 3.34 (s, 3H), 3.37 (s, 12H), 3.39 (s, 3H), 3.33-3.39 (m, 6H), 3.47 (app d, 2H, *J* = 5.1 Hz), 3.50 (app d, 2H, *J* = 4.8 Hz), 3.53 (t, 2H, *J* = 4.9 Hz), 3.57 (t, 2H, *J* = 4.7 Hz), 3.68 (t, 2H, *J* = 4.6 Hz), 3.72 (t, 2H, *J* = 4.7 Hz), 3.79 (t, 2H, *J* = 4.7 Hz), 3.96 (t, 2H, *J* = 4.7 Hz), 4.02 (t, 2H, *J* = 5.0 Hz), 4.30 (t, 2H, *J* = 4.7 Hz), 6.64 (s, 1H), 6.65 (dd, 2H, *J* = 2.7 Hz, 9.7 Hz); 6.73 (s, 1H), 7.15 (d, 2H, *J* = 2.7 Hz), 7.21 (d, 2H, *J* = 9.7 Hz); ¹³C NMR (151 MHz, CDCl₃): δ -1.15, -0.75, 40.92, 59.02, 59.10, 69.29, 69.33, 69.51, 69.55, 70.44, 70.51, 70.58, 70.72, 70.74, 70.93, 71.90, 72.00, 99.81, 113.95, 120.51, 120.51, 121.52, 122.24, 128.35, 142.01, 148.34, 153.33, 153.98, 154.18, 167.05; HRMS (ESI): Calculated for C₃₉H₅₆O₈N₅Si₁ [M-TFA]⁺ 750.3892, found 750.3899.



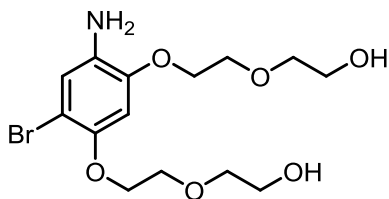
6.22 g (45.0 mmol, 3 equiv.) K₂CO₃, a white powder, was added to 50 mL diethylene glycol. Next, 1.65 mL (2.39 g, 15.0 mmol) 2,4-difluoronitrobenzene, a yellow liquid, was added. The suspension was then stirred at 80 °C under N₂ overnight (16 h). The now orange solution was cooled to rt, diluted with 100 mL cold 50% brine, and extracted with 3 x 80 mL EtOAc. The combined organic layers were washed with 5 x 100 mL sat. NaHCO₃, dried over MgSO₄, and concentrated to yield **3.16** (3.60 g, 10.87 mmol, 72%) as a yellow oil.

R_f = 0.40 (10:1 CHCl₃/MeOH, UV); ¹H NMR (500 MHz, CDCl₃): 2.00 (brs, 2H), 3.68 (t, 2H, *J* = 4.5 Hz), 3.71 (m, 2H), 3.77 (m, 4H), 4.21 (t, 2H, *J* = 4.5 Hz), 4.26 (t, 2H, *J* = 4.5 Hz), 6.53 (dd, 1H, *J* = 9.1 Hz, 2.5 Hz), 6.66 (d, 2H, *J* = 2.5 Hz), 7.98 (d, 2H, *J* = 9.1 Hz); ¹³C NMR (151 MHz, CDCl₃): δ 61.83, 61.92, 68.23, 69.33, 69.42, 69.71, 72.83, 72.92, 101.95, 105.94, 128.39, 133.60, 154.96, 163.85; HRMS (ESI): Calculated for C₁₄H₂₁NNaO₈ [M+Na]⁺ 354.1159, found 354.1159.



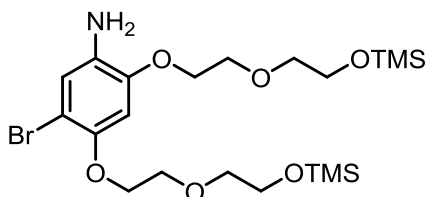
3.60 g (10.87 mmol) **3.16**, a yellow oil, was dissolved in 22 mL CHCl₃. Next, 1.58 g (11.41 mmol, 1.05 equiv.) K₂CO₃, a white powder, was added. Finally, 0.58 mL (1.82 g, 11.41 mmol, 1.05 equiv.) bromine, a red liquid, was added. The red solution was then stirred in the dark for 2 h. Another 0.1 mL bromine was added at this time and the reaction stirred another 1 h. A significant amount of gummy orange paste collected at the bottom of the flask over the course of this reaction, which was occasionally broken up with a spatula. The reaction was quenched with 50 mL sat. Na₂S₂O₃ solution, then diluted with 50 mL H₂O and extracted with 3 x 150 mL EtOAc. The combined organic layers were washed with 100 mL sat. Na₂S₂O₃ solution and 5 x 100 mL sat. NaHCO₃ solution, dried over MgSO₄, and concentrated, yielding **3.17** (3.27 g, 7.97 mmol, 73%) as a light yellow powder.

R_f = 0.40 (10:1 CHCl₃/MeOH, UV); ¹H NMR (500 MHz, CDCl₃): 2.07 (brs, 2H), 3.71 (m, 4H), 3.94 (m, 4H), 3.95 (m, 4H), 4.30 (t, 2H, *J* = 4.7 Hz), 4.30 (t, 2H, *J* = 4.7 Hz), 6.78 (s, 1H), 8.22 (s, 1H); ¹³C NMR (151 MHz, CDCl₃): δ 61.74, 61.76, 69.28, 69.31, 69.65, 70.32, 72.83, 72.85, 100.59, 102.72, 130.63, 133.37, 154.24, 160.03; HRMS (ESI): Calculated for C₁₄H₂₀BrNNaO₈ [M+Na]⁺ 432.0264, found 432.0268.



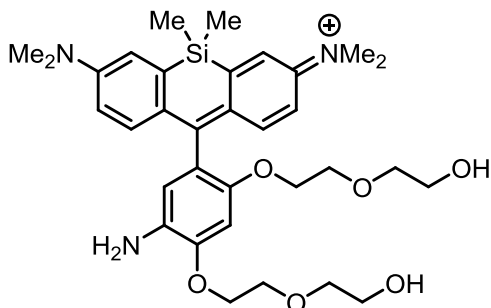
3.27 g (7.97 mmol) **3.17**, a golden oil, was suspended in 16 mL EtOH and 1.6 mL AcOH in a 100 mL round bottom flask. The cloudy solution was heated to 80 °C, during which **3.17** completely dissolved. Finally, 3.12 g (55.79 mmol, 7 equiv.) iron, a grey powder, was added, followed by 0.220 g (1.35 mmol, 0.170 equiv.) FeCl₃, a red-brown solid. A reflux condenser was attached and the grey suspension refluxed for 3 h, cooled to rt, diluted with 50 mL EtOH, and filtered through a pad of Celite. The pad was washed with another 150 mL EtOH. The solution was concentrated and the remaining brown residue purified with flash chromatography using CHCl₃ to 20:1 CHCl₃/MeOH to 7:1 CHCl₃/MeOH to yield **3.18** (2.07 g, 5.44 mmol, 68%) as a pale brown oil.

R_f = 0.40 (10:1 CHCl₃/MeOH, UV/I₂); ¹H NMR (500 MHz, CDCl₃): δ 2.93 (brs, 4H), 3.64 (t, 2H, *J* = 4.4 Hz), 3.70 (t, 2H, *J* = 4.6 Hz), 3.75 (t, 2H, *J* = 4.5 Hz), 3.77 (t, 2H, *J* = 4.5 Hz), 3.82 (t, 2H, *J* = 4.6 Hz), 3.86 (t, 2H, *J* = 4.6 Hz), 4.11 (t, 2H, *J* = 4.6 Hz), 4.17 (t, 2H, *J* = 4.4 Hz), 6.64 (s, 1H), 6.92 (s, 1H); ¹³C NMR (151 MHz, CDCl₃): δ 61.95, 62.10, 69.38, 69.82, 70.11, 71.24, 72.99, 73.01, 104.40, 105.19, 119.52, 132.97, 146.54, 148.29; HRMS (ESI): Calculated for C₁₄H₂₃BrNO₆ [M+H]⁺ 380.0703, found 380.0704.



2.07 g (5.44 mmol) **3.18**, a brown oil, was dissolved in 27 mL dry THF in a flame-dried flask. Next, 1.67 mL (1.21 g, 11.97 mmol, 2.2 equiv.) anhydrous triethylamine was added. The solution was cooled to 0 °C, then 1.52 mL (1.30 g, 11.97 mmol, 2.2 equiv.) trimethylsilyl chloride was added dropwise, immediately turning the light brown solution to a cloudy slurry. After addition was completed, the reaction was warmed to rt and stirred under N₂ overnight. After 10 h, the cloudy brown solution was filtered to remove salts, then concentrated to afford **3.19** (2.44 g, 4.65 mmol, 85%) as a brown oil.

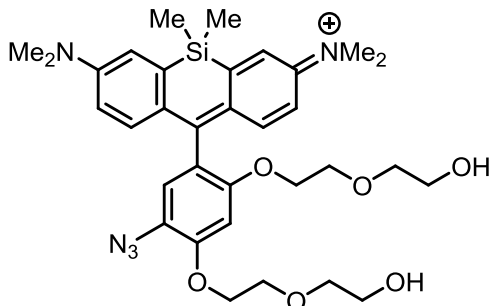
¹H NMR (400 MHz, CDCl₃): δ 0.13 (s, 18H), 3.62 (t, 2H, *J* = 5.1 Hz), 3.67 (t, 2H, *J* = 5.2 Hz), 3.75 (t, 2H, *J* = 4.6 Hz), 3.77 (t, 2H, *J* = 4.6 Hz), 3.83 (t, 2H, *J* = 4.6 Hz), 3.84 (t, 2H, *J* = 4.6 Hz), 4.08 (t, 2H, *J* = 4.9 Hz), 4.11 (t, 2H, *J* = 4.9 Hz), 6.57 (s, 1H), 6.89 (s, 1H); ¹³C NMR (151 MHz, CDCl₃): δ -0.29, -0.25, 62.14, 62.22, 69.02, 69.78, 69.98, 71.09, 72.94, 73.08, 103.72, 104.78, 118.98, 132.81, 146.28, 148.05.



1.05 g (2.00 mmol) **3.19** was converted to the bis-trimethylsilyl-protected bromoaniline (1.37 g, 2.00 mmol, quant.), a brown oil, via the general procedure.

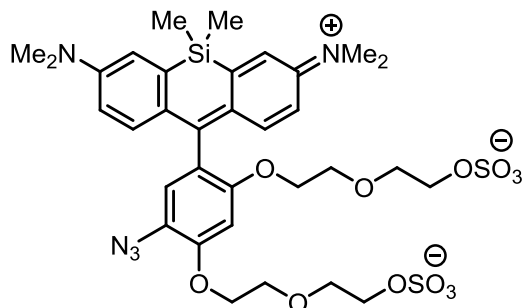
0.438 g (0.655 mmol) of this intermediate was converted to **3.20** (0.125 g, 0.194 mmol, 62% based off Si-xanthone), a blue solid, via the general procedure. Chromatography was performed using C₂-functionalized silica gel⁴⁴ to minimize loss of material on the column.

¹H NMR (600 MHz, CDCl₃): δ 0.57 (s, 3H), 0.57 (s, 3H), 3.34 (t, 2H, *J* = 4.8 Hz), 3.37 (s, 12H), 3.45 (t, 2H, *J* = 4.9 Hz), 3.53 (t, 2H, *J* = 4.6 Hz), 3.73 (t, 2H, *J* = 4.7 Hz), 3.80 (t, 2H, *J* = 4.3 Hz), 3.95 (t, 2H, *J* = 4.4 Hz), 3.99 (t, 2H, *J* = 4.6 Hz), 4.35 (t, 2H, *J* = 4.5 Hz), 6.65 (s, 1H), 6.73 (dd, 2H, *J* = 9.8 Hz, 2.7 Hz), 6.78 (s, 1H), 7.09 (d, 2H, *J* = 2.8 Hz), 7.38 (d, 2H, *J* = 9.6 Hz); ¹³C NMR (151 MHz, CDCl₃): δ -0.61, -0.56, 41.14, 61.36, 61.63, 69.51, 69.72, 69.88., 69.95, 72.55, 72.88, 101.12, 114.06, 117.78, 120.26, 120.26, 120.85, 128.66, 142.67, 148.14, 148.50, 149.48, 154.18, 169.17; HRMS (ESI): Calculated for C₃₃H₄₆N₃O₆Si [M-Cl]⁺ 608.3150, found 608.3147.



83.8 mg (0.130 mmol) **3.20** was converted to **3.21** (68 mg, 0.091 mmol, 70%), a blue solid, via the general procedure. Chromatography was performed using C₂-functionalized silica gel⁴⁴ to minimize loss of material on the column.

¹H NMR (600 MHz, CDCl₃): δ 0.56 (s, 3H), 0.59 (s, 3H), 3.35 (t, 2H, *J* = 4.9 Hz), 3.39 (s, 12H), 3.46 (t, 2H, *J* = 5.1 Hz), 3.59 (t, 2H, *J* = 4.5 Hz), 3.97 (t, 2H, *J* = 4.3 Hz), 4.11 (t, 2H, *J* = 4.6 Hz), 3.72 (t, 2H, *J* = 4.5 Hz), 3.80 (t, 2H, *J* = 4.4 Hz), 4.41 (t, 2H, *J* = 4.3 Hz), 6.64 (s, 1H), 6.75 (dd, 2H, *J* = 9.6 Hz, 2.5 Hz), 6.92 (s, 1H), 7.10 (d, 2H, *J* = 2.5 Hz), 7.27 (d, 2H, *J* = 9.6 Hz); ¹³C NMR (151 MHz, CDCl₃): δ -0.84, -0.79, 41.06, 61.19, 61.61, 69.38, 69.38, 69.49, 69.54, 72.62, 72.85, 100.52, 114.12, 120.43, 120.47, 121.27, 121.93, 128.33, 142.04, 148.13, 153.37, 154.12, 154.16, 167.02; HRMS (ESI): Calculated for C₃₃H₄₄N₅O₆Si [M-TFA]⁺ 634.3055, found 634.3054.



27.6 mg (0.0369 mmol) **3.21**, a blue solid, was dissolved in 0.4 mL dry DMF in a flame-dried flask. Next, 25.8 mg (0.201 mmol, 5 equiv.) SO₃-trimethylamine complex, a white solid, was added. The flask was covered with foil and the blue solution stirred under N₂ overnight (16 h). The solution was then carefully quenched with 3 mL sat. NaHCO₃ and concentrated. The blue residue was taken up in 20 mL MeOH, filtered, and the solution concentrated, yielding a yellow residue. The residue was dissolved in 2 mL H₂O and allowed to sit for 20 min, during which the deep blue color returned. This solution was loaded directly onto the HPLC and purified using a 20-80% MeCN/H₂O gradient on reverse-phase to yield **3.15** (17.8 mg, 0.0218 mmol, 59%) as a blue solid.

¹H NMR (500 MHz, CD₃OD): δ 0.56 (s, 3H), 0.58 (s, 3H), 3.27 (dd, 2H, *J* = 5.8 Hz, 4.4 Hz), 3.35 (s, 12H), 3.56 (dd, 2H, *J* = 5.0 Hz, 3.2 Hz), 3.63 (dd, 2H, *J* = 5.9 Hz, 4.4 Hz), 3.81-3.85 (m, 2H), 3.93-4.00 (m, 2H), 4.08 (dd, 2H, *J* = 3.1 Hz, 5.1 Hz), 4.11-4.20 (m, 2H), 4.34-4.41 (m, 2H), 6.67 (s, 1H), 6.82 (dd, 2H, *J* = 9.7 Hz, 2.9 Hz), 6.96 (s, 1H), 7.25 (d, 2H, *J* = 9.6 Hz), 7.30 (d, 2H, *J* = 2.9 Hz); ¹³C NMR (151 MHz, CD₃OD): δ -1.22, -0.90, 40.96, 67.81, 68.27, 70.40, 70.72, 70.76, 70.77, 70.86, 70.94, 115.15, 121.95, 121.95, 122.36, 123.44, 129.28, 142.66, 149.13, 154.99, 155.53, 155.66, 167.57; HRMS (ESI): Calculated for C₃₃H₄₂N₅O₁₂S₂Si [M-Na]⁺ 792.2046, found 792.2029.

References

1. For recent reviews on bioorthogonal chemistry, see: (a) Patterson, D. M.; Nazarova, L. A.; Prescher, J. A. *ACS Chem. Biol.* **2014**, *9*, 592-605; (b) Lang, K.; Chin, J. W. *ACS Chem. Biol.* **2014**, *9*, 16-20; (c) Lang, K.; Chin, J. W. *Chem. Rev.* **2014**, *114*, 4764-4806; (d) Ramil, C. P.; Lin, Q. *Chem. Commun.* **2013**, *49*, 11007-11022; (e) Debets, M. F.; van Hest, J. C. M.; Rutjes, F. P. J. T. *Org. Biomol. Chem.* **2013**, *11*, 6439-6455; (f) McKay, C. S.; Finn, M. G. *Chem. Biol.* **2014**, *21*, 1075-1101.
2. Lemieux G. A.; de Graffenried C.L.; Bertozzi, C.R. *J. Am. Chem. Soc.* **2003**, *125*, 4708-4709.
3. Hangauer M. J.; Bertozzi C. R. *Angew. Chem. Int. Ed.* **2008**, *47*, 2394-2397.
4. For a review on fluorogenic probes activated by the azide-alkyne [3+2] cycloaddition, see: Le Droumaguet, C.; Wang, C.; Wang, Q. *Chem. Soc. Rev.* **2010**, *39*, 1233-1239.
5. Sivakumar, K.; Xie, F.; Cash, B. M.; Long, S.; Barnhill, H. N.; Wang, Q. *Org. Lett.* **2004**, *6*, 4603-4606.
6. Xie, F.; Sivakumar, K.; Zeng, Q.; Bruckman, M. A.; Hodges, B.; Wang, Q. *Tetrahedron* **2008**, *64*, 2906-2914.
7. Wang, C.; Xie, F.; Suthiwangcharoen, N.; Sun, J.; Wang, Q. *Sci. China Chem.* **2012**, *55*, 125-130.
8. Sawa, M.; Hsu, T.-L.; Itoh, T.; Sugiyama, M.; Hanson, S. R.; Vogt, P. K.; Wong, C.-H. *Proc. Natl. Acad. Sci.* **2006**, *103*, 12371-12376.
9. Zhou, Z.; Fahrni, C. J. *J. Am. Chem. Soc.* **2004**, *126*, 8862-8863.
10. Jewett, J. C.; Bertozzi, C. R. *Org. Lett.* **2011**, *13*, 5937-5939.
11. Key, J. A.; Cairo, C. W. *Dyes and Pigments* **2011**, *88*, 95-102.
12. Qi J.; Han, M. S.; Chang, Y. C.; Tung, C. H. *Bioconjug. Chem.* **2011**, *22*, 1758-1762.
13. Li, J.; Hu, M.; Yao, S. Q. *Org. Lett.* **2009**, *11*, 3008-3011.
14. Friscourt, F.; Fahrni, C. J.; Boons, G. J. *J. Am. Chem. Soc.* **2012**, *134*, 18809-18815.
15. Herner, A.; Nikic, I.; Kallay, M.; Lemke, E. A.; Kele, P. *Org. Biomol. Chem.* **2013**, *11*, 3297-3306.
16. Devaraj, N. K.; Hilderbrand, S.; Upadhyay, R.; Mazitschek, R.; Weissleder, R. *Angew. Chem. Int. Ed.* **2010**, *49*, 2869-2872.
17. Lang, K.; Davis, L.; Torres-Kolbus, J.; Chou, C.; Deiters, A.; Chin, J. W. *Nat. Chem.* **2012**, *4*, 298-304.
18. Carlson, J. C. T.; Meimetis, L. G.; Hilderbrand, S. A.; Weissleder, R. *Angew. Chem. Int. Ed.* **2013**, *52*, 6917-6920.
19. Lang, K.; Davis, L.; Wallace, S.; Mahesh, M.; Cox, D. J.; Blackman, M. L.; Fox, J. M.; Chin, J. W. *J. Am. Chem. Soc.* **2012**, *134*, 10317-10320.
20. Song, W.; Wang, Y.; Qu, J.; Madden, M.M.; Lin, Q. *Angew. Chem. Int. Ed.* **2009**, *48*, 2832-2835.
21. Yu, Z.; Ho, L. Y.; Lin, Q. *J. Am. Chem. Soc.* **2011**, *133*, 11912-11915.
22. Neves, A. A.; Stockmann, H.; Wainman, Y. A.; Kuo, S. J. C.-H.; Fawcett, S.; Leeper, F. J.; Brindle, K. M. *Bioconjug. Chem.* **2013**, *24*, 934-941.
23. An, P.; Yu, Z.; Lin, Q. *Org. Lett.* **2013**, *15*, 5496-5499.
24. Fu, M.; Xiao, Y.; Qian, X.; Zhao, D.; Xu, Y. *Chem. Commun.* **2008**, *15*, 1780-1782.
25. Koide, Y.; Urano, Y.; Hanaoka, K.; Terai, T.; Nagano, T. *ACS Chem. Biol.* **2011**, *6*, 600-608.

26. Koide, Y.; Urano, Y.; Hanaoka, K.; Terai, T.; Nagano, T. *J. Am. Chem. Soc.* **2011**, *133*, 5680-5682.
27. Egawa, T.; Hanaoka, K.; Koide, Y.; Ujita, S.; Takahashi, N.; Ikegaya, Y.; Matsuki, N.; Terai, T.; Ueno, T.; Komatsu, T.; Nagano, T. *J. Am. Chem. Soc.* **2011**, *133*, 14157-14159.
28. Wang, T.; Zhao, Q. J.; Hu, H. G.; Yu, S. C.; Liu, X.; Liu, L.; Wu, Q. Y. **2012**, *Chem. Commun.* *48*, 8781-8783.
29. Lukinavicius, G.; Umezawa, K.; Olivier, N.; Honigmann, A.; Yang, G.; Plass, T.; Mueller, V.; Reymond, L.; Correa, I. R.; Luo, Z.-G.; Schultz, C.; Lemke, E. A.; Heppenstall, P.; Eggeling, C.; Manley, S.; Johnsson, K. *Nat. Chem.* **2013**, *5*, 132-139.
30. Shieh, P.; Hangauer, M. J.; Bertozzi, C. R. *J. Am. Chem. Soc.* **2012**, *134*, 17428-17431.
31. Besanceney-Webler, C.; Jiang, H.; Zheng, T.; Feng, L.; Soriano del Amo, D.; Wang, W.; Klivansky, L. M.; Marlow, F. L.; Liu, Y.; Wu, P. *Angew. Chem. Int. Ed.* **2011**, *50*, 8051-8056.
32. Staros, J. V.; Bayley, H.; Standring, D. N.; Knowles, J. R. *Biochem. Biophys. Res. Commun.* **1978**, *80*, 568-572.
33. Lin, V. S.; Chang, C. J. *Curr. Opin. Chem. Biol.* **2012**, *16*, 595-601.
34. Lord, S. J.; Conley, N. R.; Lee, H. D.; Samuel, R.; Liu, N.; Twieg, R. T.; Moerner, W. E. *J. Am. Chem. Soc.* **2008**, *130*, 9204-9205.
35. Lee, H. D.; Lord, S. J.; Iwanaga, S.; Zhan, K.; Xie, H.; Williams, J. C.; Wang, H.; Bowman, G. R.; Goley, E. D.; Shapiro, L.; Twieg, R. J.; Rao, J.; Moerner, W. E. *J. Am. Chem. Soc.* **2010**, *132*, 15099-15101.
36. Hsu, T.-L.; Hanson, S. R.; Kishikawa, K.; Wang, S.-K.; Sawa, M.; Wong, C.-H. *Proc. Natl. Acad. Sci.* **2007**, *104*, 2614-2619.
37. Chang, P. V.; Chen, X.; Smyrniotis, C.; Xenakis, A.; Hu, T. S.; Bertozzi, C. R.; Wu, P. *Angew. Chem. Int. Ed.* **2009**, *48*, 4030-4033.
38. Griffin, B. A.; Adams, S. R.; Tsien, R. Y. *Science* **1998**, *281*, 269-272.
39. Gaietta, G. M.; Giepmans, B. N. G.; Deerinck, T. J.; Smith, W. B.; Ngan, L.; Llopis, J.; Adams, S. R.; Tsien, R. Y.; Ellisman, M. H. *Proc. Natl. Acad. Sci.* **2006**, *103*, 17777-17782.
40. Dommerholt, J.; Schmidt, S.; Temming, R.; Hendriks, L. J. A.; Rutjes, F. P. J. T.; van Hest, J. C. M.; Lefeber, D. J.; Friedl, P.; van Delft, F. L. *Angew. Chem. Int. Ed.* **2010**, *49*, 9422-9425.
41. Graves, A. P.; Kallander, L. S.; Stoy, P. *PCT Int. Appl.* **2011**, 2011025798.
42. Radchenko, O. S.; Sigida, E. N.; Balaneva, N. N.; Dmitrenok, P. S.; Novikov, V. L. *J. Heterocyclic Chem.* **2011**, *48*, 209-214.
43. Zornik, D.; Meudtner, R. M.; El Malah, T.; Thiele, C. M.; Hecht, S. *Chem. Eur. J.* **2011**, *17*, 1473-1484.
44. Panne, P.; Fox, J. M. *J. Am. Chem. Soc.* **2007**, *129*, 22-23.

Chapter 4: A Universal Motif for Fluorogenic Azide Probes Across the Visible Spectrum

Note: Portions of this chapter were published in *J. Am. Chem. Soc.* **2015**, *137*, 7145-7151.

Introduction

Key to the efforts of my earlier work was the identification of a pendent aryl ring system that imparts the desired electronic effects on a given fluorophore scaffold. In an effort to accelerate the design of activatable azide probes with various photophysical and photochemical properties, I sought to identify a universal switch capable of PeT across a variety of dye structures. In this chapter, I describe my work demonstrating that the 3-azido 4,6-dialkoxyaryl group possesses this capability. Incorporation of this group into various xanthene scaffolds afforded a palette of dyes that emit at green to far red wavelengths. When functionalized with zwitterionic solubilizing groups, these probes enabled robust and sensitive detection of alkyne-labeled biomolecules under no-wash conditions and in a variety of settings, including live cells and tissue sections. This family of probes is named Click Activated Luminogenic Fluorophores, or CalFluors.

Results and Discussion

In the last chapter, I identified the 3-azido-4,6-dimethoxy benzene substituent as a fluorogenic switch that outperformed many other aryl substituents examined. To further understand the electronic basis of this superior performance, I synthesized a panel of azide- and triazole-functionalized aryl rings (**4.1-4.5**, Figure 4-1A) and determined their oxidation potentials using cyclic voltammetry (Figure 4-1B). The measured oxidation potentials reflect the compounds' propensity to donate an electron, which would result in fluorescence quenching via PeT. Consistent with calculations, I found that all the triazoles had higher oxidation potentials than their parent azides (Figure 4-1C). Among the aryl azides, compound **4.1a** was the most electron rich, underscoring its potent quenching activity, and its change in oxidation potential upon conversion to triazole **4.1b** was the most dramatic (Figure 4-1C). This large change is consistent with computational predictions that an *ortho*-substituent forces the triazole to twist further out of plane and prevents donation from the nitrogen lone pair into the aryl system (Figure 4-2). Another approach to disrupt triazole-aryl system conjugation is to install *ortho* substituents on the triazole. This tri-substituted triazole product can be generated by copper-free reaction with cyclooctynes, suggesting that the fluorescence enhancement of these azide probes should be higher on average for copper-free click chemistry than for copper-catalyzed click reactions. Alternatively, copper-catalyzed reactions with 1-iodoalkynes may also enable such a dramatic electronic switch and are worthy of future investigation as a bioorthogonal chemical reporter.¹

I found that calculated E_{HOMO} and oxidation potential correlate (Figure 4-3), though the modest fit suggests that more sophisticated approaches towards predicting PeT efficiency may be necessary for future improvements in computation-based probe design. The fit for triazole-derivatives **4.1 – 4.5b** was worse than for azides **4.1 – 4.5a**, suggesting that the more complex

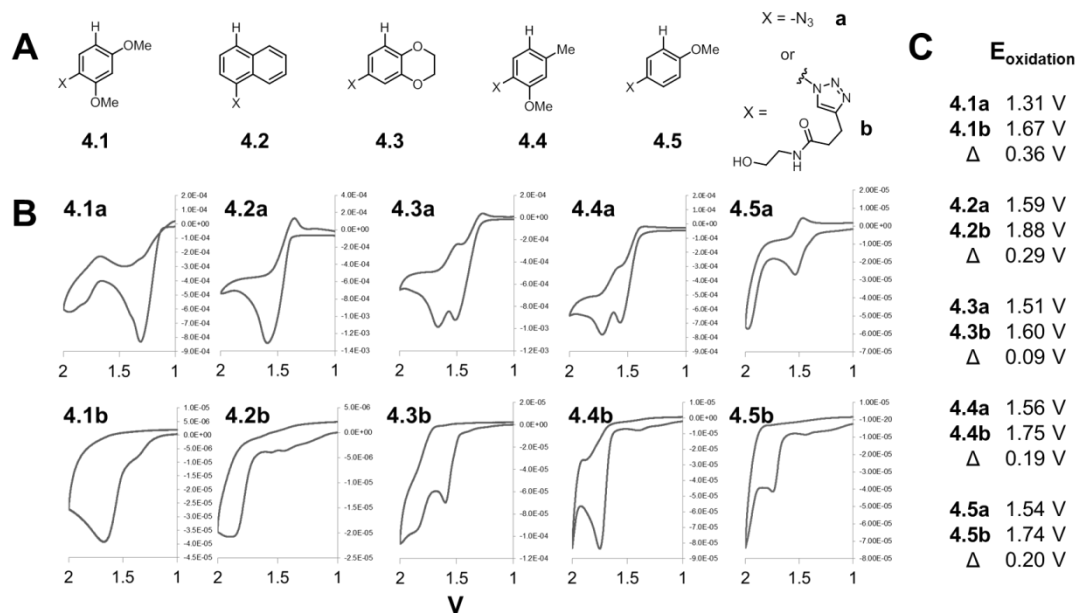


Figure 4-1. Cyclic voltammetry analysis of substituted aryl systems. (A) Aryl azides (**4.1a-4.5a**) and triazoles (**4.1b-4.5b**) synthesized and studied by cyclic voltammetry. (B) Cyclic voltammetry plots of compounds **4.1-4.5**. (C) Oxidation potentials of compounds **4.1-4.5**. Note that all redox cycles were completely or partially irreversible. Cyclic voltammetry was performed in acetonitrile containing 0.1 M NBu_4PF_6 as an electrolyte using platinum and glassy carbon electrodes, with a silver reference standard. Ferrocene was added afterwards as an internal standard. Scans were performed at 100 mV/s from 0 to 2 V.

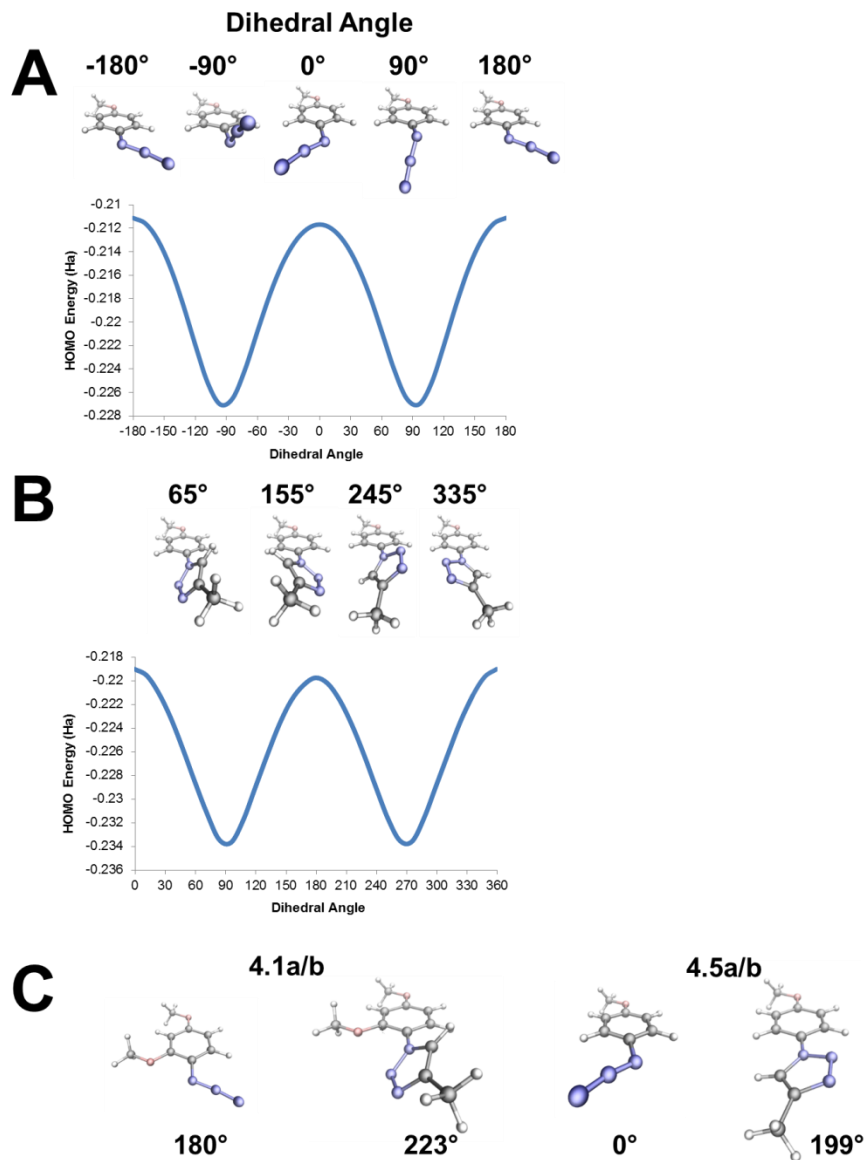


Figure 4-2. Role of azide and triazole conformation in aryl HOMO energies. HOMO energies are highest at dihedral angles of 0° , 180° , or $-180^\circ/360^\circ$, and lowest at angles of 90° and $-90^\circ/270^\circ$. (A) Plot of calculated HOMO energies of **4.5a** as a function of aryl ring-azide dihedral angle. (B) Plot of calculated HOMO energies of **4.5b** as a function of aryl ring-triazole dihedral angle. (C) Lowest energy conformations of **4.1a/b** and **4.5a/b**. Note the increased out-of-plane twist of the triazole in **4.1b** compared to **4.5b**.

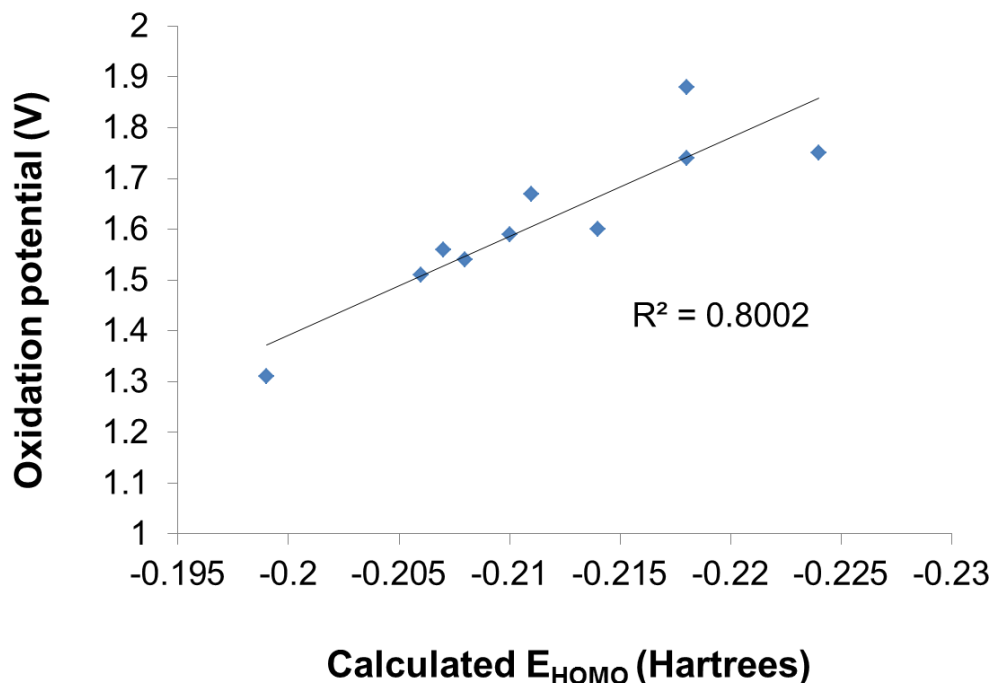


Figure 4-3. Plot of oxidation potential of aryl rings vs. calculated E_{HOMO} . Calculated E_{HOMO} values are from Ref. 3.

structure of the triazole derivatives may have electronic properties that are more difficult to predict. Nevertheless, these results gave us confidence that dimethoxy aryl ring **4.1** would efficiently switch fluorescence in a variety of fluorophore systems, regardless of subtle differences in their electronics.

To test this hypothesis, I expanded my panel of xanthene fluorophores containing the 3-azido 2,4-dimethoxy benzene substituent. I focused on fluorescein, tetramethylrhodamine (rhodamine) and dimethylsilicon-substituted fluorescein (Si-fluorescein)² scaffolds, which have emission maxima of around 520 nm (green, compound **4.6**), 580 nm (orange, compound **4.7**) and 610 nm (red, compound **4.8**), respectively (Figure 4-4). Following a general route, 3-bromo-4,6-dimethoxy aniline was protected, lithiated, and then added into various protected xanthenes to generate the corresponding amino-fluorescein, -rhodamine, and -Si-fluorescein derivatives (Scheme 4-1). While the fluorescein and Si-fluorescein xanthenes were readily prepared via literature procedures,^{2,3} I developed a new route to access the rhodamine xanthone from commercially available Pyronin Y. This route involved reduction of Pyronin Y to the corresponding xanthine, followed by oxidation using potassium permanganate. These amine-functionalized probes were converted to aryl azides by diazotization and displacement with sodium azide to generate compounds **4.6a** to **4.8a**. The corresponding triazoles, **4.6b** to **4.8b**, were prepared under Cu-catalyzed click conditions.

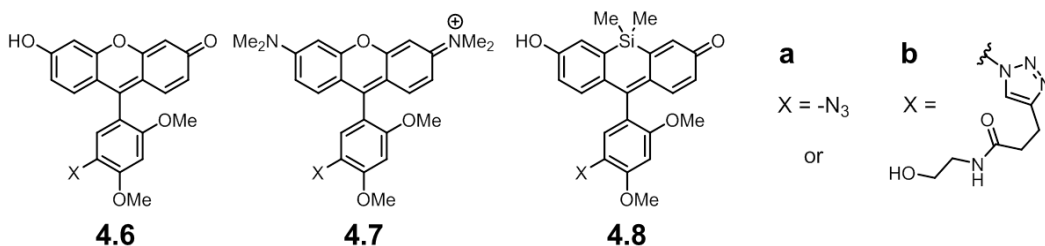
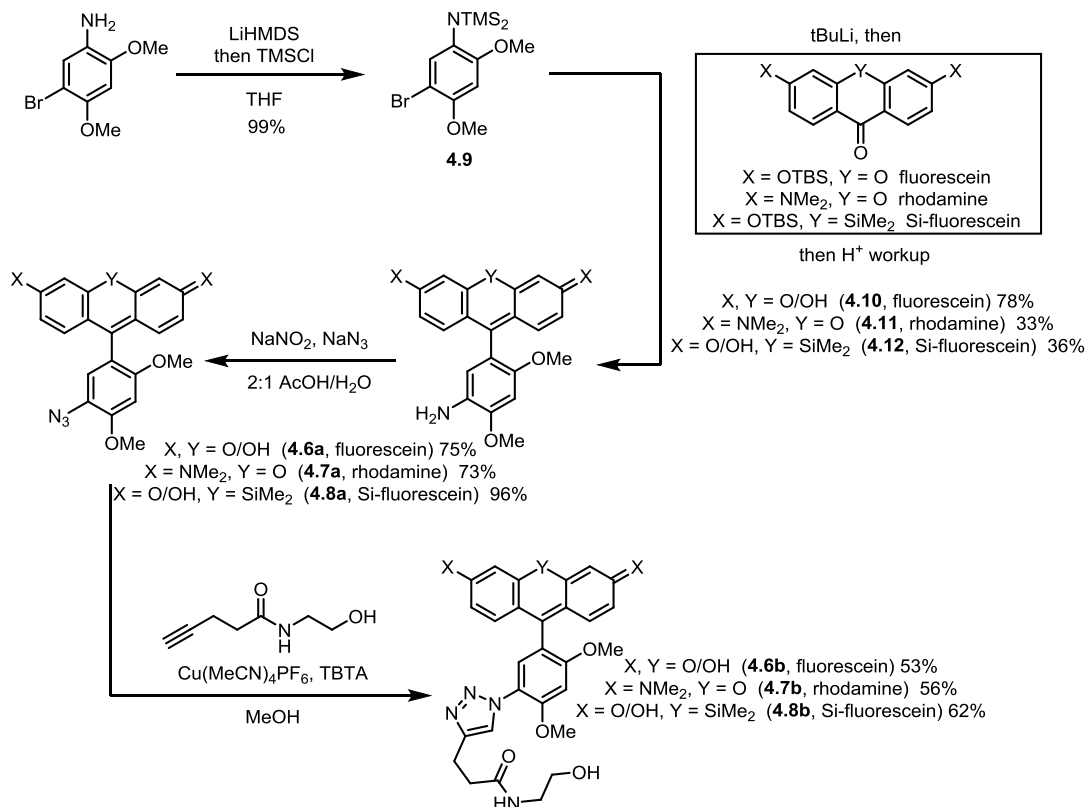


Figure 4-4. Structures of dimethoxy-substituted fluorophores **4.6** to **4.8**.



Scheme 4-1. Synthesis of dimethoxy-substituted azide fluorophores **4.6a-4.8a** and their corresponding triazole products **4.6b-4.8b**.

The fluorescence quantum yields of the azides and triazole products were measured in pH 7.4 phosphate-buffered saline. Gratifyingly, I found that their common dimethoxy aryl substituent efficiently switched fluorescence for all fluorophores tested (Table 4-1). Notably, the fluorescein and Si-fluorescein probes offered higher levels of fluorescence enhancement than any of my previously reported fluorogenic azide probes. In particular, Si-fluorescein **4.8a**, which has an emission maximum beyond 600 nm, underwent >100-fold enhancement in fluorescence upon click reaction. Rhodamine **4.7a**, however, showed a significantly lower turn-on ratio (20-fold) due to reduced quenching of the azide starting material. This poorer quenching was observed in my work in the previous chapter on Si-rhodamine probes, as well. All of the probes were good substrates for the Cu-catalyzed click reaction,⁴ achieving complete conversion to the

corresponding triazoles within 10 min using micromolar concentrations of catalyst and reagents (Figure 4-5).

Compound	λ_{max}	λ_{em}	Φ_{fl}	Enhancement
4.6a	497 nm	516 nm	0.0059	--
4.6b	498 nm	520 nm	0.437	74x
4.7a	555 nm	577 nm	0.0178	--
4.7b	557 nm	580 nm	0.351	20x
4.8a	586 nm	604 nm	0.00136	--
4.8b	588 nm	604 nm	0.240	176x
3.9	654 nm ^a	666 nm ^a	0.0042 ^a	--
3.9 triazole	665 nm ^a	668 nm ^a	0.20 ^a	48x ^a
4.13a	499 nm	519 nm	0.00589	--
5.13b	499 nm	520 nm	0.743	126x
CalFluor 488	498 nm	520 nm	0.00306	--
CalFluor 488 triazole	500 nm	521 nm	0.0747	243x
CalFluor 555	557 nm	577 nm	0.0174	--
CalFluor 555 triazole	561 nm	583 nm	0.604	35x
CalFluor 580	588 nm	611 nm	0.00250	--
CalFluor 580 triazole	591 nm	609 nm	0.473	189x
CalFluor 647	655 nm	678 nm	0.0056	--
CalFluor 647 triazole	657 nm	674 nm	0.25	45x

Table 4-1. Photophysical properties of all fluorophores. Measurements were made in pH 7.4 phosphate-buffered saline. ^aData from Ref. 5.

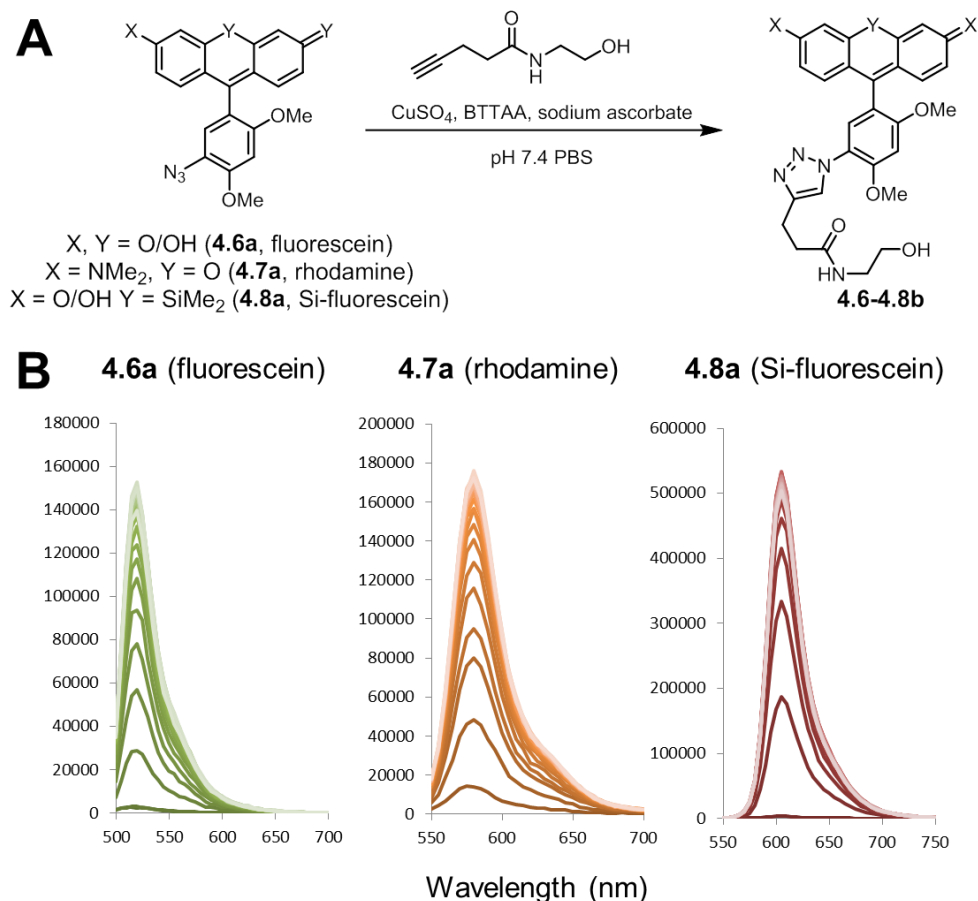
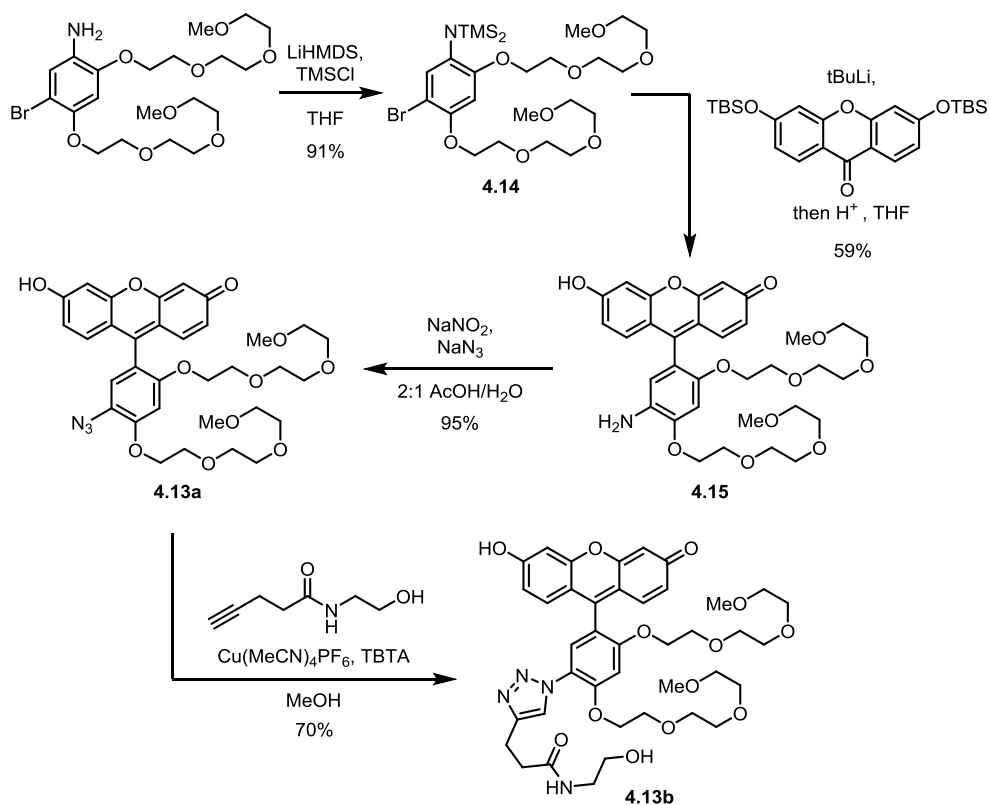


Figure 4-5. Fluorescence enhancement of dimethoxy azide probes. (A) Reaction of fluorophores **4.6a-4.8a** with a model alkyne under copper-catalyzed click conditions. (B) Fluorescence enhancement of fluorophores **4.6a-4.8a** over the course of the reaction. Scans were taken every 30 seconds, with the first scan taken immediately before the addition of alkyne.

A significant advantage of these probes is that, by replacing the methoxy groups with other alkyloxy functionalities, their physical properties can be altered without perturbing the electronics of the system. As described in the previous chapter, I found that introducing oligoethylene glycol tails significantly improved the water solubility of my probes while maintaining fluorescence enhancement. Therefore, I synthesized the bis-oligoethylene glycol functionalized azidofluorescein derivative **4.13a** as well as its triazole derivative **4.13b** (Scheme 4-2). This fluorescein analog maintained the enhancement in fluorescence of the parent fluorophore while showing good water solubility, making it very well-suited for biological labeling experiments (Table 4-1, Figure 4-21). The robustness of this route enabled us to access oligoethylene glycol functionalized rhodamine and Si-fluorescein probes as well (Figure 4-6A). Consistent with predictions, all these analogs showed similar fluorescence enhancements as compared to their parent dimethoxy compounds.



Scheme 4-2. Synthesis of oligoethylene-glycol substituted probe **4.13a** and its corresponding triazole product **4.13b**.

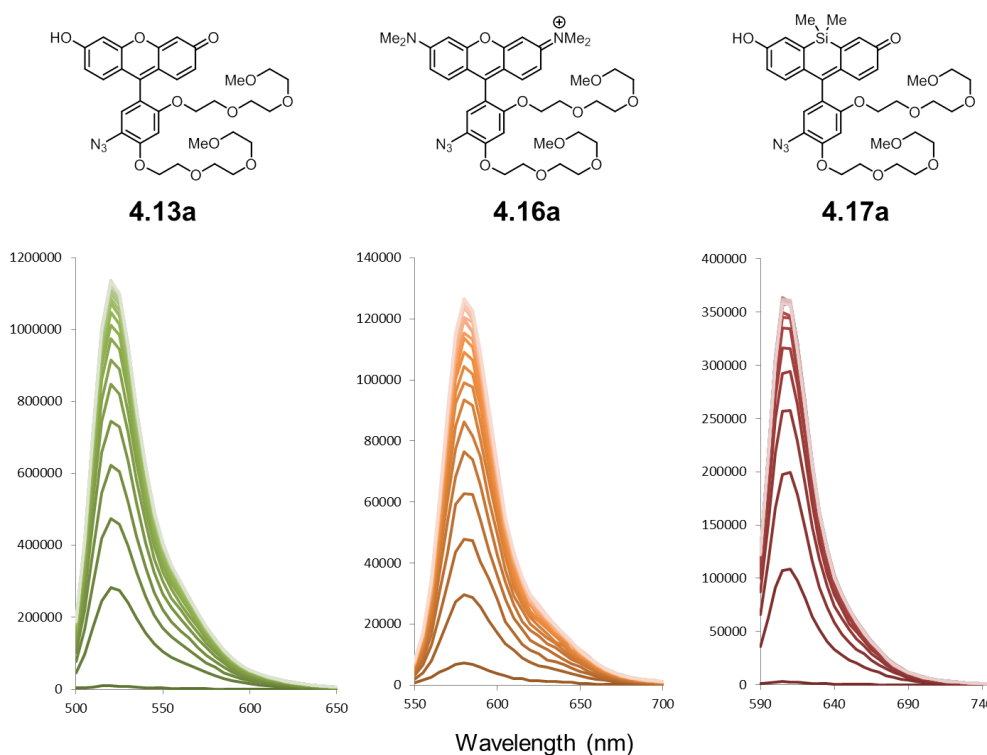


Figure 4-6. Fluorescence enhancement of bis-oligoethylene glycol azide probes **4.13a**, **4.16a**, and **4.17a**. (A) Reaction of fluorophores **4.13a**, **4.16a**, and **4.17a** with a model alkyne under copper-catalyzed click conditions. (B) Fluorescence enhancement of fluorophores **4.13a**, **4.16a**, and **4.17a** over the course of the reaction. Scans were taken every 30 seconds, with the first scan taken immediately before the addition of alkyne.

However, I found their aqueous solubility to be limiting for biological labeling purposes. I was concerned that the potential for nonspecific protein binding would lead to spurious fluorescence turn-on, as documented by Nagano and coworkers in other systems.⁶ While we were able to improve water solubility of the Si-rhodamine derivative by adding sulfate esters at the termini of oligoethylene glycol chains (**4.15**), but this compound was still subject to fluorescence enhancements due to protein and lipid binding (Figure 4-7). As well, selective sulfation would have been difficult to achieve for fluorescein-based probes that possess competing phenolic hydroxyl groups.

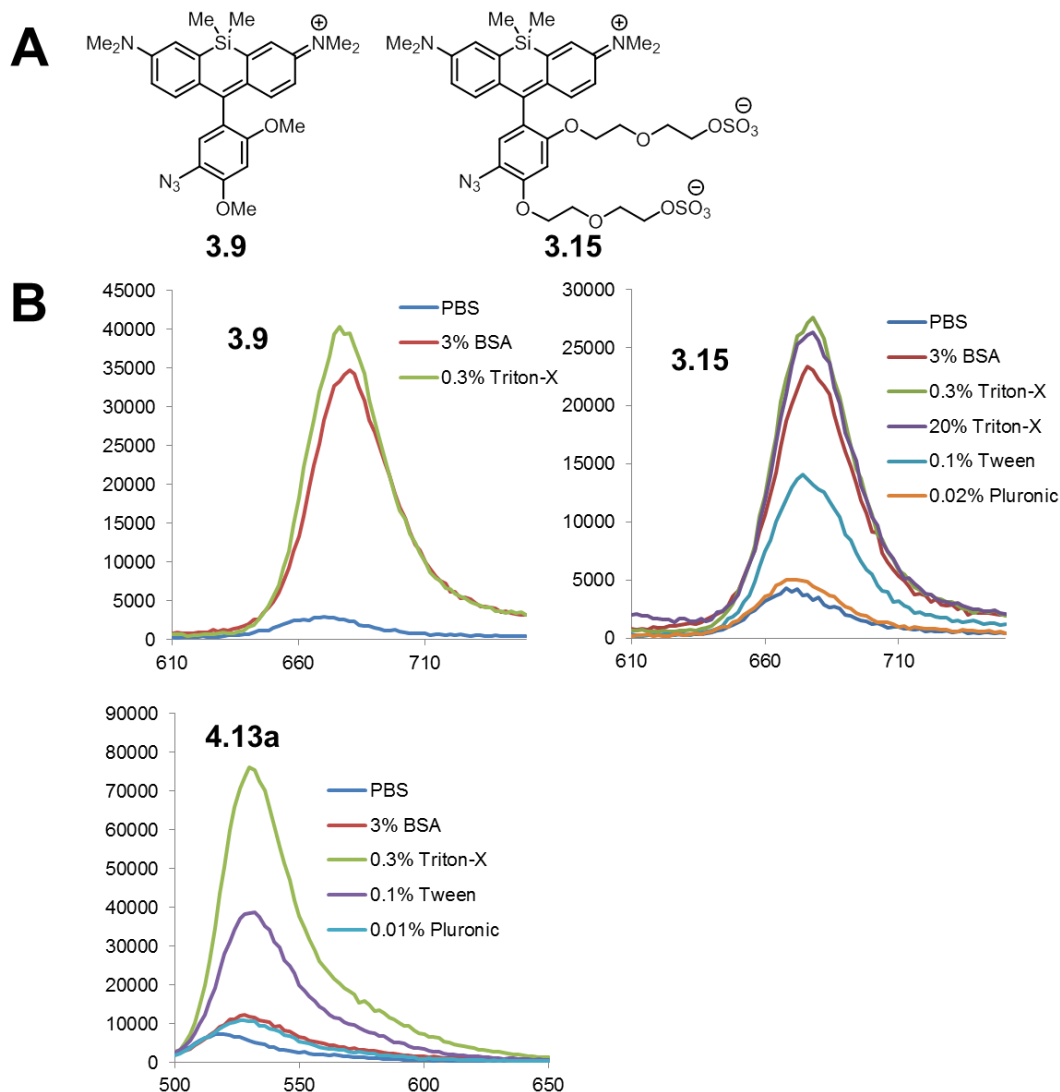
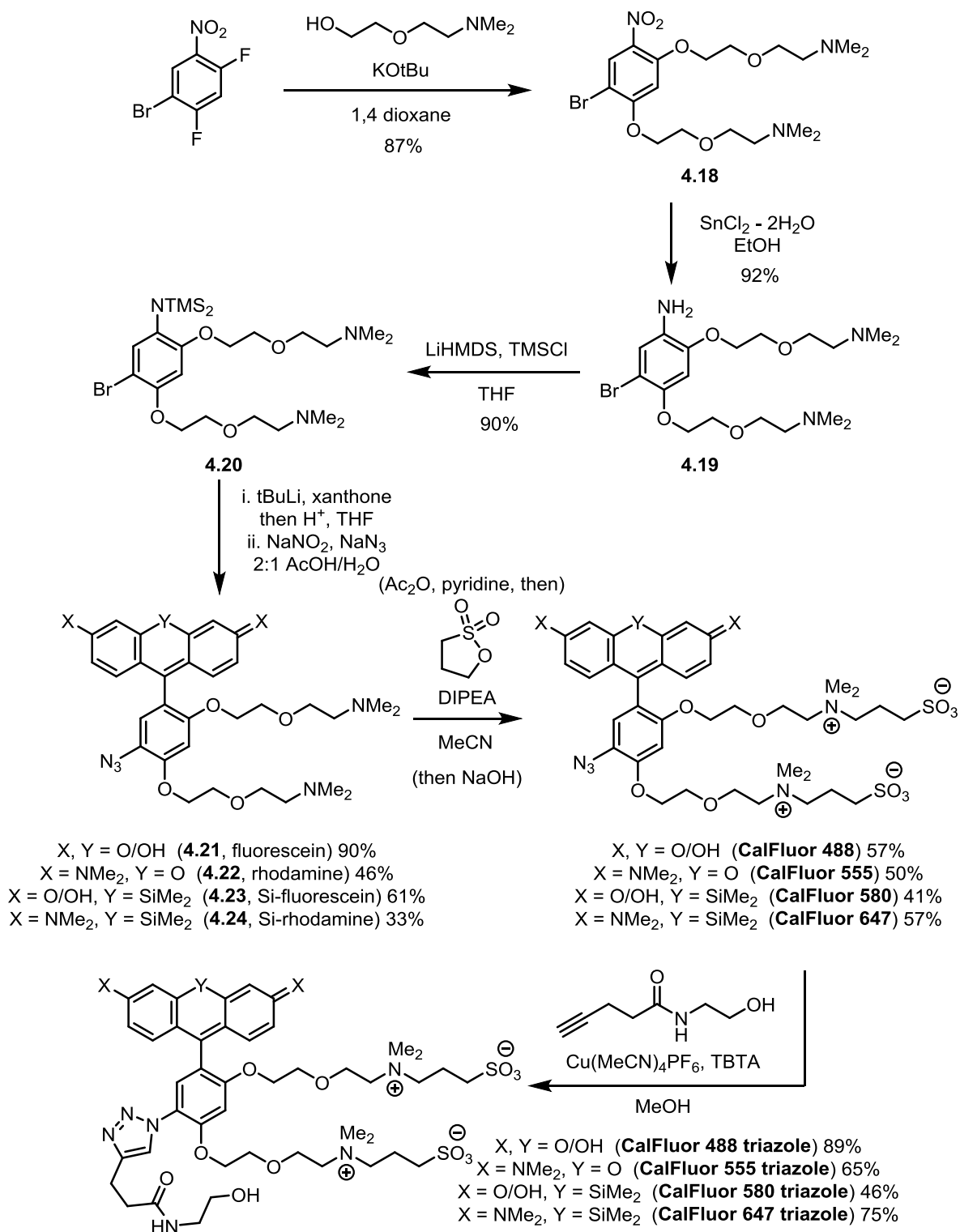


Figure 4-7. Fluorescence spectra of equimolar concentrations of probes in various environments. (A) Structure of Si-rhodamine probes **3.9** and **3.15**. (B) Fluorescence spectra of 1 μM fluorophores in pH 7.4 PBS containing various additives.

In a search for alternative solubilizing groups, I was drawn to zwitterions, which are growing in popularity as anti-fouling agents in biomaterials applications.⁷ Indeed, zwitterionic coatings have been shown to outperform polyethylene glycols in many situations.⁸⁻¹⁰ Additionally, zwitterionic fluorophores have been recently demonstrated to have dramatically reduced serum binding compared to anionic counterparts.¹¹ To generate fluorophores containing zwitterionic tails, I was drawn to the sulfo-betaine scaffold, which can be generated by the reaction of tertiary amines with 1,3-propanesultone.¹² The mild reaction conditions suggested that these functionalities could be introduced at the end of my synthetic route, thereby minimizing difficulties in product isolation. Importantly, as the fluorescein phenols could be selectively protected in the presence of tertiary amines via simple acetylation, alkylation of the xanthene could be avoided. Accordingly, I prepared a panel of zwitterionic azide fluorophores according



Scheme 4-3. Synthesis of CalFluors and their corresponding triazole products.

to the route shown in Scheme 4-3. In keeping with tradition in this field, I gave the azide fluorophore products the common names CalFluor 488, 555, 580 and 647, respectively (wherein the numbers represent their excitation wavelengths) (Figure 4-8A).

All the CalFluors underwent significant fluorescence enhancement upon triazole formation at a level that was at least as high as their dimethoxy substituted counterparts (Figure 4B, Table 1). CalFluor 488 and 580 showed higher levels of fluorescence enhancement compared to their parent derivatives, potentially due to subtle electronic differences conferred by the oligoethylene glycol tails. Additionally, the fluorescence of these probes remained virtually unaltered in proteinaceous environments (e.g., 3% BSA or neat fetal bovine serum, Figure 4-9) or in the presence of detergents such as Triton X-100 and Tween-20 (Figure 4-10), demonstrating how effectively these zwitterionic tails minimize non-specific interactions.

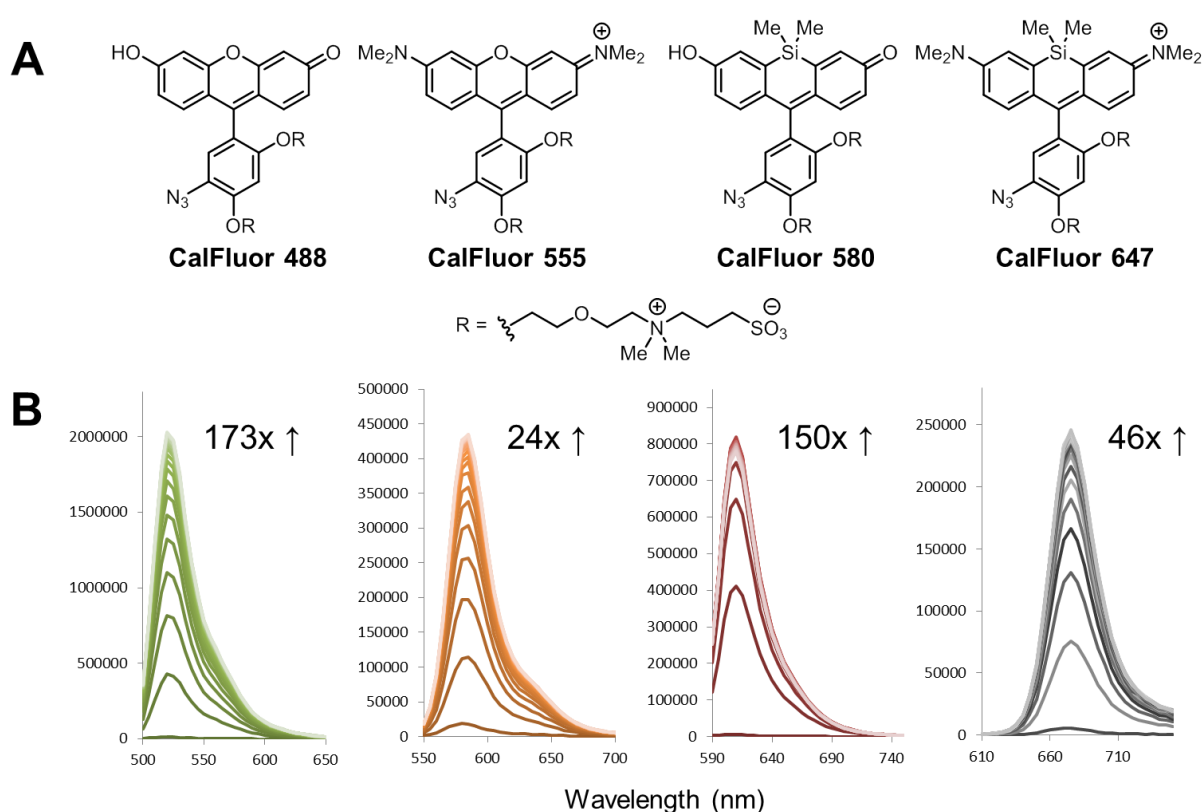


Figure 4-8. CalFluors and their fluorescence enhancements. (A) Structures of CalFluors 488, 555, 580, and 647. (B) Fluorescence enhancements of CalFluors during copper-catalyzed click reactions. To a mixture of 2 μM fluorophore, 50 μM , 300 μM BTAA ligand, and 2.5 mM sodium ascorbate was added 100 μM alkyne and emission scans were taken every 30 seconds. The first scan was taken immediately before addition of alkyne.

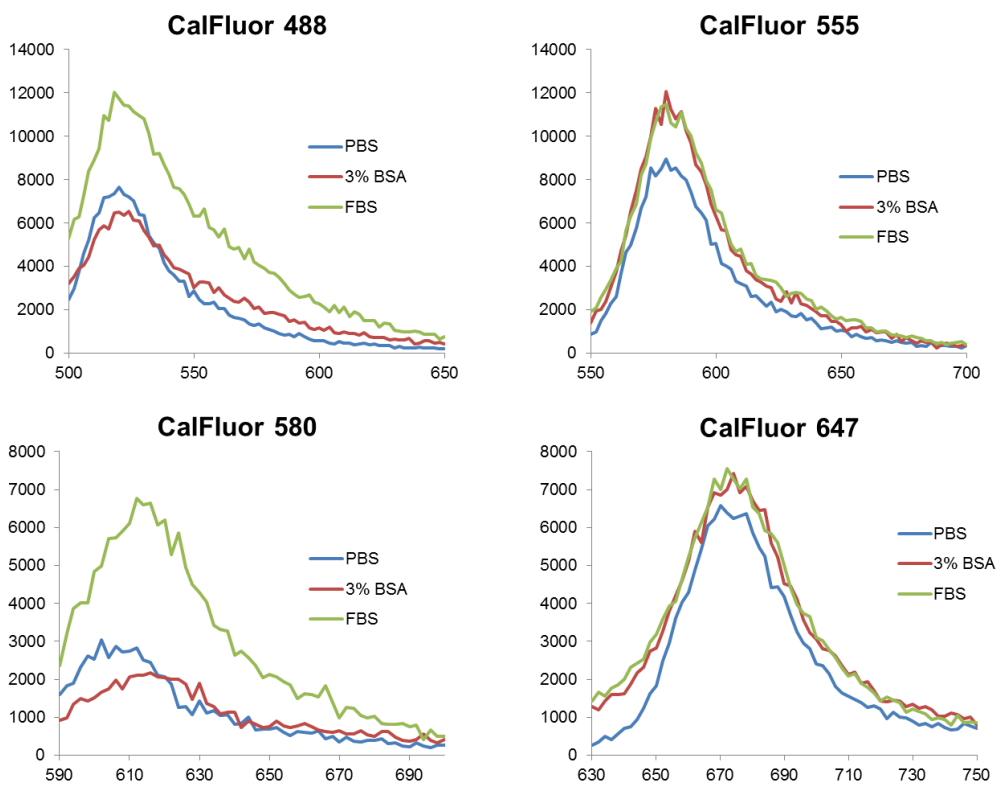


Figure 4-9. Fluorescence spectra of 1 μ M CalFluors in the presence of various additives. Compare with data from Figure S4B. FBS = neat fetal bovine serum.

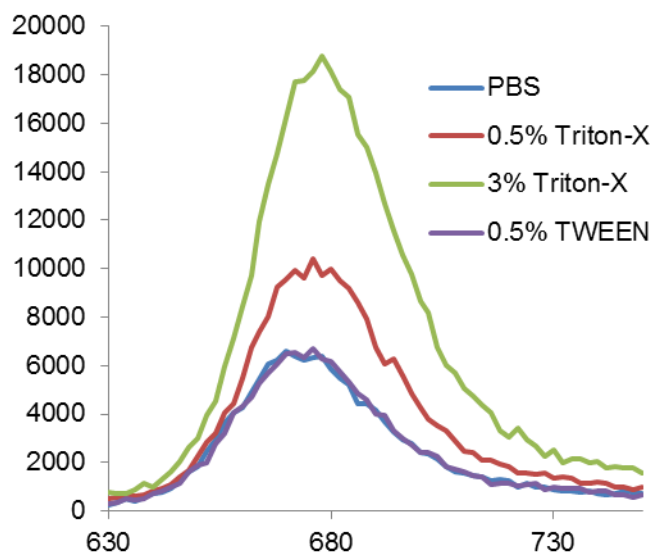


Figure 4-10. Fluorescence of CalFluor 647 in the presence of various detergents. Compare to the results for 3.15 in Figure 4-7.

My next goal was to evaluate the CalFluors' performance in no-wash cell imaging experiments. Using established methods, we metabolically labeled cell-surface glycoconjugates with peracetylated *N*-pentynoyl mannosamine (Ac₄ManNAI), which introduces terminal alkyne groups into sialic acid residues (SiaNAI).^{13,14} HEK 293T cells treated in this fashion were then incubated, without fixation, with a cocktail containing 50 μM CuSO₄, 300 μM BTAA, 5 mM sodium ascorbate and 10 μM CalFluor dye.⁴ After 15 min, cell surface glycans were robustly labeled with the given fluorophore, whereas control cells treated with peracetylated *N*-acetylmannosamine (Ac₄ManNAc) showed no detectable fluorescence (Figure 4-11A). The only background fluorescence was from free fluorophore in solution (Figure 4-12, only observable at

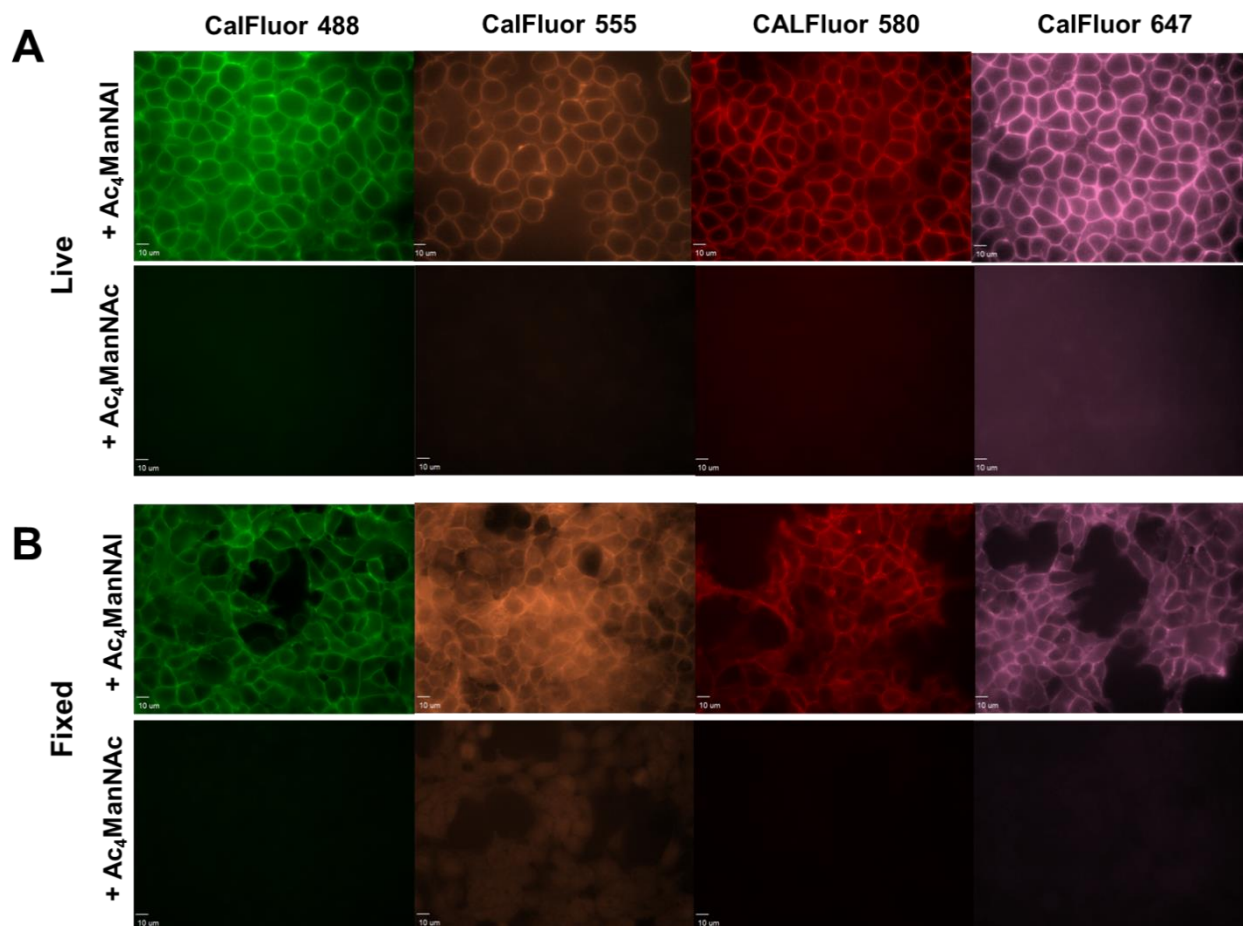


Figure 4-11. No-wash labeling of cell-surface glycoproteins on HEK 293T cells. Cells were grown with 50 μM Ac₄ManNAI or Ac₄ManNAc for 3 days, then subjected to click labeling with CalFluor probes. (A) Labeling glycoproteins on live cell surfaces. Cells were treated with 10 μM azide probe, 50 μM CuSO₄, 300 μM BTAA ligand, and 5 mM sodium ascorbate. The reaction was quenched with 1 mM BCS and the cells imaged without further wash steps. (B) Labeling glycoproteins on fixed cells. Cells were fixed with 3% paraformaldehyde, then treated with 10 μM CalFluor probe, 1 mM CuSO₄, 100 μM TBTA ligand, and 2 mM sodium ascorbate. 0.1 mg/mL BSA was added to prevent the TBTA from precipitating over the course of the reaction. Scale bar = 10 μm.

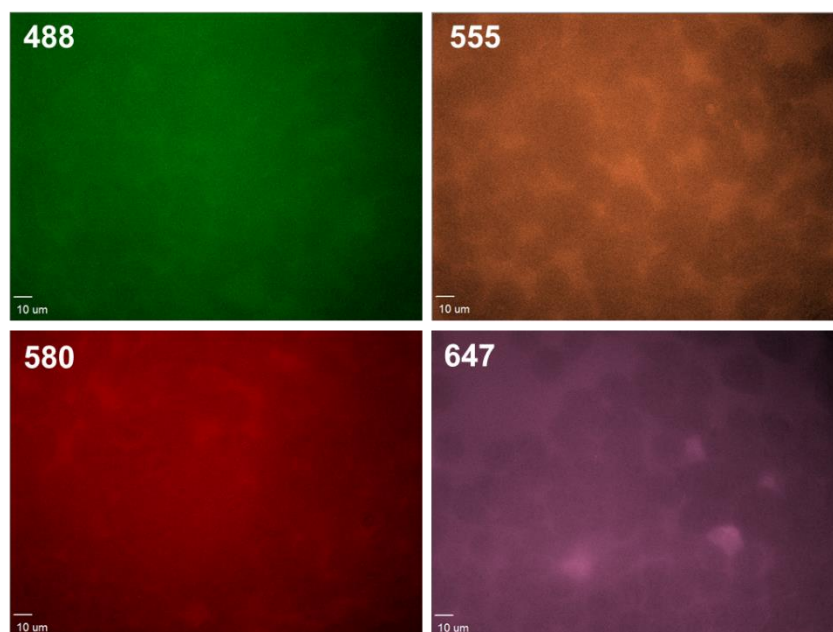


Figure 4-12. Higher-contrast images of cells labeled with Ac₄ManNAc control and treated with CalFluors. Scale bar = 10 μ m.

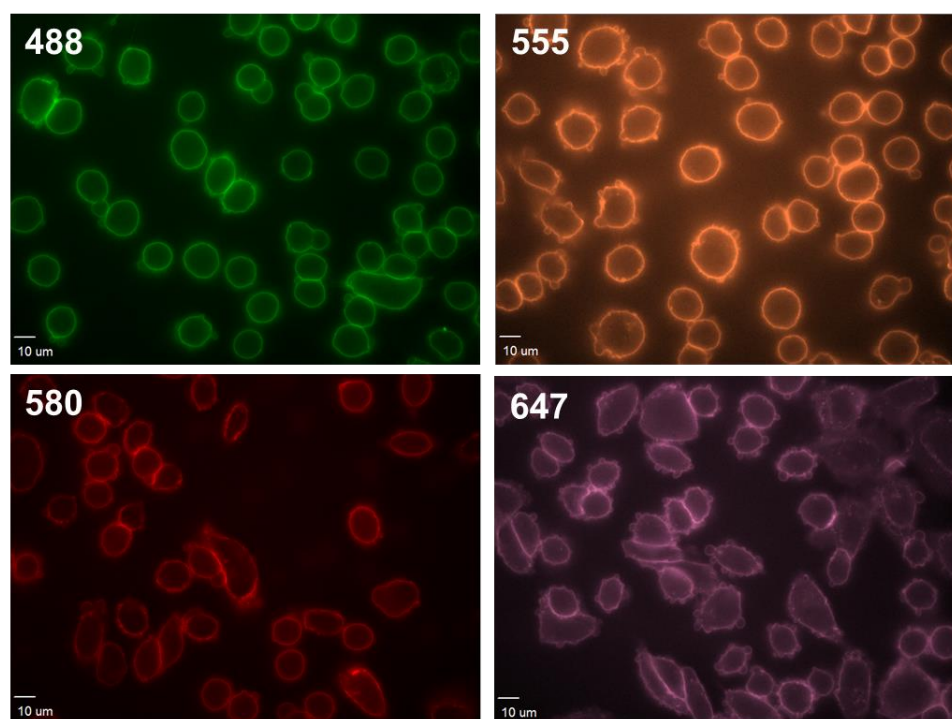


Figure 4-13. No-wash labeling of cell surface glycans on CHO K1 cells with 10 μ M CalFluors. Exposure times were 500 ms for CalFluor 488, 250 ms for CalFluor 555, and 1000ms for CalFluors 580 and 647. Scale bar = 10 μ m.

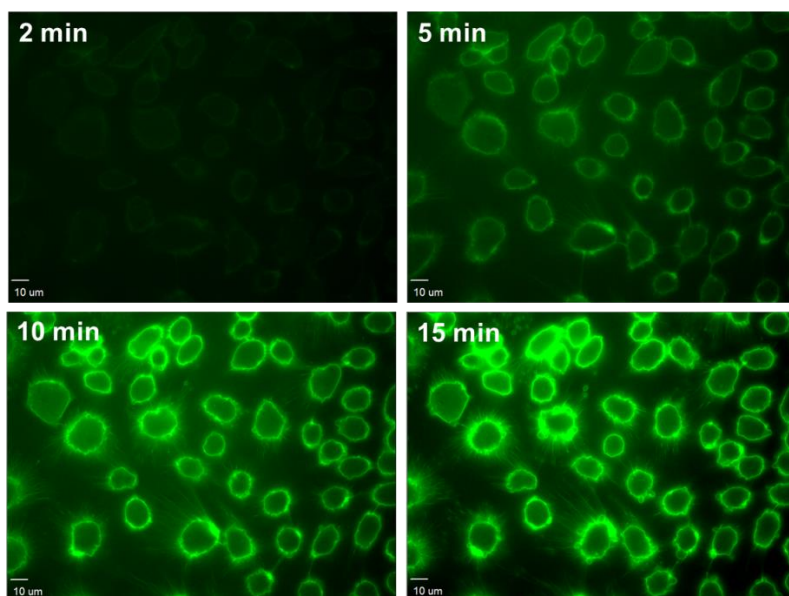


Figure 4-14. Real-time imaging of glycans on live cell surfaces. 10 μ M CalFluor 488 was used in this experiment to label Ac₄ManNAI-treated CHO K1 cells. Scale bar = 10 μ m. Contrast is kept constant in all images.

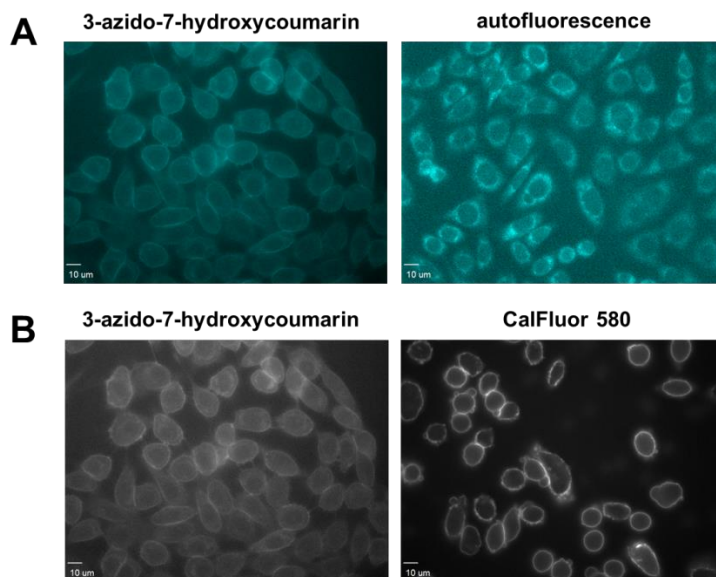


Figure 4-15. Labeling cell surface glycoproteins on live CHO K1 cells using 3-azido-7-hydroxycoumarin for BTAA-catalyzed click reactions. (A) Labeling of cell surface glycans, and autofluorescence of cells. The faint intracellular staining corresponds to background autofluorescence. (B) Comparison of labeling with this probe vs. CalFluor 580 (from Figure 4-13). Scale bar = 10 μ m. Exposure times for both fluorophores were 1000 ms. Scale bar = 10 μ m.

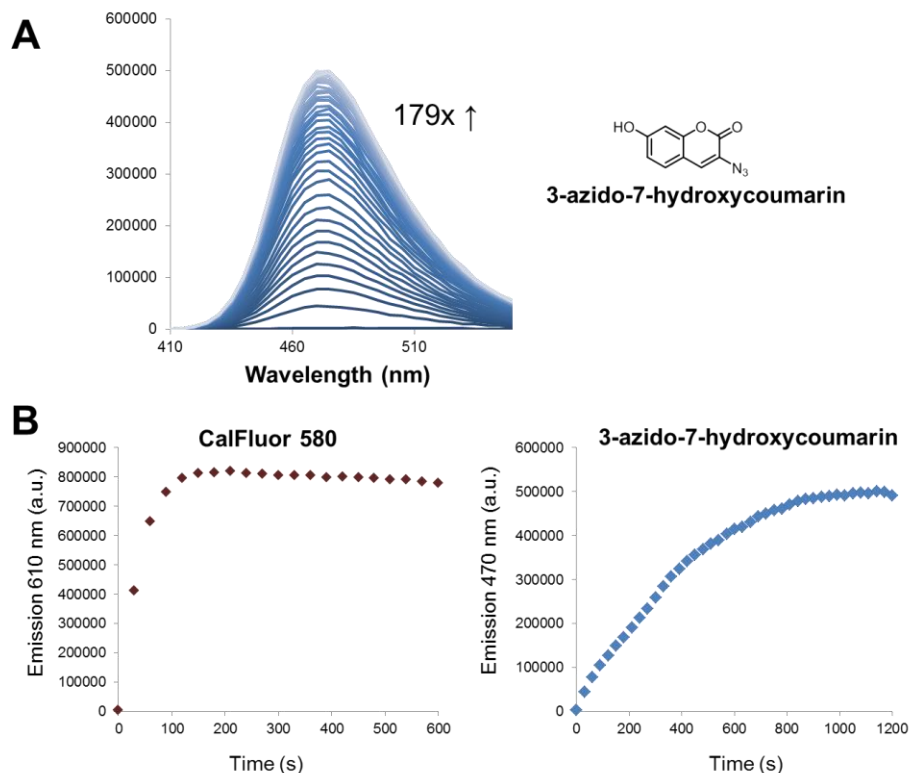


Figure 4-16. Fluorescence enhancement of 3-azido-7-hydroxycoumarin. (A) Fluorescence enhancement of 2 μM 3-azido-7-hydroxycoumarin during click reaction. The solution was excited at 400 nm, and emission spectra were taken every 30 seconds. (B) Plotting single wavelength emission intensity of 2 μM CalFluor 580 or 2 μM 3-azido-7-hydroxycoumarin plotted versus time. CalFluor 580 fluorescence saturates much more rapidly versus the coumarin probe. See also Figure 4-8B.

high contrast). Similar results were achieved with CHO K1 cells (Figure 4-13). Labeling with CalFluor probes could be observed in real time and clear fluorescence over background was visible just minutes into the reaction (Figure 4-14). Notably, under the same reaction conditions, CalFluors labeled cells far more intensely than the blue fluorogenic probe 3-azido-7-hydroxycoumarin (Figure 4-15),¹⁵ which I attribute in part to the CalFluors' superior reactivity (Figure 4-16). This observation is consistent with studies by Finn and coworkers showing that electron-rich aryl azides undergo more rapid copper-catalyzed click reactions.¹⁶

I also evaluated fixed (3% paraformaldehyde) Ac₄ManNAI-treated HEK 293T cells as substrates CalFluor labeling. In this case, copper-click reaction with 50 μM CuSO₄ and 300 μM BTTAA gave poor labeling, potentially due to sequestration of the copper catalyst by denatured proteins. However, use of higher catalyst concentrations (100 μM TBTA, 1 mM CuSO₄, 2 mM sodium ascorbate) gave robust labeling with 10 μM CalFluor dyes (Figure 4-11B). Similar results were achieved when performing the same experiments on fixed CHO K1 cells (Figure 4-17). While some background was apparent when using CalFluor 555 at this concentration, a single wash step was sufficient to eliminate this background fluorescence (Figure 4-18, 4-19).

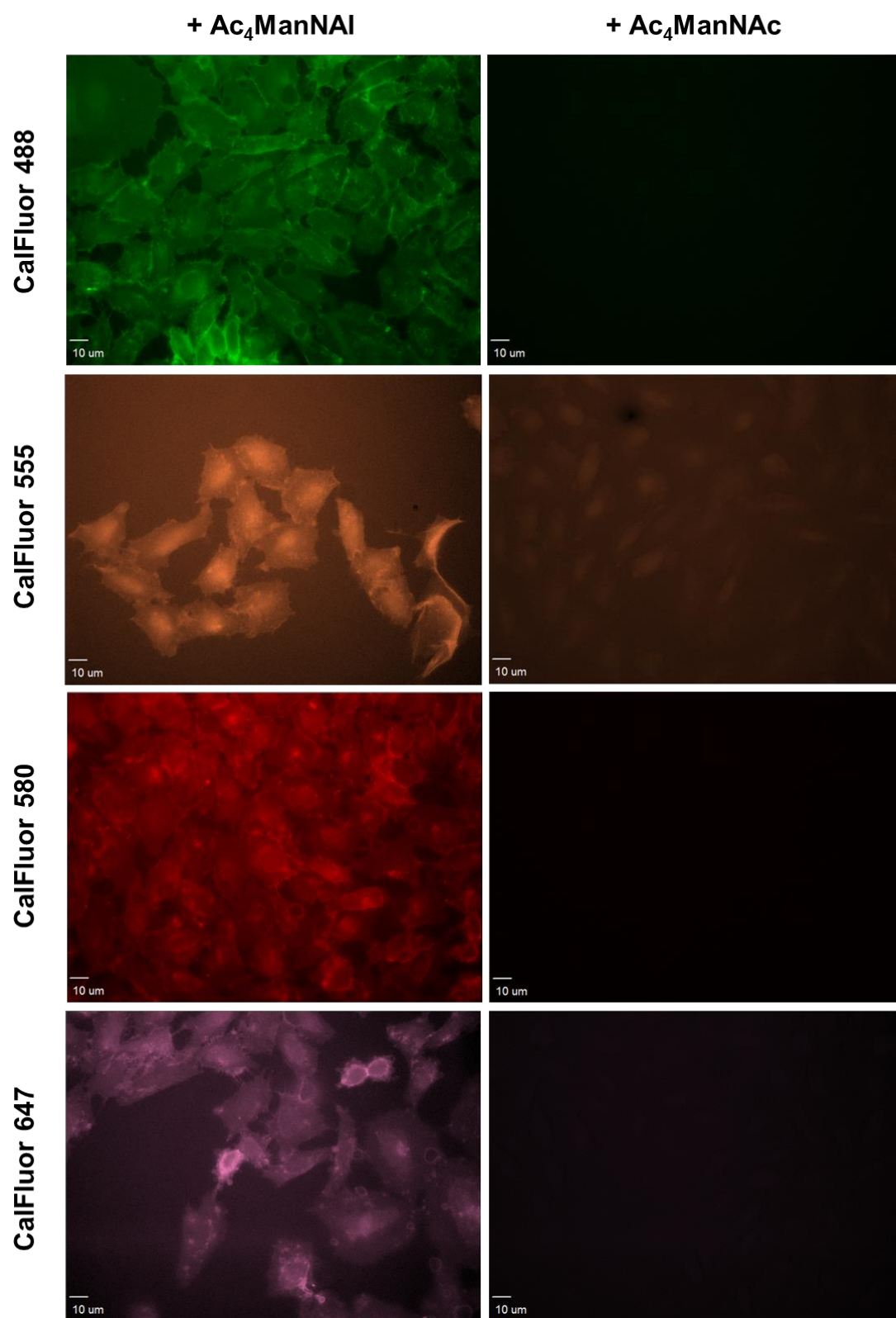


Figure 4-17. No-wash labeling of glycoproteins on fixed CHO K1 cells with 10 μ M CalFluors. Scale bar = 10 μ m.

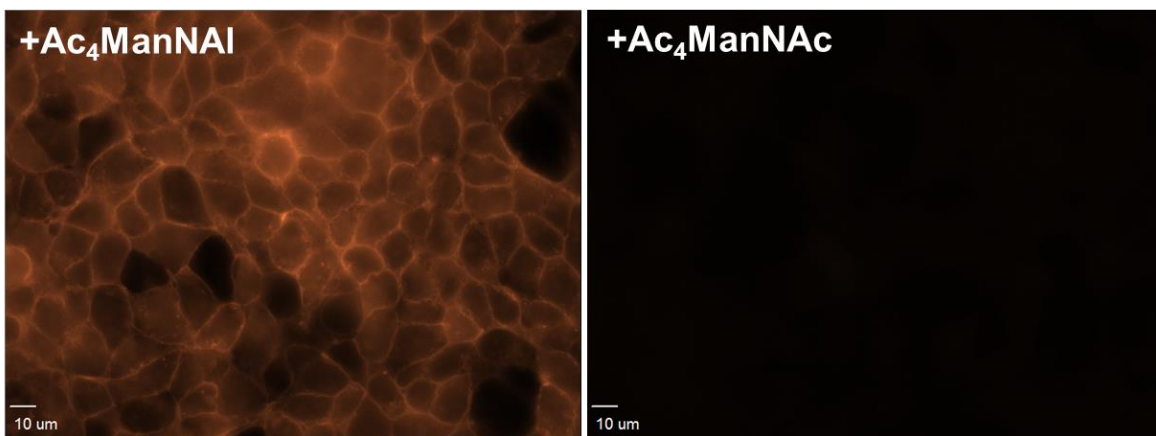


Figure 4-18. Labeling fixed HEK 293T cells with 10 μ M CalFluor 555. A single wash step was performed after cell surface labeling by replacing the reaction mixture with fresh PBS. Scale bar = 10 μ m.

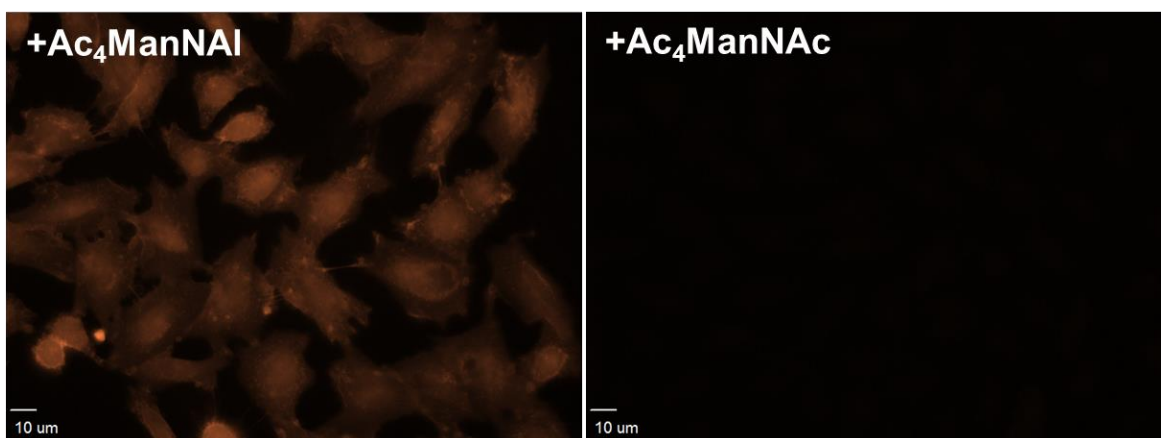


Figure 4-19. Labeling fixed CHO K1 cells with 10 μ M CalFluor 555. A single wash step was performed after cell surface labeling by replacing the reaction mixture with fresh PBS. Scale bar = 10 μ m.

Under these copper-click conditions, the 3-azido-7-hydroxycoumarin probe performed comparably to the CalFluors when labeling fixed cells (Figure 4-20). By contrast, the sulfated predecessor **3.15** or the oligoethylene glycol containing probe **4.13a** gave higher background fluorescence, underscoring the benefit of the zwitterionic tails in reducing non-specific interactions. (Figure 4-21, 4-22). The advantage of the fluorescence turn-on of CalFluors was clear when comparing labeling by the always fluorescent AlexaFluor 647 alkyl azide. (Figure 4-23). Even with a washing step, background from unreacted fluorophore obscured any alkyne-dependent signal in the latter case. Overall, these experiments conclusively demonstrate the extreme robustness of the family of CalFluor probes for *in vitro* imaging applications.

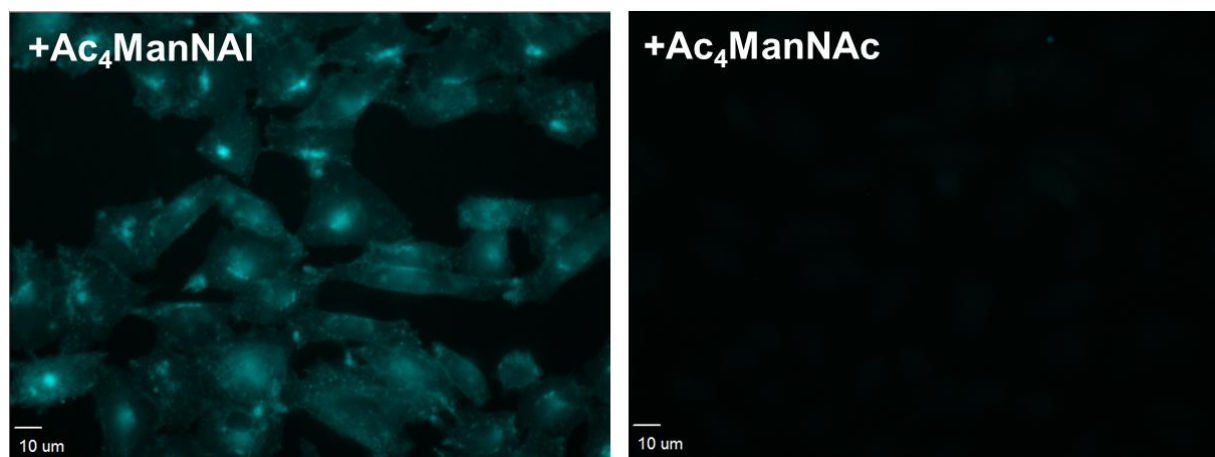


Figure 4-20. No-wash labeling of fixed CHO K1 cells with 10 μ M 3-azido-7-hydroxycoumarin. Scale bar = 10 μ m.

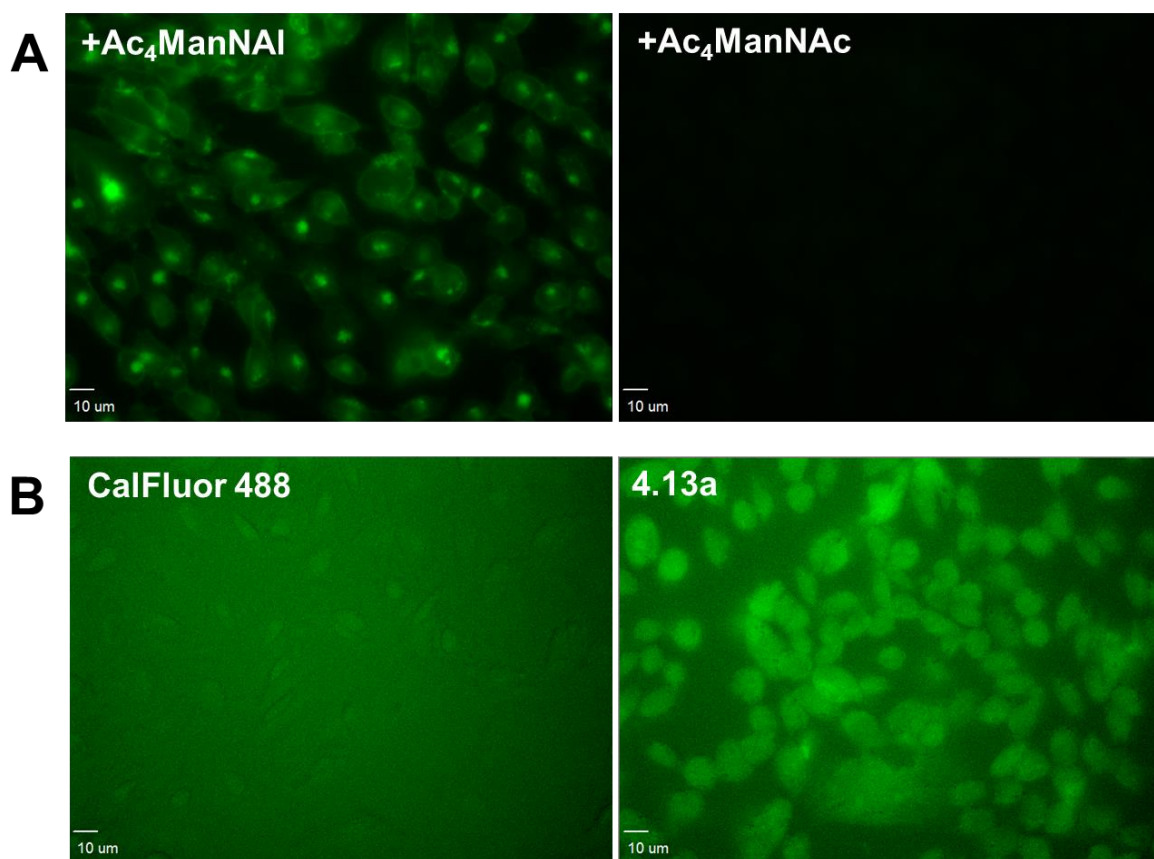


Figure 4-21. No-wash labeling of fixed CHO K1 cells with 10 μ M bis-oligoethylene glycol functionalized azidofluorescein **4.13a**. (A) CHO K1 cells treated with Ac₄ManNAI or Ac₄ManNAc and labeled with 10 μ M **4.13a** under TBTA-catalyzed click conditions. (B) High contrast images of control cells labeled with CalFluor 488 or **4.13a**. Note the slightly higher non-specific background when using **4.13a** when compared to CalFluor 488. Scale bar = 10 μ m.

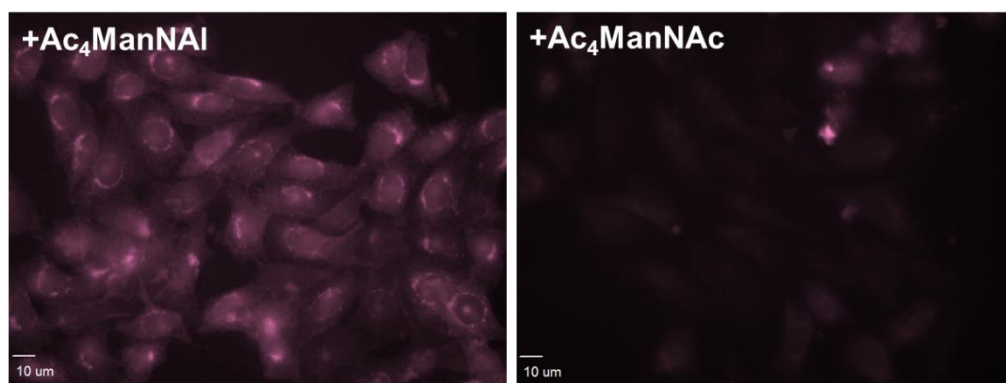


Figure 4-22. No-wash labeling of fixed CHO K1 cells with 10 μ M Si-rhodamine probe **3.15** under TBTA-catalyzed click conditions. Note the higher non-specific background when compared to CalFluor 647. Scale bar = 10 μ m.

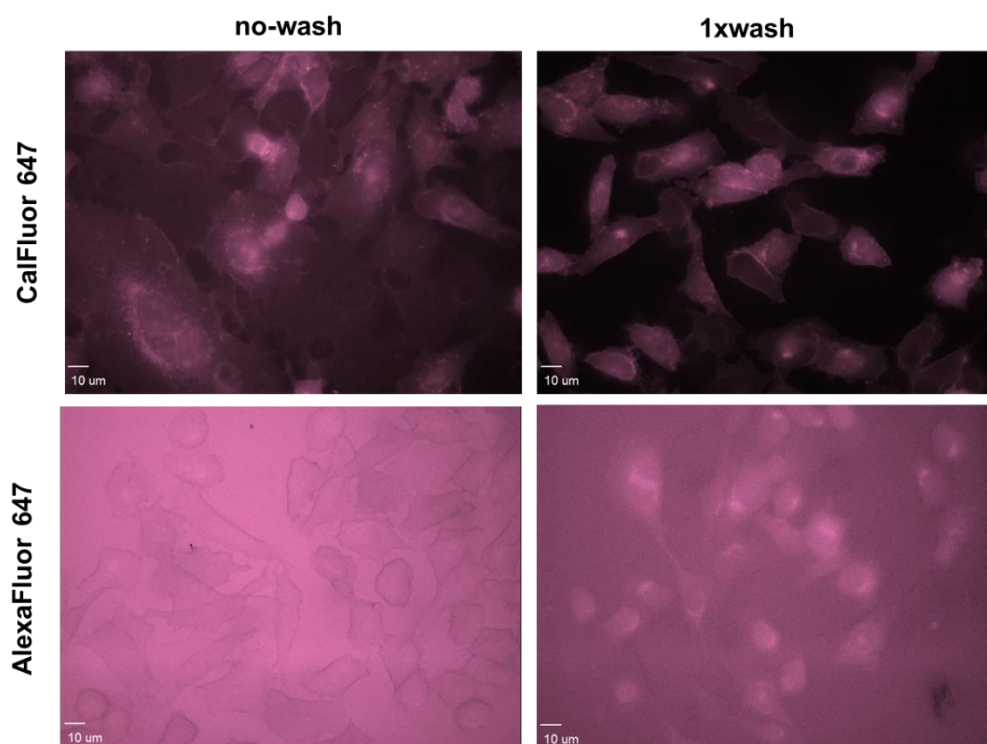


Figure 4-23. Labeling fixed CHO K1 cells with 10 μ M CalFluor 647 or AlexaFluor 647 alkyl azide. Cells were imaged directly without washing or after a single wash step. Exposure time was 500 ms for CalFluor 647 and 30 ms for AlexaFluor 647 alkyl azide. Scale bar = 10 μ m.

I next tested my probes for visualization of glycans *in vivo*. Zebrafish have been powerful model system for the study of development using optical methods due to their optical transparency. Our lab has had a longstanding interest in imaging glycans during zebrafish development.¹⁷⁻²¹ To test the utility of CalFluors in this system for such applications, we injected zebrafish embryos at the single-cell stage with SiaNAI.^{14,20} After either 24 or 36 hours post fertilization (hpf), the embryos

were bathed in a solution containing a CalFluor probe along with copper catalyst. We observed bright alkyne-dependent fluorescence on cells of the enveloping layer without washing (Figure 4-24). Fluorescence signal increased over time and maximized after 20 minutes. Importantly, in similar labeling experiments performed with the always fluorescent AlexaFluor 594 alkyl azide probe or the blue-emitting 3-azido-7-hydroxycoumarin (Figure 4-24B), high levels of background fluorescence from unreacted probe or endogenous biomolecules, respectively, obscured alkyne-dependent labeling. These results clearly demonstrate the potential advantages of developing a longer-wavelength fluorogenic azide probe for *in vivo* applications. An extremely compelling application of these fluorophores would be for systemic imaging of biomolecules. I found that the rate of biocompatible copper-catalyzed click reactions decreased dramatically in the presence of serum proteins, likely due to sequestration of copper catalyst. This complication, as well as copper toxicity, may limit the immediate application of these fluorophores for systemic imaging of linear alkynes.

Beyond glycans, the small size of linear alkynes has enabled its incorporation into a wide variety of intracellular biomolecules. For example, linear alkynes have been used to label newly synthesized DNA and RNA via 5-ethynyl deoxyuridine (EdU) and 5-ethynyl uridine (EU), respectively. In particular, this click-chemistry based approach to visualizing newly synthesized DNA/RNA remains superior to related methods such as BrdU labeling as a harsh denaturation step is not necessary.²²⁻²⁵ Additionally, linear alkynes can be incorporated into newly synthesized proteins by the incorporation of homopropargylglycine (HPG) in methionine-starved cells.²⁶⁻²⁹

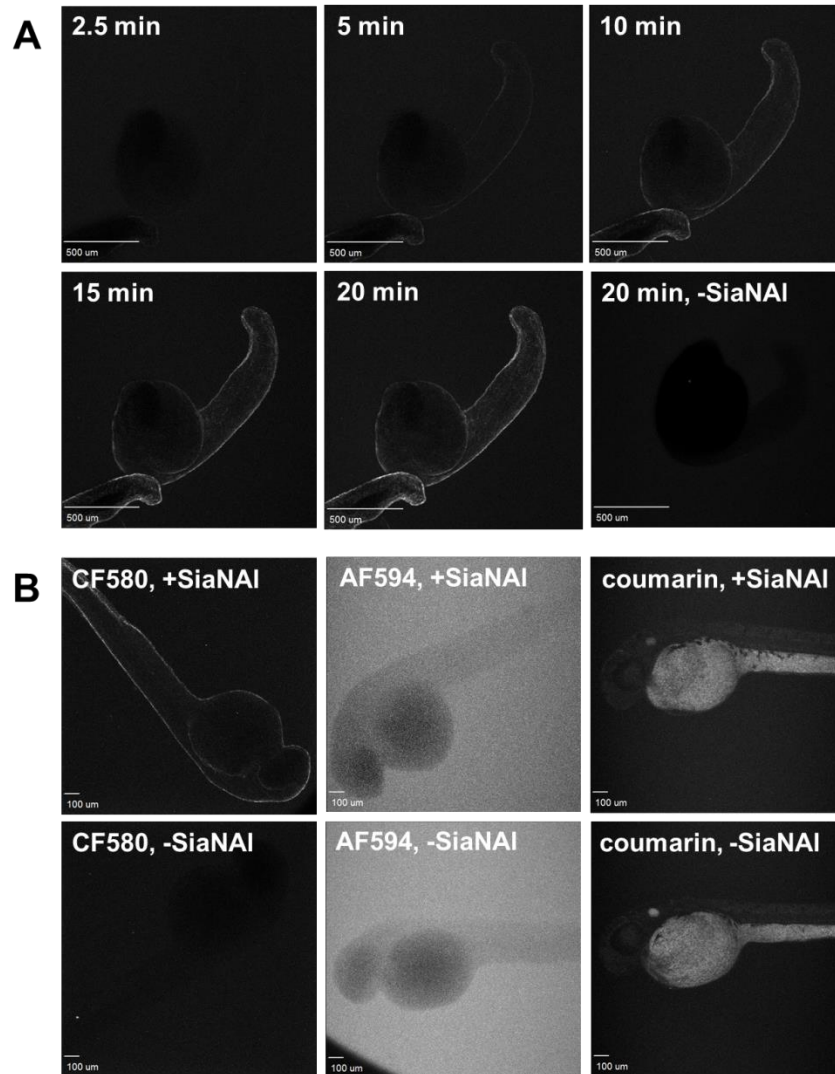


Figure 4-24. Visualizing sialic acids on live developing zebrafish with CalFluors. Zebrafish were injected with 50 pmol SiaNAI at the one to four-cell stage and allowed to develop over time. (A) Real-time labeling of sialic acids. After 24 hpf, zebrafish were incubated in a solution containing 1 μ M CalFluor 580 and copper catalyst. Alkyne-dependent labeling was observable after 5 minutes, and appeared to saturate at 20 minutes. Scale bar = 500 μ m. (B) Comparing no-wash labeling performance by azide probes. After 36 hpf, the embryos were transferred to a solution containing the fluorophore (1 μ M for CalFluor 580 and AlexaFluor 594 alkyl azide, or 5 μ M for 3-azido-7-hydroxycoumarin) and copper catalyst and imaged without washing after 20 minutes. Only zebrafish labeled with CalFluor 580 show alkyne-dependent fluorescence signal. Scale bar = 100 μ m.

I first tested the suitability of my probes for imaging EdU-labeled DNA. I treated HEK 293T cells with 10 μ M EdU for 12 h, fixed and permeabilized the cells, then labeled them with my azide probes under copper-click conditions. I hoped that the use of fluorogenic azide probes for EdU detection would streamline the visualization of newly synthesized DNA. Gratifyingly, I saw

robust labeling using all four of my probes without the need to wash away excess reagent (Figures 4-25A, 4-25B). Results were significantly better than those achieved using other azide fluorophores under similar labeling conditions. (Figures 4-25B, 4-26, and 4-27). I noticed that the fluorescein-based probes (CalFluors 488 and 580) labeled intracellular DNA more weakly than the related rhodamine-based probes (CalFluors 555 and 647, Figures 4-25B). Similar results were achieved when I labeled newly synthesized RNA by treatment of cells with 1 mM EU (Figures 4-28 – 4-30). This difference may be due to the pH sensitivity of my fluorescein-based dyes, especially when conjugated to the anionic oligonucleotides (Figures 4-31, 4-32).³⁰ To avoid such complications, an important future direction is to utilize rhodamine-based azide probes to span the visible spectrum. For example, rhodamine 110 has excitation and emission wavelengths comparable to fluorescein, but is significantly more photostable and pH insensitive. Additionally, the lack of electron-donating methyl groups in rhodamine 110, as compared to tetramethylrhodamine, may enable more efficient quenching via PeT and higher fluorescence enhancement upon click reaction. Preliminary work towards a rhodamine 110 molecule, however, has been hampered by difficulties in selectively converting the aryl amine to an azide while leaving the xanthene untouched. Texas Red derivatives have emission in a red to far-red region and are worthwhile targets as well.

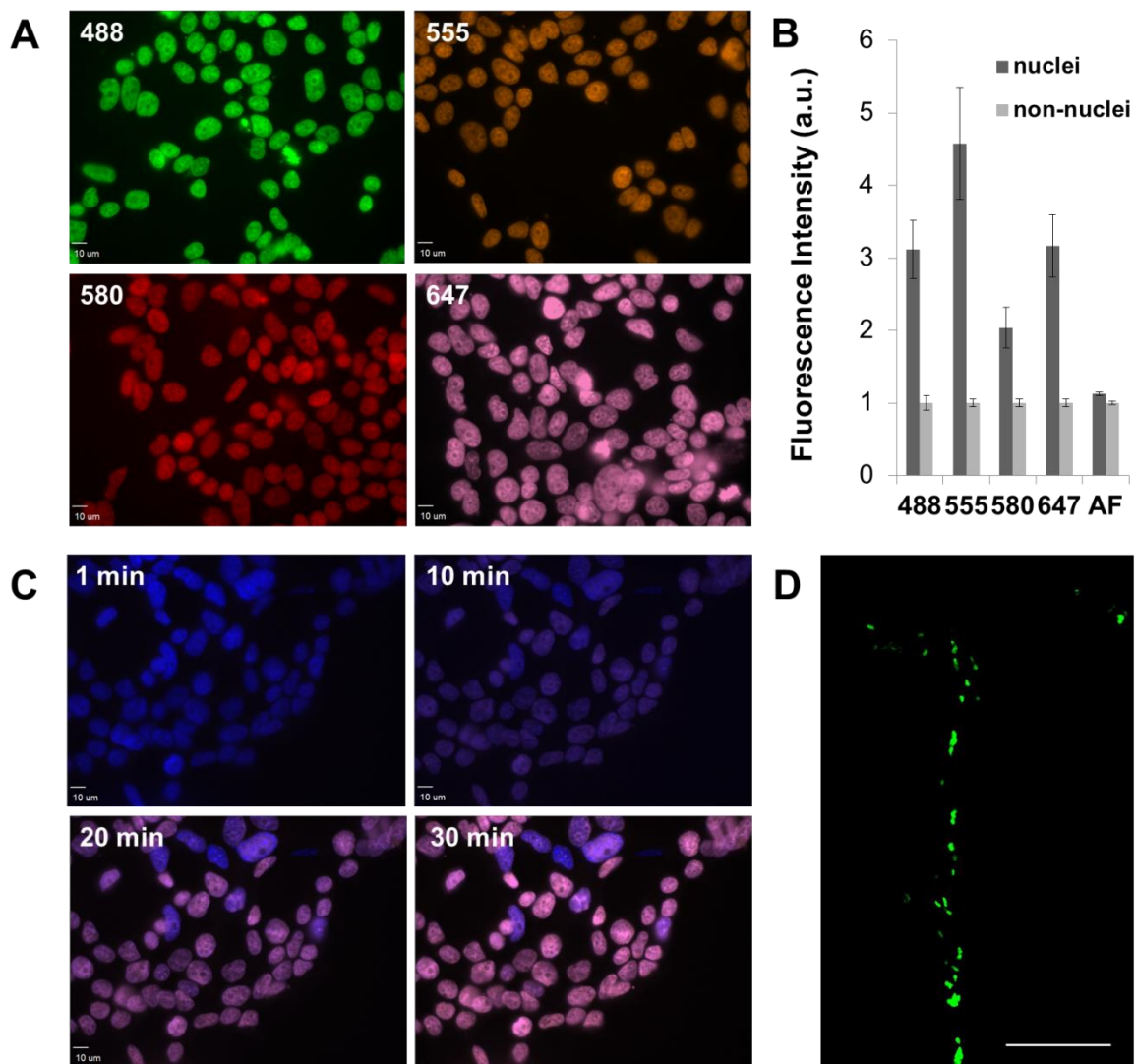


Figure 4-25. Visualizing EdU-labeled DNA in fixed and permeabilized samples using fluorogenic azide probes. (A) No-wash labeling of EdU-labeled HEK 293T cells. Cells were treated with EdU for 16 h, fixed and permeabilized, then treated with 10 μ M CalFluor probe, 1 mM CuSO_4 , 100 μ M TBTA ligand, 2 mM sodium ascorbate, and 0.1 mg/mL BSA and imaged without further wash steps after 1 hour. Scale bar = 10 μ m. (B) Quantification of normalized signal over background for the four panels in (A), and comparison to labeling under identical conditions using the always fluorescent AlexaFluor 647 alkyl azide (AF). (C) Two-color labeling using Hoescht 33342 and CalFluor 555. After staining with Hoescht, the cells were incubated with a solution of 1 μ M CalFluor probe and copper catalyst and imaged in real-time. Scale bar = 10 μ m. (D) Visualization of EdU-labeled newly proliferating cells in mouse brain slices with CalFluor 647. Scale bar = 100 μ m.

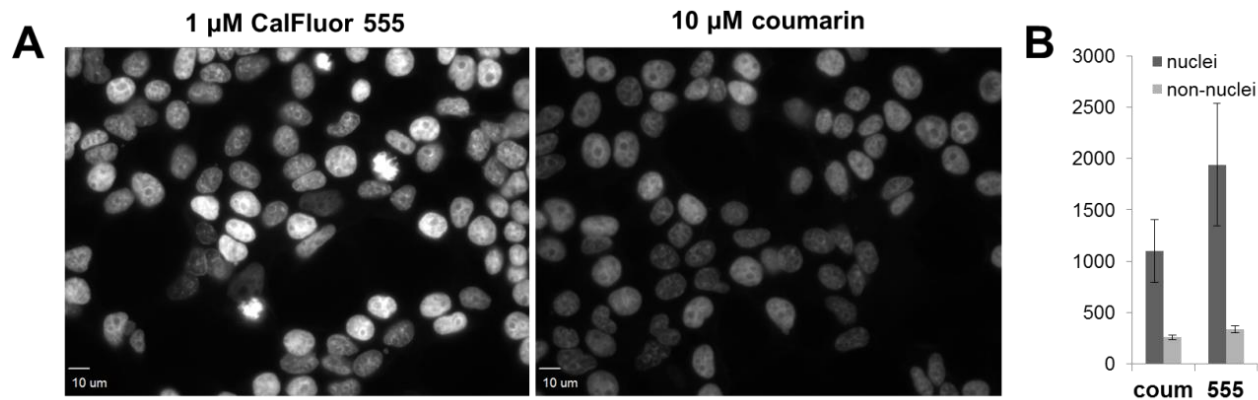


Figure 4-26. Comparing no-wash labeling of newly synthesized DNA by 1 μ M CalFluor 555 and 10 μ M 3-azido-7-hydroxycoumarin in HEK 293T cells. Exposure times were 1000 ms for both probes. (A) DNA labeling of the two probes. (B) Quantification of labeling intensity between the two probes. Scale bar = 10 μ m.

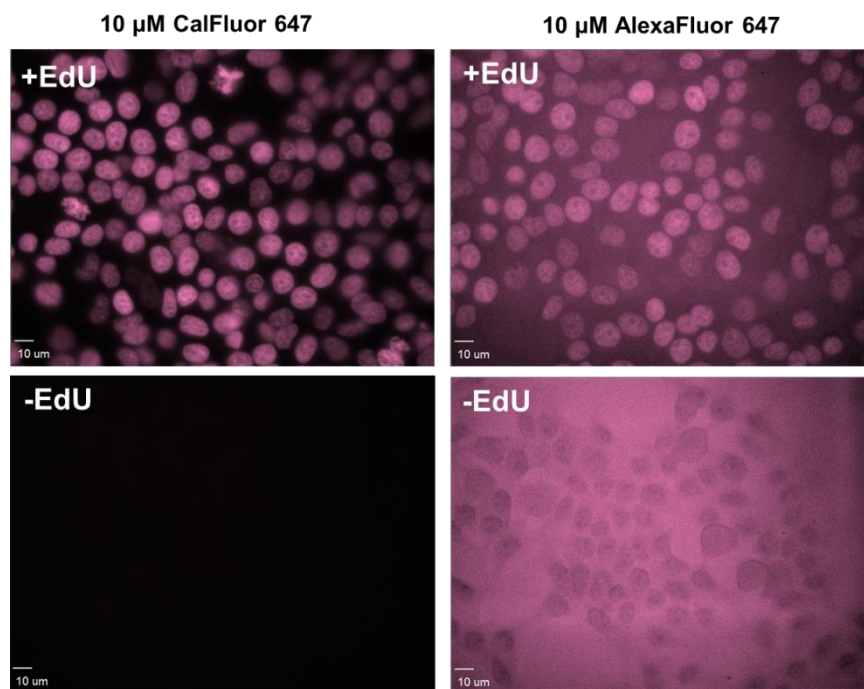


Figure 4-27. Comparison of no-wash EdU labeling using 10 μ M CalFluor 647 or AlexaFluor 647 alkyl azide in HEK 293T cells. After allowing the click reaction to proceed for one hour, the cells were imaged without washing. Scale bar = 10 μ m. Exposure times were 500 ms for CalFluor 647 and 10 ms for AlexaFluor 647 alkyl azide.

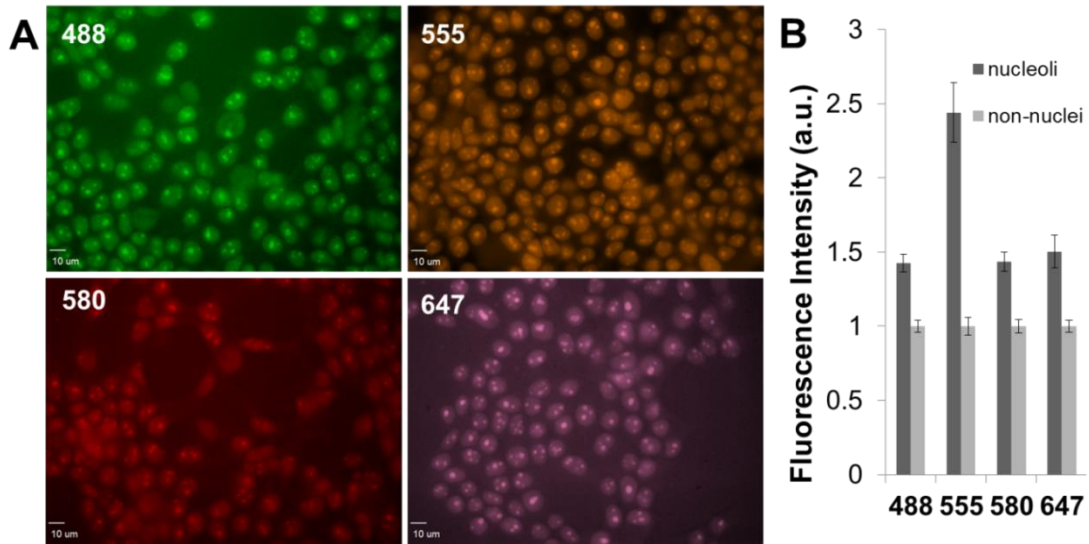


Figure 4-28. No-wash labeling newly of synthesized RNA using 5-ethynyluridine and 5 μ M CalFluors (A) RNA labeling with CalFluor probes (B) Quantification of labeling intensity by all four probes. Scale bar = 10 μ m.

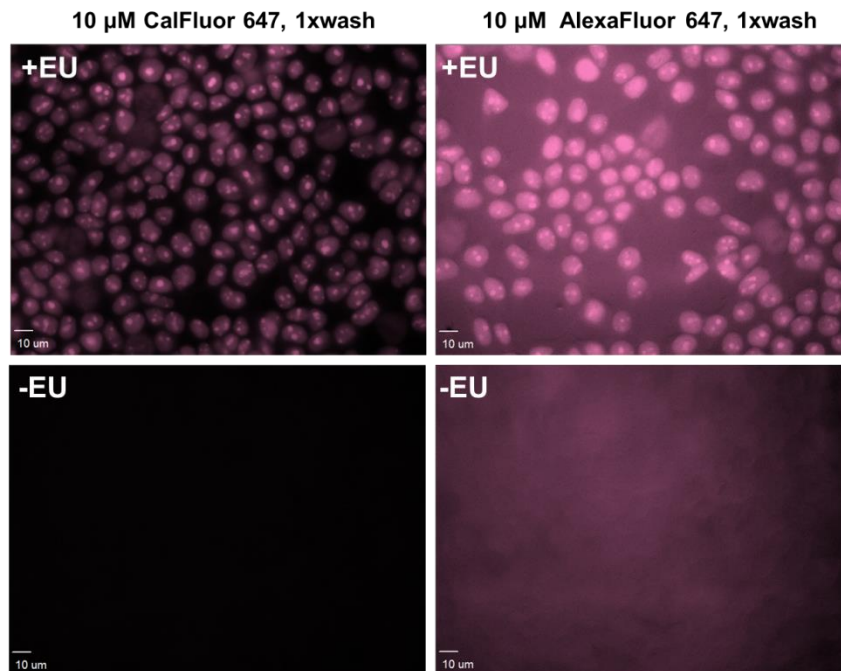


Figure 4-29. Labeling newly synthesized RNA using EU. HEK 293T cells were imaged after a single wash step involving removing the reaction mixture and replacing the mixture with fresh PBS. Scale bar = 10 μ m.

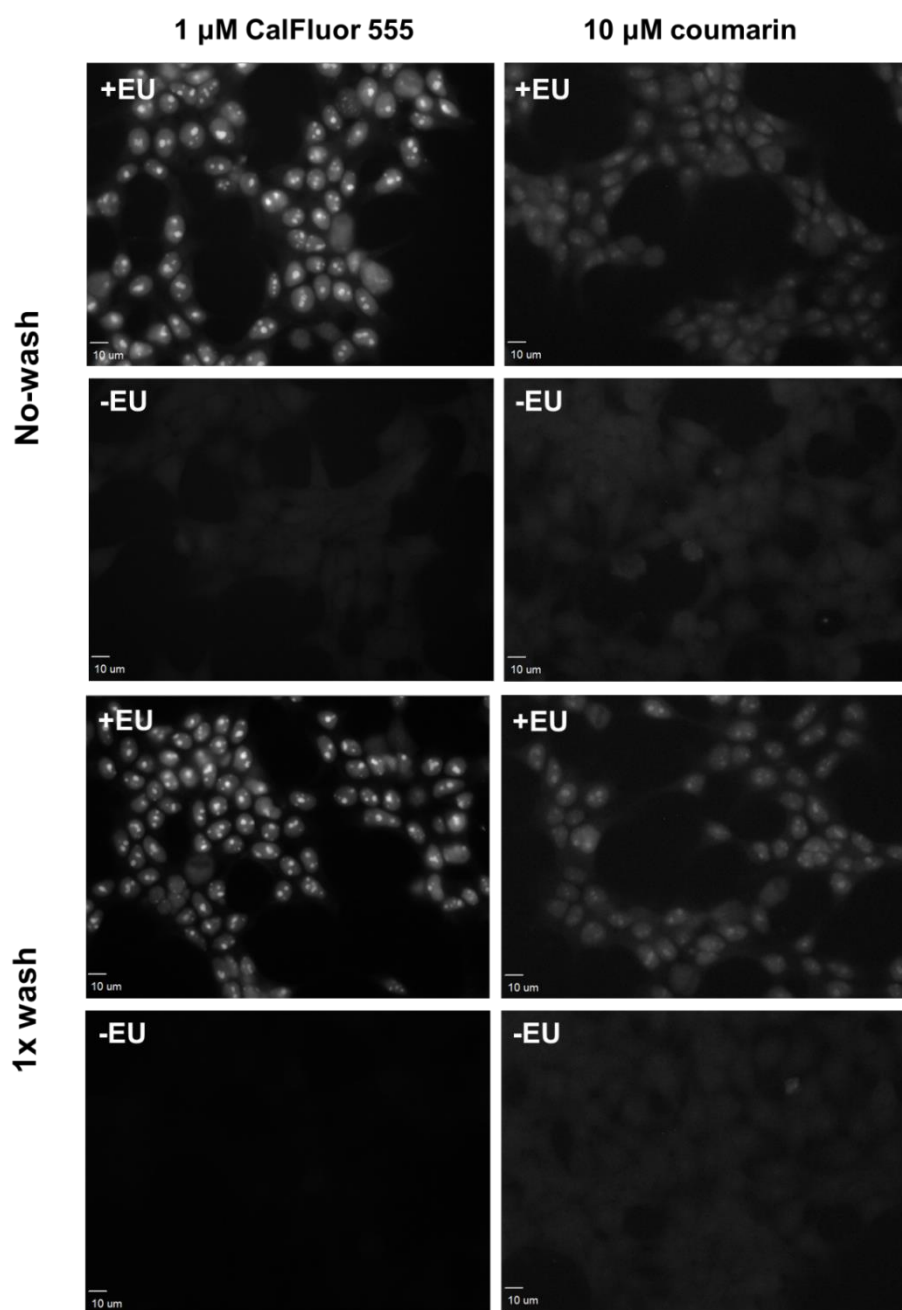


Figure 4-30. Comparing EU labeling in HEK 293T cells between 1 μM CalFluor 555 and 10 μM 3-azido-7-hydroxycoumarin under TBTA-catalyzed click conditions. 10 μM of coumarin probe and 1 μM of CalFluor 555 were used. Exposure times were 1000 ms for both probes. Scale bar = 10 μm .

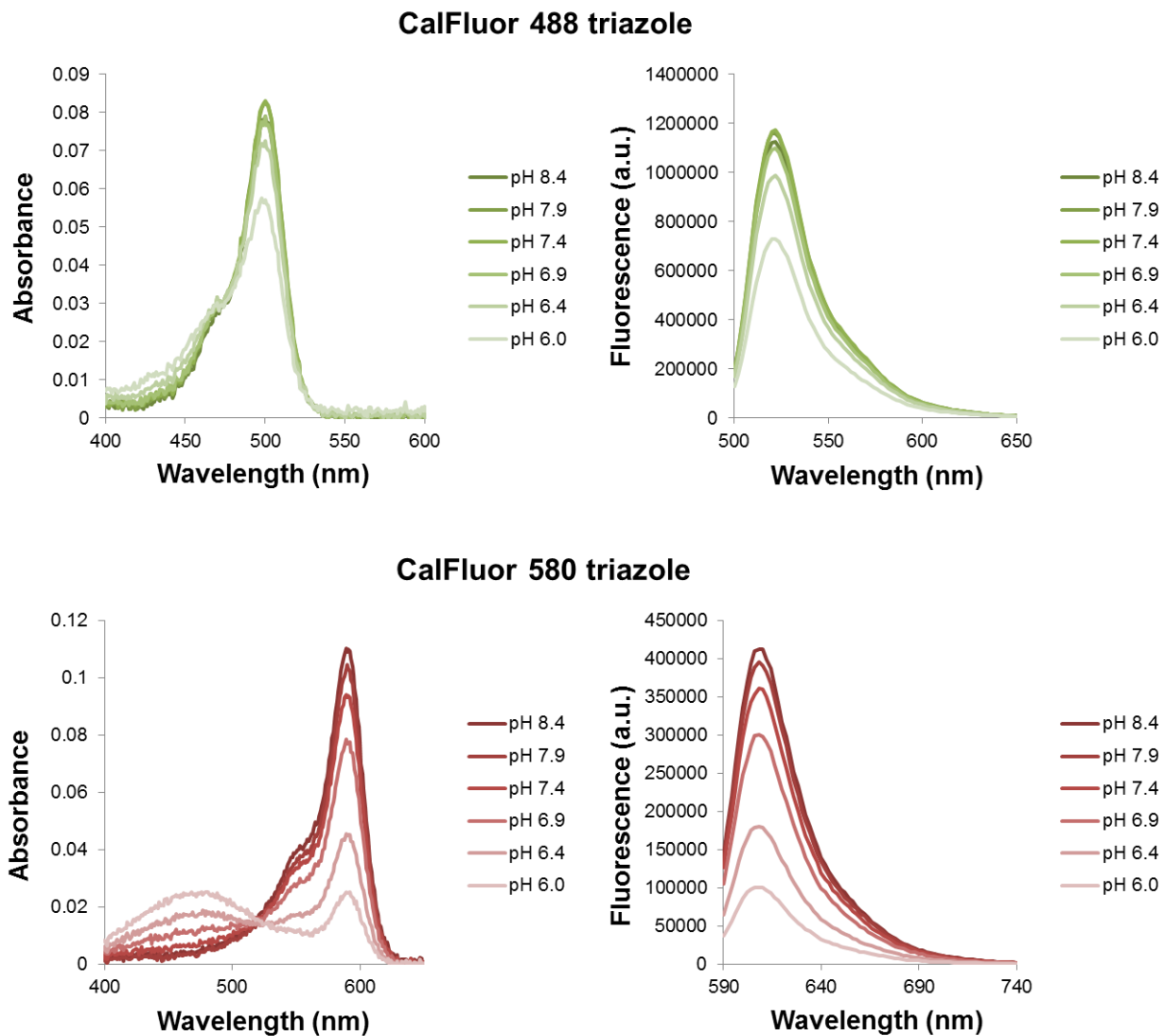


Figure 4-31. pH sensitivity of the fluorescein-based CalFluor 488 and CalFluor 580-derived triazole products. The absorption and emission spectra of 1 μM of either CalFluor 488 triazole or CalFluor 580 triazole at various pHs were determined. The dramatic change in absorbance of the Si-fluorescein derived CalFluor 580 is attributed to protonation of the xanthene and disruption of hyperconjugative interactions with the Si-C σ^* orbitals, as described in Ref. 2.

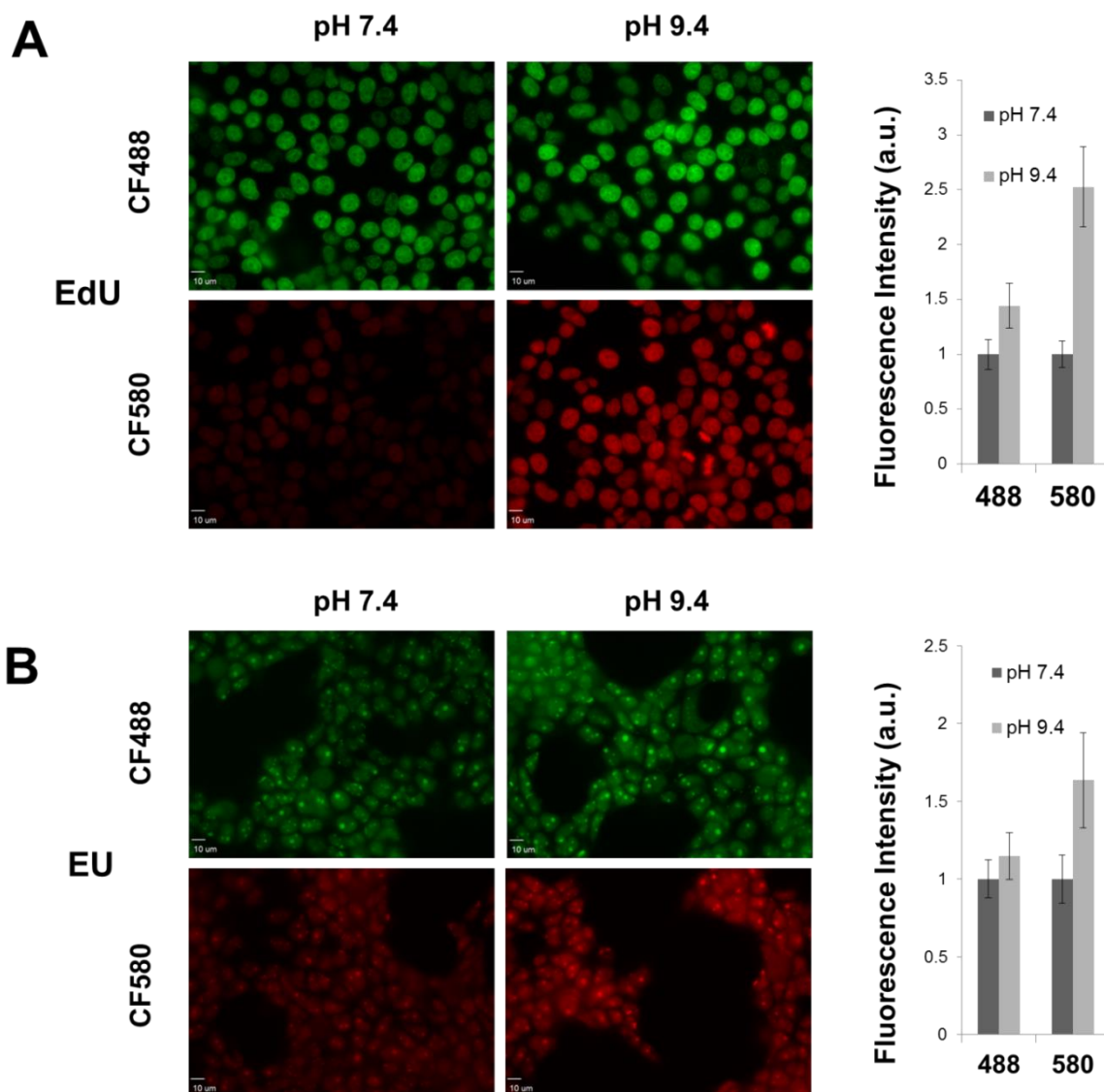


Figure 4-32. pH sensitivity of CalFluor 488 and CalFluor 580-oligonucleotide conjugates in fixed and permeabilized cells. EdU or EU-treated HEK 293T cells were fixed and permeabilized as described above, and labeled with 10 μ M CalFluor 488 or CalFluor 580 under TBTA-catalyzed click conditions. After washing three times with pH 7.4 PBS, the cells were covered with pH 7.4 PBS and imaged. The same set of cells were then covered with pH 9.4 PBS and imaged again. Exposure times were 200 ms for all images acquired. (A) pH-dependent fluorescence of CalFluor 488 and 580 clicked onto EdU in newly synthesized DNA. (B) The same experiment performed with EU for newly synthesized RNA.

Importantly, my palette of probes enabled two-color imaging with other well established probes, such as with cells pre-labeled with the blue-emitting Hoescht 33342 nuclear stain (Figure 4-25C). No-wash labeling was also suitable for CHO K1 cells labeled with EdU and EU under identical conditions, although specific signal was lower for all probes tested, likely due to poorer alkyne incorporation (Figures 4-33 – 4-35). Beyond imaging mammalian cells in culture, EdU

has also been used to label newly synthesized DNA in bacteria.³¹ *E. coli* were grown in the presence of EdU, fixed, permeabilized, and labeled with CalFluor 647; robust alkyne-dependent labeling was observed by flow cytometry, and significantly higher signal over background was achieved compared to AlexaFluor 647 alkyl azide (Figure 4-36). The ability to image perform sensitive EdU labeling may open the door to future studies tracking the role of mycobacterial DNA in the context of infection.³²

One of the more exciting applications of EdU labeling is to visualize actively proliferating cells *in vivo*. Tissue slices were obtained from the subventricular zone of mice injected with 150 mg/kg EdU two hours before perfusion. Gratifyingly, CalFluor 647 were able to efficiently visualize EdU from these tissue sections with excellent signal over background (Figure 4-25D). Finally, all four CalFluor probes were suitable for the robust detection of newly synthesized proteins containing homopropargylglycine (HPG, Figure 4-37). These experiments show that this series of fluorophores are extremely well suited for imaging metabolites beyond glycans.

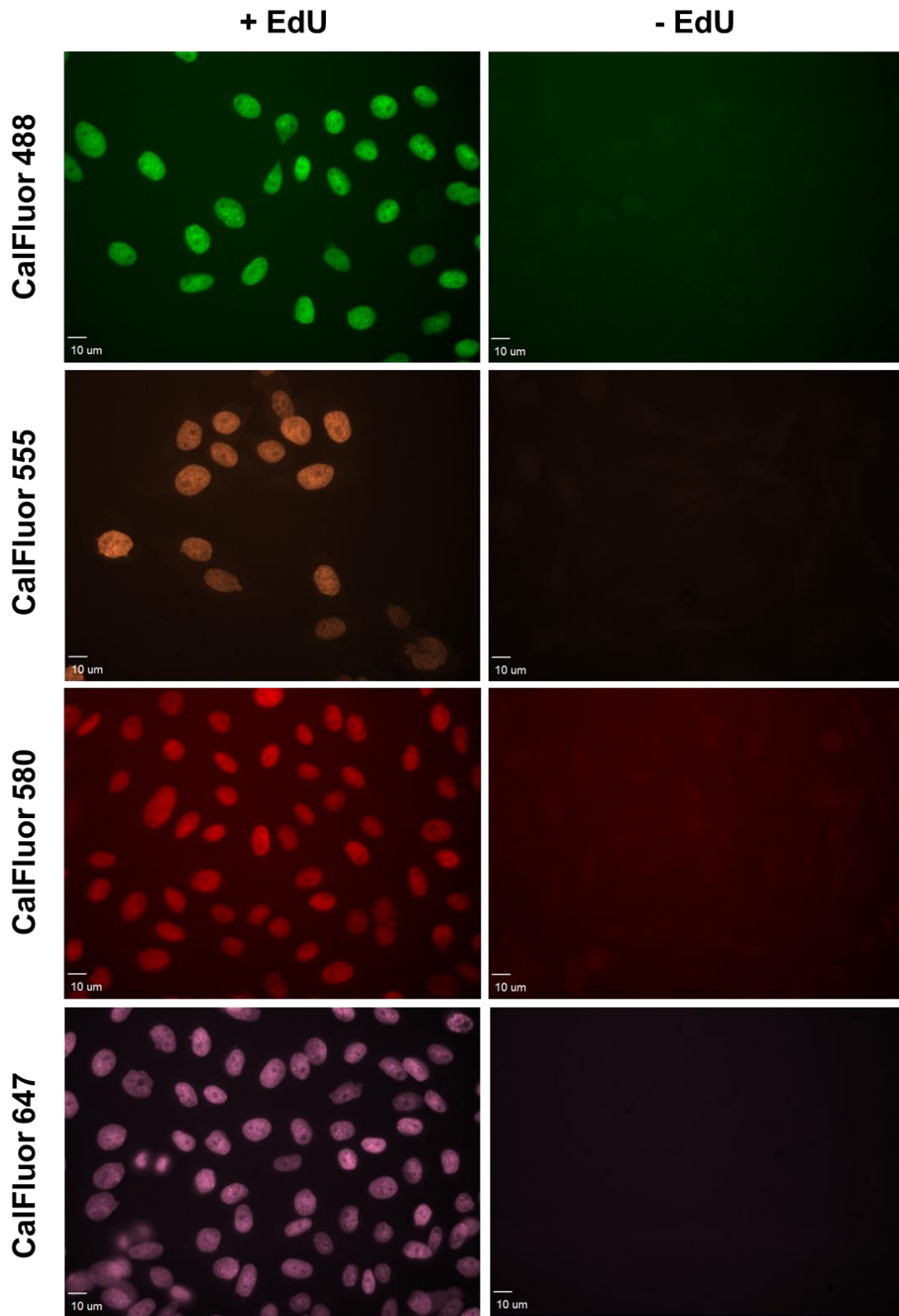


Figure 4-33. No-wash labeling of EdU in fixed and permeabilized CHO K1 cells with CalFluors. Scale bar = 10 μ m.

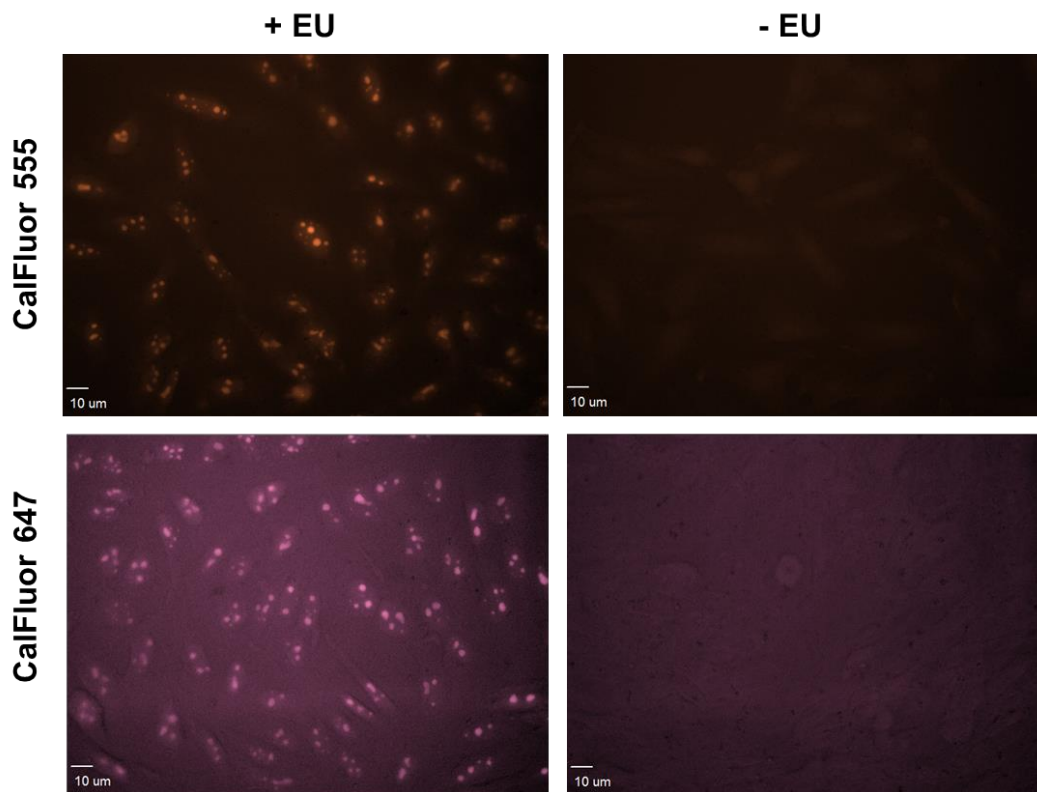


Figure 4-34. No-wash labeling of EU in fixed and permeabilized CHO K1 cells with 5 μ M CalFluors. Insufficient signal over background was observed when using the fluorescein-based probes. Scale bar = 10 μ m.

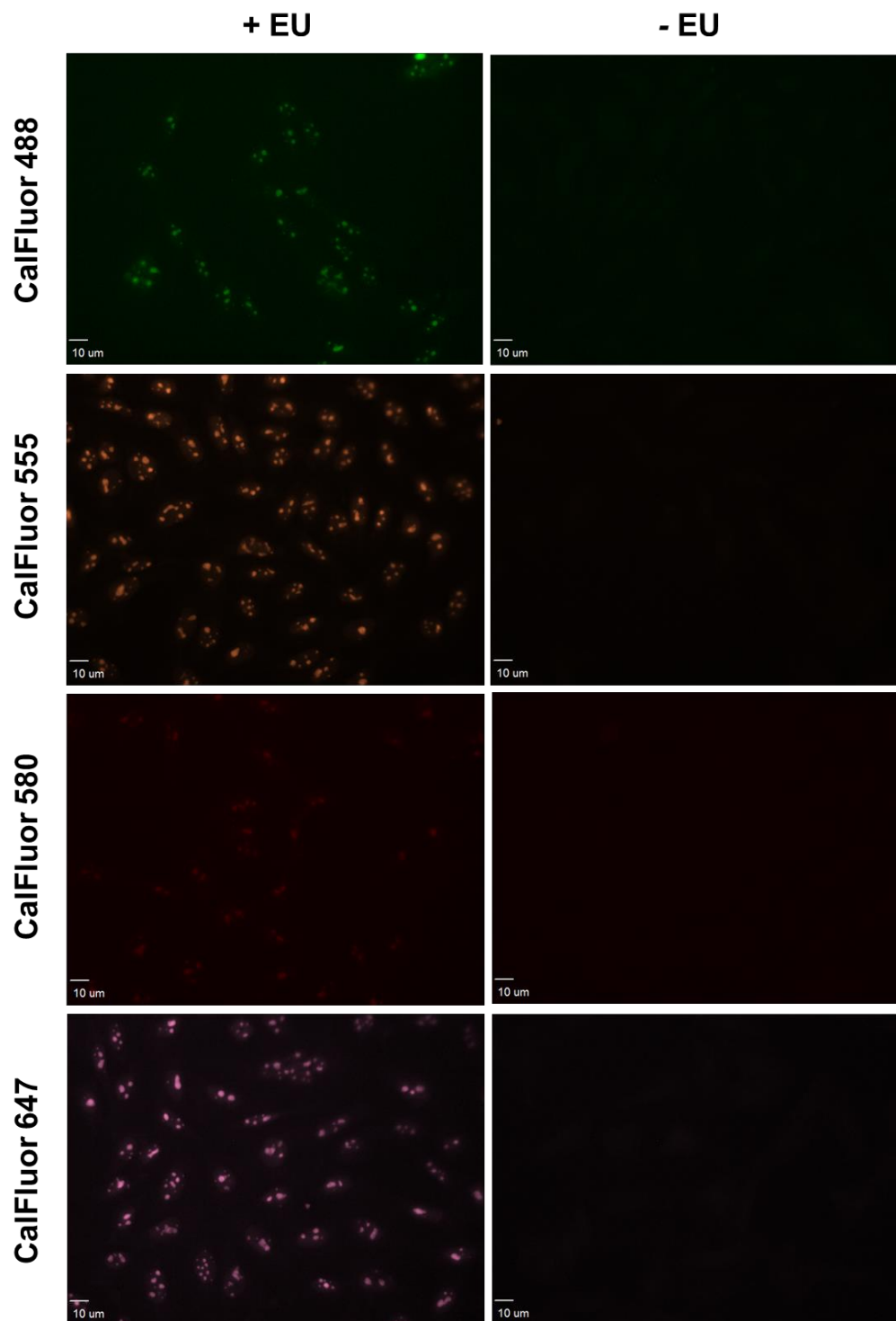


Figure 4-35. Labeling of EU in fixed and permeabilized CHO K1 cells with 5 μ M CalFluors. A single wash step was performed after click reaction. Scale bar = 10 μ m.

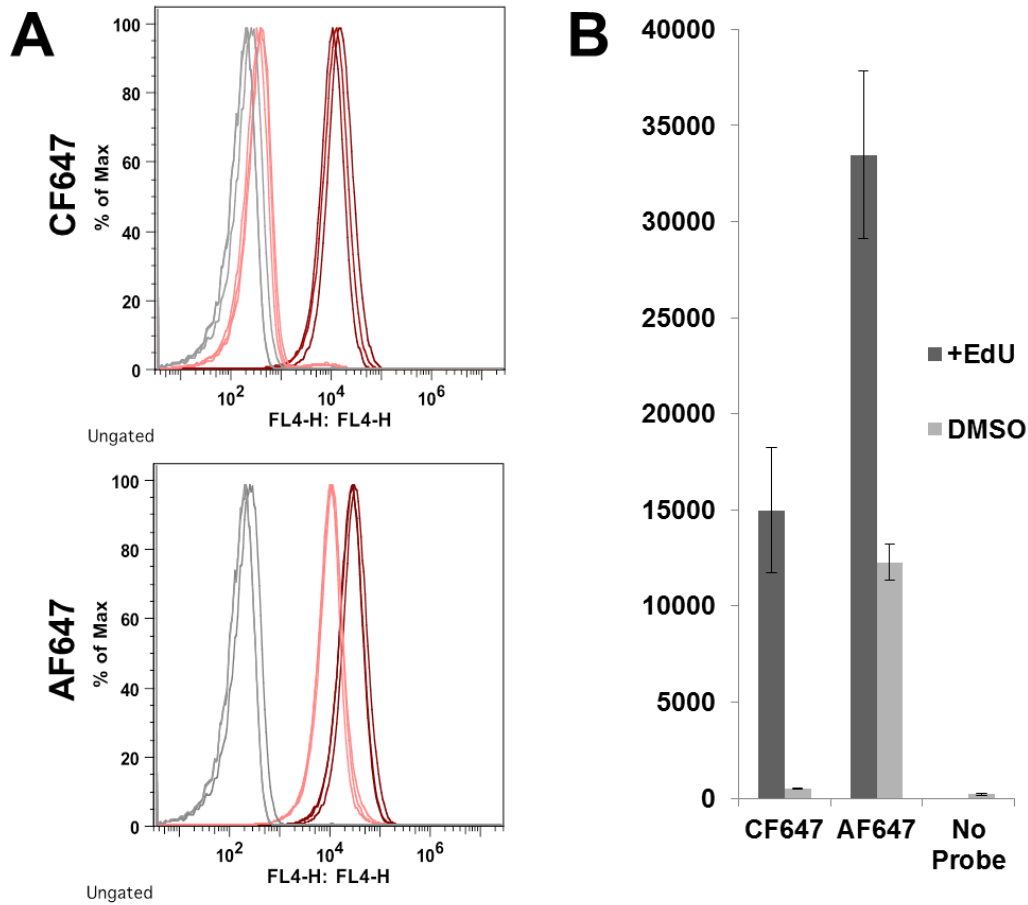


Figure 4-36. Labeling EdU-containing DNA in fixed and permeabilized *E. coli*. Cells were grown in the presence of 12 μ M EdU for 1.5 h and labeled with 10 μ M CalFluor 647 or AlexaFluor 647 alkyl azide. (A) Raw flow cytometry data of bacteria labeled with CalFluor 647 or AlexaFluor 647 alkyl azide. Grey traces are from cells not treated with fluorophore, pink traces are from DMSO-incubated cells treated with fluorophore, and red traces are from EdU-incubated cells treated with fluorophore. (B) Quantification of the data in (A).

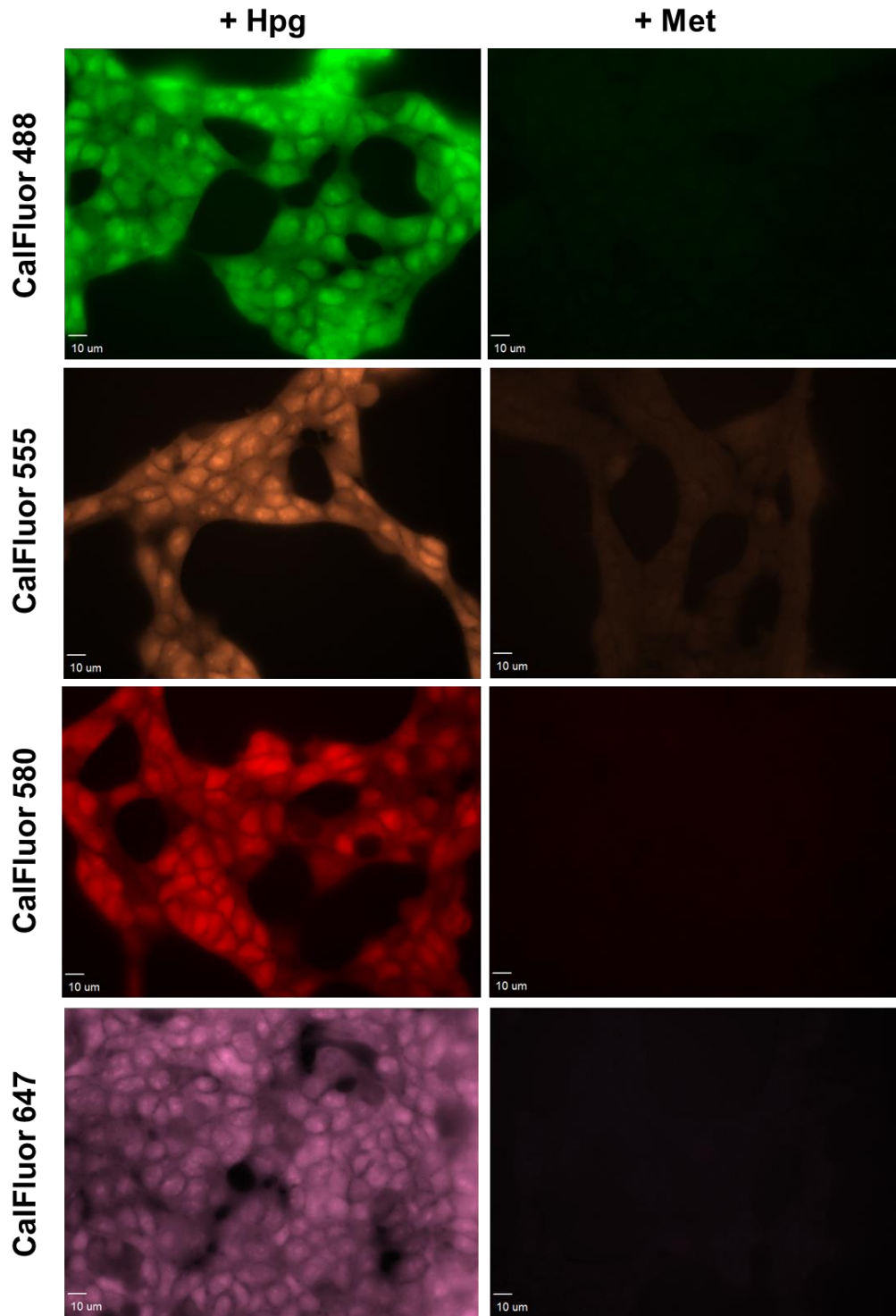


Figure 4-37. No-wash labeling newly synthesized proteins in fixed and permeabilized in HEK 293T cells with 10 μ M CalFluors. Cells were treated with 1 mM Hpg or Met for 90 minutes. Scale bar = 10 μ m.

Conclusion

In this chapter, I report the realization of general platform to generate fluorogenic azide probes across the visible spectrum. My experiments clearly demonstrate the broad applicability of these optimized probes for labeling a large panel of alkyne-functionalized biomolecules in both live and fixed cells, in tissue and *in vivo*. Given the generality of PeT, I anticipate that this bis-zwitterionic dialkoxy aryl azide motif will switch fluorescence in a wide variety of fluorophores beyond the xanthenes. For example, other fluorophore scaffolds, such as BODIPY, cyanines, and pyrazolines, can all be efficiently switched via PeT.³³⁻³⁵

Consistent with this prediction, a recent report from Wong and coworkers demonstrated that the BODIPY scaffold can also be used as a platform for PeT-based fluorogenic azide probes.³⁶ Beyond developing probes with higher photostability, using my optimized aryl ring in conjunction with cyanine probes or modified Si-rhodamine probes may push emission maxima into the near-infrared.³⁷ PeT has also been used to modulate other properties besides fluorescence, such as the rate of singlet oxygen generation or luminescence from metal complexes.^{38,39} This transportable design element is reminiscent of the 1,2-diaminobenzene-based trigger for nitric oxide sensing that has been integrated into myriad dye scaffolds.⁴⁰⁻⁴³ In addition, the incorporation of zwitterionic sulfobetaine tails, which significantly outperformed both oligoethylene glycol or sulfated modifications in my hands, may be a general strategy for increasing the performance of PeT-based probes in complex environments.⁴⁴ These modifications prevent probe access to the interior of living cells, but the cytotoxicity of copper catalysts likewise limits reactions with linear alkyne-functionalized biomolecules to fixed samples or the live cell surface. Future work to overcome these shortcomings may benefit from the modularity of my synthetic route towards a wide variety of fluorogenic azide probes. Beyond the applications described here, CalFluor probes may find use in visualizing linear alkyne-tagged biomolecules in large tissue samples, where reagents are difficult to wash out.⁴⁵

Ultimately, the work described in this chapter completes the panel of fluorogenic azide probes with emission maxima across the visible spectrum. With recent advances in increasing the efficiency of Cu-catalyzed click reactions, these technologies will further enhance the ease and sensitivity of detecting linear alkyne-functionalized biomolecules in biological systems.⁴⁶⁻⁴⁸

Experimental Procedures

DFT calculations

Calculations were performed using Gaussian. 09 software package using the B3LYP/6-31G(d) level of theory. Structures were first minimized in energy. Next, dihedral scans about the aryl-azide or aryl-triazole bond were performed in 12° increments. For each fixed dihedral angle, structures were minimized in energy and the E_{HOMO} calculated. Calculations were performed at the UC Berkeley College of Chemistry Molecular Graphics and Computation Facility.

Cyclic voltammetry

Experiments were performed on a BASi Epsilon potentiostat. Solutions of the aromatic azides or triazoles were dissolved in acetonitrile containing 0.1 M NBu_4PF_6 as an electrolyte. Argon was bubbled through the solution for 10 minutes before acquiring any measurements. Measurements were made using platinum and glassy carbon electrodes, with a silver reference electrode. A small amount of ferrocene was added as a standard. A scan rate of 100 mV/s was used for all measurements.

Measuring fluorescence quantum yields

Fluorescence quantum yields were measured by creating 2 mM stocks of dyes in MeOH. The dyes were then diluted to 20 μM in PBS, then further diluted in PBS to various final concentrations. The absorbance and emission spectra of five different concentrations of dye were measured while keeping maximum absorbance under 0.2. For Si-rhodamine based probes, solutions of probe were excited at 600 nm, and emission was integrated from 600 to 800 nm. Plotting integrated emission vs. absorbance at 600 nm yielded a line, whose slope corresponds to the fluorescence quantum yield. Absolute quantum yields were determined by comparison with the slope of the line measured for cresyl violet in MeOH ($\Phi_{\text{fl}} = 0.54$). A similar strategy was used for fluorescein ($\lambda_{\text{ex}} = 500 \text{ nm}$, $\lambda_{\text{em}} = 500 - 700 \text{ nm}$), rhodamine ($\lambda_{\text{ex}} = 550 \text{ nm}$, $\lambda_{\text{em}} = 550 - 700 \text{ nm}$), and Si-fluorescein ($\lambda_{\text{ex}} = 550 \text{ nm}$, $\lambda_{\text{em}} = 550 - 700 \text{ nm}$) based probes. Fluorescein in 0.1M NaOH ($\Phi_{\text{fl}} = 0.85$, fluorescein-based probes) and rhodamine B in EtOH ($\Phi_{\text{fl}} = 0.95$, for rhodamine and Si-fluorescein-based probes) were used as standards. The reported quantum yields are the average of three sets of measurements. Absorbance spectra were recorded on a Varian Cary 50 UV-Visible spectrophotometer. Fluorescence spectra were recorded on a Photon Technology International Quanta Master 4 L-format scanning spectrofluorometer equipped with an LPS-220B 75-W xenon lamp and power supply, A-1010B lamp housing with an integrated igniter, switchable 814 photon counting/analog photomultiplier detection unit, and MD5020 motor driver. Measurements were made in 1 cm x 0.4 cm quartz cuvettes with a total sample volume of 1 mL.

Monitoring fluorescence during copper-catalyzed click reactions

To a 1 cm x 0.4 cm quartz cuvette was added 944 μL PBS. Next, 2 μL 50 mM BTAA in PBS and 1 μL 50 mM CuSO_4 in H_2O were added and the solution mixed with a glass pipette. Next, 50 μL freshly prepared 100 mM sodium ascorbate in PBS was added and the solution mixed again. Then, 2 μL of a 1 mM stock of azide fluorophore (in 4:1 $\text{H}_2\text{O}/\text{MeCN}$ for CalFluors and MeOH

for all other fluorophores) was added and the solution mixed. The emission spectra were recorded at this time ($t = 0$ s). Finally, 1 μL 100 mM alkyne **4.25** in DMSO was added and the solution vigorously mixed and monitored every 30 s for 10 min. Final concentrations for all reagents are 2 μM azido probe, 100 μM alkyne, 100 μM BTAA, 50 μM CuSO_4 , and 5 mM sodium ascorbate with a total volume of 1 mL. Fluorescence spectra were recorded on a Photon Technology International Quanta Master 4 L-format scanning spectrofluorometer equipped with an LPS-220B 75-W xenon lamp and power supply, A-1010B lamp housing with an integrated igniter, switchable 814 photon counting/analog photomultiplier detection unit, and MD5020 motor driver.

Measuring fluorescence in the presence of various additives

1 μL of a 1 mM stock of fluorophore was placed into 1 mL of PBS solution containing various additives or 1 mL of alternative solvent, and fluorescence spectra were measured.

Measuring absorbance and fluorescence at various pHs

pH 7.4 PBS was adjusted to various pHs with the addition of NaOH or HCl. 1 μL of a 1 mM stock of fluorophore was placed into these solutions, and the absorption and fluorescence spectra were measured.

Epifluorescence microscopy of cultured cells

For mammalian cells, microscopy was performed using a Zeiss AxioVert 200M inverted microscope using a Plan-Neofluar 40x/0.75 objective. A 175W xenon lamp housed in a Sutter DG4 illuminator linked to the microscope by an optical fiber assured shuttering and illumination. Images were acquired using the Cy5 filter for labeling with Si-rhodamines or AlexaFluor 647 alkyl azide, the Cy3 filter for Si-fluoresceins or rhodamines, the FITC filter for labeling with fluoresceins, and the DAPI filter for labeling with 3-azido-7-hydroxycoumarin. Images were acquired and processed using SlideBook 5.0, and are shown as a single z-plane. Images acquired using the Cy5 filter are false-colored pink, the FITC filter are false-colored green, and the DAPI filter are false-colored blue. For the Cy3 filter, labeling with rhodamine probes were false-colored orange while labeling with Si-fluorescein probes were false-colored red. Greyscale images were used for comparisons between probes of different emission wavelengths.

No-wash labeling of glycoproteins on live mammalian cells

Cells were grown in 8-well Lab-Tek Chambered Coverglass systems in 300 μL media (HAM-F12 for CHO K1 cells, DMEM for HEK 293T cells) containing 10% fetal bovine serum, penicillin/streptomycin, and either 50 μM Ac_4ManNAI or Ac_4ManNAc for 3 d at 37 $^\circ\text{C}$, as described previously.¹⁴ The cells were then washed with 3 x 300 μL PBS, then incubated with 100 μL freshly prepared click solution. Click solution comprised of 50 μM CuSO_4 , 300 μM BTAA, 2.5 mM sodium ascorbate, and 10 μM azide fluorophore. This was prepared by first adding 0.5 μL 50 mM CuSO_4 in H_2O and 3 μL 50 mM BTAA in H_2O to 481.5 μL PBS. Next, 12.5 μL freshly prepared 100 mM sodium ascorbate in PBS was added. Finally, 2.5 μL 1 mM

azido fluorophore in 4:1 H₂O/MeCN was added. After 15 min, the reactions were quenched with the addition of 1 μL of 100 mM bathocuproine disulfonate (BCS) in H₂O (final concentration 1 mM). No changes in fluorescence were observed before or after the addition of BCS. For real-time imaging, images were acquired as the labeling progressed without quenching the reaction.

No-wash fixed mammalian cell labeling

Cells were grown in 8-well Lab-Tek Chambered Coverglass systems in media (HAM-F12 for CHO K1 cells, DMEM for HEK 293T cells) containing 10% fetal bovine serum, penicillin/streptomycin. For labeling cell surface glycoproteins, cells were grown in the presence of 50 μM Ac₄ManNAI or Ac₄ManNAc for 3d. For EdU labeling, cells were grown for 2d, then 0.15 μL of 20 mM EdU in DMSO (final concentration of 10 μM) or DMSO control were added and the cells grown for another 12 h. Alternatively, for EU labeling, cells were grown in the presence of 0.3 μL of 1 M EU in DMSO (final concentration of 1 mM) or DMSO control. Finally, for HPG labeling, before labeling, HEK 293T were incubated in methionine-free DMEM for 30 minutes at 37 °C. The media was replaced with fresh methionine-free DMEM supplemented with either 1 mM HPG or 1 mM methionine control for 1 h. The cells were washed with three 5 minute incubations in regular DMEM at 37 °C before fixation.

The media was removed and the cells were fixed with 200 μL 3% paraformaldehyde in PBS at room temperature for 10 minutes. The paraformaldehyde was removed and the cells were washed with 300 μL PBS. The cells were then permeabilized with 200 μL 0.5% Triton-X for 20 minutes. The Triton-X was removed and the cells were washed twice with 300 μL PBS, then covered with 200 μL click solution. For labeling cell surface glycoproteins, this permeabilization step was omitted. The click solution comprised of 100 μM TBTA, 1 mM CuSO₄, 2 mM sodium ascorbate, and various concentrations of azide probe. 0.1 mg/mL BSA was found to be an important additive to prevent precipitation of the TBTA ligand over the course of the labeling experiment. To prepare this solution, to 930 μL PBS was added 3.3 μL 3% BSA, 20 μL 50 mM CuSO₄ in H₂O, and 25 μL 4 mM TBTA in 4:1 DMSO/tBuOH. After mixing the reagents by vortexing, 20 μL of freshly prepared 100 mM sodium ascorbate solution in PBS was added and the reagents vortexed again. Finally, the required amount of fluorophore (from a 1 mM stock) was added, the reagents mixed, and the solution used immediately (never letting the reaction mixture sit out for longer than 10 minutes). After 1 h, the cells were imaged without washing. For real-time labeling experiments, images were taken after the addition of the reagents at designated time points. Afterwards, if needed, the cells were washed by replacing the labeling cocktail with 300 μL PBS.

Two color DNA imaging of cells

HEK 293T cells were incubated with EdU as described above. After 12h, 0.15 μL of 2 mg/mL Hoescht 33342 in H₂O was added to the cells (final concentration of 10 μg/mL) and the cells allowed to incubate at 37 °C for 20 minutes. The cells were then fixed, permeabilized, labeled, and imaged as described above.

pH dependent fluorescence of CalFluor-DNA or RNA conjugates in cells

HEK 293T cells were treated with EdU or EU and clicked with azide probe as described above. After the click reaction, the cells were washed three times with 300 μ L pH 7.4 PBS. After acquiring images, the pH 7.4 PBS was replaced with 300 μ L pH 9.4 PBS (adjusted with NaOH) and cells imaged again.

Quantification of labeling intensity

Intensities were acquired from random points in various raw fluorescence micrographs. A minimum of 120 points were acquired for EdU labeling, and a minimum of 30 points were acquired for analysis of EU labeling. Intensities were normalized to the fluorescence intensities from extranuclear regions.

No-wash labeling of glycoproteins on developing zebrafish

AB-derived (wild-type) adult zebrafish were kept at 28.5 °C on a 14 h light/10 h dark cycle. Embryos were collected from natural spawning. Embryos were developmentally staged according to Kimmel and coworkers.

2 nL of a 25 mM SiaNAI in 0.2 M KCl + 0.2% phenol red was injected into the yolk sac of embryos at the one to four-cell stage. After 4-5 h, healthy embryos were transferred to plates in fresh embryo media (EM) and placed in an incubator at 28.5 °C. EM consisted of 150 mM NaCl, 0.5 mM KCl, 1.0 mM CaCl₂, 0.37 mM KH₂PO₄, 0.05 mM Na₂HPO₄, 2.0 mM MgSO₄, 0.71 mM NaHCO₃ in diH₂O.

At 24 hpf, the embryos were manually dechorionated and placed into plates containing fresh EM with 0.14 mg/mL tricaine. Phenylthiourea (PTU) was not included as it was found to interfere with the reaction. Embryos in 100 μ L of media from the plate were transferred onto a glass cover slide.

500 μ L of a 2x stock of click labeling solution was prepared by first combining 383 μ L of EM, 6 μ L of 50 mM BTAA in H₂O, and 1 μ L 50 mM of CuSO₄ in H₂O. After mixing, 100 μ L of a freshly prepared stock of 100 mM sodium ascorbate in EM was added. The reagents were mixed once more, 1 μ L of 1 mM CalFluor 580 in 4:1 H₂O/MeCN was added, the solution mixed, and 100 μ L was added to the embryos on the slide. Another slide was placed on top of the embryos, supported by four drops of vacuum grease, and the embryos were imaged by confocal microscopy on a Zeiss LSM 780 NLO AxioExaminer using a Plan Neofluar 5x/0.16 or a Plan-Apochromat 20x/1.0 objective. Final concentrations of reagents were 50 μ M CuSO₄, 300 μ M BTAA, 10 mM sodium ascorbate, and 1 μ M CalFluor 580. Control zebrafish embryos were not injected at the one to four-cell stage.

For the data in Figure 4-24B, embryos were allowed to develop to 36 hpf in the absence of PTU, but were labeled as described above using either 1 μ M CalFluor 580, 1 μ M AlexaFluor 594 alkyl azide, or 5 μ M 3-azido-7-hydroxycoumarin. After 20 minutes, the embryos were imaged without further washing steps.

EdU labeling in E. coli

E. coli were grown from a single colony in 1 mL LB with continuous shaking overnight at 37 °C. The bacteria were then diluted to an OD of 0.2 in LB. To 3.6 mL of OD 0.2 culture was added 2.2 µL of 20 mM EdU or DMSO. After shaking for 1.5 h at 37 °C, the bacteria were transferred to Eppendorfs and the bacteria pelleted by centrifugation at 6000 rpm for 5 minutes. The supernatant was removed and the bacteria were resuspended in 1% formaldehyde and gently shaken for 30 minutes. The bacteria were then pelleted by centrifugation at 6000 rpm for 5 minutes, then resuspended in PBS. This wash step was repeated twice more. The bacteria were then resuspended in 0.25% Triton-X for 15 minutes. After washing three more times with PBS, the bacteria were transferred to a Costar 96-well V-bottom plate (200 µL per well), pelleted by centrifugation at 3500 rpm for 5 minutes, then resuspended in 200 µL of click solution. Click solution consisted of PBS containing 1 mM CuSO₄, 100 µM TBTA, 2 mM sodium ascorbate, and 10 µM CalFluor 647 or AlexaFluor 647 alkyl azide. Bacteria not treated with probe were resuspended in PBS. After shaking for 1 h at rt, then bacteria were pelleted by centrifugation at 3500 rpm for 5 minutes, then resuspended in 200 µL of PBS. After washing two more times, the bacteria were analyzed using a BD Accuri C6 flow cytometer.

EdU labeling in mouse brain tissue slices

2 month-old C57Bl/6J mice were injected (intraperitoneal) with 150 mg/kg EdU. After 2h, mice were sacrificed by injection with 3.8% chloral hydrate, followed by transcardial perfusion using chilled phosphate-buffered saline. Following extraction, brains were post-fixed in 4% paraformaldehyde for 48 h at 4 °C and stored in 30% sucrose thereafter. Coronal sections at a thickness of 40 µm were prepared using a freezing sliding microtome. Prior to staining, sections were stored in cryoprotective medium at -20 °C.

Brain sections containing the subventricular zone were placed into pH 7.4 PBS. The PBS was removed by aspiration and 1 mL of 0.5% Triton-X in PBS was added to each well. After 20 minutes, the Triton-X was removed and the cells were covered with 500 µL of click solution. Click solution consisted of PBS containing 1 mM CuSO₄, 100 µM TBTA, 2 mM sodium ascorbate, and 10 µM CalFluor 647, and 0.1 mg/mL BSA. After 30 minutes, the cocktail was removed, and tissue slices were mounted under Prolong Gold and imaged.

All animal handling and use was in accordance with institutional guidelines approved by the VA Palo Alto Committee on Animal Research.

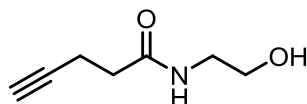
Synthetic procedures

All chemical reagents obtained from commercial suppliers were used without further purification. Anhydrous dichloromethane, tetrahydrofuran and acetonitrile were passed through an activated alumina column prior to use. Anhydrous DMF and 1,4-dioxane were used as purchased. Water was double distilled prior to use. Ac₄ManNAI¹⁴, SiaNAI¹⁴, BTAA⁴, and 3-azido-7-hydroxycoumarin¹⁵ were prepared according to literature procedures.

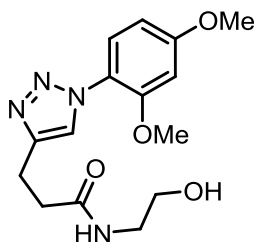
Flash chromatography was performed using Silicycle SiliaFlash P60 silica gel. Analytical thin layer chromatography was performed using glass-backed Analtech Uniplat silica gel plates containing a fluorescent indicator. Reversed-phase HPLC was performed on a Varian Pro Star system with a Varian UV-Vis detector model 345 (210, 254 nm) on a Dynamax Microsorb C-18

preparative column (21.4 x 250 mm) at a flow rate of 20 mL/min or on a Dynamax Microsorb C-18 semi-preparative column (10.0 x 250 mm) at a flow rate of 4 mL/min.

NMR spectra were obtained on Bruker AVQ-400, AVB-400, DRX-500, AV-500, or AV-600 spectrometers at ambient temperature at the UC Berkeley College of Chemistry NMR Facility. ^1H NMR shifts are calibrated to residual undeuterated solvent: δ 7.26 for CHCl_3 , 2.50 for d_5 -DMSO, 4.79 for HDO, 1.94 for CHD_2CN , and 3.31 for CHD_2OD . ^{13}C NMR shifts are calibrated to solvent peaks: δ 77.16 for CDCl_3 , 39.52 for d_6 -DMSO, 1.39/118.69 for CD_3CN , and 49.00 for CD_3OD . High resolution mass spectrometry was performed at the UC Berkeley Mass Spectrometry Laboratory.

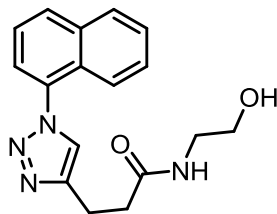


Alkyne **4.25** was prepared according to Ref. 5.



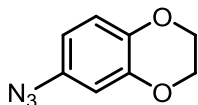
44.8 mg 1-azido-2,4-dimethoxybenzene **4.1a**⁴⁹ (0.250 mmol), a brown oil, was dissolved in 1.25 mL 2:1 *t*BuOH/ H_2O . Next, 35.5 mg alkyne **4.25** (0.250 mmol, 1 equiv.), a white solid, was added. The solution was placed under a nitrogen atmosphere, and 3.5 mg $\text{Cu}(\text{MeCN})_4\text{PF}_6$, a white powder, and 5.4 mg THPTA, a white powder, (both 0.0125 mmol, 0.05 equiv.) were added. The brown solution was stirred under N_2 overnight. Afterwards, the reaction was diluted with 10 mL H_2O and extracted with 3 x 10 mL EtOAc. The organic layers were washed with 3 x 10 mL H_2O , dried over MgSO_4 , and concentrated, yielding a brown oil. The oil was purified with CHCl_3 to 20:1 $\text{CHCl}_3/\text{MeOH}$ to 7:1 $\text{CHCl}_3/\text{MeOH}$ to yield **4.1b** (45.8 mg, 0.143 mmol, 57%) as a white solid.

R_f = 0.40 (10:1 $\text{CHCl}_3/\text{MeOH}$, UV) ^1H NMR (500 MHz, CDCl_3): δ 7.81 (s, 1H), 7.58 (d, J = 9.3 Hz, 1H), 6.59 (s, 1H), 6.58 (d, J = 9.3 Hz, 1H), 6.48 (br, 1H), 3.86 (s, 3H), 3.85 (s, 3H), 3.58 (t, 5.3 Hz, 2H), 3.40 (q, J = 5.3 Hz, 2H), 3.14 (t, J = 6.9 Hz, 2H), 2.72 (t, J = 6.9 Hz, 2H), 2.22 (br, 1H); ^{13}C NMR (126 MHz, CDCl_3) δ 173.44, 161.34, 152.71, 145.70, 126.57, 124.03, 119.92, 104.81, 99.65, 62.18, 56.04, 55.82, 42.77, 35.98, 21.74; HRMS (ESI): $\text{C}_{15}\text{H}_{21}\text{O}_4\text{N}_4$ $[\text{M}+\text{H}]^+$ 321.1557, found 321.1552.



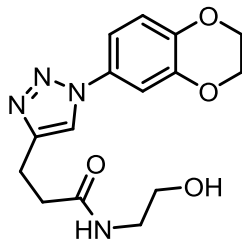
84.6 mg 1-azidonaphthalene **4.2a**⁵⁰ (0.500 mmol), a light yellow liquid, was dissolved in 2.5 mL 2:1 tBuOH/H₂O. Next, 71 mg mg alkyne **4.25** (0.500 mmol, 1 equiv.), a white solid, was added. The solution was placed under a nitrogen atmosphere, and 9.3 mg Cu(MeCN)₄PF₆, a white solid, and 13.3 mg THPTA, a brown solid, (both 0.0332 mmol, 0.066 equiv.) were added. The cloudy brown solution was stirred under N₂ overnight. After 16 h, the solution was diluted with 10 mL H₂O and extracted with 3 x 10 mL EtOAc. The combined organic layers were dried over MgSO₄ and concentrated, yielding a brown oil. The oil was purified with CHCl₃ to 15:1 CHCl₃/MeOH, yielding **4.2b** (61.1 mg, 0.197 mmol, 39% yield) as a clear oil.

R_f = 0.45 (10:1 CHCl₃/MeOH, UV/CAM); ¹H NMR (400 MHz, CDCl₃): δ 8.01 (q, *J* = 4.0, 3.3 Hz, 1H), 7.98 – 7.91 (m, 1H), 7.77 (s, 1H), 7.65 – 7.47 (m, 5H), 6.37 (br, 1H), 3.71 (dd, *J* = 5.5, 4.3 Hz, 2H), 3.44 (q, *J* = 5.3 Hz, 2H), 3.23 (t, *J* = 6.9 Hz, 2H), 2.78 (t, *J* = 6.9 Hz, 2H); ¹³C NMR (150 MHz, CDCl₃): δ 173.20, 146.49, 134.20, 133.68, 128.52, 128.38, 128.00, 127.17, 125.08, 124.59, 123.61, 122.27, 61.93, 42.61, 35.70, 21.61; HRMS (ESI): Calculated for C₁₇H₁₉O₂N₄ [M+H]⁺ 311.1503, found 311.1503.



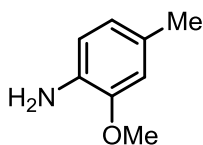
0.171 g 2,3-dihydrobenzo[b][1,4]dioxin-6-amine (1.13 mmol), a brown oil, was dissolved in 6 mL 2:1 AcOH/H₂O. The solution was cooled to 0 °C, then 0.117 g (1.69 mmol, 1.5 equiv) sodium nitrite, a white powder, was added. The solution was stirred for 10 minutes at 0 °C, then 0.149 g (2.26 mmol, 2 equiv.) sodium azide was added. Bubbling was observed. The solution was stirred for 1 h at 0 °C and 1 h at rt. The solution was then diluted with 20 mL H₂O and extracted with 3 x 25 mL Et₂O. The combined organic layers were washed with sat. Na₂CO₃ (caution: gas evolution!), dried over MgSO₄, and concentrated to yield a brown oil. The oil was purified with hexanes to 10:1 hexanes/EtOAc to yield **4.3a** (0.156 g, 0.881 mmol, 78%) as a brown oil.

R_f = 0.40 (10:1 hex/EtOAc, UV) HRMS (EI): ¹H NMR (400 MHz, CDCl₃): δ 6.83 (d, *J* = 8.6 Hz, 1H), 6.56 (d, *J* = 2.7 Hz, 1H), 6.52 (dd, *J* = 8.5, 2.7 Hz, 1H), 4.30 – 4.20 (m, 4H); ¹³C NMR (126 MHz, CDCl₃): δ 144.34, 141.05, 133.14, 118.21, 112.06, 108.04, 64.50, 64.27. Calculated for C₈H₇N₃O₂ [M]⁺ 177.0538, found 177.0539.



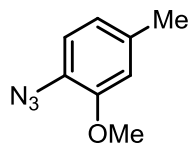
44.3 mg **4.3a** (0.250 mmol), a brown oil, was dissolved in 1.25 mL 2:1 tBuOH/H₂O. Next, 35.5 mg alkyne **4.25** (0.250 mmol, 1 equiv.), a white solid, was added. The solution was placed under a nitrogen atmosphere, and 3.5 mg Cu(MeCN)₄PF₆, a white powder, and 5.4 mg THPTA, a white powder, (both 0.0125 mmol, 0.05 equiv.) were added. The brown solution was stirred under N₂ overnight. Afterwards, the reaction was diluted with 10 mL H₂O and extracted with 3 x 10 mL EtOAc. The organic layers were washed with 3 x 10 mL H₂O, dried over MgSO₄, and concentrated, yielding a brown oil. The oil was purified with CHCl₃ to 20:1 CHCl₃/MeOH to 7:1 CHCl₃/MeOH to yield **4.3b** (41.4 mg, 0.130 mmol, 52%) as a white solid.

R_f = 0.40 (10:1 CHCl₃/MeOH, UV); ¹H NMR (400 MHz, CDCl₃): δ 7.71 (s, 1H), 7.23 (d, *J* = 2.5 Hz, 1H), 7.16 (dd, *J* = 8.7 Hz, 2.6 Hz, 1H), 6.96 (d, *J* = 8.7 Hz, 1H), 6.27 (br, 1H), 4.31 (br, 4H), 3.68 (q, *J* = 5.0 Hz, 3H), 3.40 (q, *J* = 5.5 Hz, 2H), 3.13 (t, *J* = 6.8 Hz, 2H), 2.73 – 2.61 (m, 2H); ¹³C NMR (151 MHz, CDCl₃): δ 173.23, 144.17, 144.07, 130.91, 120.22, 118.11, 113.75, 110.26, 64.51, 64.45, 62.09, 42.65, 35.73, 21.63; HRMS (ESI): Calculated for C₁₅H₁₉O₄N₄ [M+H]⁺ 319.1401, found 319.1401.



1-bromo-4-methoxy-2-methyl-5-nitrobenzene⁵¹ (0.793 g, 3.24 mmol), an orange solid, was dissolved in 16 mL 1:1 EtOAc/EtOH. The solution was purged with nitrogen, then 0.345 g 10% Pd/C (0.1 equiv., 0.324 mmol) was added. The solution was purged with nitrogen, then placed under an atmosphere of hydrogen and stirred overnight (24h). The product was filtered over a pad of Celite and the pad washed with 200 mL EtOAc, then concentrated to yield a brown oil. The brown oil was purified by silica gel chromatography (10:1 to 4:1 hex/EtOAc) to yield **4.26** (0.361 g, 2.61 mmol, 81%) as a brown oil.

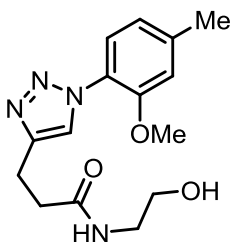
R_f = 0.45 (4:1 hex/EtOAc, UV/I₂); ¹H NMR (500 MHz, CDCl₃): δ 6.68–6.65 (m, 3H), 3.87 (s, 3H), 3.67 (brs, 2H), 2.33 (s, 3H); ¹³C NMR (151 MHz, CDCl₃): δ 147.34, 133.56, 127.99, 121.21, 115.06, 111.55, 55.40, 20.97. HRMS (ESI): Calculated for C₈H₁₂ON [M+H]⁺ 138.0913, found 138.0910.



0.361 g (2.61 mmol) **4.26**, a brown oil, was dissolved in 13.5 mL 2:1 AcOH/H₂O. The solution was cooled to 0 °C. Next, 0.272 g (3.95 mmol, 1.5 equiv.) sodium nitrite was added in one

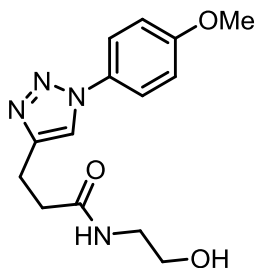
portion. The solution was allowed to stir at 0° C for 10 minutes. Next, 0.347 g (5.22 mmol, 2 equiv.) sodium azide was added in one portion. Bubbling was observed. The reaction was stirred for 1 h at 0 C and 1 h at rt, then diluted with 40 mL H₂O and extracted with 3 x 40 mL Et₂O, washed with sat. Na₂CO₃ (caution: gas evolution!), dried over MgSO₄, and concentrated. The brown oil was purified by silica gel chromatography (7:1 to 4:1 hex/EtOAc) with to yield **4.4a** (0.209 g, 1.28 mmol, 49%) as a brown oil.

R_f = 0.50 (10:1 hex/EtOAc, UV); ¹H NMR (500 MHz, CDCl₃): δ 6.90 (d, *J* = 7.9 Hz, 1H), 6.74 (dd, *J* = 8.0, 1.7 Hz, 1H), 6.70 (d, *J* = 1.7 Hz, 1H), 3.86 (s, 3H), 2.33 (s, 3H). ¹³C NMR (126 MHz, CDCl₃): δ 151.54, 135.80, 125.38, 121.73, 119.96, 112.96, 55.81, 21.32. HRMS (EI): Calculated for C₈H₉N₃O [M]⁺ 163.0746, found 163.0747.



40.8 mg (0.250 mmol) **4.4a**, a light brown oil, was dissolved in 1.25 mL 2:1 tBuOH/H₂O. Next, 35.5 mg alkyne (1 equiv, 0.250 mmol), a white solid, was added. Finally, the solution was placed under N₂ and 3.5 mg Cu(MeCN)₄PF₆ and 5.4 mg THPTA (both 0.0125 mmol, 0.05 equiv.) were added. The solution was stirred under N₂ overnight. Afterwards, the solution was diluted with 10 mL H₂O and extracted with 3x10 mL EtOAc. The organic layers were washed with 3 x 10 mL H₂O, dried over MgSO₄, and concentrated, yielding a brown oil. The oil was purified with CHCl₃ to 20:1 CHCl₃/MeOH to 7:1 CHCl₃/MeOH to yield **4.4b** (40.0 mg, 0.132 mmol, 53%) as a light brown oil.

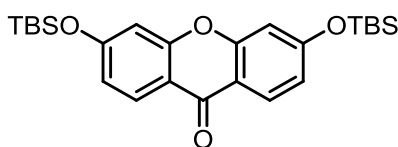
R_f = 0.45 (10:1 CHCl₃/MeOH, UV); ¹H NMR (600 MHz, CDCl₃): δ 7.85 (s, 1H), 7.53 (d, *J* = 8.0 Hz, 1H), 6.86 (m, 3H), 3.87 (br, 1H), 3.84 (s, 3H), 3.66 (d, *J* = 5.1 Hz, 2H), 3.38 (q, *J* = 5.2 Hz, 2H), 3.11 (t, *J* = 7.2 Hz, 2H), 2.67 (t, *J* = 7.2 Hz, 2H), 2.40 (s, 3H); ¹³C NMR (151 MHz, CDCl₃): δ 173.39, 151.12, 145.79, 140.79, 125.29, 123.94, 121.84, 113.06, 62.11, 55.98, 42.73, 35.94, 21.77, 21.73; HRMS (ESI): Calculated for C₁₅H₂₁O₄N₄ [M+H]⁺ 321.1557, found 321.1559.



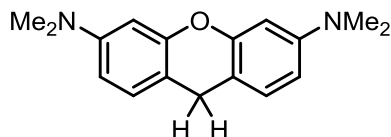
37.2 mg 1-azido-4-methoxybenzene **4.5a**⁶ (0.250 mmol), a light brown oil, was dissolved in 1.25 mL 2:1 tBuOH/H₂O. Next, 35.2 mg alkyne (1 equiv, 0.250 mmol), a white solid, was added.

Finally, the solution was placed under N₂ and 4.6 mg Cu(MeCN)₄PF₆ and 5.4 mg THPTA (both 0.0125 mmol, 0.05 equiv.) were added. The solution was stirred under N₂ overnight. Afterwards, the solution was diluted with 10 mL H₂O and extracted with 3 x 10 mL EtOAc. The organic layers were washed with 3 x 10 mL H₂O, dried over MgSO₄, and concentrated, yielding a brown oil. The oil was purified with CHCl₃ to 20:1 CHCl₃/MeOH to 7:1 CHCl₃/MeOH to yield **4.5b** (40.0 mg, 0.132 mmol, 55%) as a light brown oil.

R_f = 0.40 (10:1 CHCl₃/MeOH, UV); ¹H NMR (400 MHz, CDCl₃) δ 7.74 (s, 1H), 7.60 (d, *J* = 8.9 Hz, 2H), 7.00 (d, *J* = 8.9 Hz, 2H), 6.28 (brs, 1H), 3.86 (s, 3H), 3.67 (d, *J* = 5.1 Hz, 2H), 3.41 (q, *J* = 5.3 Hz, 2H), 3.14 (t, *J* = 6.8 Hz, 2H), 3.04 (brs, 1H), 2.69 (t, *J* = 6.8 Hz, 2H); HRMS (ESI): Calculated for C₁₄H₁₈N₄O₃Na [M+Na]⁺ 313.1271, found 313.1270.

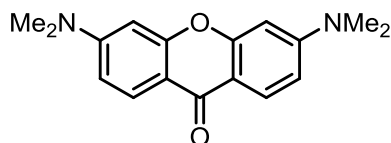


Fluorescein xanthone **4.27** was prepared according to Ref. 3.



1.00 g (3.31 mmol) Pyronin Y, a violet solid, was suspended in 300 mL methanol. The solution was heated to 60 °C, during which a significant portion of the starting material dissolved. To the solution was added 3 x 250 mg (3 x 6.62 mmol, 3 x 2 equiv.) sodium borohydride (caution: vigorous gas evolution!) over the course of 30 minutes. The solution was stirred for another 30 minutes, cooled to rt, then concentrated. The violet residue was taken up in 100 mL water and 100 mL DCM and the organic layer collected. The aqueous layer was further extracted with 4 x 100 mL DCM, dried over MgSO₄, and concentrated to yield (0.486 g, 1.82 mmol, 55%) **4.28** as a magenta solid.

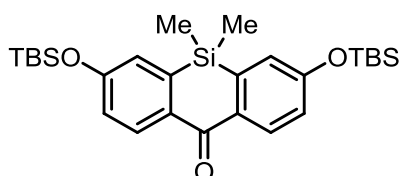
R_f = 0.65 (4:1 hex/EtOAc, UV/I₂); ¹H NMR (500 MHz, CDCl₃): δ 7.04 (d, *J* = 8.3 Hz, 2H), 6.48 (dd, *J* = 8.3, 2.5 Hz, 2H), 6.45 (d, *J* = 2.5 Hz, 2H), 3.89 (s, 2H), 2.96 (s, 12H); ¹³C NMR (126 MHz, CDCl₃): δ 152.19, 150.14, 129.12, 108.49, 107.66, 99.94, 40.37, 25.73. HRMS (ESI): Calculated for C₁₇H₂₁ON₂ [M+H]⁺ 269.1648, found 269.1647.



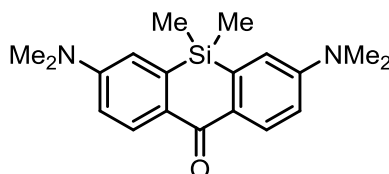
0.384 g (1.43 mmol) **S5**, a magenta solid, was dissolved in 14 mL acetone. The solution was purged with Ar, and cooled to 0 °C. To the solution was added 3 x 74 mg (3 x 0.468 mmol, 3 x 0.33 equiv.) potassium permanganate over 30 minutes. After 15 minutes, TLC analysis showed full consumption of starting material. The solution was then filtered over a pad of Celite, the pad

washed with 100 mL acetone, and concentrated under vacuum. The resulting solid was purified by silica gel chromatography with CHCl_3 to 20:1 $\text{CHCl}_3/\text{MeOH}$ to yield **4.29** (0.157 g, 0.557 mmol, 39%) as a red-orange solid.

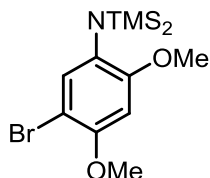
$R_f = 0.40$ (CHCl_3 , UV); $^1\text{H NMR}$ (500 MHz, CDCl_3): δ 8.13 (d, $J = 9.0$ Hz, 2H), 6.69 (dd, $J = 9.0, 2.5$ Hz, 2H), 6.48 (d, $J = 2.4$ Hz, 2H), 3.10 (s, 12H); $^{13}\text{C NMR}$ (126 MHz, CDCl_3): δ 175.28, 158.23, 154.35, 127.68, 112.03, 109.01, 97.05, 40.28. HRMS (ESI): Calculated for $\text{C}_{17}\text{H}_{19}\text{O}_2\text{N}_2$ $[\text{M}+\text{H}]^+$ 283.1441, found 283.1440.



Si-fluorescein xanthone **4.30** was prepared according to Ref. 2.

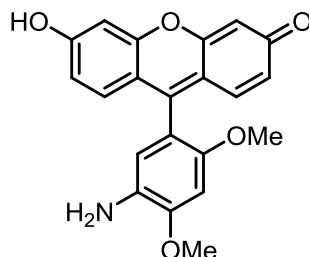


Si-rhodamine xanthone **4.31** was prepared according to Ref. 5.



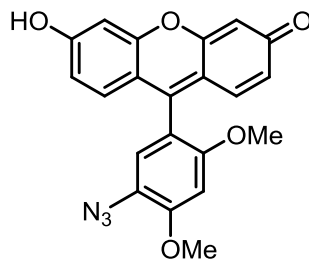
Dimethoxybromoaniline **4.9** was prepared according to Ref. 5. 0.880 mL (4.2 mmol, 2.1 equiv.) hexamethyldisilazane was dissolved in 3 mL dry THF. The solution was cooled to 0 °C, then 1.68 mL 2.5 M *n*-butyllithium solution (4.2 mmol, 2.1 equiv.) was slowly added. The solution was stirred for 15 minutes, then cooled to -78 °C. While the LiHMDS was being prepared, 0.464 g 5-bromo-2,4-dimethoxyaniline (2.00 mmol), a light brown solid, was dissolved in 4 mL THF and cooled to -78 °C. The LiHMDS was added dropwise via cannula, turning the light brown solution a deep red-brown color. The solution was stirred for 10 minutes at -78 °C, then allowed to warm to rt for 5 minutes, then cooled back to -78 °C. Finally, 0.533 mL (4.2 mmol, 2.1 equiv.) trimethylsilyl chloride was added. The solution was warmed to rt and allowed to stir overnight, during which a white precipitate had formed on the sides of the flask. The THF was removed under vacuum. The brown residue was then taken up in 50 mL hexanes, filtered to remove lithium chloride, and reconcentrated to yield the bis-trimethylsilyl protected bromoaniline **4.9** along with small amounts of tris-trimethylamine as a brown oil (0.742 g, 1.98 mmol, 99%).

^1H NMR (500 MHz, CDCl_3): δ 7.03 (s, 1H), 6.41 (s, 1H), 3.88 (s, 3H), 3.76 (s, 3H), 0.02 (s, 18H); ^{13}C NMR (126 MHz, CDCl_3): δ 157.09, 152.83, 134.49, 130.95, 100.21, 96.57, 56.67, 55.29, 1.89.



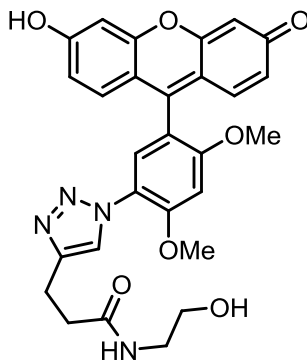
0.111 g (0.296 mmol, 1 equiv.) bromoaniline **4.9**, a brown oil, was dissolved in 1.48 mL dry THF in a flame-dried flask for a final concentration of 0.2 M. The solution was cooled to -78°C . To the solution was added dropwise 0.368 mL (0.592 mmol, 2 equiv.) tBuLi (freshly titrated, from a ~ 1.61 M solution in pentanes). After 30 minutes, 0.149 g (0.325 mmol, 1.1 equiv.) xanthone **4.27**, a white solid, was dissolved in 3.25 mL dry THF (concentration of 0.1 M) and added in one portion. The solution was immediately warmed to rt and stirred for 1 h. The reaction was then quenched by the slow addition of 0.22 mL (1.5 equiv.) 2M HCl, turning the solution a light brown. The brown solution was neutralized with 1 M NaOH and concentrated to yield an orange solid. The solid was purified by flash chromatography with CHCl_3 to 20:1 $\text{CHCl}_3/\text{MeOH}$ to 7:1 $\text{CHCl}_3/\text{MeOH}$ to yield **4.10** (83.7 mg, 0.230 mmol, 78%) as an orange solid.

^1H NMR (500 MHz, CD_3OD): δ 7.12 (d, $J = 9.3$ Hz, 2H), 6.83 (s, 1H), 6.66 (s, 1H), 6.55 (dtd, $J = 9.4, 2.0$ Hz, 2H), 6.50 (d, $J = 2.1$ Hz, 2H), 4.00 (s, 3H), 3.67 (s, 3H); HRMS (ESI): Calculated for $\text{C}_{21}\text{H}_{18}\text{O}_5\text{N}$ $[\text{M}+\text{H}]^+$ 364.1179, found 364.1176.



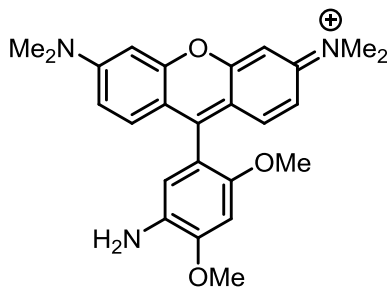
40.0 mg (0.110 mmol) **4.10**, an orange solid, was dissolved in 4.40 mL of a 2:1 AcOH/ H_2O mixture to a final concentration of 0.025 M. The dark orange solution was cooled to 0°C . Next, 11.0 mg (0.165 mmol, 1.5 equiv.) sodium nitrite, a white powder, was added. The solution was stirred for 5 min at 0°C , during which the solution lightened slightly. Next, 14.3 mg (0.220 mmol, 2 equiv.) sodium azide, a white solid, was added. Bubbling was observed. The solution was stirred for 1 h at 0°C and 1 h at rt, then concentrated *in vacuo*. The remaining orange residue was purified with flash chromatography using CHCl_3 to 20:1 $\text{CHCl}_3/\text{MeOH}$ to 10:1 $\text{CHCl}_3/\text{MeOH}$ to yield **4.6a** (32.0 mg, 0.082 mmol, 75%) as an orange solid. For photophysical measurements, the solid was further purified by reverse-phase HPLC using a 20-100% MeCN/ H_2O gradient.

^1H NMR (500 MHz, CD_3OD) δ 7.04 (d, $J = 9.3$ Hz, 2H), 6.92 (s, 1H), 6.80 (s, 1H), 6.55 (dd, $J = 9.3, 2.2$ Hz, 2H), 6.50 (d, $J = 2.1$ Hz, 2H), 4.05 (s, 3H), 3.76 (s, 3H); ^{13}C NMR (126 MHz, CD_3OD): δ 182.72, 160.13, 156.49, 155.86, 153.64, 131.91, 124.32, 123.41, 121.84, 115.32, 113.12, 104.51, 98.45, 56.98, 56.76. HRMS (ESI): Calculated for $\text{C}_{21}\text{H}_{16}\text{O}_5\text{N}_3$ $[\text{M}+\text{H}]^+$ 390.1084, found 390.1080.



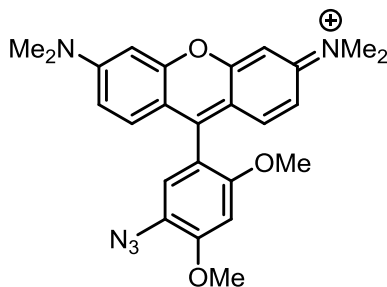
1.95 mg (0.005 mmol) **4.6a**, an orange solid, was dissolved in 0.25 mL MeOH to a final concentration of 0.02 M. The purple solution was placed under a N_2 atmosphere, then 3.53 mg (0.025 mmol, 5 equiv.) alkyne **4.25**, a white solid, was added. Next, 0.940 mg (0.0025 mmol, 0.5 equiv.) $\text{Cu}(\text{MeCN})_4\text{PF}_6$, a white powder, was added, followed by 10 μL (0.01 equiv) TBTA (added from a 10 mM solution in MeOH). The orange solution was stirred for 15 h, after which consumption of starting material was confirmed by LC-MS. The solution was concentrated and the purple residue purified by reverse-phase HPLC using a 20-100% MeCN/ H_2O gradient to yield **4.6b** (1.40 mg, 0.0026 mmol, 53%) as a purple solid.

HRMS (ESI): Calculated for $\text{C}_{28}\text{H}_{27}\text{O}_7\text{N}_4$ $[\text{M}+\text{H}]^+$ 531.1874, found 531.1872.



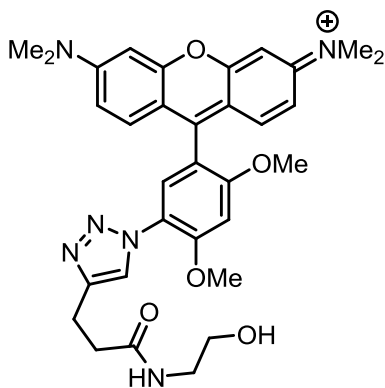
0.224 g (0.5950 mmol, 2.1 equiv.) bromoaniline **4.9**, a brown oil, was dissolved in 2.98 mL dry THF in a flame-dried flask for a final concentration of 0.2 M. The solution was cooled to -78 $^\circ\text{C}$. To the solution was added dropwise 0.78 mL (1.19 mmol, 4.2 equiv.) $t\text{BuLi}$ (freshly titrated, from a ~ 1.53 M solution in pentanes). After 30 minutes, 0.080 g (0.283 mmol.) rhodamine xanthone **4.28** a yellow solid, was suspended in 2.8 mL dry THF (concentration of 0.1 M) and added in one portion. The solution was immediately warmed to rt and stirred for 1 h. The reaction was then quenched by the slow addition of 0.8 mL 2M HCl, turning the solution a magenta color. The magenta solution was quickly poured into 60 mL 50% sat. NaHCO_3 and extracted with 5 x 100 mL CH_2Cl_2 , dried over MgSO_4 , and concentrated to yield a purple solid. The solid was purified by flash chromatography with CHCl_3 to 20:1 $\text{CHCl}_3/\text{MeOH}$ to 3:1 $\text{CHCl}_3/\text{MeOH}$ to yield **4.11** (38.9 mg, 0.093 mmol, 33%) as a purple solid.

^1H NMR (500 MHz, CD_3OD): δ 7.44 (d, $J = 9.5$ Hz, 2H), 7.08 (dd, $J = 9.5, 2.5$ Hz, 2H), 6.90 (d, $J = 2.5$ Hz, 2H), 6.87 (s, 1H), 6.70 (s, 1H), 4.03 (s, 3H), 3.69 (s, 3H), 3.35 (s, 12H). HRMS (ESI): Calculated for $\text{C}_{25}\text{H}_{28}\text{O}_3\text{N}_3$ $[\text{M}-\text{Cl}]^+$ 318.2125, found 418.2117



28.4 mg (0.067 mmol) **4.11**, a magenta solid, was dissolved in 2.72 mL of a 2:1 AcOH/ H_2O mixture to a final concentration of 0.025M. The magenta solution was cooled to 0 °C. Next, 7.02 mg (0.102 mmol, 1.5 equiv.) sodium nitrite, a white powder, was added. The solution was stirred for 10 min at 0 °C, during which the solution lightened slightly. Next, 8.82 mg (0.136 mmol, 2 equiv) sodium azide, a white solid, was added. Bubbling was observed. The solution was stirred for 1 h at 0 °C and 1 h at rt, then concentrated *in vacuo*. The remaining magenta residue was purified with flash chromatography using CHCl_3 to 20:1 $\text{CHCl}_3/\text{MeOH}$ to 3:1 $\text{CHCl}_3/\text{MeOH}$ to yield a magenta solid, which was dissolved in CHCl_3 and washed 2 times with 0.1% TFA in H_2O to yield **4.7a** (26.6 mg, 0.048 mmol, 71%) as the TFA salt. For photophysical measurements, the solid was further purified by reverse-phase HPLC using a 20-100% MeCN/ H_2O + 0.1% TFA gradient.

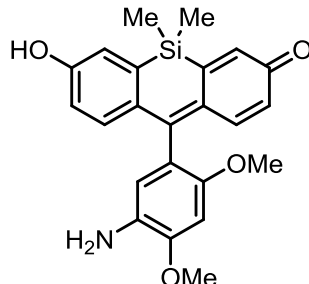
^1H NMR (400 MHz, CD_3OD): δ 7.36 (d, $J = 9.6$ Hz, 2H), 7.10 (dd, $J = 9.6, 2.3$ Hz, 2H), 6.98 (s, 1H), 6.95 (d, $J = 2.6$ Hz, 2H), 6.88 (d, $J = 1.6$ Hz, 1H), 4.07 (s, 3H), 3.77 (s, 3H), 3.32 (s, 12H); ^{13}C NMR (126 MHz, CD_3OD): δ 159.04, 158.74, 156.96, 156.70, 156.45, 132.74, 123.91, 122.33, 115.32, 115.02, 113.76, 98.63, 97.31, 57.04, 56.77, 40.93. HRMS (ESI): Calculated for $\text{C}_{25}\text{H}_{26}\text{O}_3\text{N}_5$ $[\text{M}-\text{Cl}]^-$ 444.2030, found 444.2025.



2.2 mg (0.005 mmol, 1 equiv.) **4.7a**, a purple solid, was dissolved in 0.25 mL MeOH to a final concentration of 0.02 M. The purple solution was placed under a N_2 atmosphere, then 3.53 mg (0.025 mmol, 5 equiv.) alkyne **4.25**, a white solid, was added. Next, 0.940 mg (0.0025 mmol, 0.5 equiv.) $\text{Cu}(\text{MeCN})_4\text{PF}_6$, a white powder, was added, followed by 5 μL (0.01 equiv) TBTA (added from a 10 mM solution in MeOH). The purple solution was stirred for 15 h, after which

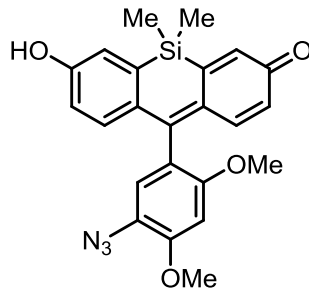
consumption of starting material was confirmed by LC-MS. The solution was concentrated and the purple residue purified by reverse-phase HPLC using a 20-100% MeCN/H₂O + 0.1% TFA gradient to yield **4.7b** (1.96 mg, 0.0028 mmol, 56%) as a purple solid.

HRMS (ESI): Calculated for C₃₂H₃₇O₅N₆ [M-TFA]⁻ 585.2820, found 585.2806.



0.132 g (0.350 mmol, 2.1 equiv.) bromoaniline **4.9**, a brown oil, was dissolved in 1.75 mL dry THF. The solution was cooled to -78°C. To the solution was added dropwise 0.46 mL (0.70 mmol, 4.2 equiv.) tBuLi (freshly titrated, from a ~1.53 M solution in pentanes). After 30 minutes, 0.083 g (0.167 mmol) Si-fluorescein xanthone **4.29**, a white solid, was dissolved in 1.7 mL dry THF (concentration of 0.1 M) and added in one portion. The solution was immediately warmed to rt and stirred for 1 h. The reaction was then quenched by the slow addition of 1 mL 2M HCl, turning the solution a bright red. The red solution was quickly poured into 30 mL 50% sat. NaHCO₃ and extracted with 4 x 20 mL CH₂Cl₂, dried over Na₂SO₄, and concentrated to yield a brown solid. The solid was purified by flash chromatography with CHCl₃ to 50:1 CHCl₃/MeOH to yield **4.12** (24.1 mg, 0.059 mmol, 36%) as a red-orange solid.

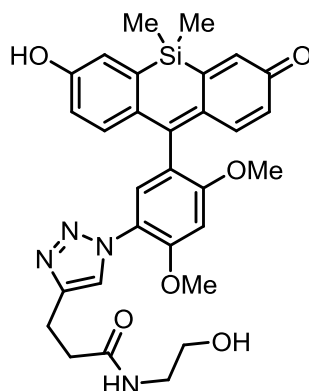
¹H NMR (600 MHz, CDCl₃): δ 7.09 (d, *J* = 9.4 Hz, 2H), 6.97 (d, *J* = 2.5 Hz, 2H), 6.57 (s, 1H), 6.47 (s, 1H), 6.46 (dd, *J* = 9.1 Hz, 2.3 Hz, 2H), 3.95 (s, 3H), 3.62 (s, 3H), 0.39 (s, 3H), 0.37 (s, 3H); ¹³C NMR (126 MHz, CDCl₃): δ 172.37, 158.67, 150.13, 148.47, 145.49, 140.73, 130.79, 128.99, 128.79, 121.88, 120.55, 117.44, 96.98, 57.02, 55.90, -1.14, -1.44; HRMS (ESI): Calculated for C₂₃H₂₄O₄NSi [M+H]⁺ 406.1469, found 406.1463.



22.0 mg (0.054 mmol, 1 equiv.) **4.12**, an orange solid, was dissolved in 2.16 mL of a 2:1 AcOH/H₂O mixture to a final concentration of 0.025M. The red solution was cooled to 0 °C. Next, 11.2 mg (0.163 mmol, 3 equiv.) sodium nitrite, a white powder, was added. The solution was stirred for 10 min at 0 °C, during which the solution lightened slightly. Next, 13.9 mg (0.217 mmol, 4 equiv.) sodium azide, a white solid, was added. Bubbling was observed. The solution was stirred for 1h at 0 °C and 1 h at rt, then concentrated *in vacuo*. The remaining red residue was purified with flash chromatography using CHCl₃ to 50:1 CHCl₃/MeOH to yield **4.8a**

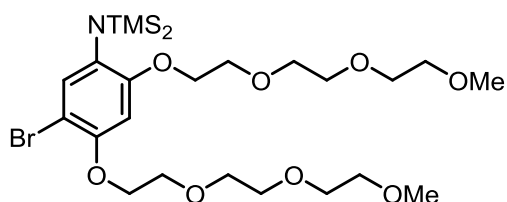
(22.5 mg, 0.052 mmol, 96%) as a red solid. For photophysical measurements, the solid was further purified by reverse-phase HPLC using a 20-100% MeCN/H₂O gradient.

¹H NMR (400 MHz, CDCl₃): δ 7.04 – 6.94 (m, 4H), 6.71 (s, 1H), 6.60 (s, 1H), 6.53 (dd, *J* = 9.5, 2.5 Hz, 2H), 3.99 (s, 3H), 3.70 (s, 3H), 0.43 (s, 3H), 0.41 (s, 3H); ¹³C NMR (126 MHz, CDCl₃) δ 172.40, 156.86, 154.77, 152.93, 145.58, 140.30, 130.73, 129.02, 129.02, 122.09, 120.93, 120.90, 96.83, 56.40, 56.38, -1.09, -1.41; HRMS (ESI): Calculated for C₂₃H₂₂O₄N₃Si [M+H]⁺ 432.1374, found 432.1373.



2.16 mg (0.005 mmol, 1 equiv.) **4.8a** a purple solid, was dissolved in 0.25 mL MeOH. The purple solution was placed under a N₂ atmosphere, then 3.53 mg (0.025 mmol, 5 equiv.) alkyne **4.25**, a white solid, was added. Next, 0.94 mg (0.0025 mmol, 0.5 equiv.) Cu(MeCN)₄PF₆, a white powder, was added, followed by 5 μL (0.01 equiv) TBTA (added from a 10 mM solution in MeOH). The purple solution was stirred for 15 h, after which consumption of starting material was confirmed by LC-MS. The solution was concentrated and the purple residue purified by reverse-phase HPLC using a 20-100% MeCN/H₂O gradient to yield **4.8b** (1.76 mg, 0.0031 mmol, 62%) as a red solid.

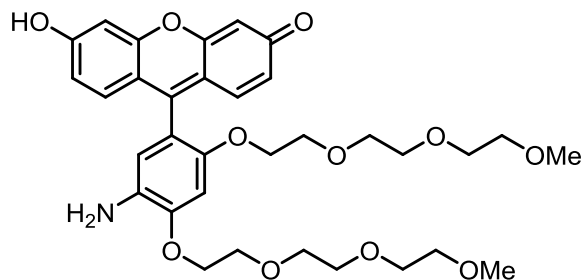
HRMS (ESI): Calculated for C₃₀H₃₃O₆N₄Si [M+H]⁺ 573.2164, found 573.2167.



Bis-TMS-bromoaniline **4.14** was prepared according to Ref. 5. 0.880 mL (4.2 mmol, 2.1 equiv.) hexamethyldisilazane was dissolved in 3 mL dry THF. The solution was cooled to 0 °C, then 1.68 mL 2.5 M n-butyllithium solution (4.2 mmol, 2.1 equiv.) was slowly added. The solution was stirred for 15 minutes, then cooled to -78 °C. While the LiHMDS was being prepared, 0.990 g bis oligoethylene glycol functionalized bromoaniline⁵ (2.00 mmol), a brown oil, was dried azeotropically with PhMe and dissolved in 4 mL THF, and cooled to -78 °C. The LiHMDS was added dropwise via cannula, turning the light brown solution a deep red-brown color. The solution was stirred for 10 minutes at -78 °C, then allowed to warm to rt for 5 minutes, then cooled back to -78 °C. Finally, 0.533 mL (4.2 mmol, 2.1 equiv.) trimethylsilyl chloride was added. The solution was warmed to rt and allowed to stir overnight, during which a white

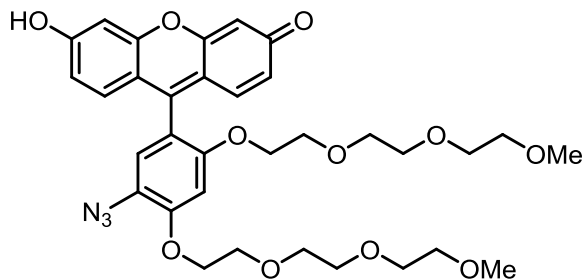
precipitate had formed on the sides of the flask. The THF was removed under vacuum. The brown residue was then taken up in 50 mL PhMe, filtered to remove lithium chloride, and reconcentrated to yield the bis-trimethylsilyl protected bromoaniline **4.14** along with small amounts of tris-trimethylamine as a brown oil (1.16 g, 1.82 mmol, 91%).

^1H NMR (600 MHz, CDCl_3): δ 7.01 (s, 1H), 6.45 (s, 1H), 4.13 (t, $J = 5.0$ Hz, 2H), 4.01 (t, $J = 5.2$ Hz, 2H), 3.89 (t, $J = 5.0$ Hz, 2H), 3.84 (t, $J = 5.1$ Hz, 2H), 3.80 (t, $J = 4.85$ Hz, 2H), 3.72 – 3.63 (m, 10H), 3.55 (app. q, $J = 4.9$ Hz, 4H), 3.38 (s, 3H), 3.368(s, 3H), 0.01 (s, 18H); ^{13}C NMR (126 MHz, CDCl_3) δ 156.15, 152.20, 134.70, 131.09, 101.13, 99.01, 71.99, 71.98, 71.14, 70.78, 70.78, 70.71, 70.66, 70.60, 69.72, 69.67, 69.64, 67.26, 59.12, 59.12, 1.84.



0.320 g bis-TMS-bromoaniline **4.14** (0.500 mmol) was dissolved in 4 mL dry THF in a flame-dried flask. The solution was cooled to -78 °C. Next, 0.650 mL (1.00 mmol, 2 equiv.) *t*-butyllithium was added dropwise. The solution was stirred for 30 minutes at -78 °C. Next, 0.229 g (0.500 mmol, 1 equiv.) fluorescein xanthone **4.27**, a white solid, in 4 mL dry THF, was added in one portion. The reaction was warmed to rt and stirred for 1 h. The reaction was quenched by the addition of 0.6 mL 2M HCl, followed by the addition of 0.6 mL 1M NaOH. After stirring for 10 minutes, 0.1 mL AcOH was added and the solution concentrated. The resulting red-orange residue was purified by silica gel column (CHCl_3 to 10:1 $\text{CHCl}_3/\text{MeOH}$) to yield 0.192 g **4.15** (0.296 mmol, 59%) as a red-orange solid.

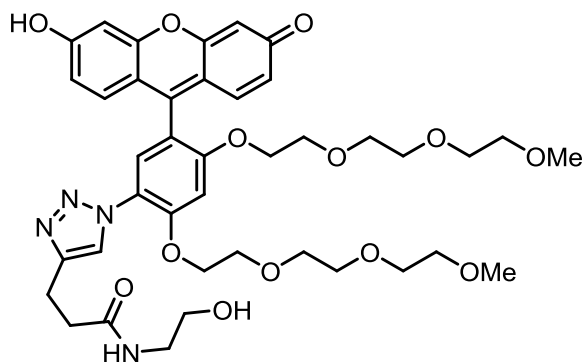
^1H NMR (600 MHz, CD_3OD): δ 7.31 (d, $J = 9.2$ Hz, 2H), 6.91 (s, 1H), 6.70 (dd, $J = 9.3, 2.3$ Hz, 2H), 6.68 (s, 1H), 6.67 (d, $J = 2.2$ Hz, 2H), 4.31 (dd, $J = 5.6, 3.4$ Hz, 2H), 4.04 – 3.99 (m, 2H), 3.94 (dd, $J = 5.5, 3.5$ Hz, 2H), 3.76 (dd, $J = 5.8, 3.4$ Hz, 2H), 3.70 (dd, $J = 5.8, 3.4$ Hz, 2H), 3.66 (dd, $J = 5.8, 3.5$ Hz, 2H), 3.57 – 3.54 (m, 2H), 3.50 – 3.46 (m, 2H), 3.46 – 3.40 (m, 4H), 3.36 (s, 3H), 3.30 (s, 3H), 3.31 (dd, $J = 6.0, 3.4$ Hz, 2H), 3.27 (dd, $J = 6.0, 3.4$ Hz, 2H); ^{13}C NMR (126 MHz, CD_3OD): δ 177.14, 159.32, 154.96, 150.45, 150.44, 133.27, 132.47, 122.42, 118.21, 116.46, 115.14, 104.05, 101.38, 72.96, 72.79, 71.71, 71.57, 71.42, 71.38, 71.32, 71.18, 70.81, 70.63, 70.61, 69.77, 59.11, 59.03; HRMS (ESI): Calculated for $\text{C}_{33}\text{H}_{42}\text{O}_{11}\text{N}$ $[\text{M}+\text{H}]^+$ 628.2752, found 628.2737.



57.5 mg (0.092 mmol, 1 equiv.) **4.15**, an orange solid, was dissolved in 3.68 mL of a 2:1 AcOH/H₂O mixture to a final concentration of 0.025 M. The dark orange solution was cooled to 0°C. Next, 9.48 mg (0.137 mmol, 1.5 equiv.) sodium nitrite, a white powder, was added. The solution was stirred for 5 min at 0 °C, during which the solution lightened slightly. Next, 11.9 mg (0.183 mmol, 2 equiv) sodium azide, a white solid, was added. Bubbling was observed. The solution was stirred for 1 h at 0 °C and 1 h at rt, then concentrated *in vacuo*. The remaining orange residue was purified with flash chromatography using CHCl₃ to 20:1 CHCl₃/MeOH to 10:1 CHCl₃/MeOH to yield **4.13a** (57.1 mg, 0.0874 mmol, 95%) as an orange solid. For photophysical measurements and biological experiments, the solid was further purified by reverse-phase HPLC using a 20-100% MeCN/H₂O gradient.

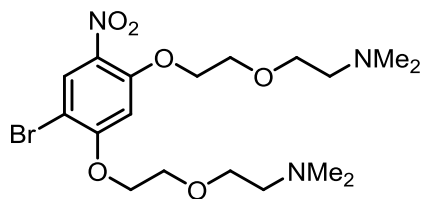
¹H NMR (500 MHz, CDCl₃): δ 7.23 (d, *J* = 9.2 Hz, 2H), 7.00 (s, 1H), 6.80 (s, 1H), 6.70 (dd, *J* = 9.2, 2.2 Hz, 2H), 6.68 (d, *J* = 2.2 Hz, 2H), 4.41 – 4.31 (m, 2H), 4.15 – 4.07 (m, 2H), 3.97 – 3.90 (m, 2H), 3.74 (dd, *J* = 5.9, 3.3 Hz, 2H), 3.68 (dd, *J* = 5.8, 3.4 Hz, 2H), 3.66 – 3.62 (m, 2H), 3.58 – 3.52 (m, 2H), 3.52 – 3.47 (m, 2H), 3.46 – 3.38 (m, 4H), 3.35 (s, 3H), 3.28 (d, *J* = 3.8 Hz, 3H), 3.32 – 3.26 (m, 4H); ¹³C NMR (126 MHz, CD₃OD): δ 176.63, 159.04, 155.79, 155.73, 152.60, 132.79, 123.87, 122.46, 122.46, 116.55, 114.91, 104.19, 100.83, 72.93, 72.78, 71.76, 71.58, 71.43, 71.34, 71.32, 71.16, 70.55, 70.39, 70.39, 70.16, 59.11, 59.04.

HRMS (ESI): Calculated for C₃₃H₄₀O₁₁N₃ [M+H]⁺ 654.2657, found 654.2642.



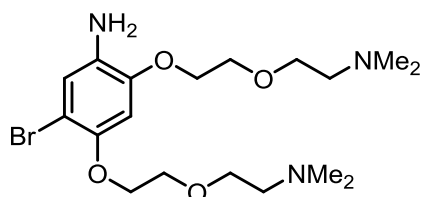
3.3 mg (0.0050 mmol) was dissolved in 0.25 mL MeOH. 3.5 mg (0.025 mmol, 5 equiv.) alkyne **4.25** was added, followed by 0.94 mg (0.0025 mmol, 0.5 equiv.) Cu(MeCN)₄PF₆ and 5 μL (0.01 equiv.) TBTA (from a 10 mM stock in MeOH). The solution was stirred under N₂ overnight in the dark. After 15 h, the reaction was concentrated and purified by HPLC using a 20-100% MeCN/H₂O gradient to yield 2.26 mg **4.13b** (0.0035 mmol, 70%) as an orange-red solid.

HRMS (ESI): Calculated for C₄₀H₅₁O₁₃N₄ [M+H]⁺ 795.3447, found 795.3434.



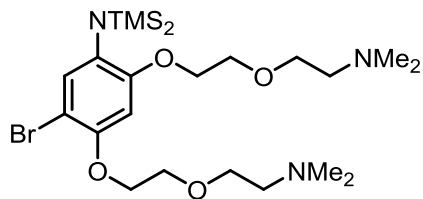
2.59 g (23.1 mmol, 2.59 equiv.) KOtBu, a white powder, was covered with 22 mL dry 1,4-dioxane in a flame-dried flask. Next, 3.24 mL 2-(2-(dimethylamino)ethoxy)ethan-1-ol (3.08 g, 23.1 mmol, 2.1 equiv.) was added. The white suspension turned to a slightly cloudy pale yellow solution. After stirring for 10 min at room temperature, the solution was cooled on ice, turning slightly cloudy. 2.62 g 1-bromo-2,4-difluoro nitrobenzene (11.00 mmol), a pale yellow liquid, was added dropwise, turning the solution to a clear brown color. The mixture was allowed to warm to rt and stirred overnight. After 12 h, the brown solution was diluted with 200 mL 50% brine and extracted with 3 x 100 mL DCM. The organic layers were washed with 3 x 200 mL sat. Na₂CO₃, dried over MgSO₄, and concentrated to yield 4.46 g **4.18** (87%, 9.6 mmol) as a brown oil.

¹H NMR (600 MHz, CDCl₃): δ 8.20 (s, 1H), 6.66 (s, 1H), 4.25 (app. dt, *J* = 7.1, 4.7 Hz, 4H), 3.89 (app. dt, *J* = 9.9, 4.8 Hz, 4H), 3.72 – 3.69 (m, 3H), 3.68 (t, *J* = 6.1 Hz, 2H), 2.51 (app. dt, *J* = 8.4, 5.6 Hz, 4H), 2.26 (s, 6H), 2.25 (s, 6H); ¹³C NMR (126 MHz, CDCl₃): δ 159.87, 154.15, 132.56, 130.28, 101.91, 99.41, 69.95, 69.57, 69.55, 69.41, 68.86, 68.75, 58.62, 58.60, 45.58, 45.52. HRMS (ESI): Calculated for C₁₈H₃₁O₆N₃Br [M+H]⁺ 464.1391, found 464.1389.



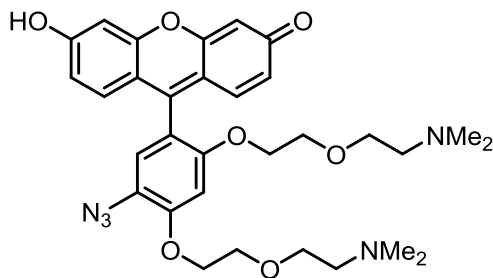
4.51 g **4.18** (9.73 mmol), a brown oil, was dissolved in 30 mL absolute ethanol. Next, 8.78 g (38.92 mmol, 4 equiv.) SnCl₂·2H₂O, a white crystalline solid, was added. The solution immediately turned to a thick yellow slurry. The slurry was vigorously stirred under N₂ at 80 °C for 30 min, during which a brown oil began to accumulate at the bottom of the flask. The solution was cooled on ice, then to the mixture was added 75 mL sat. Na₂CO₃ and 75 mL DCM. Solid was scraped off the sides of the flask with a spatula as needed. After all the solid in the flask was suspended, the mixture was stirred for an hour under N₂. The still cloudy solution diluted with 200 mL H₂O and extracted with 3 x 100 mL DCM. The combined organic extracts were then washed with 3 x 150 mL sat. Na₂CO₃ to remove residual tin salts. The organic extracts were then dried over MgSO₄ and concentrated to yield **4.19** (3.89 g, 8.96 mmol, 92%) as a brown oil.

¹H NMR (500 MHz, CDCl₃): δ 6.86 (s, 1H), 6.56 (s, 1H), 4.14 – 4.10 (m, 2H), 4.10 – 4.06 (m, 2H), 3.81 (app. q, *J* = 4.7 Hz, 4H), 3.68 (t, *J* = 5.8 Hz, 2H), 3.62 (t, *J* = 5.7 Hz, 2H), 2.58 – 2.49 (m, 4H), 2.27 (s, 6H), 2.26 (s, 6H); ¹³C NMR (126 MHz, CDCl₃) δ 147.99, 146.25, 132.56, 118.93, 104.41, 103.15, 70.93, 69.75, 69.74, 69.63, 69.57, 68.78, 59.06, 58.96, 46.03, 46.02; HRMS (ESI): Calculated for C₁₈H₃₃O₄N₃Br [M+H]⁺ 434.1649, found 434.1649.



0.880 mL (4.2 mmol, 2.1 equiv.) hexamethyldisilazane was dissolved in 3 mL dry THF. The solution was cooled to 0 °C, then 1.68 mL 2.5 M n-butyllithium solution (4.2 mmol, 2.1 equiv.) was slowly added. The solution was stirred for 15 minutes, then cooled to -78 °C. While the LiHMDS was being prepared, 0.869 g **4.19** (2.00 mmol), a brown oil, was dried azeotropically with PhMe and dissolved in 4 mL THF, and cooled to -78 °C. The LiHMDS was added dropwise via cannula, turning the light brown solution a deep blue color. The solution was stirred for 10 minutes at -78 °C, then allowed to warm to rt for 5 minutes, then cooled back to -78 °C. Finally, 0.533 mL (4.2 mmol, 2.1 equiv.) trimethylsilyl chloride was added. The solution was warmed to rt and allowed to stir overnight, during which a white precipitate had formed on the sides of the flask. The THF was removed under vacuum. The brown residue was then taken up in 50 mL PhMe, filtered to remove lithium chloride, and re-concentrated to yield the bis-trimethylsilyl protected bromoaniline **4.20** along with small amounts of tris-trimethylamine as a brown oil (1.05 g, 1.81 mmol, 90%).

¹H NMR (400 MHz, CDCl₃): δ 7.01 (s, 1H), 6.46 (s, 1H), 4.14 (t, *J* = 5.0 Hz, 2H), 4.02 (t, *J* = 5.2 Hz, 2H), 3.86 (t, *J* = 5.0 Hz, 2H), 3.80 (t, *J* = 5.2 Hz, 2H), 3.72 (t, *J* = 5.7 Hz, 2H), 3.61 (t, *J* = 5.8 Hz, 2H), 2.53 (app. dt, *J* = 10.9, 5.7 Hz, 4H), 2.28 (s, 6H), 2.27 (s, 6H), 0.02 (s, 18H); ¹³C NMR (126 MHz, CDCl₃): δ 156.12, 152.18, 134.69, 131.08, 101.09, 99.06, 69.70, 69.53, 69.45, 67.16, 58.95, 58.93, 45.98, 45.91, 1.86.

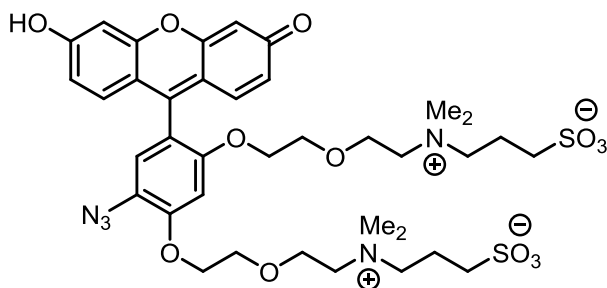


121 mg (0.210 mmol, 2.1 equiv.) **4.20** a brown oil, was dissolved in 1.5 mL dry THF in a flame-dried flask. The solution was cooled to -78 °C. Next, tBuLi (0.42 mmol, 4.2 equiv.) was added. The solution was stirred at -78 °C for 30 minutes. Next, 45.6 mg (0.100 mmol, 1 equiv.) fluorescein xanthone **4.27** was dissolved in 1.5 mL dry THF and added in one portion. The reaction was warmed to room temperature and allowed to stir for 3 hours. The reaction was quenched by the addition of 0.45 mL 2M HCl, immediately turning the solution a deep red color. After 30 seconds, 0.9 mL 1M NaOH was added and the reaction was stirred for 10 minutes. Finally, the solution was reacidified with 0.1 mL AcOH and the solution concentrated to yield the crude aminofluorescein (and excess aniline) as a red solid, which was carried on to the next step without further purification.

The residue was dissolved in 2:1 AcOH/H₂O and cooled to 0 °C. Next, 21.7 mg sodium nitrite (0.32 mmol, 1.5 equiv. relative to aniline) was added and the reaction allowed to stir for 5

minutes. Next, sodium azide (0.42 mmol, 2.0 equiv. relative to aniline) was added. Bubbling was observed. The reaction was stirred for 1 h at 0 °C and 1 h at rt, then concentrated. The orange residue was then taken up in 25 mL acetonitrile and filtered to remove salts. After concentration, the resulting red-orange residue was dissolved in H₂O and purified by reverse-phase HPLC (20 minute gradient from 20-80% MeCN in H₂O + 0.1% TFA) to yield **4.21** (74.1 mg, 0.0904 mmol, 90%) as a red solid.

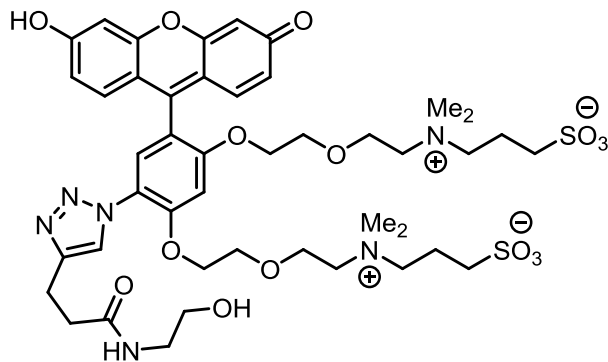
¹H NMR (500 MHz, CD₃OD): δ 7.71 (d, *J* = 9.2 Hz, 2H), 7.28 (d, *J* = 2.2 Hz, 2H), 7.21 (dd, *J* = 9.3, 2.3 Hz, 2H), 7.03 (s, 1H), 7.03 (s, 1H), 4.51 – 4.41 (m, 2H), 4.22 (t, *J* = 4.5 Hz, 2H), 4.09 – 4.01 (m, 2H), 3.99 – 3.93 (m, 2H), 3.54 (t, *J* = 4.5 Hz, 2H), 3.43 (td, *J* = 6.4, 4.6 Hz, 4H), 3.08 – 3.03 (m, 2H), 2.97 (s, 6H), 2.70 (s, 6H); ¹³C NMR (101 MHz, CD₃OD) δ 173.29, 160.79, 156.59, 155.62, 134.81, 124.29, 123.12, 121.48, 121.48, 118.10, 113.87, 103.50, 100.38, 70.48, 70.27, 70.19, 69.62, 65.91, 65.44, 58.16, 57.75, 43.81, 43.51; ..HRMS (ESI): Calculated for C₃₁H₃₈O₇N₅ [M+H]⁺ 592.2766, found 592.2761.



22.0 mg (0.0268 mmol) **4.21** was dissolved in 0.8 mL 1:1 pyridine/Ac₂O and allowed to stir for 2 h. The orange residue was then concentrated and further azeotroped with PhMe to yield crude acetylated fluorescein.

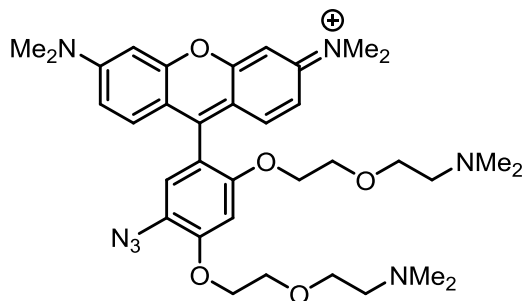
Next, the material was dissolved in 1 mL anhydrous acetonitrile. 32.7 mg propane sultone (0.268 mmol, 10 equiv.), a white solid, was added. Finally, 47 μL dry N,N-diisopropylethylamine was added (0.268 mmol, 10 equiv.) and the solution stirred in the dark overnight (16 h). The solution was then concentrated and diluted with 0.3 mL 0.5 M NaOH. After 5 minutes, the solution was reacidified with a drop of AcOH and immediately purified by reverse phase HPLC (20-80% gradient of MeCN in H₂O) to yield 11.3 mg **CalFluor 488** (0.0135 mmol, 50%) as an orange solid.

¹H NMR (500 MHz, CD₃OD): δ 7.25 (d, *J* = 9.3 Hz, 2H), 7.05 (s, 1H), 6.88 (s, 1H), 6.73 (dd, *J* = 9.2, 2.2 Hz, 2H), 6.68 (d, *J* = 2.2 Hz, 2H), 4.52 – 4.42 (m, 2H), 4.31 – 4.17 (m, 2H), 4.11 – 4.04 (m, 2H), 4.04 – 3.96 (m, 2H), 3.70 – 3.60 (m, 6H), 3.59 – 3.53 (m, 2H), 3.43 – 3.36 (m, 2H), 3.33 (m, 2H), 3.22 (s, 6H), 2.94 (s, 6H), 2.82 (t, *J* = 6.9 Hz, 2H), 2.77 (t, *J* = 6.9 Hz, 2H), 2.26 (dtd, *J* = 14.5, 7.1, 4.5 Hz, 2H), 2.17 – 2.08 (m, 2H); ¹³C NMR (126 MHz, CD₃OD): δ 178.62, 159.48, 155.68, 155.41, 152.95, 132.81, 123.79, 123.26, 122.43, 115.68, 115.33, 104.37, 100.88, 70.42, 70.38, 69.99, 69.67, 65.78, 65.43, 65.00, 64.79, 64.43, 64.21, 52.67, 52.43, 20.12, 20.02; ..HRMS (ESI): Calculated for C₃₇H₅₀O₁₃N₅S₂ [M+H]⁺ 836.2841, found 836.2844.



2.5 mg (0.0030 mmol) **CalFluor 488** was dissolved in 300 μ L 1:1 MeOH/H₂O. Next, 2.1 mg (0.015 mmol, 5 equiv.) alkyne **4.25**, a white solid, was added. The solution was briefly placed under vacuum and backfilled with N₂. Then, 0.6 mg Cu(MeCN)₄PF₆ (0.0015 mmol, 0.5 equiv.) was added. Finally, 0.75 μ L of a 4 mM stock of TBTA in 4:1 tBuOH/DMSO was added. The reaction was allowed to stir under nitrogen in the dark overnight. After 15 hours, LC-MS showed full conversion to product. The solution was concentrated, taken up in H₂O, and purified by HPLC (15-60% gradient) to yield **CalFluor 488 triazole** (2.6 mg, 0.0027 mmol, 89%) as an orange solid.

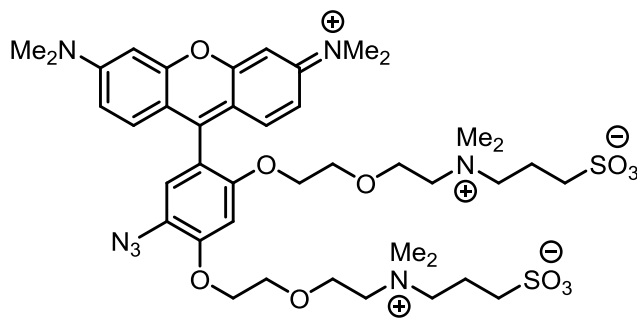
HRMS (ESI): Calculated for C₄₄H₆₁O₁₅N₆S₂ [M+H]⁺ 977.3631, found 977.3639.



215 mg (0.372 mmol, 2.1 equiv.) **4.20**, a brown oil, was dissolved in 1.5 mL dry THF in a flame-dried flask. The solution was cooled to -78 °C. Next, 0.486 mL 1.53 M tBuLi (0.744 mmol, 4.2 equiv.) was added. The solution was stirred at -78 °C for 30 minutes. Next, 50 mg (0.177 mmol, 1 equiv.) rhodamine xanthone **4.28** was suspended in 1.5 mL dry THF and added in one portion. The reaction was warmed to room temperature and allowed to stir for 3 hours. The reaction was quenched by the 0.4 mL 1:1 AcOH/H₂O. The solution immediately turned a deep magenta color. After stirring for 5 minutes, the solution was concentrated to yield a magenta residue, which was carried on to the next step without further purification.

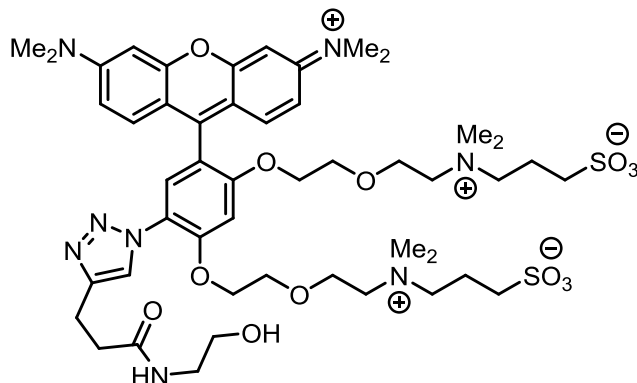
The residue was dissolved in 15 mL 2:1 AcOH/H₂O and cooled to 0 °C. Next, 37.9 mg sodium nitrite (0.558 mmol, 1.5 equiv. relative to aniline) was added and the reaction allowed to stir for 5 minutes. Next, 49.1 mg sodium azide (0.744 mmol, 2.0 equiv. relative to aniline) was added. Bubbling was observed. The reaction was stirred for 1 h at 0 °C and 1 h at rt, then concentrated. The orange residue was then taken up in 25 mL acetonitrile and filtered to remove salts. After concentration, the resulting magenta residue was dissolved in H₂O and purified by reverse-phase HPLC (gradient of 20-80% MeCN in H₂O + 0.1% TFA) to yield **4.22** (71.1 mg, 0.0814 mmol, 46%) as a red solid.

^1H NMR (500 MHz, CD_3OD): δ 7.38 (d, $J = 9.5$ Hz, 2H), 7.11 (dd, $J = 9.6, 2.5$ Hz, 2H), 7.02 (s, 1H), 6.96 (d, $J = 2.5$ Hz, 2H), 6.87 (s, 1H), 4.40 (dd, $J = 5.4, 3.5$ Hz, 2H), 4.17 – 4.10 (m, 2H), 3.96 – 3.89 (m, 2H), 3.74 (t, $J = 5.6$ Hz, 2H), 3.51 – 3.43 (m, 2H), 3.33 (s, 12H), 3.25 (t, $J = 5.5$ Hz, 2H), 2.65 (t, $J = 5.6$ Hz, 2H), 2.34 (s, 6H), 2.21 (t, $J = 5.5$ Hz, 2H), 2.06 (s, 6H); ^{13}C NMR (126 MHz, CDCl_3): δ 159.11, 158.80, 156.60, 156.28, 155.81, 132.95, 124.05, 122.65, 115.35, 115.09, 114.36, 100.64, 97.36, 70.46, 70.35, 70.15, 70.05, 69.93, 69.64, 59.51, 59.21, 45.81, 45.63, 40.97; HRMS (ESI): Calculated for $\text{C}_{35}\text{H}_{48}\text{O}_5\text{N}_7$ $[\text{M-TFA}]^+$ 646.3711, found 646.3700.



25.0 mg **4.22** (0.0286 mmol), a blue solid, was dissolved in 1.5 mL dry MeCN. To the solution was added 34.9 mg 1,3-propane sultone (0.286 mmol, 10 equiv.), a white crystalline solid, followed by 49 μL of *N,N*-diisopropylethylamine (0.286 mmol, 10 equiv.). The solution was stirred in the dark overnight. The solution was then concentrated, taken up in H_2O , and purified by reverse phase HPLC (20-80% gradient of MeCN in H_2O) to yield **CalFluor 555** (25.7 mg, 0.0211 mmol, 57%) as a magenta solid.

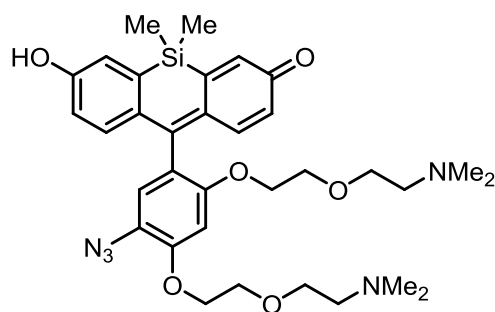
^1H NMR (500 MHz, CD_3OD): δ 7.45 (d, $J = 9.5$ Hz, 2H), 7.16 (dd, $J = 9.5, 2.5$ Hz, 2H), 7.10 (s, 1H), 6.98 (d, $J = 2.5$ Hz, 2H), 6.90 (s, 1H), 4.53 – 4.42 (m, 2H), 4.27 (dd, $J = 5.7, 3.8$ Hz, 2H), 4.12 – 4.04 (m, 2H), 4.04 – 3.96 (m, 2H), 3.68 (app. qd, $J = 9.8, 8.5, 5.5$ Hz, 6H), 3.59 – 3.50 (m, 2H), 3.39 – 3.35 (m, 4H), 3.34 (s, 12H), 3.22 (s, 6H), 2.92 (s, 6H), 2.76 (t, $J = 7.0$ Hz, 2H), 2.71 (t, $J = 6.8$ Hz, 2H), 2.32 – 2.20 (m, 2H), 2.14 – 2.02 (m, 2H); ^{13}C NMR (126 MHz, CDCl_3): δ 159.13, 158.93, 156.55, 155.83, 155.72, 133.16, 123.99, 122.53, 115.64, 115.08, 114.56, 101.01, 97.41, 70.35, 70.19, 70.05, 69.41, 65.76, 65.33, 64.82, 64.69, 64.23, 64.13, 52.80, 52.40, 41.03, 20.21, 19.97; HRMS (ESI): Calculated for $\text{C}_{41}\text{H}_{60}\text{O}_{11}\text{N}_7\text{S}_2$ $[\text{M-TFA}]^+$ 890.3787, found 890.3774.



3.01 mg (0.0030 mmol) **CalFluor 555** was dissolved in 300 μL 1:1 MeOH/ H_2O . Next, 2.1 mg (0.015 mmol, 5 equiv.) alkyne **4.25**, a white solid, was added. The solution was briefly placed

under vacuum and backfilled with N₂. Then, 0.6 mg Cu(MeCN)₄PF₆ (0.0015 mmol, 0.5 equiv.) was added. Finally, 0.75 uL of a 4 mM stock of TBTA in 4:1 tBuOH/DMSO was added. The reaction was allowed to stir under nitrogen in the dark overnight. After 15 hours, LC-MS showed full conversion to product. The solution was concentrated, taken up in H₂O, and purified by HPLC (15-60% gradient) to yield **CalFluor 555 triazole** (2.0 mg, 0.0019 mmol, 65%) as a magenta solid.

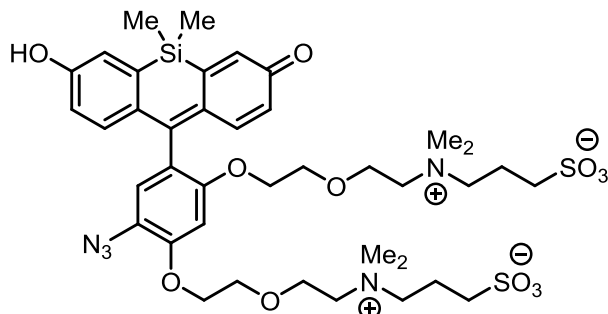
HRMS (ESI): Calculated for C₄₈H₇₁O₁₃N₈S₂ [M-TFA]⁺ 1031.4577, found 1031.4569.



0.121 g **4.20** (0.210 mmol, 2.1 equiv.), a brown oil, was dissolved in 1 mL dry THF. The solution was cooled to -78 °C. Next, 0.31 mL (0.420 mmol, 4.2 equiv.) 1.36 M t-butyllithium was added, turning the solution a darker brown. The solution was stirred at -78 C for 30 minutes, then 50 mg (0.100 mmol) Si-fluorescein xanthone **4.29**, a pale yellow solid, dissolved in 1 mL dry THF was added. The solution was warmed to rt and stirred for 3 h. The solution was quenched with 0.2 mL 2M HCl, turning it a red-orange color. After 30 seconds, 0.4 mL 1M NaOH was added, turning the solution purple. After 10 minutes, 0.1 mL AcOH was added and the solution was concentrated to yield crude amino-Si-fluorescein (and excess aniline).

The residue was dissolved in 9 mL 2:1 AcOH/H₂O and cooled to 0 °C. Next, 21.7 mg sodium nitrite (0.32 mmol, 1.5 equiv. relative to aniline) was added and the reaction allowed to stir for 5 minutes. Next, 27.7 mg sodium azide (0.42 mmol, 2.0 equiv. relative to aniline) was added. Bubbling was observed. The reaction was stirred for 1 h at 0 °C and 1 h at rt, then concentrated. The orange residue was then taken up in 25 mL acetonitrile, filtered, and reconcentrated to remove salts. The resulting red-orange residue was dissolved in H₂O and purified by reverse-phase HPLC (20-80% gradient of MeCN in H₂O) to yield **4.23** (52.5 mg, 0.0609 mmol, 61%) as a red solid.

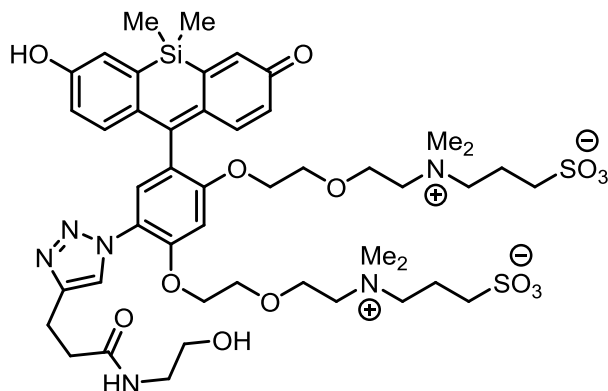
¹H NMR (400 MHz, CD₃CN): δ 8.16 (br, 1H), 8.01 (br, 1H), 7.15 – 7.07 (m, 4H), 6.80 (s, 1H), 6.79 (s, 1H), 6.55 (dd, *J* = 9.4, 2.5 Hz, 2H), 4.39 – 4.23 (m, 2H), 4.07 (dd, *J* = 5.4, 3.2 Hz, 2H), 3.96 – 3.90 (m, 2H), 3.90 – 3.81 (m, 2H), 3.59 – 3.48 (m, 2H), 3.42 – 3.35 (m, 2H), 3.30 (app. q, *J* = 5.2 Hz, 2H), 2.95 – 2.88 (m, 2H), 2.87 (d, *J* = 5.0 Hz, 6H), 2.61 (d, *J* = 4.9 Hz, 6H), 0.47 (s, 3H), 0.47 (s, 3H); ¹³C NMR (126 MHz, CDCl₃): δ 172.63, 155.01, 153.84, 148.37, 142.78, 132.06, 129.28, 123.40, 122.21, 122.04, 121.94, 115.96, 100.54, 70.24, 69.94, 65.34, 65.12, 58.03, 57.71, 44.19, 43.87, -1.45, -1.52; HRMS (ESI): Calculated for C₃₃H₄₄O₆N₅Si [M+H]⁺ 634.3055, found 634.3057.



21.0 mg **4.23** (0.0243 mmol) was dissolved in 0.8 mL 1:1 pyridine/Ac₂O and stirred in the dark for 2h. The solvent was removed under vacuum and azeotroped with toluene to remove any residual solvent to yield the crude acetylated Si-fluorescein as a very pale orange residue, which was used directly in the next step.

The material was dissolved in 1 mL dry acetonitrile and 29.7 mg 1,3-propane sultone (0.243 mmol, 10 equiv.) was added. Finally, 42 μ L dry N,N-diisopropylethylamine was added (0.243 mmol, 10 equiv.) and the solution stirred in the dark overnight (16 h). The solution was then concentrated and diluted with 0.3 mL 0.5 M NaOH, turning the solution a purple color. After 5 minutes, the solution was reacidified with a drop of AcOH and immediately purified by reverse phase HPLC (20-80% gradient of MeCN in H₂O) to yield **CalFluor 580** (8.7 mg, 0.0990 mmol, 41%) as an orange solid.

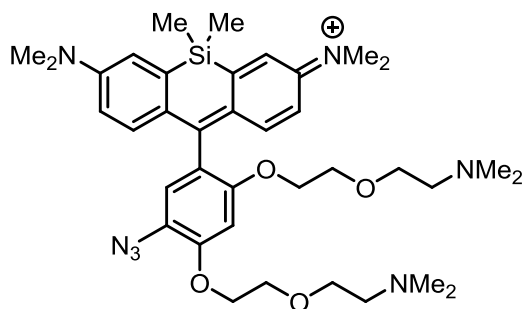
¹H NMR (500 MHz, D₂O) δ 7.06 (d, J = 2.5 Hz, 2H), 6.88 (d, J = 9.5 Hz, 2H), 6.69 (s, 1H), 6.48 (s, 1H), 6.22 (dd, J = 9.5, 2.5 Hz, 2H), 4.16 (br, 2H), 4.03 (br, 2H), 3.97 (br, 2H), 3.81 (app. d, J = 5.0 Hz, 2H), 3.61 (app. d, J = 6.4 Hz, 2H), 3.52 (app. dt, J = 11.3, 5.6 Hz, 6H), 3.27 – 3.17 (m, 2H), 3.15 (s, 6H), 2.86 (d, J = 7.2 Hz, 2H), 2.83 (s, 6H), 2.77 (t, J = 7.3 Hz, 2H), 2.20 (m, 2H), 2.02 (m, 2H), 0.43 (s, 3H), 0.39 (s, 3H); ¹³C NMR (151 MHz, CD₃CN): δ 157.39, 154.47, 153.76, 152.03, 143.19, 136.36, 130.54, 129.10, 121.83, 121.12, 120.84, 118.69, 116.01, 99.93, 69.06, 69.00, 68.66, 68.50, 64.33, 63.96, 63.76, 63.66, 63.10, 63.03, 51.58, 51.23, 47.27, 47.20, 18.47, 18.34, -2.34, -2.62. HRMS (ESI): Calculated for C₃₉H₅₆O₁₂N₅S₂Si [M+H]⁺ 878.3131, found 878.3134.



3.0 mg (0.0030 mmol) **CalFluor 580** was dissolved in 300 μ L 1:1 MeOH/H₂O. Next, 2.1 mg (0.015 mmol, 5 equiv.) alkyne **4.25**, a white solid, was added. The solution was briefly placed

under vacuum and backfilled with N₂. Then, 0.6 mg Cu(MeCN)₄PF₆ (0.0015 mmol, 0.5 equiv.) was added. Finally, 0.75 μL of a 4 mM stock of TBTA in 4:1 tBuOH/DMSO was added. The reaction was allowed to stir under nitrogen in the dark overnight. After 15 hours, LC-MS showed full conversion to product. The solution was concentrated, a few drops of AcOH were added, then the solution was diluted in H₂O and purified by HPLC (15-60% gradient) to yield **CalFluor 580 triazole** (1.4 mg, 0.014 mmol, 46%) as an orange solid.

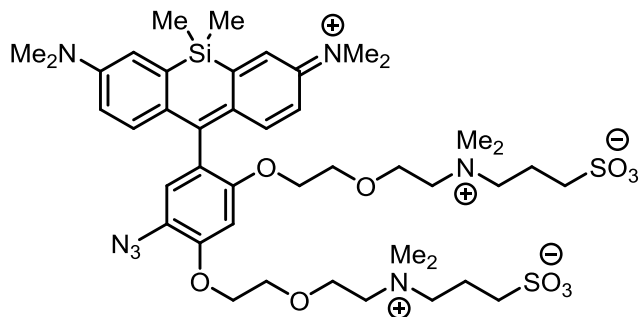
HRMS (ESI): Calculated for C₄₆H₆₅O₁₄N₆S₂Si [M-H]⁻ 1017.3775, found 1017.3765.



0.187 g **4.20** (0.323 mmol, 2.1 equiv.), a brown oil, was dissolved in 1 mL dry THF in a flame-dried flask. The solution was cooled to -78 °C, then 0.38 mL 1.70 M tBuLi (0.646 mmol, 4.2 equiv.) was added. The solution was stirred for 30 min at -78 °C, then 50 mg (0.154 mmol) Si-xanthone **4.30**, a yellow solid, was suspended in 1 mL dry THF and added in one portion. The solution turned from a deep brown to a reddish color. The reaction was stirred at rt for 3 h, then quenched with 0.6 mL 1:1:1 MeOH/H₂O/AcOH, immediately turning the solution a deep blue color. The blue solution was stirred for 15 minutes, then concentrated and taken directly onto the next step.

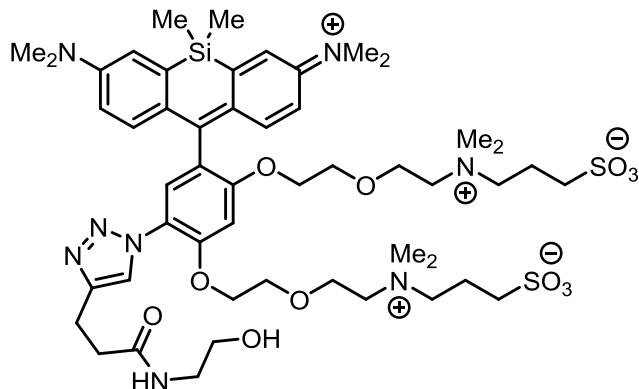
The blue residue was dissolved in 13 mL 2:1 AcOH/H₂O and cooled to 0 °C. Next, 32.5 mg sodium nitrite (0.484 mmol, 1.5 equiv. relative to aniline) was added and the reaction allowed to stir for 5 minutes. Next, 42.0 mg sodium azide (0.646 mmol, 2.0 equiv. relative to aniline) was added. Bubbling was observed. The reaction was stirred for 1 h at 0 °C and 1 h at rt, then concentrated. The blue residue was then taken up in 25 mL acetonitrile and filtered to remove salts. After concentration, the resulting blue residue was dissolved in H₂O and purified by reverse-phase HPLC (20 minute gradient from 20-80% MeCN in H₂O + 0.1% TFA) to yield 46.5 mg **4.24** (0.0507 mmol, 33%) as a blue solid.

¹H NMR (500 MHz, CD₃OD): δ 7.34 (d, *J* = 2.9 Hz, 2H), 7.24 (d, *J* = 9.7 Hz, 2H), 6.92 (s, 1H), 6.81 (dd, *J* = 9.6, 2.8 Hz, 2H), 6.74 (s, 1H), 4.43 – 4.31 (m, 2H), 4.19 – 4.10 (m, 2H), 4.06 – 3.98 (m, 2H), 3.98 – 3.91 (m, 2H), 3.61 (app. q, *J* = 5.2, 4.6 Hz, 2H), 3.53 – 3.47 (m, 2H), 3.47 – 3.39 (m, 2H), 3.36 (s, 12H), 3.05 – 2.99 (m, 2H), 2.97 (s, 6H), 2.70 (s, 6H), 0.59 (s, 3H), 0.59 (s, 3H); ¹³C NMR (126 MHz, CDCl₃): δ 167.60, 155.63, 154.60, 149.31, 142.65, 129.22, 123.67, 122.30, 121.95, 121.77, 115.04, 100.16, 70.56, 70.48, 70.05, 70.01, 65.88, 65.59, 58.11, 57.73, 43.75, 43.41, 40.91, -0.97, -1.30; HRMS (ESI): Calculated for C₃₇H₅₄O₄N₇Si [M-TFA]⁺ 688.4001, found 688.3993.



34.0 mg **4.24** (0.0372 mmol), a blue solid, was dissolved in 1.5 mL dry MeCN. To the solution was added 51.9 mg 1,3-propane sultone (0.372 mmol, 10 equiv.), a white crystalline solid, followed by 74 μ L (0.372 mmol, 10 equiv.) of N,N-diisopropylethylamine. The solution was stirred in the dark overnight. The solution was then concentrated, taken up in H₂O, and purified by reverse phase HPLC (20-80% gradient) to yield **CalFluor 647** (22.1 mg, 0.0211 mmol, 57%) as a blue solid.

¹H NMR (400 MHz, CD₃CN): δ 7.28 – 7.18 (m, 4H), 7.06 (s, 1H), 6.81 (dd, *J* = 9.7, 2.9 Hz, 2H), 6.74 (s, 1H), 4.45 (app. dd, *J* = 5.5, 3.7 Hz, 2H), 4.19 (app. dd, *J* = 5.7, 3.7 Hz, 2H), 4.00 (app. d, *J* = 5.2 Hz, 2H), 3.96 – 3.89 (m, 2H), 3.68 (app. d, *J* = 5.2 Hz, 2H), 3.66 – 3.58 (m, 2H), 3.58 – 3.53 (m, 12), 3.53 – 3.47 (m, 2H), 3.45 (app. dd, *J* = 8.2, 4.1 Hz, 2H), 3.30 (s, 12H), 3.28 – 3.22 (m, 2H), 3.12 (s, 6H), 2.87 (s, 6H), 2.57 (app. t, *J* = 6.8 Hz, 4H), 2.14 (m, 2H), 2.07 – 1.98 (m, 2H), 0.56 (s, 3H), 0.55 (s, 3H); ¹³C NMR (151 MHz, CD₃CN): δ 165.40, 154.09, 153.85, 152.36, 147.78, 141.29, 127.65, 121.90, 121.06, 120.94, 118.86, 114.03, 100.23, 69.11, 69.09, 68.80, 68.63, 64.44, 64.09, 63.85, 63.71, 63.17, 63.09, 51.77, 51.33, 47.39, 47.28, 18.61, 18.47, -1.83, -2.00; HRMS (ESI): Calculated for C₄₃H₆₆O₁₀N₇S₂Si [M-TFA]⁺ 932.4076, found 932.4070.



3.0 mg (0.0030 mmol) **CalFluor 647** was dissolved in 300 μ L 1:1 MeOH/H₂O. Next, 2.1 mg (0.015 mmol, 5 equiv.) alkyne **4.25**, a white solid, was added. The solution was briefly placed under vacuum and backfilled with N₂. Then, 0.6 mg Cu(MeCN)₄PF₆ (0.0015 mmol, 0.5 equiv.) was added. Finally, 0.75 μ L of a 4 mM stock of TBTA in 4:1 tBuOH/DMSO was added. The reaction was allowed to stir under nitrogen in the dark overnight. After 15 hours, LC-MS showed full conversion to product. The solution was concentrated, a few drops of AcOH were added, then the solution was diluted in H₂O and purified by HPLC (15-60% gradient) to yield **CalFluor 647 triazole** (2.4 mg, 0.0022 mmol, 75%) as a blue solid.

HRMS (ESI): Calculated for $C_{50}H_{77}O_{12}N_8S_2Si$ [M-TFA]⁺ 1073.4866, found 1073.4860.

References

1. Hein, J. E.; Tripp, J. C.; Krasnova, L. B.; Sharpless, K. B.; Fokin, V. V. *Angew. Chem. Int. Ed.* **2009**, *48*, 8018-8021.
2. Egawa, T.; Koide, Y.; Hanaoka, K.; Komatsu, T.; Terai, T.; Nagano, T. *Chem. Commun.* **2011**, *47*, 4162-4164.
3. Shieh, P. Hangauer, M. J.; Bertozzi, C. R. *J. Am. Chem. Soc.* **2012**, *134*, 17428-17431.
4. Besanceney-Webler, C.; Jiang, H.; Zheng, T.; Feng, L.; Soriano del Amo, D.; Wang, W.; Klivansky, L. M.; Marlow, F. L.; Liu, Y.; Wu, P. *Angew. Chem. Int. Ed.* **2011**, *50*, 8051-8056.
5. Shieh, P.; Siegrist, M. S.; Cullen, A. J.; Bertozzi, C. R. *Proc. Natl. Acad. Sci.* **2014**, *111*, 5456-5461.
6. Sunahara, H.; Urano, Y.; Kojima, H.; Nagano, T. *J. Am. Chem. Soc.* **2007**, *129*, 5597-5604.
7. For selected references, see: (a) Butun, V.; Bennett, C. E.; Vamvakaki, M.; Lowe, A. B.; Billingham, N. C.; Armes, S. P. *J. Mater. Chem.* **1997**, *7*, 1693-1695. (b) Homlin, R. E.; Chen, X.; Chapman, R. G.; Takayama, S.; and Whitesides, G. M. *Langmuir* **2001**, *17*, 2841-2850. (c) Zhang, Z.; Chao, T.; Chen, S.; Jiang, S. *Langmuir* **2006**, *22*, 10072-10077. (d) Yang, R.; Xu, J.; Ozaydin-Ince, G.; Wong, S. Y.; and Gleason, K. K. *Chem. Mater.* **2011**, *23*, 1263-1272.
8. Jiang, S. Y.; Cao, Z. Q. *Adv. Mater.* **2010**, *22*, 920-932.
9. Zhang, L.; Cao, Z.; Bai, T.; Carr, L.; Ella-Menye, J.-R.; Irvin, C.; Ratner, B. D.; Jiang, S. *Nat. Biotechnol.* **2012**, *31*, 553-556.
10. Smith, R. S.; Zhang, Z.; Bouchard, M.; Li, J.; Lapp, H. S.; Brotske, G. R.; Lucchino, D. L.; Weaver, D.; Roth, L. A.; Coury, A.; Biggerstaff, J.; Sukavaneshvar, S.; Langer, R.; Loose, C. *Sci. Transl. Med.* **2012**, *4*, 153ra132.
11. Choi, H. S.; Nasr, K.; Alyabyev, S.; Feith, D.; Lee, J. H.; Kim, S. H.; Ashitate, Y.; Hyun, H.; Patonay, G.; Strekowski, L.; Henary, M.; Frangioni, J. V. *Angew. Chem. Int. Ed.* **2011**, *50*, 6258-6263.
12. Huang, J.; Xu, W. J. *Appl. Polymer Sci.* **2011**, *122*, 1251-1257.
13. Hsu, T.-L.; Hanson, S. R.; Kishikawa, K.; Wang, S.-K.; Sawa, M.; Wong, C.-H. *Proc. Natl. Acad. Sci.* **2007**, *104*, 2614-2619.
14. Chang, P. V.; Chen, X.; Smyrniotis, C.; Xenakis, A.; Hu, T. S.; Bertozzi, C. R.; Wu, P. *Angew. Chem. Int. Ed.* **2009**, *48*, 4030-4033.
15. Sivakumar, K.; Xie, F.; Cash, B. M.; Long, S.; Barnhill, H. N.; Wang, Q. *Org. Lett.* **2004**, *6*, 4603-4606.
16. Rodionov, V. O.; Presolski, S. I.; Diaz, D. D.; Fokin, V. V.; Finn, M. G. *J. Am. Chem. Soc.* **2007**, *129*, 12705-12712.
17. Laughlin, S. T.; Baskin, J. M.; Amacher, S. L.; Bertozzi, C. R. *Science* **2008**, *320*, 664-667.
18. Baskin, J. M.; Dehnert, K. W.; Laughlin, S. T.; Amacher, S. L.; Bertozzi, C. R. *Proc. Natl. Acad. Sci.* **2010**, *107*, 10360-10365.
19. Dehnert, K. W.; Beahm, B. J.; Huynh, T. T.; Baskin, J. M.; Laughlin, S. T.; Wang, W.; Wu, P.; Amacher, S. L.; Bertozzi, C. R. *ACS Chem. Biol.* **2011**, *6*, 547-552.
20. Dehnert, K. W.; Baskin, J. M.; Laughlin, S. T.; Beahm, B. J.; Naidu, N. N.; Amacher, S. L.; Bertozzi, C. R. *ChemBioChem* **2012**, *13*, 353-357.

21. Beahm, B. J.; Dehnert, K. W.; Derr, N. L.; Kuhn, J.; Eberhart, J. K.; Spillmann, D.; Amacher, S. L.; Bertozzi, C. R. *Angew. Chem. Int. Ed.* **2014**, *53*, 3347-3352.
22. Salic, A.; Mitchison, T. J. *Proc. Natl. Acad. Sci.* **2008**, *105*, 2415-2420.
23. Li, K.; Lee, L. A.; Lu, X.; Wang, Q. *Biotechniques* **2010**, *49*, 525-527.
24. Jao, C. Y.; Salic, A. *Proc. Natl. Acad. Sci.* **2008**, *105*, 15779-15784.
25. Rieder, U.; Luedtke, N. W. *Angew. Chem. Int. Ed.* **2014**, *53*, 916.
26. Sasaki, E.; Kojima, H.; Hiroaki, N.; Urano, Y.; Kikuchi, K.; Hirata, Y.; Nagano, T. *J. Am. Chem. Soc.* **2005**, *127*, 3684-3685.
27. van Hest, J. C. M.; Kiick, K. L.; Tirrell, D. A. *J. Am. Chem. Soc.* **2000**, *122*, 1282-1288.
28. Beatty, K. E.; Xie, F.; Wang, Q.; Tirrell, D. A. *J. Am. Chem. Soc.* **2005**, *127*, 14150-14151.
29. Beatty, K. E.; Liu, J. C.; Xie, F.; Dieterich, D. C.; Schuman, E. M.; Wang, Q.; Tirrell, D. A. *Angew. Chem. Int. Ed.* **2006**, *45*, 7364-7367.
30. Sjoback, R.; Nygren, J.; Kubista, M. *Biopolymers* **1998**, *46*, 445-453.
31. Spahn, C.; Endesfelder, U.; Heilemann, M. *J. Struct. Biol.* **2014**, *185*, 243-249.
32. Watson, R. O.; Manzanillo, P. S.; Cox, J. S. *Cell* **2012**, *150*, 803-815.
33. Boens, N.; Leen, V.; Dehaen, W. *Chem. Soc. Rev.* **2012**, *41*, 1130-1172.
34. Song, F.; Peng, X.; Lu, E.; Wang, Y.; Zhou, W.; Fan, J. *Tet. Lett.* **2005**, *46*, 4817-4820.
35. Fahrni, C. J.; Yang, L.; VanDerveer, D. G. *J. Am. Chem. Soc.* **2003**, *125*, 3799-3812.
36. Shie, J.-J.; Liu, Y.-C.; Lee, Y.-M.; Lim, C.; Fang, J.-M.; Wong, C.-H. *J. Am. Chem. Soc.*, **2014**, *136*, 9953-9961.
37. Koide, Y.; Urano, Y.; Hanaoka, K.; Piao, W.; Kusakabe, M.; Saito, N.; Terai, T.; Okabe, T.; Nagano, T. *J. Am. Chem. Soc.* **2012**, *134*, 5029-5031.
38. Yogo, T.; Urano, Y.; Mizushima, A.; Sunahara, H.; Inoue, T.; Hirose, K.; Iino, M.; Kikuchi, K.; Nagano, T. *Proc. Natl. Acad. Sci.* **2008**, *105*, 28-32.
39. Terai, T.; Urano, Y.; Izumi, S.; Kojima, H.; Nagano, T. *Chem. Commun.* **2012**, *48*, 2840-2842.
40. Kojima, H.; Nakatsubo, N.; Kikuchi, K.; Kawahara, S.; Kirino, Y.; Nagoshi, H.; Hirata, Y.; Nagano, T. *Anal. Chem.* **1998**, *70*, 2446-2453.
41. Kojima, H.; Hirotani, M.; Nakatsubo, N.; Kikuchi, K.; Urano, Y.; Higuchi, T.; Hirata, Y.; Nagano, T. *Anal. Chem.* **2001**, *73*, 1967-1973.
42. Gabe, Y.; Urano, Y.; Kikuchi, K.; Kojima, H.; Nagano, T. *J. Am. Chem. Soc.* **2004**, *126*, 3357-3367.
43. Zhang, H.-X.; Chen, J.-B.; Guo, X.-F.; Wang, H.; Zhang, H.-S. *Anal. Chem.* **2014**, *86*, 3115-3123.
44. Romieu, A.; Massif, C.; Rihn, S.; Ulrich, G.; Ziessel, R.; Renard, P.-Y. *New J. Chem.* **2013**, *37*, 1016-1027.
45. Renier, N.; Wu, Z.; Simon, D. J.; Yang, J.; Ariel, P.; Tessier-Lavigne, M. *Cell* **2014**, *159*, 896-910.
46. Uttamapinant, C.; Tangpeerachaikul, A.; Grecian, S.; Clarke, S.; Singh, U.; Slade, P.; Gee, K. R.; Ting, A. Y. *Angew. Chem. Int. Ed.* **2012**, *51*, 5852-5856.
47. Bevilacqua, V.; King, M.; Chaumontet, M.; Nothisen, M.; Gabillet, S.; Buisson, D.; Puente, C.; Wagner, A.; Taran, F. *Angew. Chem. Int. Ed.* **2014**, *53*, 5872-5876.
48. Jiang, H.; Zheng, T.; Lopez-Aguilar, A.; Feng, L.; Marlow, F. L.; Wu, P. *Bioconjug. Chem.* **2014**, *25*, 698-706.

49. Pagliai, F; Pirali, T.; Del Grosso, E.; Di Brisco, R.; Cesare Tron, G.; Sorba, G.; Genazzani, A. A. *J. Med. Chem.* **2006**, *49*, 467-470.
50. Hu, M.; Li, J.; Yao, S. Q. *Org. Lett.* **2008**, *10*, 5529-5531.
51. Radchenko O. S.; Sigida E. N.; Balaneva N. N.; Dmitrenok P. S.; Novikov V. L.; *J. Heterocyclic Chem.* **2011**, *48*, 209-214.

Chapter 5: Metabolic Incorporation of Cyclooctynes into Bacterial Peptidoglycan

Introduction

Peptidoglycan is a major component of the bacterial cell wall.¹ The peptidoglycan polymer is crucial for bacterial viability, giving bacteria the structural integrity needed to survive under conditions of osmotic stress. Peptidoglycan consists of alternating chains of the glycans *N*-acetylmuramic acid (MurNAc) and *N*-acetylglucosamine (GlcNAc, Figure 5-1).² Attached to the *N*-acetylmuramic acid is a stem peptide comprised of anywhere from three to five amino acids. Crosslinking between adjacent peptidoglycan chains forms a mesh-like network that comprises the peptidoglycan polymer. Slight variations in peptidoglycan structure exist between bacterial species, such as the types of amino acids incorporated into the stem peptide, the site and chemical structure of the peptide crosslinks, and chemical modifications to the glycans. Nevertheless, the overall structure and functional significance of peptidoglycan remains the same across all bacterial species, including Gram-positive and Gram-negative bacteria.

As peptidoglycan has no human analog but is so crucial to bacterial survival, it has been a popular target for antibacterials. For example, the body naturally produces lysozyme, an enzyme that cleaves and depolymerizes peptidoglycan, as a first-line defense against bacterial invaders. Additionally, myriad antibiotics target peptidoglycan biosynthesis, such as the β -lactams, fosfomycin, vancomycin, D-cycloserine, and teixobactin. Given this, chemical tools to study peptidoglycan biosynthesis in an infection setting may open up new therapeutic avenues to target bacterial pathogens.

Ample evidence exists that the bacterial cell wall changes dramatically in an infection setting as compared to *in vitro*. For example, *Mycobacterium tuberculosis* isolated from patients shows dramatically different cell-wall staining as compared to bacteria grown in media.³ Moreover, analysis of the bacterial peptidoglycan molecular structure shows that the types of crosslinks also change dramatically in an infection setting.⁴ Such structural changes in different environments are not too surprising given the important role that the cell wall plays in bacterial survival.

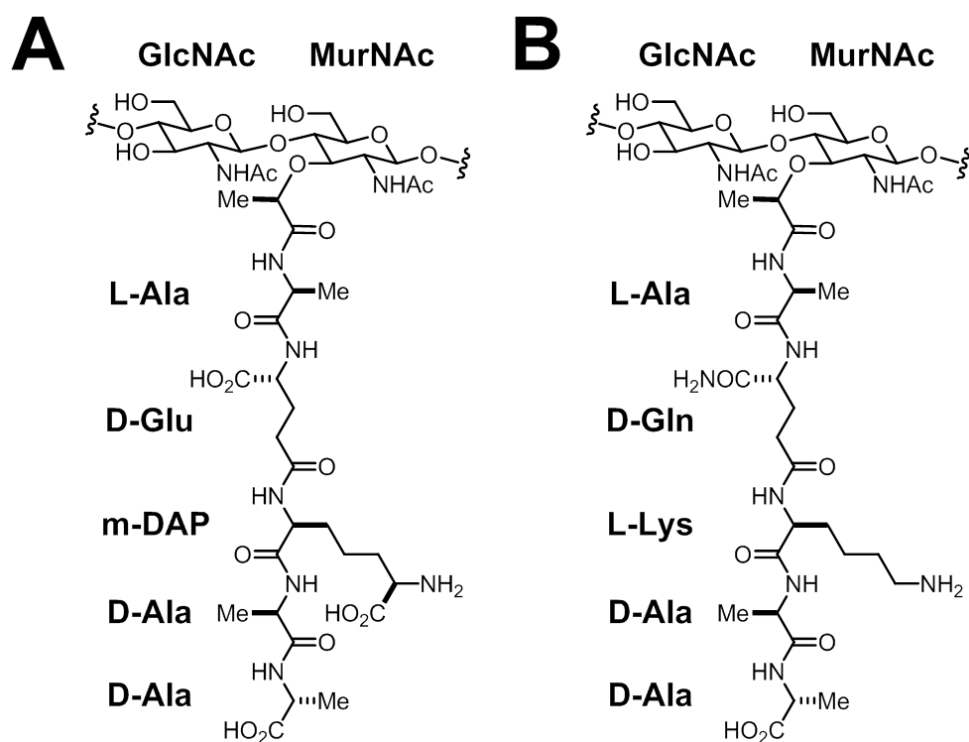


Figure 5-1. Structure of un-crosslinked peptidoglycan in (A) Gram-negative bacteria and Gram-positive bacilli and (B) most other Gram-positive bacteria.

Many approaches exist for visualizing the bacterial cell wall, but none have been successfully applied to study cell wall synthesis in an infection setting. Fluorescent lectins, for example, bind the glycans of peptidoglycan with high affinity and selectivity.^{5,6} However, lectins are not selective for nascent peptidoglycan, preventing their specific visualization. Similar limitations apply to strategies involving enzymatic ligation of fluorescent substrates onto the cell wall.^{7,8} To mark nascent peptidoglycan, fluorescent vancomycin derivatives have been developed.¹⁰ Vancomycin binds newly installed stem peptides with high affinity, enabling their selective labeling and detection. This high affinity binding, however, prevents peptidoglycan crosslinking and maturation, leading to the observed toxicity of vancomycin and preventing long-term imaging experiments. Beyond these limitations, none of these strategies are applicable to Gram-negative bacteria and intracellular pathogens due to poor permeability of the detection reagent. Therefore, we aimed to develop a metabolic labeling approach that address these limitations and would enable the long-term visualization of peptidoglycan synthesis of bacterial pathogens during infection. In this chapter, I discuss the development of D-amino acid analogs bearing cyclooctynes as powerful tools for the visualization and study of newly synthesized peptidoglycan in bacteria.

Results and Discussion

To incorporate unnatural metabolites into peptidoglycan, one must first consider the biosynthetic pathway for peptidoglycan synthesis (Figure 5-2).¹⁰ Peptidoglycan biosynthesis begins from

Uridine diphosphate-*N*-acetylmuramic acid (UDP-MurNAc). Over the course of multiple enzymatic steps, the pentapeptide is assembled as a mix of D- and L- amino acids. The UDP-MurNAc pentapeptide is then anchored to the cell membrane by covalent attachment to the bactoprenol, forming the Lipid I intermediate. Another enzyme then attaches UDP-*N*-acetylglucosamine to form the Lipid II intermediate. Lipid II is flipped across the membrane, and then the muropeptide transferred onto existing peptidoglycan. Further enzymatic steps then truncate and crosslink the stem peptides to form mature peptidoglycan.

Our laboratory initially sought to metabolically incorporate unnatural monosaccharides into peptidoglycan. Preliminary results suggested that *N*-azidoacetylglucosamine (GlcNAz) was incorporated into nascent peptidoglycan, as judged by inhibition of labeling by various cell wall synthesis inhibitors. While promising, this compound would likely label other bacterial glycoconjugates as well.¹¹ More importantly, in an infection setting, GlcNAz would be efficiently processed and incorporated into host glycoproteins, and therefore prevent the selective visualization of bacterial pathogens.¹²

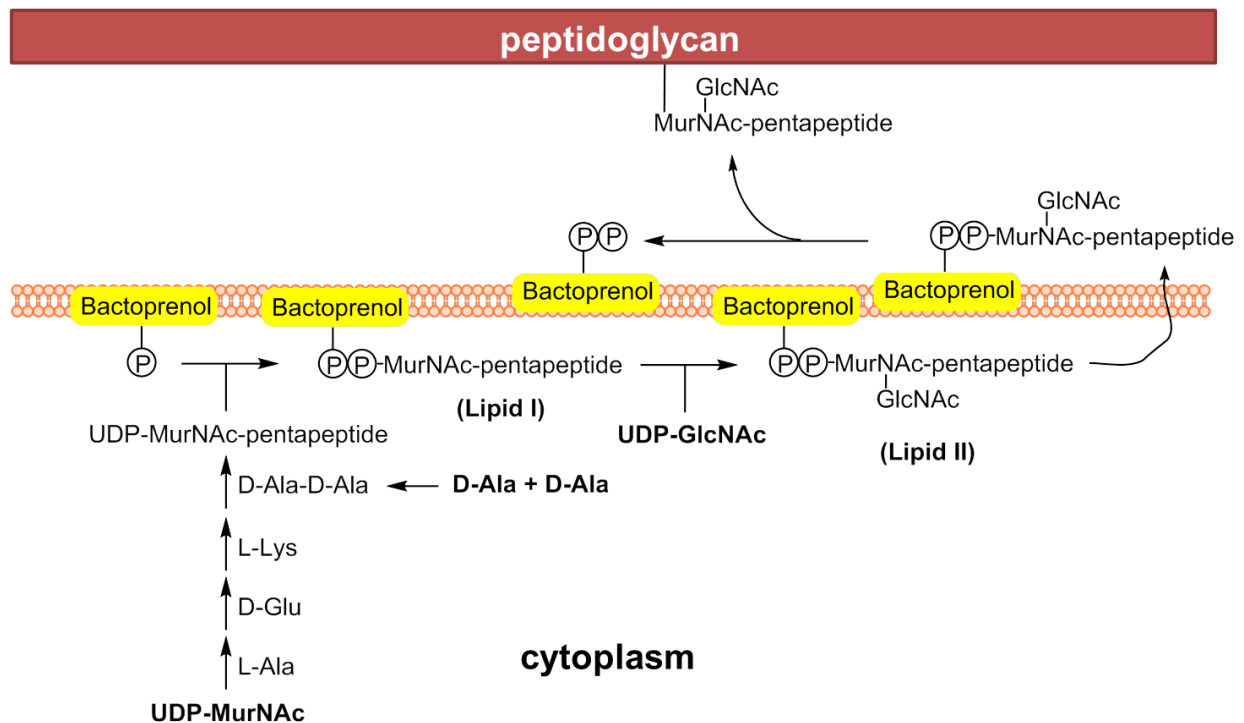


Figure 5-2. Biosynthesis of peptidoglycan from UDP-*N*-acetylmuramic acid, UDP-*N*-acetylglucosamine, and *D*-alanine.

To identify a better entry point for metabolic labeling, we next hoped that unnatural *D*-alanine derivatives would be incorporated into newly synthesized peptidoglycan (Figure 5-3A). Bacteria naturally incorporate *D*-amino acids besides *D*-alanine into peptidoglycan, suggesting that the biosynthetic machinery may tolerate larger unnatural functionalities.¹³⁻¹⁵ Importantly, as *D*-

amino acids are not present in mammalian systems, these metabolites should not be incorporated into host biomolecules. Initial studies focused on the sterically minimized azide and linear alkyne handles (Figure 5-3B, **5.1** and **5.2**), which had the highest likelihood of being accepted by the biosynthetic machinery that utilizes the natural substrate D-alanine.¹⁶ Of the two, the linear alkyne could be efficiently labeled under copper-catalyzed click conditions with azide probes in fixed cells. Catalyst-free reaction of azides with cyclooctyne-fluorophore conjugates, however, was considerably less effective, potentially due to poor probe access. At this juncture, no efficient method existed for the live cell labeling of nascent peptidoglycan using bioorthogonal chemistry. To enable two-step peptidoglycan labeling of pathogenic bacteria either intracellularly or *in vivo*, I hoped to identify a suitable chemical reporter/secondary detection agent pair that would label the bacterial cell wall in the absence of a cytotoxic copper catalyst.

The promiscuity of peptidoglycan metabolic enzymes towards both natural and unnatural D-amino acid substrates suggested that incorporation of the relatively large cyclooctyne moiety might be possible.^{13-15,17} If so, metabolic labeling with a cyclooctyne D-alanine analog would enable copper-free PG imaging using the fluorogenic azide probes I had developed. In addition, I hoped that using an azide-functionalized secondary detection agent rather than a cyclooctyne would prevent fluorescence background arising from the non-specific reactions of cyclooctynes with biological nucleophiles in serum or living cells.¹⁸⁻²⁰

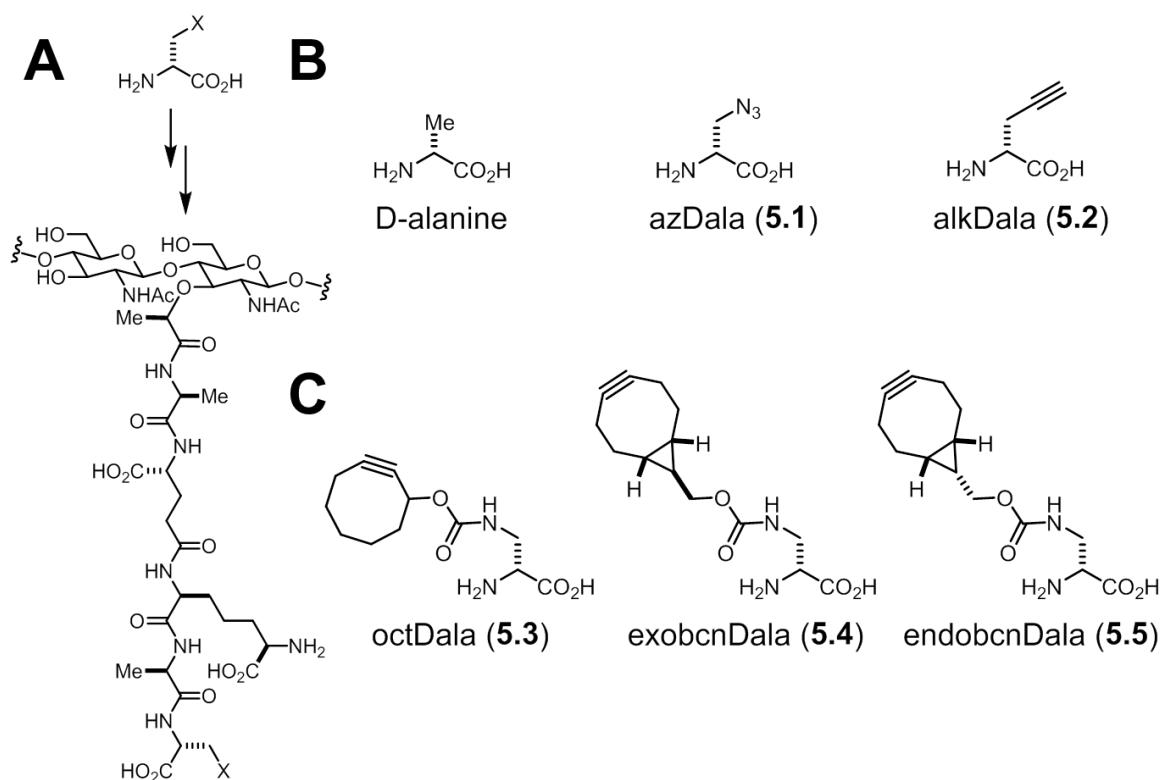
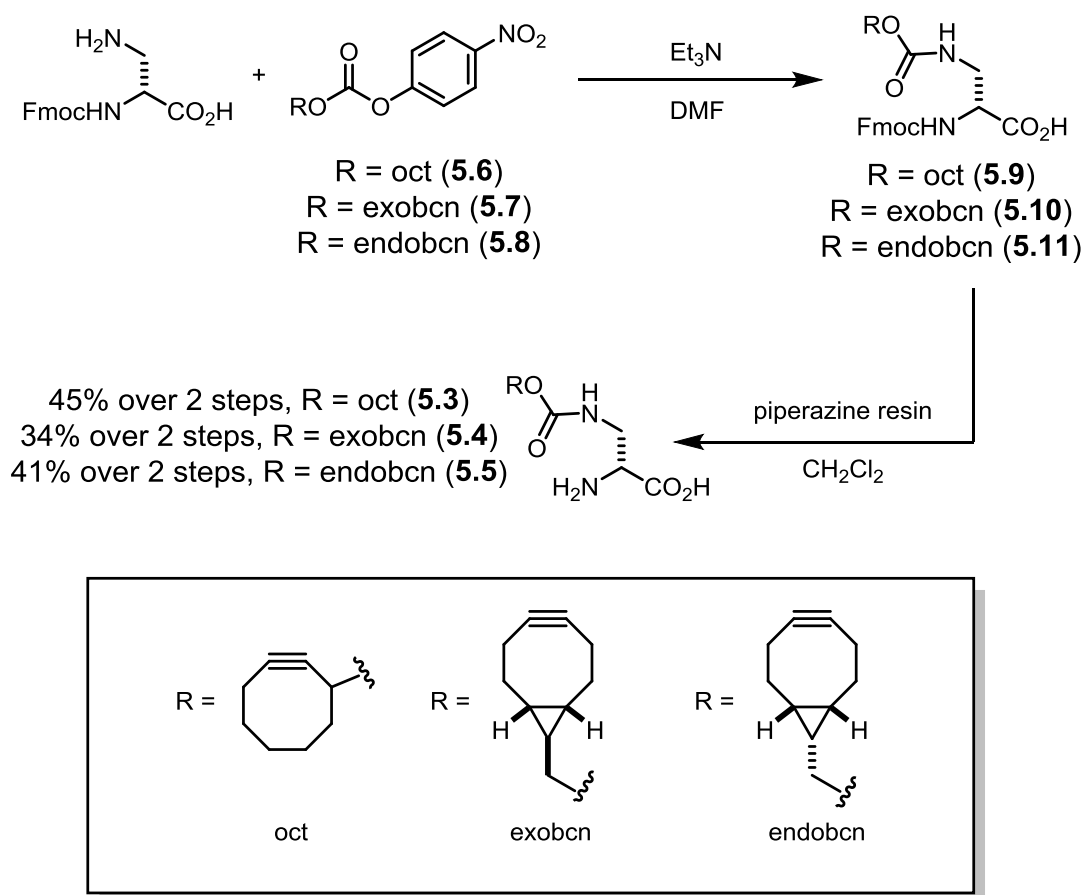


Figure 5-3. Incorporation of unnatural D-amino acids into peptidoglycan. (A) D-amino acids bearing unnatural functionalities are incorporated into the stem peptide of nascent peptidoglycan. (B) Initial, sterically-minimized D-amino acids evaluated. (C) Cyclooctyne D-amino acids **5.3** to **5.5**.

Accordingly, I synthesized cyclooctyne-functionalized D-alanine analog **5.3** (octDala) as well as the bicyclononyne derivatized stereoisomers **5.4** (exobcnDala) and **5.5** (endobcnDala) (Figure 5-3C).^{21,22} The minimally substituted cyclooctyne ring of **5.3** offers the least steric bulk, but is less reactive than the bicyclononyne moiety of **5.4** and **5.5**.²² I chose to evaluate all three compounds because I was unsure whether reactivity or incorporation efficiency would dominate fluorophore labeling using our two-step protocol. Although there are other means of enhancing cyclooctyne reactivity, such as aryl ring fusions, these would impose much additional steric bulk and thus were not pursued further.²³ The sterically minimized and kinetically fast 3,3,6,6-tetramethylcycloheptyne, however, was unable to be functionalized for attachment onto a D-amino acid scaffold.²⁴

The synthesis of cyclooctyne-functionalized D-amino acids began from Fmoc-protected D-diaminopropionic acid, which was prepared in one step from commercially available Fmoc-D-asparagine following literature procedure.^{22,25,26} (Scheme 5-1) The Fmoc-protected D-diaminopropionic acid was then coupled to known cyclooctynol-*para*-nitrophenol carbonates **5.6** to **5.8** to generate Fmoc-protected cyclooctyne D-amino acids **5.9** to **5.11**. Finally, the Fmoc group was removed using a polymer supported piperazine resin to yield the free cyclooctyne D-amino acids.²⁷ While **5.3** could also be prepared using the Boc protected D-diaminopropionic acid, I found that the highly strained bicyclononyne in **5.4** and **5.5** rapidly decomposed under the acidic deprotection conditions.



Scheme 5-1. Synthesis of cyclooctyne-functionalized D-alanine analogs **5.3** to **5.5**.

With all three cyclooctyne D-amino acids in hand, I first tested their metabolic incorporation in *Listeria monocytogenes*. *L. monocytogenes* are facultative intracellular pathogens and a common cause of food-borne illness. Given the diverse environments in which *Listeria* can live and grow, I hoped to that our metabolic labeling strategy would enable a study of cell wall synthesis both *in vitro* as well as in an infection setting. *Listeria* were grown for one doubling time in the presence of 5 mM **5.3**, **5.4** or **5.5**, washed to remove excess amino acid, and then reacted with 20 μM commercially available azido-PEG₃-carboxyrhodamine 110, a reagent our group previously used to image alkDala-labeled peptidoglycan under copper-catalyzed conditions.¹⁶ The cells were washed to remove excess probe, fixed, and analyzed by flow cytometry and microscopy (Figure 5-4).

Cells treated with all three cyclooctyne D-alanine derivatives showed fluorescence signal over D-alanine control, suggesting that the derivatives were incorporated into peptidoglycan and could be covalently modified by azide probes. Additionally, the fluorescence intensities observed correlated with the relative reactivities of the parent cyclooctynes. This suggested that the larger bicyclic D-amino acid derivatives were also incorporated with high efficiency. Cells incubated with **5.4** and **5.5** followed by copper-free reaction with azido-PEG₃-carboxyrhodamine

110 showed somewhat lower fluorescence intensity to cells metabolically labeled with alkDala followed by copper-catalyzed reaction with the same probe.

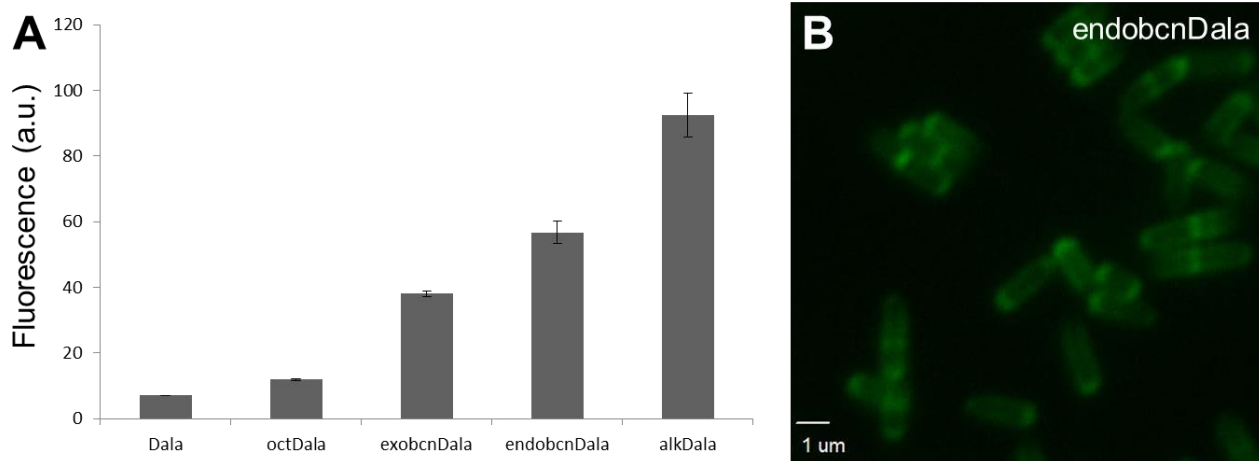


Figure 5-4. Labeling of wild-type *L. monocytogenes* with azido-PEG₃-carboxyrhodamine 110. (A) Flow cytometry data of labeling with various D-amino acids. (B) A representative image showing cell surface localization of fluorescence signal for cells treated with endobcnDala **5.5**. (Scale bar: 1 μm.)

While the observed fluorescence appeared to concentrate at the bacterial cell walls, consistent with incorporation of cyclooctyne D-alanine analogs into peptidoglycan, I sought additional evidence that these unnatural amino acids access the same metabolic pathways as natural D-alanine. I performed a competition experiment showing that excess D-alanine decreases the fluorescence intensity of *L. monocytogenes* incubated with **5.3**, **5.4** or **5.5** (Figure 5-5). The relatively modest competition by D-alanine may suggest the presence of a large endogenous D-alanine pool within *L. monocytogenes*.

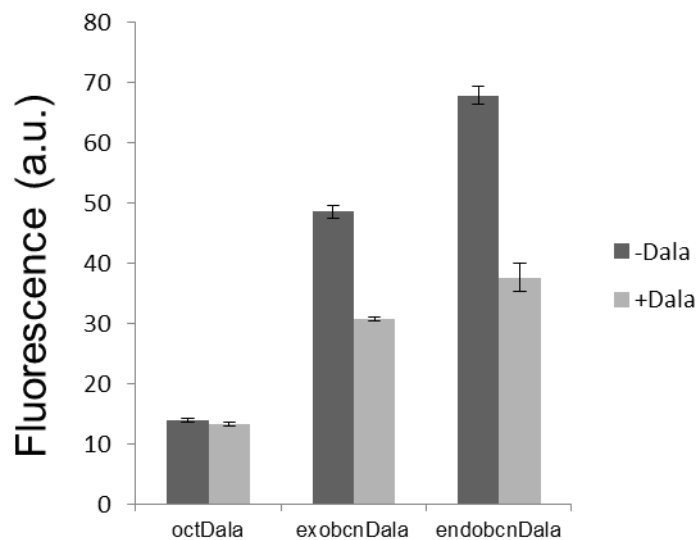


Figure 5-5. Competition experiment using wild-type *L. monocytogenes*. The bacteria were incubated with 5 mM cyclooctyne amino acid, in the presence of either 0 or 20 mM D-alanine, and labeled following the general procedure.

To test this, I performed a competition experiment in the *dal⁻ dat⁻* strain of *L. monocytogenes* auxotrophic for D-alanine.²⁸ In this D-alanine auxotroph, as endogenous D-alanine is absent, one would expect that unnatural D-amino acid incorporation would increase relative to wild-type bacteria and that incorporation would be more effectively competed out by exogenous D-alanine. Indeed, labeling by alkDala **5.2** was significantly higher in the *dal⁻ dat⁻* strain as compared to wild-type, and signal decreased dramatically when exogenous D-alanine was added. In stark contrast, when I performed a similar experiment using cyclooctyne D-amino acid analogs **5.3** to **5.5** in the D-alanine auxotroph, I observed that additional D-alanine increased the efficiency of incorporation of our unnatural analogs (Figure 5-6).

Recent work has shown that bulkier D-amino acids are incorporated into nascent peptidoglycan by transpeptidase enzymes involved in peptidoglycan crosslinking.²⁹ Typically, these enzymes form an amide bond between the amino group from the *meso*-diaminopimelic acid of the stem peptide with the carboxy-terminus of the third or fourth amino acid of a neighboring stem peptide. This transpeptidation reaction proceeds via an intermediate where a serine in the enzyme active site is covalently attached to the stem peptide via an ester linkage. Larger unnatural D-amino acid residues mimic the *meso*-diaminopimelic acid residue, intercepting this acyl enzyme intermediate and resulting in D-amino acid incorporation into the fourth or fifth position of the stem peptide. As these intermediates of peptidoglycan crosslinking are present only in nascent peptidoglycan, bulky D-amino acid chemical reporters are still able to effectively report on cell wall synthesis. The enhanced labeling of the auxotrophic strain in the presence of excess D-alanine is likely a result of increased concentrations of this stem peptide, which can be displaced by cyclooctyne D-alanine derivatives. Therefore, this data suggests that compounds **5.3** to **5.5** are incorporated primarily through this transpeptidation reaction.

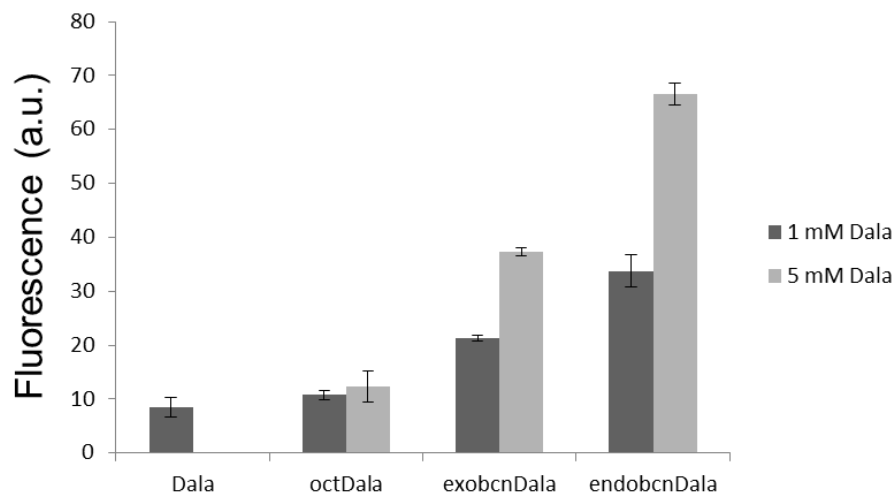


Figure 5-6. Competition experiment using the D-alanine auxotroph *L. monocytogenes dal⁻ dat⁻*. The bacteria were incubated with 5 mM cyclooctyne amino acid, in the presence of either 1 or 5 mM D-alanine, and labeled following the general procedure.

Additionally, I tested out my analogs in a mutant of *L. monocytogenes* lacking the PBP5 carboxypeptidase³⁰, which trims the terminal D-alanine residues from the pentapeptide peptidoglycan crosslink. I found that this mutant shows enhanced labeling compared to wild type bacteria (Figure 5-7A). The labeling enhancement in the absence of PBP5 is comparable for both the relatively small alkDala and the bulkier cyclooctyne amino acids, suggesting that this carboxypeptidase is tolerant of larger, unnatural D-amino acids.

I also observed that the PBP5 mutant showed a noticeable change in the localization of D-amino acid label as compared to wild-type. In wild-type *Listeria*, labeling was most prominent in the polar and septal regions, with minimal sidewall labeling. In the PBP5 transposon mutant, bright labeling was observed across the entire length of the bacterium (Figure 5-7B). This differential labeling is consistent with the known role of PBP5 in processing newly synthesized peptidoglycan. As *L. monocytogenes* grows primarily along the sidewall, PBP5 activity would be expected to localize in that region.³¹

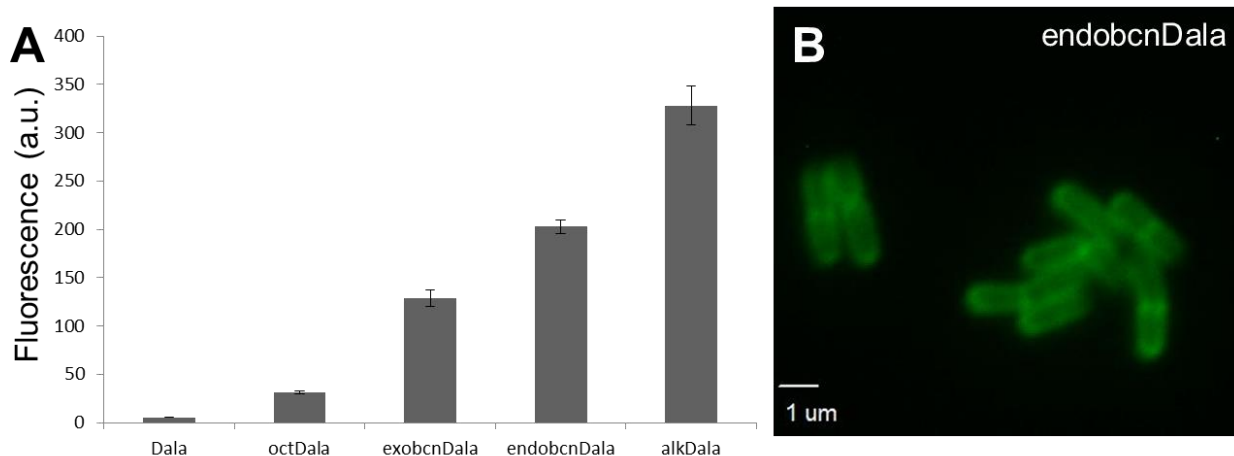


Figure 5-7. Labeling of *L. monocytogenes* *pbp5::tn* with azido-PEG₃-carboxyrhodamine 110. (A) Flow cytometry data of labeling with various D-amino acids. (B) A representative image showing cell surface localization of fluorescence signal for cells treated with endobcnDala. Note the increased sidewall labeling versus wild-type *L. monocytogenes*. (Scale bar: 1 μ m.)

Finally, I found that *L. monocytogenes* showed a negligible growth phenotype in the presence of 5 mM D-amino acids, suggesting that incorporation of these unnatural functionalities into the cell wall is minimally perturbative (Figure 5-8). This is beneficial for long term experiments and is a significant advantage over fluorescent antibiotics.

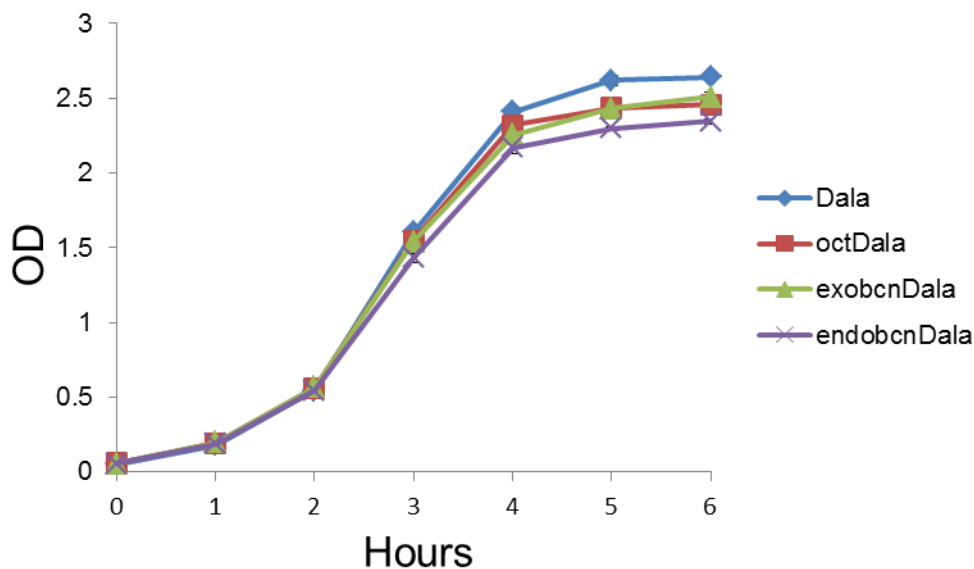


Figure 5-8. Optical density of wild-type *L. monocytogenes* grown in the presence of 5 mM D-alanine or cyclooctyne D-alanine derivatives **5.3** to **5.5**.

I next tested the metabolic incorporation of **5.3** to **5.5** into the cell walls of a variety of other bacterial species. I evaluated labeling in the Gram-positive bacteria *Mycobacterium smegmatis* and *Corynebacterium glutamicum* (Figures 5-9, 5-10). In both species, I observed robust labeling using our analogs in conjunction with azido-PEG₃-carboxyrhodamine 110. Notably, I found that the cyclooctyne D-alanine analogs **5.4** and **5.5** labeled more brightly with azide probes than alkDala **5.2**. Therefore, these two analogs enable peptidoglycan imaging with the same or higher sensitivity as the earlier methods, but without the need for a cytotoxic copper catalyst. I found that probe access was not problematic in these two bacterial species even with the presence of a mycobacterial outer membrane, which prevents cell wall staining by fluorescent lectins. Notably, the labeling efficiency in these two bacterial species dramatically exceeded that of *L. monocytogenes*, suggesting a higher tolerance for unnatural functionalities by the biosynthetic machinery.

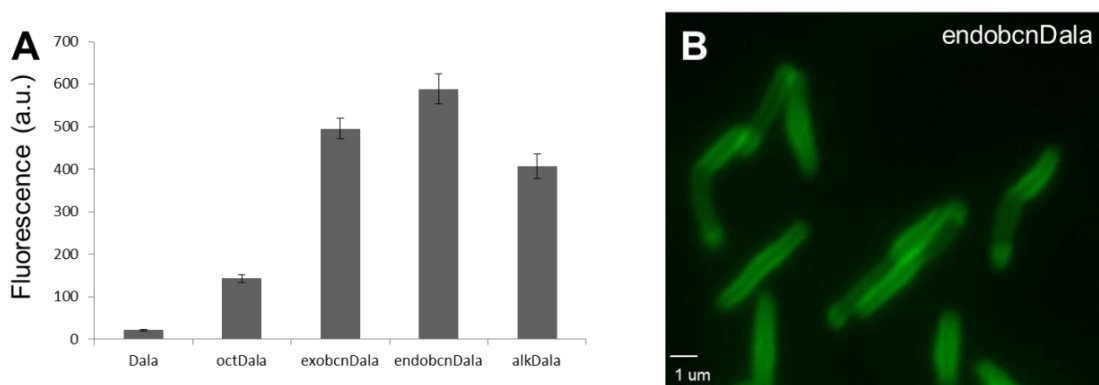


Figure 5-9. Labeling of *M. smegmatis* with azido-PEG₃-carboxyrhodamine 110. (A) Flow cytometry data of labeling with various D-amino acids. (B) A representative image showing cell surface localization of fluorescence signal for cells treated with endobcnDala. (Scale bar: 1 μm.)

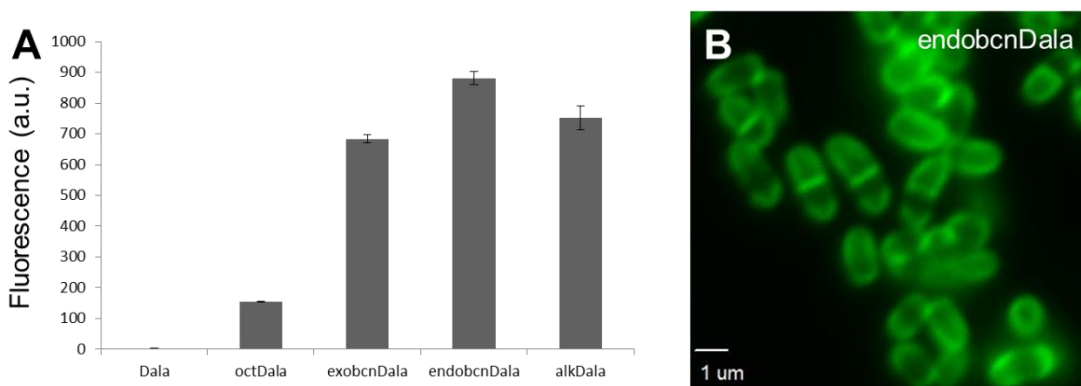


Figure 5-10. Labeling of *C. glutamicum* with azido-PEG₃-carboxyrhodamine 110. (A) Flow cytometry data of labeling with various D-amino acids. (B) A representative image showing cell surface localization of fluorescence signal for cells treated with endobcnDala. (Scale bar: 1 μm.)

I next evaluated these D-amino acid analogs in the Gram-negative bacterium *Escherichia coli* (Figure 5-11). As Gram-negative bacteria are not amenable to labeling via other methods such as fluorescent vancomycin or fluorescent lectins, a strategy to visualize the cell wall in this organism would find considerable utility. Gratifyingly, I found that D-amino acid **5.5** was able to label *E. coli*, although a smaller fluorophore that lacked the oligoethylene glycol spacer was needed for efficient reaction with the amino acid. This suggests that the Gram-negative outer membrane of *E. coli* is considerably less permeable than the outer membranes of *C. glutamicum* and *M. smegmatis*. For all three bacterial species, fluorescence signal localized to the cell wall.

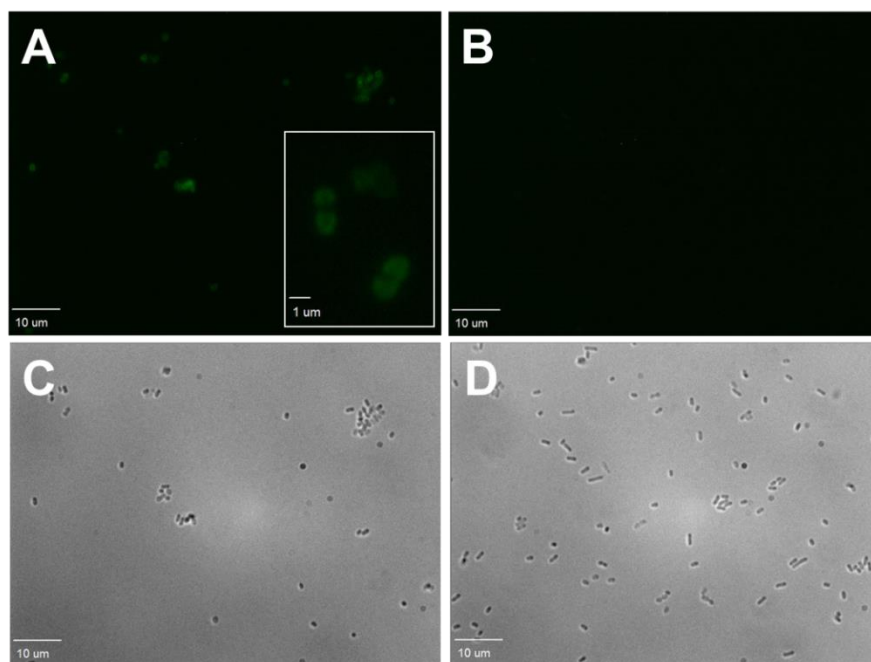


Figure 5-11. Labeling *E. coli* with azido-carboxyrhodamine 110. *E. coli* were incubated with 5 mM endobcnDala **5.5** or D-alanine for 2 h from a starting OD of 0.05, washed, and labeled with using 20 μ M of azido-carboxyrhodamine 110 (note the lack of a PEG spacer) for 1 h. The cells were then washed, fixed, and imaged as described above for labeling with azido-PEG₃-carboxyrhodamine 110. (A and C) Fluorescence and brightfield images of *E. coli* incubated with 5 mM endobcnDala **5.5**. (B and D) Fluorescence and brightfield images of *E. coli* incubated with 5 mM D-alanine. (Scale bar: 10 μ m.) Inset in (A) shows cells enlarged to highlight cell surface labeling. (Scale bar: 1 μ m.)

Recent work has demonstrated that smaller fluorophore D-amino acids are efficiently incorporated into nascent peptidoglycan.¹⁷ For example, nitrobenzoxadiazole and coumarin functionalized D-amino acids are incorporated into a variety of bacterial species, which enable the direct visualization of cell wall synthesis without the need for a second, bioorthogonal labeling step. The comparatively small size of our chemical reporter groups, however, should result in higher incorporation efficiency, enabling cell wall labeling with a higher fluorophore density as compared to one-step labeling. Additionally, our two-step labeling strategy should

enable the incorporation of long-wavelength fluorophores into peptidoglycan, absent in the existing palette of fluorophore D-amino acids. To test this, I incubated *L. monocytogenes* *pbp5::tn* with 1 mM endocytosin 5.5 or nitrobenzoxadiazole D-amino acid (NADA) for one doubling time (Figure 5-12A). I next incubated the bacteria with 5 μ M of azide-cyanine fluorophore. I found that a one-hour incubation with 5 μ M of an azide-substituted cyanine fluorophore enabled comparable fluorescence intensity to that of NADA-treated bacteria, but with near-infrared fluorescence (Figure 5-12B). Incubation with 5 μ M of a tetrazine-substituted cyanine fluorophore yielded dramatically higher fluorescence intensity due to the more rapid kinetics of this bioorthogonal reaction, again with the added benefit of near-infrared fluorescence (Figure 5-12C). These results demonstrate that our two-step labeling protocol enables the modification of bacterial peptidoglycan with high densities of long-wavelength fluorophores.

Beyond brighter labeling, the diverse types of fluorophores that can be incorporated using our two-step labeling approach will open the door to advanced imaging applications. For example, the installation of cyanine fluorophores onto peptidoglycan will enable super-resolution microscopy of the bacterial cell wall. In addition, the incorporation of fluorophores with extremely high photostability will allow for long term imaging of single bacteria over the course of infection.

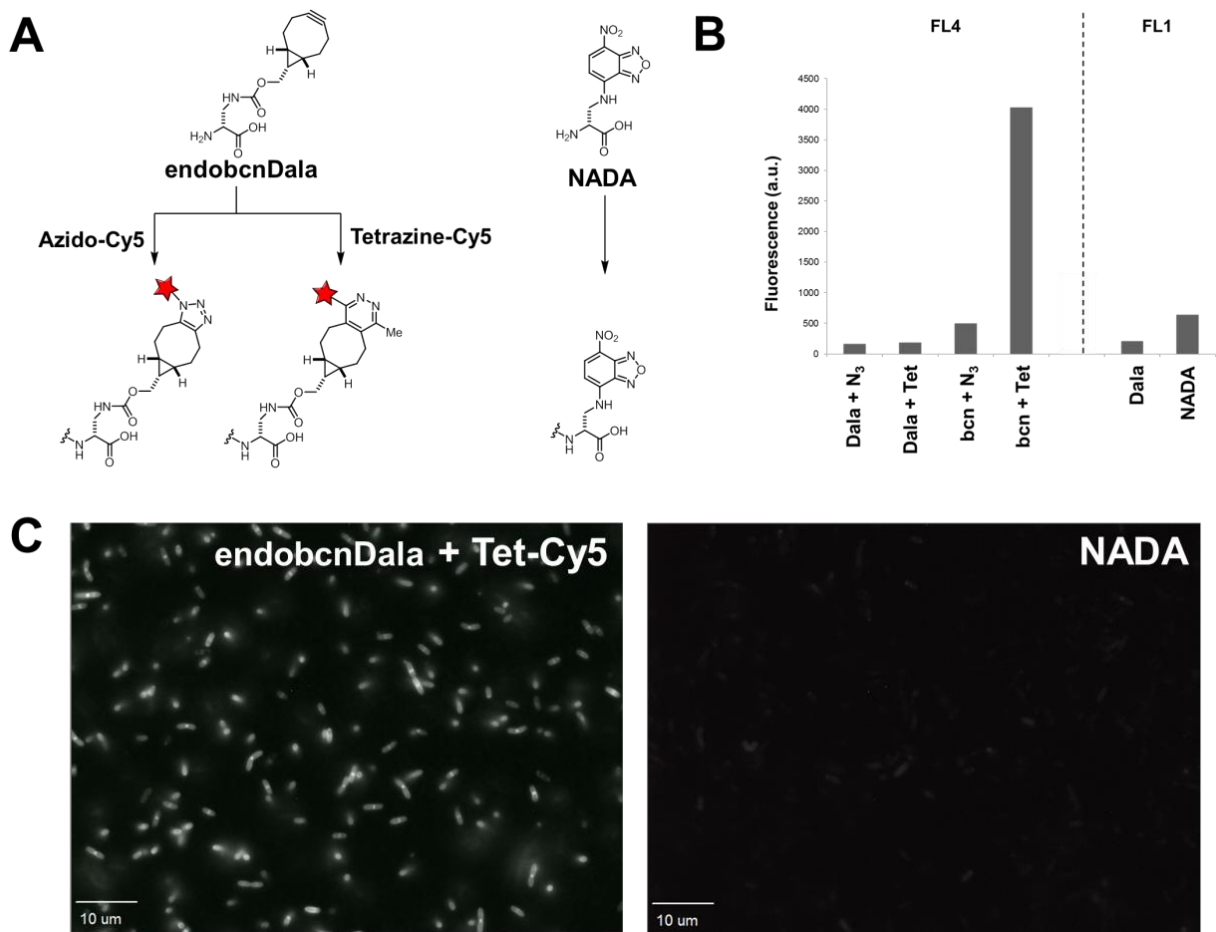


Figure 5-12. A comparison of two-step versus one-step labeling approaches for peptidoglycan imaging. (A) The D-amino acids and cyclooctyne-reactive fluorophores used. (B) Fluorescence intensities of bacteria labeled via two-step or one-step approaches. (C) Microscopy of bacteria labeled via two-step or one-step approaches.

I next imaged the bacteria using my near-infrared fluorogenic azide probes towards the *in vivo* imaging of bacterial pathogens. All three bacterial strains were incubated with endobcnDala **5.5** as before, but after washing away excess amino acid, the bacteria were incubated with 10 or 20 μM **3.15** for one hour and directly imaged without washing away excess probe. Clear fluorescence signal over background was observed in all cases, demonstrating the suitability of cyclooctyne-functionalized D-amino acids and fluorogenic azide probes for imaging peptidoglycan on live cells (Figure 5-13). This represents important first steps towards the *in vivo* visualization of bacterial pathogens. As no signal is observed until the bioorthogonal ligation occurs, simultaneous administration of a clearing agent that can rapidly react with any excess, unincorporated cyclooctyne D-amino acid will enable the direct visualization of bacterial peptidoglycan under no-wash conditions.

The cell-permeable bis-oligoethylene Si-rhodamine **3.11** accumulated in the cytosol of bacteria in a cyclooctyne-independent manner, consistent with previous literature on how lipophilic

cations behave in response to bacterial membrane potential.³² Notably, cyclooctyne-dependent labeling was observable even with the use of 500 μ M endobcnDala **5.5**, showing that the sensitivity of this method is comparable to one-step D-amino acid labeling strategies (Figure 5-14). The Gram-negative *E. coli*, however, labeled poorly, again due to limitations in probe access (Figure 5-15). The variability in *E. coli* labeling efficiency may provide insight on cell-to-cell differences in outer membrane permeability, which can be detected in real-time using fluorogenic azide probes.

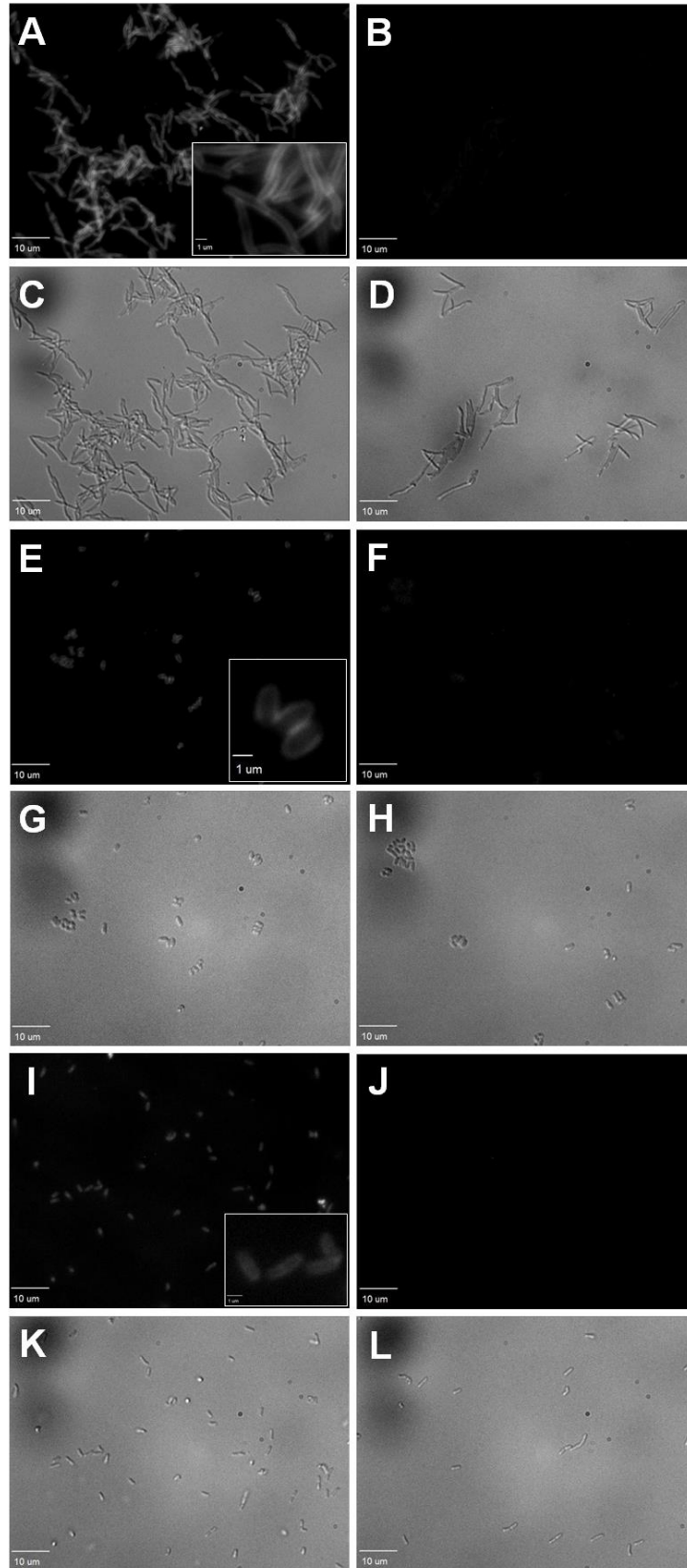


Figure 5-13. Bacterial peptidoglycan labeling with fluorogenic azide probes. Bacteria were treated with 5 mM endobcnDala **5.5** or D-alanine, then reacted with 10 or 20 μ M bis-sulfated probe **3.15** for 1 h. (A)-(D) Fluorescence and brightfield images of *M. smegmatis* treated with **5.5** or D-alanine and labeled with 10 μ M **3.15**. (E)-(H) Fluorescence and brightfield images of *C. glutamicum* treated under the same conditions. (I)-(L) Fluorescence and brightfield images of *L. monocytogenes pbp::tn* treated under the same conditions, but labeled with 20 μ M **3.15**. Scale bar = 10 μ m. Insets in (A), (E), (I) show cells enlarged to highlight cell surface labeling. Scale bar = 1 μ m.

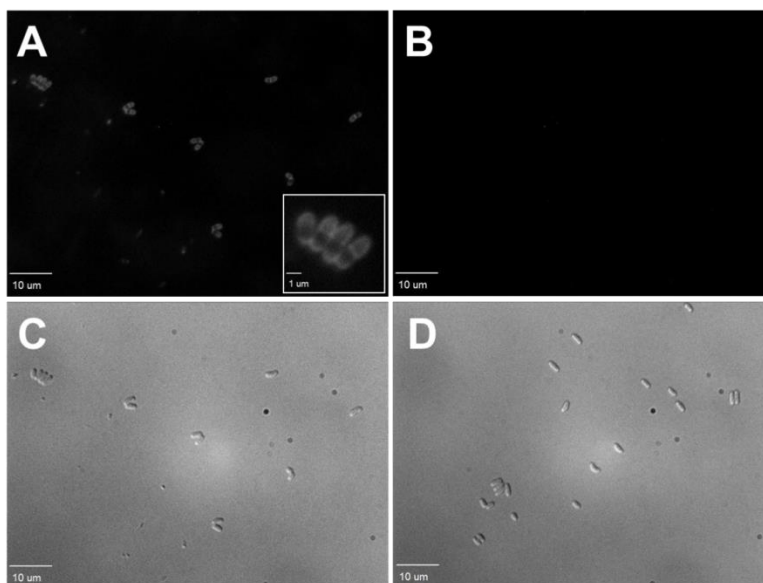


Figure 5-14. No-wash peptidoglycan labeling of *C. glutamicum* with reduced amino acid loading. Bacteria were incubated with 500 μ M endobcnDala **5.5** for one doubling time and imaged in the presence of 5 μ M of azido Si-rhodamine **3.15** as described above. (A and C) Fluorescence and brightfield images of bacteria incubated with endobcnDala **5.5**. (B and D) Fluorescence and brightfield images of bacteria incubated with D-alanine. (Scale bar: 10 μ m.) Inset in (A) shows cells enlarged to highlight cell surface labeling. (Scale bar: 1 μ m.)

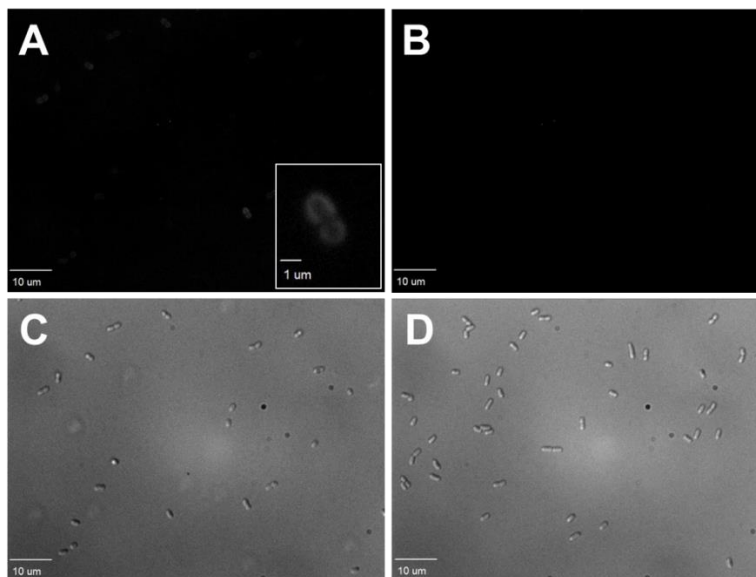


Figure 5-15. No-wash peptidoglycan labeling of the Gram-negative *E. coli*. *E. coli* incubated with 5 mM endobcnDala **5.5** or D-alanine for 2 h from a starting OD of 0.05 and imaged in the presence of 20 μ M of azido Si-rhodamine **3.15** as described above. Only a fraction of the bacteria incubated with endobcnDala **5.5** were fluorescently labeled under these conditions. (A and C) Fluorescence and brightfield images of *E. coli* incubated with 5 mM endobcnDala **5.5**. (B and D) Fluorescence and brightfield images of *E. coli* incubated with 5 mM D-alanine. (Scale bar: 10 μ m.) Inset in (A) shows cells enlarged to highlight cell surface labeling. (Scale bar: 1 μ m.)

Finally, I pursued imaging the peptidoglycan of an intracellular pathogen using bioorthogonal chemistry. *Mycobacterium marinum* is a facultative intracellular pathogen related to *Mycobacterium tuberculosis*. I first confirmed that *Mycobacterium marinum* incorporates endobcnDala **5.5**. I grew the bacteria in the presence of 1 mM **5.5** for 40 hours, then the bacteria labeled using a panel of fluorogenic azide fluorophores,³³ washed, fixed, and studied by fluorescence microscopy. Gratifyingly, I observed bright cell surface labeling of the mycobacterial cell wall using all three of these probes (Figure 5-16).

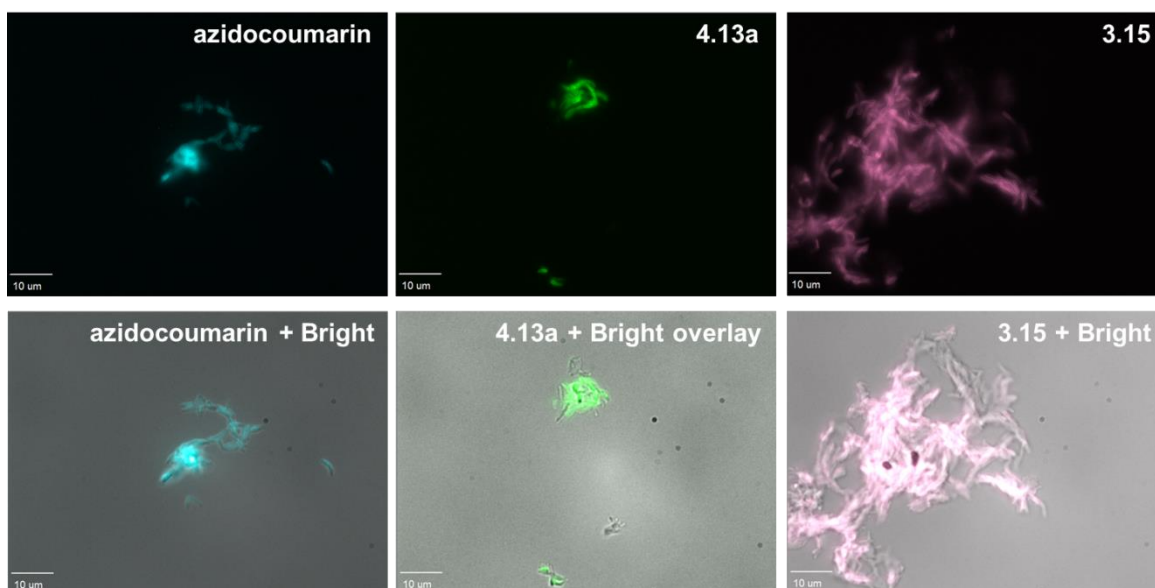


Figure 5-16. Labeling *M. marinum* with cyclooctyne D-alanine **5.5** and fluorogenic azide probes.

Next, I took a mutant of *M. marinum* that constitutively expresses RFP, labeled the bacteria with endobcnDala **5.5**, and allowed them to infect J774 macrophages. Afterwards, extracellular bacteria were removed, and a cell permeable fluorogenic azide probe, structurally related to **4.13a**, was added. After three hours, I observed cyclooctyne-dependent cell wall labeling of intracellular mycobacteria, demonstrating the potential of our fluorogenic azide probes to image targets within live mammalian cells (Figure 5-17A). As a fluorescein derivative, it does not show the mitochondrial accumulation observed with **3.11**.

After bioorthogonal labeling reaction, the infected macrophages were incubated for another sixteen hours. I observed mycobacterial growth within these macrophages, as shown by red bacterial fluorescence that extended beyond the original green fluorescence of cell wall label. The ability of these labeled mycobacteria to grow demonstrates the suitability of our approach for the long-term study of intracellular pathogens (Figure 5-17B). Direct pulse-chase labeling of intracellular pathogens, however, has been hampered by the limited permeability of endobcnDala **5.5** into and out of macrophages. Additionally, attempts to study *L. monocytogenes* during infection were dramatically less successful. The relatively rapid doubling time of *L. monocytogenes* (40 minutes) vs. *M. marinum* (6 hours) resulted a rapid dilution of cyclooctyne reporters within the cell wall during the bioorthogonal labeling reaction. These limitations can be addressed through the development of C-terminus modified D-amino acid derivatives, which have recently been demonstrated to incorporate into nascent peptidoglycan, and the use of alternative bioorthogonal reactions with more rapid labeling kinetics.^{29,34,35}

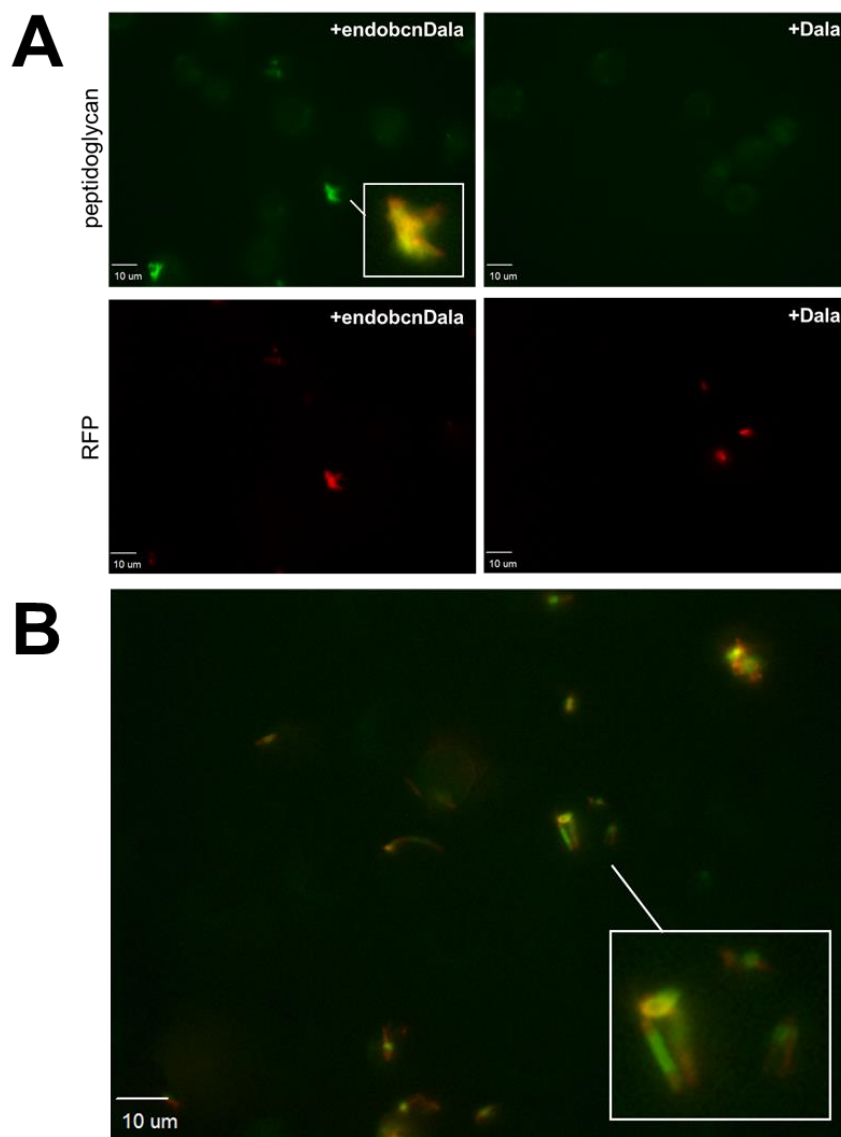


Figure 5-17. Labeling *M. marinum* within J774 murine macrophages using fluorogenic azide probes. (A) A fluorogenic azide probe enables the visualization of intracellular mycobacteria labeled with endobcnDala 5.5. (B) *M. marinum* with fluorescently labeled peptidoglycan are able to continue their growth within macrophages.

While live-cell imaging of newly synthesized peptidoglycan in intracellular bacteria is an unmet challenge, pre-labeling mycobacteria with D-amino acids will still provide insight into bacterial growth during infection. Mycobacteria add new cell wall material near its poles, and regions of old and new cell wall are clearly demarcated. Therefore, intracellular growth can be assessed, albeit indirectly, by measuring the amount of cytosolic fluorescence that extends beyond the original cell wall label (Figure 5-17B). As a result, these D-amino acid chemical tools may shed light on mycobacterial growth during infection.

Conclusion

In summary, I found that the bacterial peptidoglycan biosynthetic machinery tolerates D-alanine analogs bearing cyclooctynes. These unnatural D-amino acids are efficiently incorporated into both Gram-positive and Gram-negative bacteria, and enabled the robust, catalyst-free visualization of newly synthesized peptidoglycan. Together with the fluorogenic probes described in this thesis, this finding enabled the visualization of cell wall synthesis of a bacterial pathogen growing within live mammalian cells. Ultimately, this platform will facilitate the *in vivo* imaging of peptidoglycan in pathogenic bacteria, either in cultured host cells or model organisms, with bioorthogonal chemistry.

Experimental Procedures

Peptidoglycan labeling with unnatural D-amino acids

Bacteria were grown to an OD of 0.4 in their respective media (7H9 for *M. smegmatis*, LB for *C. glutamicum*, BHI for *L. monocytogenes*) at 37 °C (*M. smegmatis* and *L. monocytogenes*) or 30 °C (*C. glutamicum*). Then, 5 mM D-amino acid was added (from a 1 M stock in H₂O, 1 eq. NaOH was added to help solubilize compounds **5.3**, **5.4**, and **5.5**) and the cells grown for one doubling time. The bacteria were then added to a 96-well V-bottom plate at 200 µL/well and pelleted by centrifugation at 3500 rpm for 3 min. The supernatant was removed and the cells resuspended in 200 µL PBS and pelleted again. This wash process was repeated twice more. The cells were then incubated with 100 µL of 20 µM azido-PEG₃-carboxyrhodamine 110 (Click Chemistry Tools) in PBS (made by diluting a 1 mM stock in 9:1 PBS/DMSO) and placed in a 37 °C shaker for 1 h. Alternatively, for alkDala, labeling was performed by incubation with 100 µL of 20 µM azido-PEG₃-carboxyrhodamine 110, 128 µM TBTA, 1 mM CuSO₄, and 1.2 mM sodium ascorbate in PBS in a 37 °C shaker for 1 h. The cells were washed three times, then fixed with 4% paraformaldehyde for 10 min at rt. The cells were washed another three times, then studied by flow cytometry and microscopy. For flow cytometry studies with *M. smegmatis*, the cells were washed with PBS containing 0.5 mg/mL BSA and 0.1% v/v TWEEN 20 to minimize clumping.

D-alanine competition experiments

L. monocytogenes were grown in the presence of 5 mM D-amino acid as described above. An additional 20 mM of D-alanine was to compete out fluorescence signal. The bacteria were labeled with azido-PEG₃-carboxyrhodamine 110, fixed, and studied by flow cytometry. For the D-alanine auxotrophic *dal⁻ dat⁻* strain, bacteria were grown in the presence of 5 mM D-amino acid plus either 1 or 5 mM D-alanine.

L. monocytogenes growth curve

1 mL cultures of *L. monocytogenes* were grown in BHI at 37 °C in the presence of 5 mM D-amino acid, starting from an OD of 0.05. Aliquots were taken from the culture every hour, and optical densities were measured using an Eppendorf BioPhotometer.

No-wash peptidoglycan labeling with 3.15

The bacteria were incubated with either endobcnDala **5.5** or D-alanine and washed as described above. The cells were then taken up in 100 µL of 10 to 20 µM **3.15** in PBS (made by dilution of a 1 mM stock of **3.15** in 4:1 PBS/MeOH). 5 µL of cells were immediately plated on a glass slide, covered by coverslip, and imaged after 1 h.

One-step versus two-step labeling comparison

L. monocytogenes *pbp5::tn* were labeled with 1 mM of either endobcnDala **5.5**,

nitrobenzoxadiazole D-alanine (NADA), or D-alanine for one doubling time from OD 0.4 to 0.8. The bacteria were then added to a 96-well V-bottom plate at 200 μ L/well and pelleted by centrifugation at 3500 rpm for 3 min. The supernatant was removed and the cells resuspended in 200 μ L PBS and pelleted again. This wash process was repeated twice more. The cells were then incubated with 100 μ L of 5 μ M AlexaFluor 647 Azide (Life Technologies) or Tetrazine Cy5 (Click Chemistry Tools) in PBS and placed in a 37 $^{\circ}$ C shaker for 1 h. The cells were then washed three times as described above and studied by flow cytometry using a BD Accuri Flow Cytometer. The FL4 channel was used for quantifying cyanine fluorescence, while the FL1 channel was used for quantifying nitrobenzoxadiazole fluorescence.

Labeling Mycobacterium marinum with unnatural D-amino acids

M. marinum was grown from OD 0.06 in 1 mL 7H9 for 40 hours in the presence of endobcnDala **5.5** at 33 $^{\circ}$ C. The bacteria were then added to a 96-well V-bottom plate at 200 μ L/well and pelleted by centrifugation at 3500 rpm for 3 min. The supernatant was removed and the cells resuspended in 200 μ L PBS + 0.05% BSA + 0.01% TWEEN 20 (PBSTB) and pelleted again. This wash process was repeated twice more. The cells were then incubated with 100 μ L of 20 μ M 3-azido-7-hydroxycoumarin, **4.13a**, or **3.15** in PBS and placed in a 37 $^{\circ}$ C shaker for 1 h. The cells were washed three more times with PBSTB, fixed in 100 μ L 4% formaldehyde for 2 h, washed twice more with PBSTB, then imaged under a coverslip.

Labeling Mycobacterium marinum during infection

1 mL *M. marinum* containing an RFP expression plasmid with a hygromycin selection marker were grown for 48 hours in 5 mM endobcnDala **5.5** or D-alanine in 7H9 containing 50 μ g/mL hygromycin for 48 hours from OD 0.4. The bacteria were then washed three times with PBST as described above, then suspended in 200 μ L PBSTB and repeatedly passed through a 26 gauge needle to break up bacterial clumps. The cells were then centrifuged at 1000 rpm for 10 minutes, and the supernatant collected as a single cell suspension.

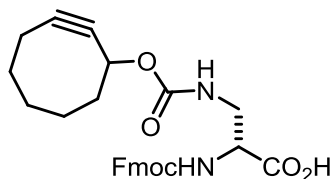
Meanwhile, J774 cells were grown to confluency in a LabTek 8-well chambered glass slide containing 250 μ L of DMEM containing fetal bovine serum but lacking antibiotics. Then, 5 μ L of the bacteria were added to the J774 cells and incubated for 3 h at 37 $^{\circ}$ C to allow the infection to proceed. Next, the media was replaced with fresh DMEM containing 50 μ g/mL gentamycin for 30 minutes to kill any extracellular bacteria, then the J774 cells washed with 200 μ L DMEM. Finally, the cells were covered with 200 μ L DMEM containing 5 μ M azide fluorophore and incubated at 37 $^{\circ}$ C for 3 h. Finally, the cells were washed with 300 μ L DMEM. The cells were allowed to continue growing within the chamber glass slides and images were taken over time.

Synthetic procedures

All chemical reagents obtained from commercial suppliers were used without further purification. Anhydrous dichloromethane, tetrahydrofuran and acetonitrile were passed through an activated alumina column prior to use. Anhydrous DMF and 1,4-dioxane were used as purchased. Water was double distilled prior to use.

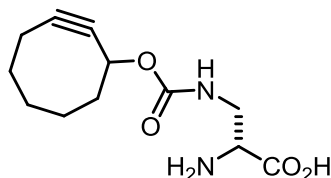
Flash chromatography was performed using Silicycle SiliaFlash P60 silica gel. Analytical thin layer chromatography was performed using glass-backed Analtech Uniplate silica gel plates containing a fluorescent indicator. Reversed-phase HPLC was performed on a Varian Pro Star system with a Varian UV-Vis detector model 345 (210, 254 nm) on a Dynamax Microsorb C-18 preparative column (21.4 x 250 mm) at a flow rate of 20 mL/min or on a Dynamax Microsorb C-18 semi-preparative column (10.0 x 250 mm) at a flow rate of 4 mL/min.

NMR spectra were obtained on Bruker AVQ-400, AVB-400, DRX-500, AV-500, or AV-600 spectrometers at ambient temperature at the UC Berkeley College of Chemistry NMR Facility. ^1H NMR shifts are calibrated to residual undeuterated solvent: δ 7.26 for CHCl_3 , 2.50 for d_5 -DMSO, 4.79 for HDO, 1.94 for CHD_2CN , and 3.31 for CHD_2OD . ^{13}C NMR shifts are calibrated to solvent peaks: δ 77.16 for CDCl_3 , 39.52 for d_6 -DMSO, 1.39/118.69 for CD_3CN , and 49.00 for CD_3OD . High resolution mass spectrometry was performed at the UC Berkeley Mass Spectrometry Laboratory.



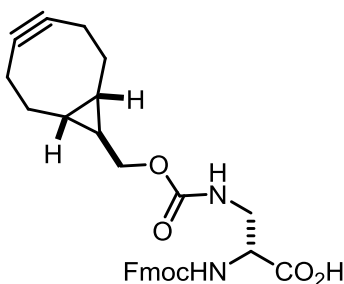
0.675 g (2.07 mmol, 1.3 equiv.) Fmoc-2,3-diaminopropionic acid⁷, a brown solid, was dissolved in 45 mL dry DMF. Next, 0.461 g (1.59 mmol) 2-cyclooctynol p-nitrophenol carbonate **5.6**⁸, a white powder, was added. Finally, 0.67 mL (0.483 g, 4.78 mmol, 3 equiv.) triethylamine, a clear liquid, was added. The now bright yellow solution was stirred for 1.5 h, after which TLC showed consumption of the carbonate. The solution was concentrated and the remaining brown oil taken up in 100 mL EtOAc. 1.5 mL AcOH was added, and the solution was washed with 3 x 100 mL 50% brine. The organic layer was dried over Na_2SO_4 and concentrated, yielding a brown oil. The oil was purified with CHCl_3 to 10:1 $\text{CHCl}_3/\text{MeOH}$ to yield 0.551 g **5.9**, contaminated with p-nitrophenol, as an off-white foamy solid.

Mixture of diastereomers. $R_f = 0.40$ (10:1 $\text{CHCl}_3/\text{MeOH}$, UV, I_2); ^1H NMR (500 MHz, CD_3OD): δ 1.44-1.54 (m, 1H), 1.54-1.64 (m, 2H), 1.70-1.80 (m, 1H), 1.81-1.87 (m, 2H), 1.95-2.05 (m, 1H), 2.05-2.25 (m, 2H), 3.40 (dd, 1H (minor), $J = 13.5$ Hz, 7.0 Hz), 3.45 (dd, 1H (major), $J = 14.0$ Hz, 7.5 Hz), 3.56 (dd, 1H (major), $J = 13.8$ Hz, 4.2 Hz), 3.61 (dd, 1H (minor), $J = 14.0$ Hz, 4.3 Hz), 4.21-4.30 (m, 2H), 4.37 (dd, 1H, $J = 9.8$ Hz, 6.9 Hz); 5.15 (app t, 1H, $J = 12.7$ Hz), 7.32 (app t, 2H, $J = 7.6$ Hz), 7.39 (app t, 2H, $J = 7.5$ Hz), 7.68 (d, 2H, $J = 7.5$ Hz), 7.80 (d, 2H, $J = 7.5$ Hz); ^{13}C NMR (151 MHz, CD_3OD): δ 20.77 (minor), 21.01 (major), 27.01, 27.03, 30.50, 35.05, 42.61, 42.97, 48.07, 48.09, 91.98/92.01, 102.06/102.09, 120.74, 126.08, 127.98, 128.58, 142.24, 144.94, 158.08, 158.22, 173.84; HRMS (ESI): Calculated for $\text{C}_{27}\text{H}_{27}\text{N}_2\text{O}_6$ $[\text{M}+\text{H}]^+$ 475.1875, found 475.1866.



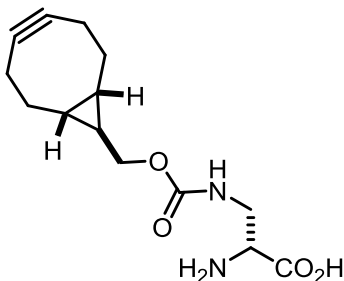
0.139 g of **5.9** from the previous step, an off-white foamy solid, and 1.16 g 1-2 mmol/g piperazine resin were added to a flame-dried flask and covered with 10 mL dry CH₂Cl₂. The yellow suspension was stirred for 5 h, then filtered. The resin was washed with 50 mL CH₂Cl₂. Finally, the product was eluted with 150 mL 2:1 CHCl₃/MeOH and concentrated. The yellowish residue was dissolved in 50 mL H₂O and washed with 3 x 50 mL EtOAc. The final wash was extracted with 2 x 10 mL H₂O. The combined aqueous layers were concentrated and lyophilized to yield 46 mg (45% over two steps) **5.3** as a white powder. For biological studies, the material was further purified by HPLC using a 5-65% MeCN/H₂O gradient.

Mixture of diastereomers. ¹H NMR (500 MHz, D₂O): δ 2.93 (brs, 4H), 3.64 (t, 2H, *J* = 4.4 Hz), 3.70 (t, 2H, *J* = 4.6 Hz), 3.75 (t, 2H, *J* = 4.5 Hz), 3.77 (t, 2H, *J* = 4.5 Hz), 3.82 (t, 2H, *J* = 4.6 Hz), 3.86 (t, 2H, *J* = 4.6 Hz), 4.11 (t, 2H, *J* = 4.6 Hz), 4.17 (t, 2H, *J* = 4.4 Hz), 6.64 (s, 1H), 6.92 (s, 1H); ¹³C NMR (151 MHz, 1:1 D₂O/d₆-DMSO + 5% 1M NaOH in H₂O): δ 21.24, 26.92, 30.37, 35.06, 42.57, 46.39, 57.01 (minor), 57.06 (major), 68.35, 92.66, 103.79, 158.01, 179.75 (major), 179.79 (minor); HRMS (ESI): Calculated for C₁₂H₁₉O₄N₂ 255.1339, found 255.1340.



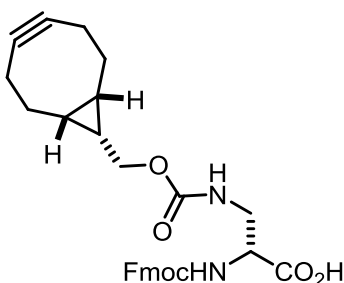
0.864 g (2.65 mmol, 1.3 equiv.) Fmoc-2,3-diaminopropionic acid⁹, a light brown solid, was dissolved in 60 mL dry DMF in a flame-dried flask. To this light brown solution was added 0.642 g (2.04 mmol) exo-bicyclononyl p-nitrophenol carbonate **5.7**¹², a white solid. Finally, 0.85 mL (0.618 g, 6.11 mmol, 3 equiv.) triethylamine, a clear liquid, was added and the yellow solution stirred for 1.5 h, after which all of the carbonate was consumed according to TLC. The solvent was then removed under vacuum and the remaining yellow oil diluted with 100 mL EtOAc. To this solution was added 2 mL AcOH in 100 mL 50% brine. The organic layer was collected, washed with 3 x 100 mL 50% brine, dried over Na₂SO₄, and concentrated to yield a light brown oil. The oil was purified with flash chromatography with CHCl₃ to 40:1 CHCl₃/MeOH to 10:1 CHCl₃/MeOH to yield 0.678 g **5.10**, contaminated with p-nitrophenol, as a white foamy solid.

R_f = 0.40 (10:1 CHCl₃/MeOH, UV, I₂); ¹H NMR (500 MHz, CD₃OD): δ 0.57-0.74 (m, 3H), 1.29 (app q, 2H, *J* = 13.0 Hz), 1.97-2.07 (m, 2H), 2.10-2.21 (m, 2H), 2.30 (d, 2H, *J* = 13.4 Hz), 3.43 (dd, 1H, *J* = 13.8 Hz, 8.0 Hz), 3.60 (dd, 1H, *J* = 14.0 Hz, 4.4 Hz), 3.88-3.97 (m, 2H), 4.22-4.30 (m, 2H), 4.36 (dd, 1H, *J* = 7.32 (t, 2H, *J* = 7.9 Hz), 7.39 (t, 2H, *J* = 7.6 Hz), 7.68 (t, 2H, *J* = 6.6 Hz), 7.80 (d, 2H, *J* = 7.7 Hz); ¹³C NMR (151 MHz, CD₃OD): δ 21.78, 21.79, 23.97, 24.75, 34.21, 43.04, 55.73, 68.18, 70.21, 99.44, 120.89, 126.21, 128.09, 128.70, 142.40, 145.08, 158.38, 159.32, 173.65; HRMS (ESI): Calculated for C₂₉H₂₉N₂O₆ [M+H]⁺ 501.2031, found 501.2019.



0.149 g **5.10** from the previous step and 1.16 g 1-2 mmol/g piperazine resin were covered with 10 mL dry CH₂Cl₂ in a flame-dried flask. The yellow suspension was stirred for 5 h, then filtered. The resin was washed with 50 mL CH₂Cl₂, then the product eluted with 150 mL 2:1 CHCl₃/MeOH and concentrated to yield a yellow solid. The solid was then taken up in 50 mL H₂O and washed with 3 x 50 mL EtOAc, then concentrated and lyophilized to yield **5.4** as a white solid. The solid was further purified by HPLC with 5-65% MeCN/H₂O for biological experiments.

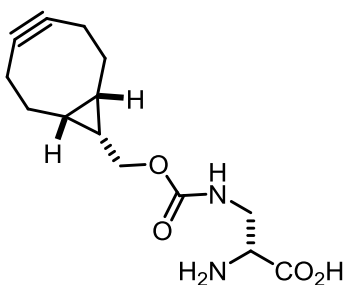
¹H NMR (500 MHz, D₂O): δ 0.71-0.83 (m, 3H), 1.37 (app q, 2H, *J* = 9.6 Hz), 2.14 (app dt, 2H, *J* = 14.2 Hz, 2.6 Hz), 2.26 (dd, 2H, *J* = 15.8 Hz, 12.4 Hz), 2.39 (dd, 2H, *J* = 13.6 Hz, 2.9 Hz), 3.49 (dd, 1H, *J* = 15.0 Hz, 6.8 Hz), 3.65 (dd, 1H, *J* = 14.9 Hz, 3.9 Hz), 3.78 (dd, 1H, *J* = 6.9 Hz, 3.9 Hz), 3.91-4.12 (m, 2H); ¹³C NMR (151 MHz, 1:1 D₂O/d₆-DMSO + 5% 1M NaOH in H₂O): 22.18, 23.86, 24.64, 46.44, 57.36, 70.92, 101.57, 159.84, 180.94; HRMS (ESI): Calculated for C₁₄H₂₁O₄N₂ [M+H]⁺ 281.1496, found 281.1498.



0.849 g (2.60 mmol, 1.3 equiv.) Fmoc-2,3-diaminopropionic acid, a light brown solid, was dissolved in 60 mL dry DMF in a flame-dried flask. To this light brown solution was added 0.630 g (2.00 mmol) endo-bicyclononyl p-nitrophenol carbonate **5.8**⁹, a white solid. Finally, 0.84 mL (0.607 g, 6.00 mmol, 3 equiv.) triethylamine, a clear liquid, was added and the yellow solution stirred for 1.5 h, after which all of the carbonate was consumed according to TLC. The solvent was then removed under vacuum and the remaining yellow oil diluted with 100 mL EtOAc. To this solution was added 2 mL AcOH in 100 mL 50% brine. The organic layer was collected, washed with 3 x 100 mL 50% brine, dried over Na₂SO₄, and concentrated to yield a light brown oil. The oil was purified with CHCl₃ to 40:1 CHCl₃/MeOH to 20:1 CHCl₃/MeOH to 10:1 CHCl₃/MeOH to yield 0.782 g **5.11**, contaminated with p-nitrophenol, as a white foamy solid.

R_f = 0.40 (10:1 CHCl₃/MeOH, UV, I₂); ¹H NMR (600 MHz, CD₃OD): δ 0.80-0.95 (m, 2H), 1.28-1.32 (m, 1H), 1.41-1.63 (m, 2H), 2.02-2.25 (m, 6H), 3.44 (dd, 1H, *J* = 14.1 Hz, 8.2 Hz),

3.61 (dd, 1H, $J = 14.4$ Hz, 4.8 Hz), 4.04 (dd, 1H, $J = 11.4$ Hz, 8.4 Hz), 4.07-4.17 (m, 2H), 4.20-4.40 (m, 3H), 7.31 (app t, 2H, $J = 8.0$ Hz), 7.38 (app t, 2H, $J = 8.2$ Hz), 7.57-7.72 (m, 2H), 7.80 (d, 2H, $J = 7.7$ Hz); ^{13}C NMR (125 MHz, CD_3OD): δ 18.78, 21.33, 21.87, 30.04, 43.16, 55.89, 64.01, 68.23, 99.50, 120.92, 126.25, 128.14, 128.76, 142.51, 145.16, 158.47, 159.42, 173.79; HRMS (ESI): Calculated for $\text{C}_{29}\text{H}_{29}\text{N}_2\text{O}_6$ $[\text{M}+\text{H}]^+$ 501.2031, found 501.2021.



0.270 g of **5.11** from the previous step, a white foamy solid, and 2.15 g 1-2 mmol/g piperazine resin were added to a flame-dried flask and covered with 18 mL dry CH_2Cl_2 . The now yellow solution was stirred for 5 h. The mixture was then filtered and washed with 100 mL CH_2Cl_2 . The product was then eluted with 150 mL 2:1 $\text{CHCl}_3/\text{MeOH}$, then concentrated. The solid was then taken up in 80 mL H_2O and washed with 3 x 80 mL EtOAc, then concentrated and lyophilized to yield **5.5** as a white solid. The solid was further purified by HPLC with 5-65% MeCN/ H_2O for biological experiments.

^1H NMR (500 MHz, D_2O): δ 0.98 (t, 2H, $J = 9.4$ Hz), 1.40 (t, 1H, $J = 8.7$ Hz), 1.53-1.61 (m, 2H), 2.19-2.31 (m, 6H), 3.54 (dd, 1H, $J = 15.1$ Hz, 6.9 Hz), 3.70 (d, 1H, $J = 15.2$ Hz), 3.85 (dd, 1H, $J = 7.0$ Hz, 3.7 Hz), 4.20 (d, 2H, $J = 8.8$ Hz); ^{13}C NMR (151 MHz, 1:1 $\text{D}_2\text{O}/\text{d}_6\text{-DMSO DMSO} + 5\%$ 1M NaOH in H_2O): 18.71, 21.10, 22.22, 46.52, 57.33, 64.43, 101.28, 159.51, 180.42; HRMS (ESI): Calculated for $\text{C}_{14}\text{H}_{21}\text{O}_4\text{N}_2$ $[\text{M}+\text{H}]^+$ 281.1496, found 281.1492.

References

1. Typas, A.; Banzhaf, M.; Gross, C. A.; Vollmer, W. *Nat. Rev. Microbiol.* **2010**, *10*, 123–136.
2. Vollmer, W.; Blanot, D.; de Pedro, M. A. *FEMS Microbiol. Rev.* **2008**, *32*, 149-167.
3. Seiler, P.; Ulrichs, T.; Bandermann, S.; Pradl, L.; Jorg, S.; Krenn, V.; Morawietz, L.; Kaufmann, S. H. E.; Aichele, P. *J. Infect. Dis.* **2003**, *188*, 1326-1331.
4. Kieser, K. J.; Rubin, E. J. *Nat. Rev. Microbiol.* **2014**, *12*, 550-562.
5. Lotan, R.; Sharon, N.; Mirelman, D. *Eur. J. Biochem.* **1975**, *55*, 257-262.
6. Sizemore, R. K.; Caldwell, J. J.; Kendrick, A. S. *Appl. Environ. Microbiol.* **1990**, *56*, 2245–2247.
7. Sadamoto, R.; Niikura, K.; Sears, P. S.; Liu, H.; Wong, C. H.; Suksomcheep, A.; Tomita, F.; Monde, K.; Nishimura, S. *J. Am. Chem. Soc.* **2002**, *124*, 9018– 9019.
8. Nelson, J. W.; Chamessian, A. G.; McEnaney, P. J.; Murelli, R. P.; Kazmierczak, B. I.; Spiegel, D. A. *ACS Chem. Biol.* **2010**, *5*, 1147–1155
9. Tiyanont, K.; Doan, T.; Lazarus, M. B.; Fang, X.; Rudner, D. Z.; Walker, S. *Proc. Natl. Acad. Sci.* **2006**, *103*, 11033–11038.
10. Barreteau, H.; Kovac, A.; Boniface, A.; Sova, M.; Gobec, S.; Blanot, D. *FEMS Microbiol. Rev.* **2008**, *32*, 168-207.
11. Geva-Zatorsky, N.; Alvarez, D.; Hudak, J. E.; Reading, N. C.; Erturk-Hasdemir, D.; Dasgupta, S.; von Andrian, U. H.; Kasper, D. L. *Nat. Med.* **2015**, *21*, 1091-1100.
12. Vocadlo, D. J.; Hang, H. C.; Kim, E.-J.; Hanover, J. A.; Bertozzi, C. R. *Proc. Natl. Acad. Sci.* **2003**, *100*, 9116-9121.
13. Caparros, M.; Pisabarro, A. G.; de Pedro, M. A. *J. Bacteriol.* **1992**, *174*, 5549–5559
14. Lam, H.; Oh, D. C.; Cava, F.; Takacs, C. N.; Clardy, J.; de Pedro, M. A.; Waldor, M. K. *Science* **2009**, *325*, 1552–1555.
15. Cava, F.; de Pedro, M. A.; Lam, H.; Davis, B. M.; Waldor, M. K. *EMBO J.* **2011**, *30*, 3442–3453.
16. Siegrist, M. S.; Whiteside, S.; Jewett, J. C.; Aditham, A.; Cava, F.; Bertozzi, C. R. *ACS Chem. Biol.* **2013**, *8*, 500-505.
17. Kuru, E.; Hughes, H. V.; Brown, P. J.; Hall, E.; Tekkam, S.; Cava, F.; de Pedro, M. A.; Brun, Y. V.; VanNieuwenhze, M. S. *Angew. Chem. Int. Ed.* **2012**, *51*, 12519-12523.
18. van Geel, R.; Pruijn, G. J. M.; van Delft, F. L.; Boelens, W. C. *Bioconjug. Chem.* **2012**, *23*, 392-398.
19. Chang, P. V.; Prescher, J. A.; Sletten, E. M.; Baskin, J. M.; Miller, I. A.; Agard, N. J.; Lo, A.; Bertozzi, C. R. *Proc. Natl. Acad. Sci.* **2010**, *107*, 1821-1826
20. Yao, J. Z.; Uttamapinant, C.; Poloukhine, A.; Baskin, J. M.; Codelli, J. A.; Sletten, E. M.; Bertozzi, C. R.; Popik, V. V.; Ting, A. Y. *J. Am. Chem. Soc.* **2012**, *134*, 3720-3728.
21. Agard, N. J.; Prescher, J. A.; Bertozzi, C. R. *J. Am. Chem. Soc.* **2004**, *126*, 15046-15047.
22. Dommerholt, J.; Schmidt, S.; Temming, R.; Hendriks, L. J. A.; Rutjes, F. P. J. T.; van Hest, J. C. M.; Lefeber, D. J.; Friedl, P.; van Delft, F. L. *Angew. Chem. Int. Ed.* **2010**, *49*, 9422-9425.
23. Jewett, J. C.; Bertozzi, C. R. *Chem. Soc. Rev.* **2010**, *39*, 1272-1279.
24. de Almeida, G.; Sletten, E. M.; Nakamura, H.; Palaniappan, K. K.; Bertozzi, C. R. *Angew. Chem. Int. Ed.* **2012**, *51*, 2443-2447.
25. Lau Y. H.; Spring D. R. *Synlett* **2011**, *13*, 1917-1919.

26. Plass T.; Milles, S.; Koehler, C.; Schultz, C.; Lemke, E. A. *Angew. Chem. Int. Ed.* **2011**, *50*, 3878-3881.
27. Lang, K.; Davis, L.; Wallace, S.; Mahesh, M.; Cox, D. J.; Blackman, M. L.; Fox, J. M.; Chin, J. W. *J. Am. Chem. Soc.* **2012**, *134*, 10317-10320.
28. Thompson, R. J.; Bouwer, H. G.; Portnoy, D. A.; Frankel, F. R. *Infect. Immun.* **1998**, *66*, 3552-3561.
29. Lebar, M. D.; May, J. M.; Meeske, A. J.; Leiman, S. A.; Lupoli, T. J.; Tsukamoto, H.; Losick, R.; Rudner, D. Z.; Walker, S.; Kahne, D. *J. Am. Chem. Soc.* **2014**, *136*, 10874-10877.
30. Korsak, D.; Popowska, M.; Markiewicz, Z. *Pol. J. Microbiol.* **2005**, *54*, 339-342.
31. Korsak, D.; Vollmer, W.; Markiewicz, Z. *FEMS Microbiol. Lett.* **2005**, *251*, 281-288
32. Ramos, S.; Schuldiner, S.; Kaback, H. R. *Proc. Natl. Acad. Sci.* **1976**, *73*, 1892-1896
33. Sivakumar, K.; Xie, F.; Cash, B. M.; Long, S.; Barnhill, H. N.; Wang, Q. *Org. Lett.* **2004**, *6*, 4603-4606.
34. Pidgeon, S. E.; Fura, J. M.; Leon, W.; Birabaharan, M.; Vezenov, D.; Pires, M. M. *Angew. Chem. Int. Ed.* **2015**, *54*, 6158-6162.
35. Blackman, M. L.; Royzen, M.; Fox, J. M. *J. Am. Chem. Soc.* **2008**, *130*, 13518-13519.

Chapter 6: New Tricks for Old Cyclooctynes

Introduction

The small size and high physiological stability of the azide allows for azide-tagged substrates to be metabolically incorporated into myriad biomolecules using native biosynthetic machinery.¹ These azide-tagged biomolecules can then be labeled by reaction with an alkyne-tagged fluorophore or affinity handle and studied using methods such as fluorescence microscopy, Western blot, or mass spectrometry. This combination of metabolic incorporation and bioorthogonal chemistry has emerged as a powerful tool for the study of biomolecules not amenable to tagging using molecular biology techniques. While the first bioorthogonal reaction of the azide was the Staudinger ligation, cyclooctynes have become the reagent of choice for the catalyst-free detection of azide-tagged biomolecules.²

As bioconjugation reactions must be performed using low concentrations of reagents, a high rate constant is necessary for efficient labeling. Modulating the strain or electronics of these alkynes has accelerated the copper-free azide-alkyne cycloaddition by three orders of magnitude over the parent cyclooctyne (from a bimolecular rate constant of $k = 1 \times 10^{-3} \text{ M}^{-1}\text{s}^{-1}$ up to $4 \text{ M}^{-1}\text{s}^{-1}$, Figure 6-1, **6.7** to **6.8**).³ For reagent concentrations of $100 \mu\text{M}$, this represents an improvement in reaction half-life from 116 days down to 42 minutes. Still, many dynamic biological processes occur on even shorter time-scales. Faster reaction kinetics are needed to study these systems with bioorthogonal chemistry. Moreover, faster kinetics mean less probe is needed to achieve the same reaction rate, crucial for situations where background from excess unreacted probe is problematic.

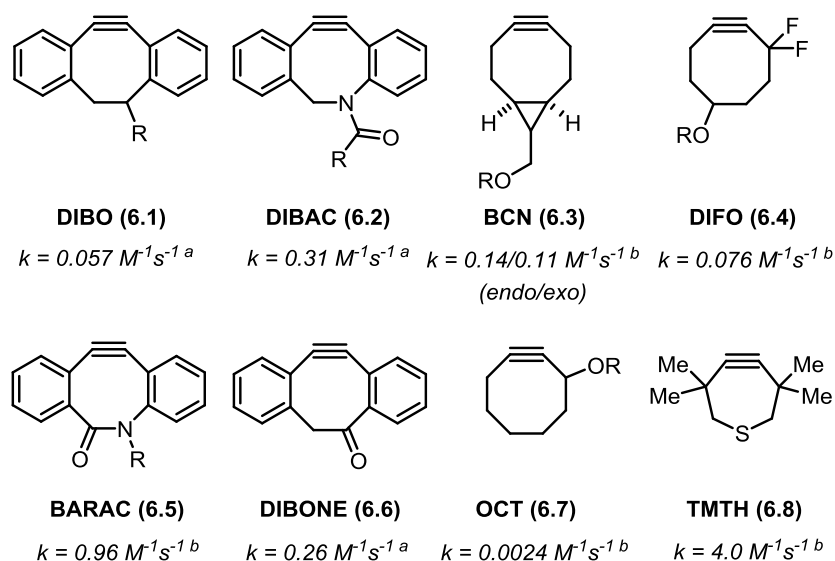


Figure 6-1. Various strained alkynes and their second-order rate constants for cycloaddition with benzyl azide.³ ^a Measured in CD_3OD . ^b Measured in CD_3CN .

Unfortunately, modification of strained alkynes can only yield a certain amount of rate acceleration before the stability of the cycloalkyne is compromised and side reactions such as nucleophilic attack by thiols or trimerization become problematic.^{4,5} Therefore, the most prudent path forward for improving cyclooctyne labeling kinetics may be to tune the other reactant.

Importantly, in recent years, cyclooctynes have evolved beyond their role as secondary reagents to label tagged biomolecules with bioorthogonal chemistry (Figure 6-1). The discovery and generation of promiscuous biosynthetic enzymes have enabled cyclooctyne incorporation into a variety of biomolecules, including proteins (**6.9**, **6.10**)⁶⁻⁹, lipids (**6.11**)¹⁰, and peptidoglycan (**6.12**)¹¹. There are still size limits on the unnatural functionalities that can be incorporated, meaning that only minimally substituted cyclooctynes are suitable substrates.

Bicyclononyne **6.3**, in particular, derives its nearly two-orders of rate acceleration over the parent cyclooctyne **6.7** from a sterically minimal cyclopropane ring fusion. In addition, it is dramatically easier to synthesize compared to other, smaller cyclooctynes, such as **6.4** and **6.8**. Overall, its comparatively small size, rapid reaction kinetics, and easy synthesis have made **6.3** the cyclooctyne chemical reporter of choice (**6.10**, **6.13**).

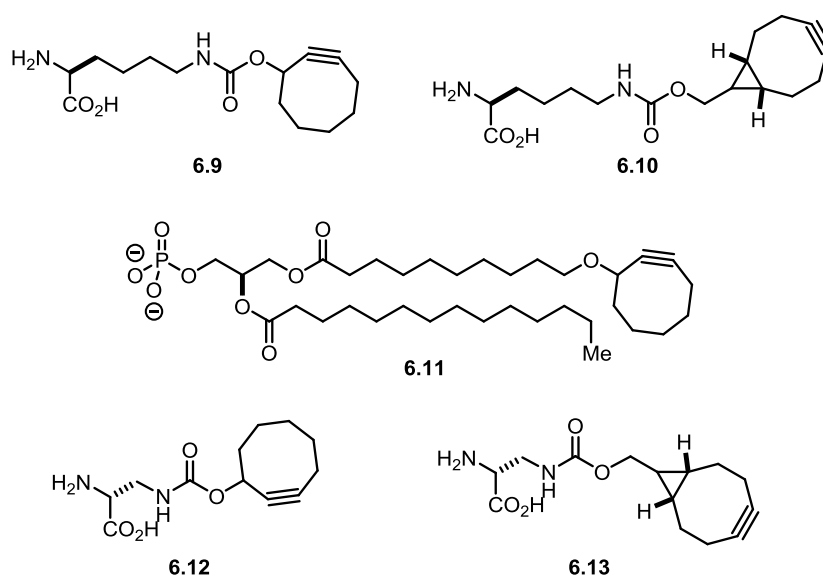


Figure 6-2. Various cyclooctyne derivatives that can be biosynthetically incorporated into proteins (**6.9**, **6.10**), lipids (**6.11**), and peptidoglycan (**6.12**, **6.13**).

The fact that the biosynthetic machinery can tolerate medium-sized functionalities like cyclooctynes means that compact fluorophores can often be directly incorporated as well, opening the door to one-step detection via fluorescence microscopy. Still, two-step labeling with bioorthogonal chemistry can accommodate tailored fluorophores with optimized photophysical properties, extremely powerful for advanced techniques such as superresolution microscopy. In addition, molecules beyond fluorophores can be attached. The installation of a diverse functional repertoire onto biomolecules opens the door to experiments such as affinity enrichments for mass

spectrometry. Finally, as covalent modification of the biomolecule does not occur until the bioorthogonal reaction occurs, methods to modulate bioorthogonal reaction rate via proximity can be exploited to study biomolecule accessibility and binding interactions.

For the purpose of increasing conjugation efficiency, cyclooctyne incorporation also means that more leeway can be made in identifying suitable reaction partners. Issues such as size and stability are less important, as the reagents are no longer required to traverse entire biosynthetic pathways. Given this flexibility, myriad alternative reaction partners have been investigated for their reactions with cyclooctynes (Figure 6-3). These include novel azides, nitrones, nitrile oxides, diazos, quinones, sydrones and tetrazines, which have resulted in dramatic improvements in reaction kinetics.

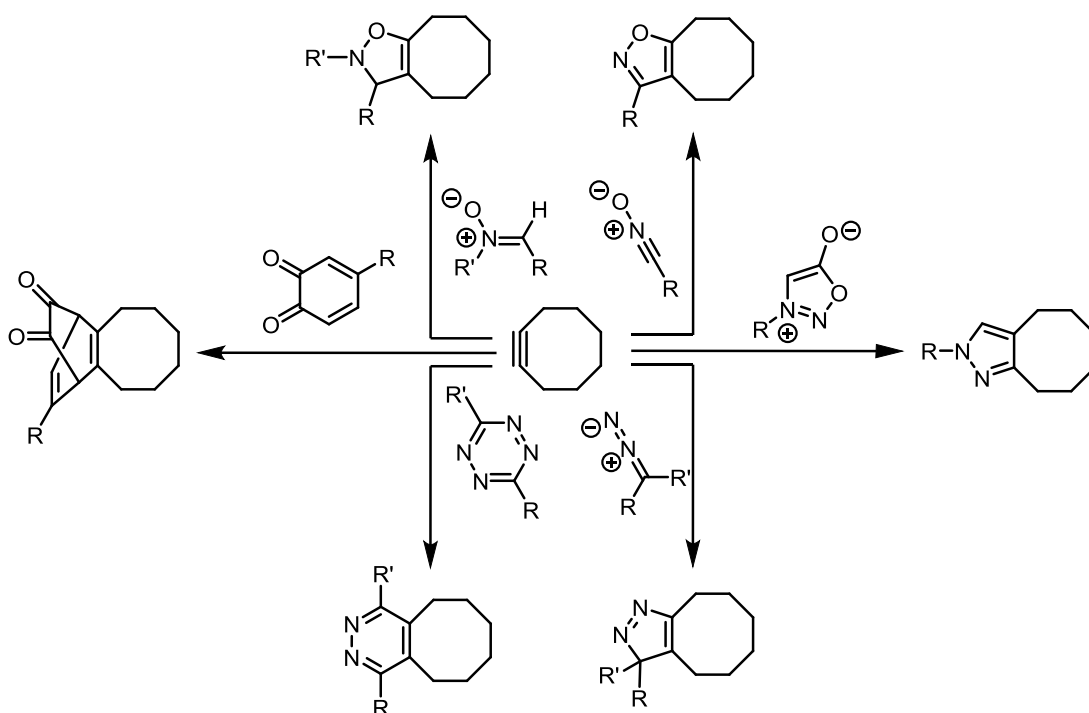


Figure 6-3. Non-azide reaction partners for bioconjugation with cyclooctynes.

Reactions with Modified Azides

As azides were the first bioorthogonal reaction partners identified for cyclooctynes, researchers have investigated how azide structure impacts cycloaddition rate. Early work from the Hosoya group found that doubly sterically hindered aryl azides show unexpectedly high reactivity towards cyclooctynes.¹² In their work, they monitored reactions of Sondheimer diyne **6.14** with alkyl and aryl azides (Figure 6-4A). They found that the reaction of **6.14** with 2,6-diisopropyl phenyl azide **6.15** was 10 times faster than the corresponding reaction with benzyl azide in methanol ($6.7 \times 10^{-1} \text{ M}^{-1}\text{s}^{-1}$ vs. $6.3 \times 10^{-2} \text{ M}^{-1}\text{s}^{-1}$, Figure 6-4B). This enhanced reactivity was not a general property of all aryl azides: the reaction of diyne **6.14** with phenyl azide **6.16** was 7 times

slower compared benzyl azide. These results suggested that the enhanced reactivity of **6.15** was likely due to conformational effects. Indeed, calculations showed that knocking the azide out of conjugation with *ortho* substituents prepaid some of distortion energy required for cycloaddition, resulting in increased reaction rate. Finally, Hosoya and coworkers found that electronic modification of sterically unhindered aryl azides with electron donating or withdrawing groups had a modest effect on reaction rate with diyne **6.14**.

More recently, the van Delft group has also invested the role of the azide in cycloaddition rate.¹³⁻¹⁵ Their interest in this area came from a serendipitous discovery that the fluorogenic 3-azido-7-hydroxycoumarin underwent a remarkably fast cycloaddition reaction with bicyclononyne **6.3** (nearly $2 \text{ M}^{-1}\text{s}^{-1}$ in 1:2 MeCN/H₂O, although the contribution from solvent effects were not delineated).¹³

A systematic investigation of the reaction of aryl azides with cyclooctynes revealed that bicyclononyne **6.3** reacted with phenyl azide 3 times more rapidly than benzyl azide (at $3.0 \times 10^{-1} \text{ M}^{-1}\text{s}^{-1}$, Figure 6-4B), in stark contrast to the Hosoya study performed with diyne **6.14**.¹⁴ In addition, reactions with bicyclononyne were also more sensitive to the electronics of the aryl azide, with extremely electron deficient aryl azides undergoing cycloadditions with **6.3** at rates of up to $2 \text{ M}^{-1}\text{s}^{-1}$ in 9:1 THF/H₂O. The authors attributed the contrasting reactivity of bicyclononyne **6.3** and diyne **6.14**/dibenzocyclooctyne **6.2** to steric effects. To take advantage of the dramatic reactivity difference between the two classes of cyclooctynes, the authors developed a bifunctional linker **6.20**, containing both an alkyl azide and an electron-deficient aryl azide (Figure 6-4C). This linker was used to couple a dibenzocyclooctyne **6.2** functionalized fluorophore with a bicyclononyne functionalized protein in a one pot reaction.

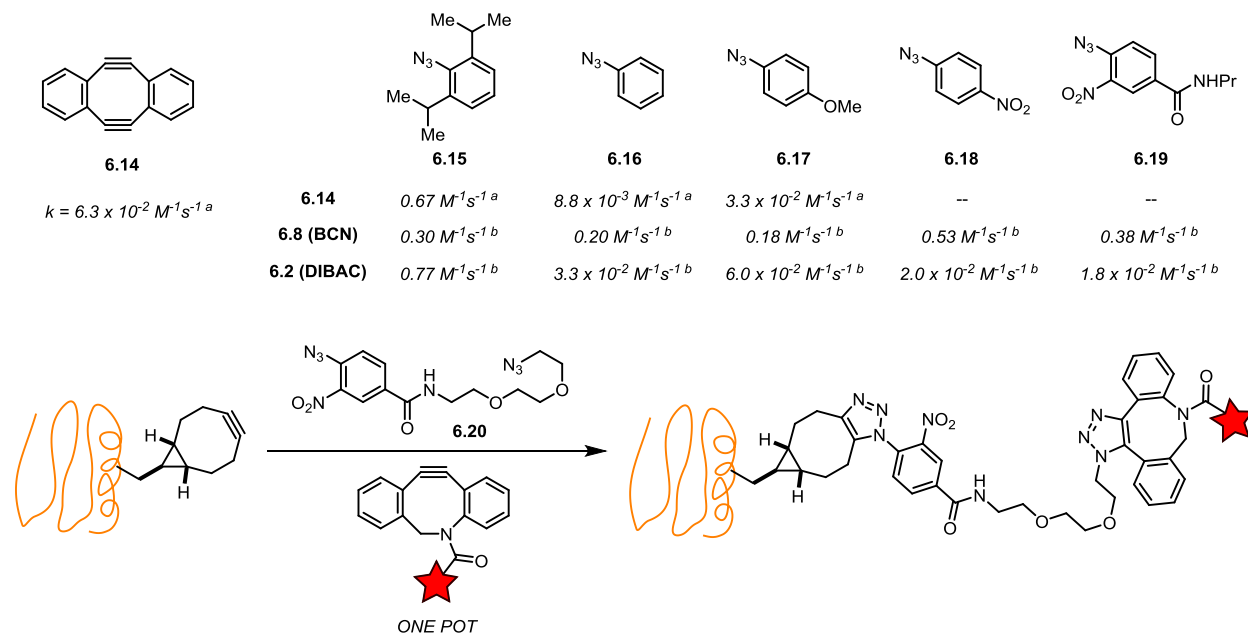


Figure 6-4. Cyclooctyne reactivity with modified azides. (A) Structure of Sondheimer diyne **6.14** and its reaction rate with benzyl azide in methanol. (B) Various aryl azides and their reaction rates with **6.14**, **6.8**, or **6.6**. (C) A one-pot ligation of two cyclooctyne-functionalized molecules enabled by bifunctional linker **6.20**.

Finally, van Delft and coworkers hypothesized that installing electron-withdrawing groups onto alkyl azides would result in the same rate-acceleration seen between aryl azides and bicyclononyne.¹⁵ Consistent with their hypothesis, they found that gem-difluorinated alkyl azides showed a two-fold enhancement in labeling efficiency with bicyclononyne. The small steric difference between hydrogen and fluorine atoms also meant that these fluorinated azide molecules could still be processed by the enzymatic machinery. This suggests that gem-difluorination of alkyl azides may be a generally useful strategy for increasing bioorthogonal labeling efficiency.

Reactions with Nitrones

Nitrones were the first alternative reaction partners investigated for bioconjugation reactions with cyclooctynes. These nitrones undergo cycloaddition reactions to form isoxazolines (**2.21**). The Boons, van Delft, and Pezacki groups have found that nitrones such as **6.22** undergo cycloaddition with alkynes at a comparable rate as azides (Figure 6-5).¹⁶⁻¹⁸ Interestingly, nitrones in conjugation with electron-withdrawing carboxy groups (such as **6.23**) were significantly more reactive, undergoing cycloaddition with dibenzocyclooctyne (DIBO, **6.1**) with a second order rate constant of $3.9 \text{ M}^{-1}\text{s}^{-1}$ in 3:1 $\text{CD}_3\text{CN}/\text{D}_2\text{O}$ (Figure 6-5B).⁷ Even higher rates could be achieved with more reactive cyclooctynes. For example, azadibenzocyclooctyne (DIBAC, **6.2**) reacted with **6.23** at $39 \text{ M}^{-1}\text{s}^{-1}$ in 3:1 $\text{CD}_3\text{CN}/\text{D}_2\text{O}$.^{7,9} Beyond electronic perturbations, Pezacki and coworkers have found that cyclic nitrones such as **6.24** also react rapidly with **6.1** (up to $3.4 \text{ M}^{-1}\text{s}^{-1}$ in CD_3CN), likely due to ring strain (Figure 6-5B).⁸ Reactions of these cyclic nitrones with faster cyclooctynes likewise yield higher reaction rates, up to $47.3 \text{ M}^{-1}\text{s}^{-1}$ in 99:1 $\text{MeCN}/\text{H}_2\text{O}$ with biarylazacyclooctynone (BARAC, **6.5**). Interestingly, ketone-derived **6.25** was virtually unreactive with cyclooctynes (Figure 6-5B). This phenomenon may be due to a combination of steric and electronic factors. The different sensitivities of bicyclononyne and dibenzo-fused cyclooctynes to such factors, as shown for reactions with aryl azides, suggest that bicyclononynes may be promising nitronone reaction partners. Recent work by Pezacki and coworkers, however, show that bicyclononynes are relatively sluggish reaction partners with most nitrones. Reaction with a close relative of **6.21**, for example, proceeded at $2.9 \times 10^{-3} \text{ M}^{-1}\text{s}^{-1}$ in MeOH.

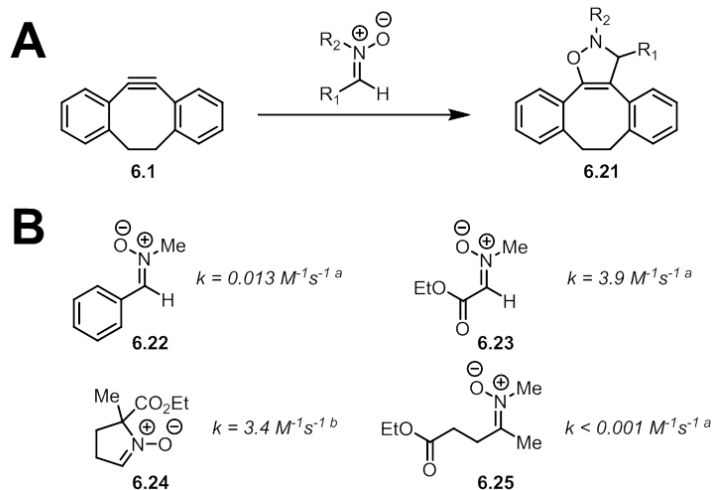
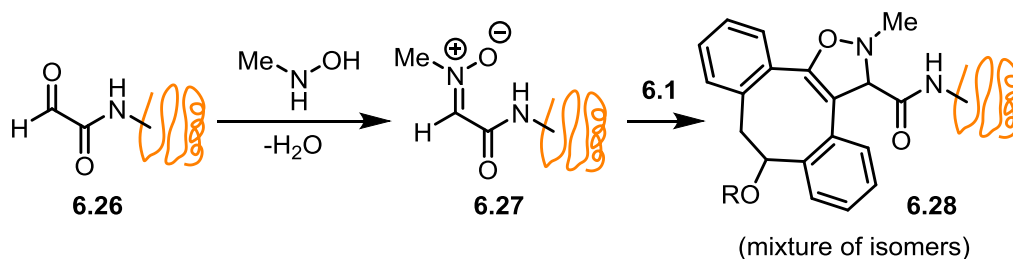


Figure 6-5. Alkyne-nitronium cycloadditions. (A) Strained alkynes and nitroniums react to form oxazolines. (B) Second-order rate constants for the cycloaddition of various nitroniums with dibenzocyclooctyne **6.1**.^{5,6} ^a Measured in 3:1 CD₃CN/D₂O ^b Measured in CD₃CN.

Unfortunately, many nitroniums are susceptible to hydrolysis under acidic or basic conditions, limiting their versatility in chemical biology applications. Boons, van Delft and coworkers found that metabolic incorporation of variety of nitronium-tagged substrates was hampered by nitronium hydrolysis in acidic cellular compartments.¹⁷ Still, nitronium-tagged protein could be prepared *in vitro* by first creating N-terminal aldehyde **6.26** through periodate cleavage of an N-terminal serine. Condensation of the aldehyde with N-methylhydroxylamine generated nitronium **6.27**. The nitronium could then be reacted with **6.1** to form isoxazoline adduct **6.28** (Scheme 6-1). Importantly, the carbon-carbon bond forming nitronium-alkyne cycloaddition produces a dramatically more stable linkage compared to oximes or hydrazones. Although isoxazolines do not benefit from aromaticity (as do triazoles), these adducts were stable at 60 °C in CHCl₃ or at room temperature in a pH 3 or 9 THF/water mixture. N-aryl isoxazolines, however, are known to rearrange to 2-acyl aziridines and 4-oxazolines at room temperature.¹⁹ Hydrolysis of these rearranged products can lead to a net deconjugation. Finally, by using functionalized hydroxylamines with this approach, two different functionalities can be attached onto the protein N-terminus.²⁰



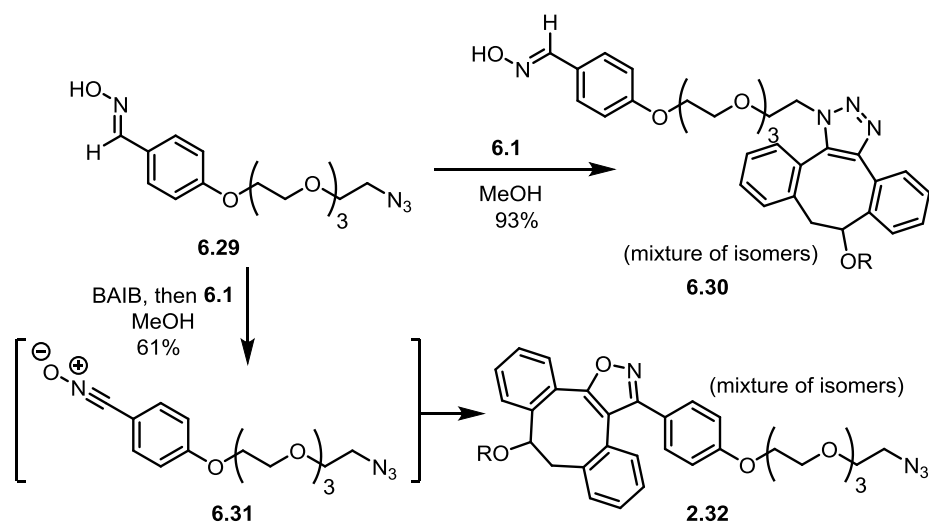
Scheme 6-1. Protein N-terminus labeling using alkyne-nitronium cycloaddition.

The Pezacki group has found that five-membered cyclic nitrones (**6.24**), unlike their acyclic counterparts, were dramatically more stable to hydrolysis and were able to survive incubation in both acidic and basic aqueous solutions.²¹ This increased stability is presumably due to the high effective molarity of the aldehyde and hydroxylamine, driving equilibrium towards the nitron. This higher stability enabled them to perform nitron-alkyne cycloadditions on the cell surface using cyclic nitrones and **6.1**, although the nitron-tagged biomolecule was prepared *in vitro* in this initial work. More recently, by taking advantage of the promiscuity of the bacterial peptidoglycan synthetic machinery, Pezacki and coworkers biosynthetically incorporated cyclic nitrones onto the bacterial cell wall for downstream visualization with cyclooctynes.²² As ketone-derived nitrones are more hydrolytically stable than their aldehyde-derived counterparts, they may be less prone to decomposition within the cell. Therefore, they may find utility in metabolic labeling experiments if their sluggish cycloaddition rates can be addressed (perhaps with more voracious dipolarophiles).

Reactions with Nitrile Oxides

Given the enhanced reactivity of nitrones compared to azides, nitrile oxides were a logical next step in the pursuit of higher cycloaddition kinetics. The Boons group found that nitrile oxides reacted two orders of magnitude faster with **6.1** compared with other similarly substituted 1,3-dipoles (up to $3.4 \text{ M}^{-1}\text{s}^{-1}$ in MeOH).²⁴ While even faster rates may be achieved with nitrile oxides in conjugation with electron-withdrawing groups (as had been seen with nitrones), these species are not known and likely to be highly unstable. Reaction rates with bicyclononyne **6.3** were comparable to those achieved with dibenzocyclooctynes, again in contrast to reactivity trends with aryl azides.²⁵ Typically, nitrile oxides can be generated from imidoyl chlorides by treatment with base. To bypass the difficult-to-generate imidoyl chloride, Boons and coworkers found that oximes generated by the condensation of aldehydes with hydroxylamine could be rapidly oxidized to the nitrile oxide using bis(acetoxy)iodobenzene (BAIB). Other suitable oxidants have since been identified.^{25,26} The *in situ* generated nitrile oxide can then react with cyclooctyne to form an isoxazole product.

To showcase the speed of nitrile oxide cycloadditions, Boons and coworkers synthesized bifunctional linker **6.29**, which contained both an oxime and an azide (Scheme 6-2).²⁴ In the absence of BAIB, **6.1** only underwent cycloaddition with the azide to generate triazole **6.30**. In the presence of BAIB, however, the newly generated nitrile oxide cleanly underwent cycloaddition to form isoxazole cycloadduct **6.31** instead (Scheme 6-2). This linker was also suitable for creating bifunctional compounds by sequential cycloadditions with two differently functionalized molecules of **6.1**. In all cases, an excess of nitrile oxide was necessary for full conversion to product, as nitrile oxides are highly unstable and susceptible to dimerization or nucleophilic attack. Indeed, their limited use, especially in biological contexts, may be a result of the practical limitations arising from their instability and poorly biocompatible conditions for generation.



Scheme 6-2. Selective cycloadditions on a bifunctional linker in the absence or presence of BAIB.

Reactions with Diazos

Another cyclooctyne-reactive 1,3-dipole is the diazo group. Pezacki, Boons and their respective coworkers first demonstrated that diazo compounds may be suitable bioorthogonal reaction partners for cyclooctynes.^{24,27} They found that highly resonance-stabilized diazo compounds reacted with **6.1** at a comparable rate as azides. Pezacki and coworkers also found that less-stabilized diazos such as TMS-diazomethane rapidly underwent cycloaddition with **6.1** in CD_3OD ($>10 \text{ M}^{-1}\text{s}^{-1}$). For monosubstituted diazos, the initially formed cyclic diazene **6.33** tautomerizes to generate aromatic pyrazole **6.34** (Figure 6-6A).

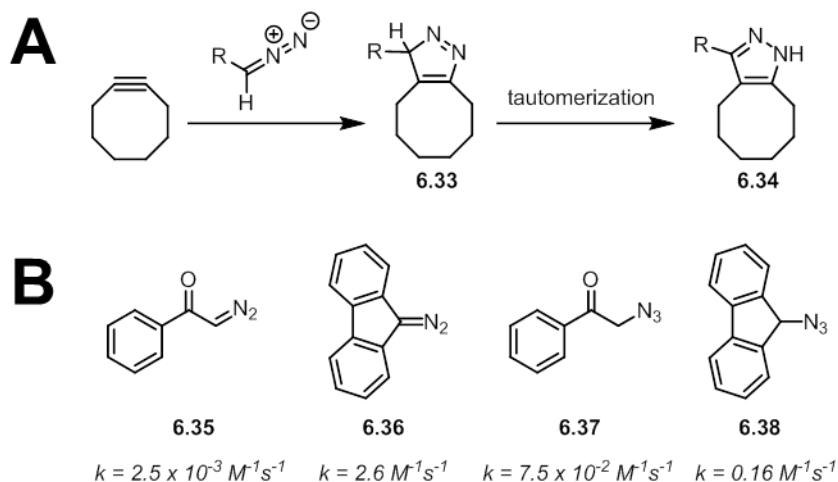


Figure 6-6. Alkyne-diazo cycloadditions. (A) Cycloaddition of diazos with cyclooctyne and subsequent tautomerization. (B) Cycloaddition rates of diazos **6.35** and **6.36** or their parent azides **6.37** and **6.38** with DIBONE **6.6**.

More recently, the Raines group undertook a computational approach to improve the rates of cycloaddition between cyclooctynes and diazo compounds.²⁸ Their interest in diazo compounds arose from their discovery of a general method to access diazo compounds from azides using an interrupted Staudinger reduction.^{29,30} They found that HOMO_{diazo}-LUMO_{alkyne} was the primary orbital interaction involved in cycloaddition. A simple FMO analysis would suggest that a smaller HOMO-LUMO gap would enhance reactivity. Indeed, the electron poor diazoacetophenone **6.35** reacted 1000-fold more slowly than the electron rich diazofluorene **6.36** with cyclooctyne **6.6** ($2.5 \times 10^{-3} \text{ M}^{-1}\text{s}^{-1}$ vs. $2.6 \text{ M}^{-1}\text{s}^{-1}$ in CD₃CN, Figure 6-6B). The structurally related azide compounds **6.37** and **6.38** showed only a two-fold difference in reaction rate, presumably because the azide is electronically decoupled from the rest of the molecule. Still, diazos appear to have significantly more tunable cycloaddition kinetics compared to azides, as shown by the modest differences in cycloaddition rates between different aryl azides and cyclooctynes. Bicyclononyne **6.3** was significantly less reactive to a diazoacetate derivative compared to dibenzocyclooctynes **6.2** or **6.6**, suggesting that sterics play a smaller role than electronic interactions in determining reaction rate.³¹

To highlight the biocompatibility of the diazo group, Raines and coworkers showed that diazofluorene was stable to 10 mM cysteine for over 18 hours.²⁸ Additionally, diazofluorene could cleanly react with **6.6** in the presence of 10 equivalents of the tripeptide glutathione, demonstrating that the reaction could occur in the presence of free amines, thiols, and carboxylic acids. The stability of the cyclic diazene product was not described, but potential decomposition or rearrangement pathways will likely preserve the newly formed carbon-carbon bond. Moreover, diazenes derived from monosubstituted diazos will rapidly tautomerize to the highly stable pyrazoles.

While promising, the ultimate test of stability for chemical reporter groups is their metabolic incorporation into biomolecules. Raines and coworkers took advantage of the promiscuity of the glycan salvage pathway to incorporate a diazo-substituted monosaccharide (**6.39**) into cell surface glycoproteins (Figure 6-7A).³¹ Excitingly, cells treated with diazosugars showed robust labeling over control when treated with a **6.2** functionalized secondary detection agent, demonstrating that the diazo group can survive the entire biosynthetic pathway. Labeling efficiency, however, was significantly lower than what was observed in a parallel experiment using azidosugar **6.40**. Since this difference cannot be explained by cycloaddition rates, poor diazosugar incorporation or decomposition of the diazo group within the cellular milieu may be operative. Raines and coworkers focused on the latter explanation, suggesting that the diazo may be decomposing within acidic cellular compartments.³² In contrast, Brindle, Leepers and coworkers observed that a related diazo-substituted monosaccharide showed only marginal labeling over control, consistent with different preferences of the biosynthetic machinery for diazo versus azide tagged substrates.³³

Importantly, the use of diazos in place of azides as cyclooctyne reaction partners enabled two-color labeling experiments. After treating cells with both diazo- and alkyne-functionalized glycans **6.39** and **6.41**, the two functional groups could be robustly detected by sequential copper-click reactions with azide probes and copper-free click reactions with cyclooctyne probes (Figure 6-7B). In contrast, when cells were fed both azido- and alkyne-functionalized sugars **6.40**

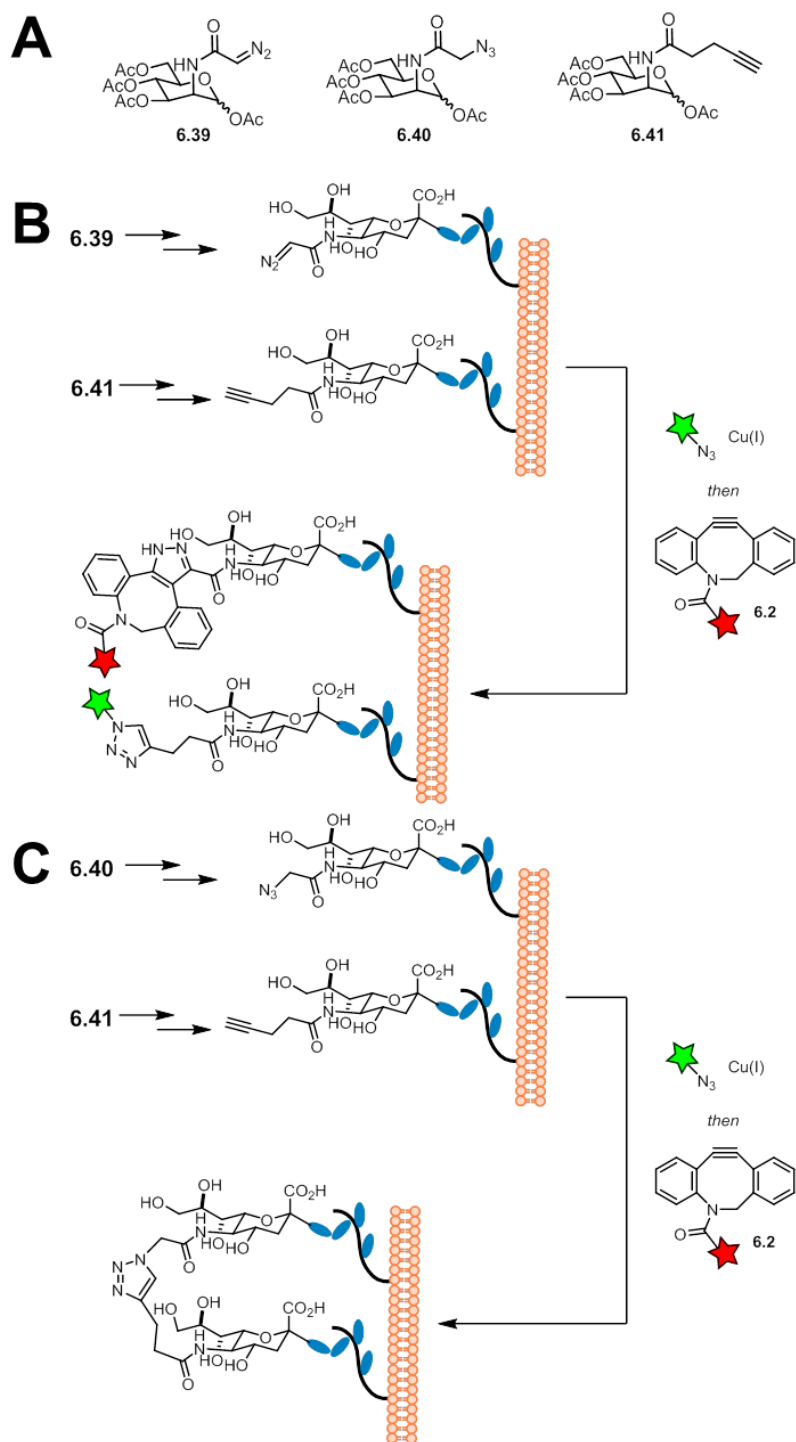


Figure 6-7. Diazo-functionalized monosaccharides enable robust two-color glycan imaging. (A) Structures of the monosaccharides used in metabolic labeling experiments. (B) Two-color labeling with both diazo- and alkyne-functionalized glycans. (C) Proposed Cell-surface crosslinking when both azide- and alkyne-glycans **6.40** and **6.41** were used.

and **6.41**, labeling of azidosugars with cyclooctynes was negligible after the first copper-catalyzed click reaction. The authors attributed this result to the undesired crosslinking of azide and alkyne-functionalized glycoproteins, which does not occur with diazosugars (Figure 6-7C). Overall, the demonstrated advantages of the diazo group: small size, reasonable stability in cells, its orthogonality to copper-catalyzed click chemistry, suggest a bright future for the diazo as a bioorthogonal chemical reporter.

Reactions with Quinones

A recent report from the van Delft and van Hest labs showed that 1,2-quinones undergo rapid Diels-Alder reactions with cyclooctynes (Figure 6-8).³⁴ While 1,2-quinones are generally unstable to storage, they can be generated *in situ* by oxidation of the corresponding catechol with sodium periodate (**6.33** to **6.34**). Notably, reactions with bicyclononynes were exceptionally fast (nearly $500 \text{ M}^{-1}\text{s}^{-1}$ in 1:1 MeOH/H₂O). Reactions with dibenzocyclooctyne **6.2**, in contrast, were significantly slower, potentially due to the same steric interactions that negatively impacted aryl azide reactivity.

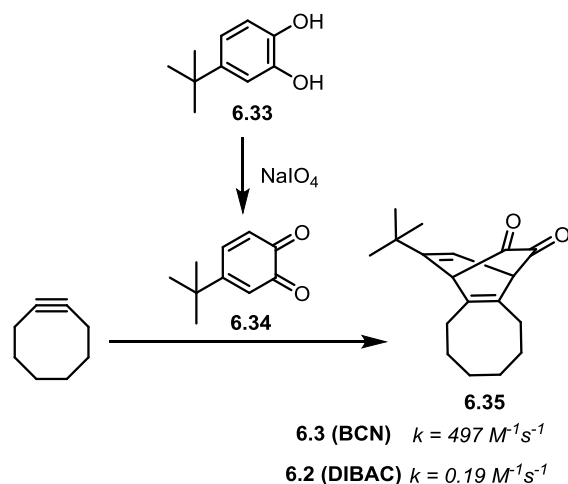


Figure 6-8. Oxidation of catechols to 1,2-quinones and their inverse electron-demand Diels-Alder reaction with cyclooctynes. Rate constants were measured in methanol.

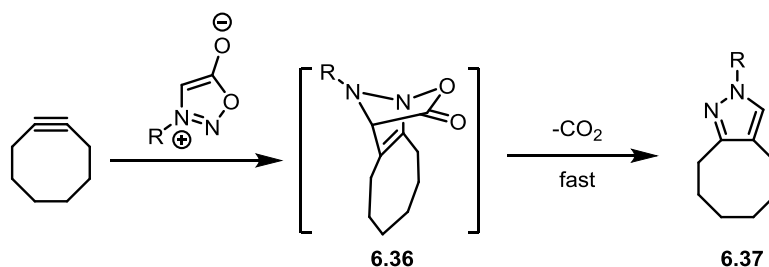
The authors next showed that 1,2-quinone-functionalized fluorophores robustly labeled bicyclononyne-functionalized proteins, demonstrating their utility for bioconjugation. A potential liability of these quinones is their high electrophilicity. For example, 1,2-quinones have been shown to react with both amines and thiols, common biological nucleophiles.³⁵ Shorter bioconjugation reaction times, enabled by fast cycloaddition kinetics, will minimize the likelihood of such side reactions.

An interesting feature of the compounds is that no reaction occurs between the catechol precursor and cyclooctyne. Therefore, oxidation may act as a switch for this bioorthogonal ligation reaction, opening the door to temporal control of reactivity. Such oxidant-controlled reactivity is

also manifested in the *in situ* generation of nitrile oxides, but 1,2-quinones are likely to be more useful due to their rapid cycloaddition kinetics. Finally, milder methods to oxidize catechols, such as with tyrosinases, may allow for the generation of reactive functionalities under milder conditions.

Reactions with Sydnone

Chin and coworkers were among the first to incorporate cyclooctynes into proteins via the pyrrolysine system.⁸ They have since placed substantial effort towards identifying new reaction partners for these genetically encoded cyclooctynes.³⁷ The copper-catalyzed reaction between linear alkynes and sydnone was identified by Taran and coworkers as a candidate for bioorthogonal reaction.³⁸ Reminiscent of strategy used to improve catalyst-free cycloaddition rates of azides and alkynes, the Chin group investigated the role that ring strain would have on sydnone-alkyne cycloadditions. As a testament to the broad utility of this strategy, sydnone and cyclooctynes were found to readily react to generate pyrazole adducts (Scheme 6-3).



Scheme 6-3. [3+2] cycloaddition/retro-Diels-Alder reaction of sydnone and cyclooctyne.

The reaction likely proceeds via a [3+2] cycloaddition reaction to generate diaza [2.2.1] bicyclic lactone intermediate **6.36**. This intermediate then undergoes a retro Diels-Alder reaction, ejecting carbon dioxide and forming pyrazole **6.37**. The reaction rate constant between bicyclononyne and phenyl sydnone was fairly modest, at $0.054 \text{ M}^{-1}\text{s}^{-1}$ in 55:45 MeOH/H₂O. Still, sydnone was found to be suitable for the quantitative labeling of proteins and is a solid contribution to the bioorthogonal toolbox.

Reactions with Tetrazines

Finally, tetrazines also undergo reactions with strained alkynes via inverse electron-demand Diels-Alder reactions. The resulting bicyclic intermediate **6.38** then undergoes a retro-Diels-Alder reaction to extrude dinitrogen and form the final pyridazine product **6.39** (Figure 6-9A). Although tetrazines were initially paired with strained alkenes for bioconjugation, their reactions with strained alkynes have been investigated by multiple groups and are growing in popularity.³⁸

The first systematic investigation of cyclooctyne-tetrazine reactivity was performed by Wang and coworkers, who took a computational approach similar to that performed by Raines and coworkers in their study of diazo reactivity.³⁹ In contrast to cyclooctyne-diazo cycloadditions, HOMO_{alkyne}-LUMO_{tetrazine} was the primary electronic driver of tetrazine ligation rates.

Calculations indicated that the more strained bicyclononyne **6.3** had a higher HOMO energy than parent cyclooctyne **6.7**. Consistent with such predictions, bicyclononyne **6.3** reacted significantly faster than cyclooctyne **6.7** with diphenyltetrazine **6.40** (at $3.3 \text{ M}^{-1}\text{s}^{-1}$ vs. $0.07 \text{ M}^{-1}\text{s}^{-1}$ in MeOH, Figure 6-9B). Furthermore, the more electron poor dipyridyltetrazine **6.41** (lower energy LUMO) had faster rates of reaction with both cyclooctynes ($2.0 \text{ M}^{-1}\text{s}^{-1}$ and $44.8 \text{ M}^{-1}\text{s}^{-1}$ with **6.7** and **6.3** in MeOH, respectively). These different combinations of cyclooctynes and tetrazines spanned a 640-fold range in reaction rates.

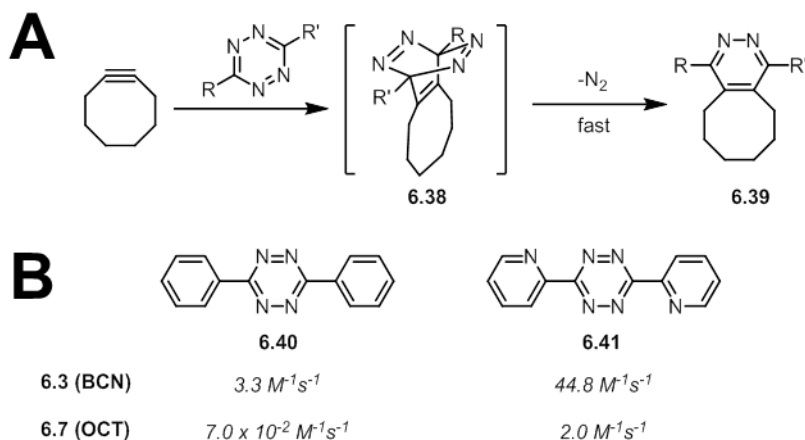


Figure 6-9. Alkyne-tetrazine cycloadditions. (A) Inverse-electron demand Diels-Alder/retro-Diels-Alder reaction of tetrazine and cyclooctyne. (B) Reaction rate constants of various cyclooctynes and tetrazines in methanol.

Notably, Wang and coworkers found that the electron-poor difluorinated cyclooctyne DIFO (**6.4**) which reacts more rapidly with azides than **6.7**, showed no appreciable reactivity with tetrazines. This observation is consistent with an increased $\text{HOMO}_{\text{alkyne}}\text{-LUMO}_{\text{tetrazine}}$ gap from the electron-withdrawing fluorine substituents on DIFO. This observation is also important for dual-labeling studies using cyclooctynes/azides and strained alkenes/tetrazines. Simultaneous detection of azide- and strained alkene-tagged biomolecules with cyclooctynes and tetrazines, respectively, may fail if the cyclooctyne and tetrazine secondary reagents react with each other instead of their intended targets.

Another solution to mitigate cross-reactivity was identified by Hildebrand and coworkers.³⁹ They found that dibenzo-fused cyclooctynes are unreactive with tetrazines. The contrasting reactivity of bicyclononynes and dibenzo-fused cyclooctynes, as seen with aryl azides and 1,2-quinones, is again likely due to unfavorable steric interactions. Consistent with this hypothesis, Houk and coworkers observed such a steric clash in the transition state of the reaction between tetrazines and dibenzocyclooctynes.⁴⁰ In that work, they also suggested that thiacycloheptyne **6.8** may be inert to tetrazines due to steric shielding by the tetramethyl substituents.

The Chin and Lemke groups were the first to demonstrate the utility of tetrazines for tagging cyclooctyne-functionalized biomolecules.⁷⁻⁹ The two groups used the pyrrolysine system to site-

specifically incorporate cyclooctyne-functionalized amino acids **6.9** and **6.10** into proteins, which could subsequently be visualized using tetrazine-functionalized fluorophores (Figure 6-10). These tetrazine ligations were found to be extraordinarily fast. Proteins bearing amino acid **6.9** reacted with dipyridyltetrazine-fluorophore conjugations at $400 \text{ M}^{-1}\text{s}^{-1}$ in water.⁷ As may be expected, faster reaction kinetics can be achieved with the bicyclononyne-functionalized amino acid **6.10**. Indeed, proteins bearing **6.10** appear to react with dipyridyltetrazines at rates exceeding $10^4 \text{ M}^{-1}\text{s}^{-1}$ in water.⁹ While these on-protein rates are not directly comparable to rates determined for other reaction partners, the impressive reactivity of tetrazines is clear. As a better comparison, free amino acid **6.10** reacted with a derivative of **6.41** with a rate constant of $1245 \text{ M}^{-1}\text{s}^{-1}$ in 55:45 MeOH/H₂O.⁸ A potential liability of electron-poor tetrazines such as **6.41** is their susceptibility to hydrolysis. Reactions with the stable methyl-substituted tetrazine, however, still show rates in excess of $10 \text{ M}^{-1}\text{s}^{-1}$.

Importantly, these tetrazine-functionalized probes were suitable for labeling metabolically incorporated **6.10** in live mammalian cells. Their high reactivity enabled efficient labeling using sub-micromolar concentrations of probe in under an hour.⁸ More recently, the incorporation of **6.10** enabled the live-cell superresolution microscopy of bicyclononyne-functionalized proteins using tetrazine probes.⁴² The rapid reaction kinetics of tetrazines with bicyclononynes enabled quantitative labeling in cells, providing the high labeling density needed for superresolution microscopy. The small size of unnatural amino acids versus genetic protein fusions provides a distinct advantage for the non-perturbative study of proteins.

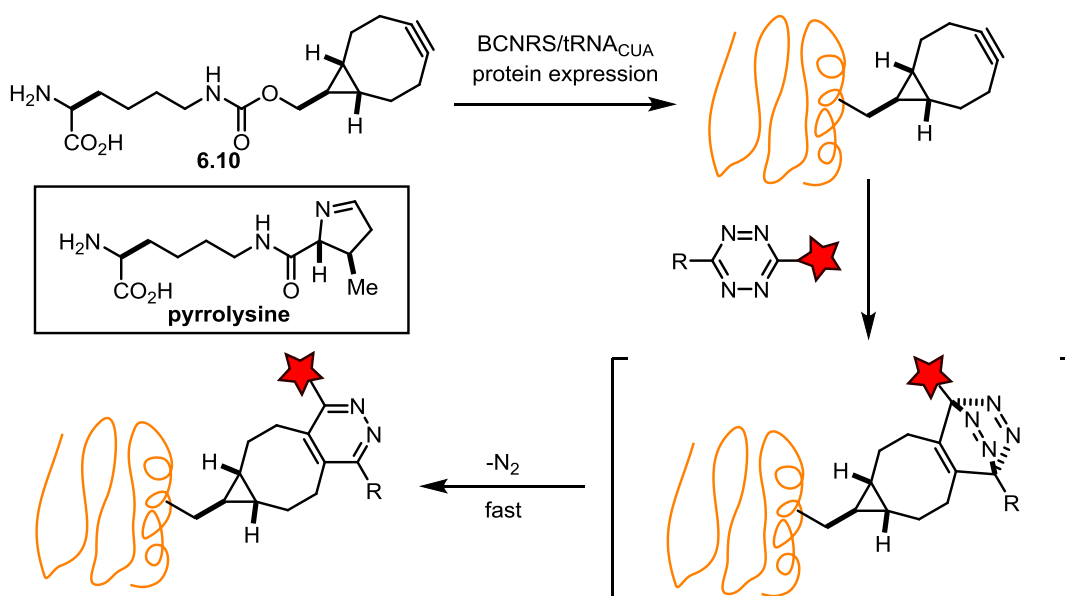


Figure 6-10. Biomolecule labeling through the reaction of a genetically encoded cyclooctyne **6.10** with a tetrazine-fluorophore conjugate.

Tetrazines have also been developed as chemical reporter groups.⁴³ Specifically, tetrazine-functionalized unnatural amino acids have been site-specifically incorporated into proteins. To mitigate unwanted hydrolysis, the tetrazines were stabilized with electron-donating groups. Although the reactivity of these tetrazine-functionalized biomolecules with cyclooctynes is not known, they will likely show significantly reduced reaction kinetics compared to the tetrazines **6.40** or **6.41**. As *trans*-cyclooctenes undergo even more rapid cycloaddition reactions with tetrazines (over an order-of-magnitude greater than cyclooctynes), they will likely remain the reagent of choice over cyclooctynes for labeling tetrazine-tagged biomolecules.

The kinetic advantage of the tetrazine ligation also proved beneficial for the production of bispecific antibodies. These antibodies, which target two different antigens, offer an additional layer of selectivity over single-antigen binding antibodies and may represent the next generation of targeted chemotherapeutics. Direct expression of antibody fusions, however, has proven extremely challenging. The Bertozzi and Schultz groups have identified an alternative approach towards bispecific antibodies using bioorthogonal chemistry (Figure 6-11).^{44,45} In their work, carbonyls were introduced into individual antibody fragments using formylglycine generating enzyme or unnatural amino acids. Next, bifunctional linkers bearing a hydroxylamine and a cyclooctyne or azide (**6.42** or **6.43**) were attached to the fragments with oxime chemistry. Finally, the azide- or cyclooctyne-functionalized antibody fragments could be coupled together to prepare the final bispecific antibody. While effective, this strategy required overnight incubation with fairly high concentrations of proteins for quantitative conversion. By swapping out the azide for a tetrazine, significant conversion to the bispecific antibody was observed within minutes.⁴⁶ Interestingly, conversion never exceeded 60% using this chemistry, potentially due to decomposition of the tetrazine-biomolecule conjugate. Ultimately, tetrazines, with their demonstrated bioorthogonality and extremely high reaction kinetics, will likely supplant the azide as the reagent of choice for tagging cyclooctyne-tagged biomolecules.

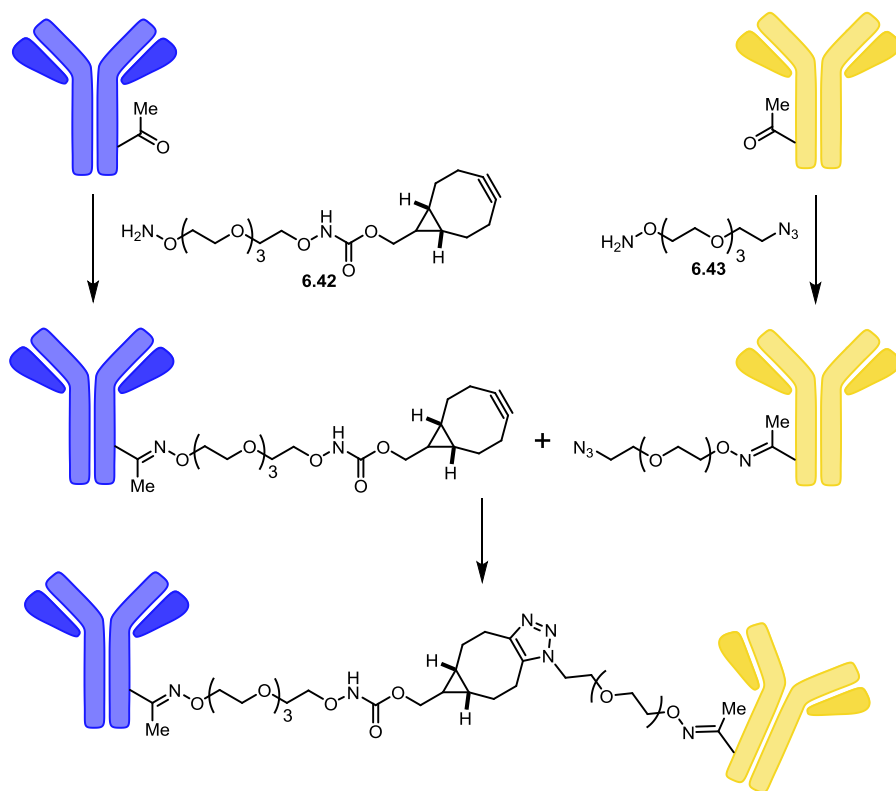


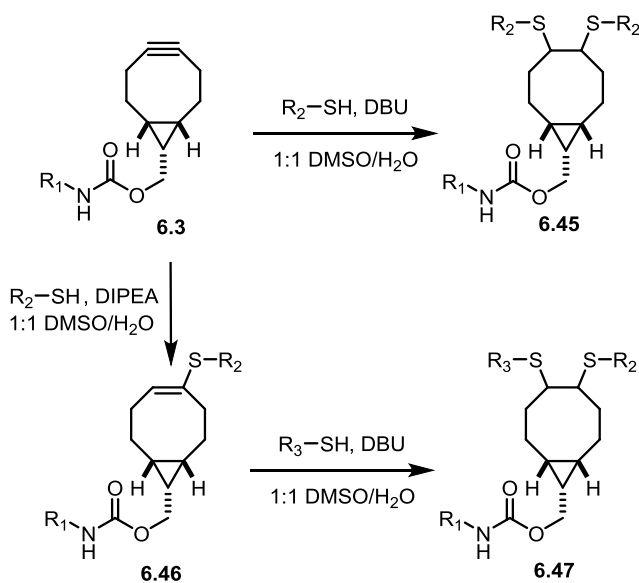
Figure 6-11. Generation of bispecific antibodies using bioorthogonal chemistry. Bifunctional linkers **6.42** and **6.43** are first conjugated onto two separate monoclonal antibodies bearing ketone handles. Afterwards, the two antibodies are coupled together using copper-free click chemistry.

Reactions with Thiols and Higher-Order Sulfur Compounds

Cyclooctynes have also been found to suffer from some side reactions in biological systems, exacerbated by the same modifications intended to increase their cycloaddition rates with azides. In particular, much of their background reactivity has been attributed to thiols, which can add to cyclooctynes to form covalent adducts.⁴ Originally, thiol addition into cyclooctynes was anticipated to only proceed via Michael addition. This belief motivated the use of difluorination instead of carbonyls to decrease alkyne electron density for enhanced azide reactivity (as in DIFO **6.4**).⁴⁷ Still, it has been discovered that the diradical character of strained alkynes still enables thiol addition via radical pathways. For cell surface labeling *in vitro*, this background reactivity is negligible due to the fact that most cysteines are tied up in disulfide bonds. For lysates, intracellular, or *in vivo* labeling applications, however, background labeling by cyclooctynes is a more serious concern.⁴⁸⁻⁵⁰ In lysates, this problem can be addressed by capping free thiols with iodoacetamide before copper-free click ligation.⁴

Making lemonade out of lemons, cyclooctyne-thiol reactivity has been used as a platform to create multi-functional probes (Scheme 6-4).⁵¹ Hong, Cheng, and their respective coworkers found that two thiol molecules could add into bicyclononyne **6.3** in the presence of catalytic

DBU to form adduct **6.45**. The radical scavenger TEMPO inhibited this reaction, consistent with a reaction proceeding via radical intermediates. Interestingly, by switching to a weaker base, DIPEA, they could cleanly isolate monoadduct **6.46**. Treatment of this monoadduct with a different thiol in the presence of DBU forms a trifunctional probe **6.47**. By conjugating bicyclononynes bearing targeting agents with thiol-functionalized imaging probes, the groups could readily prepare a targeted probe suitable for simultaneous fluorescence and PET imaging.



Scheme 6-4. Addition of thiols into bicyclononyne **6.3** enables the facile generation of multifunctional probes.

More recently, rapid reactions between cyclooctynes and oxidized sulfur species were identified.^{52,53} Sulfenic acids are most commonly found as oxidized cysteine residues, and play an important role in oxidative signaling pathways in biology (Figure 6-12A). Bicyclononyne was found to undergo a cycloaddition-like mechanism with sulfenic acids to generate alkenyl sulfoxide **6.48** (Figure 6-12B).⁵² This reaction was impressively fast, with a rate constant between cyclooctynes and sulfenic acids of up to $25 \text{ M}^{-1}\text{s}^{-1}$ with model sulfenic acid **6.49** in acetonitrile and $16.7 \text{ M}^{-1}\text{s}^{-1}$ on cysteine sulfenic acid in proteins (Figure 6-12C). The resulting sulfoxide adducts were also highly stable, showing no degradation after prolonged exposure to reducing agents such as DTT or TCEP. Interestingly, *trans*-cyclooctene also reacted with sulfenic acids to generate alkyl sulfoxides, but at a dramatically slower rate compared to bicyclononyne ($0.02 \text{ M}^{-1}\text{s}^{-1}$). Sulfenic acids reacted two-orders of magnitude more rapidly with bicyclononyne than with dimedones, the most widely used tool for sulfenic acids; therefore, the authors suggested that **6.3** may be the reagent of choice for studying sulfenic acid biology.⁵⁴

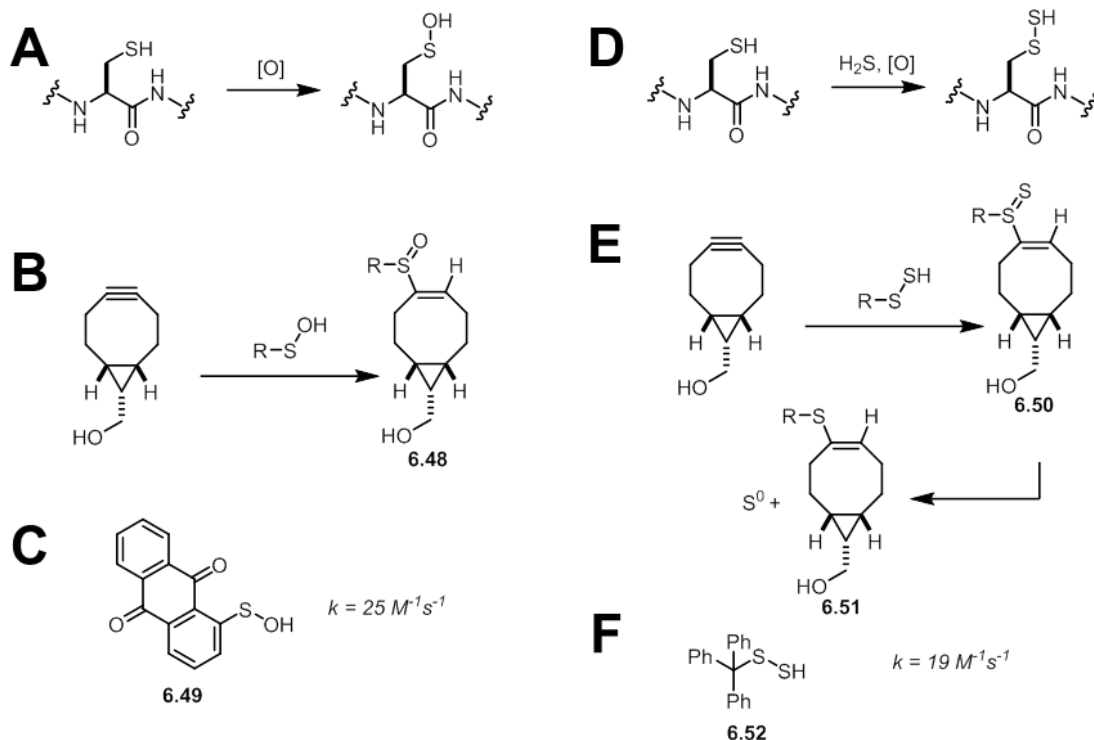


Figure 6-12. Reactions of cyclooctynes with oxidized sulfur species. (A) Conversion of cysteines to sulfenic acids. (B) Reactions of sulfenic acids with bicyclononyne to form adduct **6.48**. (C) Sulfenic acid **6.49** and its reaction rate with bicyclononyne. (D) Conversion of cysteines to persulfides. (E) Reactions of persulfides with bicyclononyne to form adduct **6.51**. (F) Persulfide **6.52** and its reaction rate with bicyclononyne. Reaction rates were measured in acetonitrile.

A subsequent report demonstrated that cyclooctynes also react with persulfides.⁵³ Persulfides, another form of oxidative cysteine modification in biological systems, can be viewed as disulfides derived from the signaling molecule hydrogen sulfide (Figure 6-12D).⁵⁵ Bicyclononyne likely undergoes a cycloaddition reaction to generate the thiosulfoxide intermediate **6.50**, similar to its reaction with sulfenic acids. This intermediate is highly unstable due to the weak sulfur-sulfur double bond. As a result, it rapidly decomposes to form alkenyl thioether **6.51** and elemental sulfur (Figure 6-12E). The reaction of bicyclononyne **6.3** with persulfide **6.52** proceeded at $19 \text{ M}^{-1}\text{s}^{-1}$ in acetonitrile, almost identical to the reaction rate with sulfenic acids (Figure 6-12F). This lack of selectivity is problematic, as a significant fraction of cysteines exist as persulfides, and represents a caveat for using **6.3** to probe sulfenic acid biology. The fact that persulfides react rapidly with cyclooctynes also provides another explanation for the background observed in cellular lysates that has been attributed to cysteines. Capping of persulfides with iodoacetamide will also prevent cycloaddition, and the resulting adducts are also identical to what would be observed by direct cysteine addition.⁴ While these side-reactions are problematic in the context of bioorthogonal chemistry, they also suggest an exciting second life for cyclooctynes as tools to probe the biology of cysteine-mediated redox signaling.

Conclusion

Novel reaction partners of cyclooctynes have enabled bioconjugations at rates three orders of magnitude higher than the fastest known copper-free azide-alkyne cycloaddition reaction. The ability of cyclooctyne to robustly react with a variety of 1,3-dipoles and dienes is a testament to its versatile reactivity. Beyond these cycloaddition reactions, their interactions with thiols and oxidized sulfur species add another layer of complexity to our understanding of cyclooctyne reactivity. Furthermore, the contrasting reactivity trends observed with different reaction partners (such as alkyl vs. aryl azides) hint at limits to our understanding of how steric interactions impact cycloaddition rate. While important early work has been done on this front, a comprehensive computational study of how these two classes of cyclooctynes react with the reaction partners described here may enable the development of powerful predictive tools. The importance of these reactivity differences is clear, as showcased in the one-pot three-component ligation reaction in Figure 6-4C.

These systematic investigations of cycloaddition reactions have also established the broad utility of cyclooctynes beyond its original role as a tool to detect azides. Cyclooctynes, for example, provide superior cycloaddition kinetics over virtually any other alkene and alkyne reaction partner. Their reactivity appears to only be surpassed by the closely related *trans*-cyclooctene. In practice, however, cyclooctynes offer many advantages over the *trans*-cyclooctene that may be worth the slightly slower kinetics. For instance, *trans*-cyclooctenes (but not cyclooctynes) undergo cis-trans isomerization, a major liability when these molecules are exposed to biological systems for prolonged periods of time, such as during biosynthetic incorporation. Additionally, the adducts formed by cyclooctynes are also generally more stable and homogenous than those of the *trans*-cyclooctene. This is due to the extra degree of unsaturation of alkynes, which often leads to aromatic cycloaddition products. For example, cycloaddition of tetrazines with cyclooctynes results in the formation of aromatic pyrazine adducts. The tetrazine ligation, as first described with *trans*-cyclooctenes, results in the formation of a mixture of dihydropyrazine adducts. Autoxidation of these adducts to pyrazines has also been observed.⁵⁶ As another example, whereas the classic cyclooctyne-azide cycloaddition forms an aromatic triazole, the adduct between *trans*-cyclooctenes and azides is highly unstable. Finally, the physical properties of the two probes are also somewhat different; Chin, for example, has found that amino acid **6.10** washes out of cells significantly better than the related *trans*-cyclooctene functionalized amino acid.

Similar to how Huisgen and coworkers were unlikely to predict the impact their seminal work on the chemistry of 1,3-dipoles would have on the field of chemical biology, cyclooctynes have found new roles and reaction partners well beyond their initial development as a tool to detect azides. This chapter has covered the exciting developments that have occurred almost exclusively in the past six years. It will be exciting to see what new applications cyclooctynes may find in the future.

References

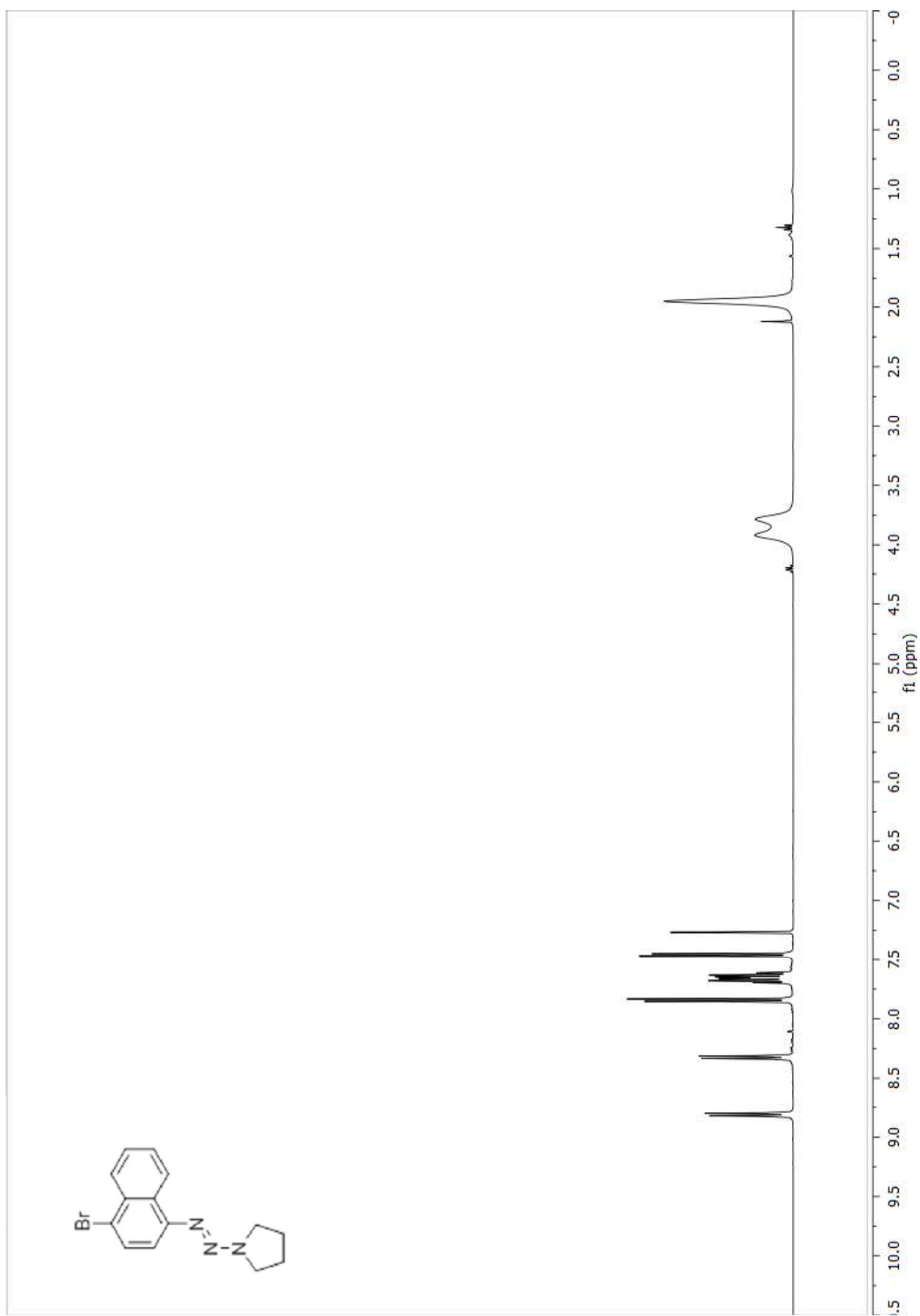
1. Boyce, M.; Bertozzi, C. R. *Nat. Methods* **2011**, *8*, 638-642.
2. Jewett, J. C.; Bertozzi, C. R. *Chem. Soc. Rev.* **2010**, *39*, 1272-1279.
3. (a) See Ref. 2 and references therein. (b) Debets, M. F.; van Berkel, S. S.; Schoffelen, S.; Rutjes, F. P. J. T.; van Hest, J. C. M.; van Delft, F. L. *Chem. Comm.* **2010**, *46*, 97-99. (c) Dommerholt, J.; Schmidt, S.; Temming, R.; Hendriks, L. J. A.; Rutjes, F. P. J. T.; van Hest, J. C. M.; Lefeber, D. J.; Friedl, P.; van Delft, F. L. *Angew. Chem. Int. Ed.* **2010**, *49*, 9422-9425. (d) Jewett, J. C.; Sletten, E. M.; Bertozzi, C. R. *J. Am. Chem. Soc.* **2010**, *132*, 3688-3690. (e) Mbua, N. E.; Guo, J.; Wolfert, M. A.; Steet, R.; Boons, G.-J. *ChemBioChem* **2011**, *12*, 1912-1921. (f) de Almeida, G.; Sletten, E. M.; Nakamura, H.; Palaniappan, K. K.; Bertozzi, C. R. *Angew. Chem. Int. Ed.* **2012**, *51*, 2443-2447.
4. van Geel, R.; Pruijn, G. J. M.; van Delft, F. L.; Boelens, W. C. *Bioconjug. Chem.* **2012**, *23*, 392-398.
5. Sletten, E. M.; Nakamura, H.; Jewett, J. C.; Bertozzi, C. R. *J. Am. Chem. Soc.* **2010**, *132*, 11799-11805.
6. Plass, T.; Milles, S.; Koehler, C.; Schultz, C.; Lemke, E. A. *Angew. Chem. Int. Ed.* **2011**, *50*, 3878-3881.
7. Plass, T.; Milles, S.; Koehler, C.; Szymanski, J.; Mueller, R.; Wiessler, M.; Schultz, C.; Lemke, E. A. *Angew. Chem. Int. Ed.* **2012**, *51*, 4166-4170.
8. Lang, K.; Davis, L.; Wallace, S.; Mahesh, M.; Cox, D. J.; Blackman, M. L.; Fox, J. M.; Chin, J. W. *J. Am. Chem. Soc.* **2012**, *134*, 10317-10320.
9. Borrmann, A.; Milles, S.; Plass, T.; Dommerholt, J.; Verkade, J. M.; Wiessler, M.; Schultz, C.; van Hest, J. C.; van Delft, F. L.; Lemke, E. A. *ChemBioChem* **2012**, *13*, 2094-2099.
10. Neef, A. B.; Schultz, C. *Angew. Chem. Int. Ed.* **2009**, *48*, 1498-1500.
11. Shieh, P.; Siegrist, M. S.; Cullen, A. J.; Bertozzi, C. R. *Proc. Natl. Acad. Sci.* **2014**, *111*, 5456-5461.
12. Yoshida, S.; Shiraishi, A.; Kanno, K.; Mtasushita, T.; Johmoto, K.; Uekusa, H.; Hosoya, T. *Sci. Rep.* **2011**, *1*, 82.
13. Leunissen, E. H. P.; Meuleners, M. H. L.; Verkade, J. M. M.; Dommerholt, J.; Hoenderop, J. G. J.; van Delft, F. L. *ChemBioChem*, **2014**, *15*, 1446-1451.
14. Dommerholt, J.; van Rooijen, O.; Borrmann, A.; Guerra, C. F.; Bickelhaupt, F. M.; van Delft, F. L. *Nat. Commun.* **2014**, *5*, 5378.
15. Van Geel, R.; Wijdeven, M. A.; Heesbeen, R.; Verkade, J. M. M.; Wasiel, A. A.; van Berkel, S. S.; van Delft, F. L. *Bioconj. Chem.* **2015**, *26*, 2233-2242.
16. For a review of nitron-alkyne cycloadditions, see: MacKenzie, D. A.; Sherratt, A. R.; Chigrinova, M.; Cheung, L. L. W.; Pezacki, J. P. *Curr. Opin. Chem. Biol.* **2014**, *21*, 81-88.
17. Ning, X.; Temming, R. P.; Dommerholt, J.; Guo, J.; Ania, D. B.; Debets, M. F.; Wolfert, M. A.; Boons, G.-J.; van Delft, F. L. *Angew. Chem. Int. Ed.* **2010**, *49*, 3065-3068.
18. McKay, C. S.; Chigrinova, M.; Blake, J. A.; Pezacki, J. P. *Org. Biomol. Chem.* **2012**, *10*, 3066-3070.
19. Baldwin, J. E.; Pudusery, R. G.; Qureshi, A. K.; Sklarz, B. *J. Am. Chem. Soc.* **1968**, *90*, 5325-5326.
20. Temming, R. P.; Eggermont, L.; van Eldijk, M. B.; van Hest, J. C. M.; van Delft, F. L. *Org. Biomol. Chem.* **2013**, *11*, 2772-2779.

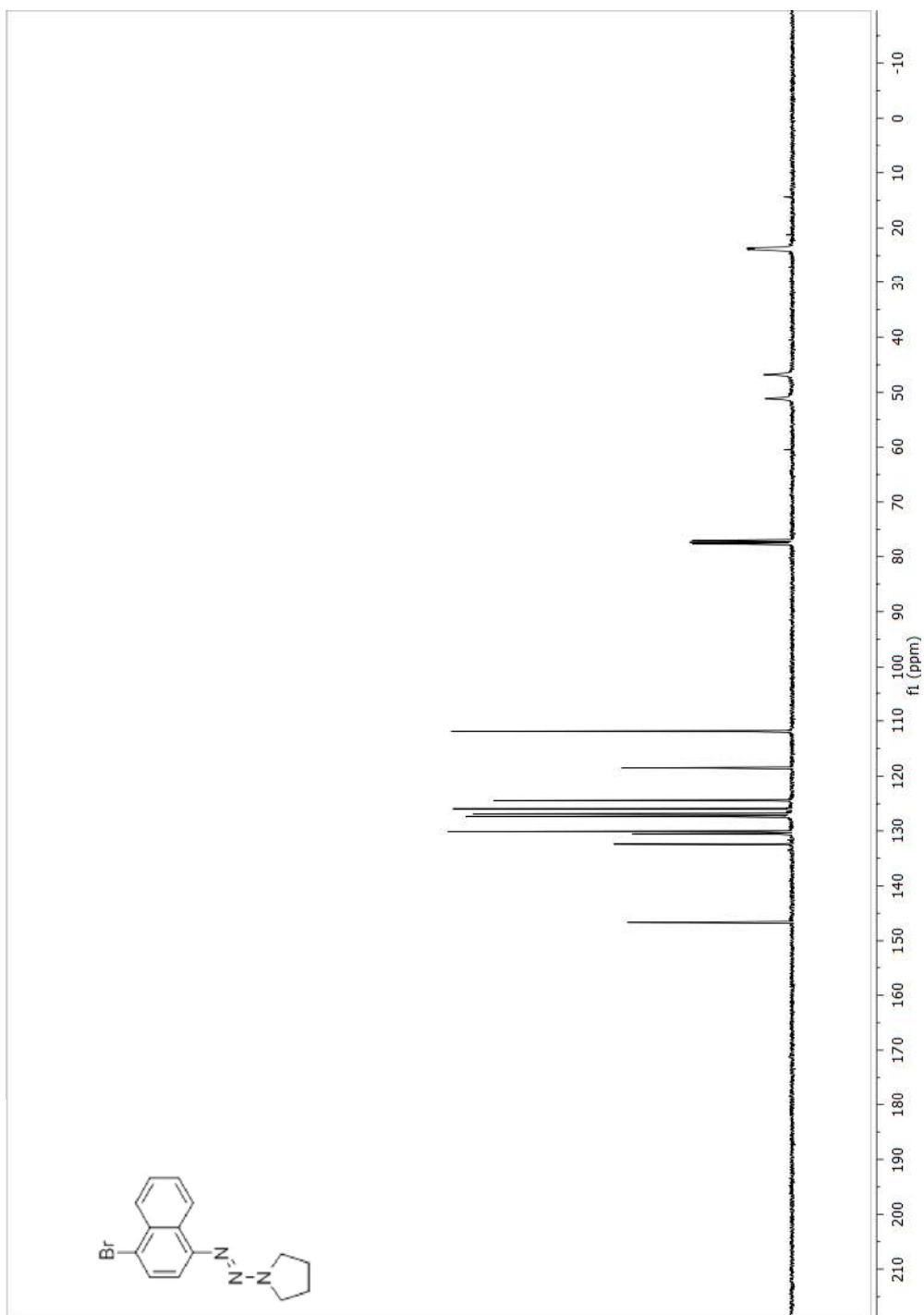
21. McKay, C. S.; Blake, J. A.; Cheng, J.; Danielson, D. C.; Pezacki, J. P. *Chem. Commun.* **2011**, *47*, 10040-10042.
22. MacKenzie, D. A.; Sherratt, A. R.; Chigrinova, M.; Kell, A. J.; Pezacki, J. P. *Chem. Commun.* **2015**, *51*, 12501-12054.
23. MacKenzie, D. A.; Pezacki, J. P. *Can. J. Chem.* **2014**, *92*, 337-340.
24. Sanders, B. C.; Friscourt, F.; Ledin, P. A.; Mbua, N. E.; Arumugam, S.; Guo, J.; Boltje, T. J.; Popik, V. V.; Boons, G.-J. *J. Am. Chem. Soc.* **2011**, *133*, 949-957.
25. Jawalekar, A. M.; Reubsaet, E.; Rutjes, F. P. J. T.; van Delft, F. L. *Chem. Commun.* **2011**, *47*, 3198-3200.
26. Singh, I.; Heaney, F. *Chem. Commun.* **2011**, *47*, 2706-2708.
27. Moran, J.; McKay, C. S.; Pezacki, J. P. *Can. J. Chem.* **2011**, *89*, 148-151.
28. McGrath, N. A.; Raines, R. T. *Chem. Sci.* **2012**, *3*, 3237-3240.
29. Myers, E. L.; Raines, R. T. *Angew. Chem. Int. Ed.* **2009**, *48*, 2359-2363.
30. Chou, H.-H.; Raines, R. T. *J. Am. Chem. Soc.* **2013**, *135*, 14936-14939.
31. Andersen, K. A.; Aronoff, M. R.; McGrath, N. A.; Raines, R. T. *J. Am. Chem. Soc.* **2015**, *137*, 2412-2415.
32. McGrath, N. A.; Andersen, K. A.; Davis, A. K. F.; Lomax, J. E.; Raines, R. T. *Chem. Sci.* **2015**, *6*, 752-755.
33. Josa-Cullere, L.; Wainman, Y. A.; Brindle, K. M.; Leeper, F. J. *RSC Adv.* **2014**, *4*, 52241-52244.
34. Borrmann, A.; Fatunsin, O.; Dommerholt, J.; Jonker, A. M.; Lowik, D. W. P. M.; van Hest, J. C. M.; van Delft, F. L. *Bioconjug. Chem.* **2015**, *26*, 257-261.
35. Liu, B.; Burdine, L.; Kodadek, T. *J. Am. Chem. Soc.* **2006**, *126*, 15228-15235.
36. Wallace, S.; Chin, J. W. *Chem. Sci.* **2014**, *5*, 1742-1744.
37. Kolodych, S.; Rasolofonjatovo, E.; Chaumontet, M.; Nevers, M.-C.; Creminon, C.; Taran, F. *Angew. Chem. Int. Ed.* **2013**, *52*, 12056-12060.
38. Devaraj, N. K.; Weissleder, R. *Acc. Chem. Res.* **2011**, *44*, 816-827.
39. Chen, W.; Wang, D.; Dai, C.; Hamelberg, D.; Wang, B. *Chem. Commun.* **2012**, *48*, 1736-1738.
40. Karver, M. R.; Weissleder, R.; Hilderbrand, S. A. *Angew. Chem. Int. Ed.* **2012**, *51*, 920-922.
41. Liang, Y.; Mackey, J. L.; Lopez, S. A.; Liu, F.; Houk, K. N. *J. Am. Chem. Soc.* **2012**, *134*, 17904-17907.
42. Uttamapinant, C.; Howe, J. D.; Lang, K.; Beranek, V.; Davis, L.; Mahesh, M.; Barry, N. P.; Chin, J. W. *J. Am. Chem. Soc.* **2015**, *137*, 4602-4605.
43. Seitchik, J. L.; Peeler, J. C.; Taylor, M. T.; Blackman, M. L.; Rhoads, T. W.; Cooley, R. B.; Refakis, C.; Fox, J. M.; Mehl, R. A. *J. Am. Chem. Soc.* **2012**, *134*, 2898-2901.
44. Hudak, J. E.; Barfield, R. M.; de Hart, G. W.; Grob, P.; Nogales, E.; Bertozzi, C. R.; Rabuka, D. *Angew. Chem. Int. Ed.* **2012**, *51*, 4161-4165.
45. Kim, C. H.; Axup, J. Y.; Dubrovskaya, A.; Kazane, S. A.; Hutchins, B. A.; Wold, E. D.; Smider, V. V.; Schultz, P. G. *J. Am. Chem. Soc.* **2012**, *134*, 9918-9921.
46. Ramadoss, N. S.; Schulman, A. D.; Choi, S.; Rodgers, D. T.; Kazane, S. A.; Kim, C. H.; Lawson, B. R.; Young, T. S. *J. Am. Chem. Soc.* **2015**, *137*, 5288-5291.
47. Sletten, E. M.; Bertozzi, C. R. *Acc. Chem. Res.* **2011**, *44*, 666-676.

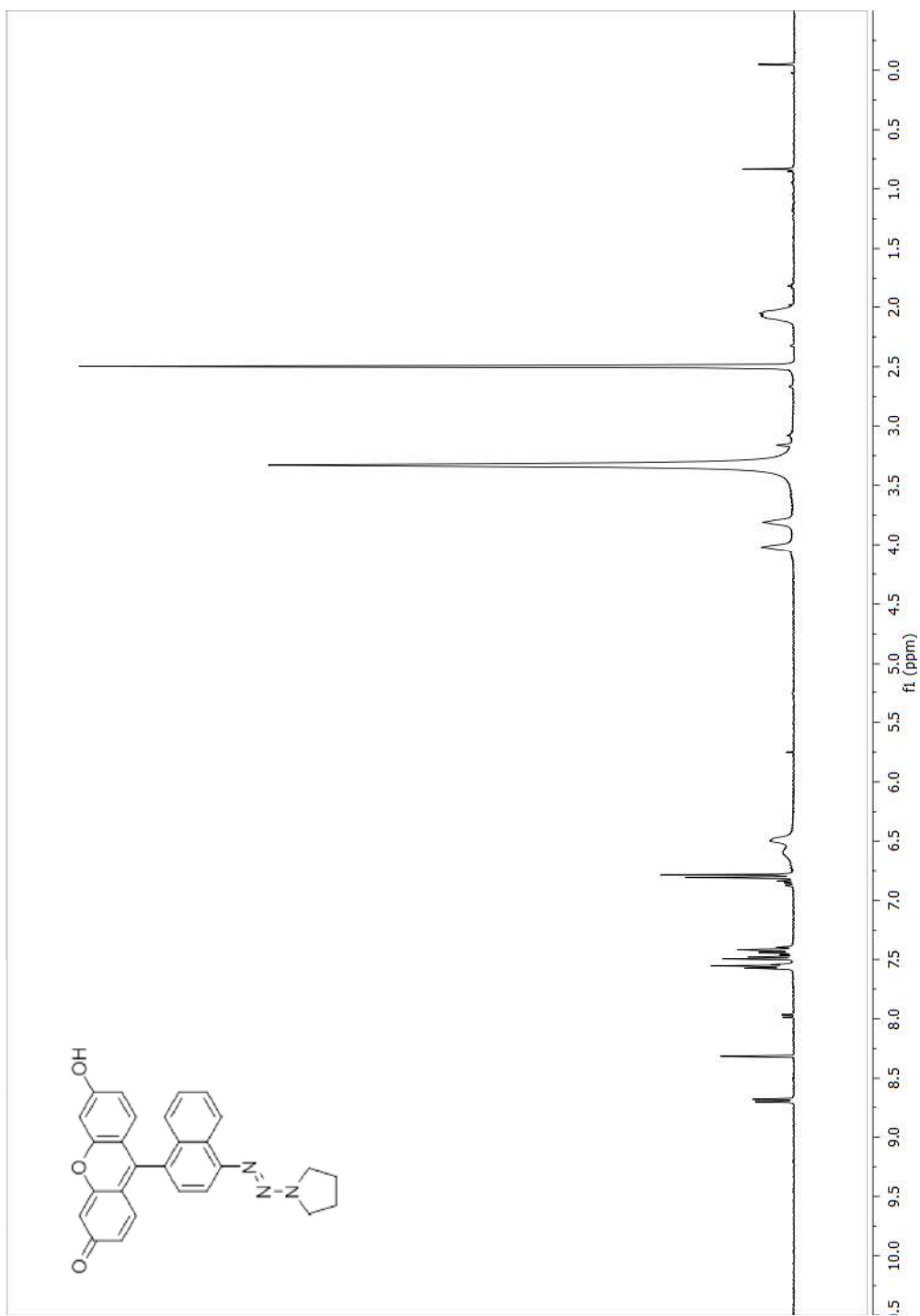
48. van der Linder, W. A.; Li, N.; Hoogendoorn, S.; Ruben, M.; Verdoes, M.; Guo, J.; Boons, G. J.; van der Marel, G. A.; Florea, B. I.; Overkleeft, H. S. *Bioorg. Med. Chem. Lett.* **2012**, *20*, 662-666.
49. Yao, J. Z.; Uttamapinant, C.; Poloukhine, A.; Baskin, J. M.; Codelli, J. A.; Sletten, E. M.; Bertozzi, C. R.; Popik, V. V.; Ting, A. Y. *J. Am. Chem. Soc.* **2012**, *134*, 3720-3728.
50. Chang, P. V.; Prescher, J. A.; Sletten, E. M.; Baskin, J. M.; Miller, I. A.; Agard, N. J.; Lo, A.; Bertozzi, C. R. *Proc. Natl. Acad. Sci.* **2010**, *107*, 1821-1826.
51. Sun, Y.; Ma, X.; Cheng, K.; Wu, B.; Duan, J.; Chen, H.; Bu, L.; Zhang, R.; Hu, X.; Deng, Z.; Xing, Z.; Hong, X.; Cheng, Z. *Angew. Chem. Int. Ed.* **2015**, *54*, 5981-5984.
52. Poole, T. H.; Reisz, J. A.; Zhao, W.; Poole, L. B.; Furdui, C. M.; King, S. B. *J. Am. Chem. Soc.* **2014**, *136*, 6167-6170.
53. Galardon, E.; Padovani, D. *Bioconjug. Chem.* **2015**, *26*, 1013-1016.
54. Paulsen, C. E.; Carroll, K. S. *Chem. Rev.* **2013**, *113*, 4633-3679.
55. Szabo, C. *Nat. Rev. Drug Discov.* **2007**, *6*, 917-935.
56. Xu, H.; Yang, J.; Seckute, J.; Devaraj, N. K. *Angew. Chem. Int. Ed.* **2014**, *53*, 5805-5809.

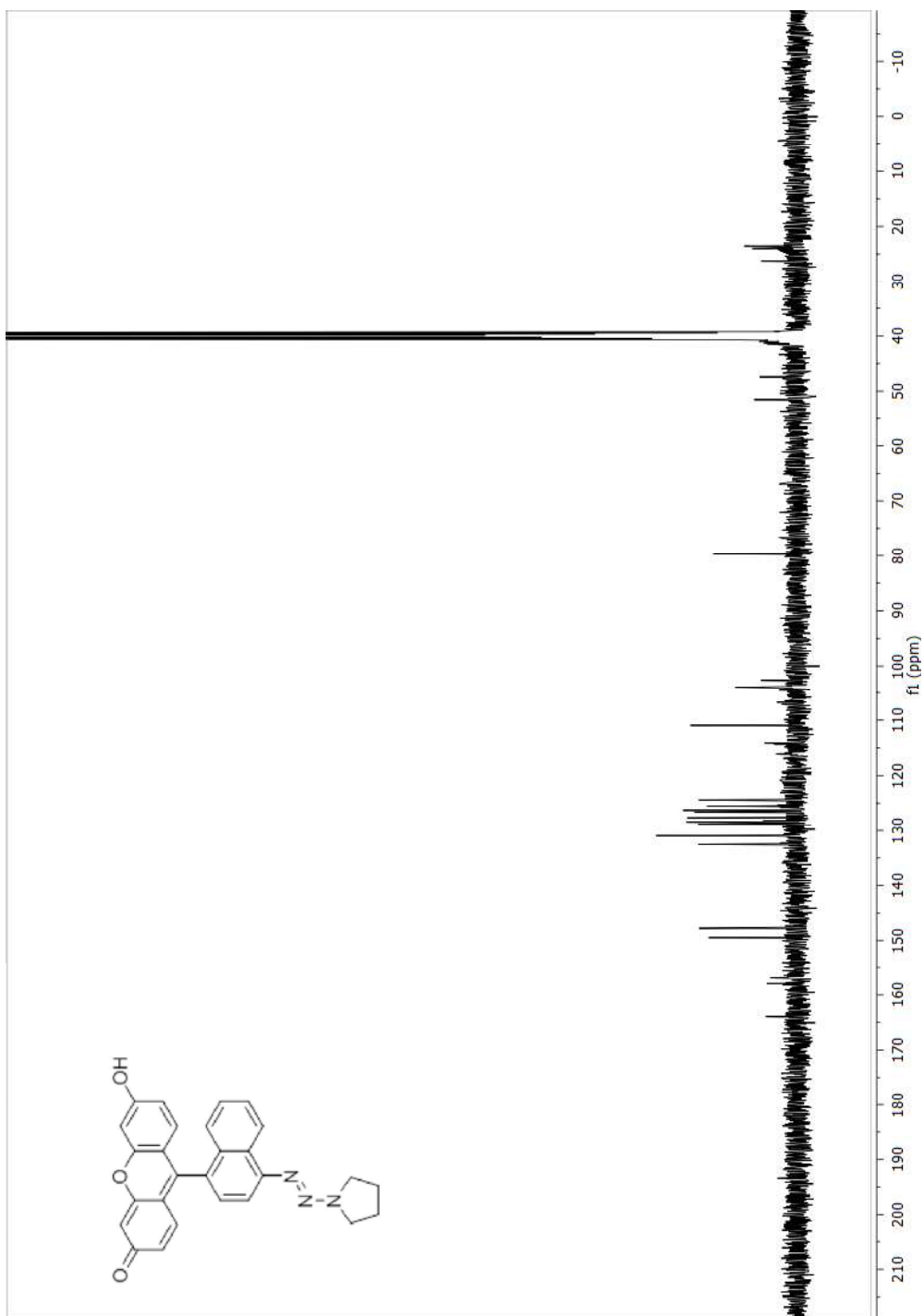
Appendix

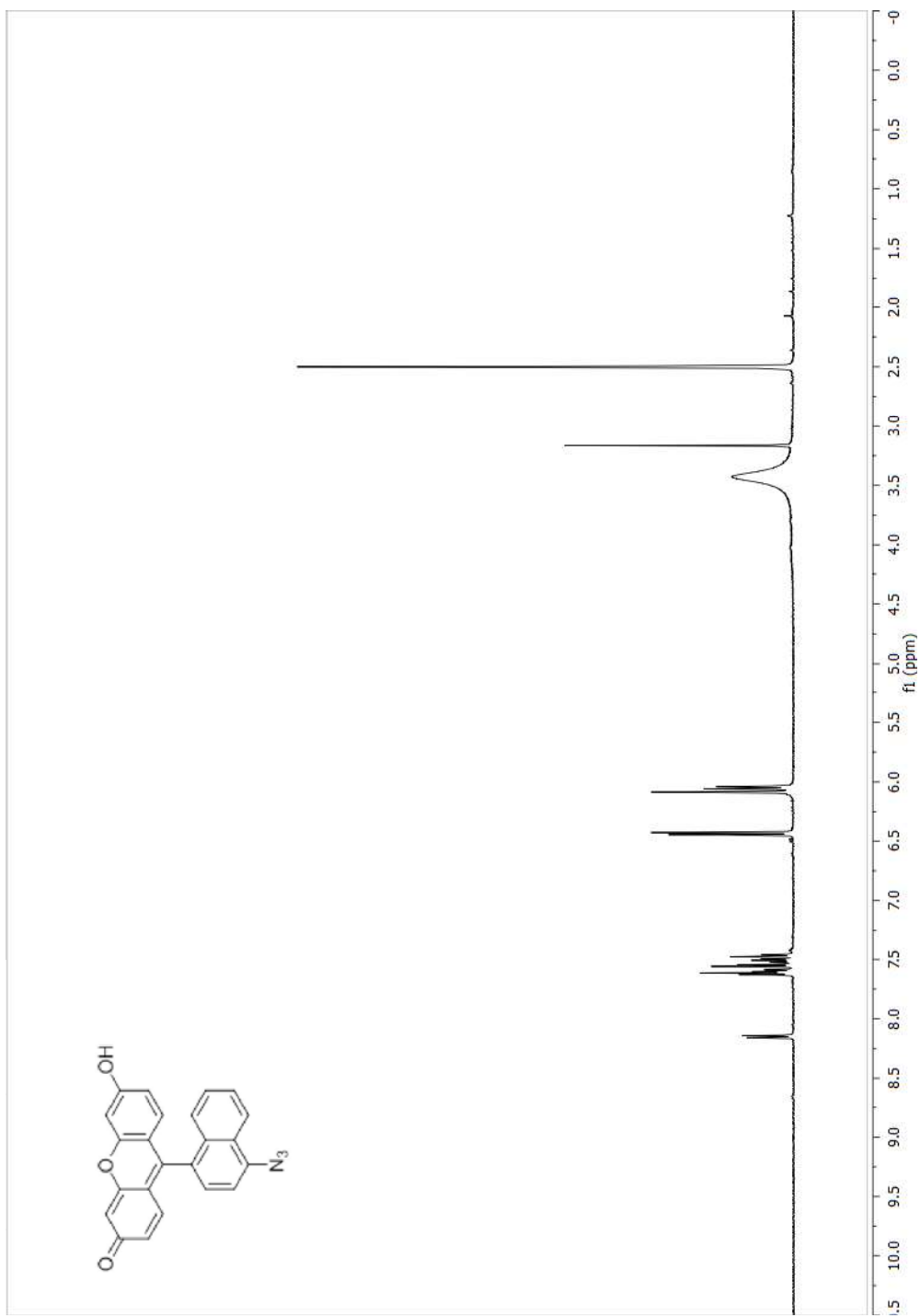
NMR Spectra

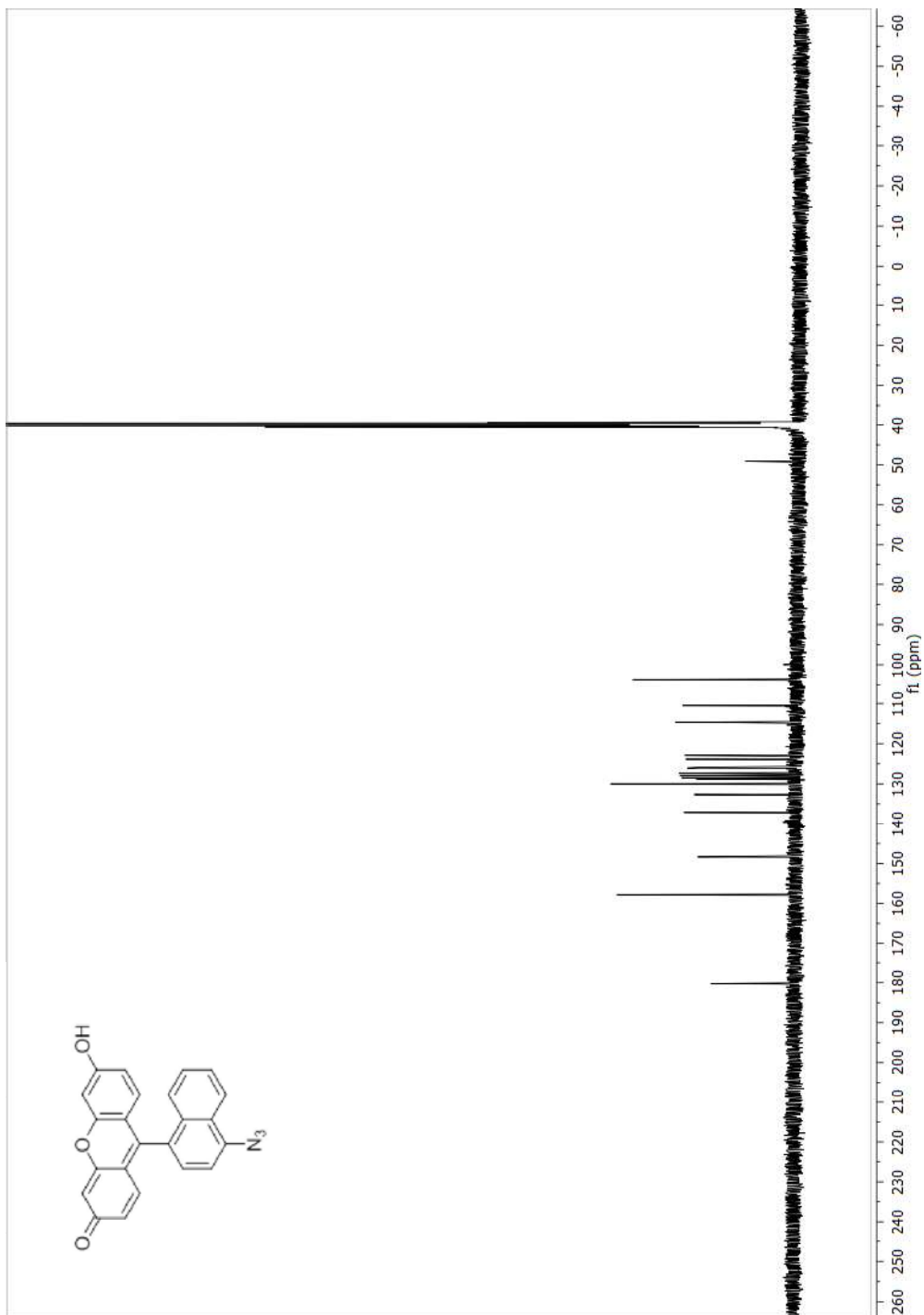


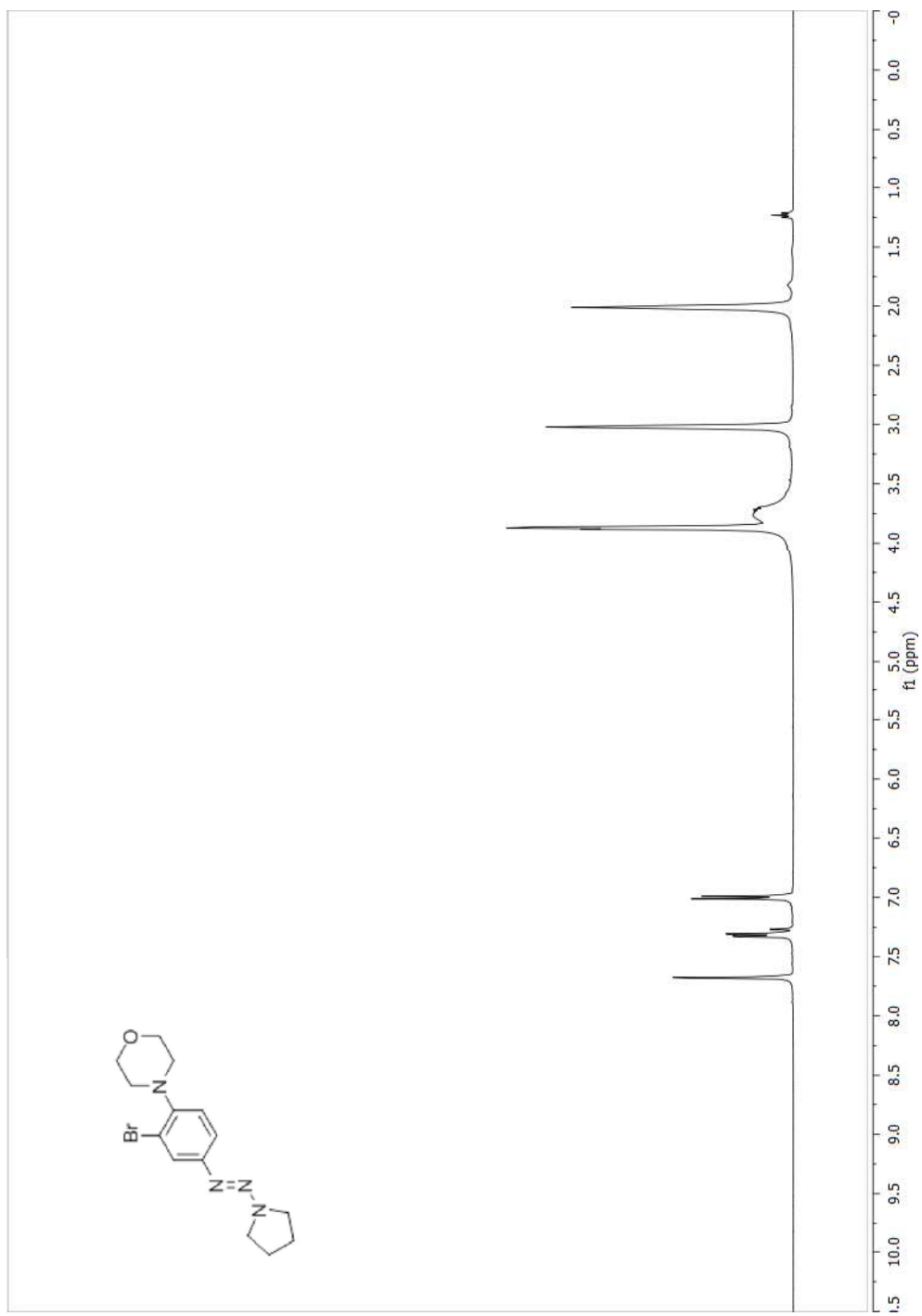


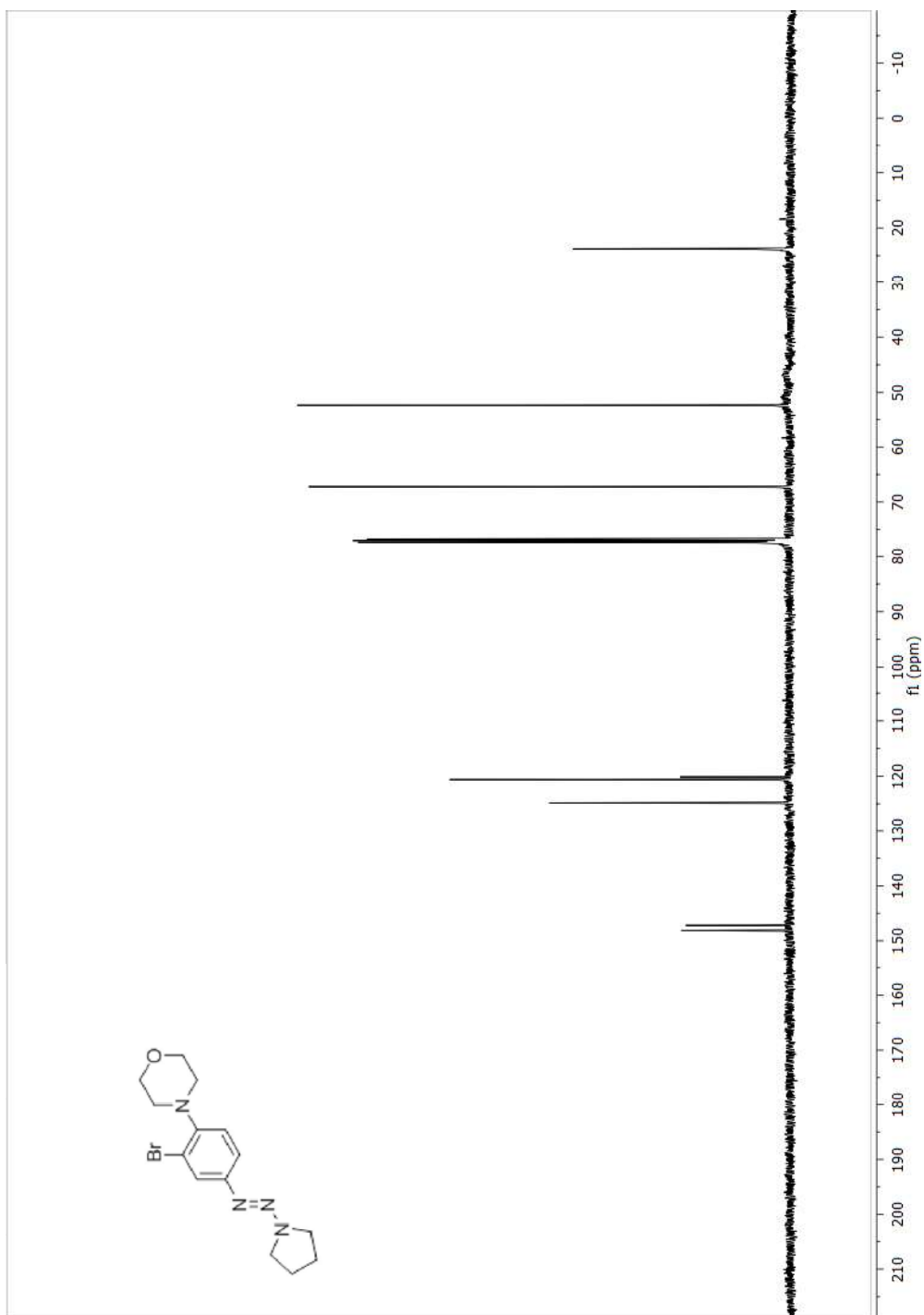


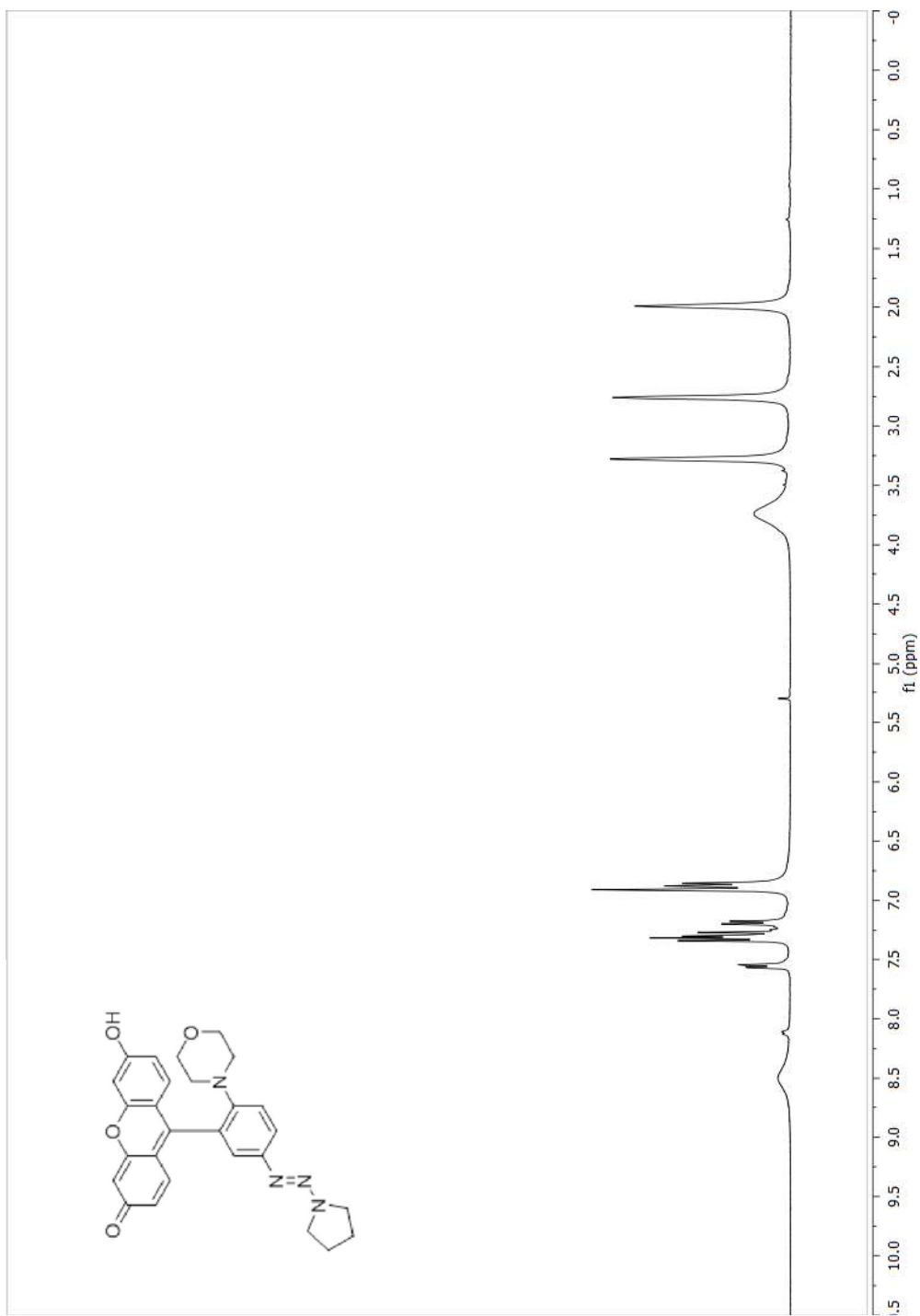


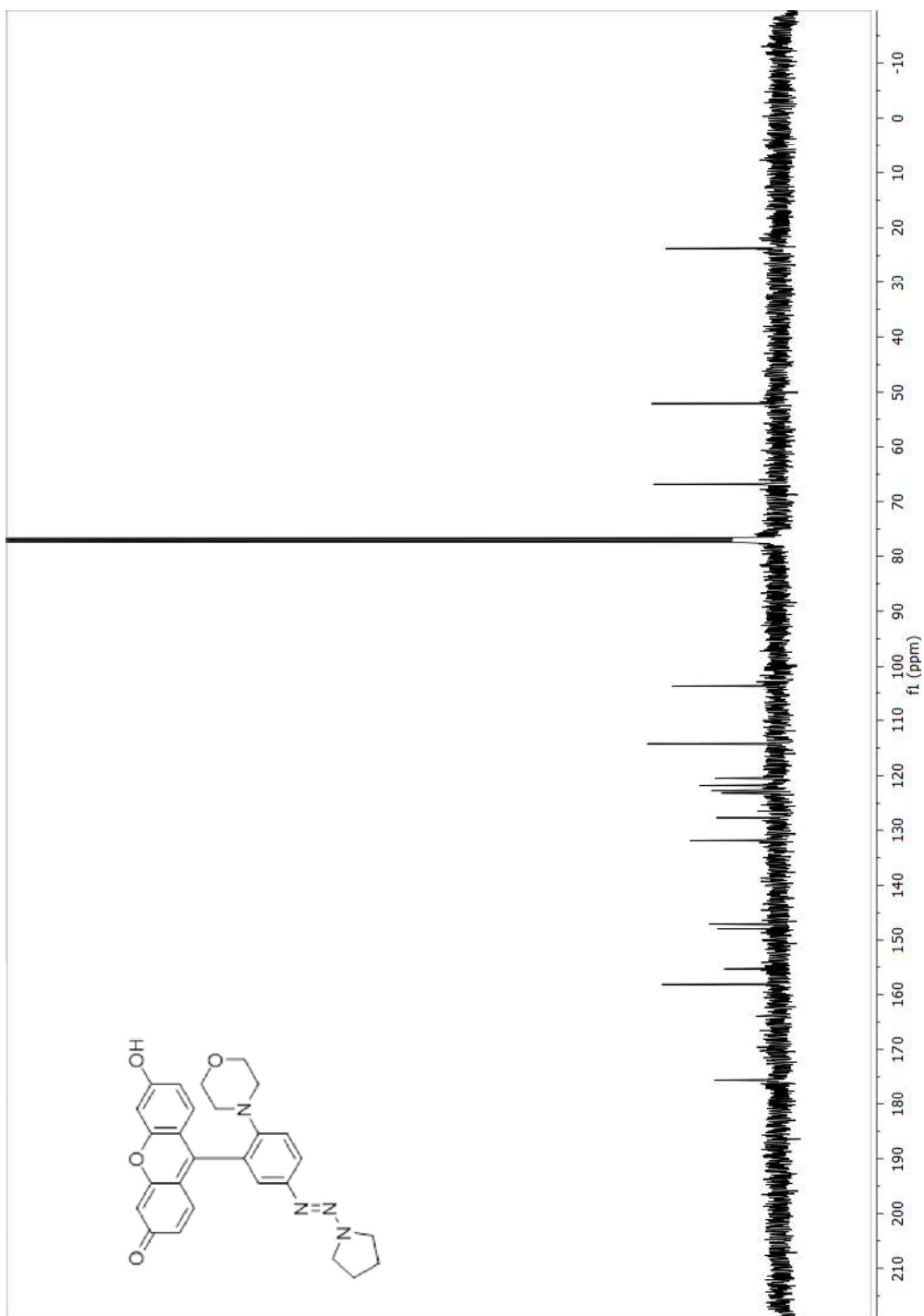


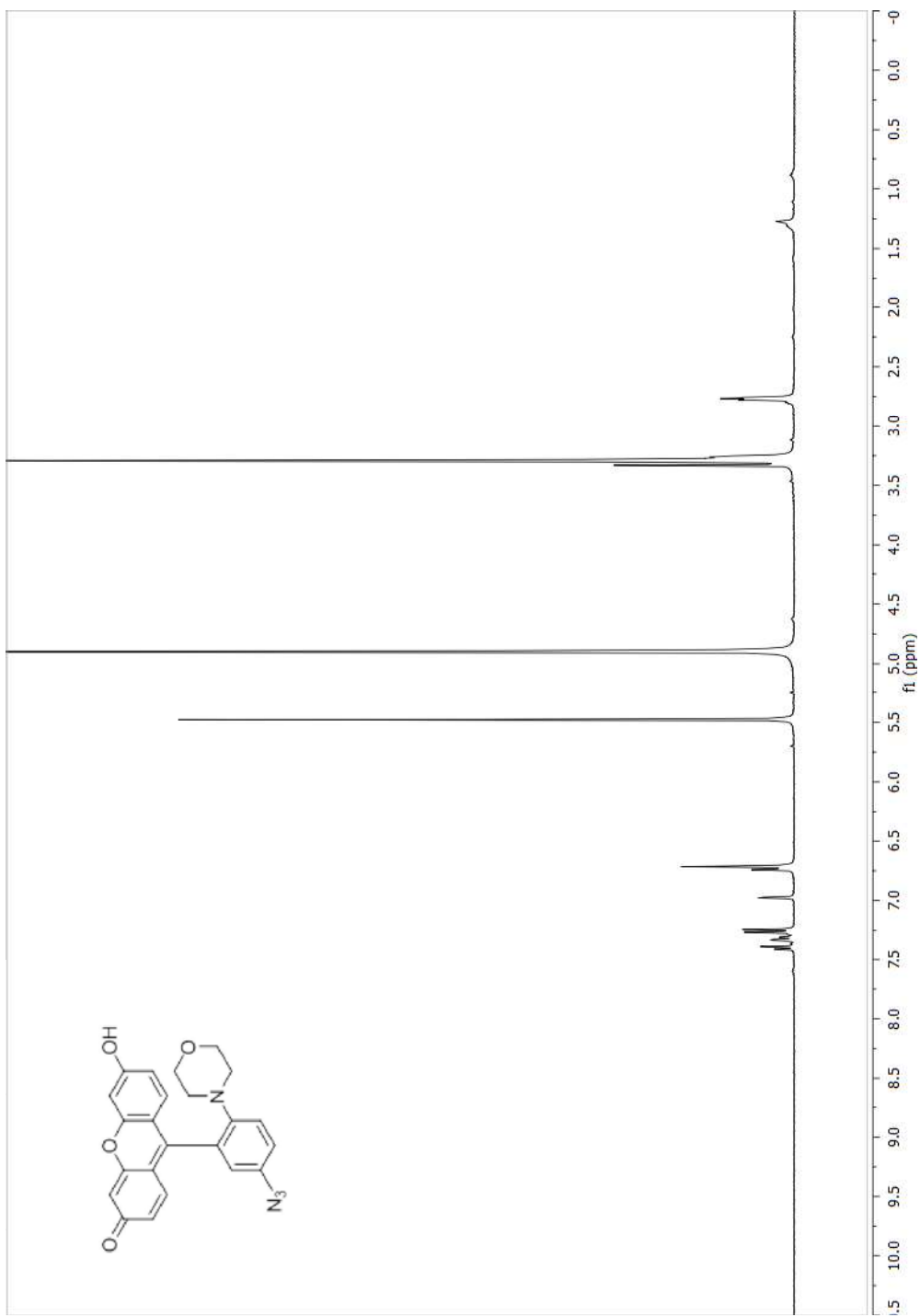


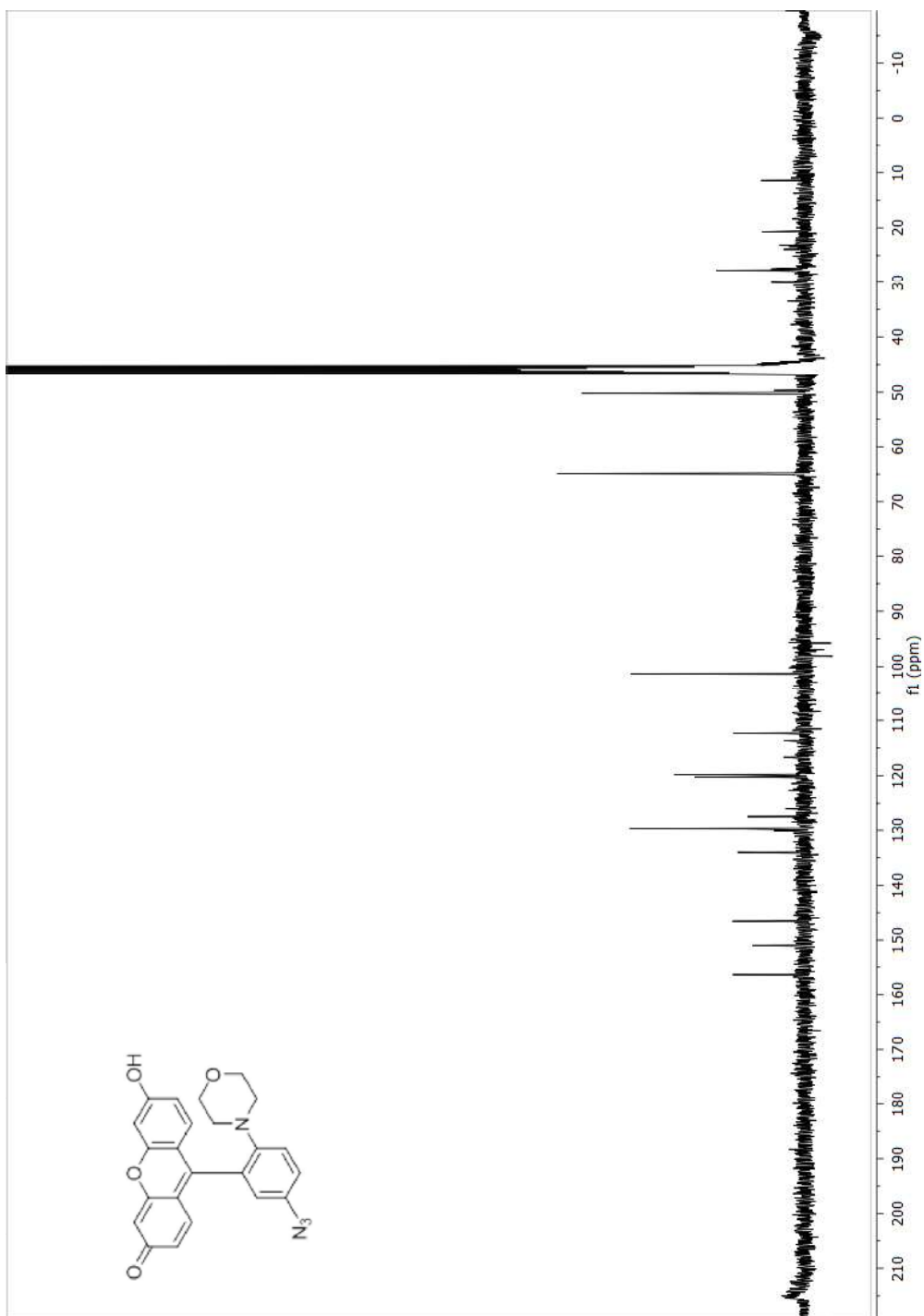


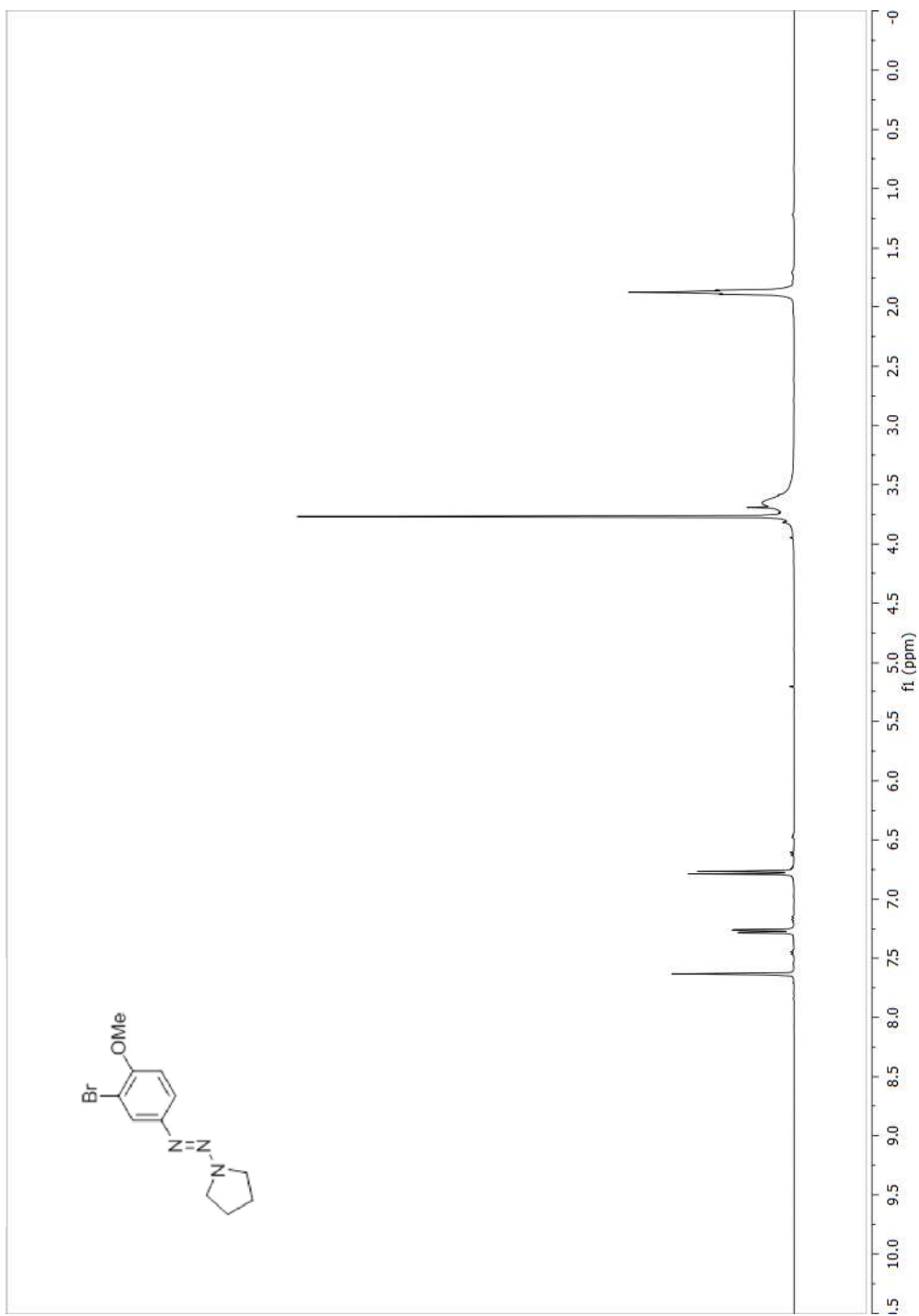


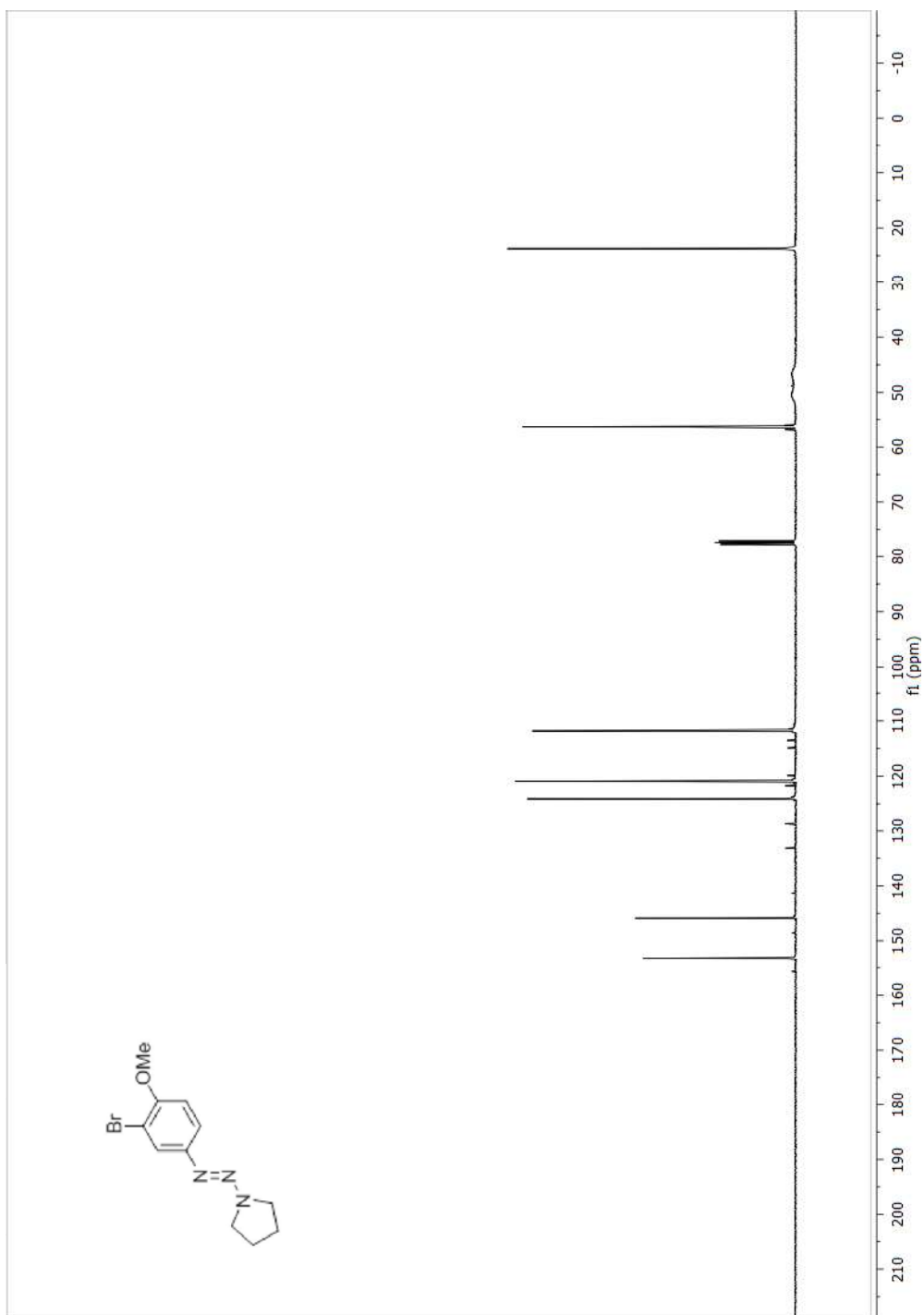


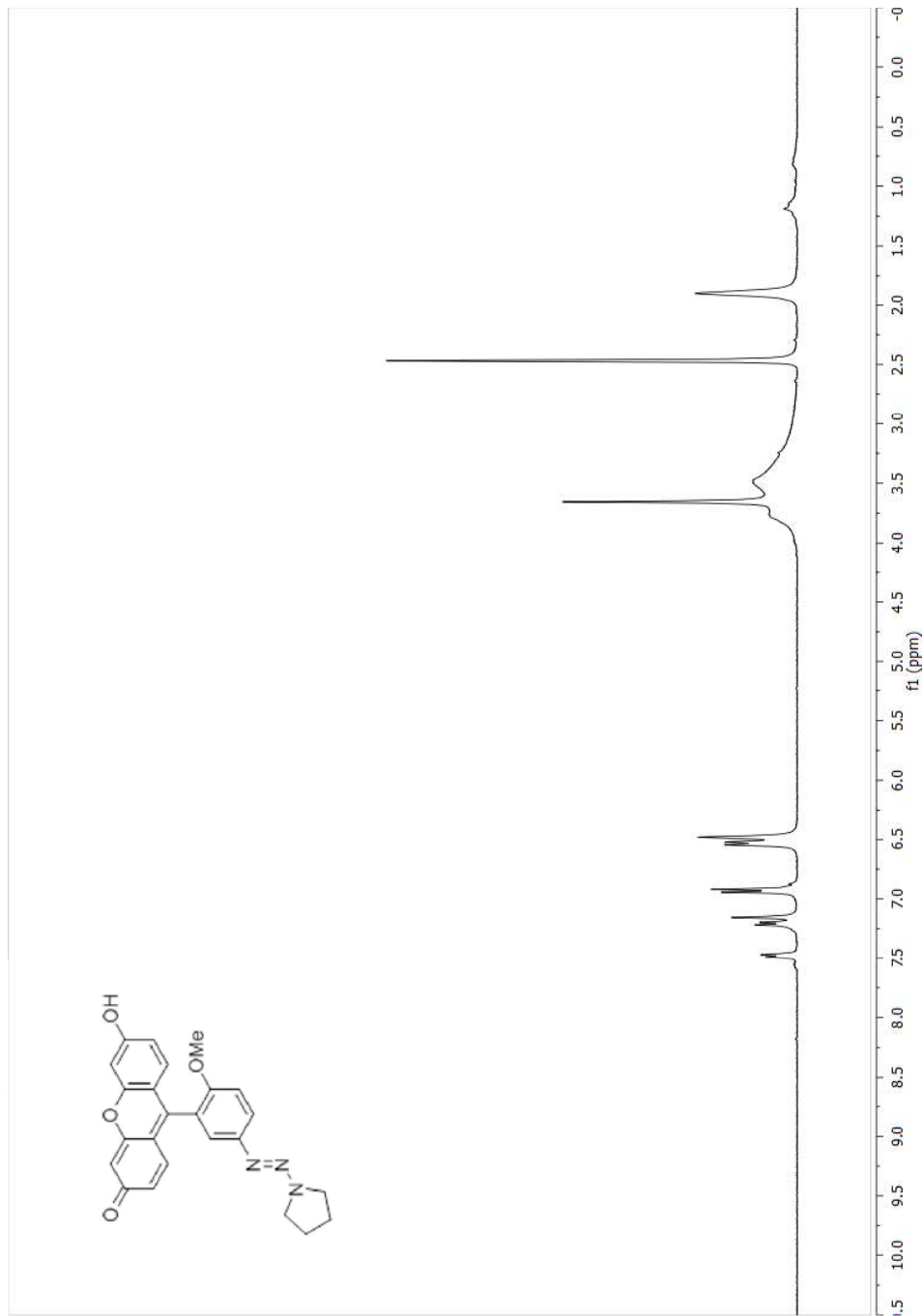


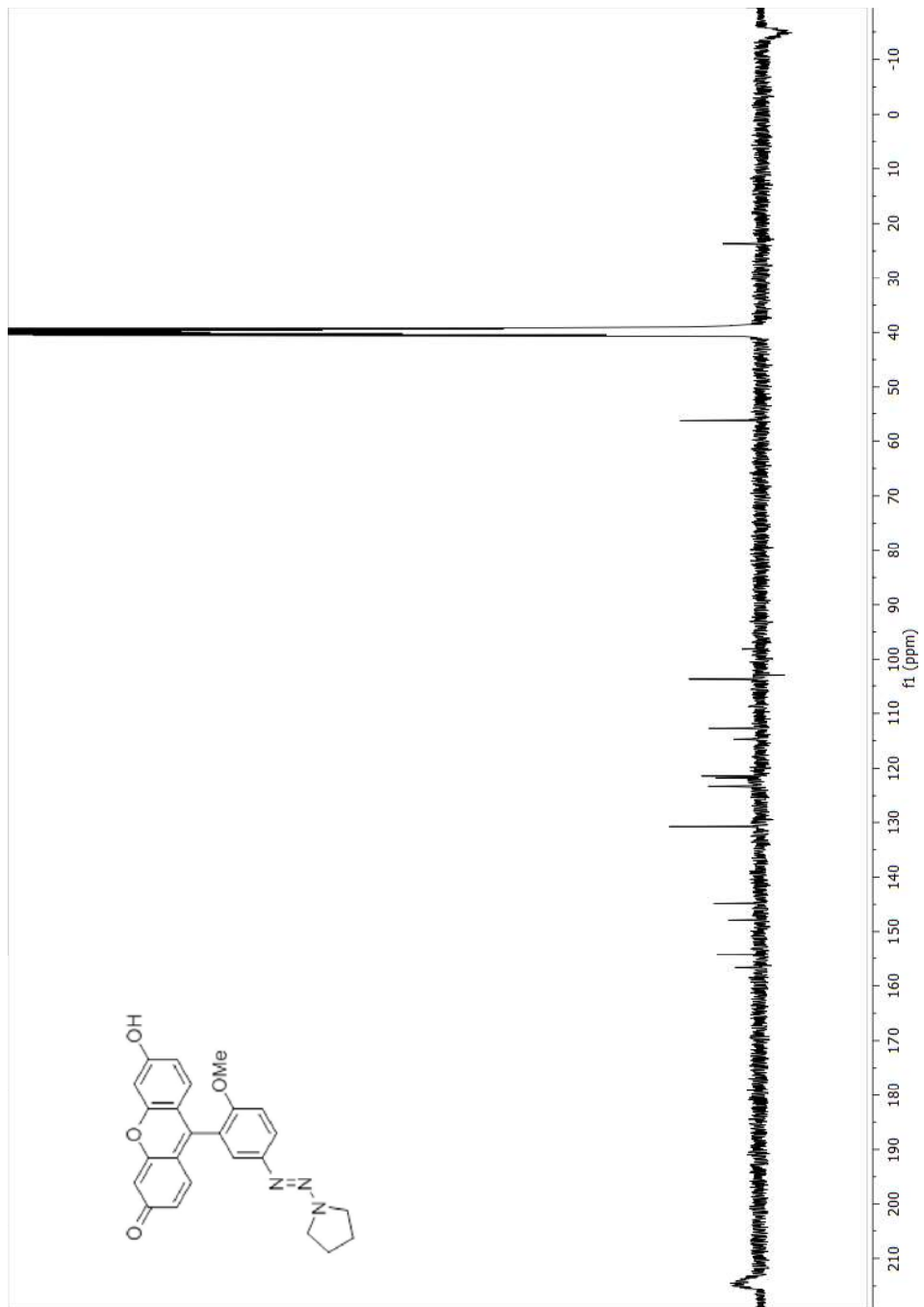


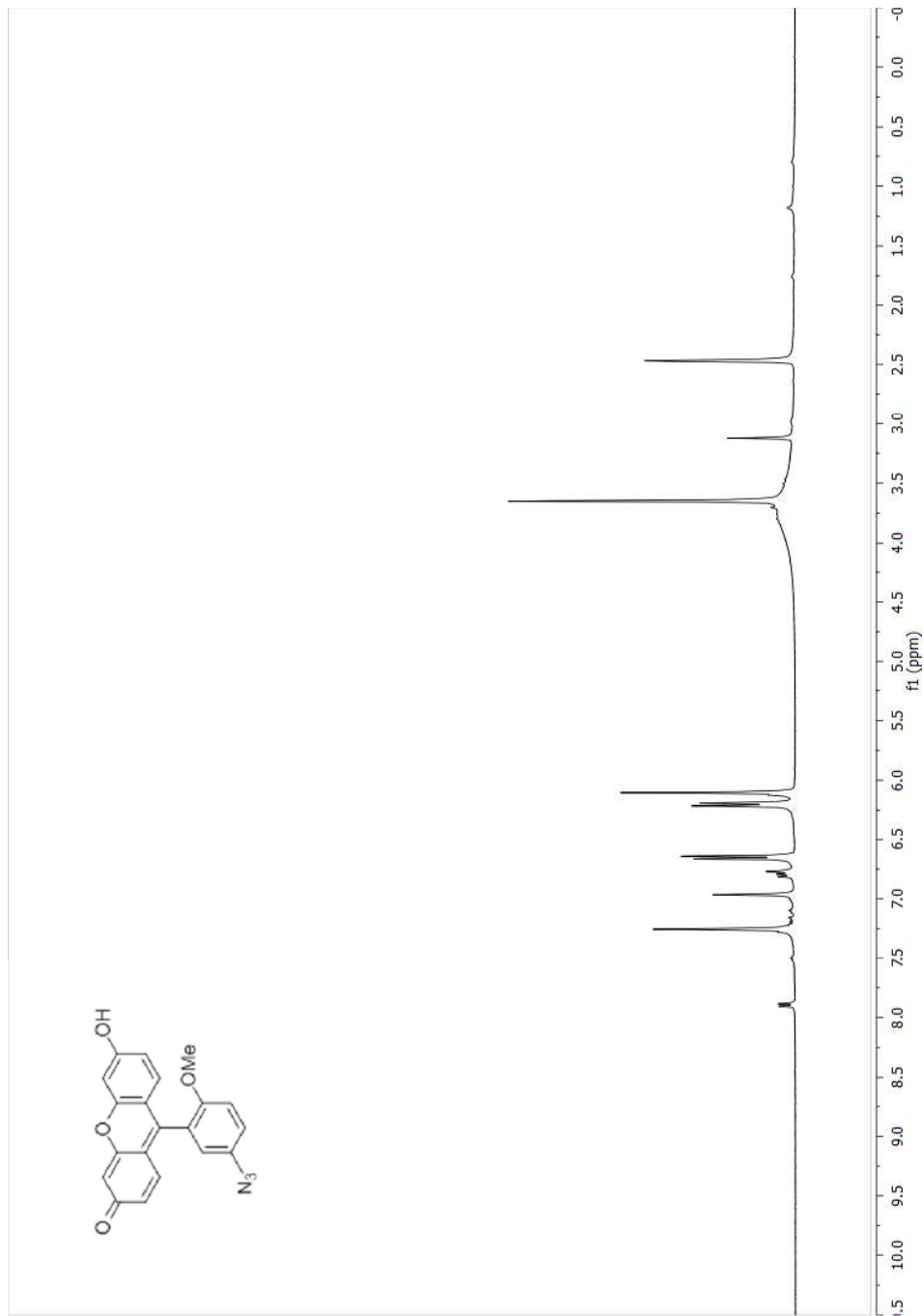


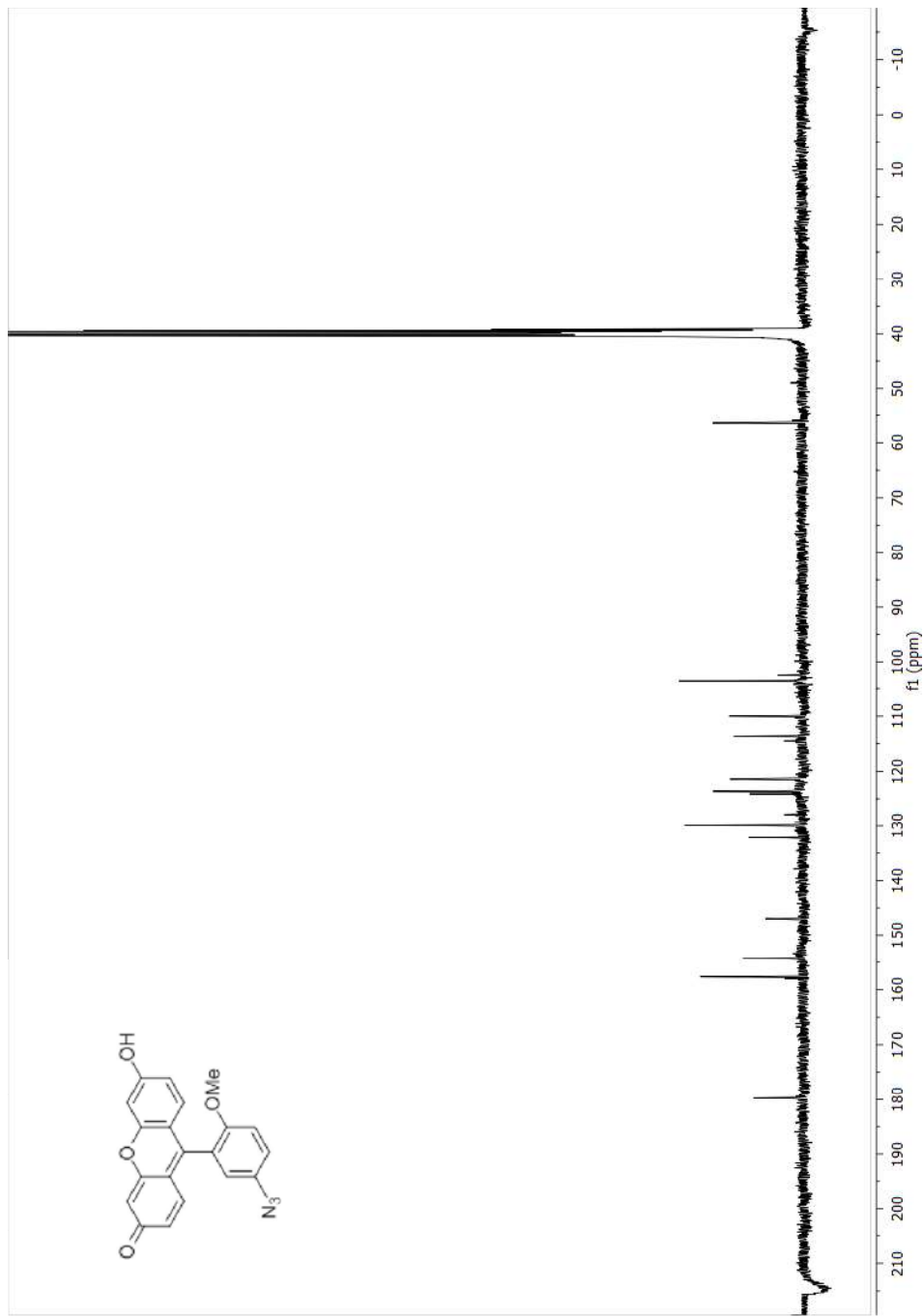


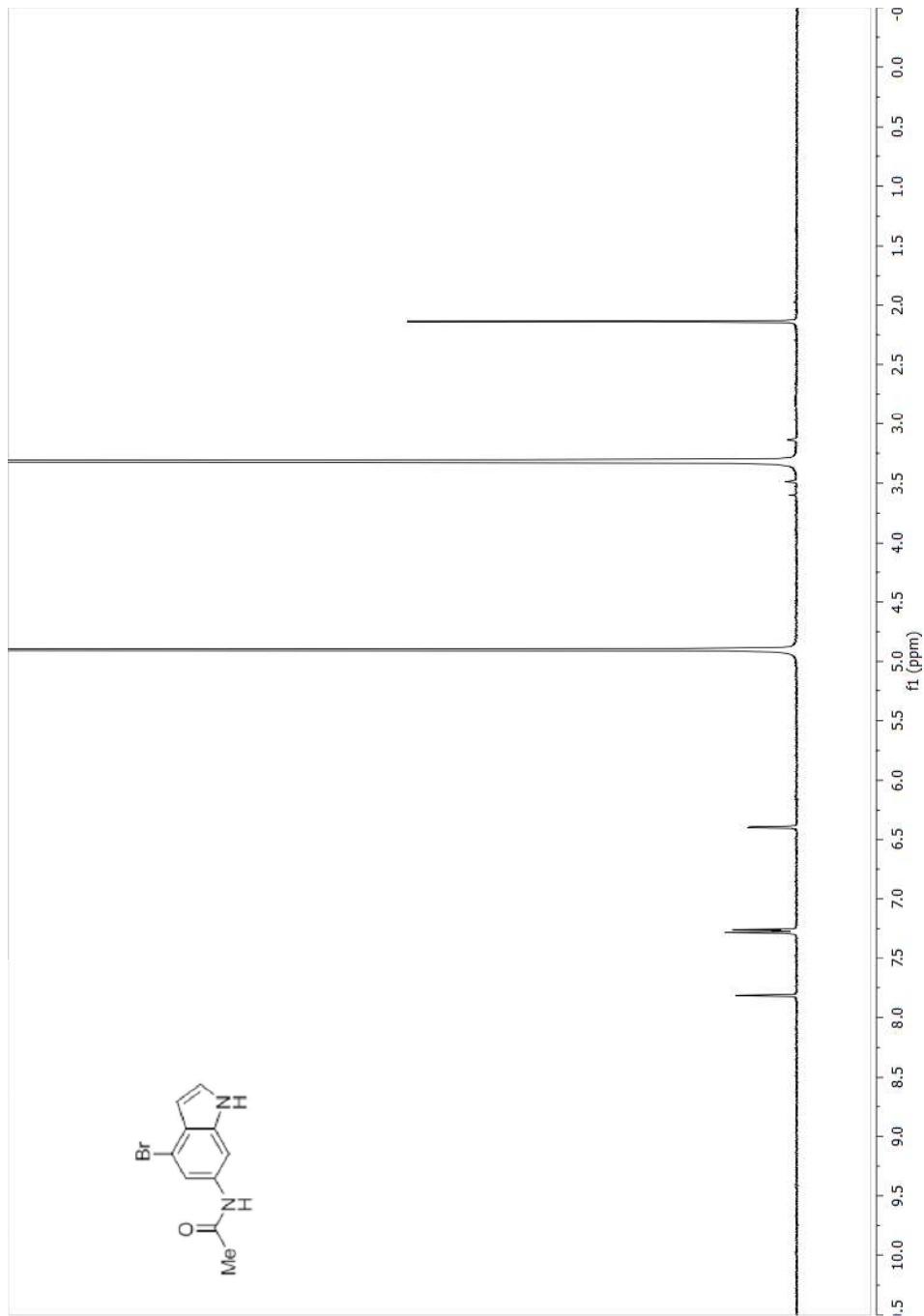


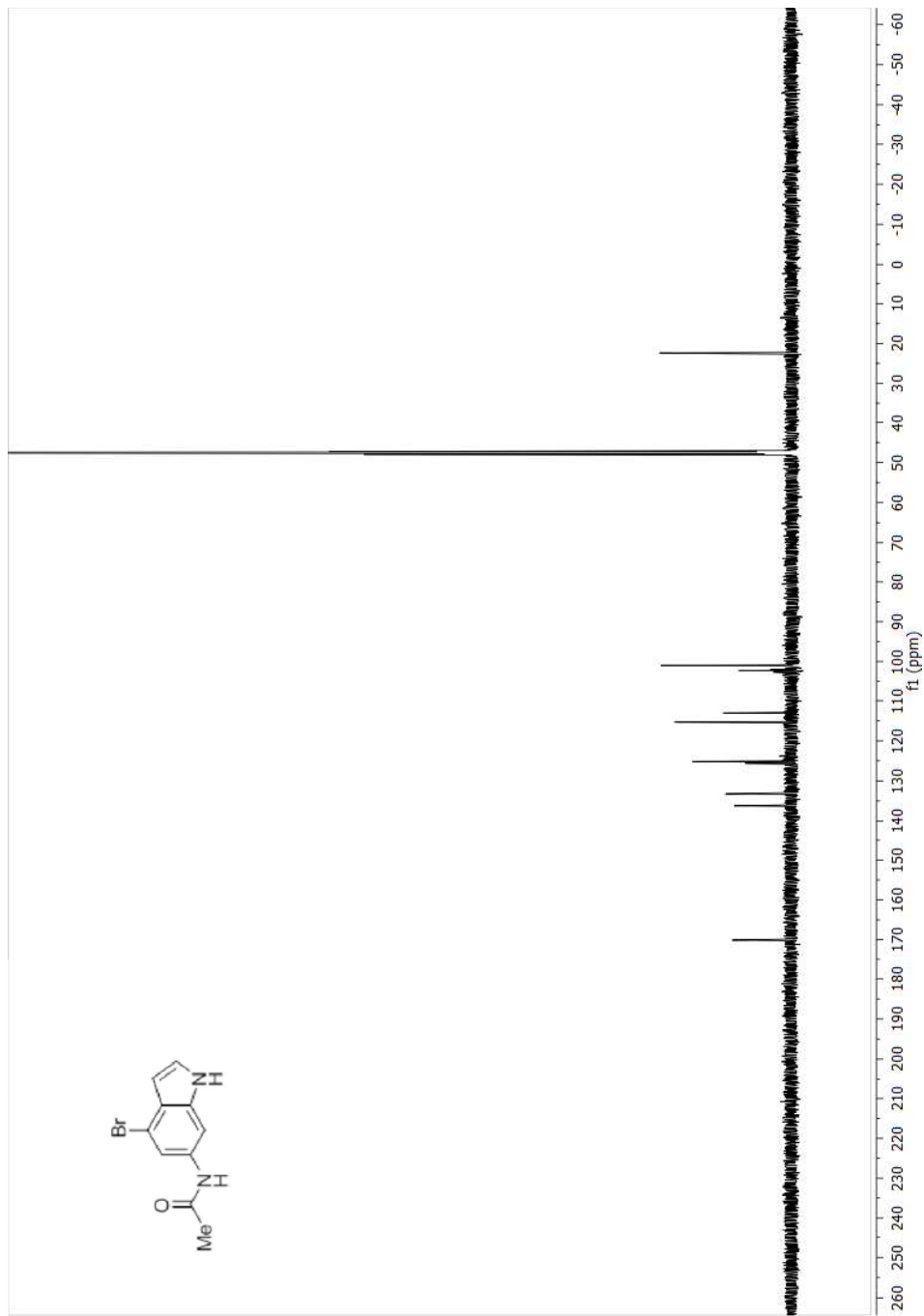


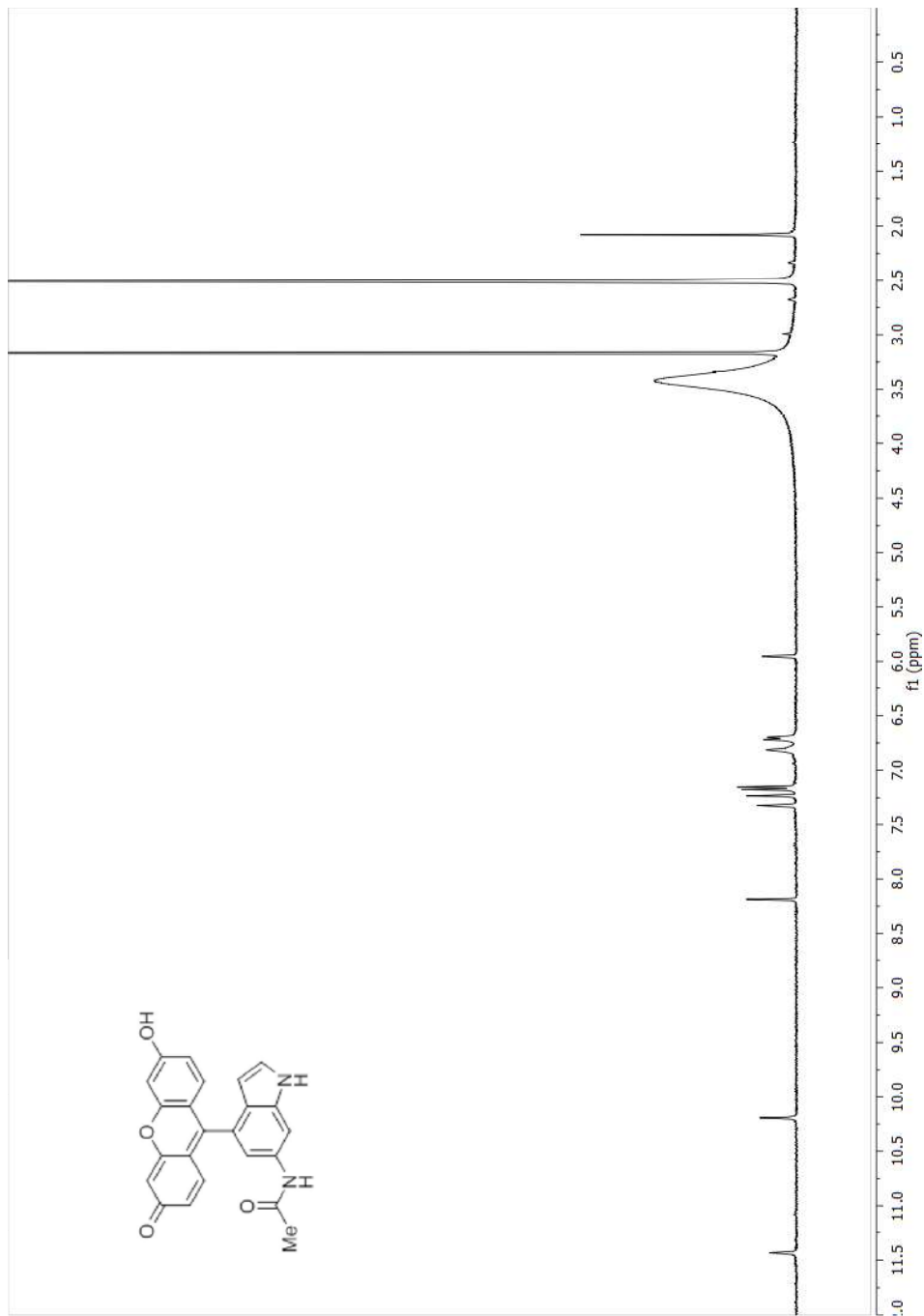


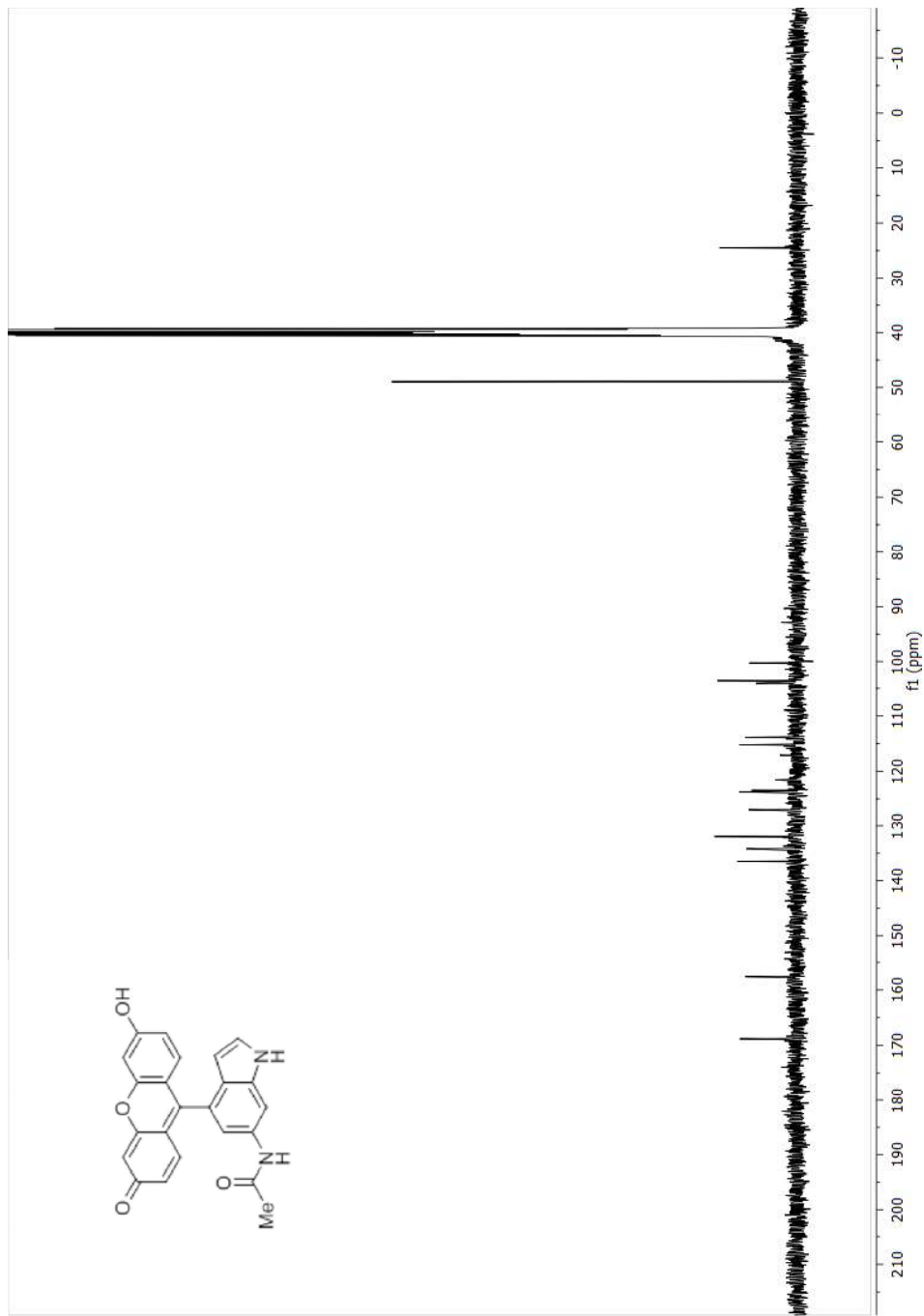


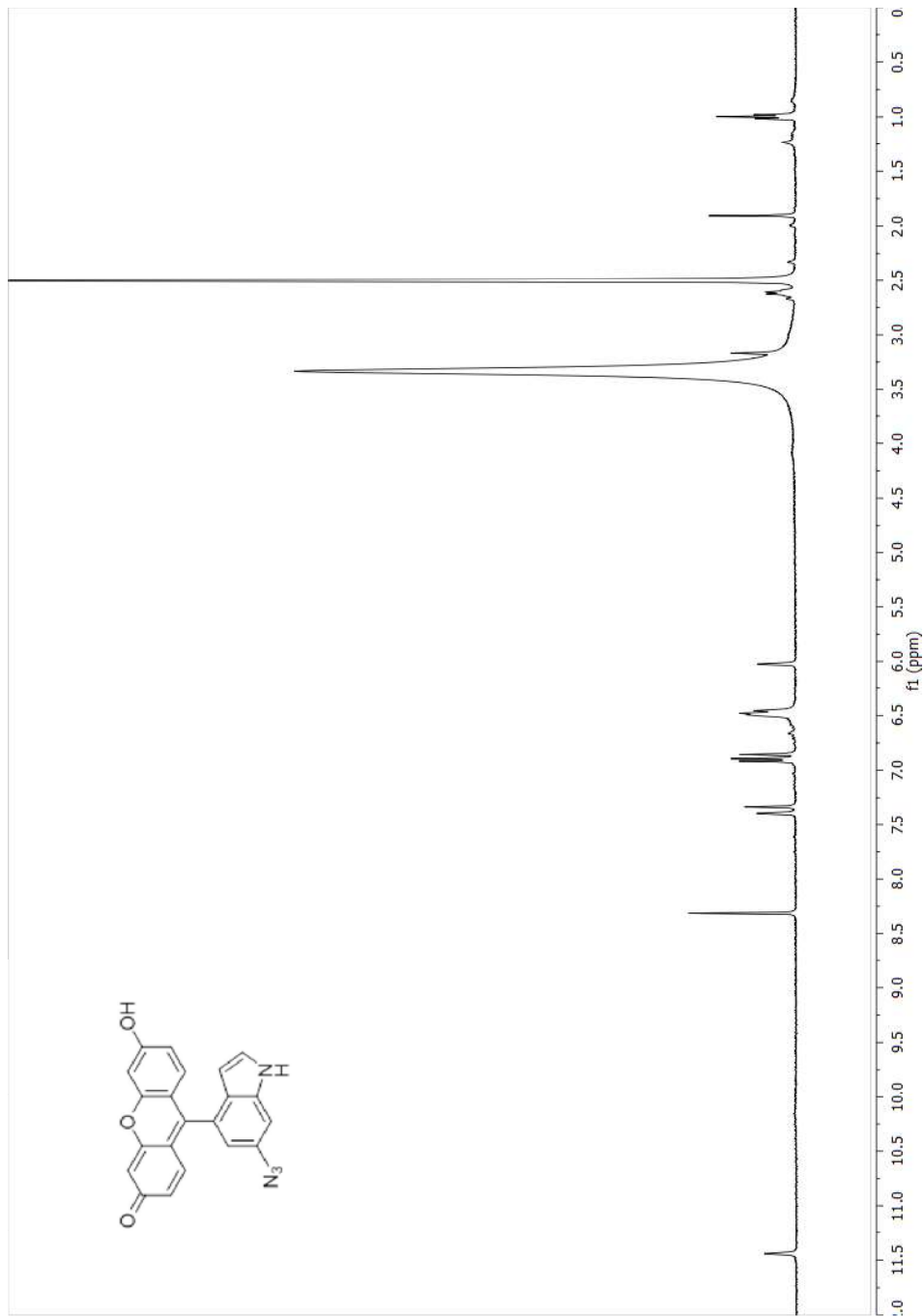


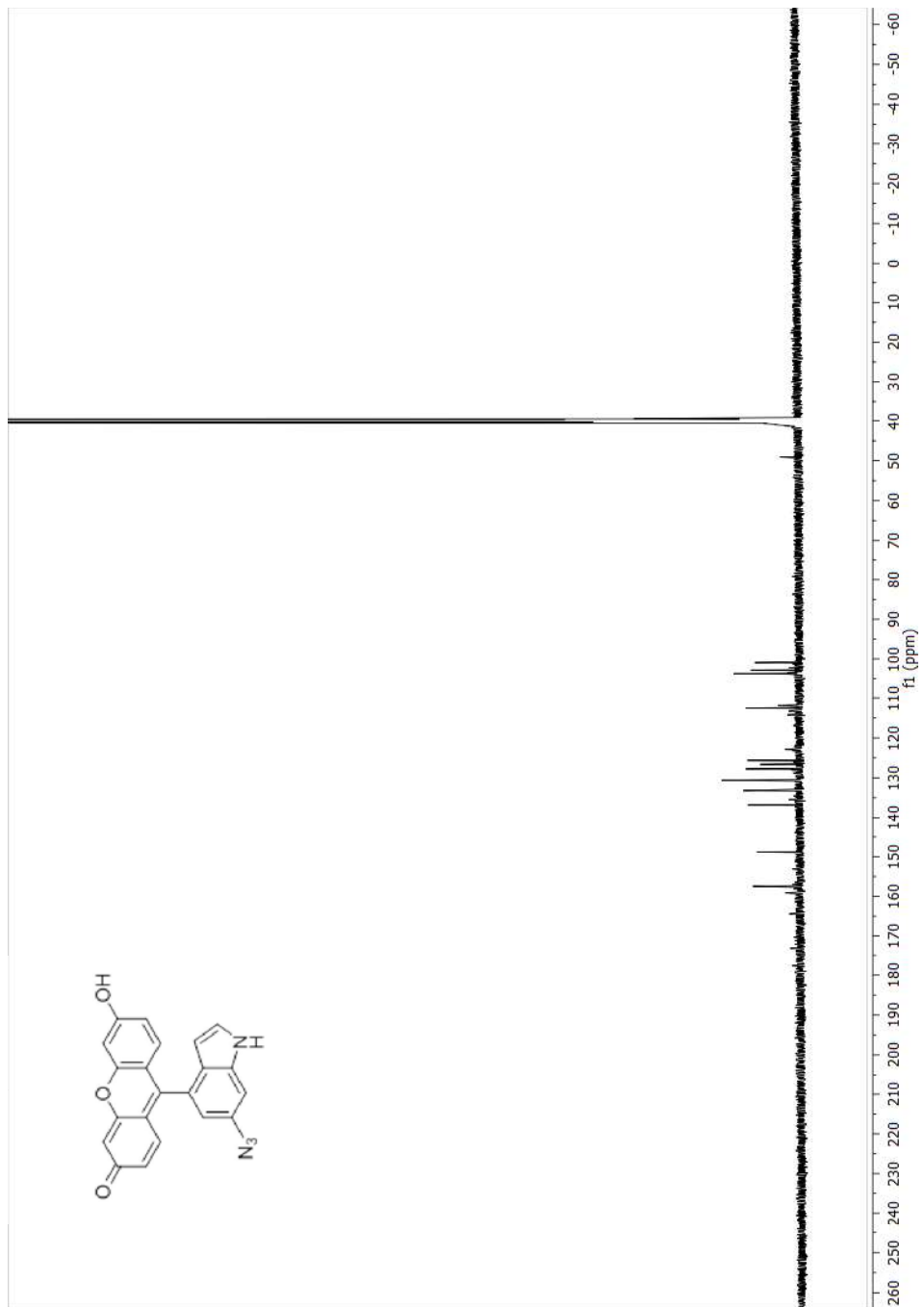


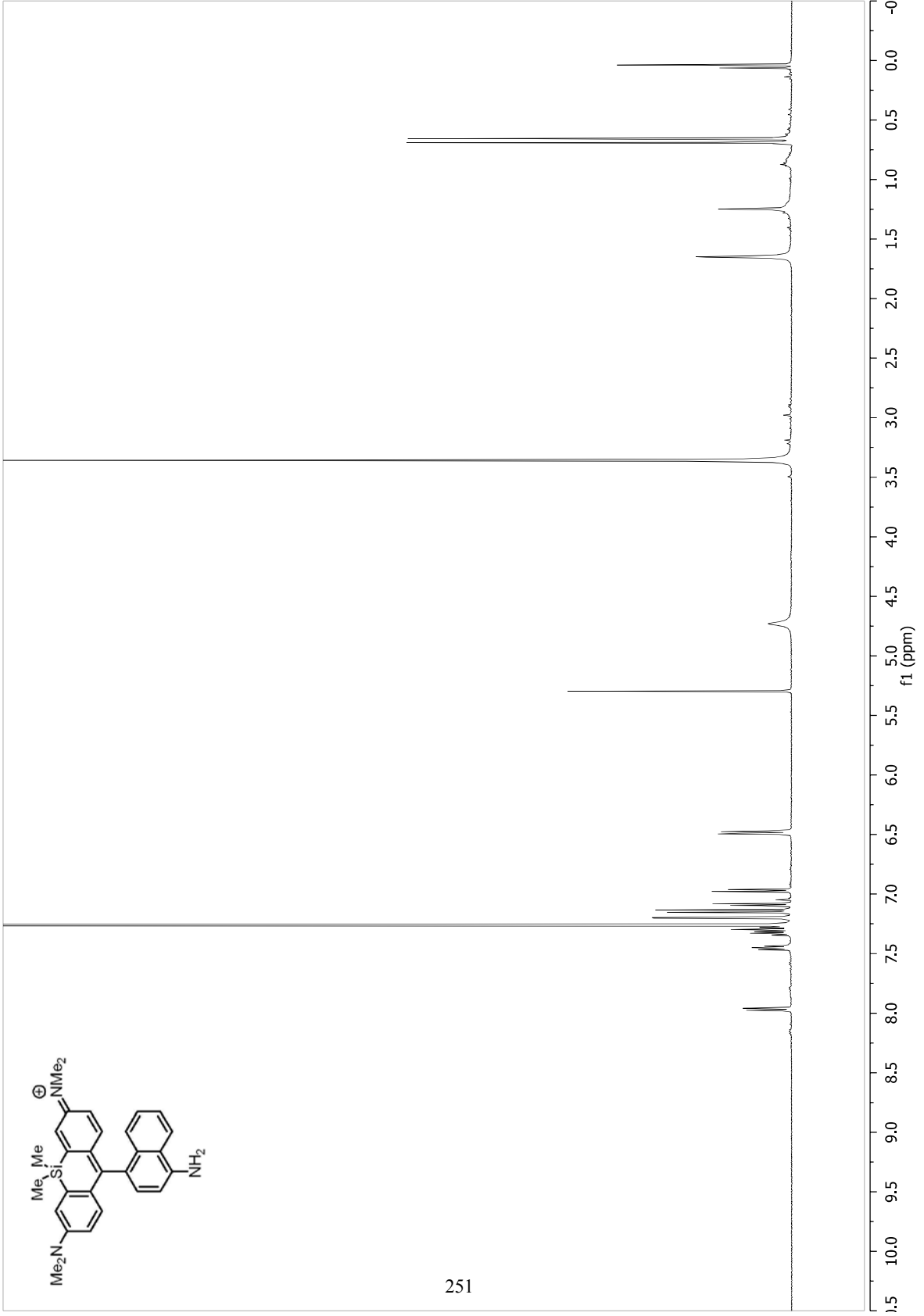


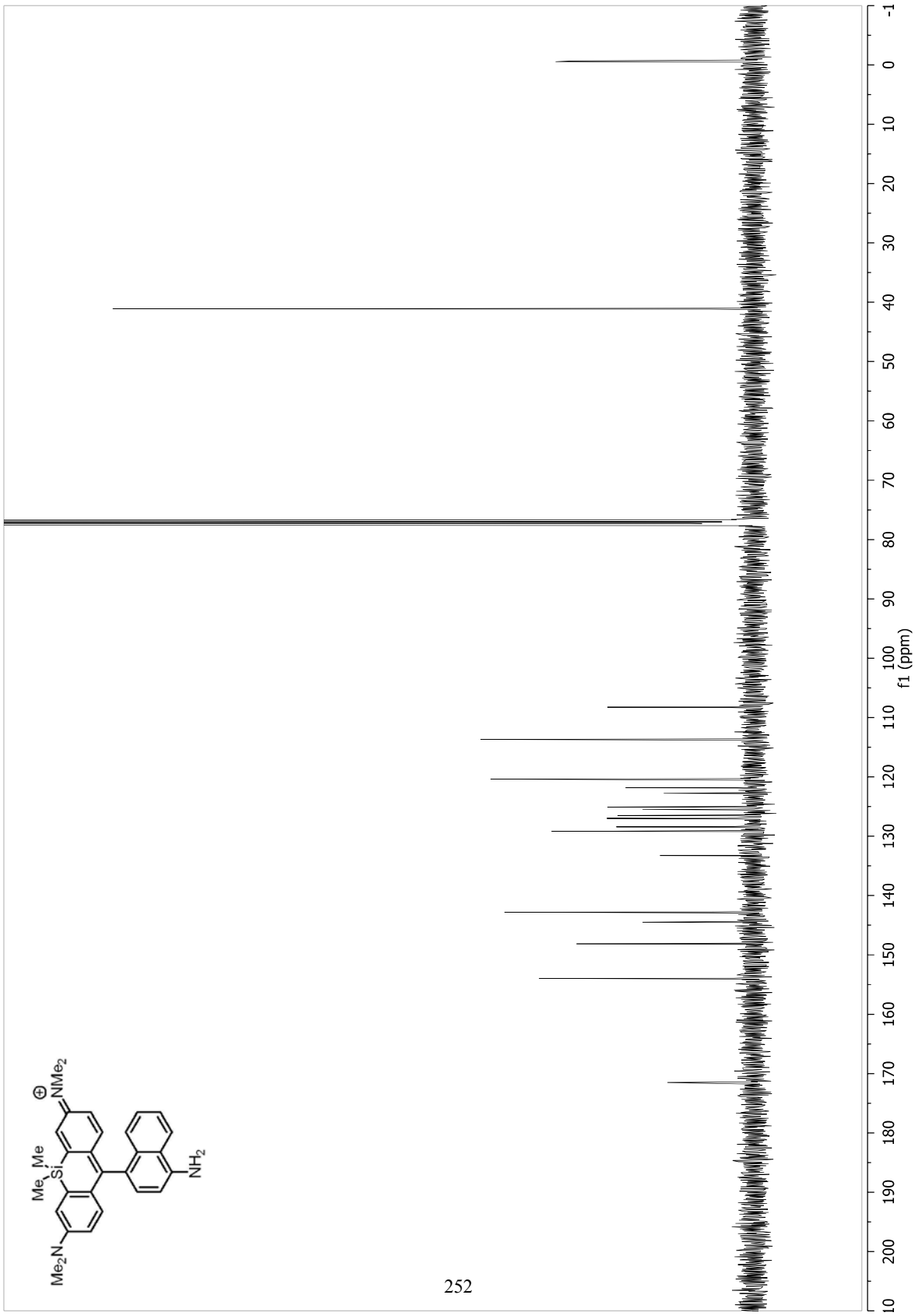


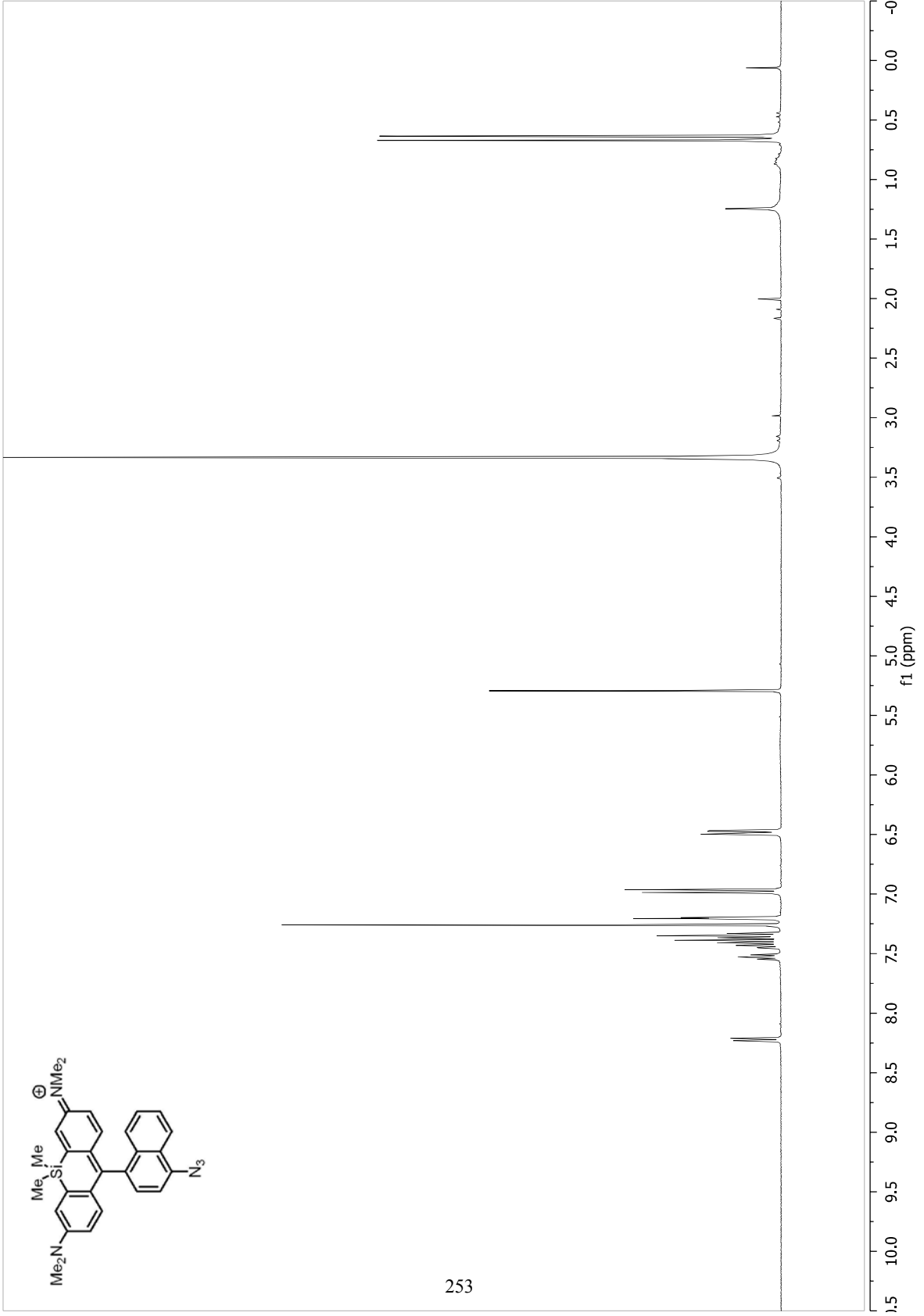


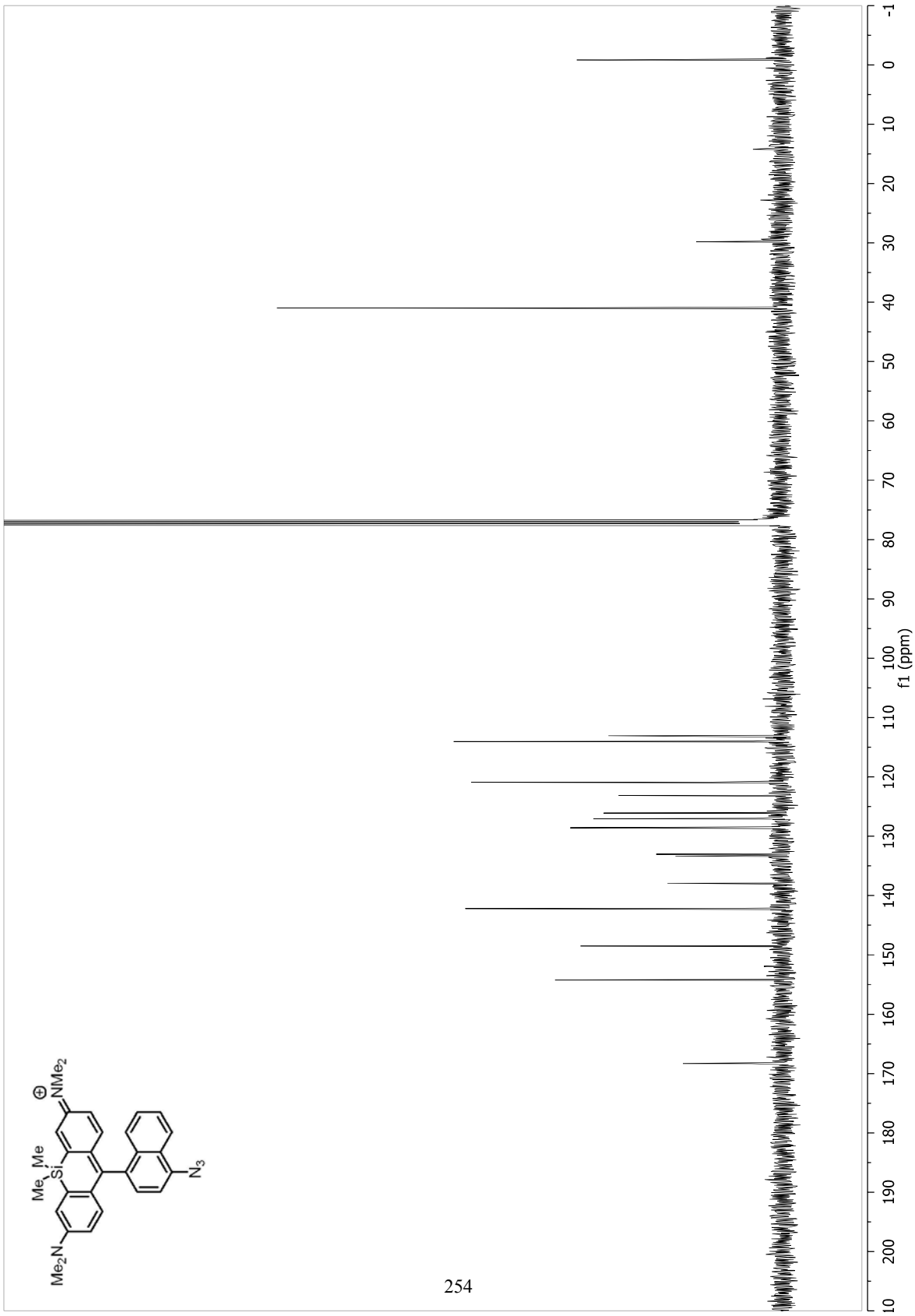


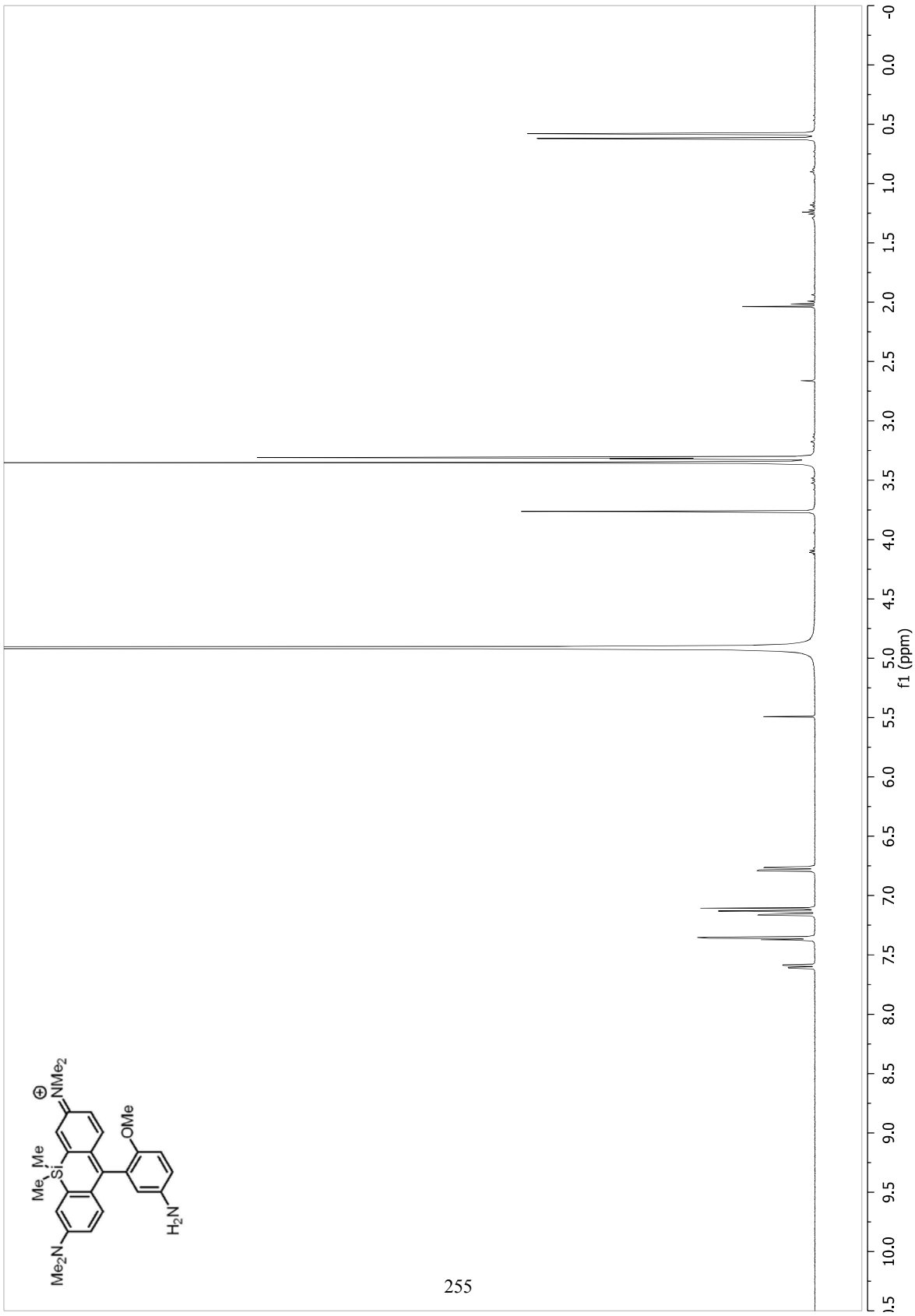


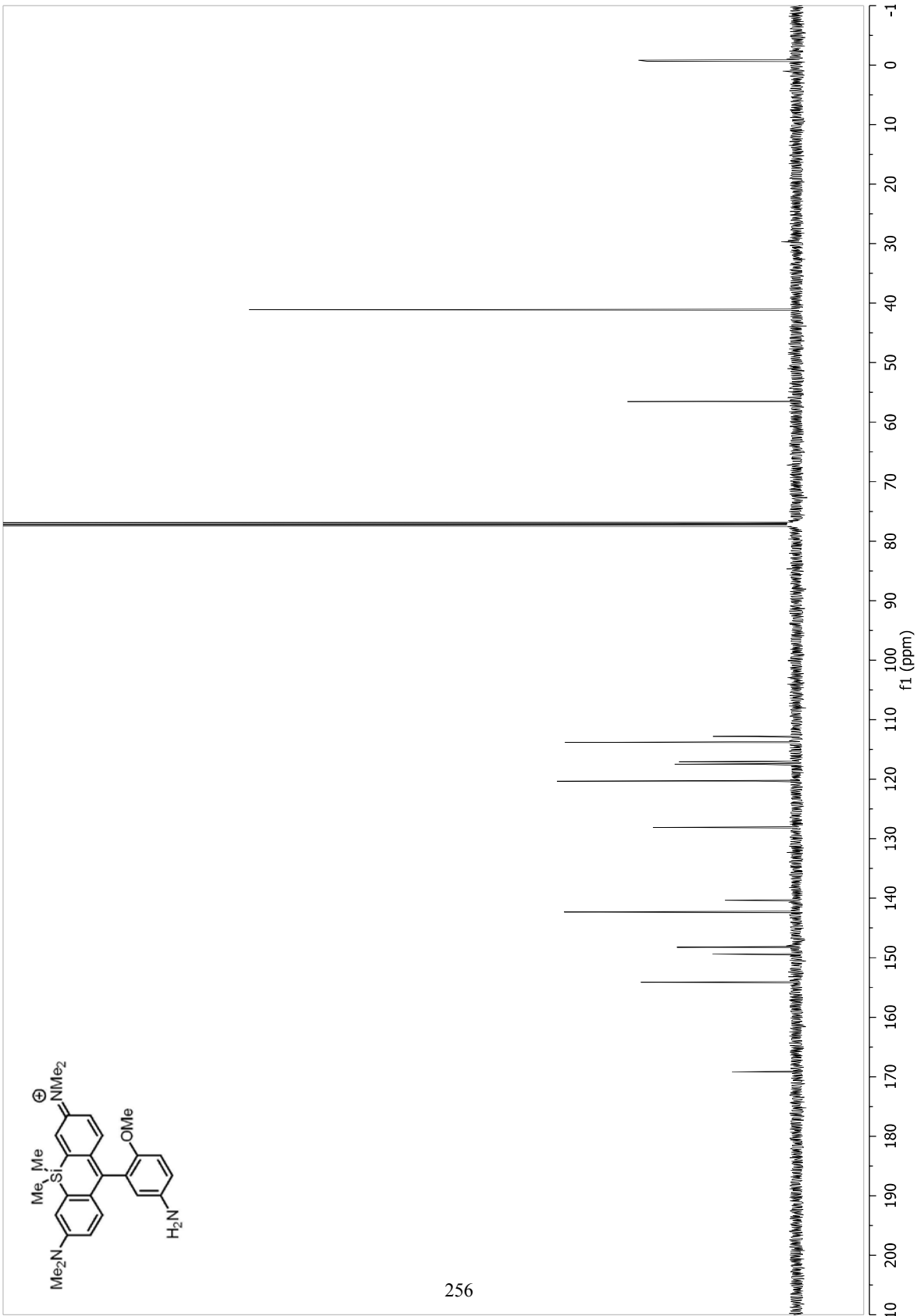


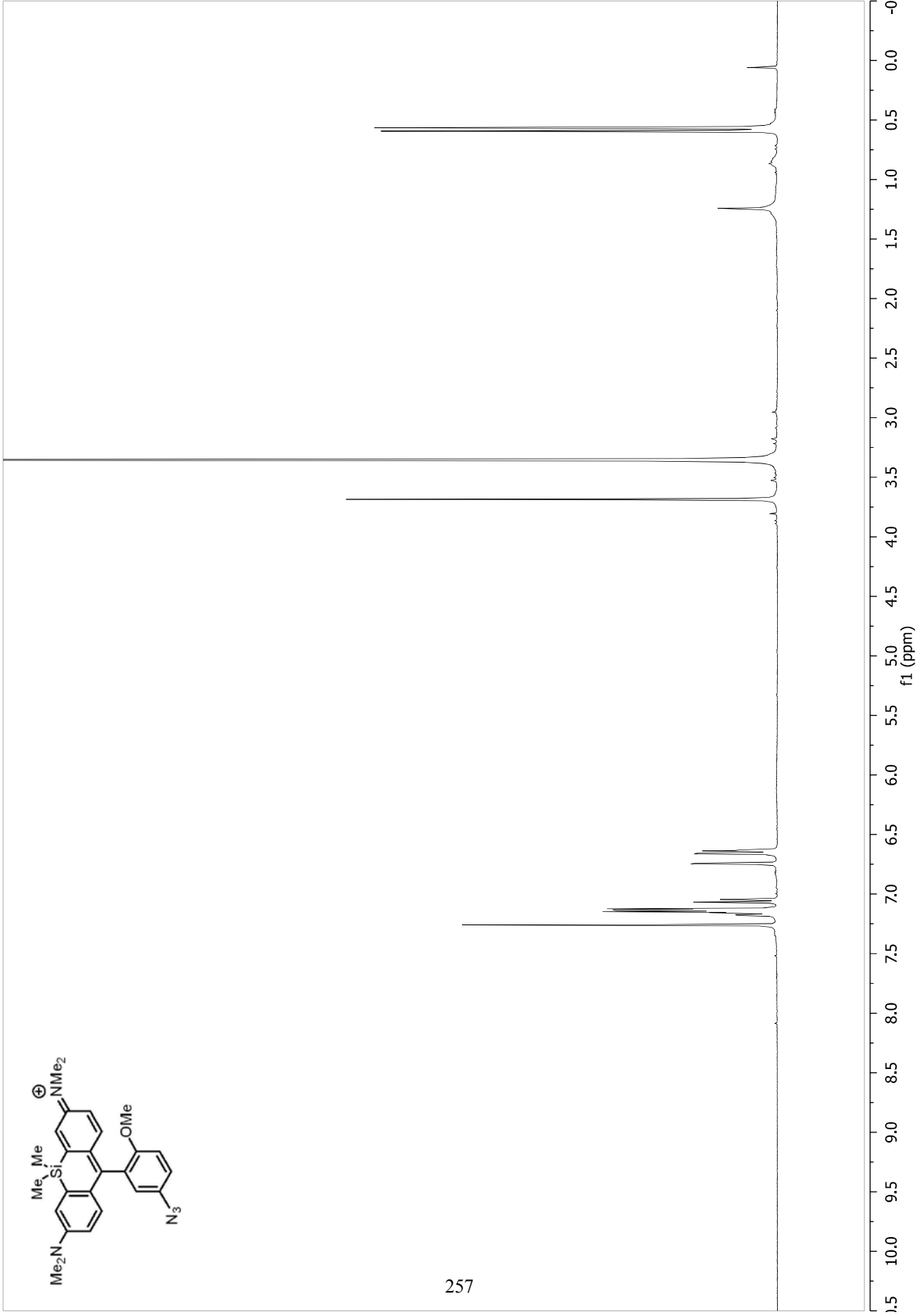


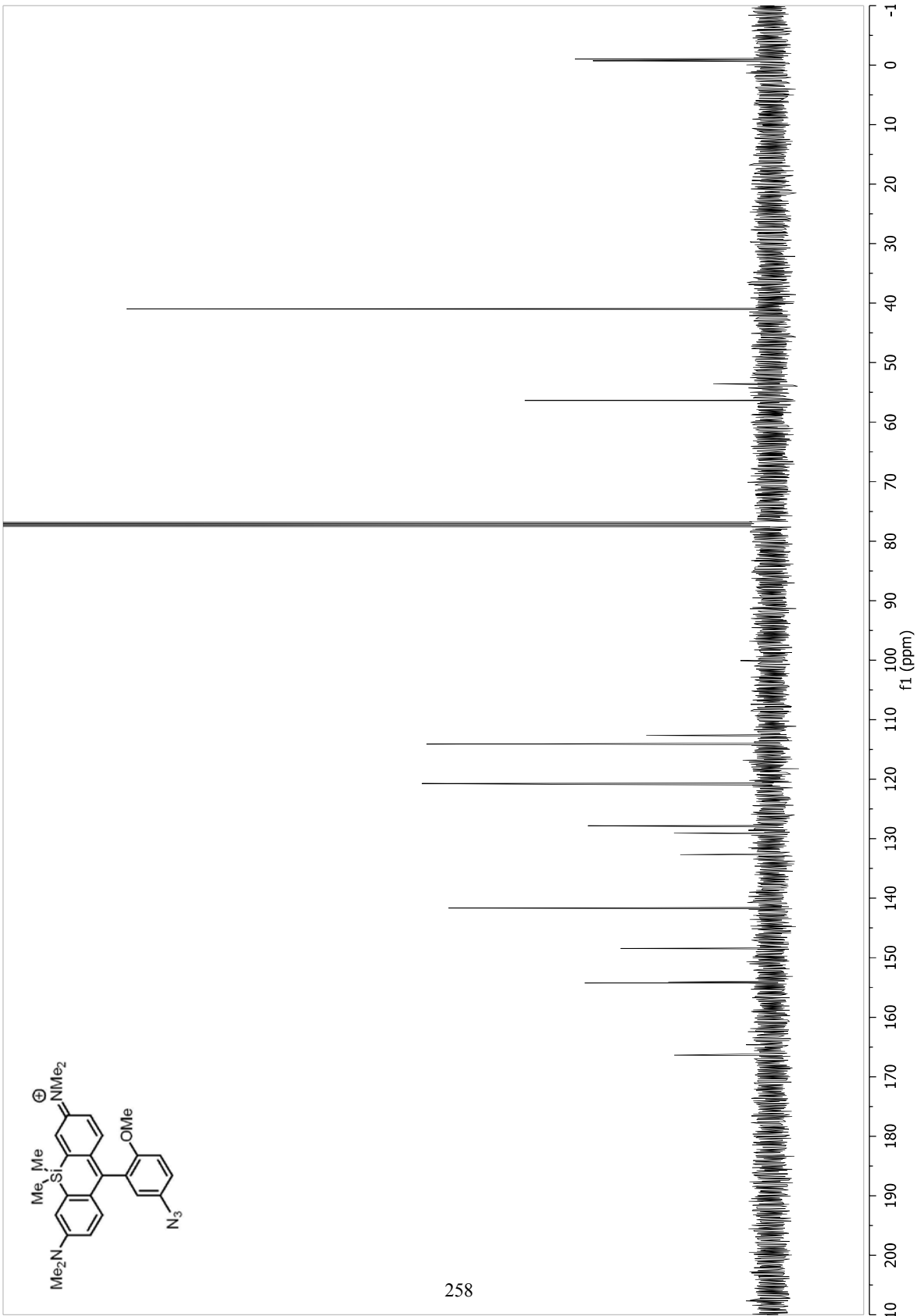


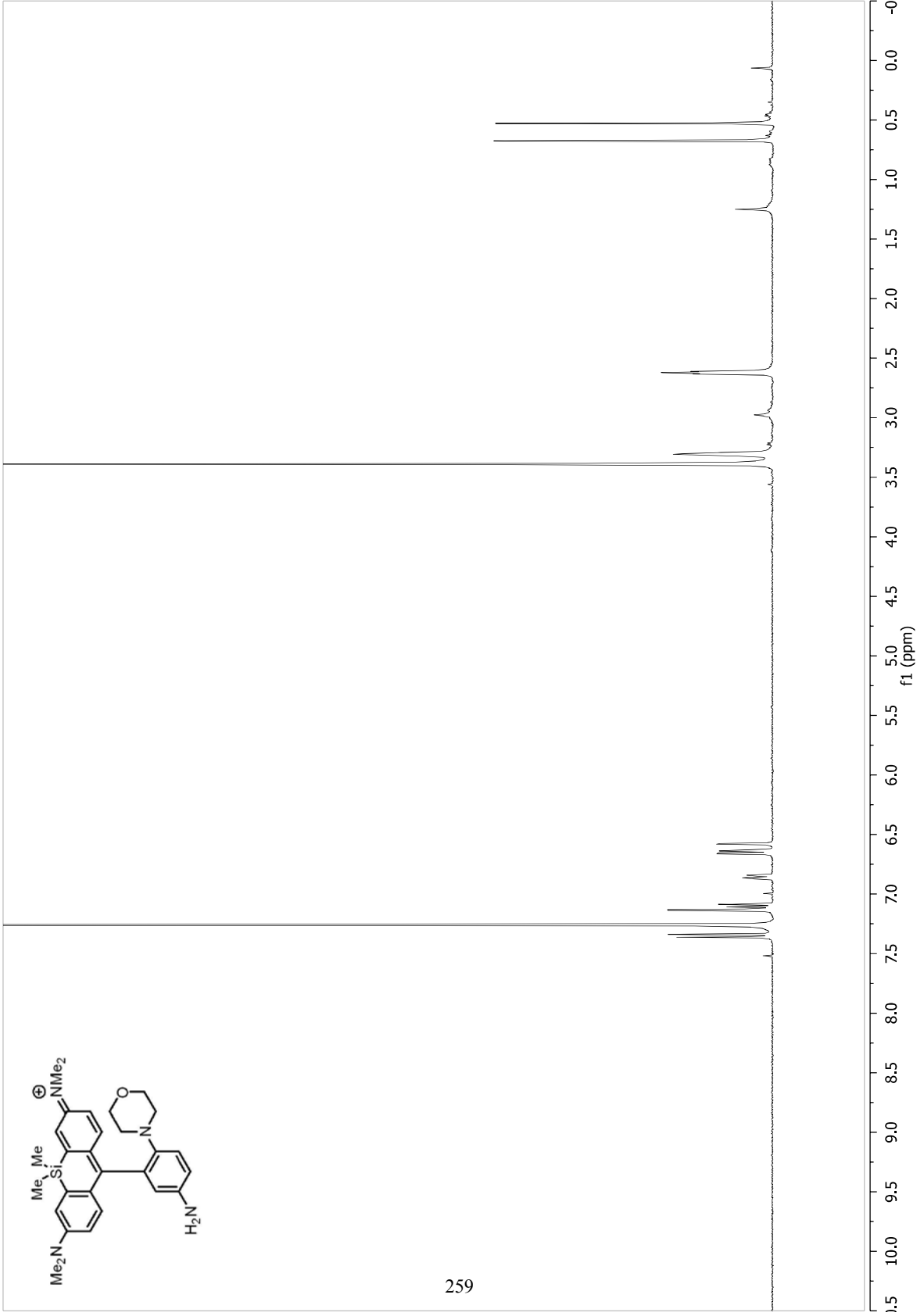


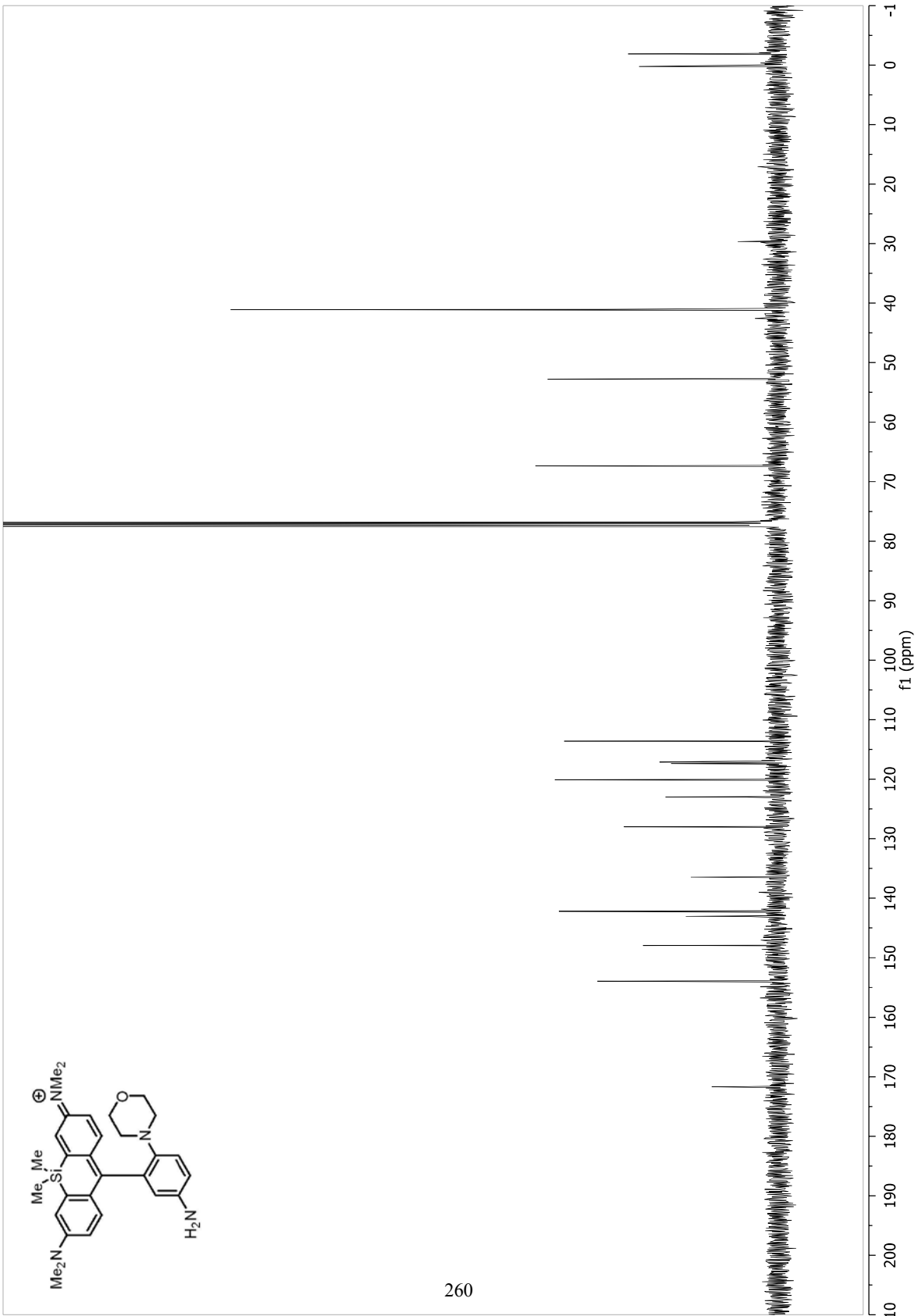


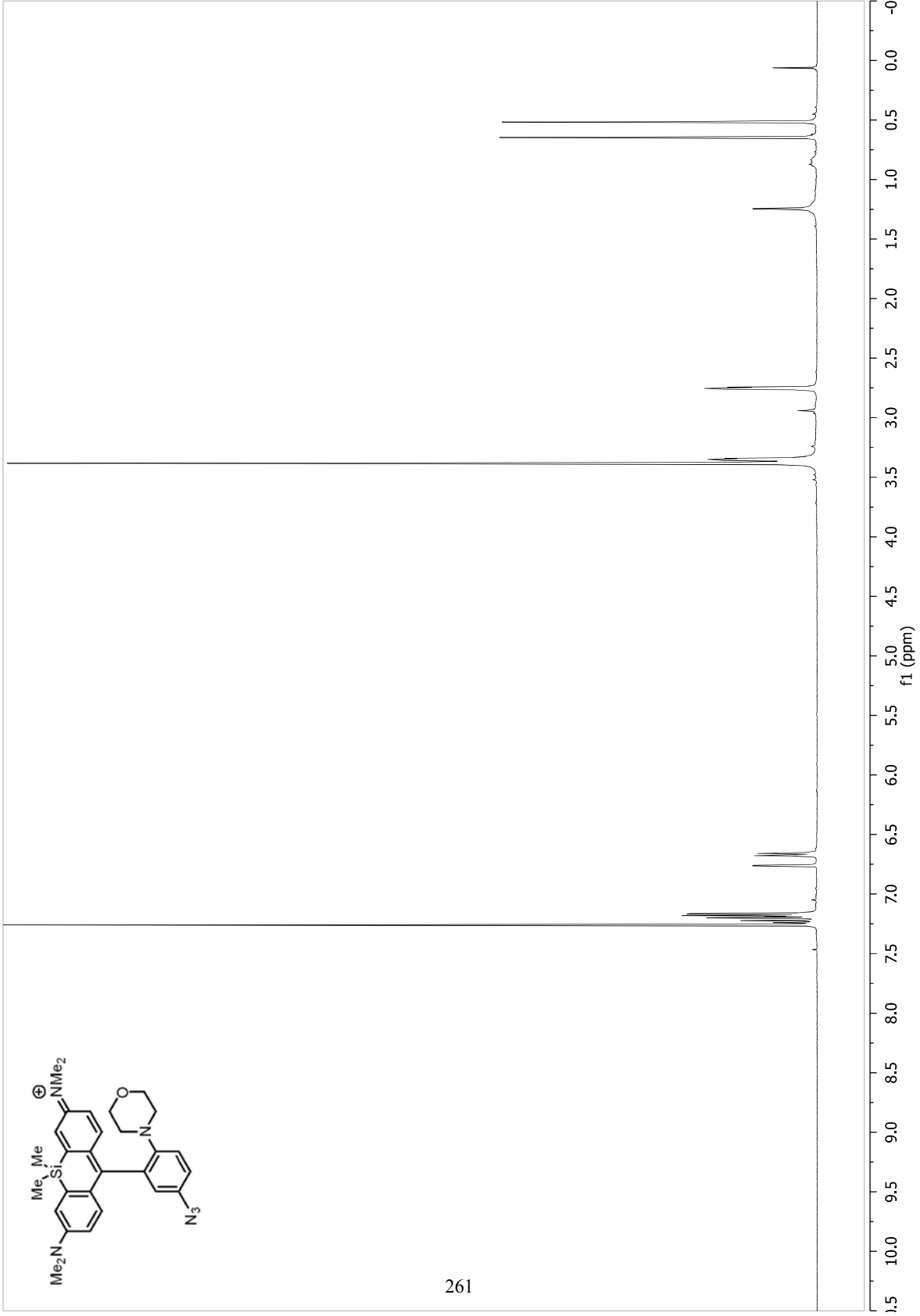


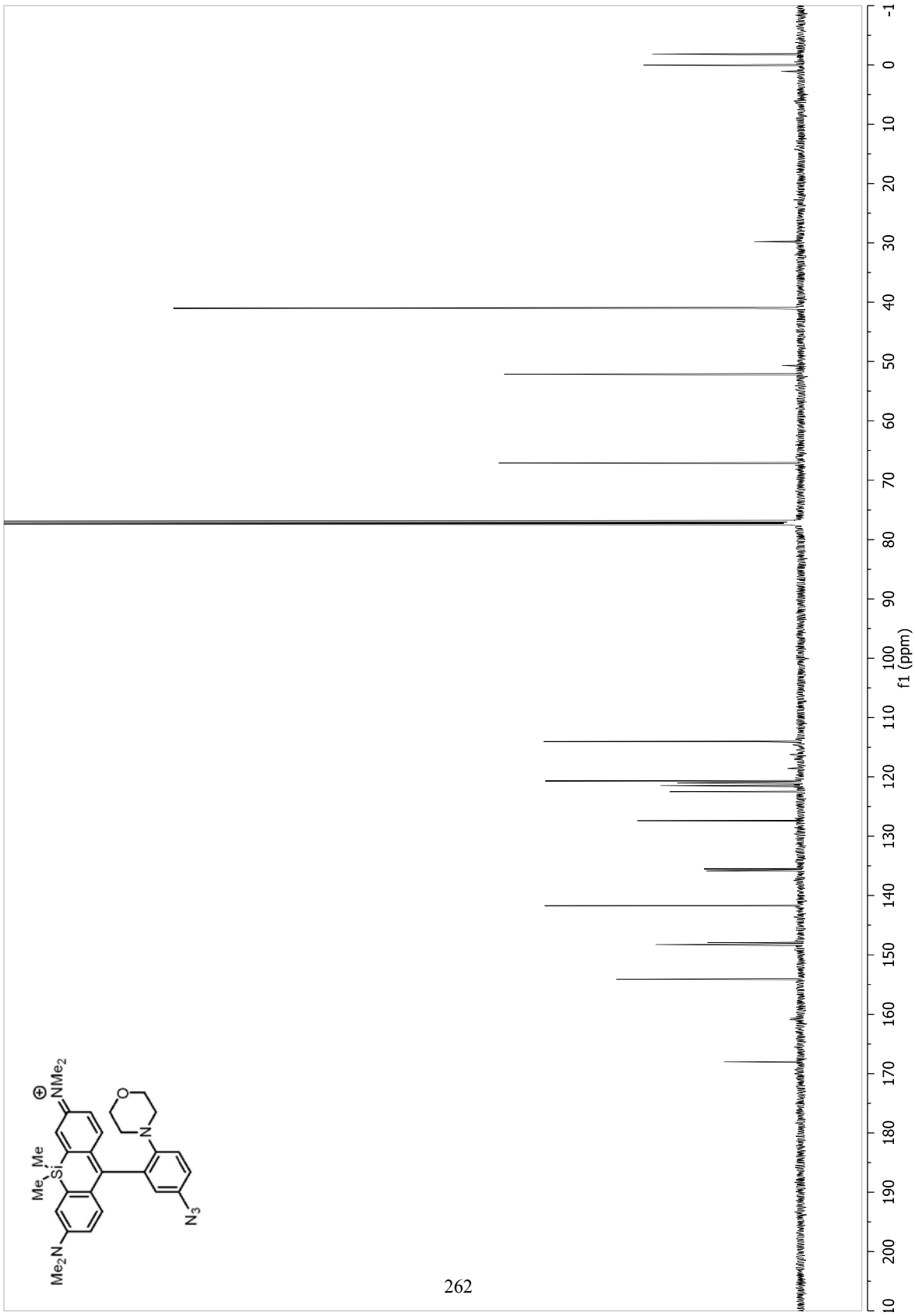


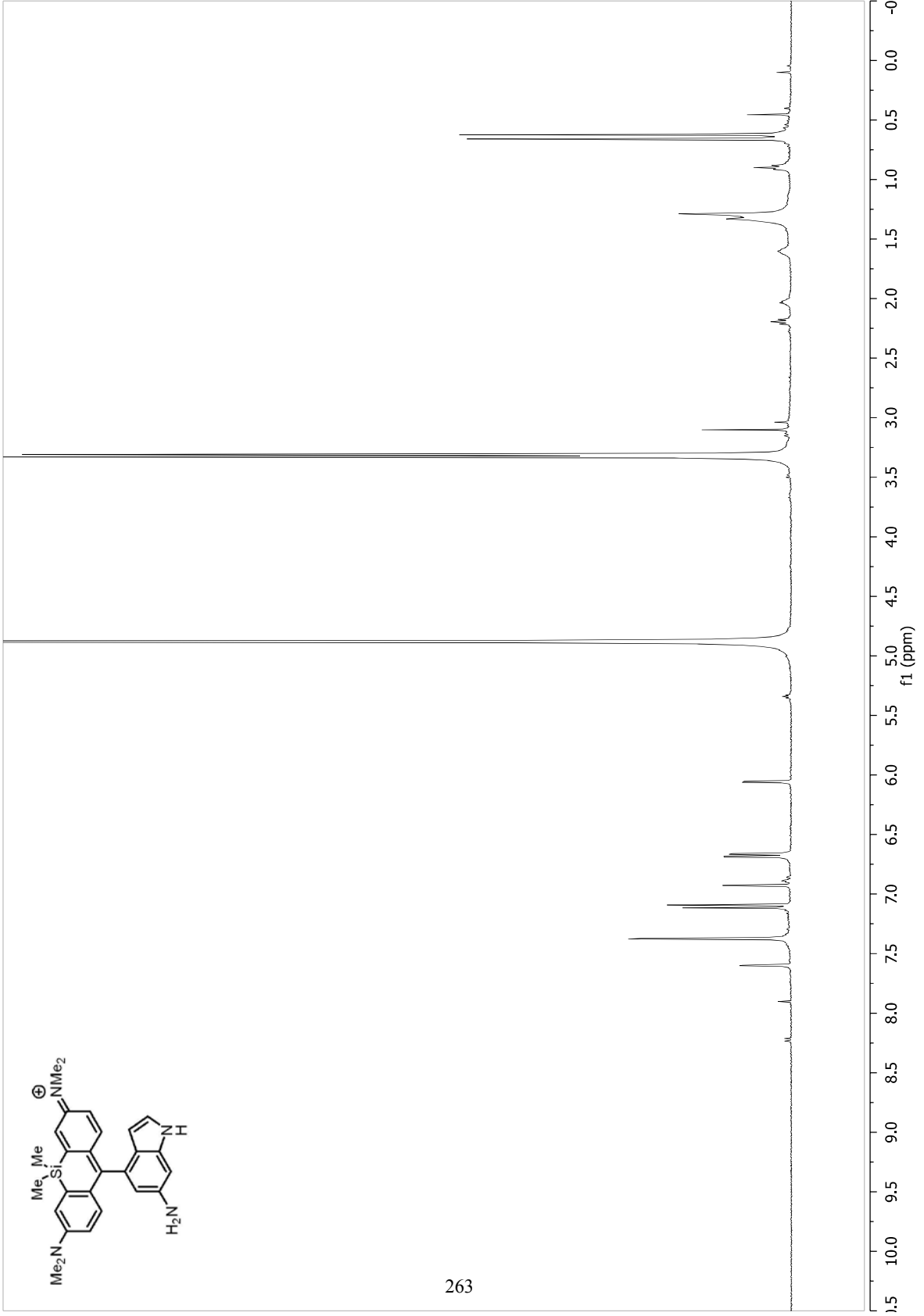


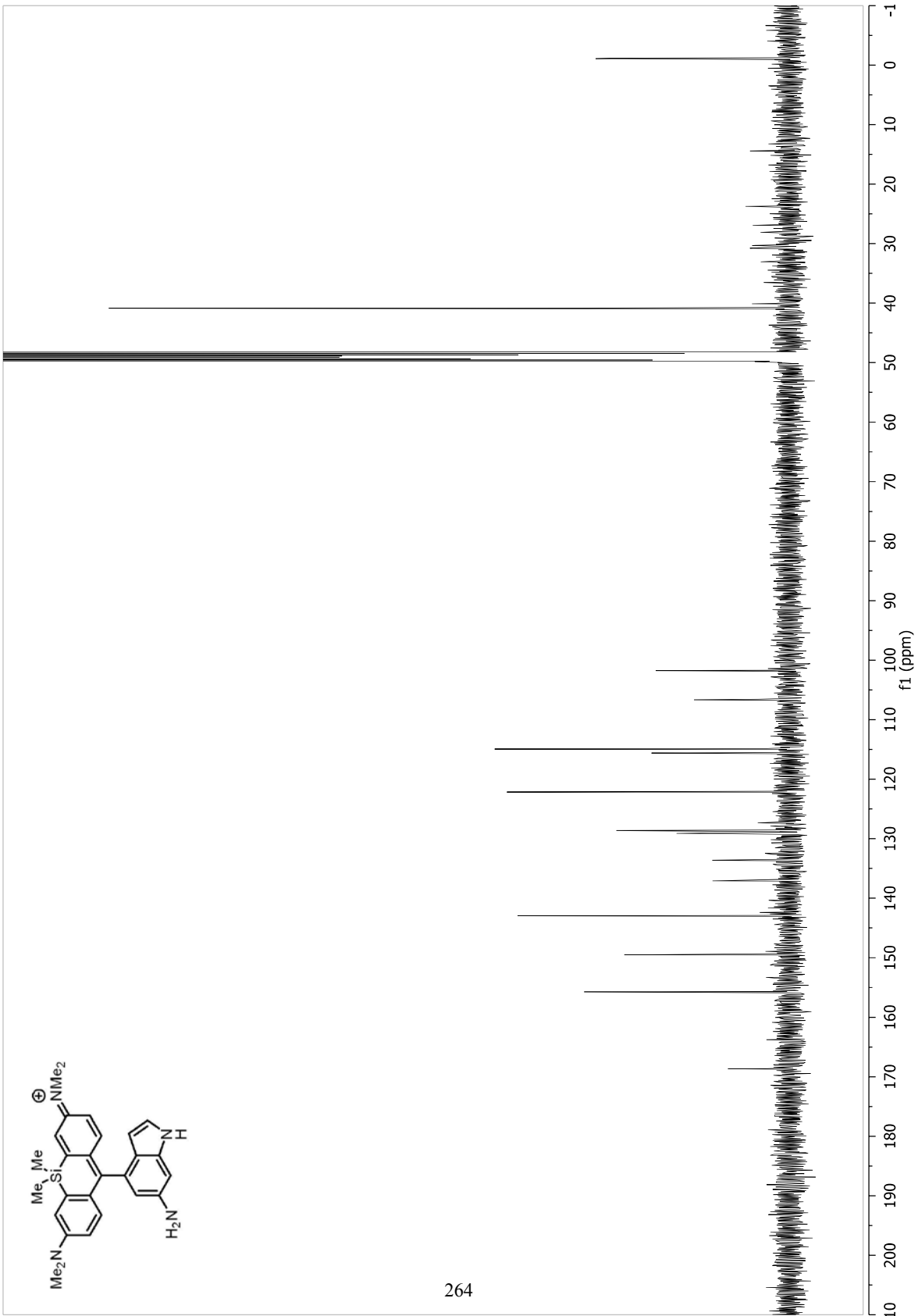


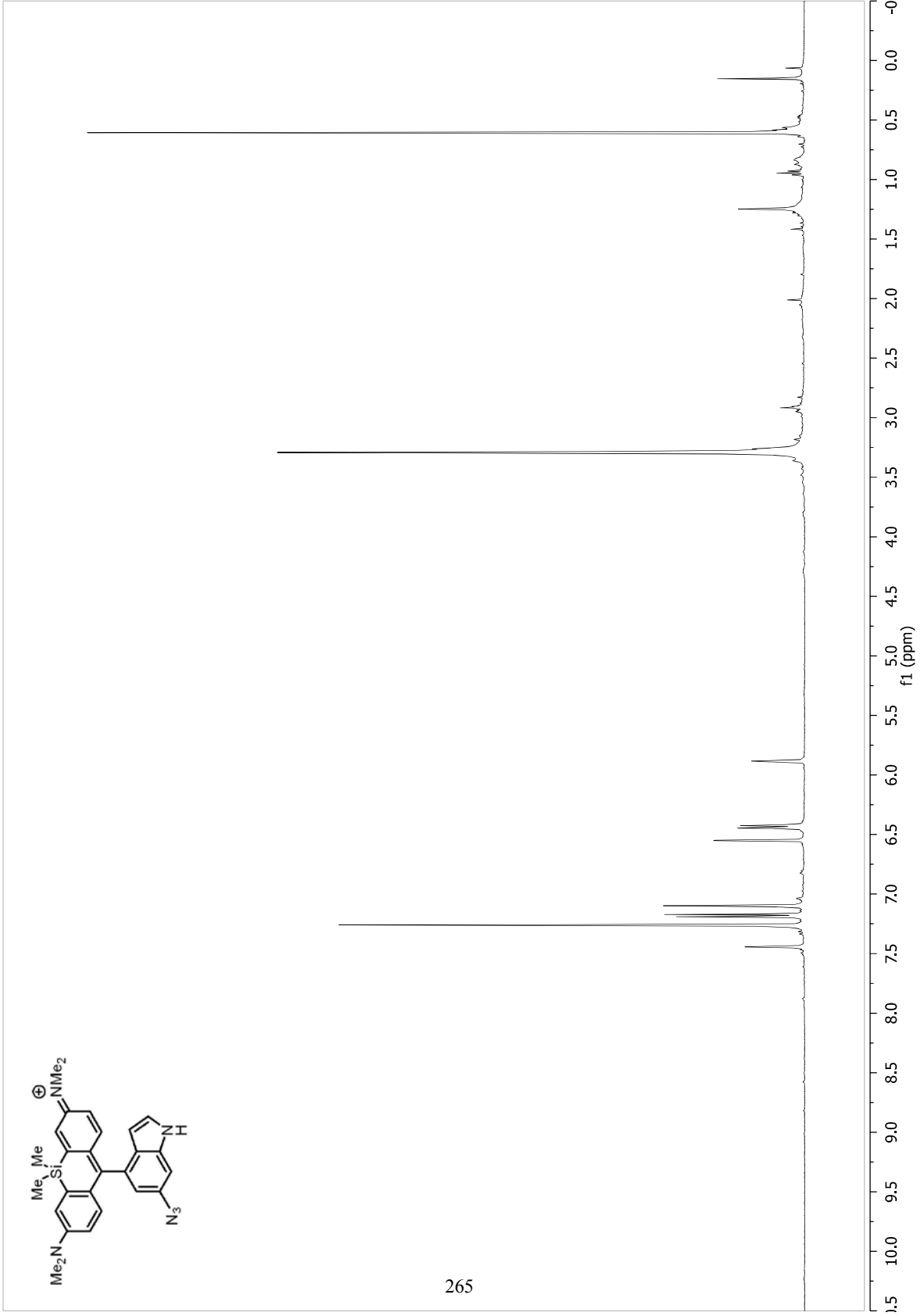


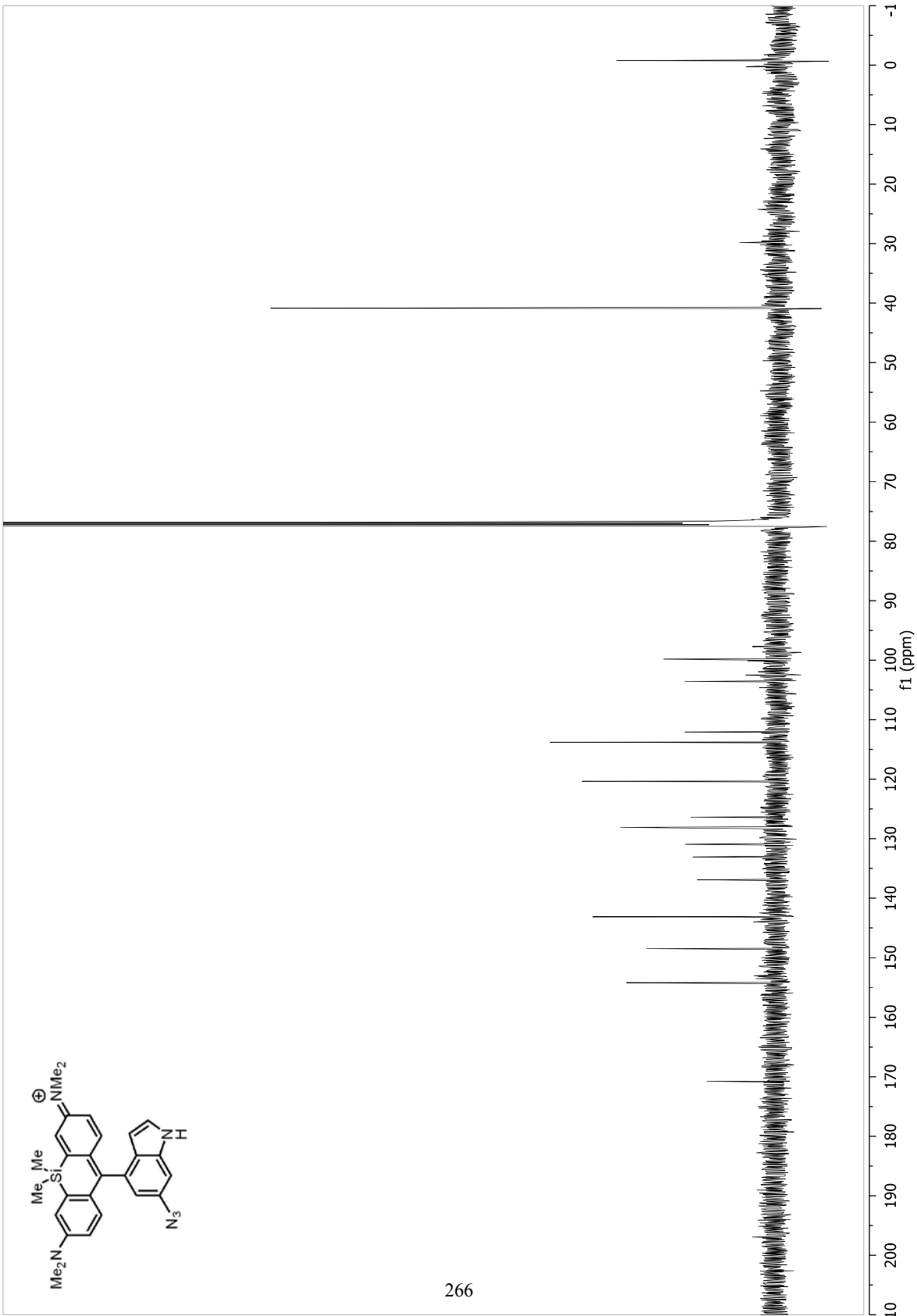


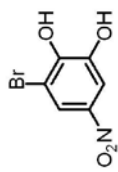




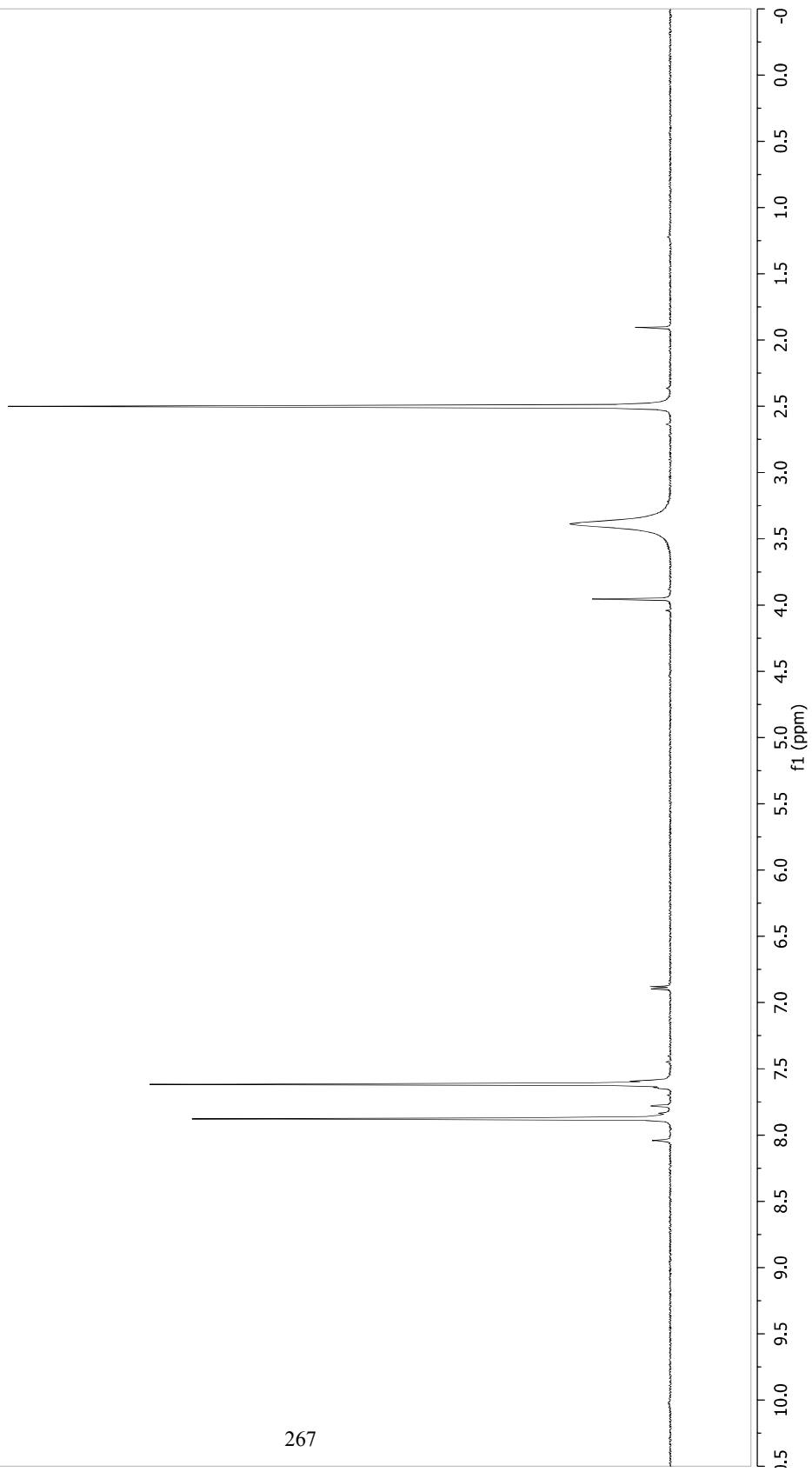


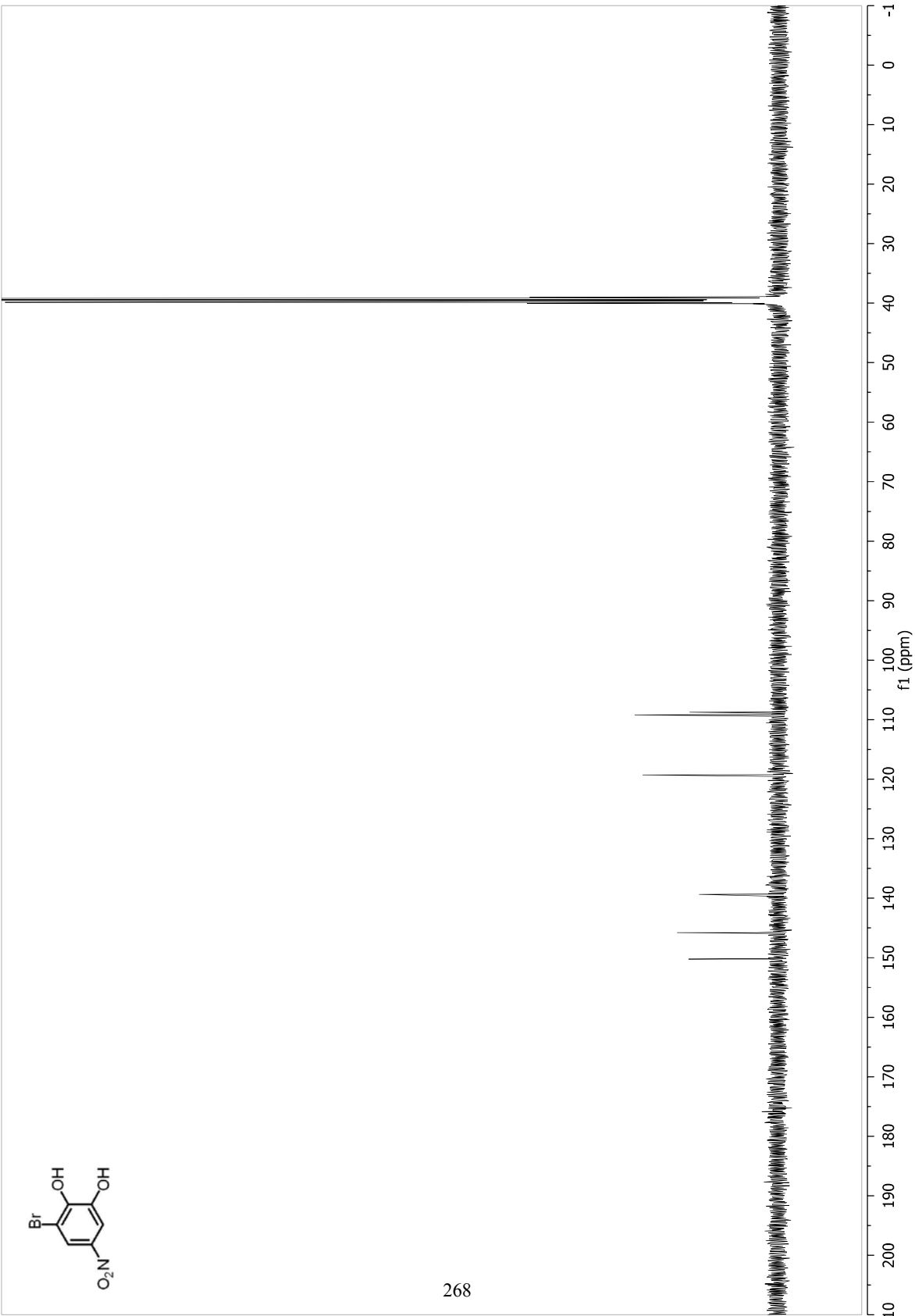


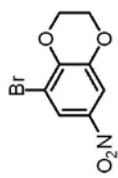




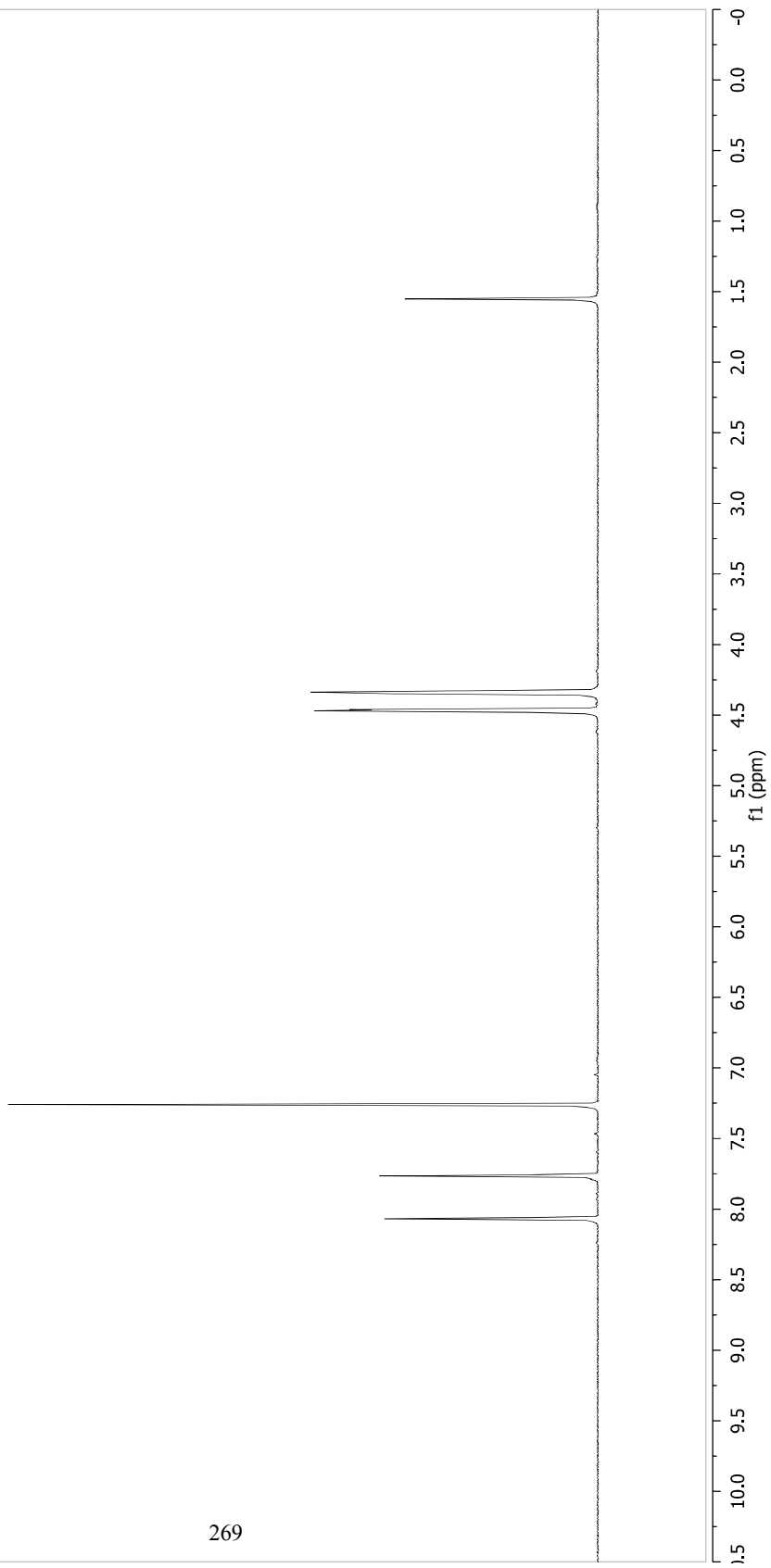
267

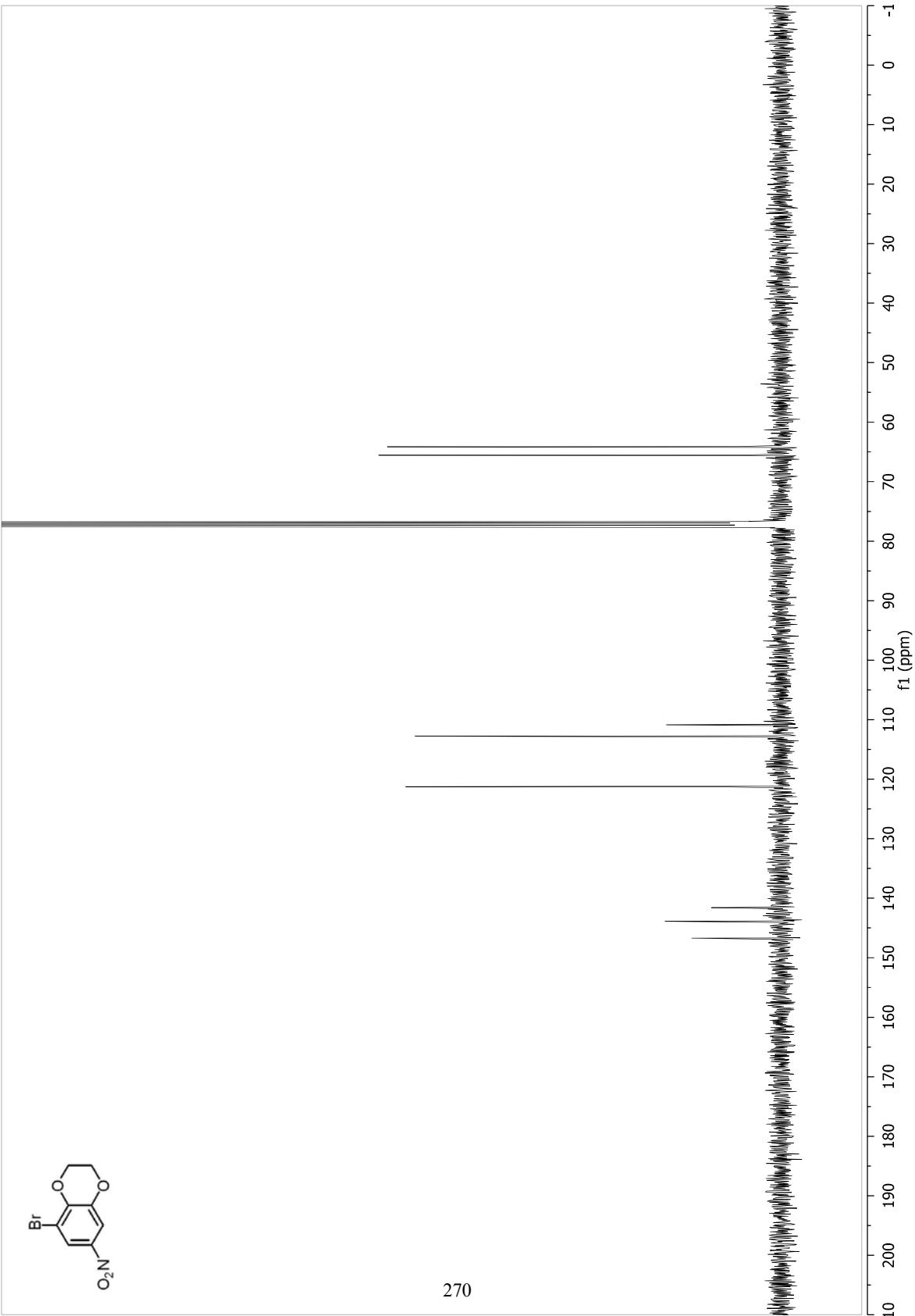


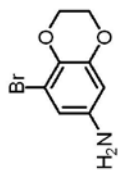




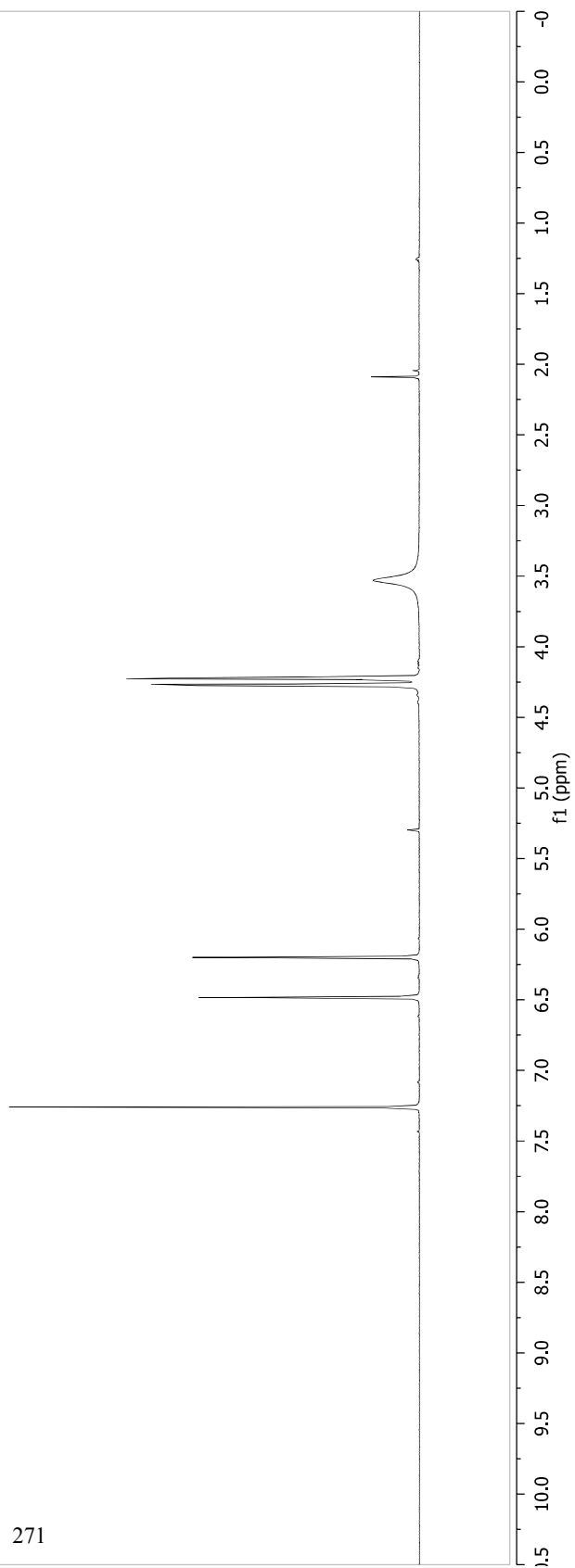
269

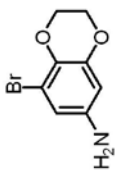




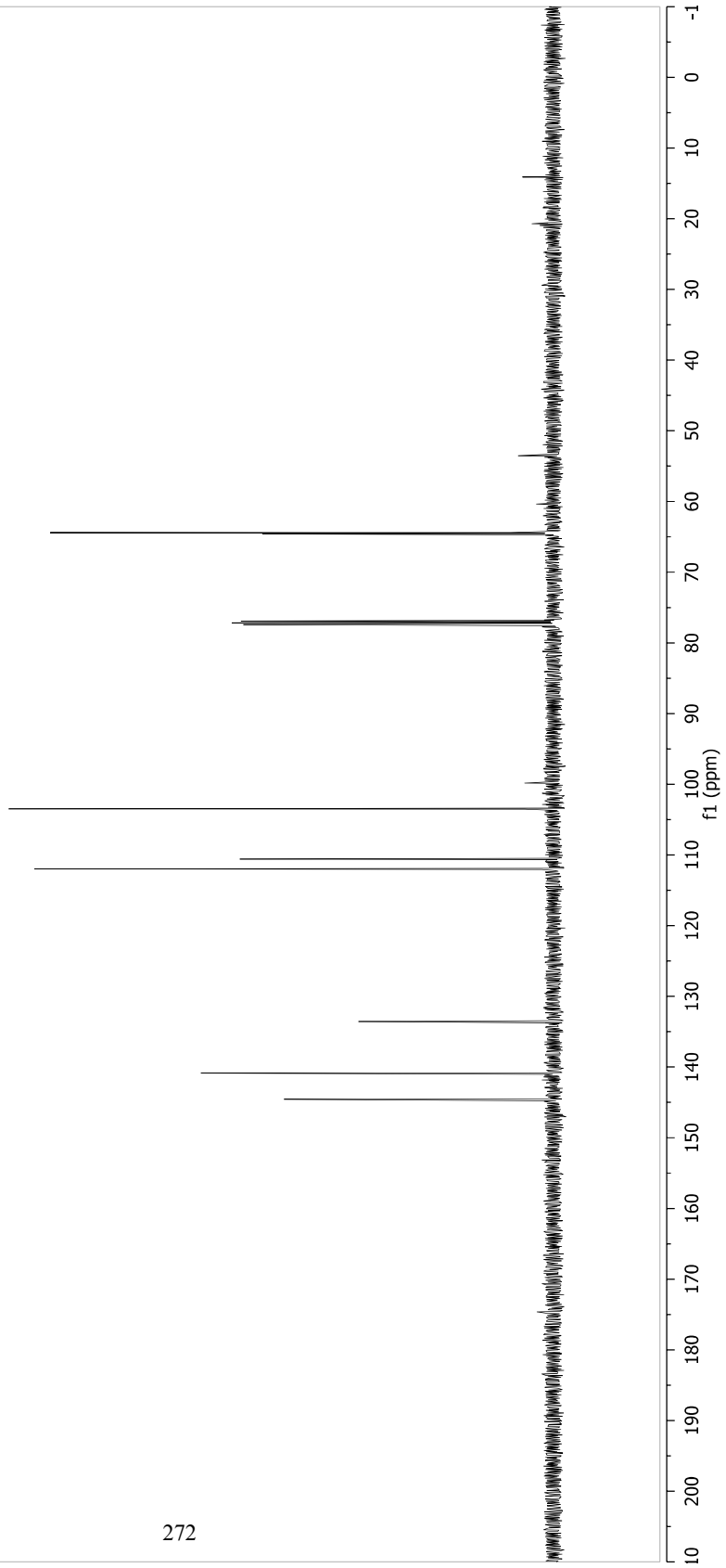


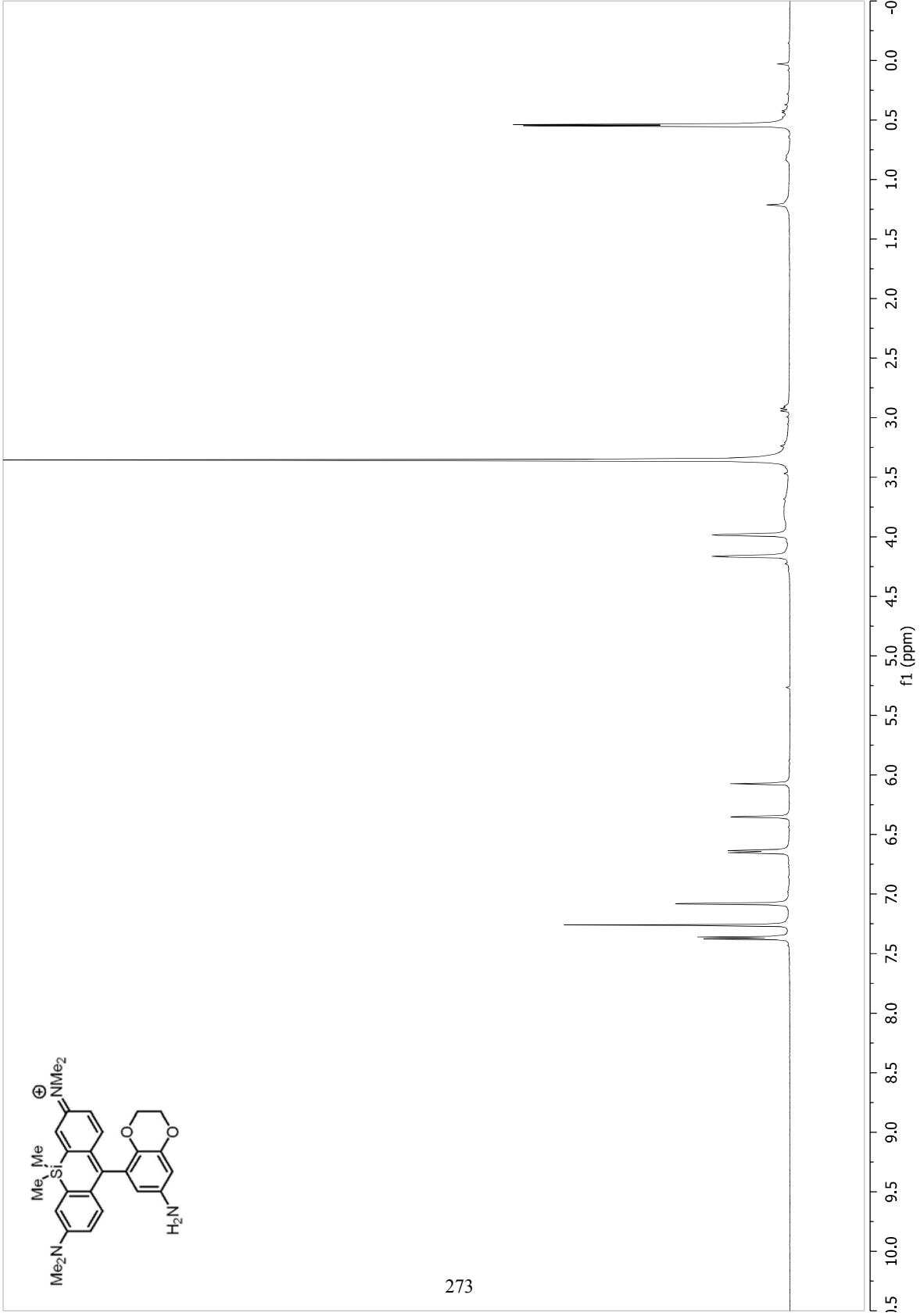
271

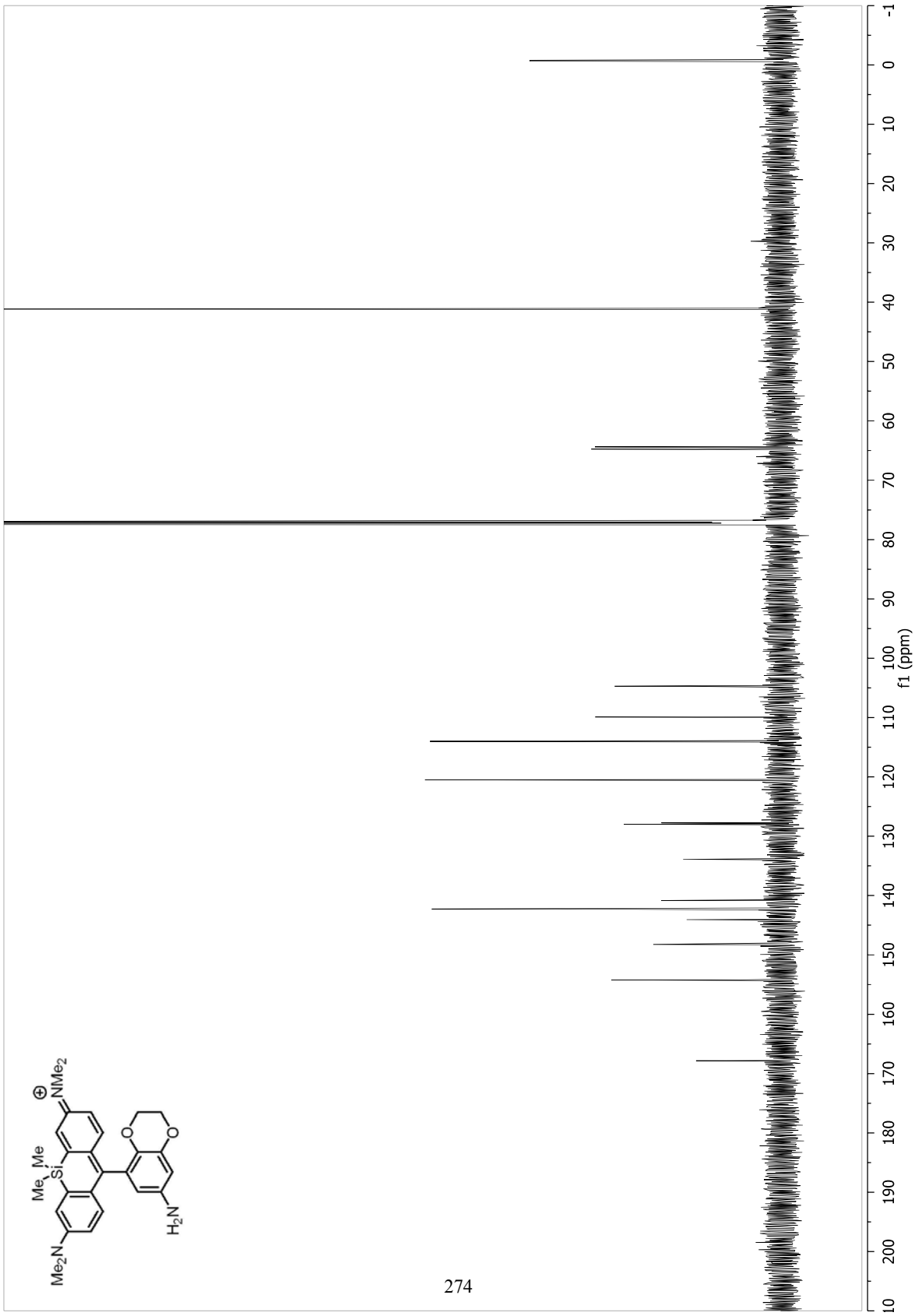


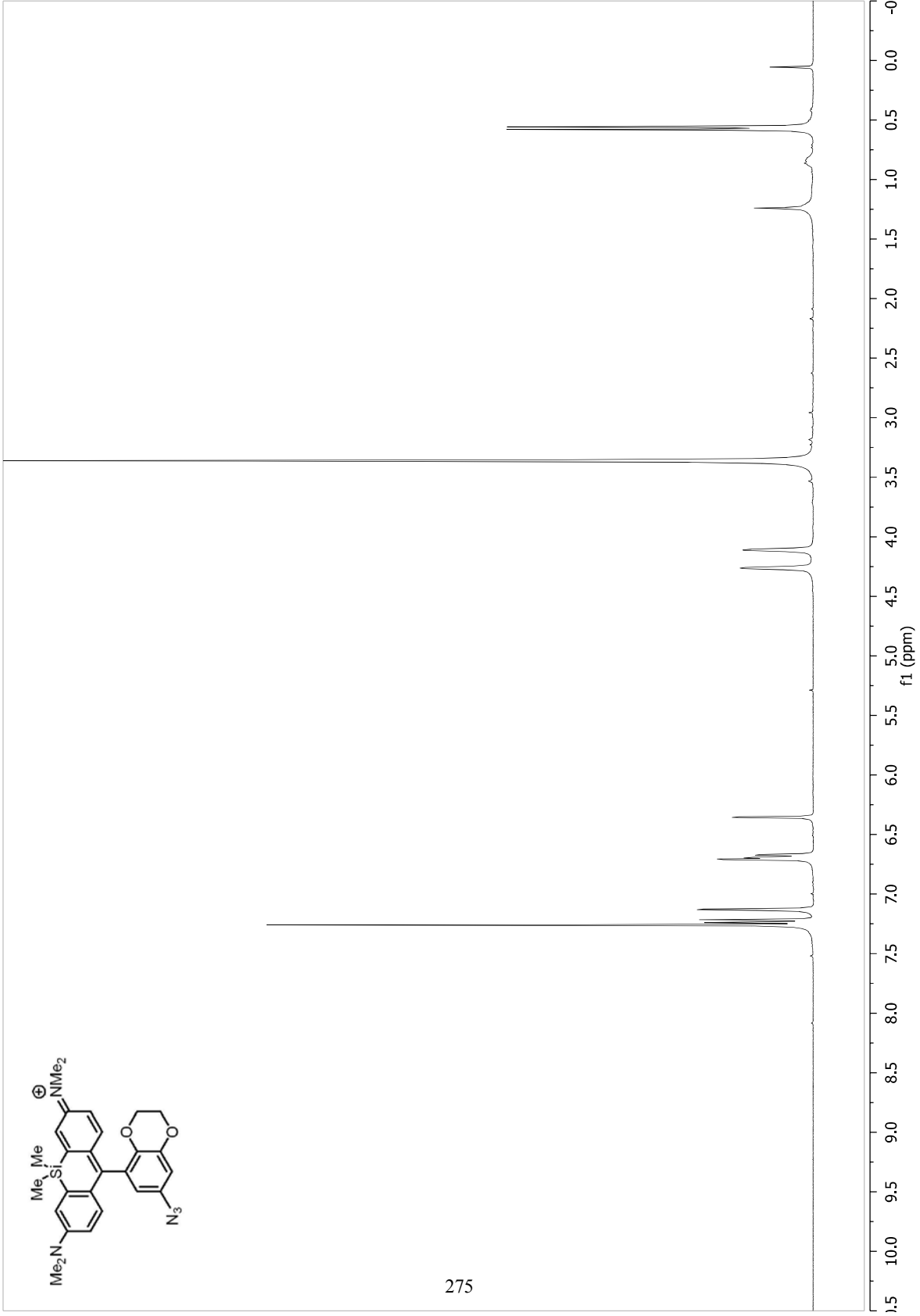


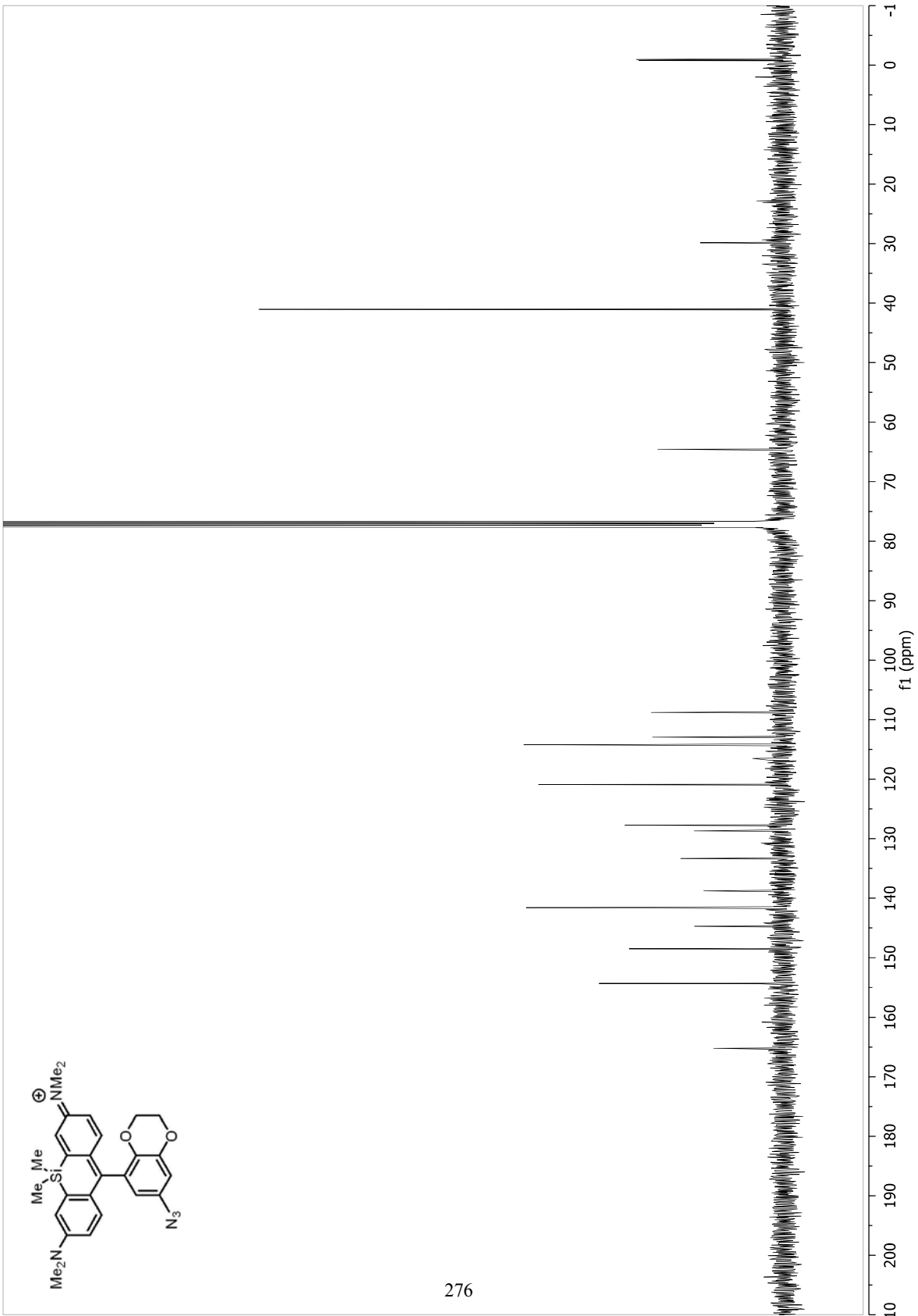
272

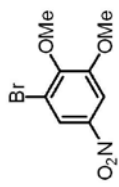




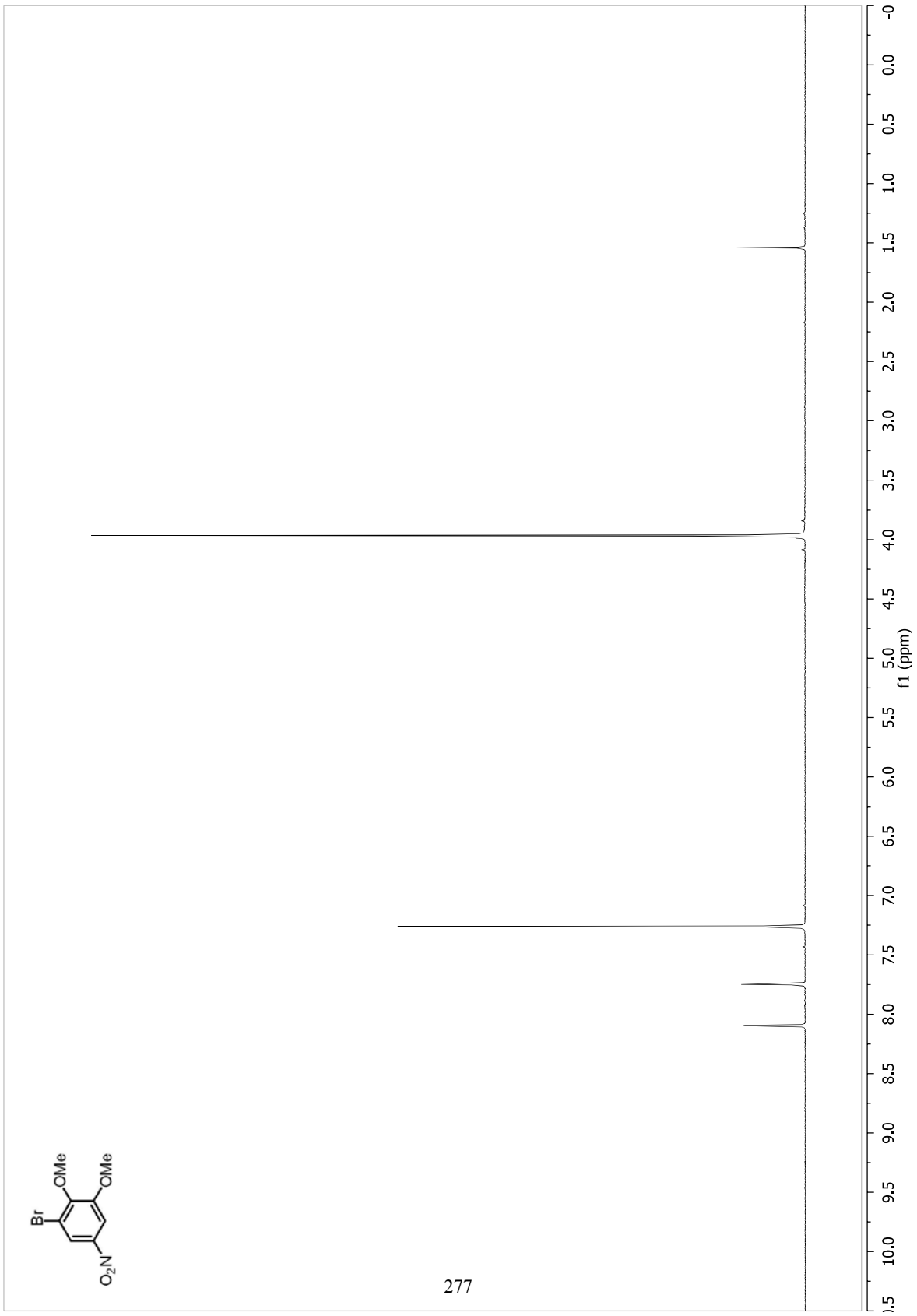


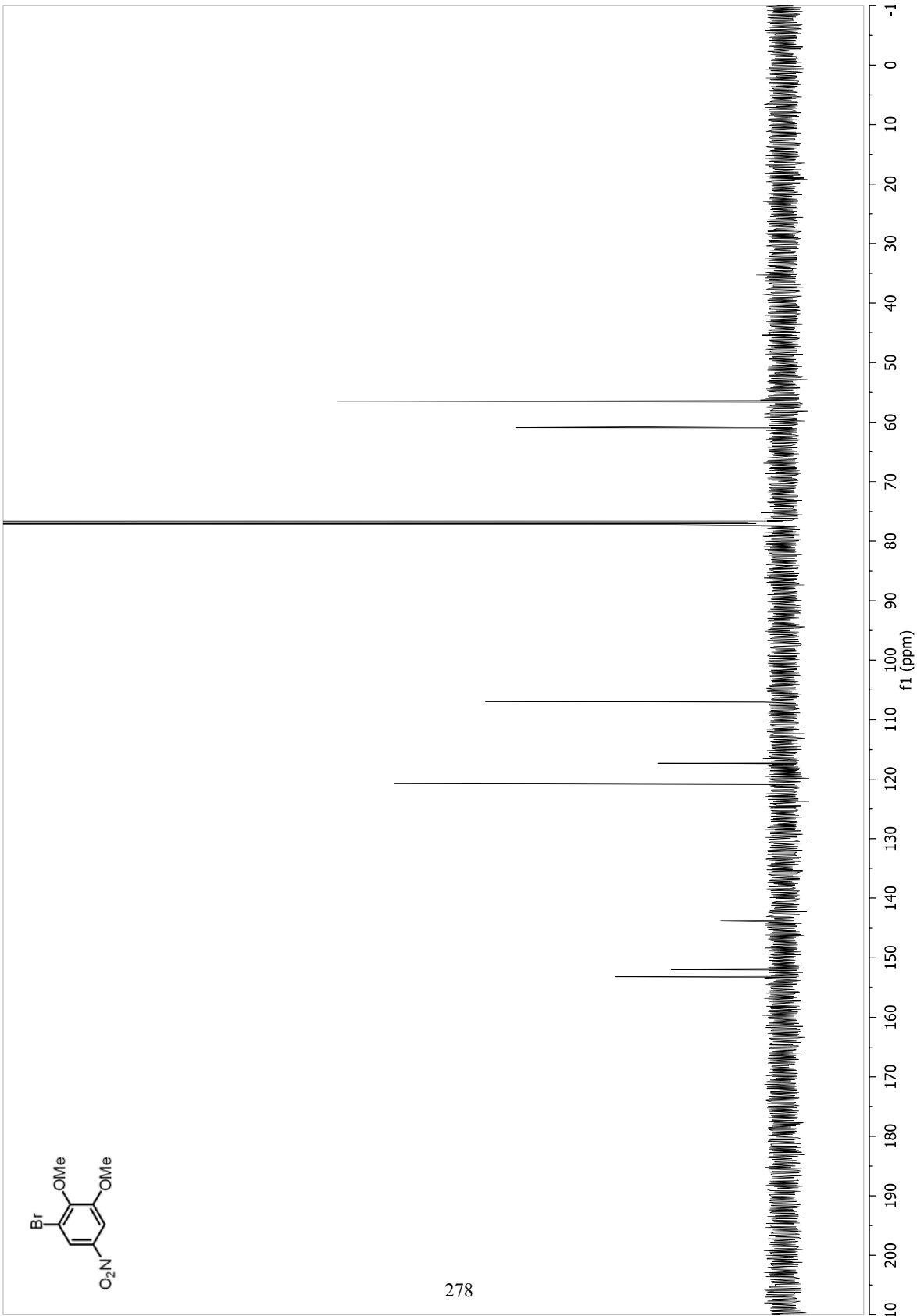


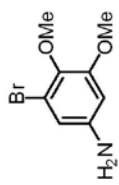




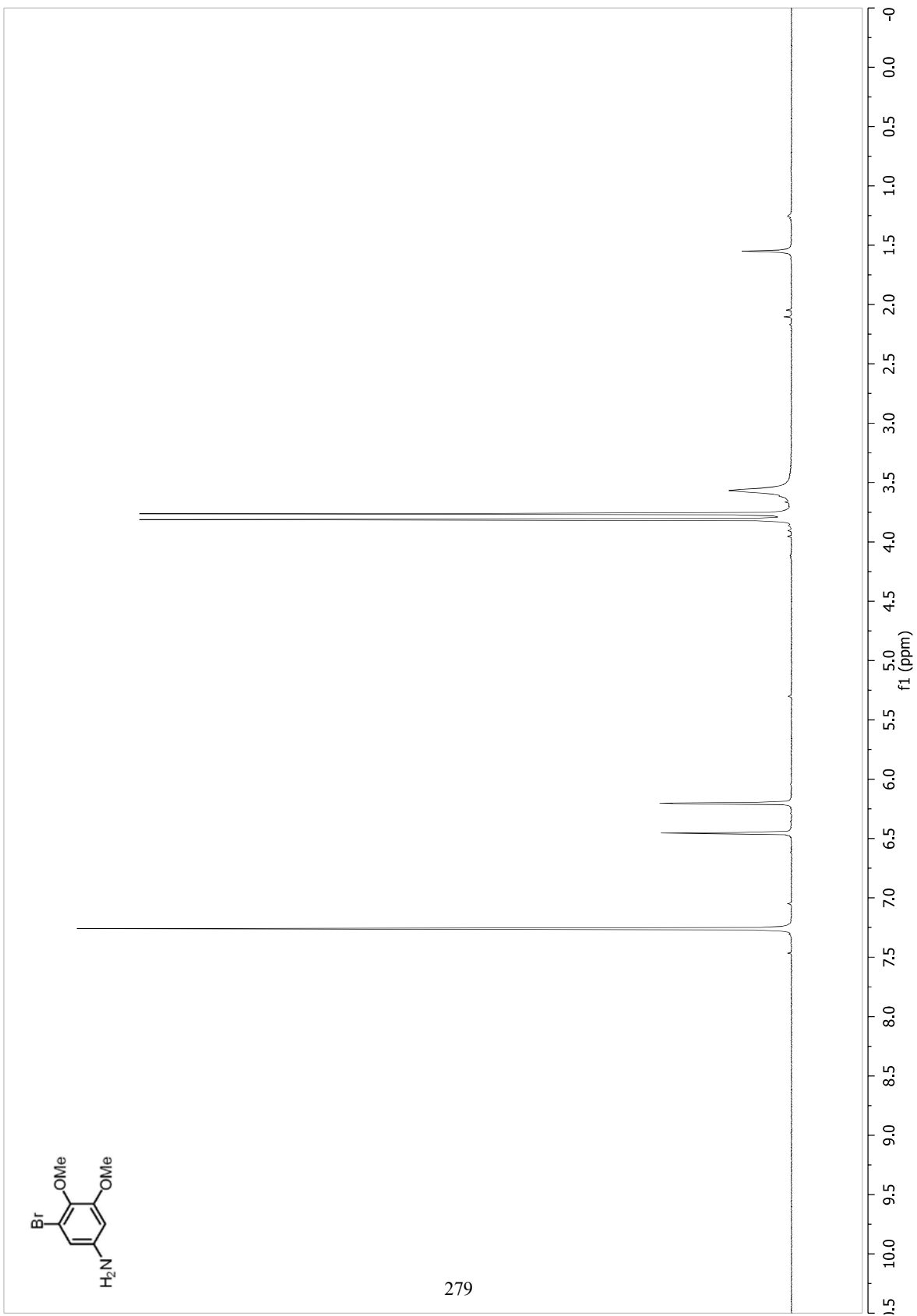
277

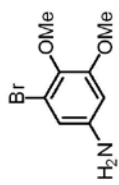




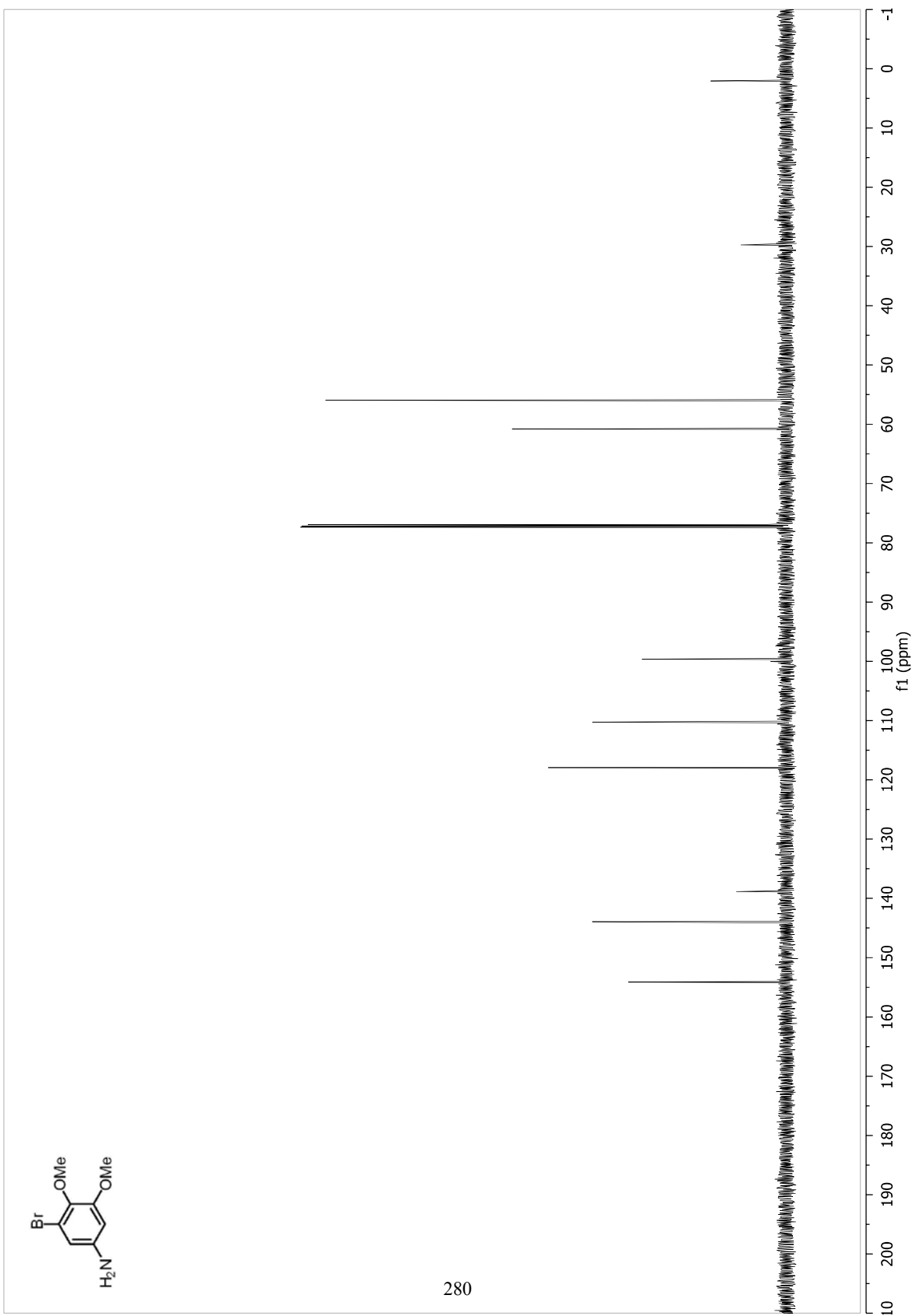


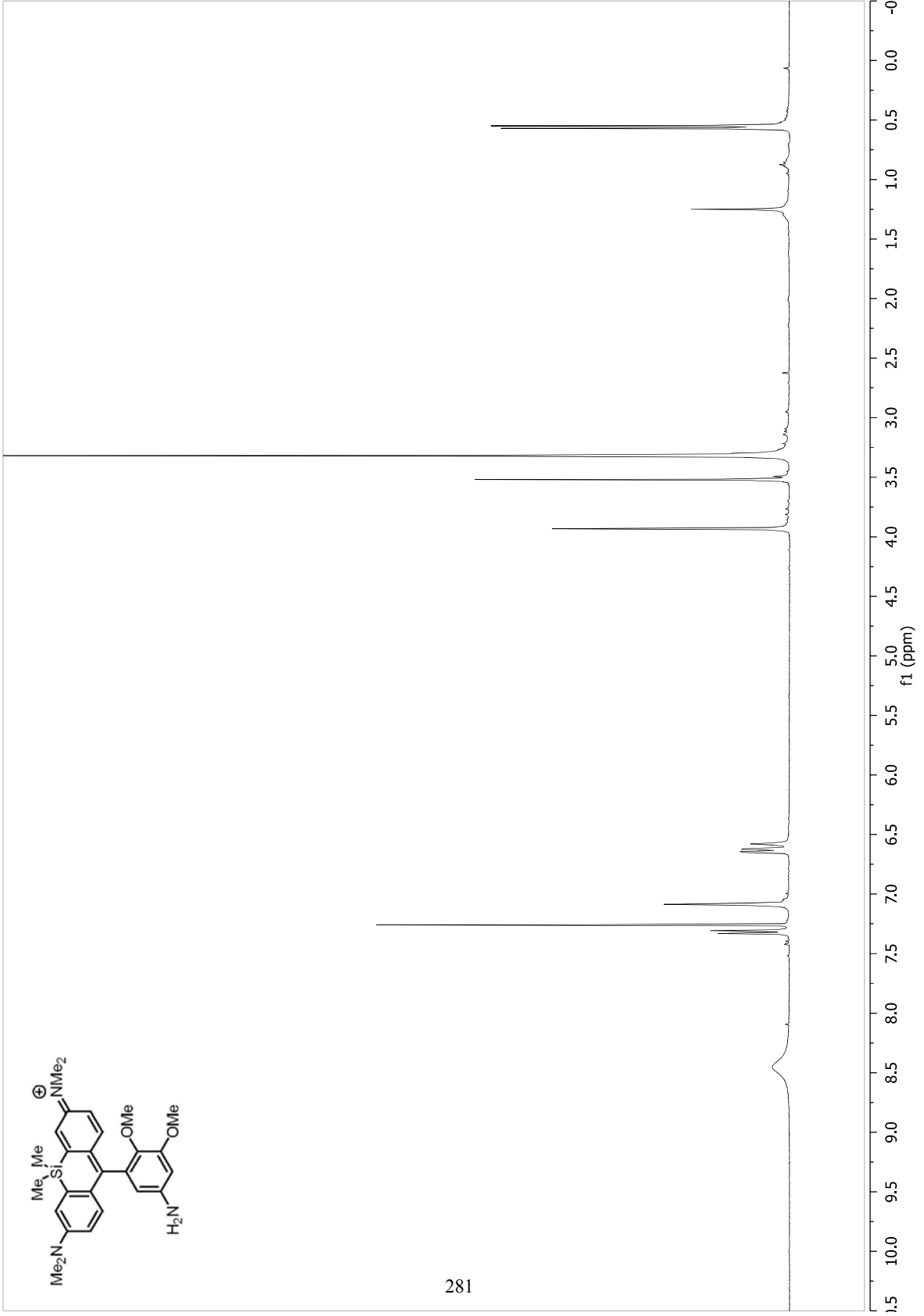
279

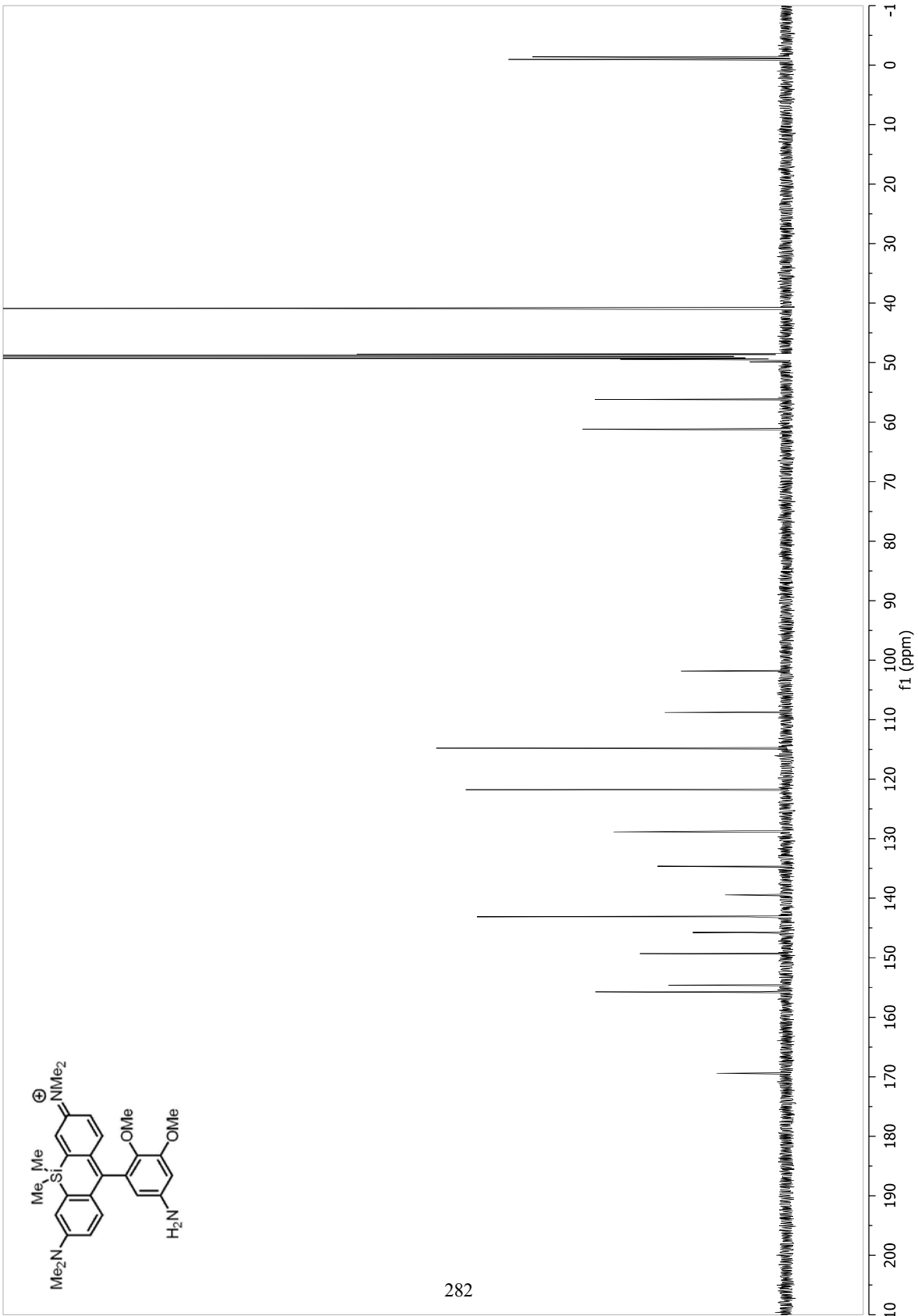


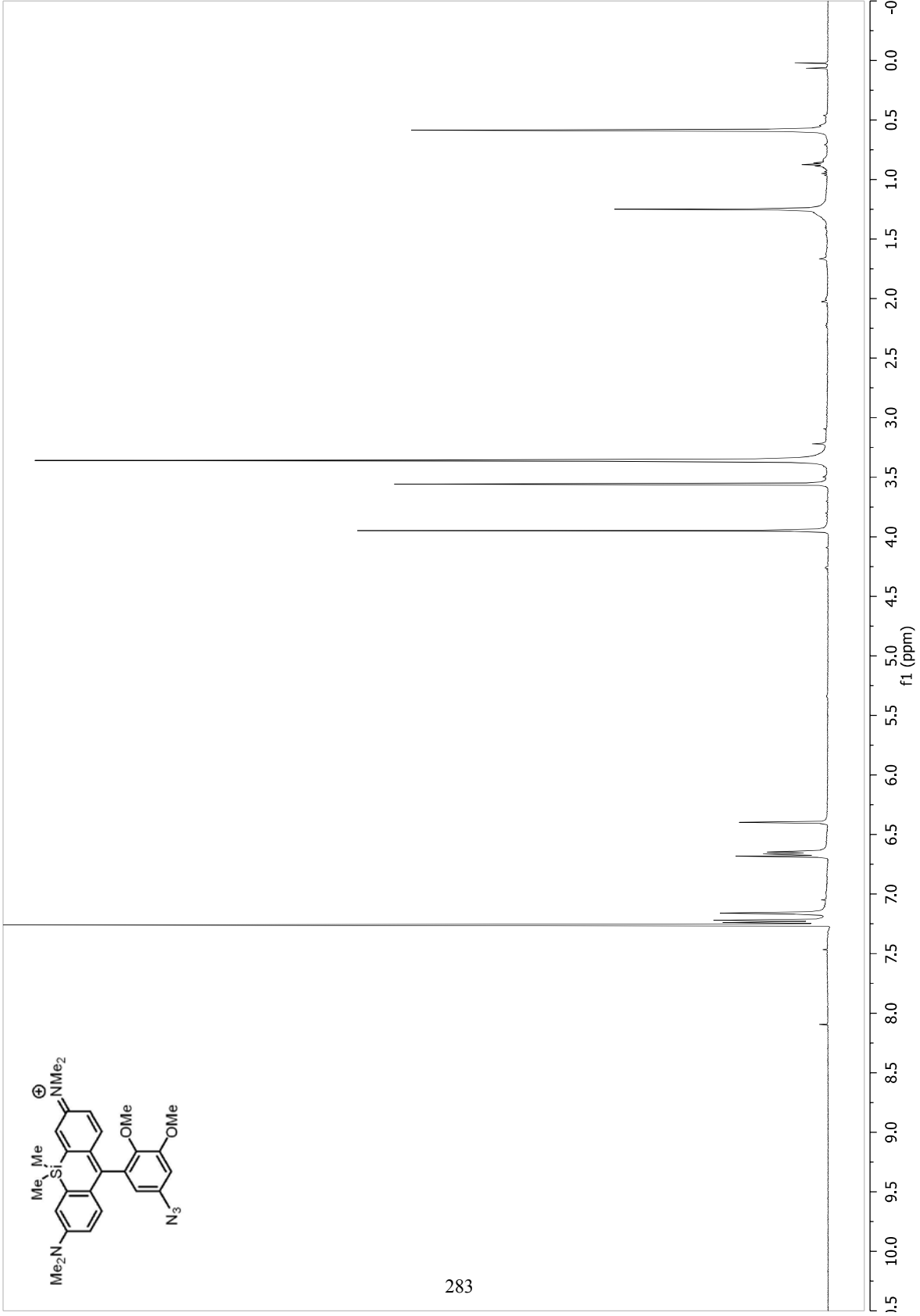


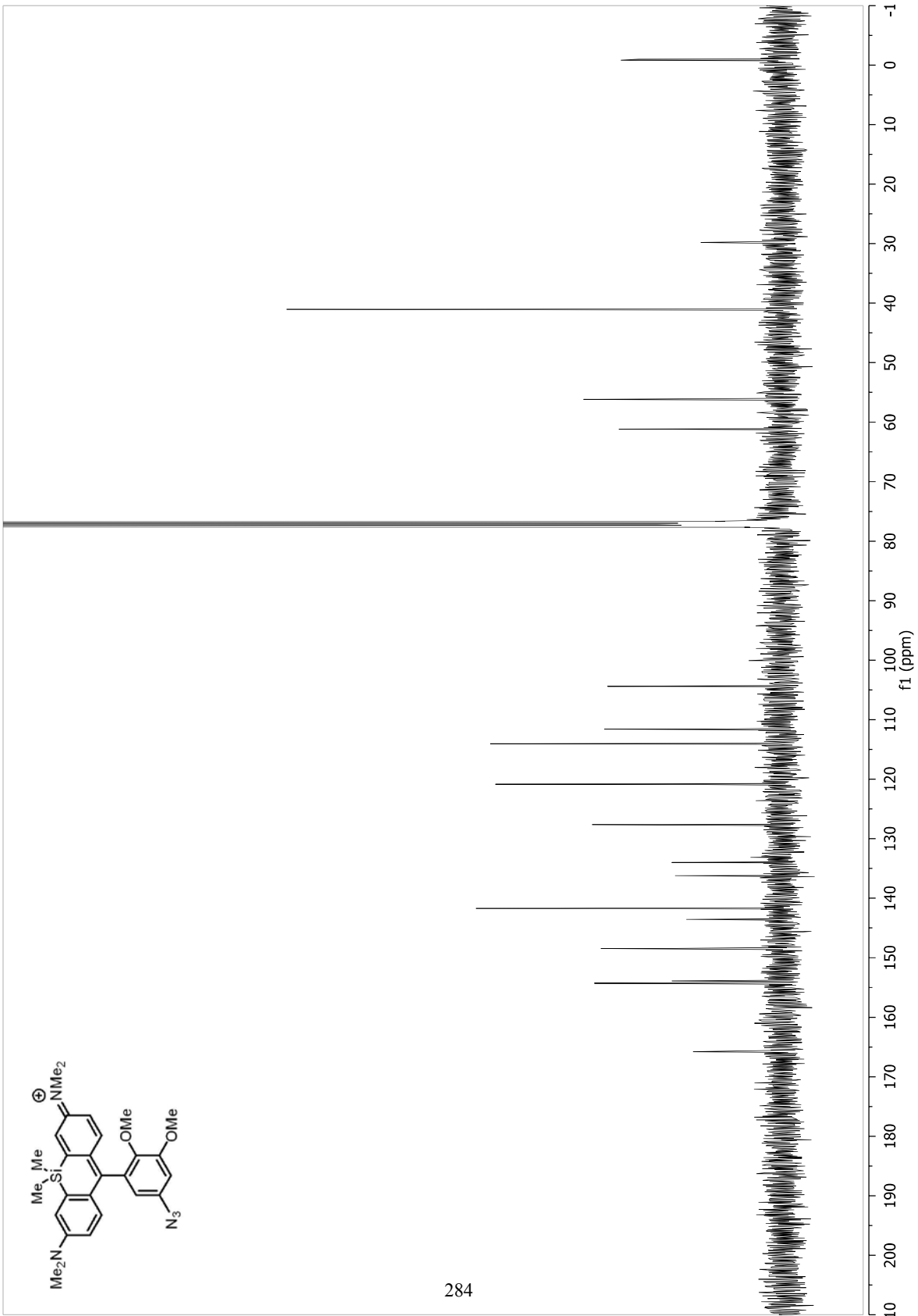
280

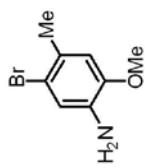




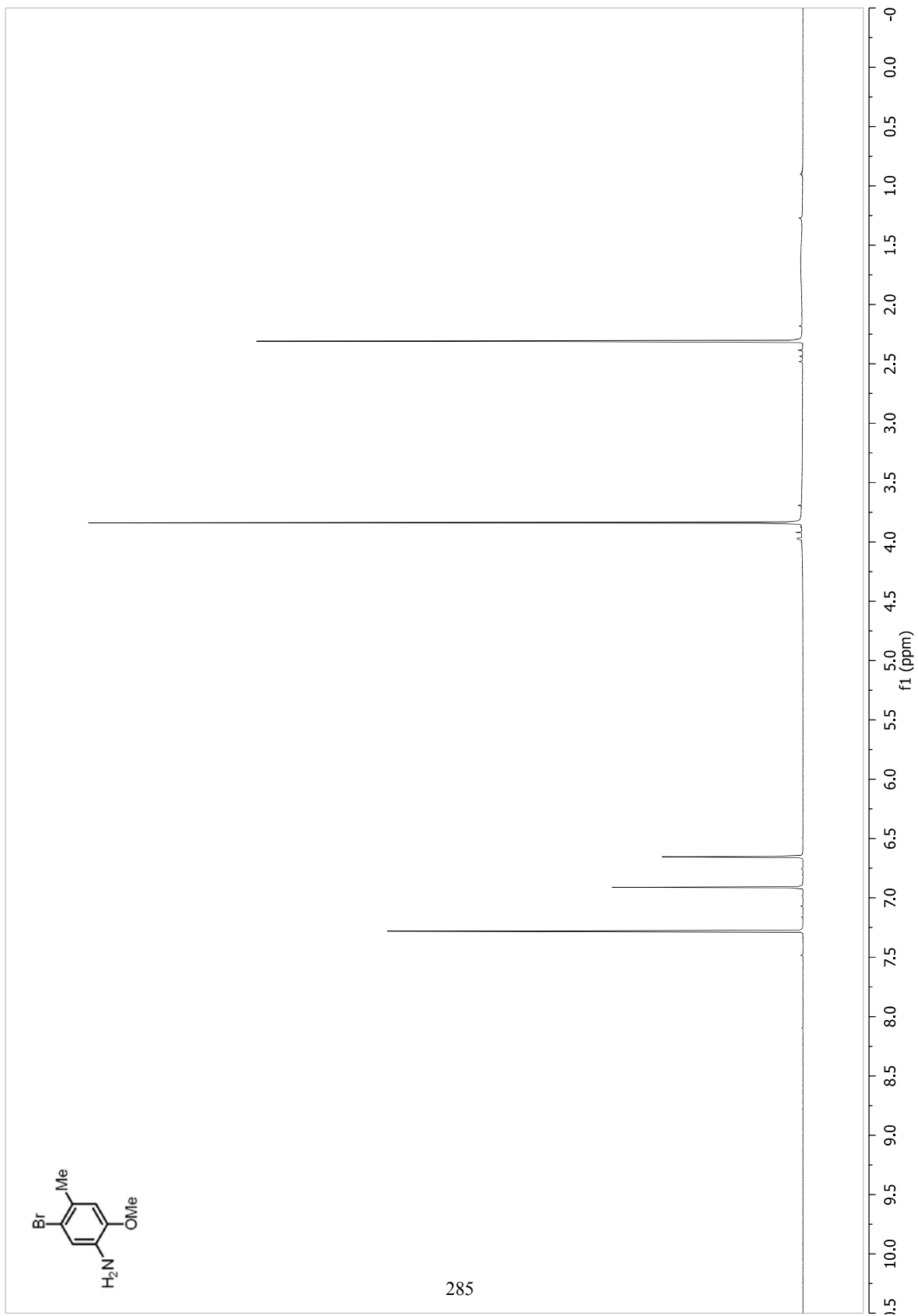


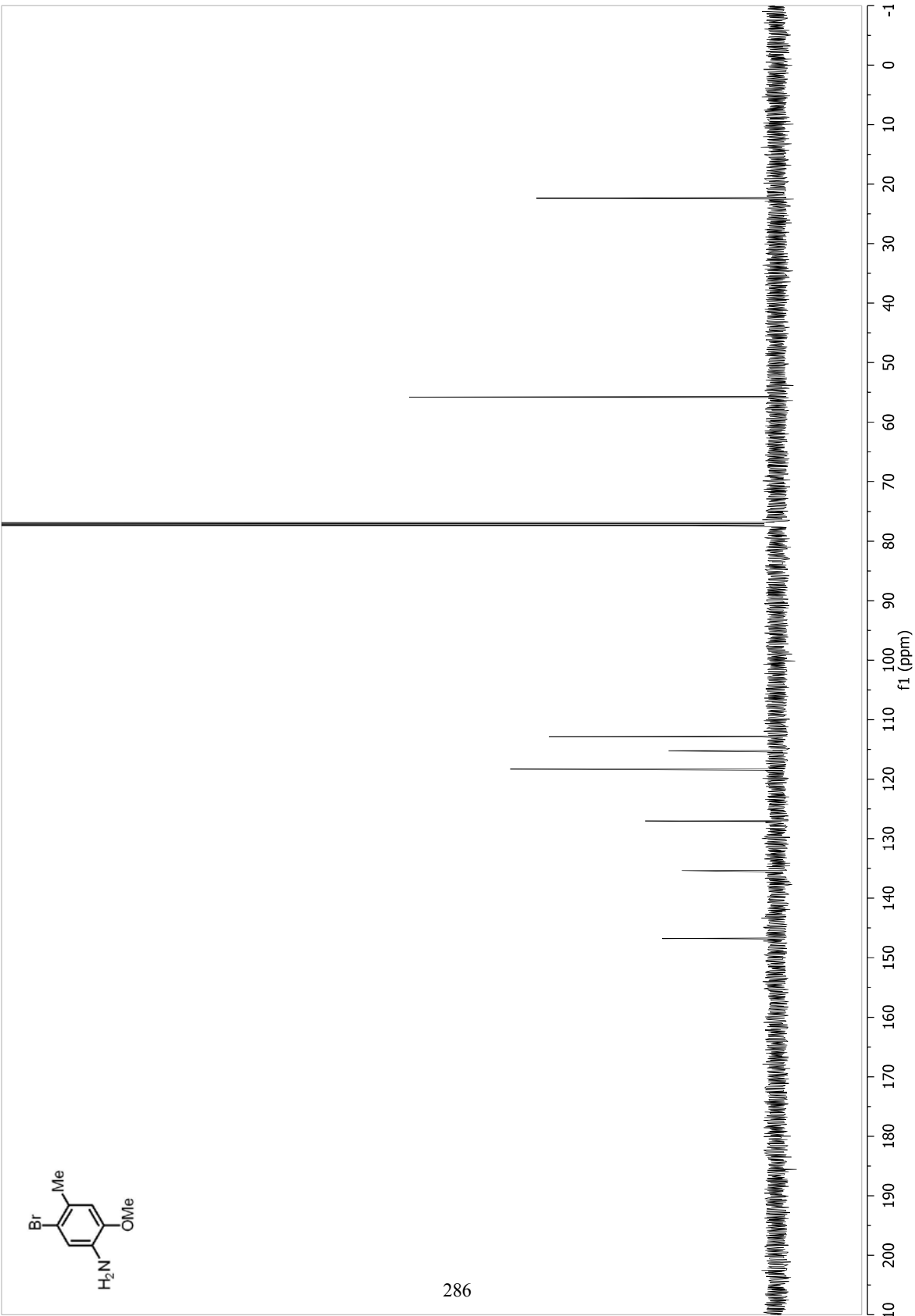


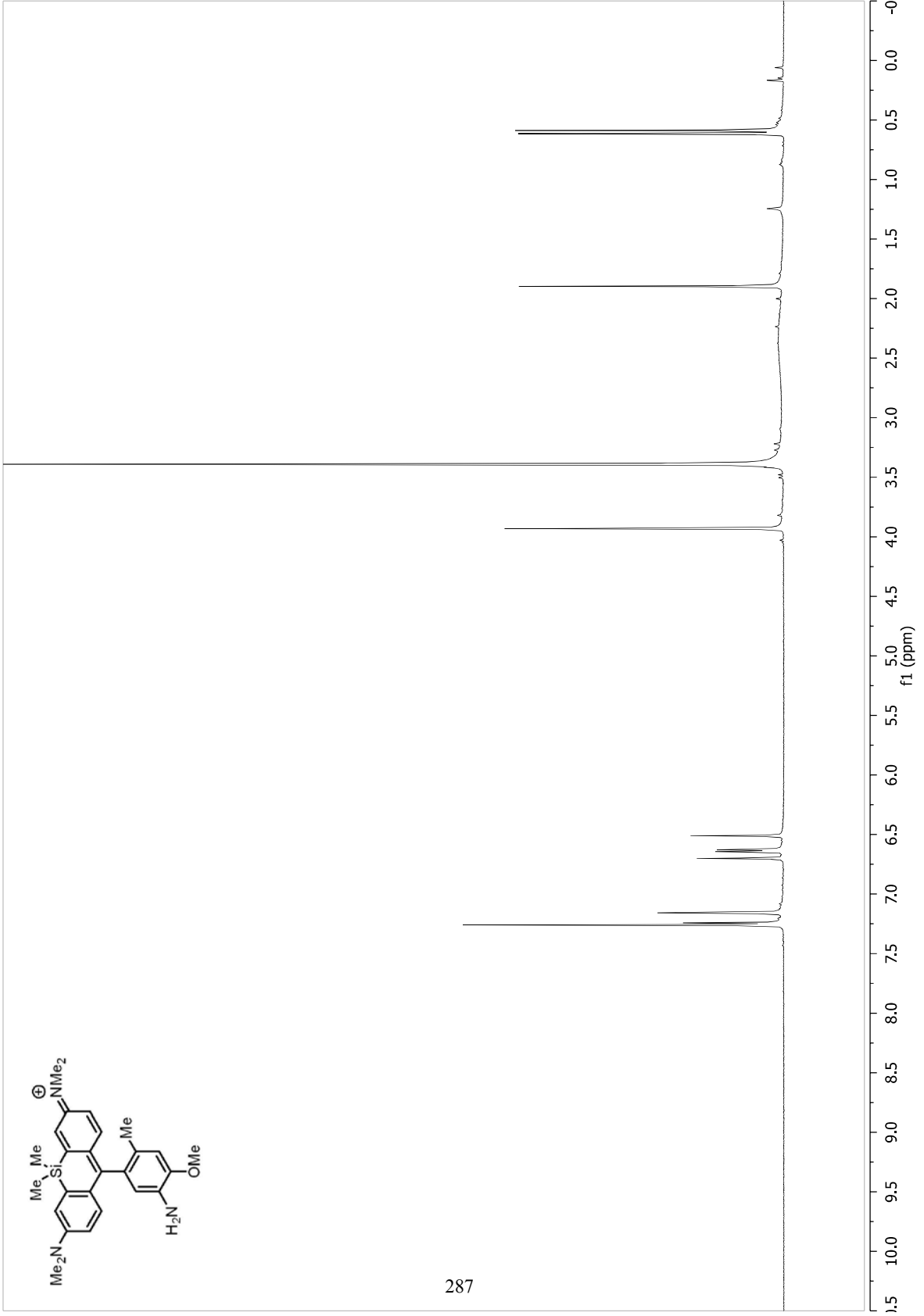


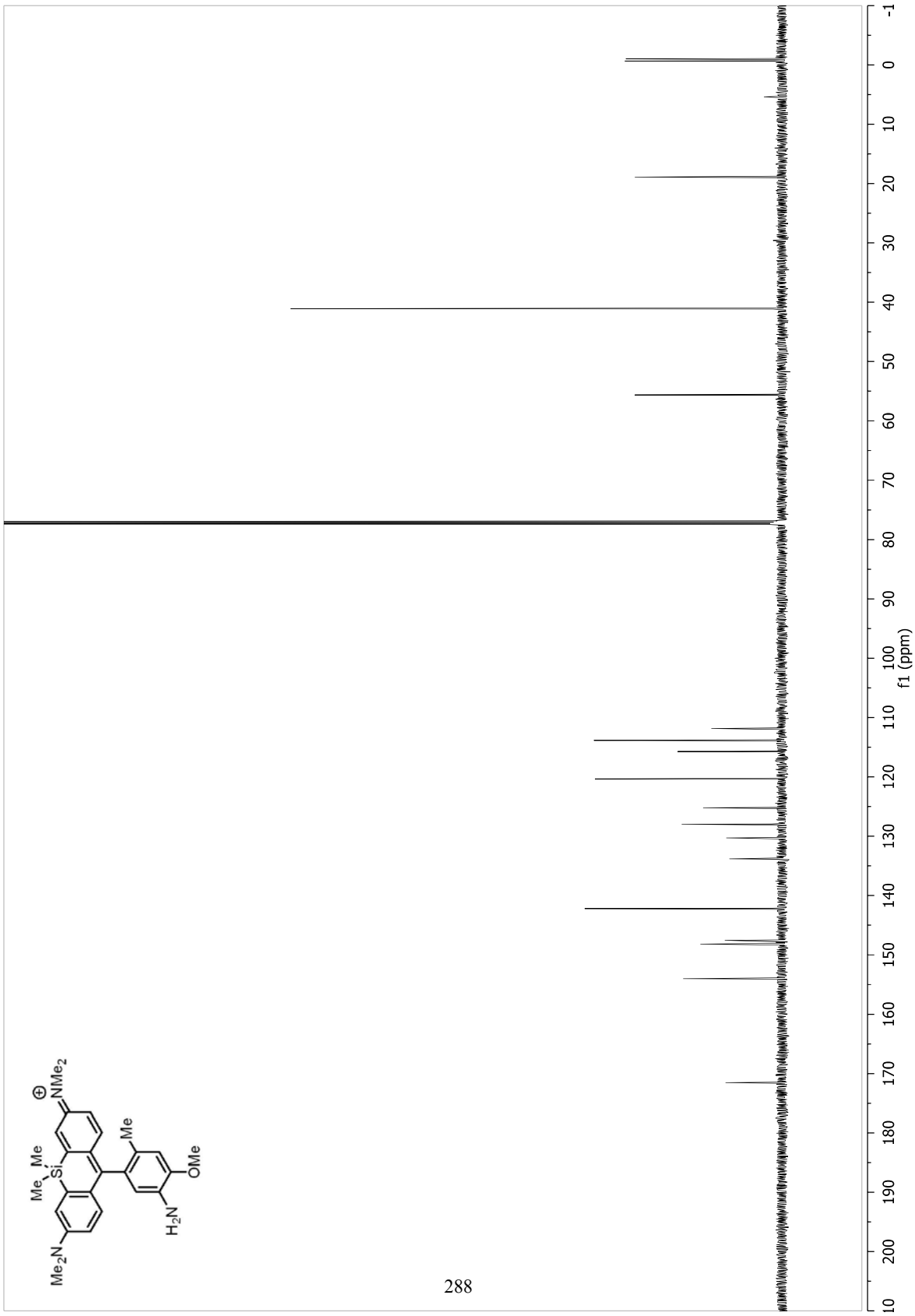


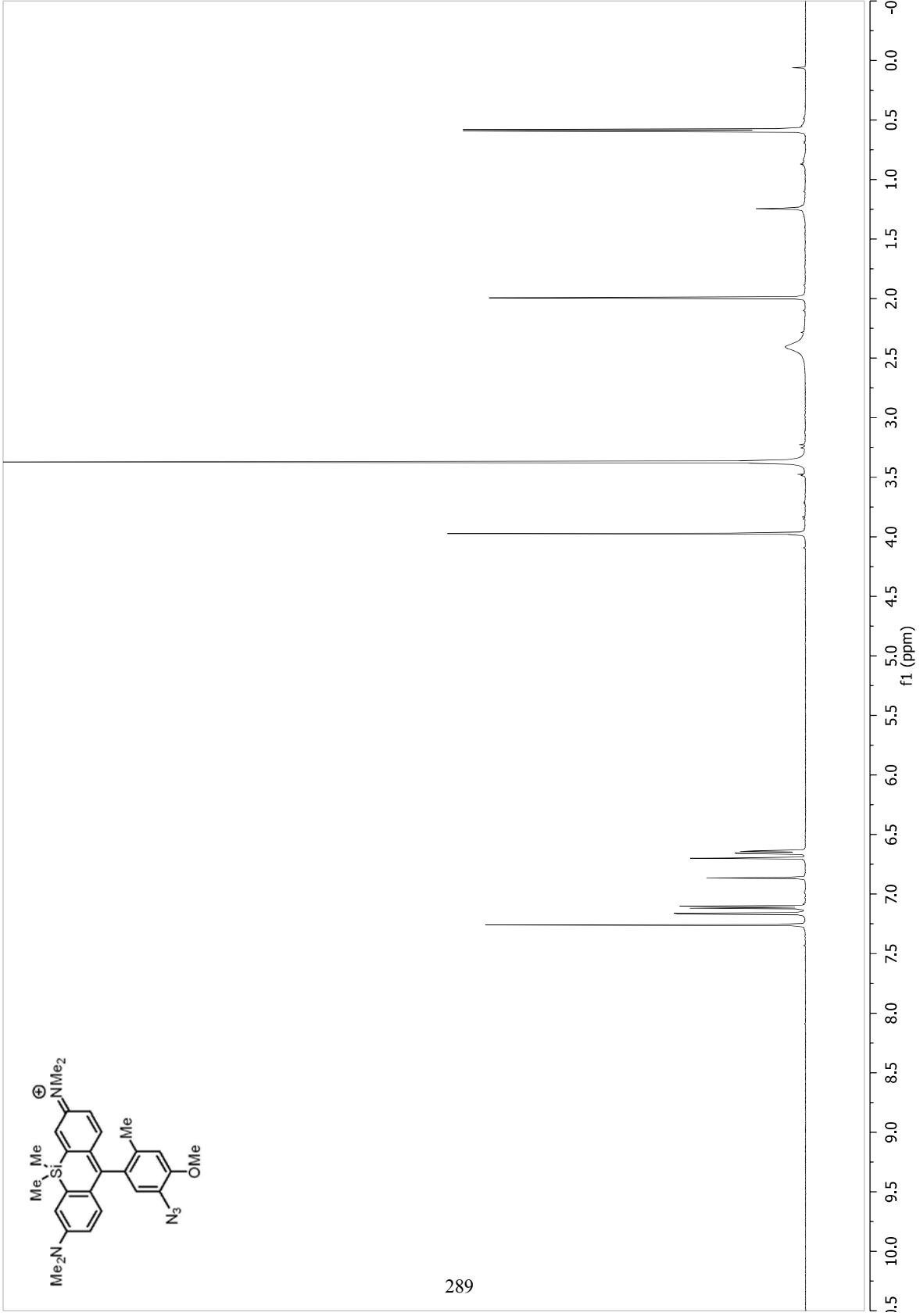
285

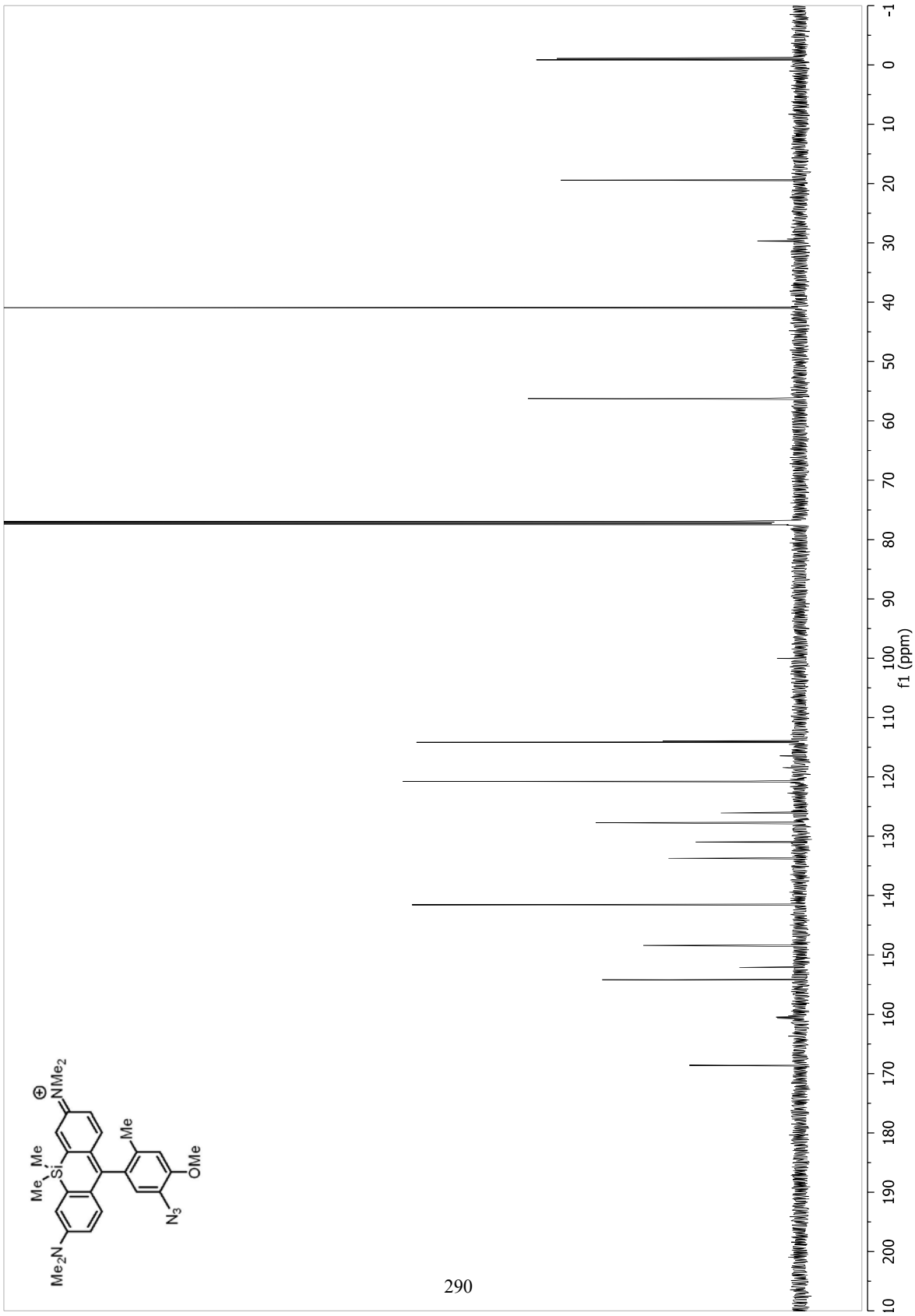


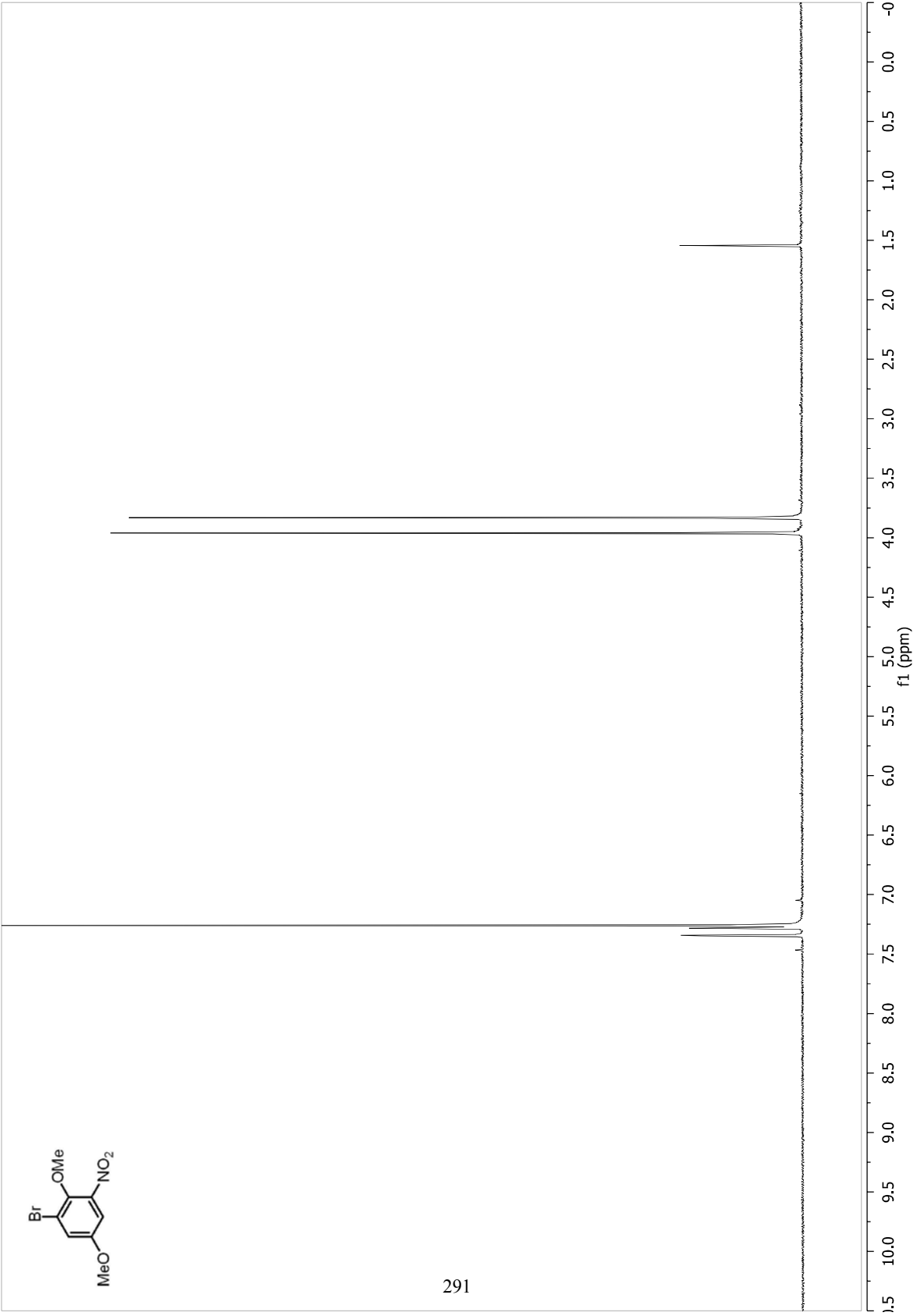


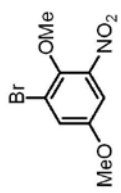




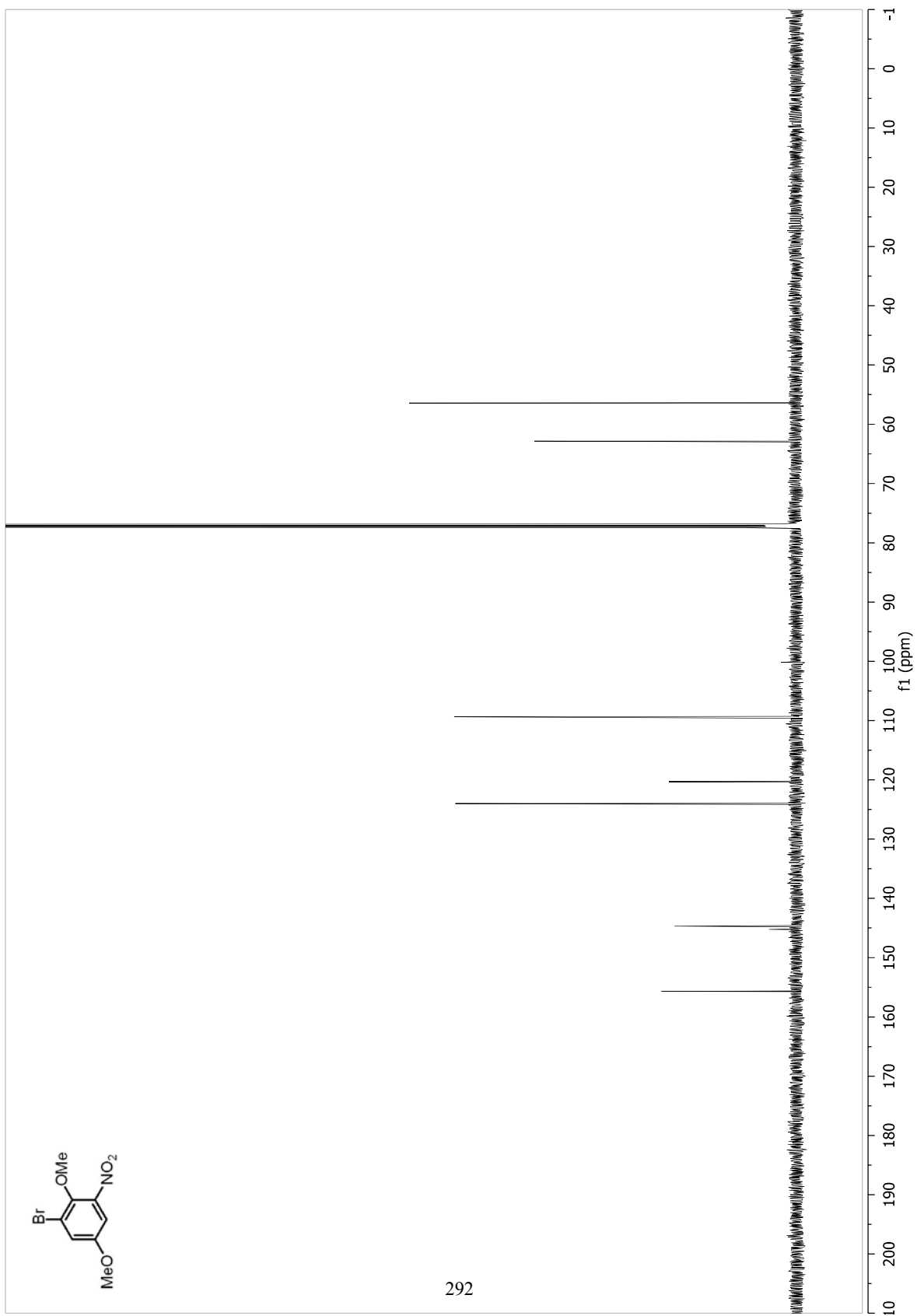


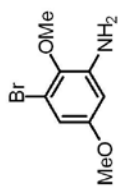




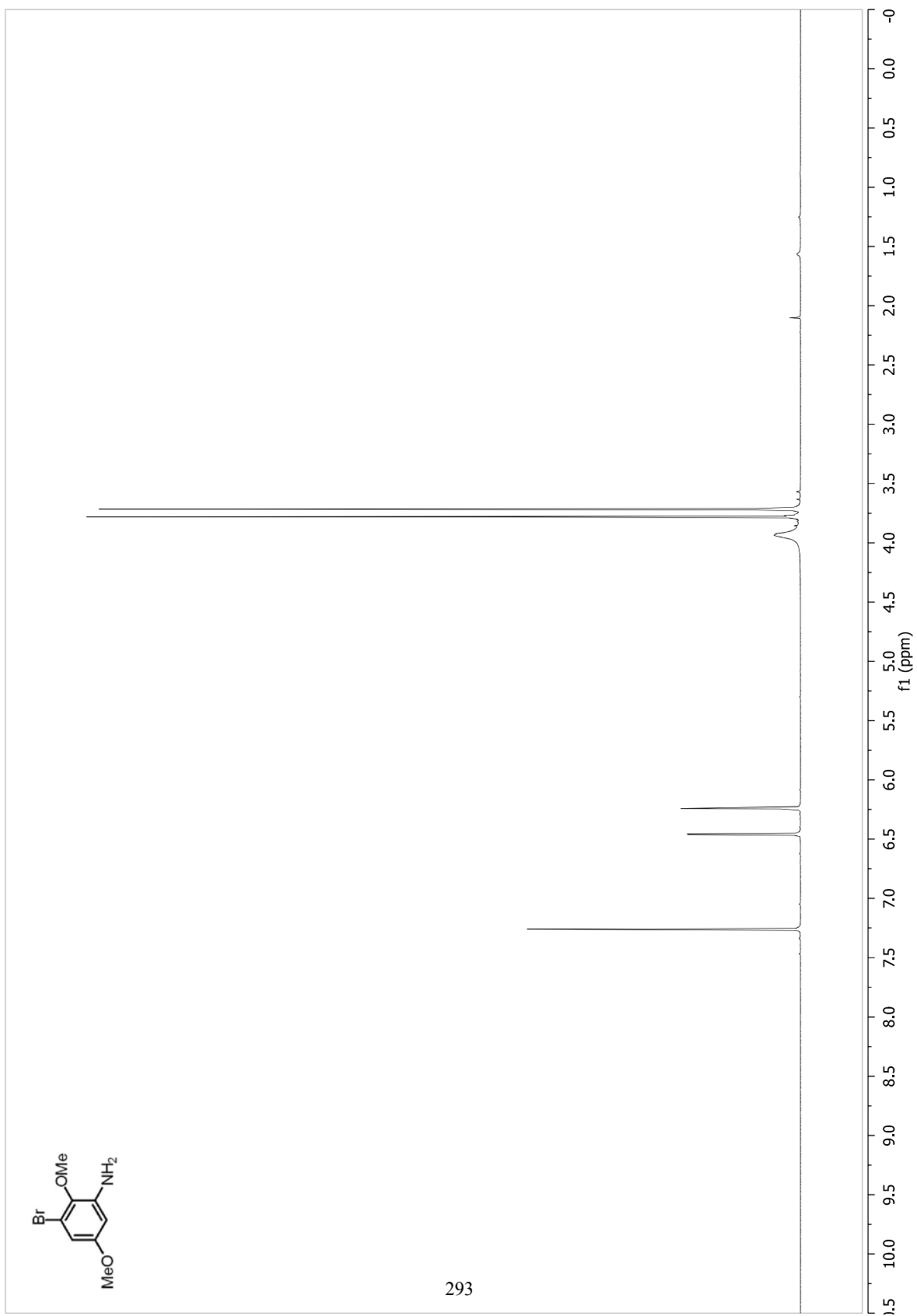


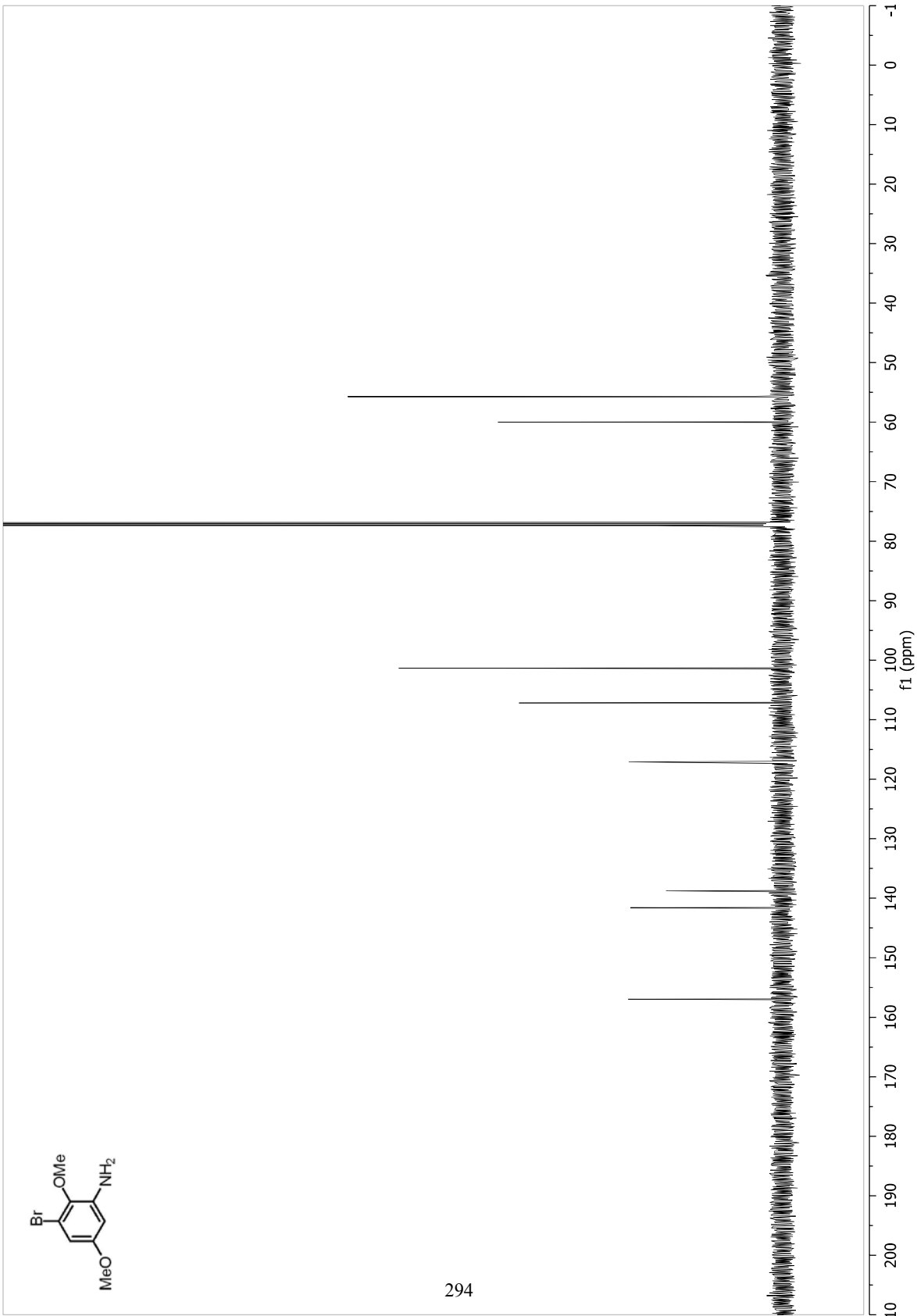
292

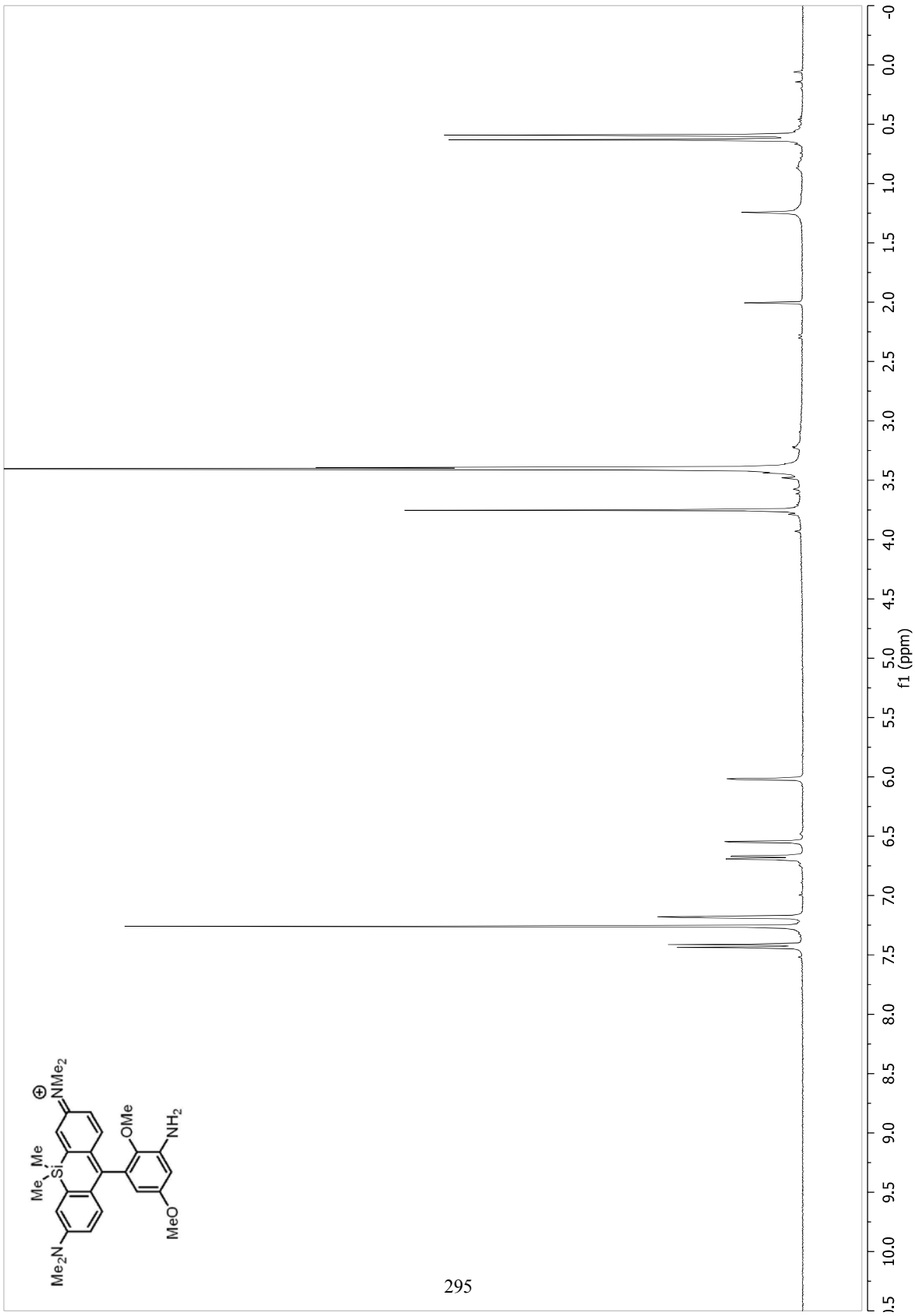


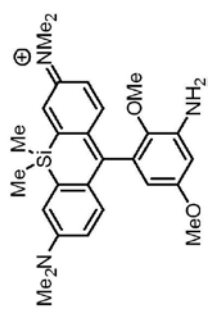


293

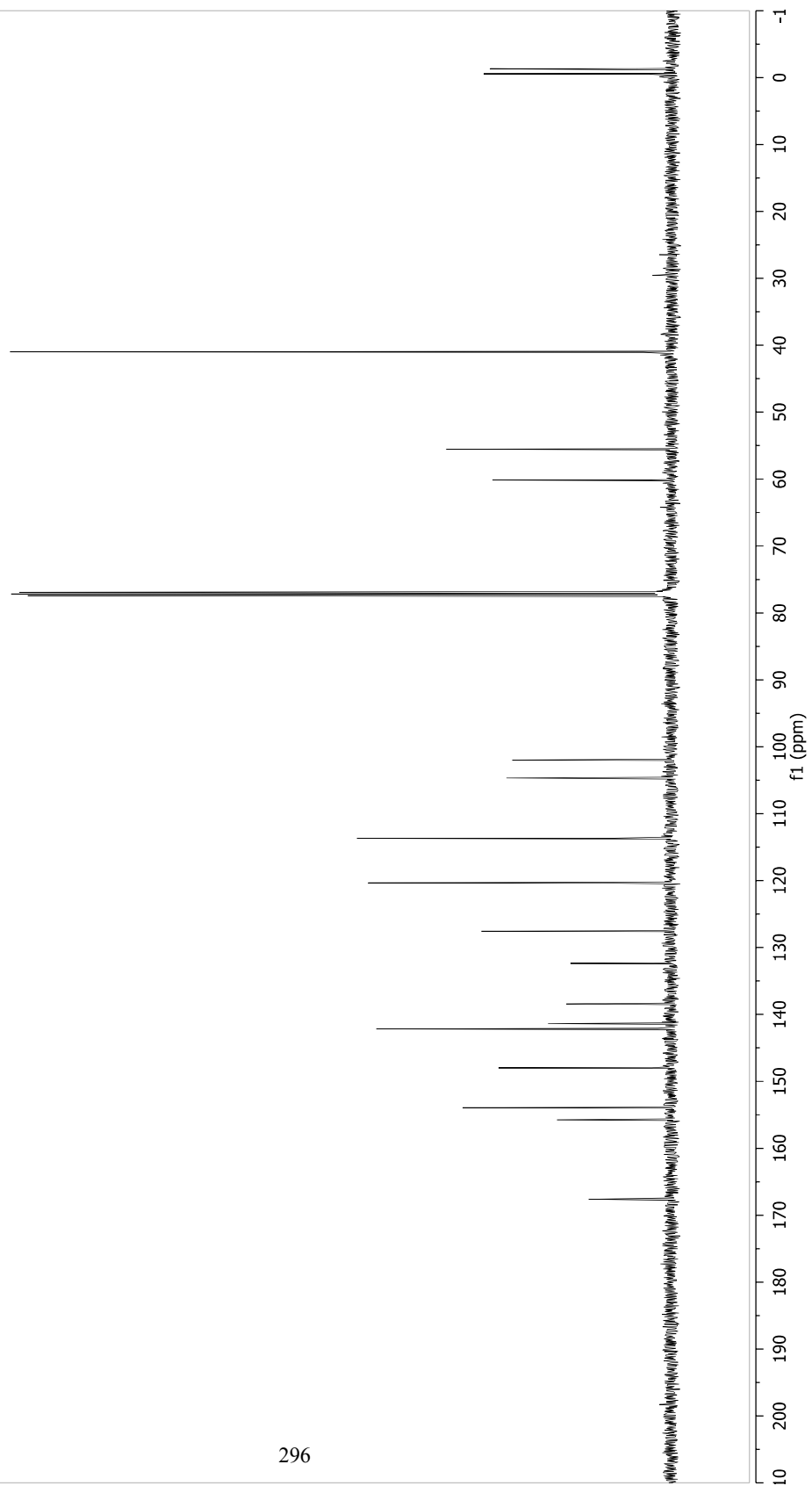


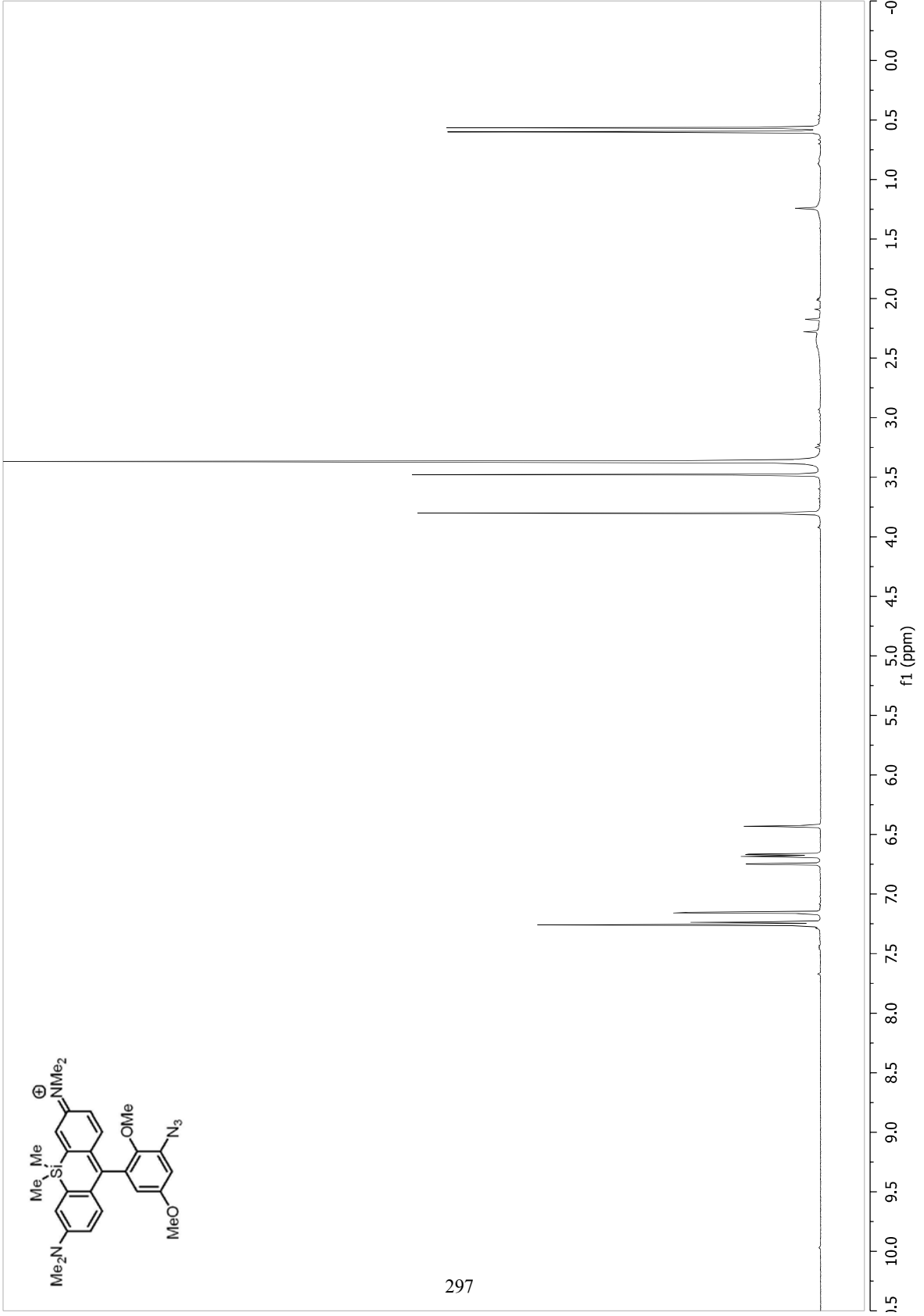


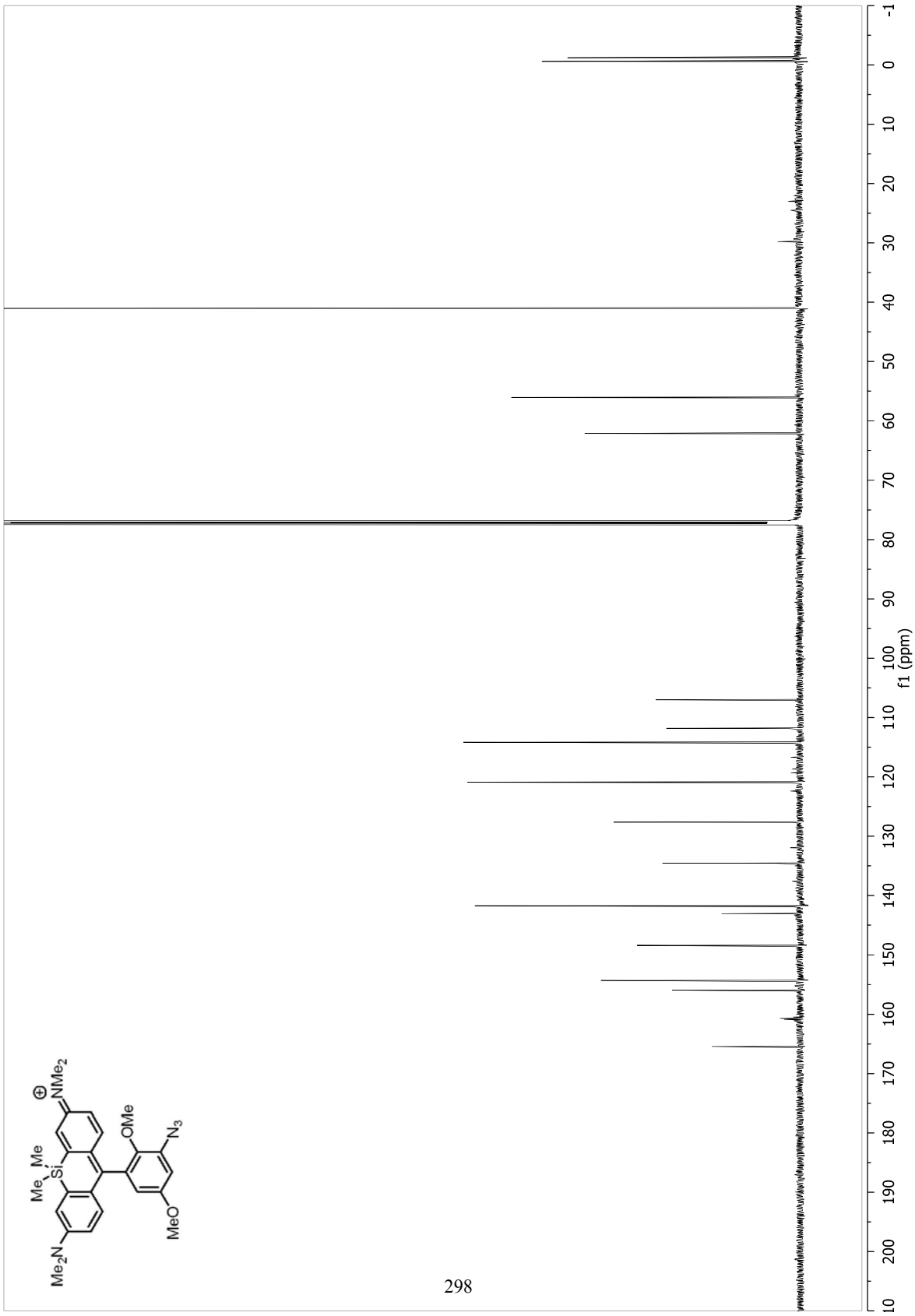


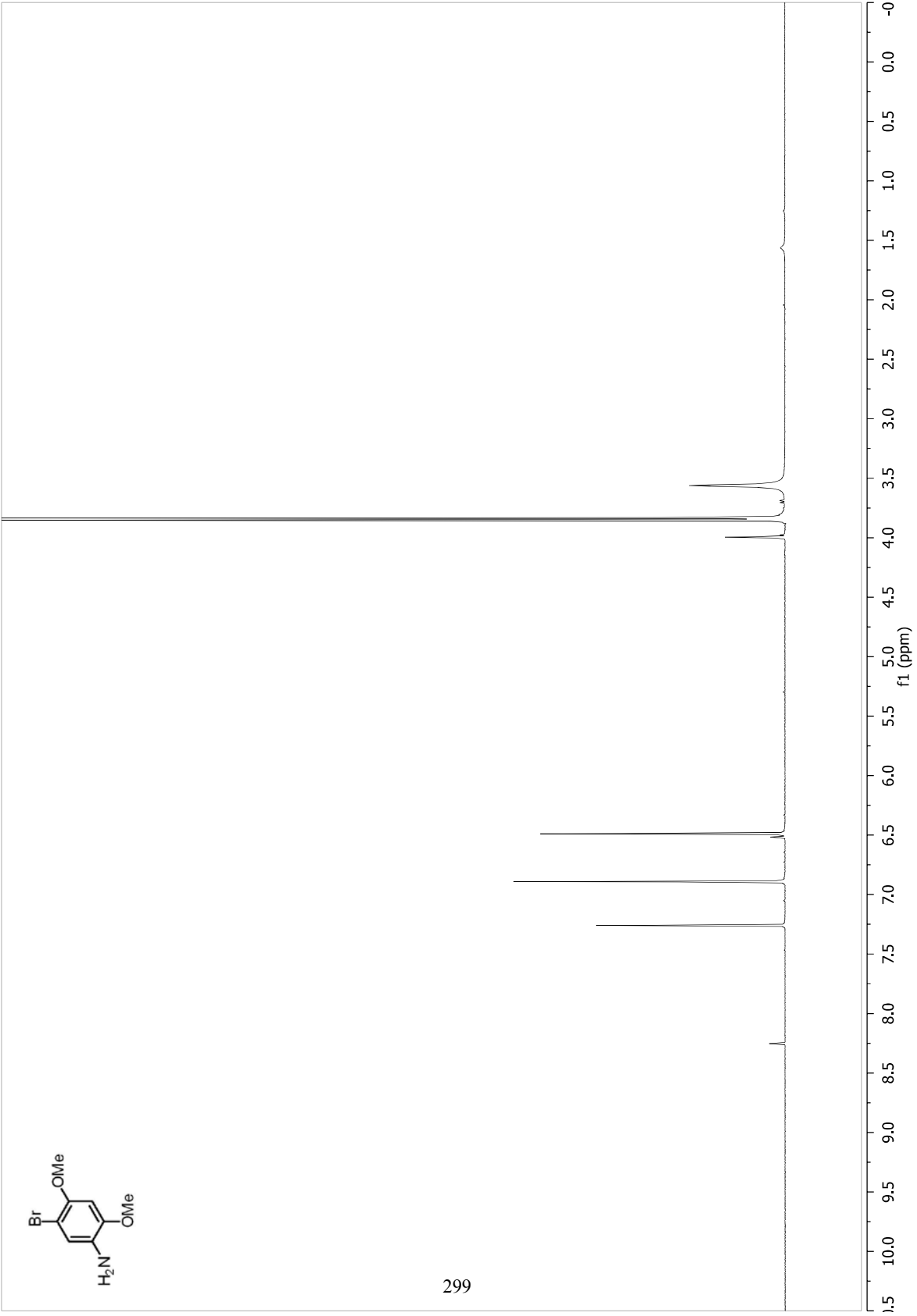


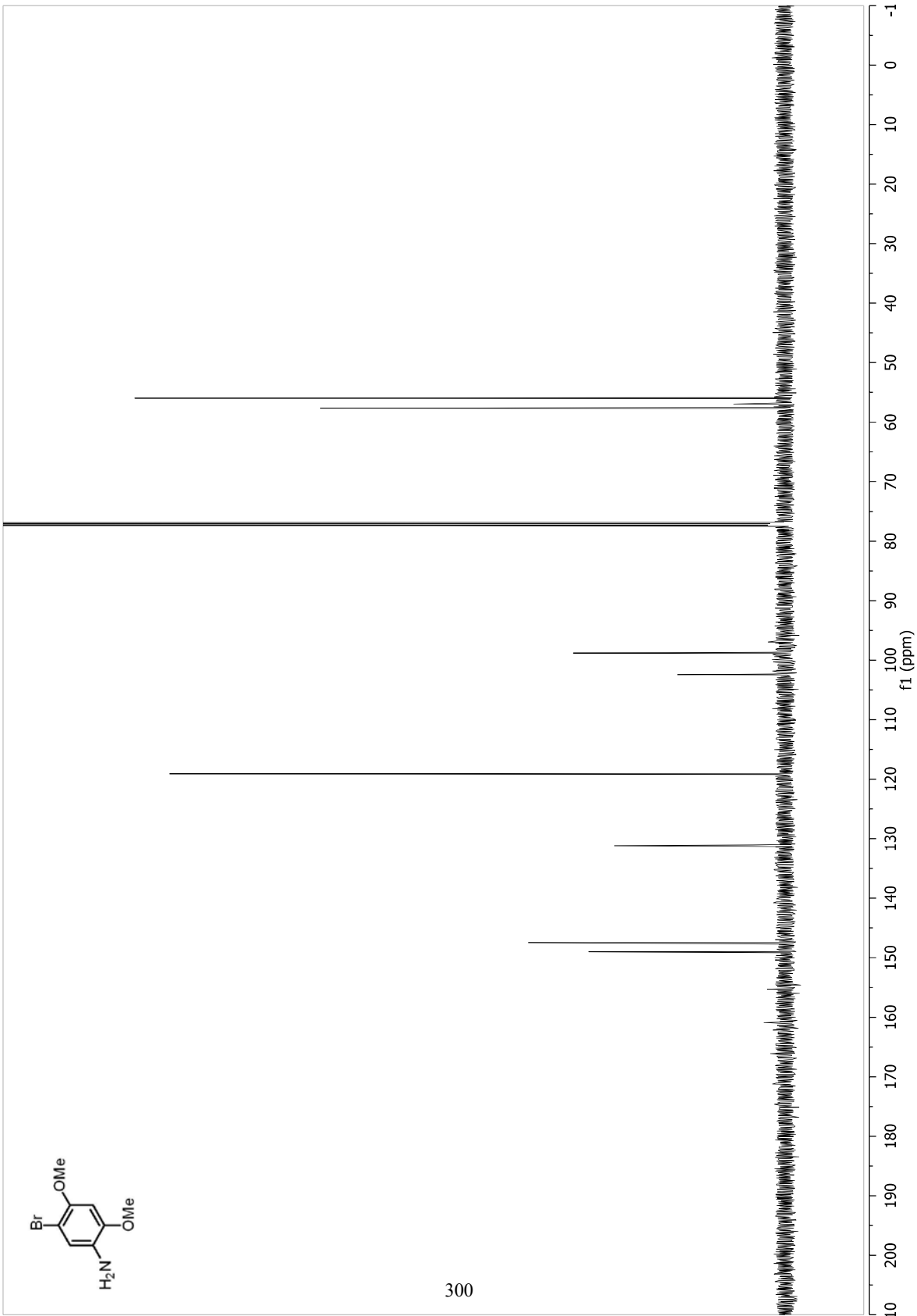
296

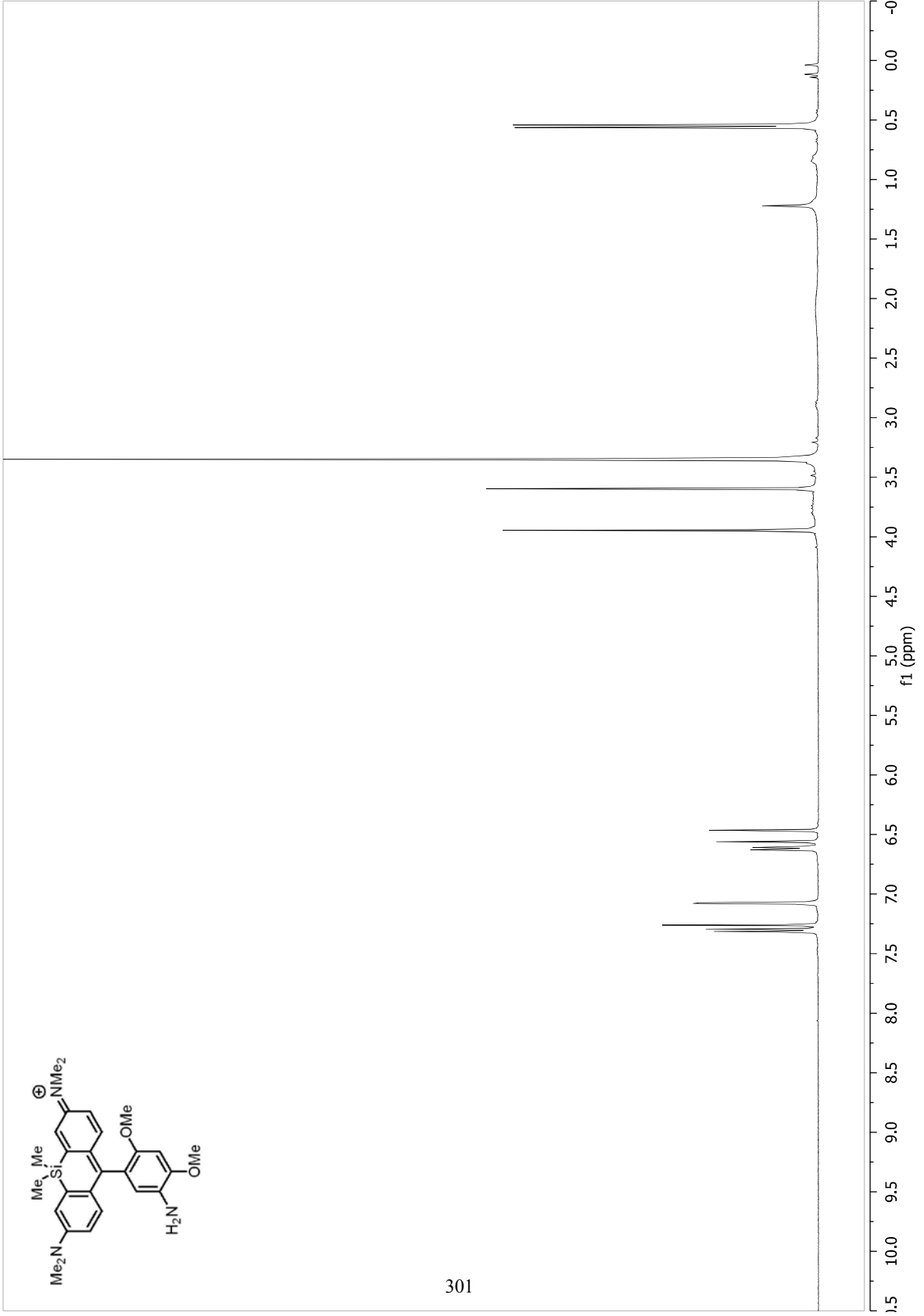


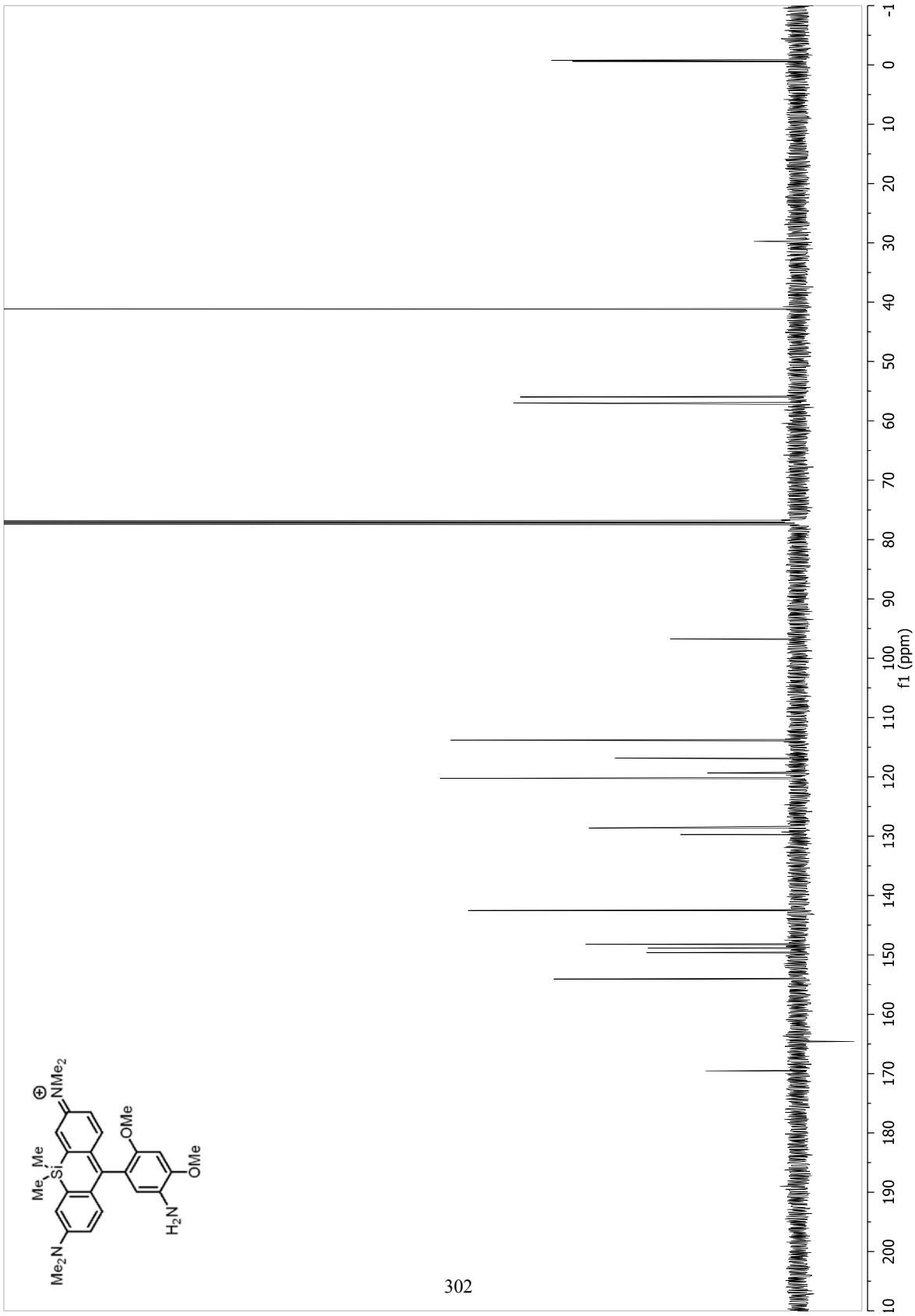


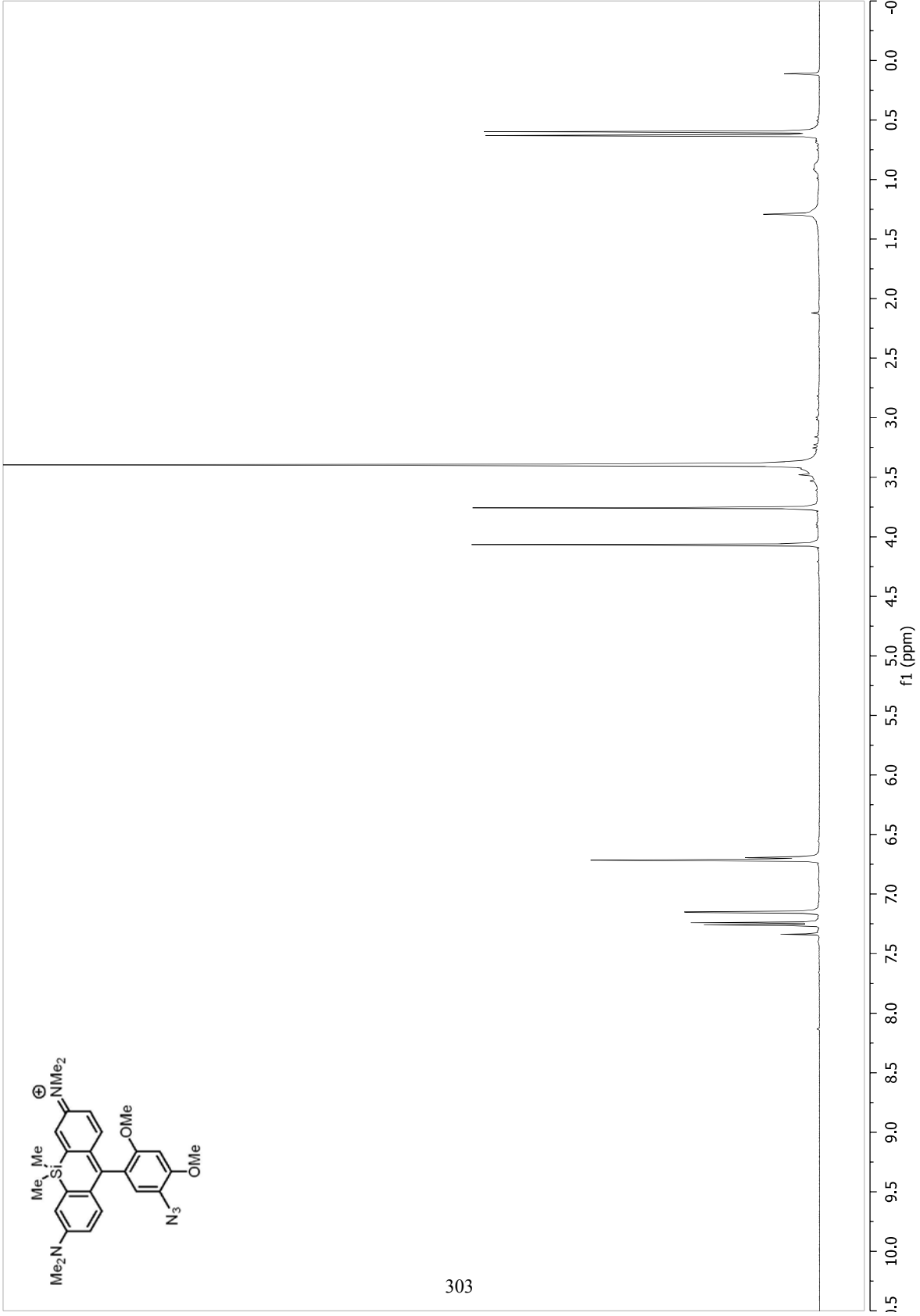


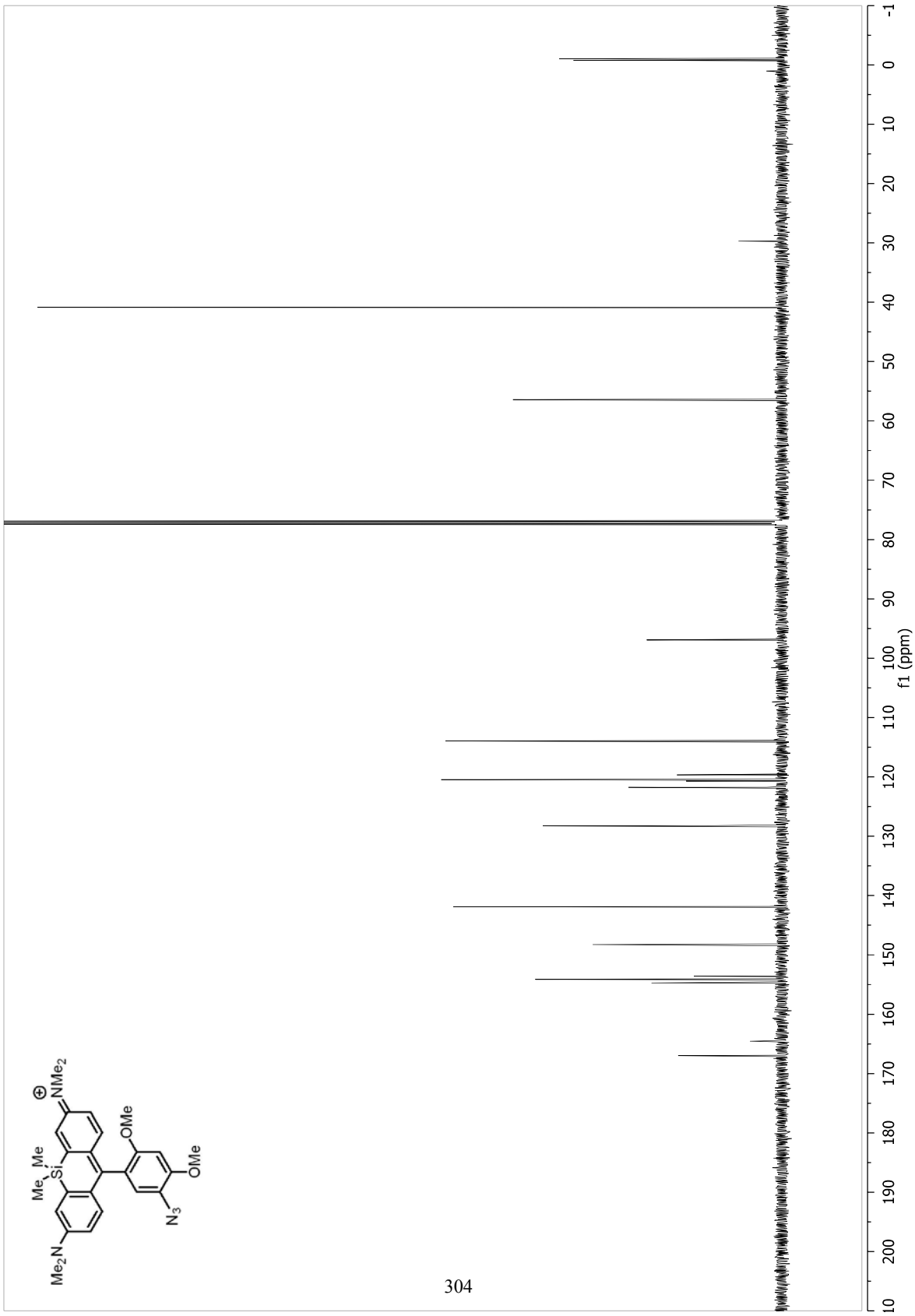


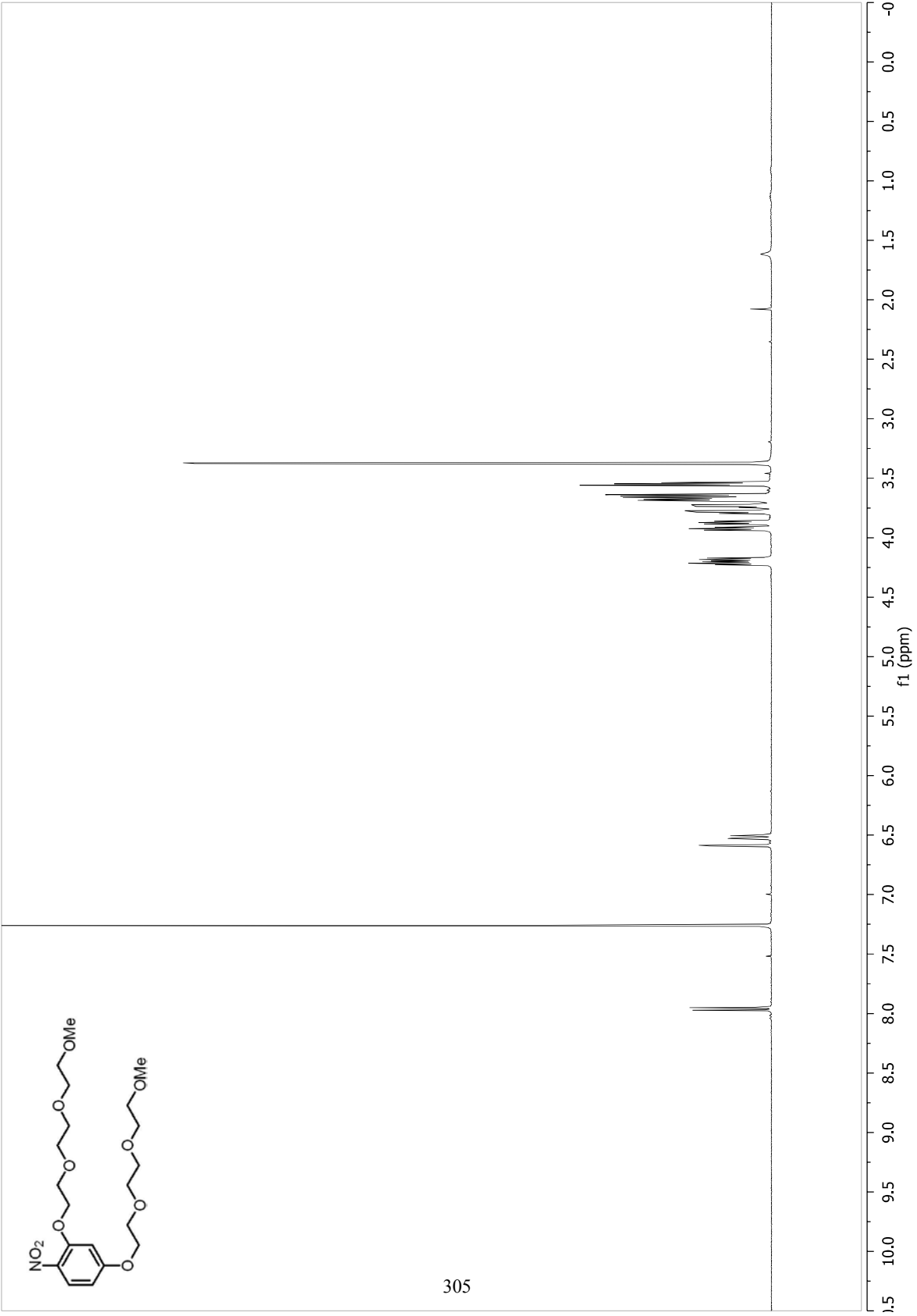


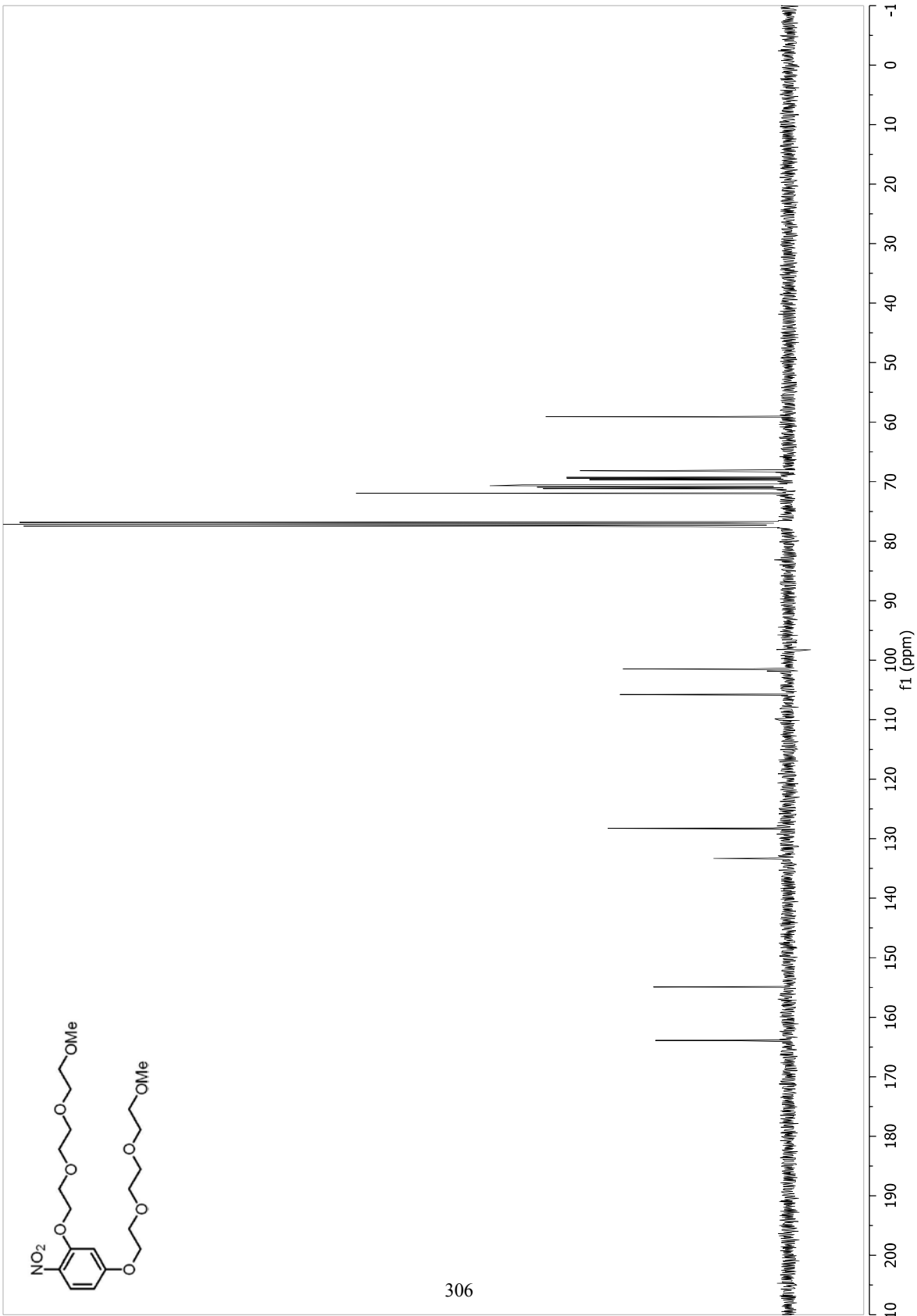


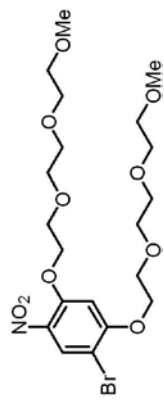




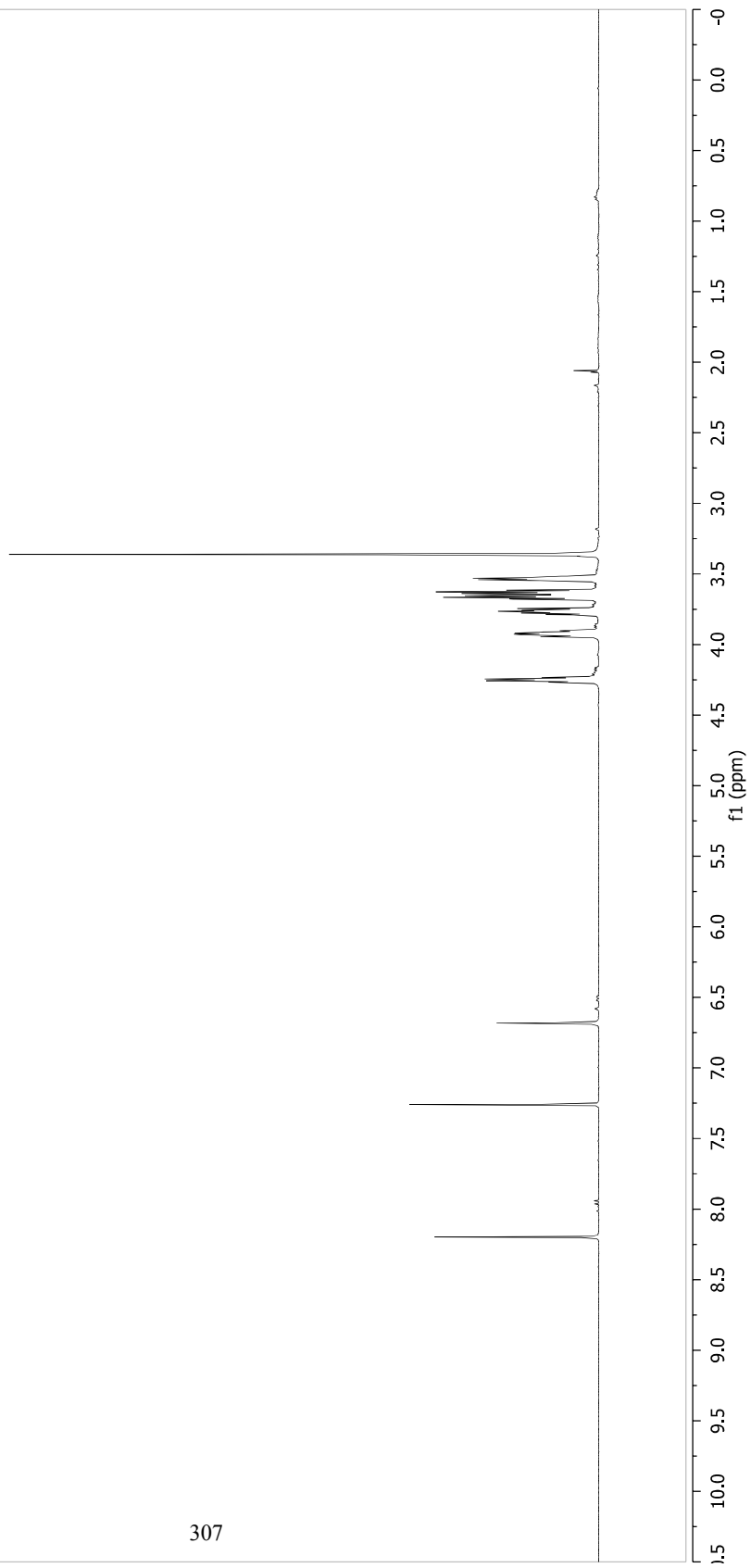


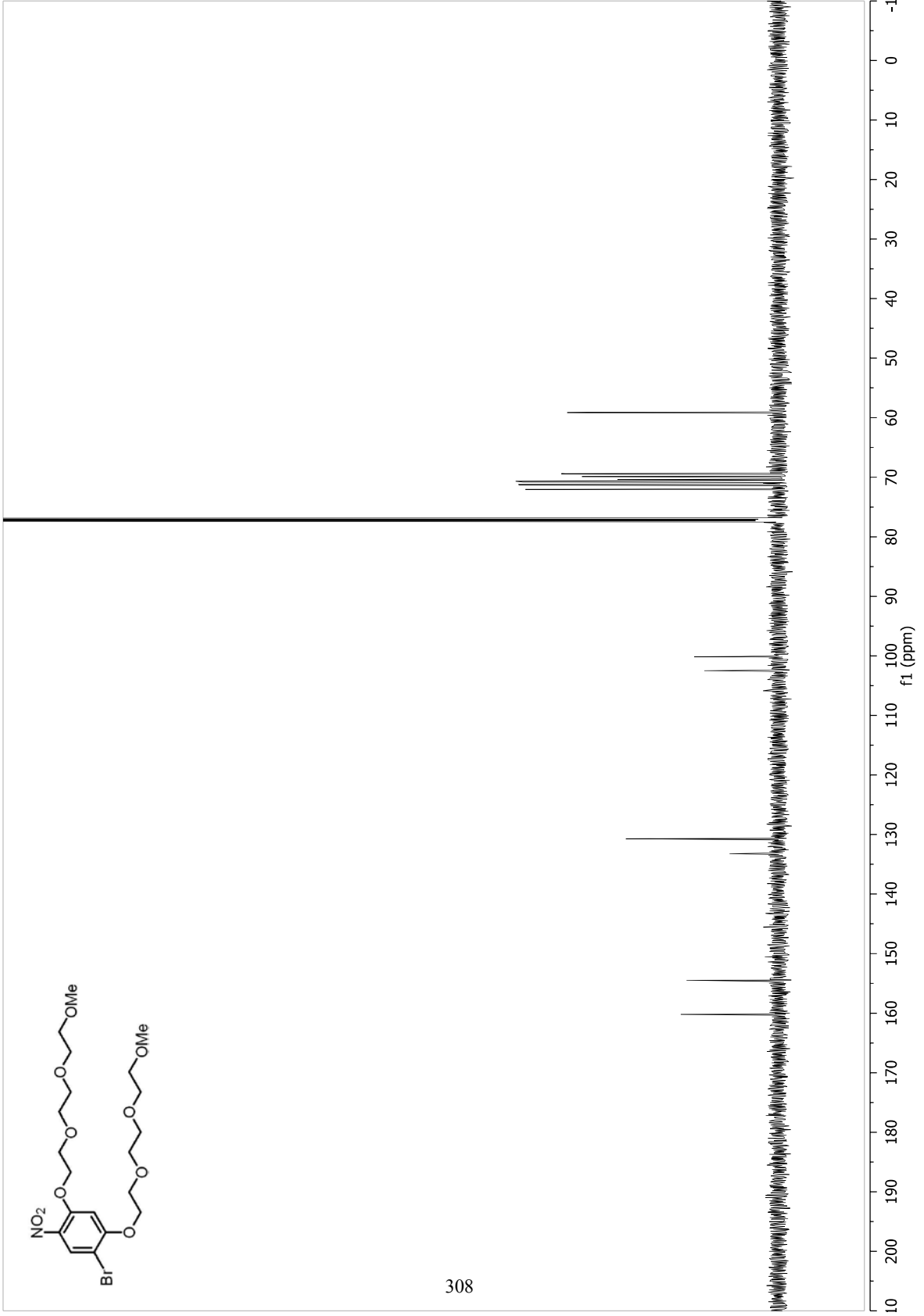


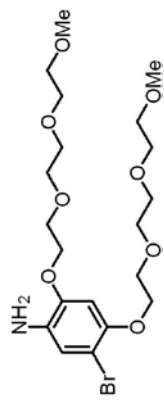




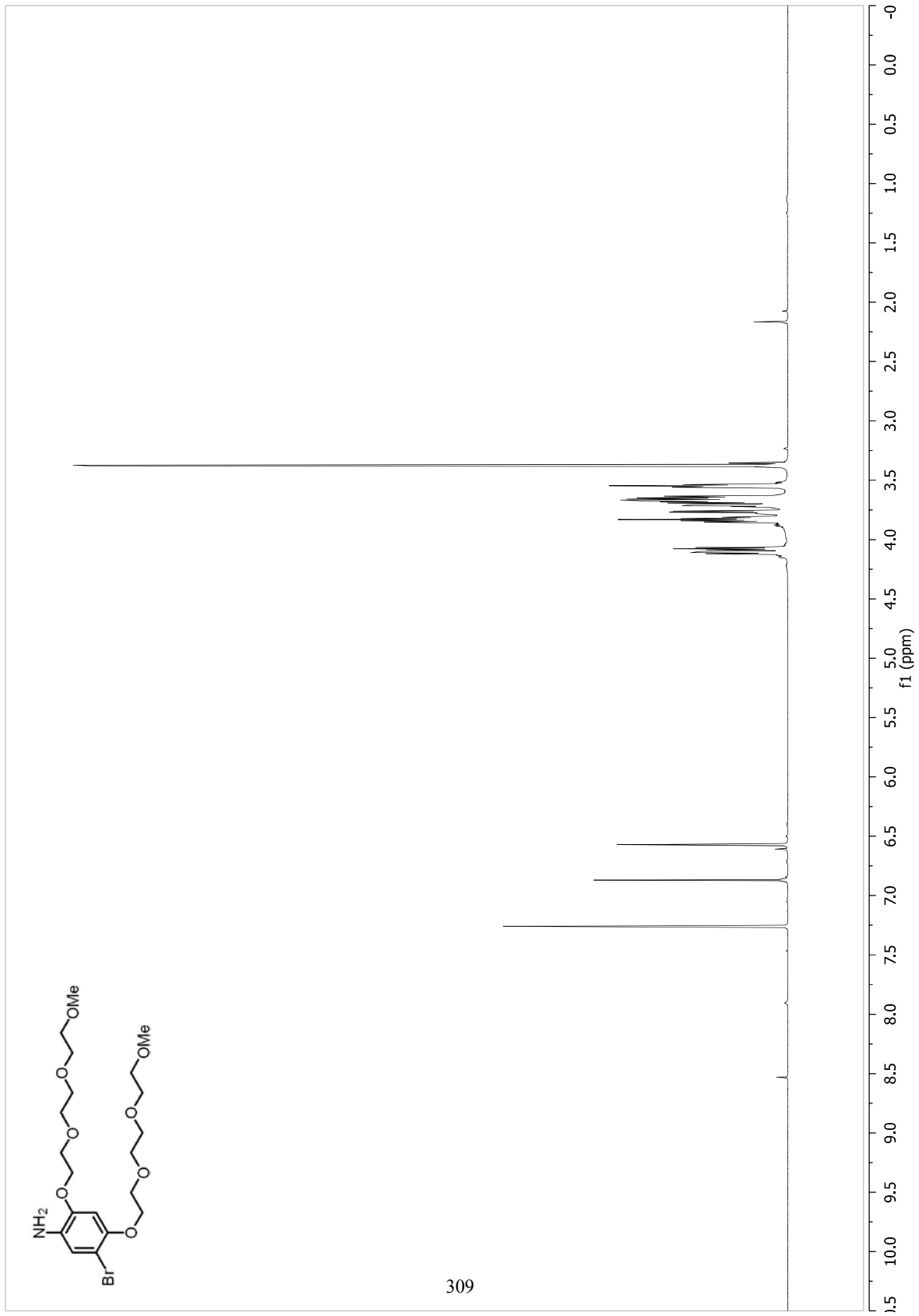
307

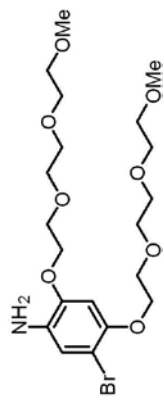




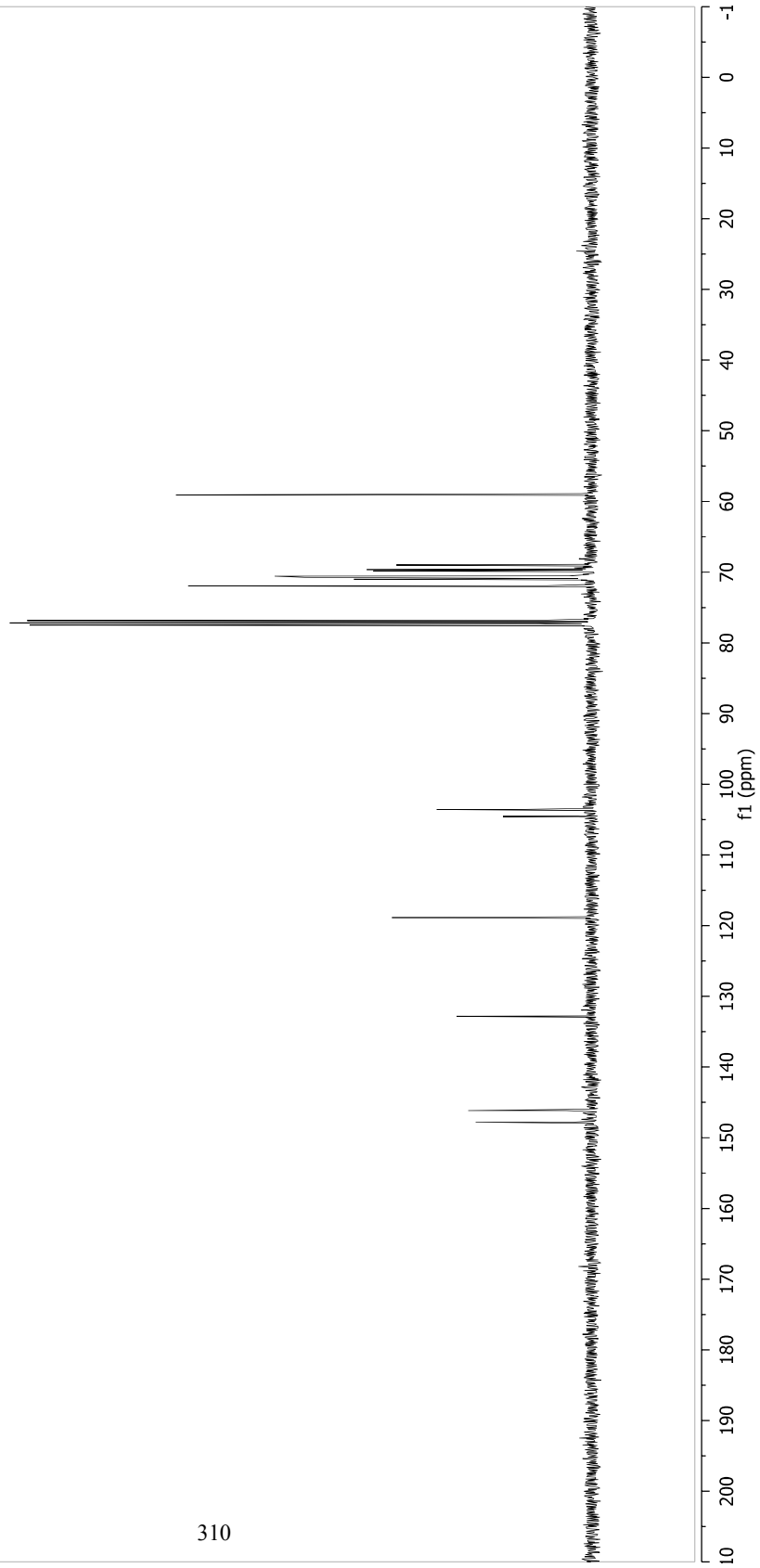


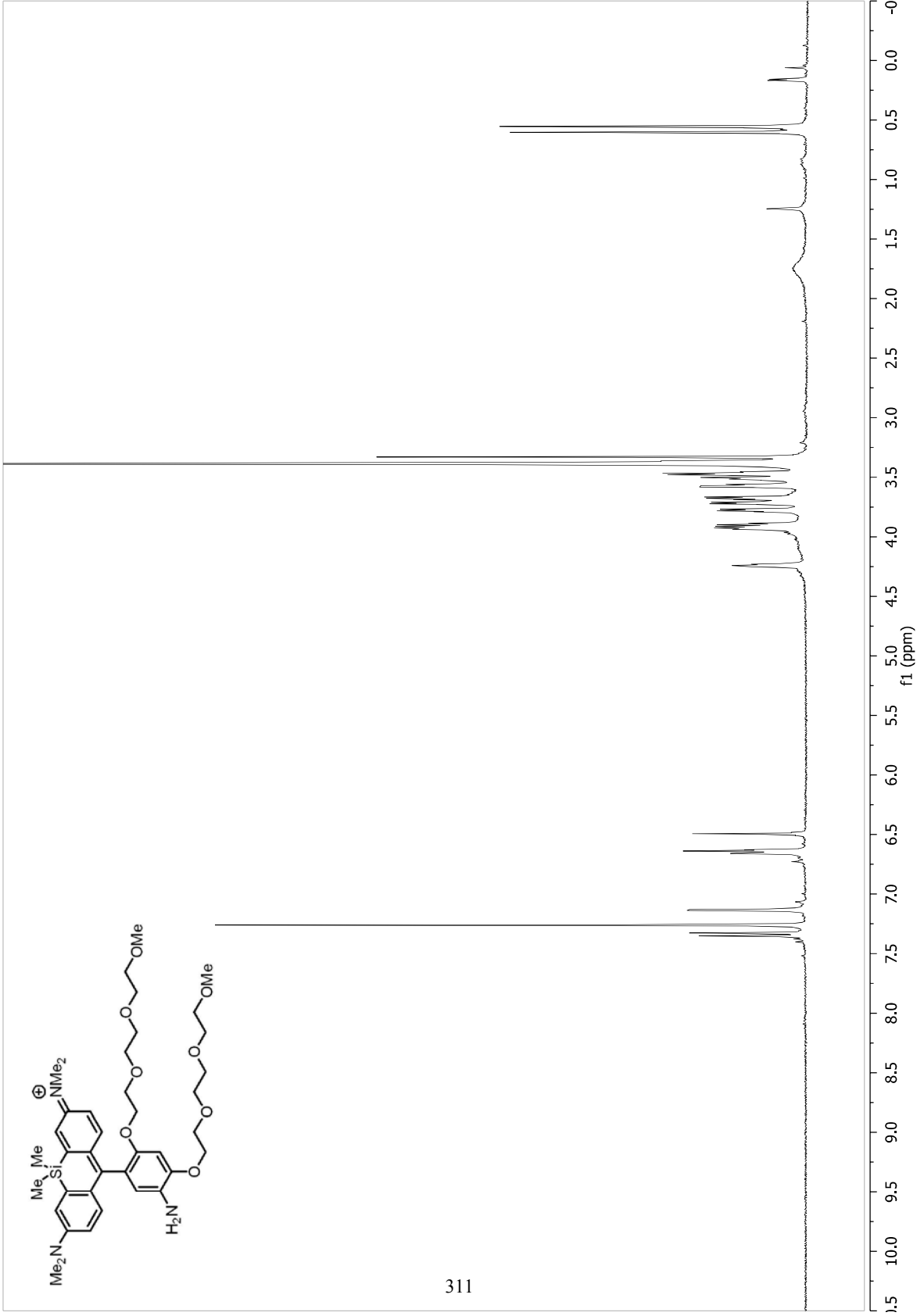
309

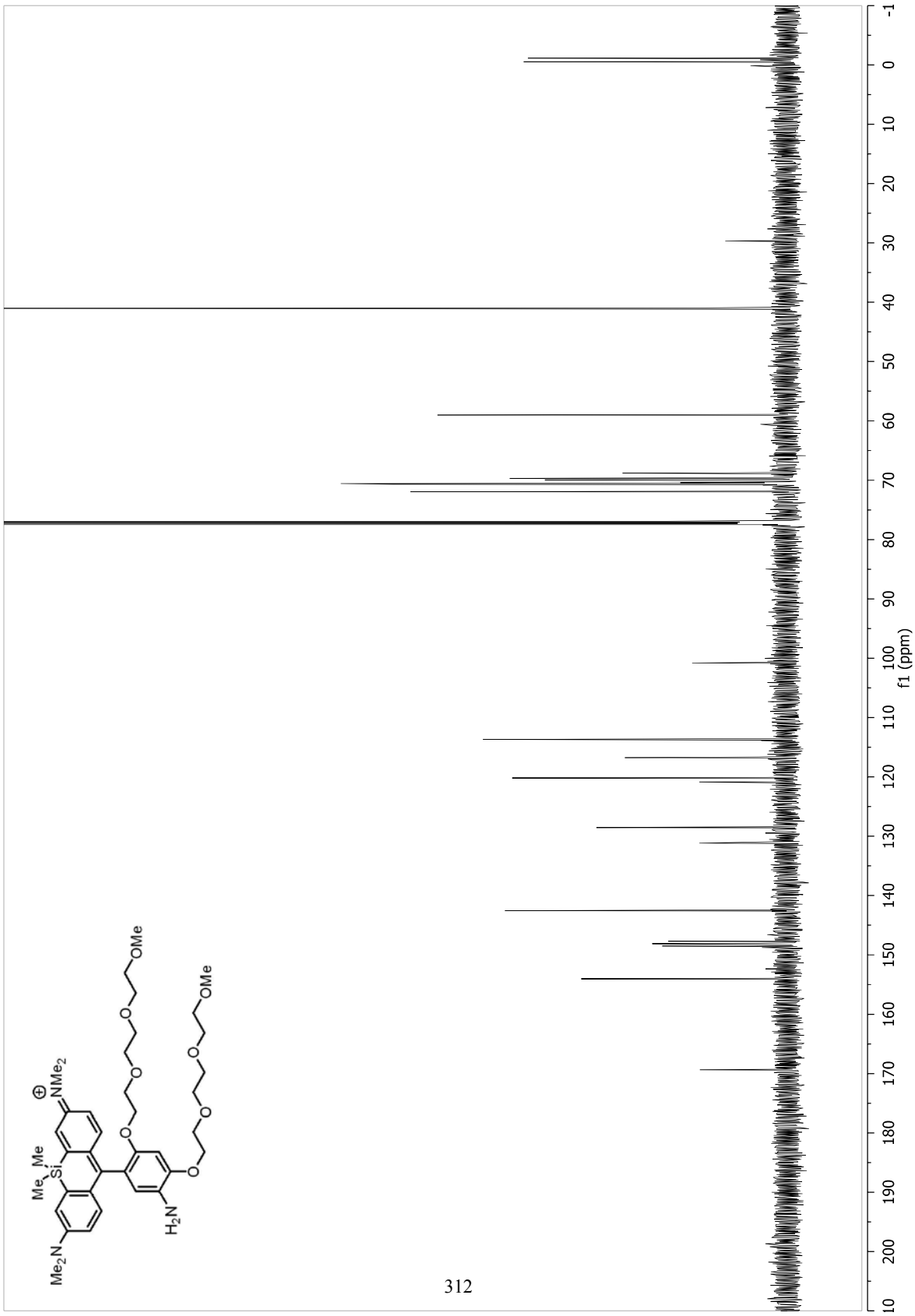


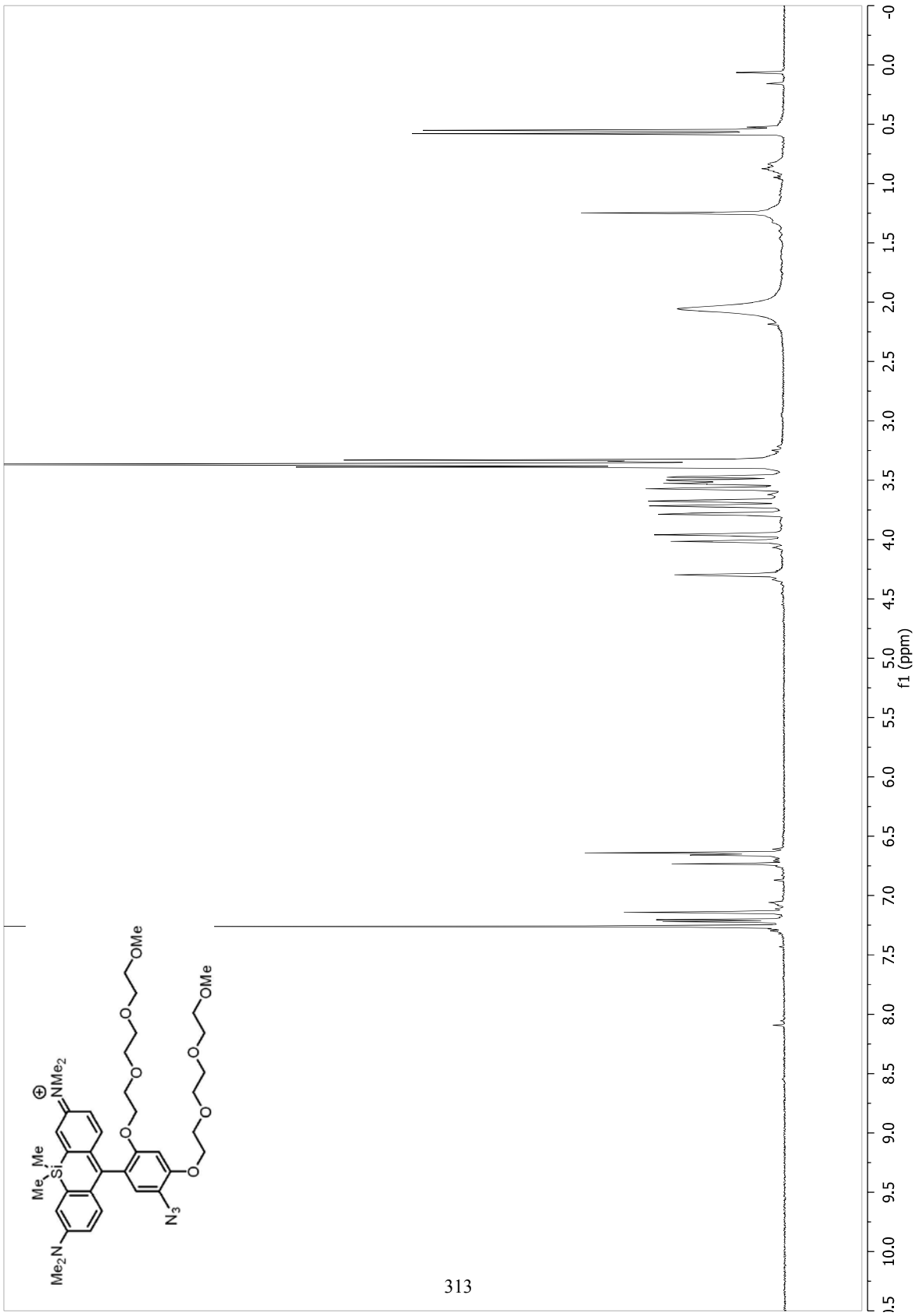


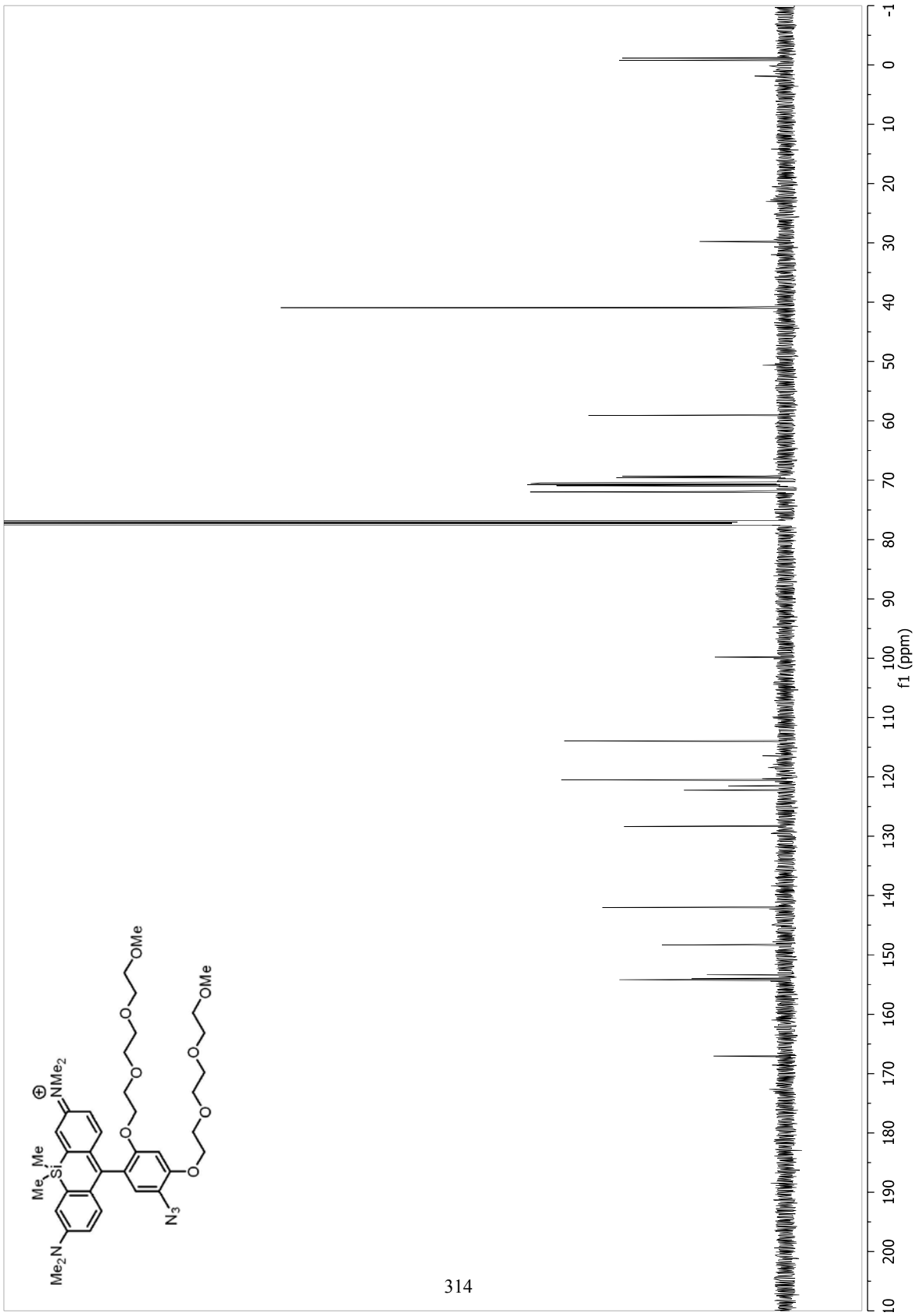
310

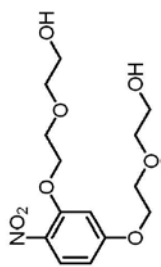




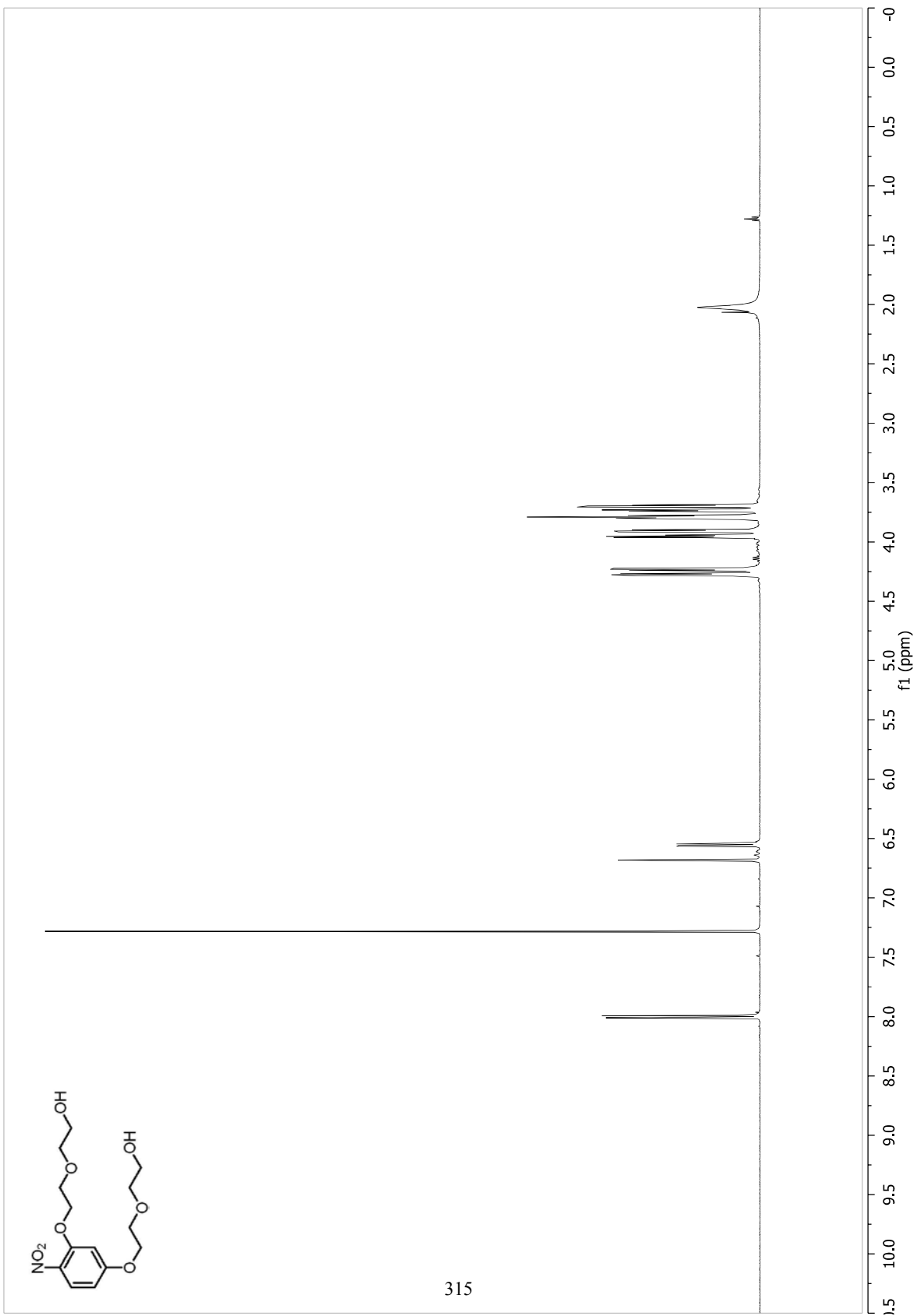


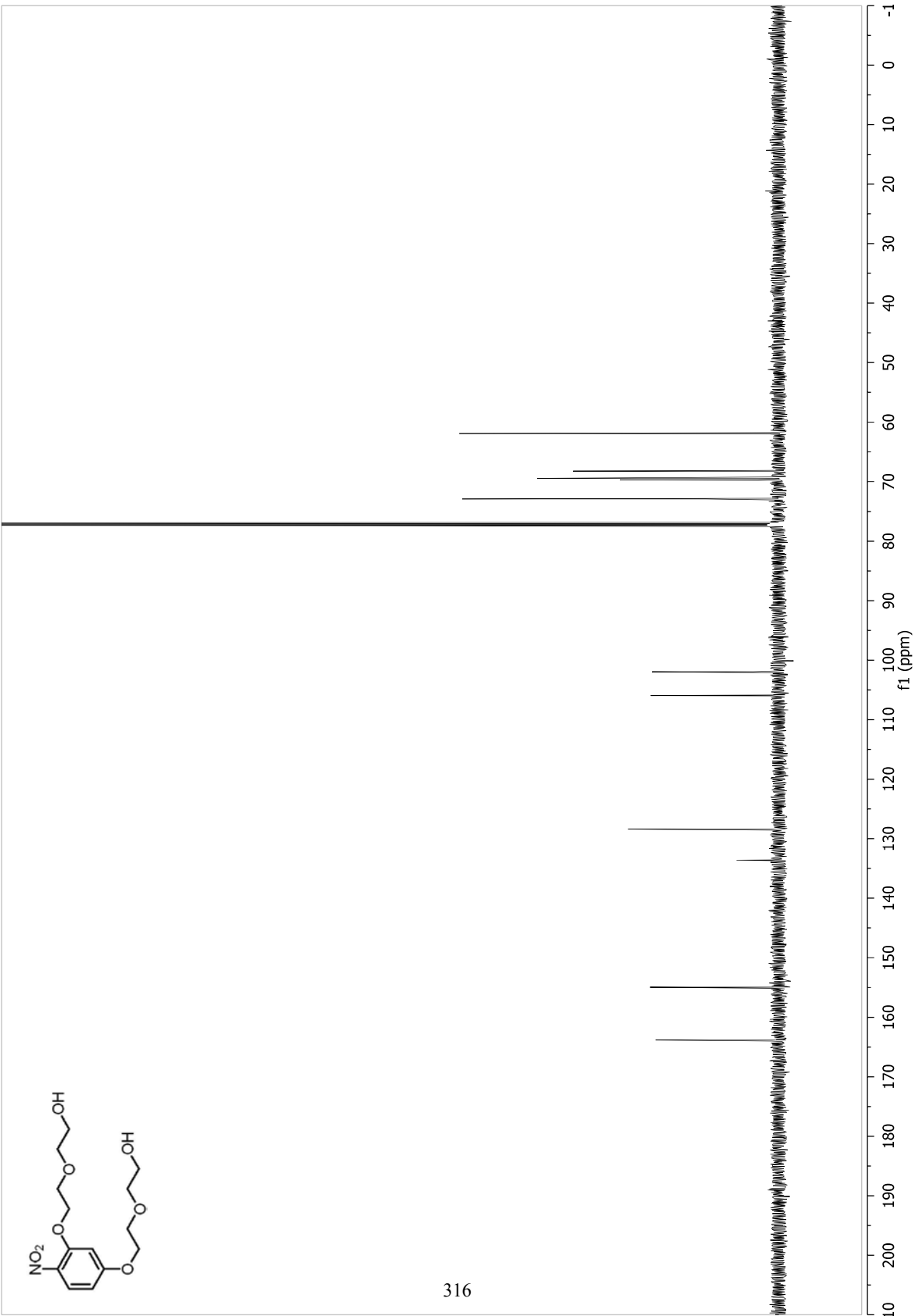


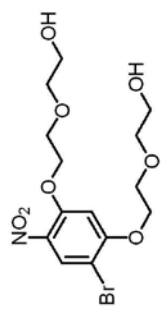




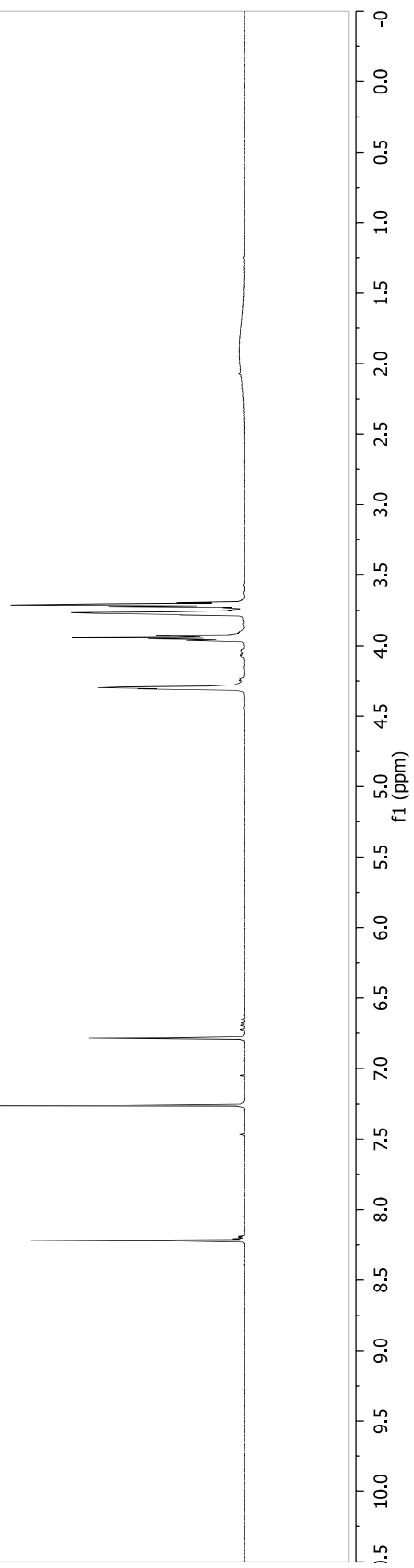
315

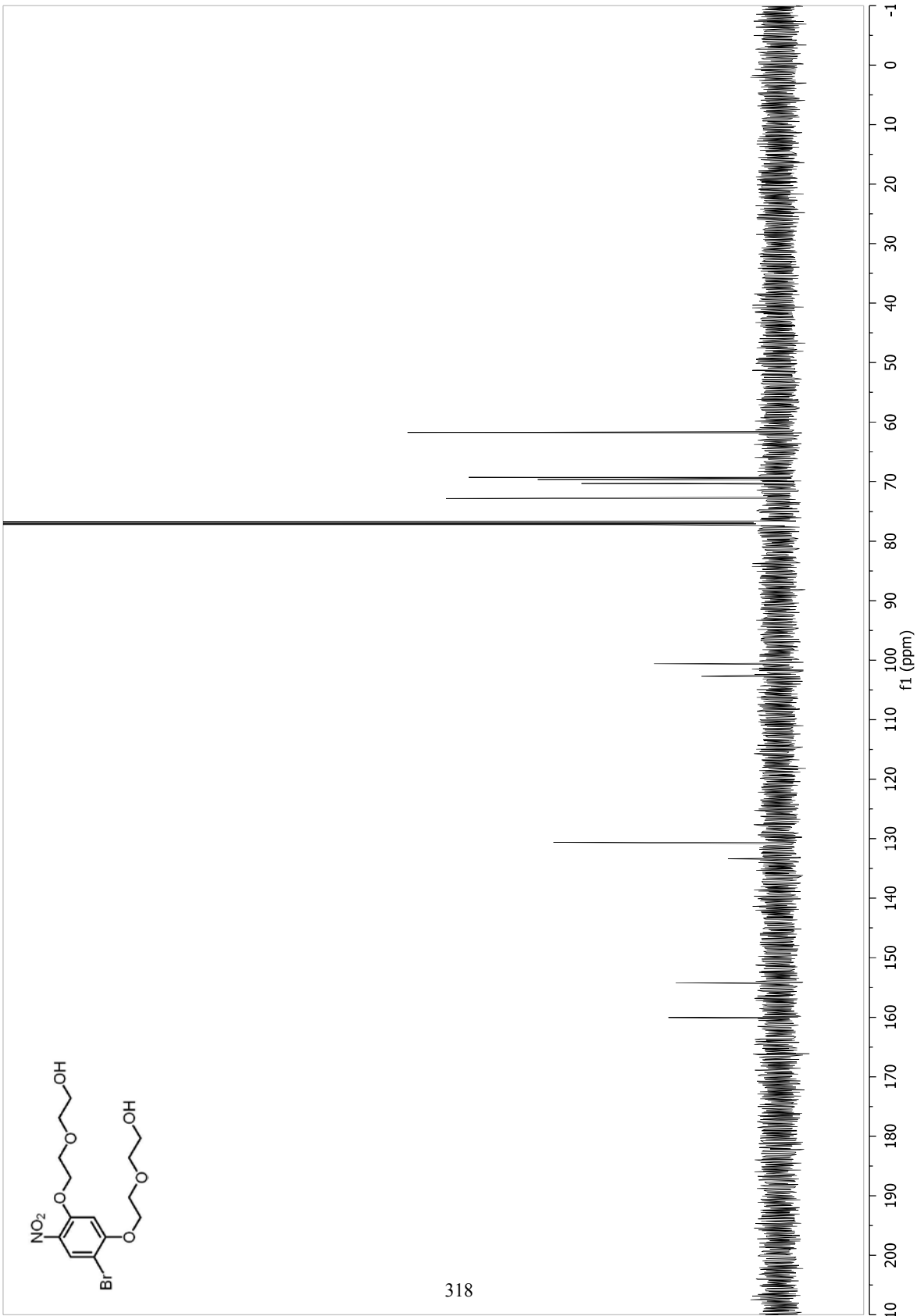


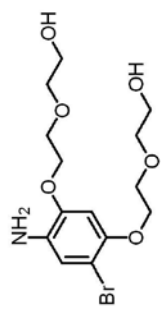




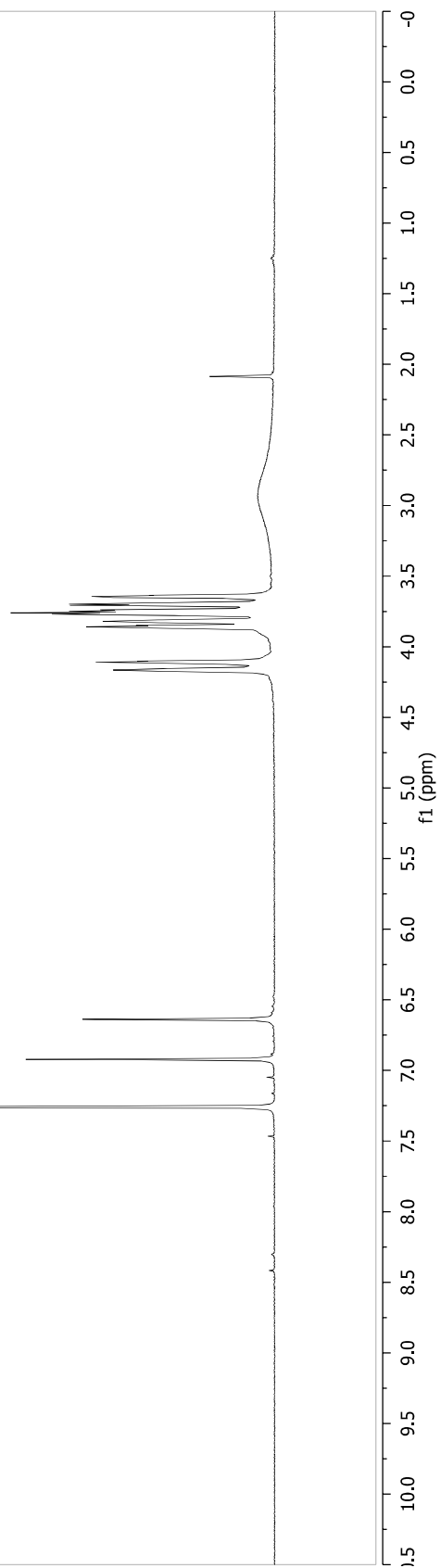
317

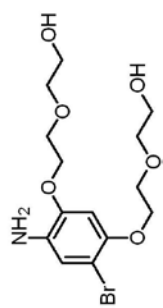




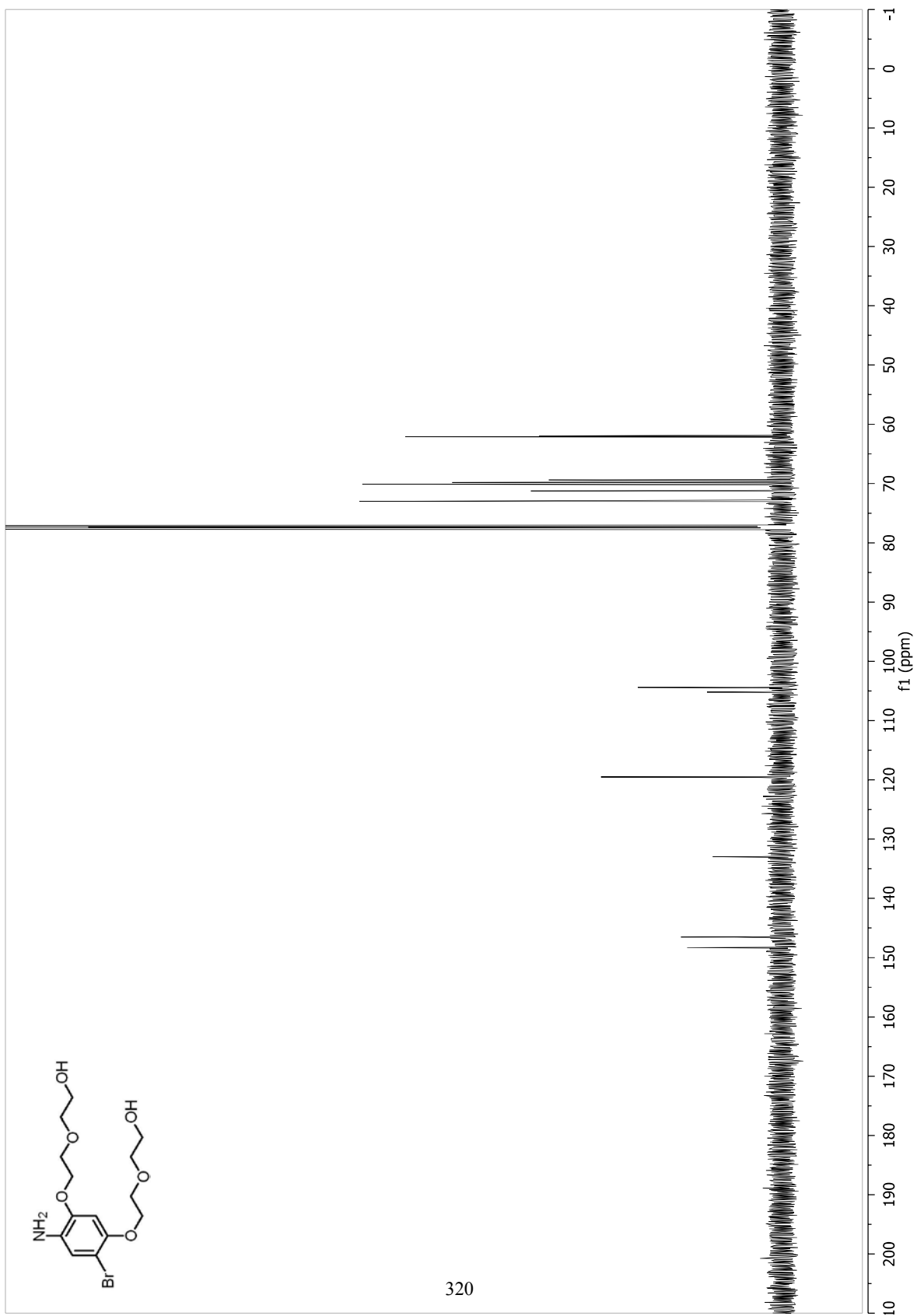


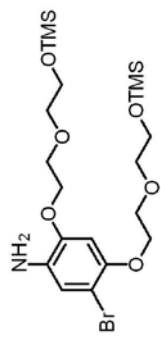
319



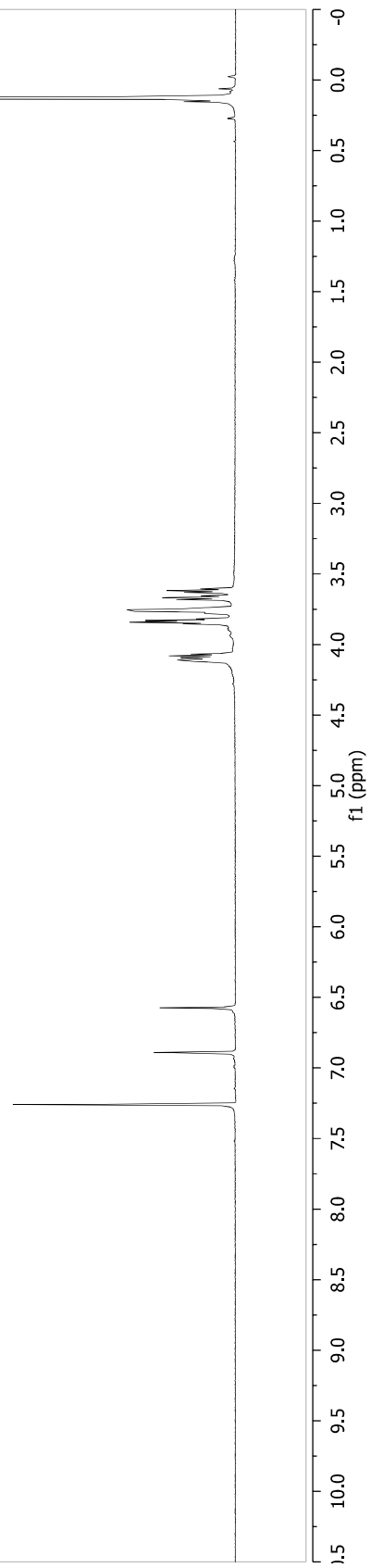


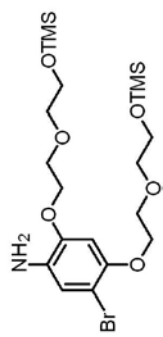
320



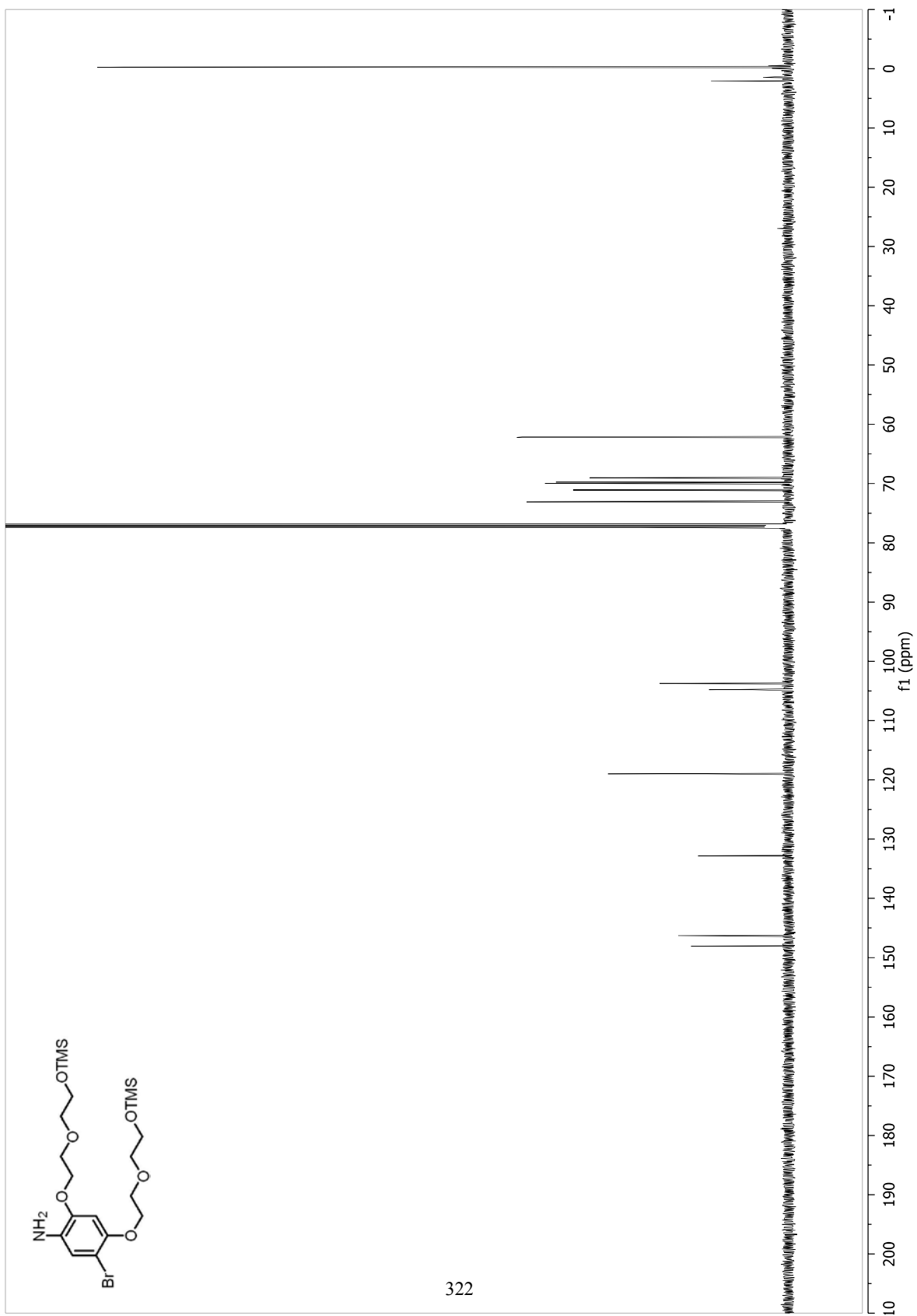


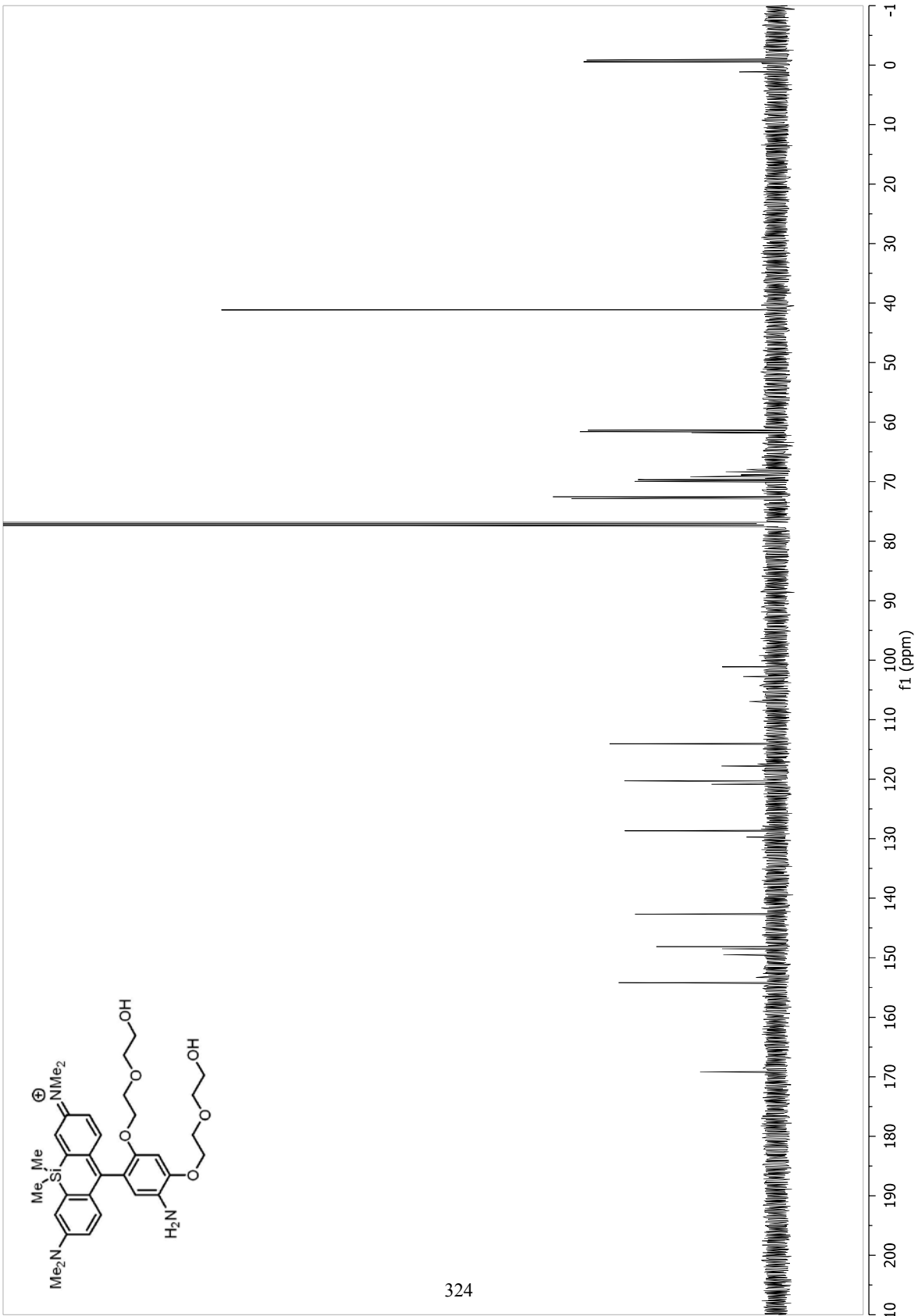
321

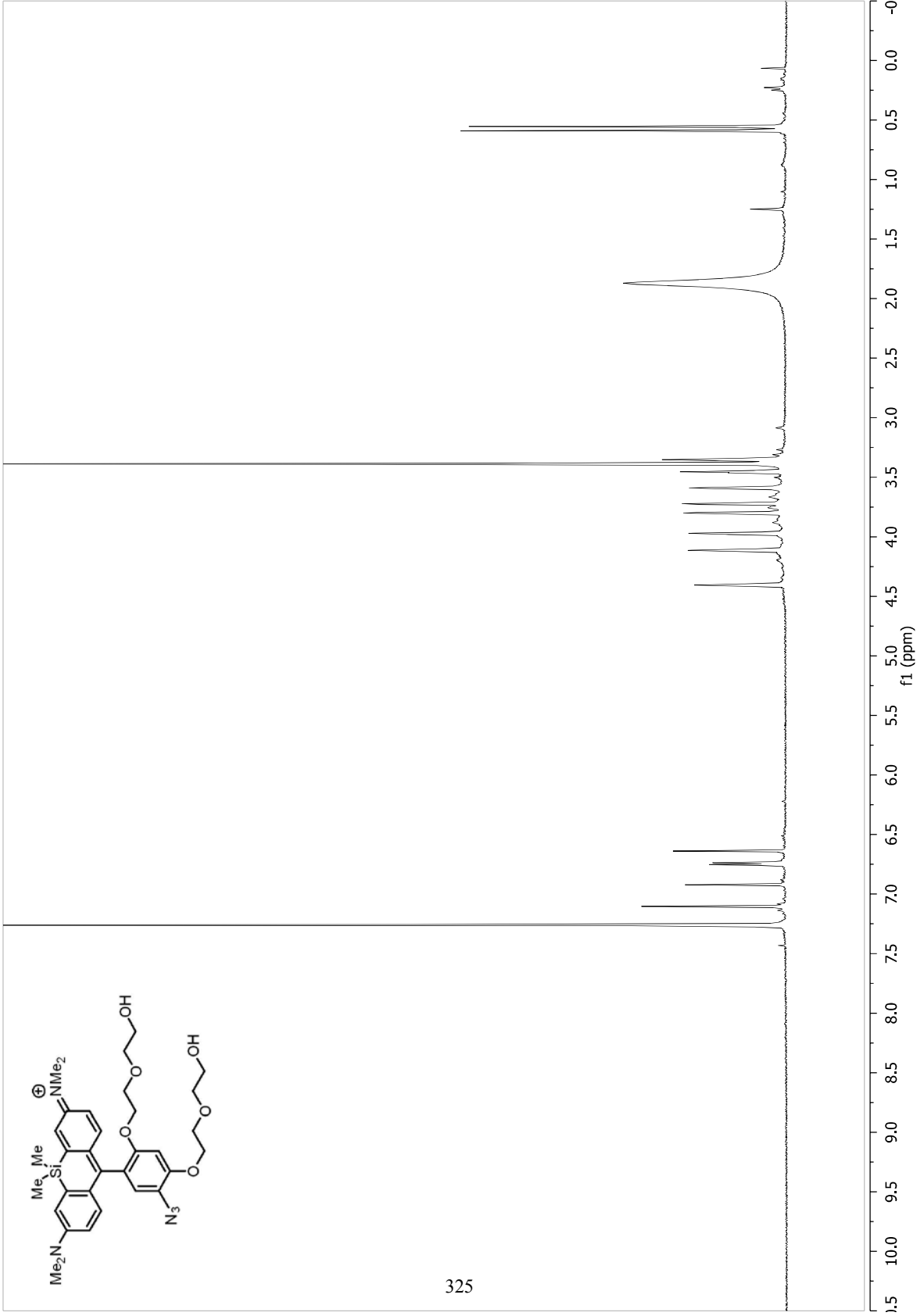


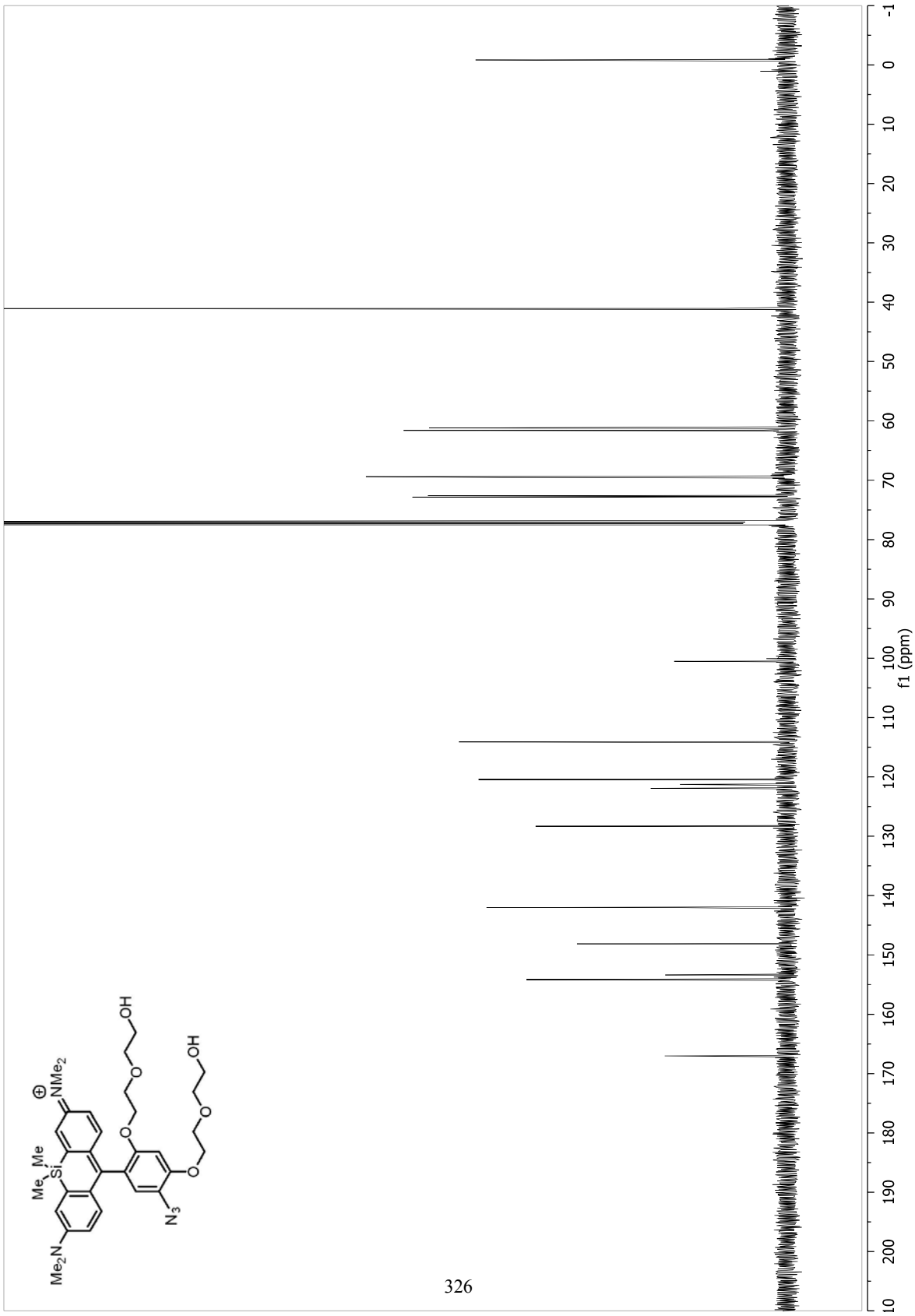


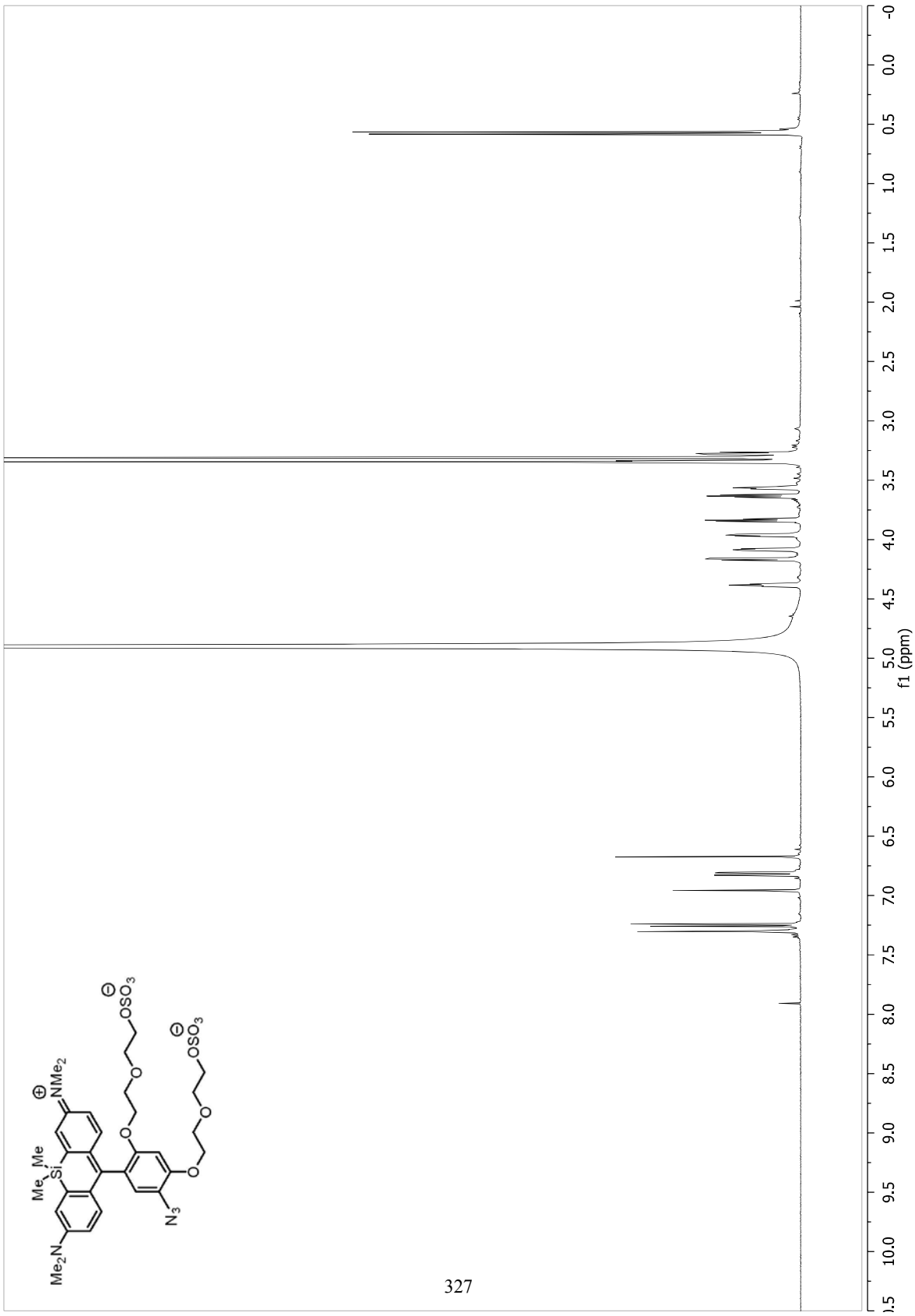
322

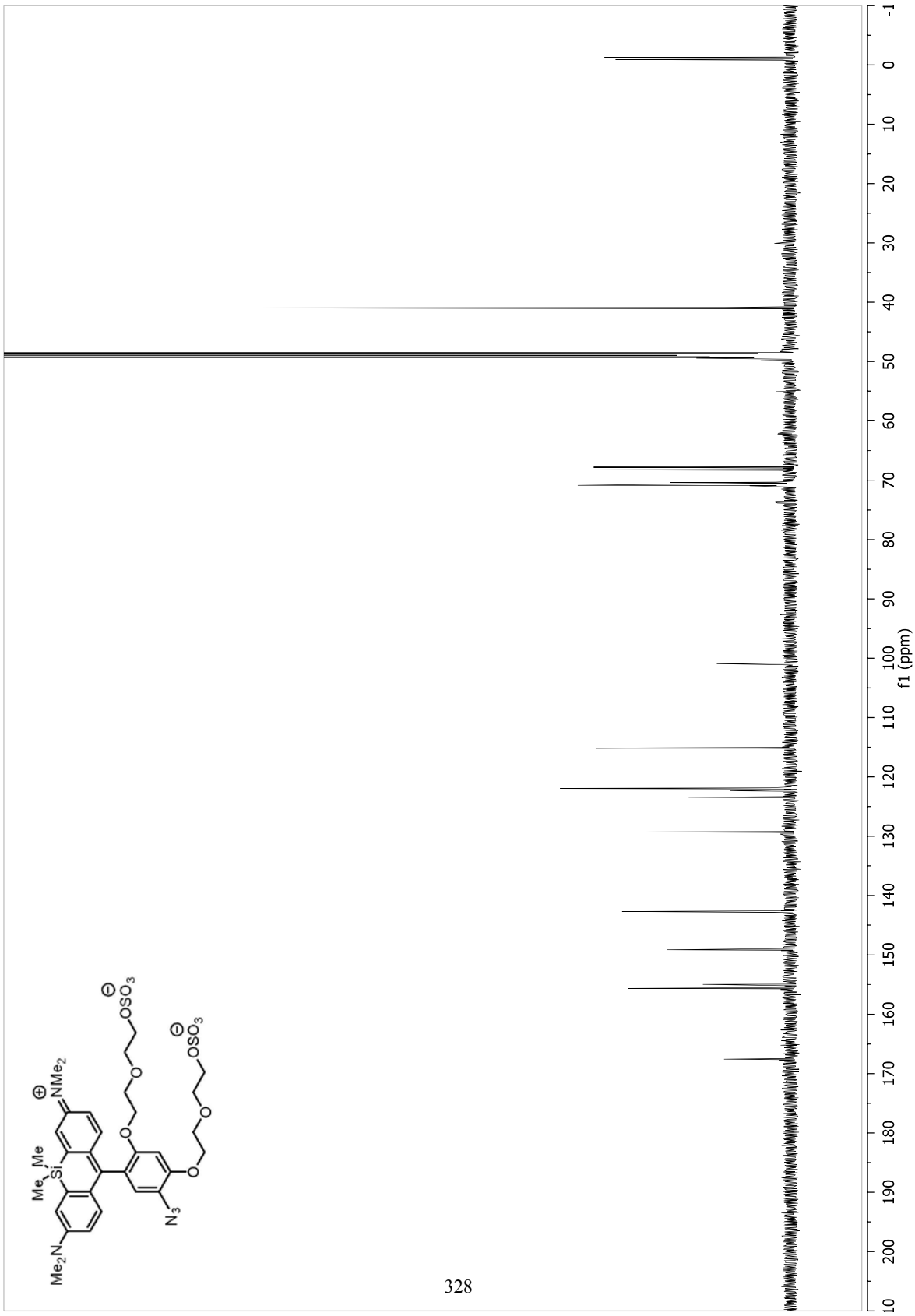


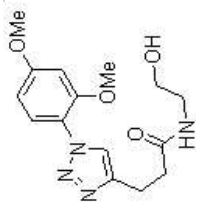




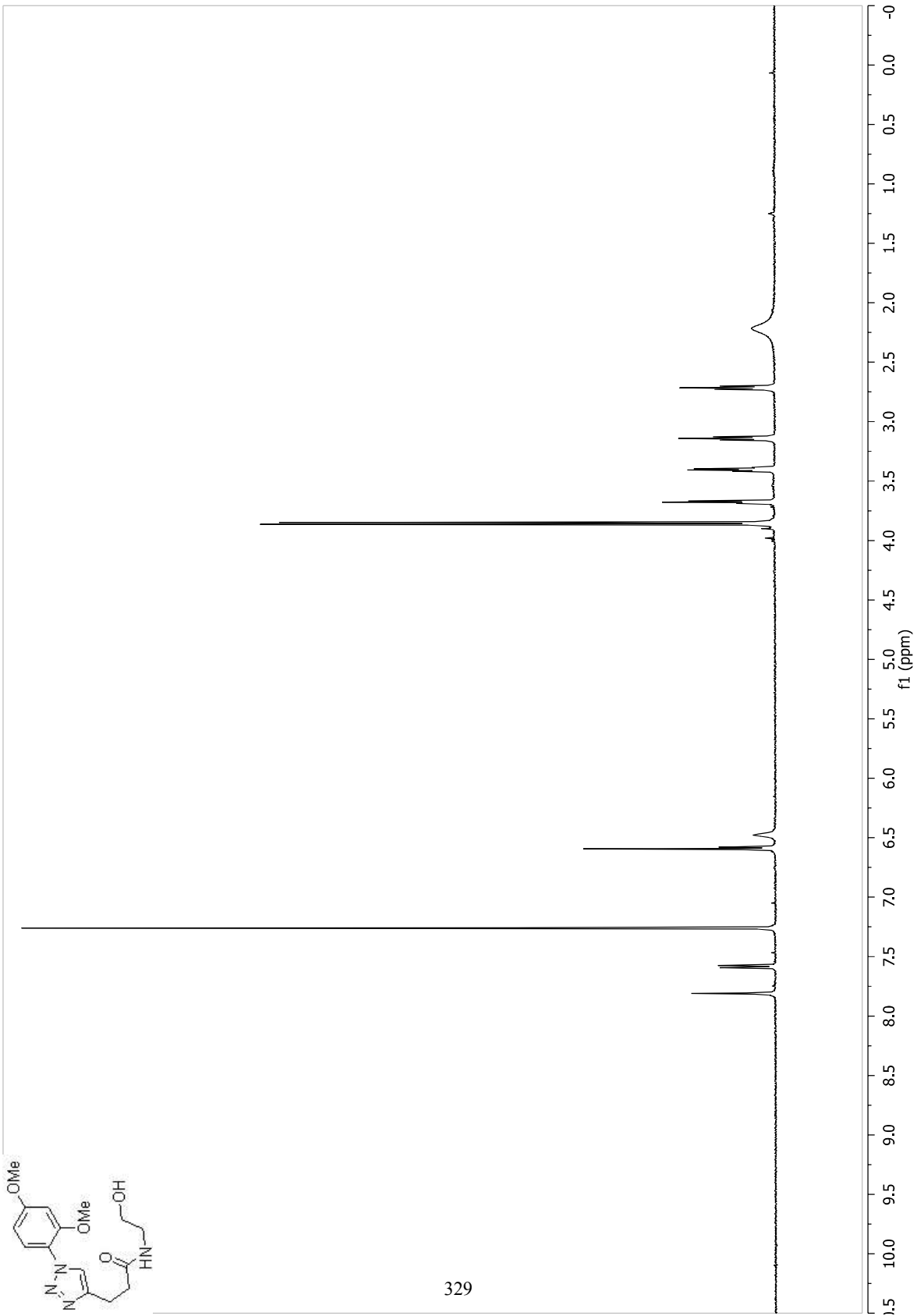


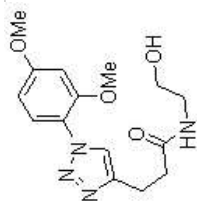




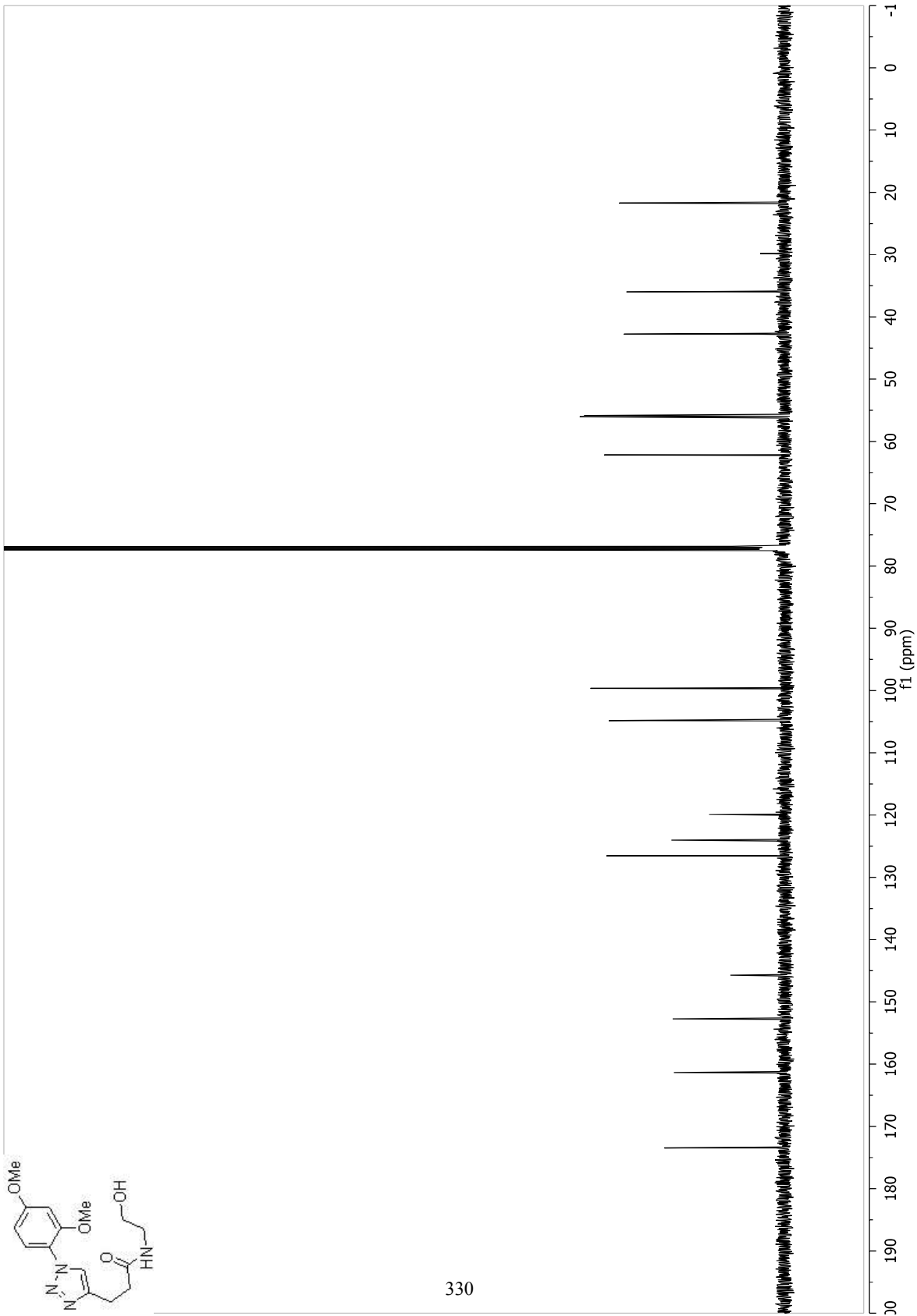


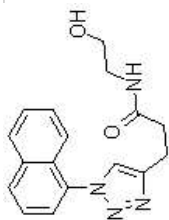
329



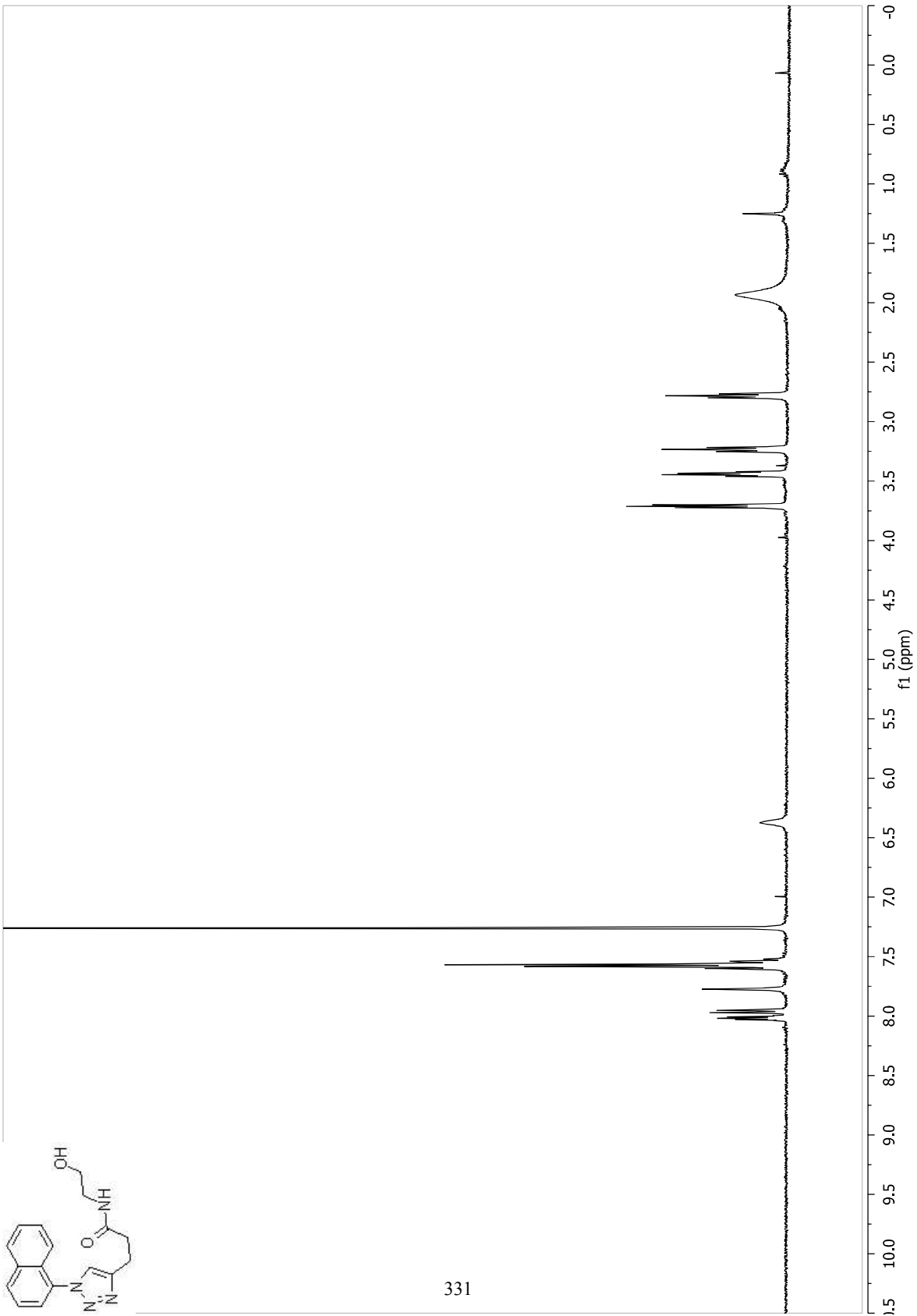


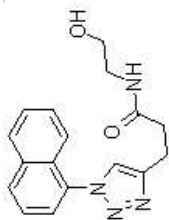
330



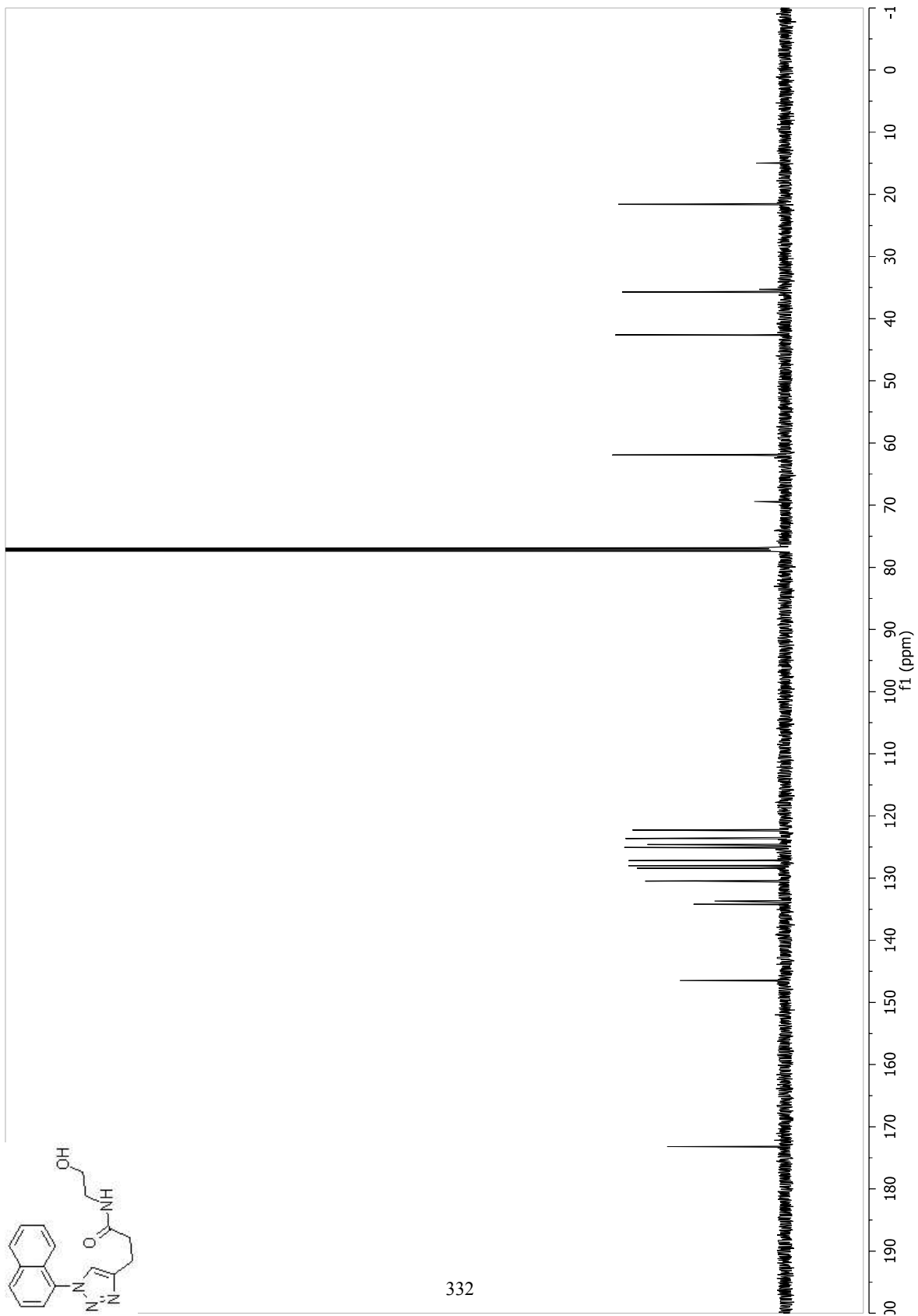


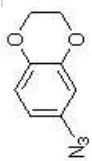
331



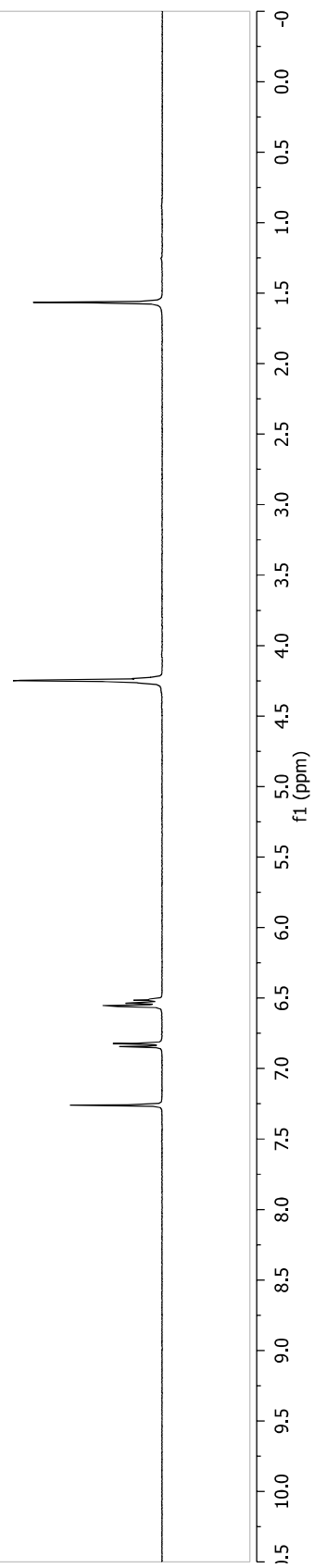


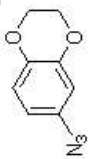
332



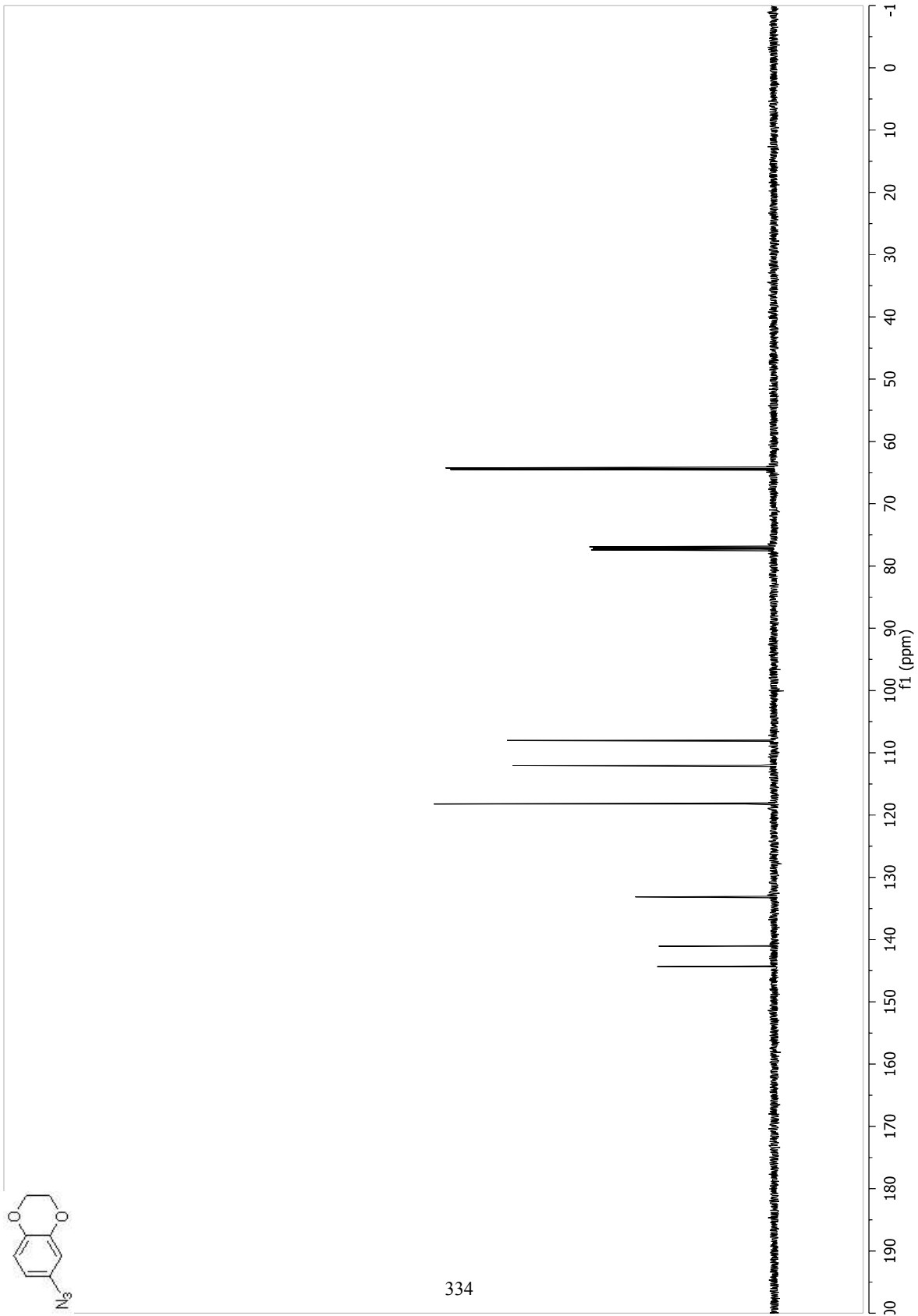


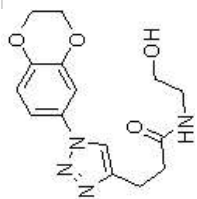
333



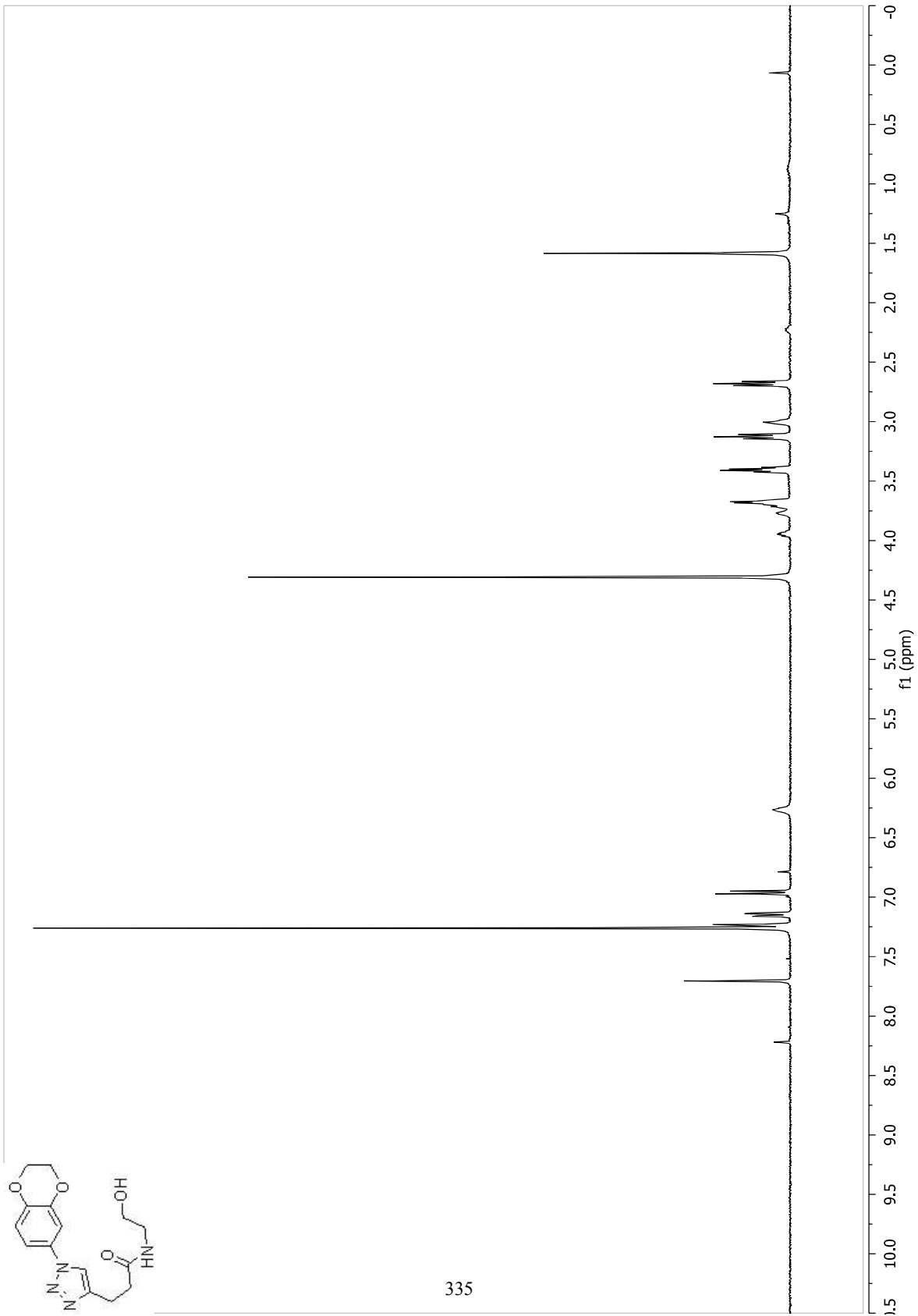


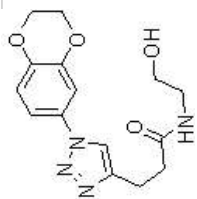
334



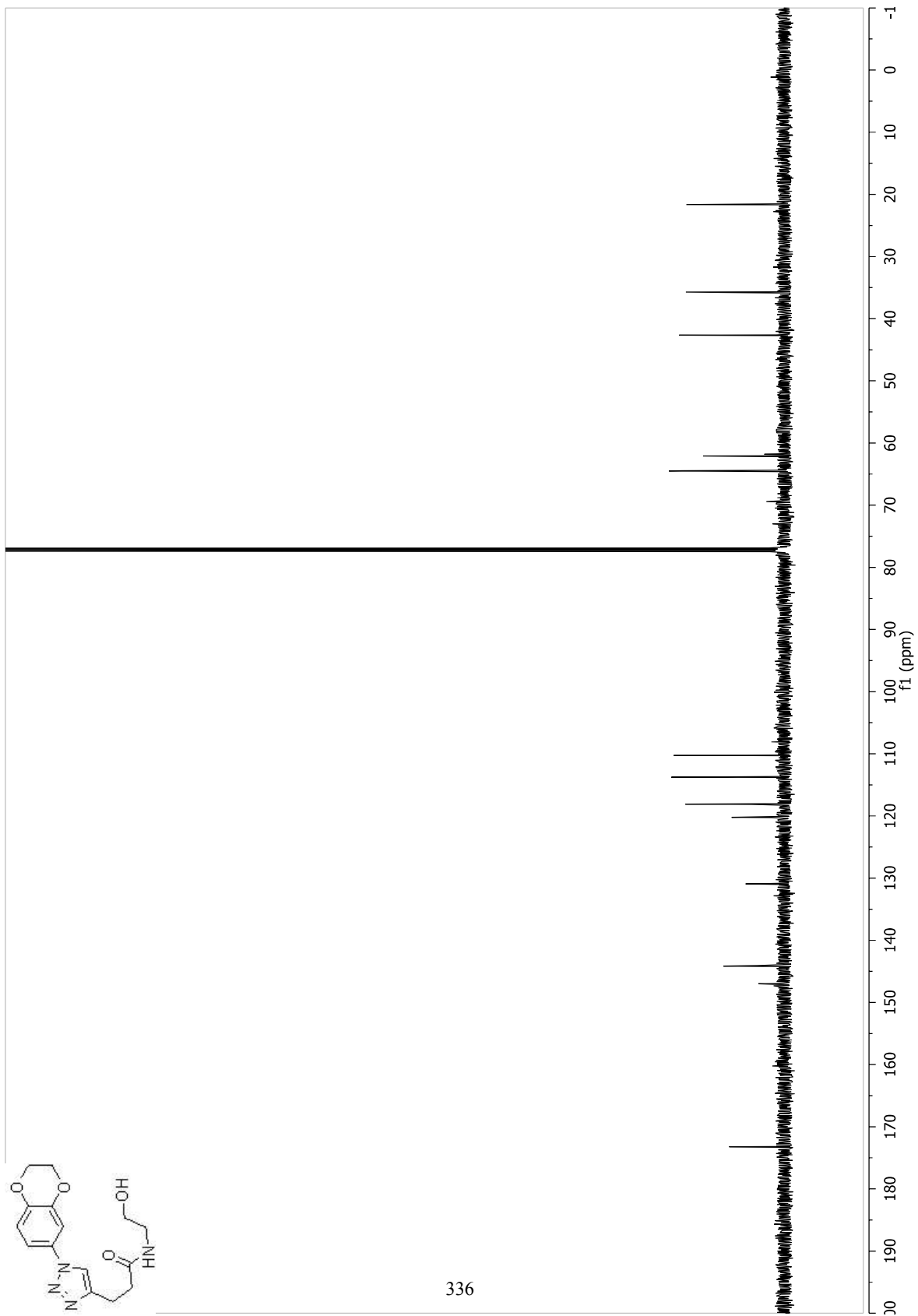


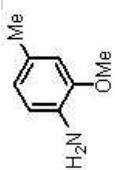
335



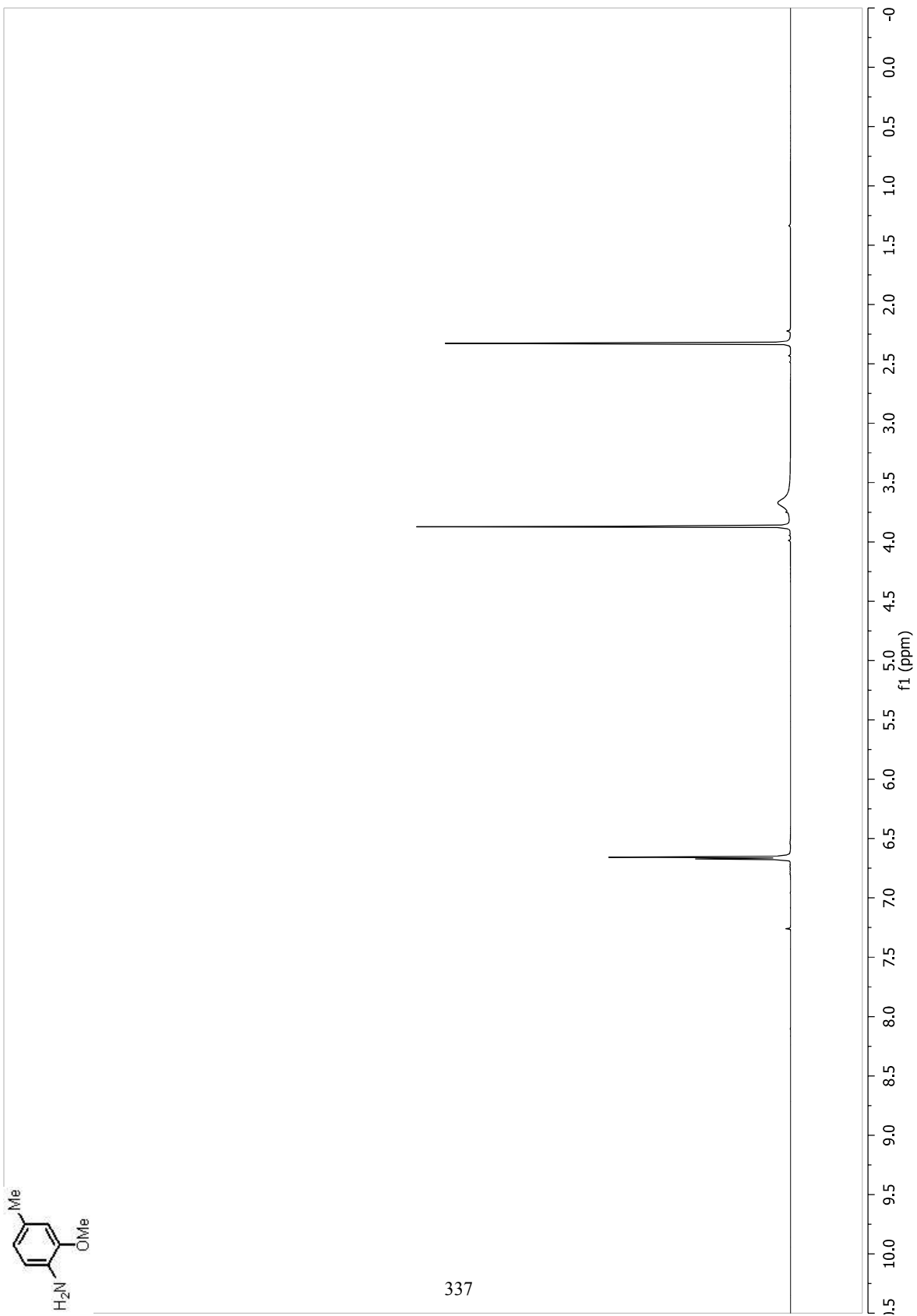


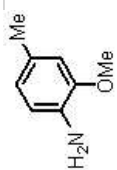
336



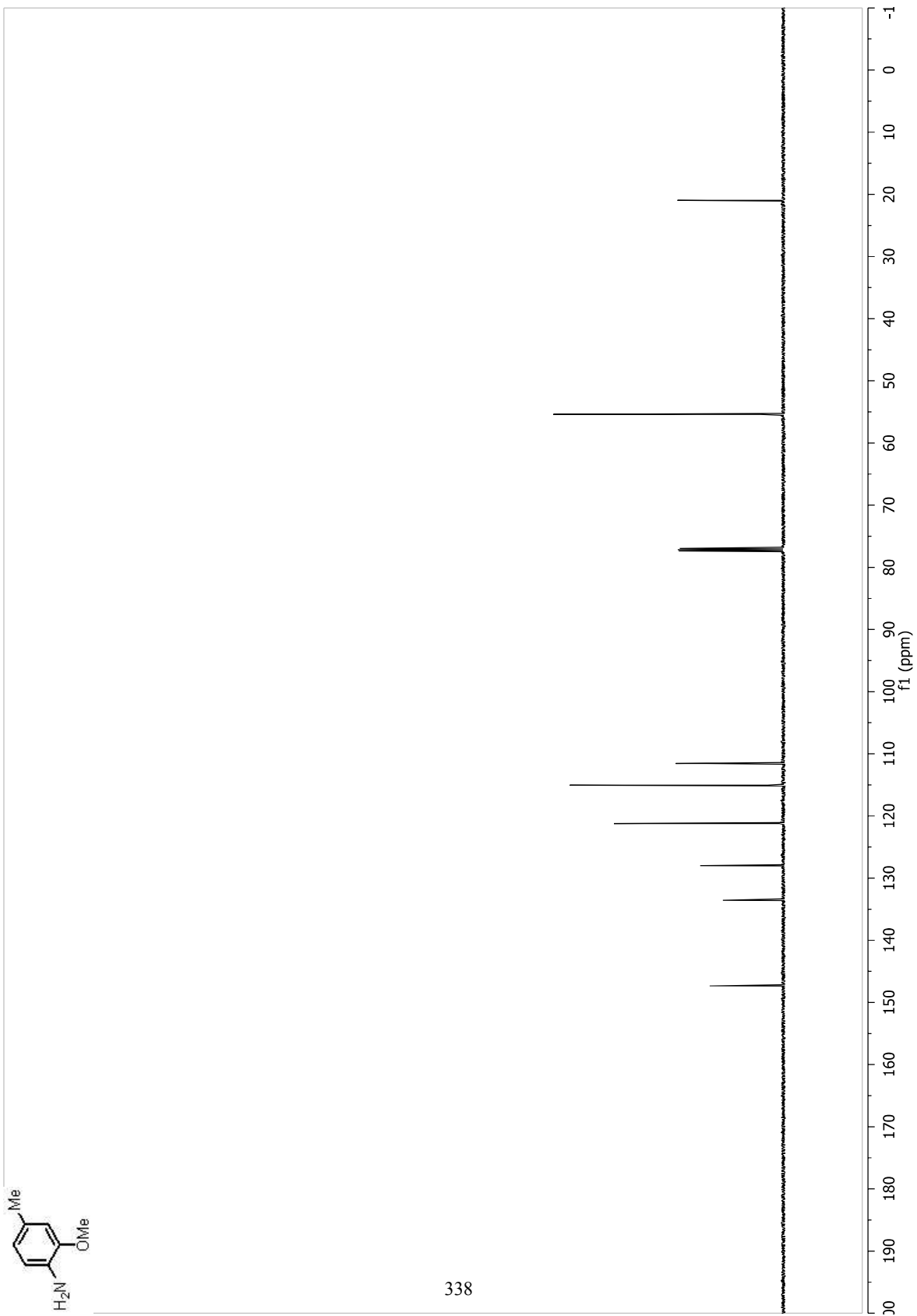


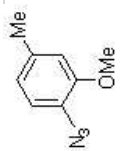
337



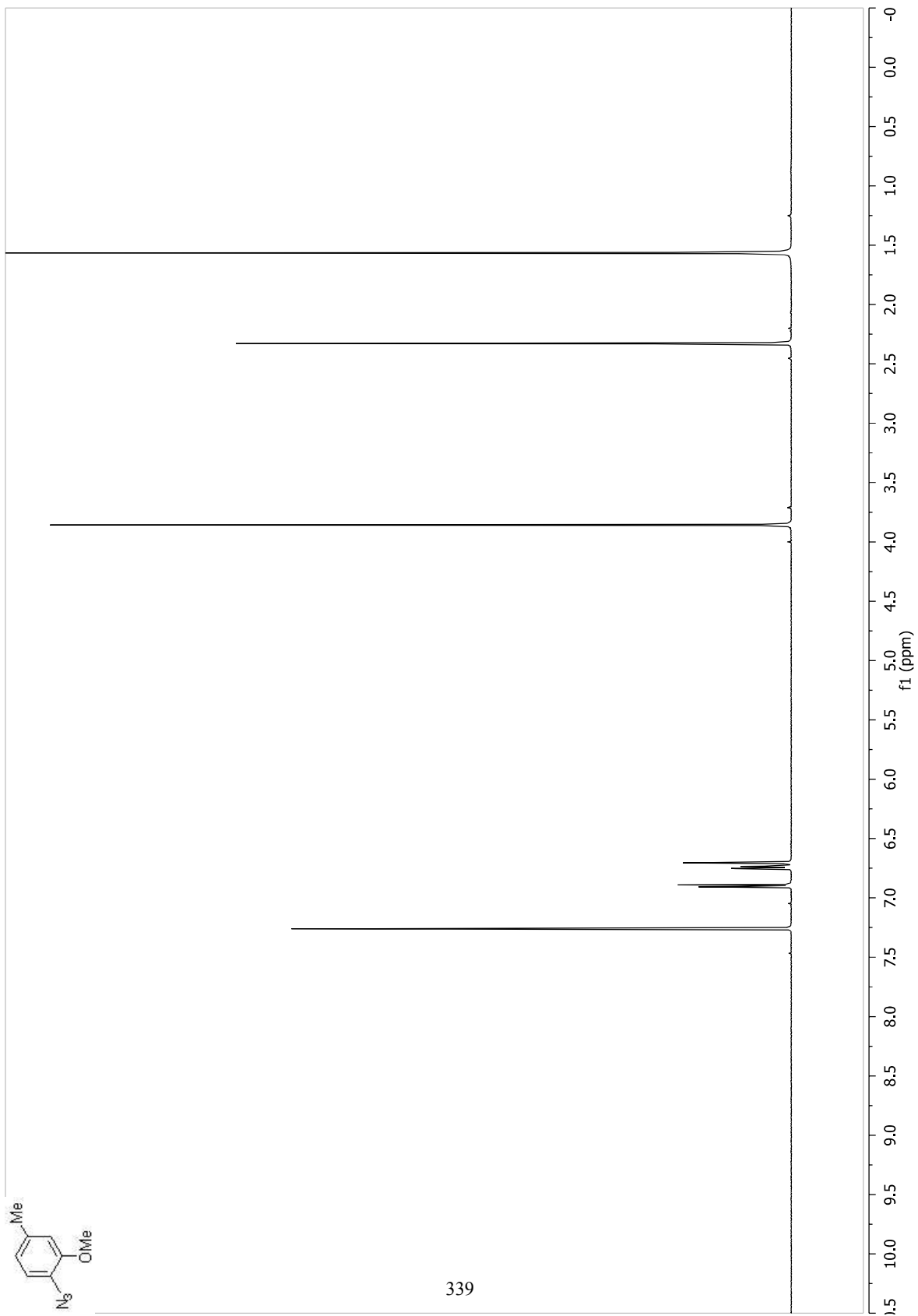


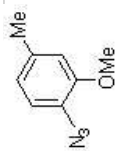
338



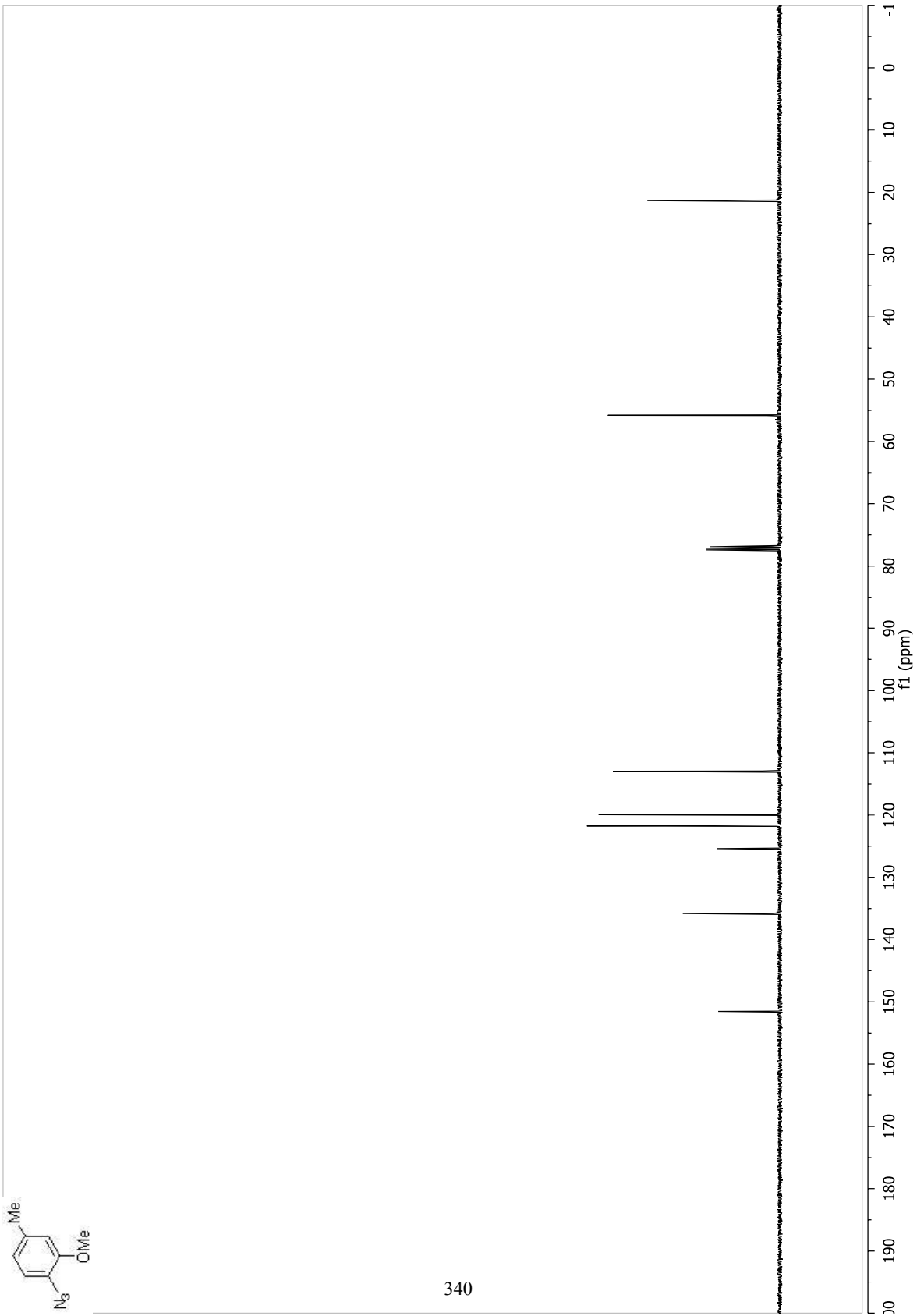


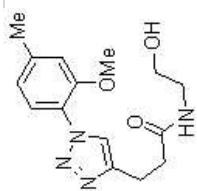
339



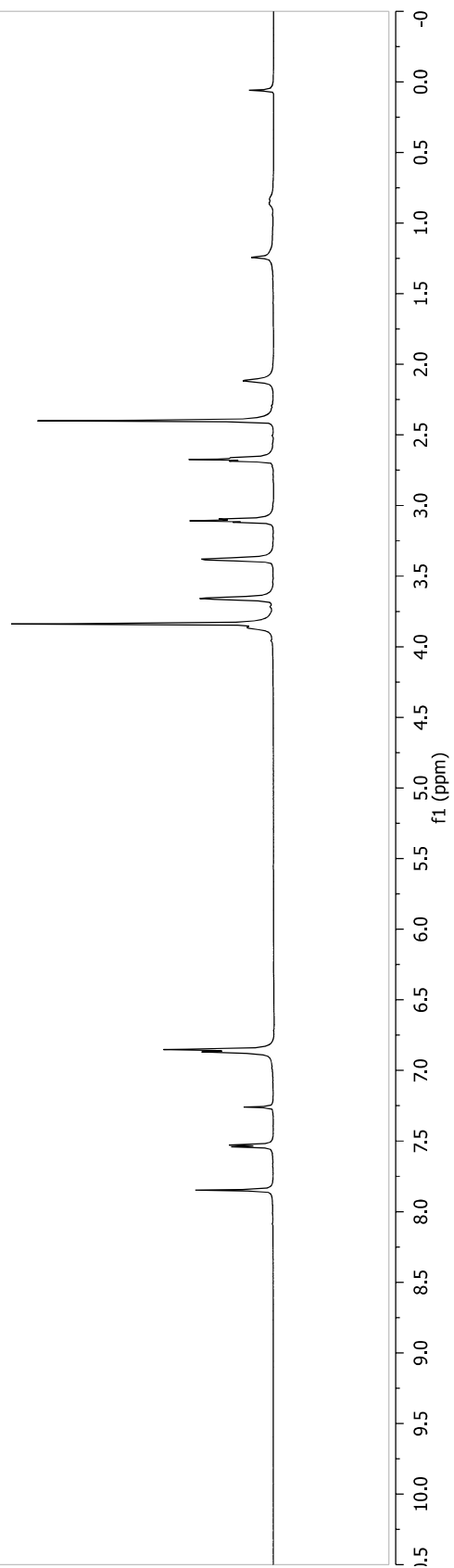


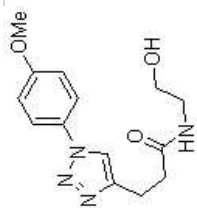
340



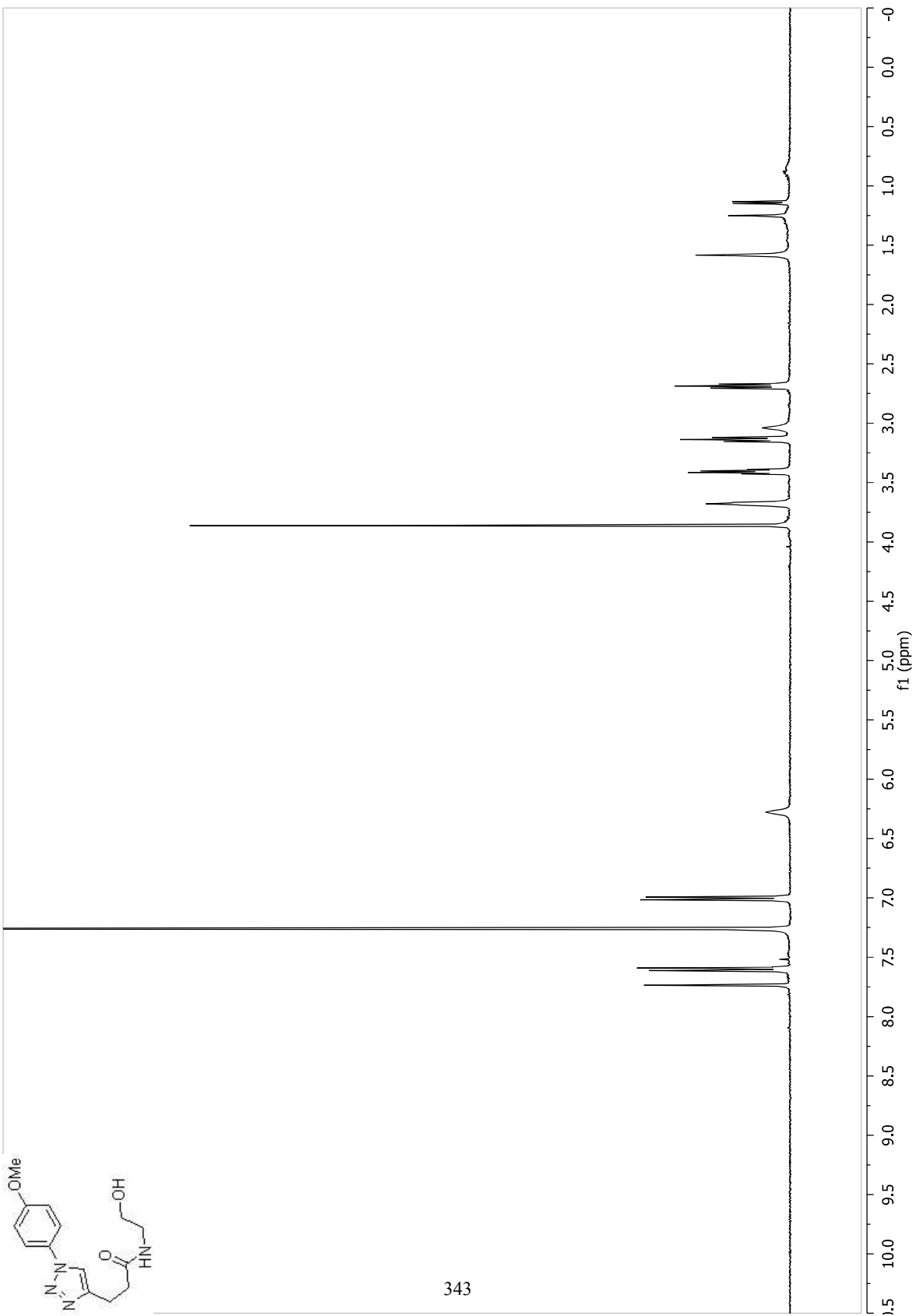


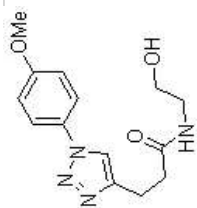
341



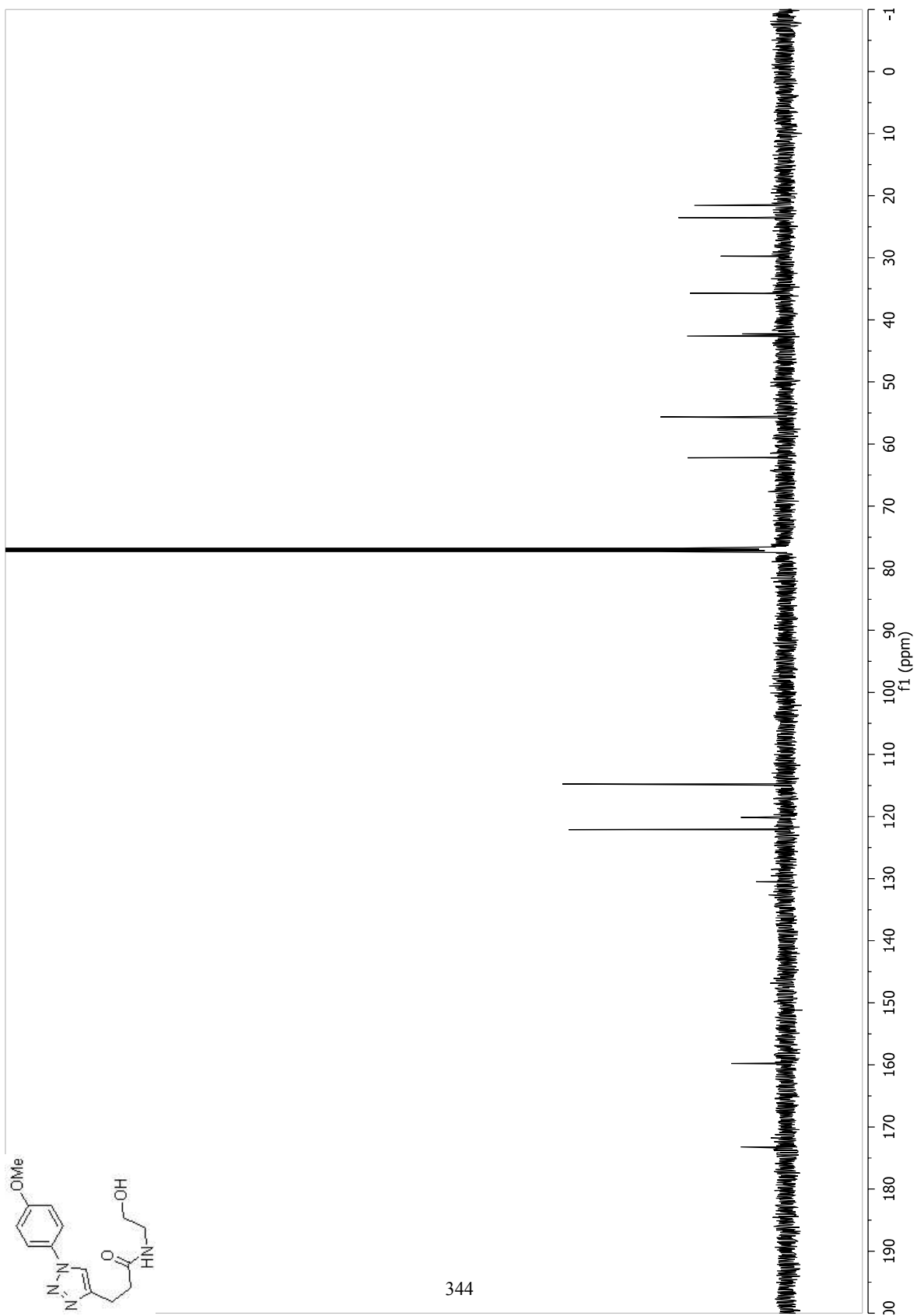


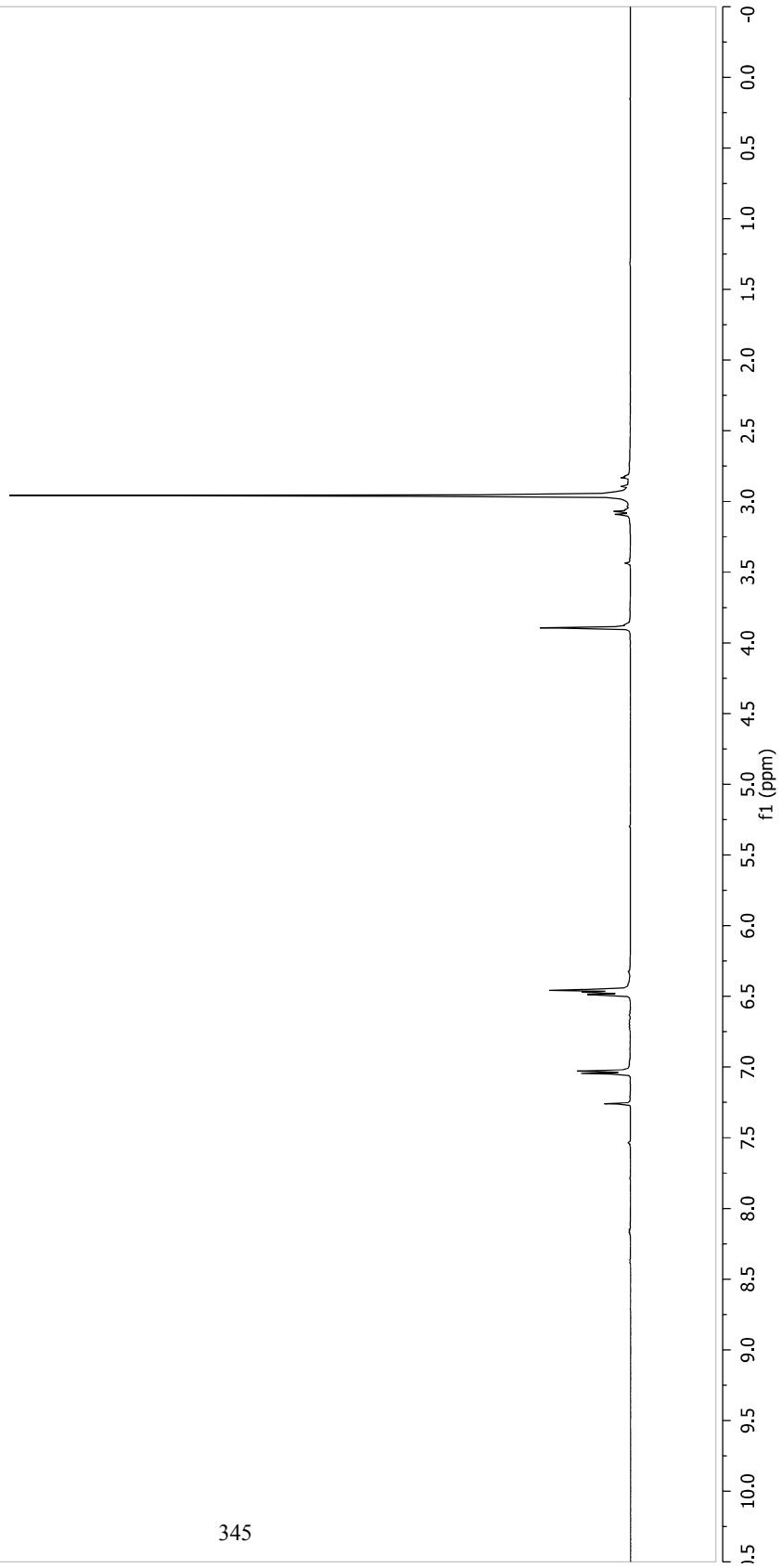
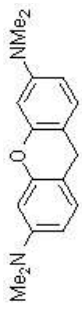
343

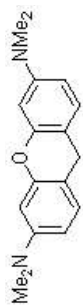




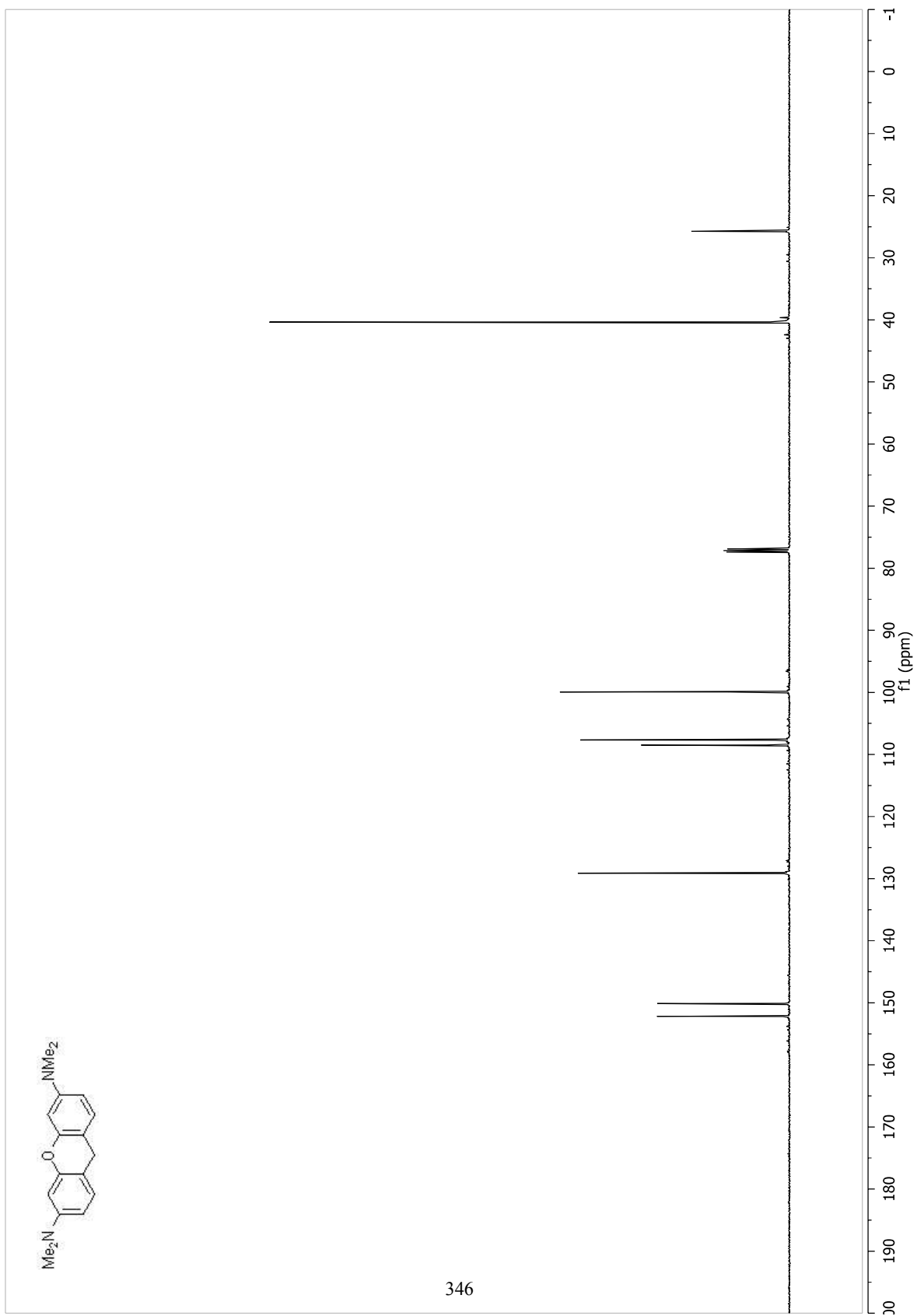
344

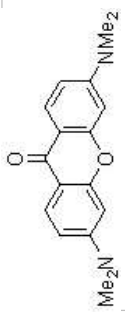




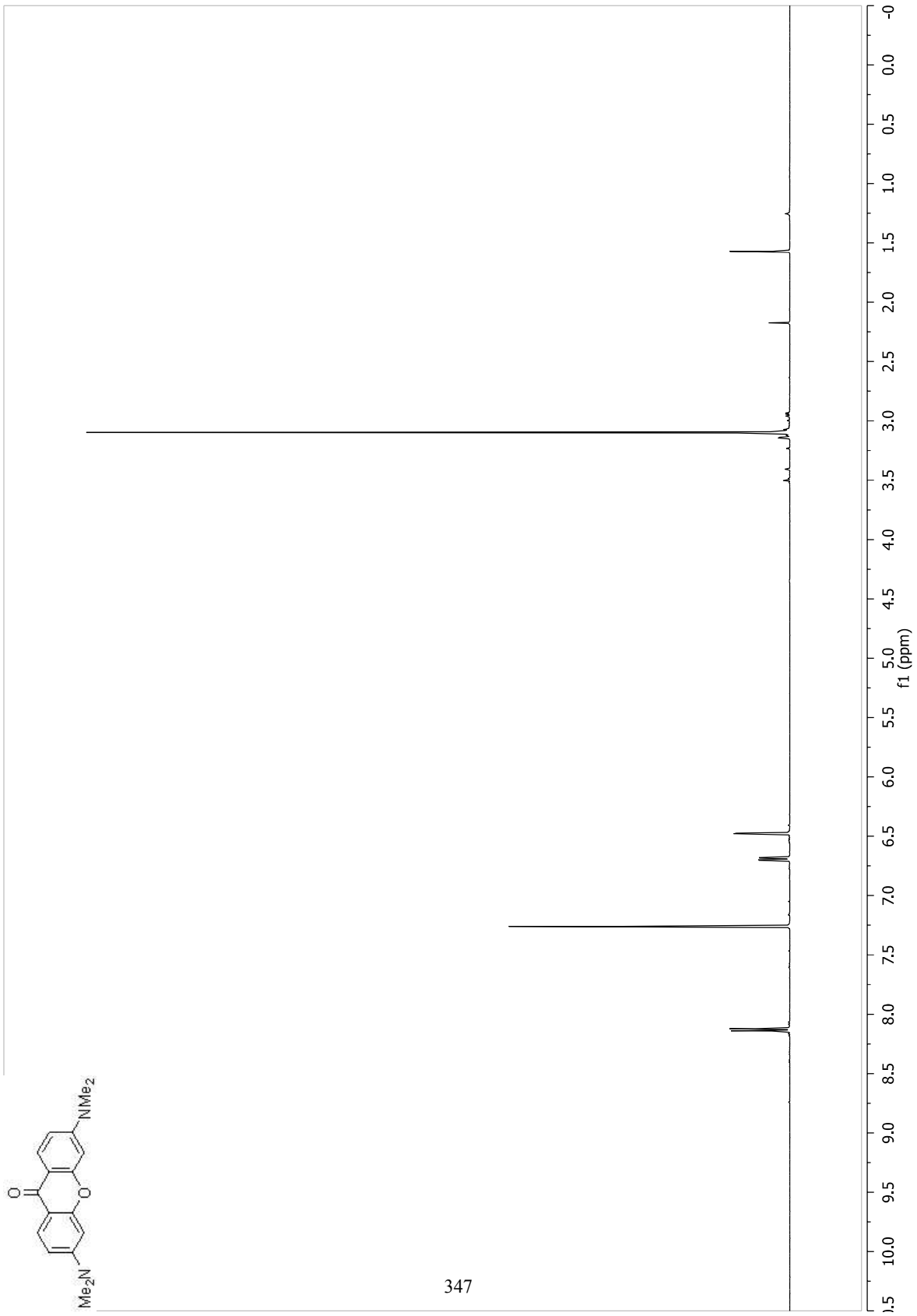


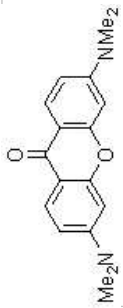
346



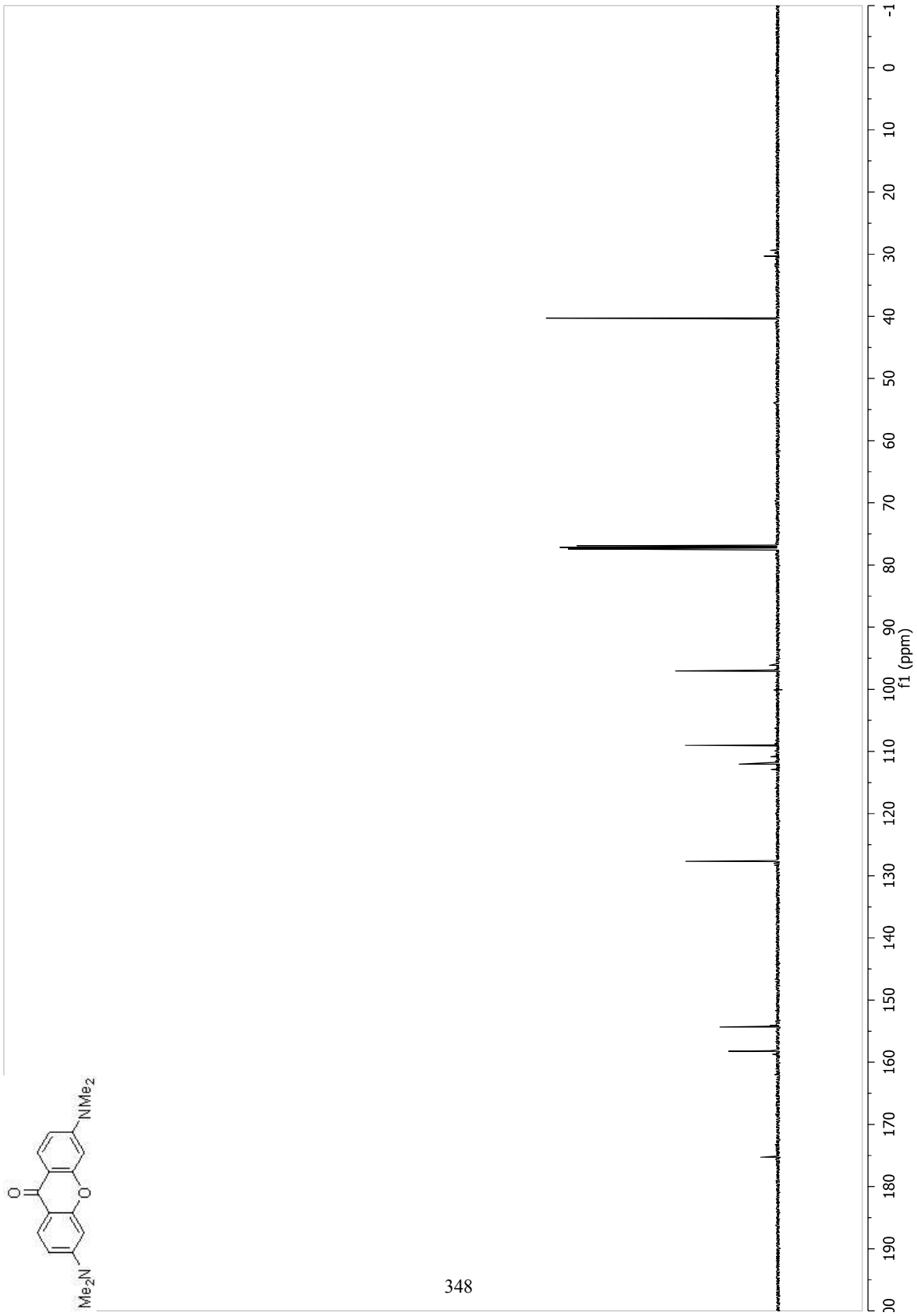


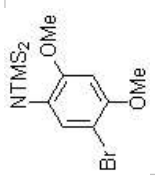
347



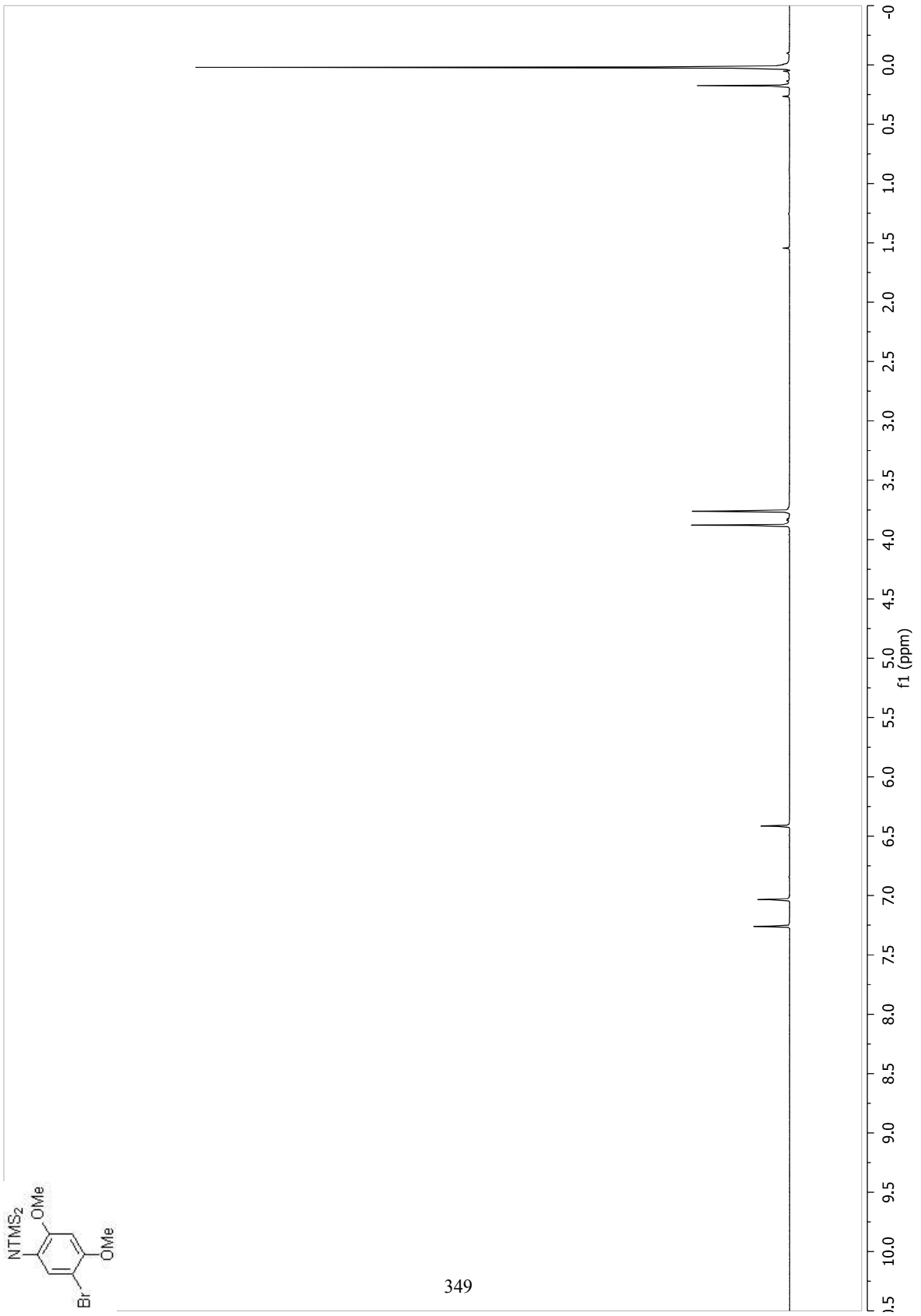


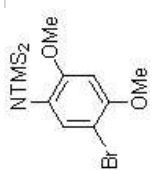
348



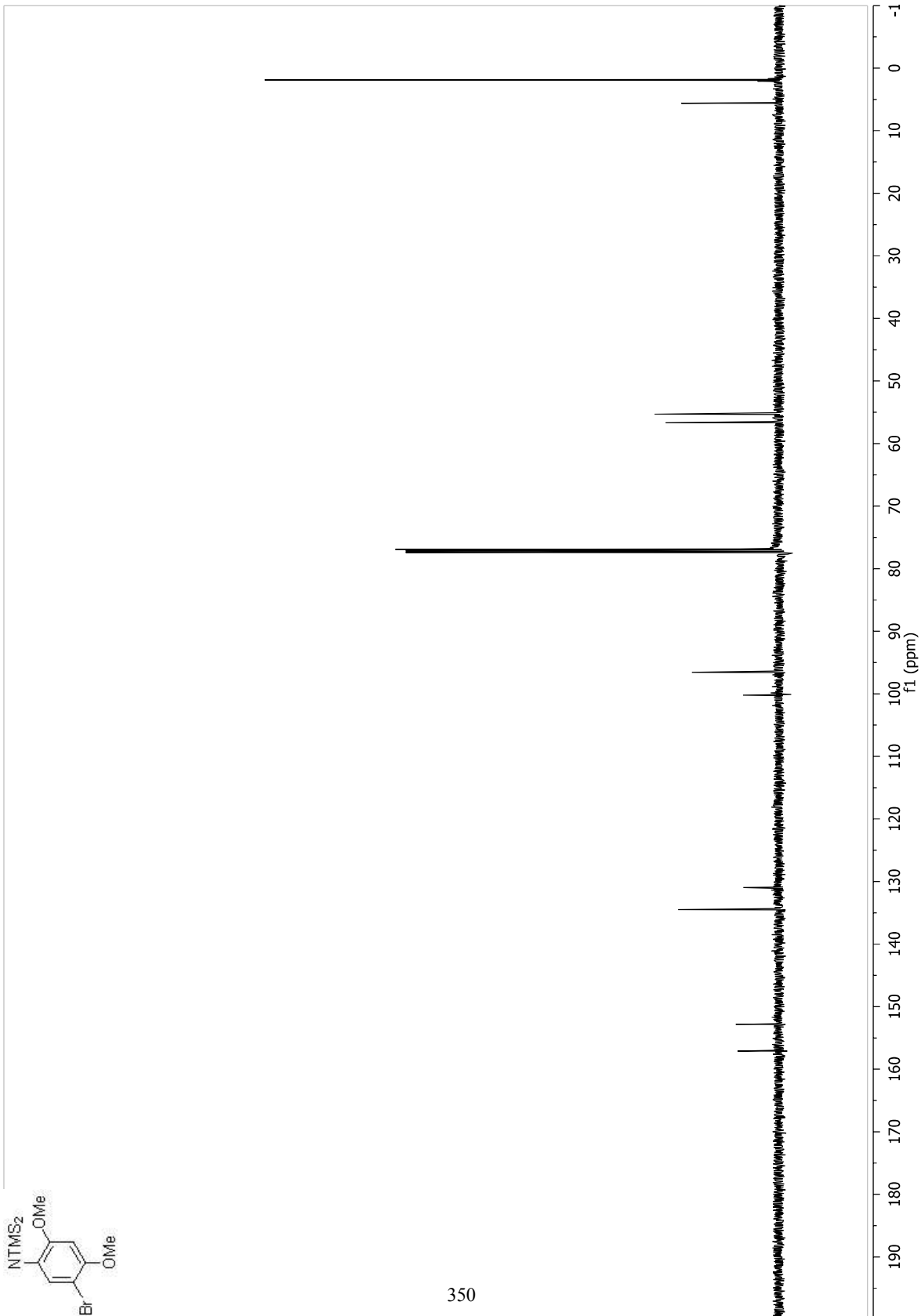


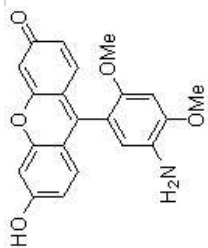
349



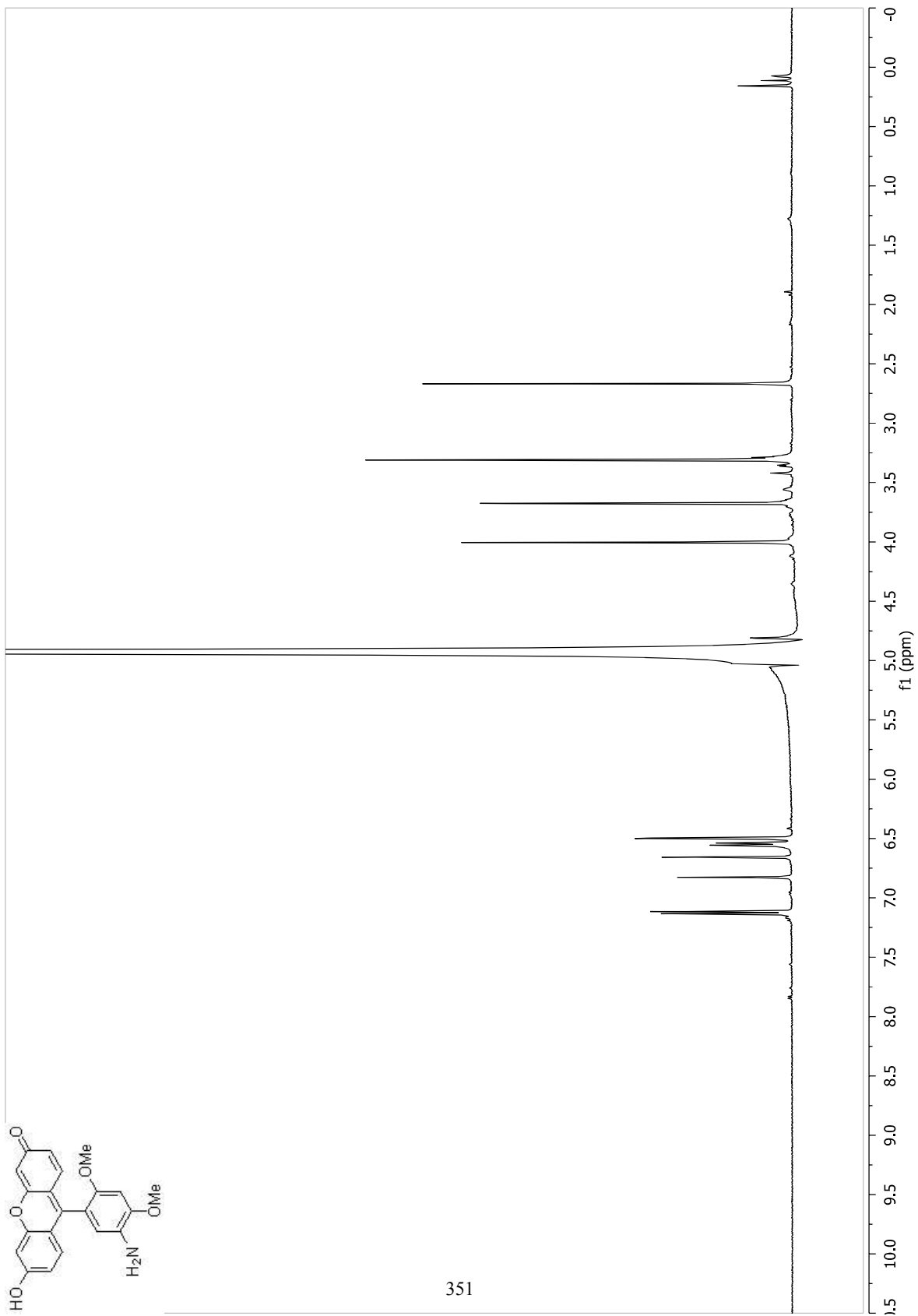


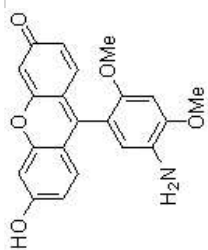
350



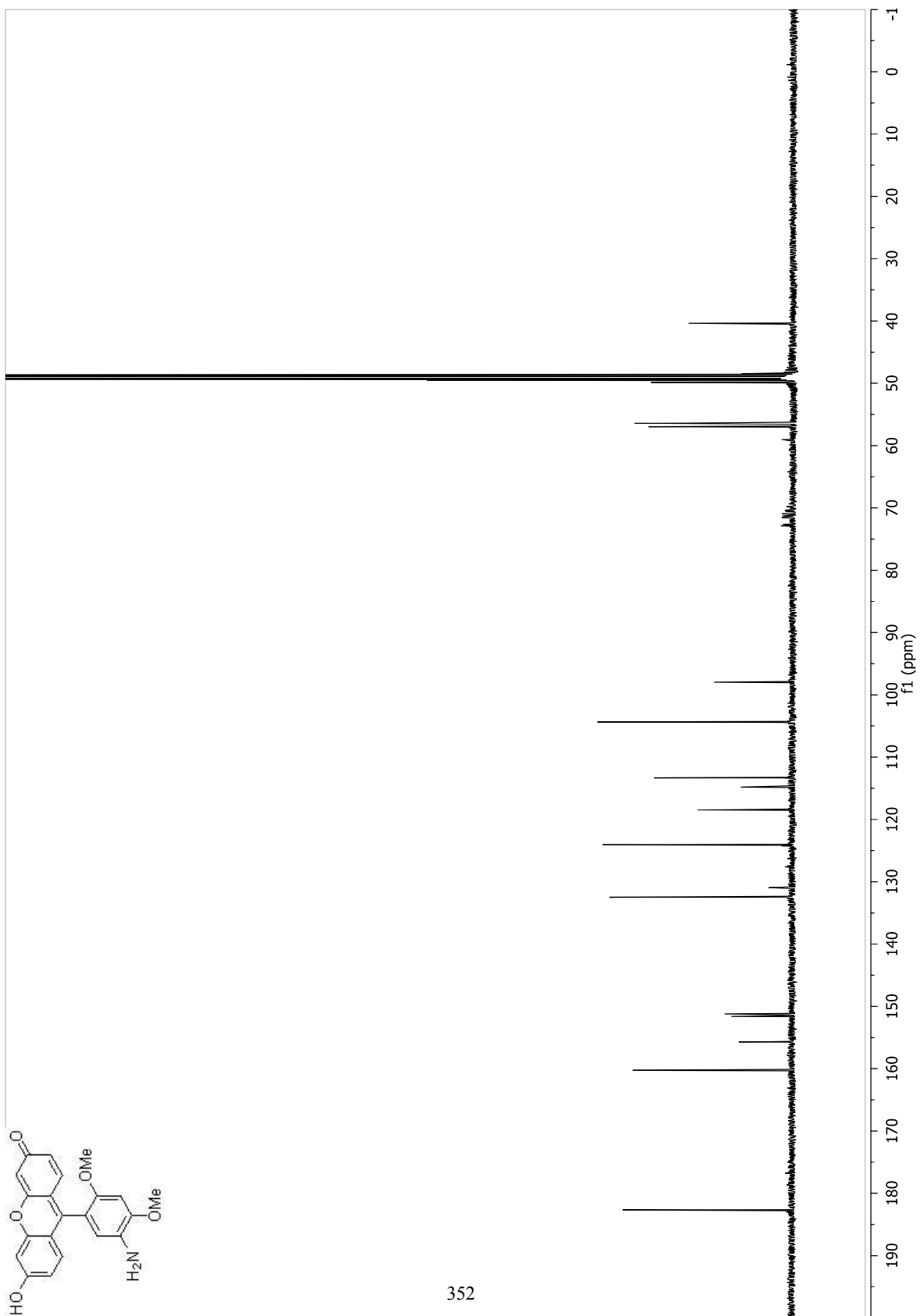


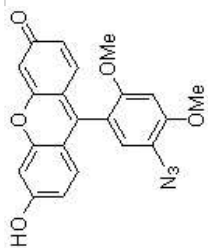
351



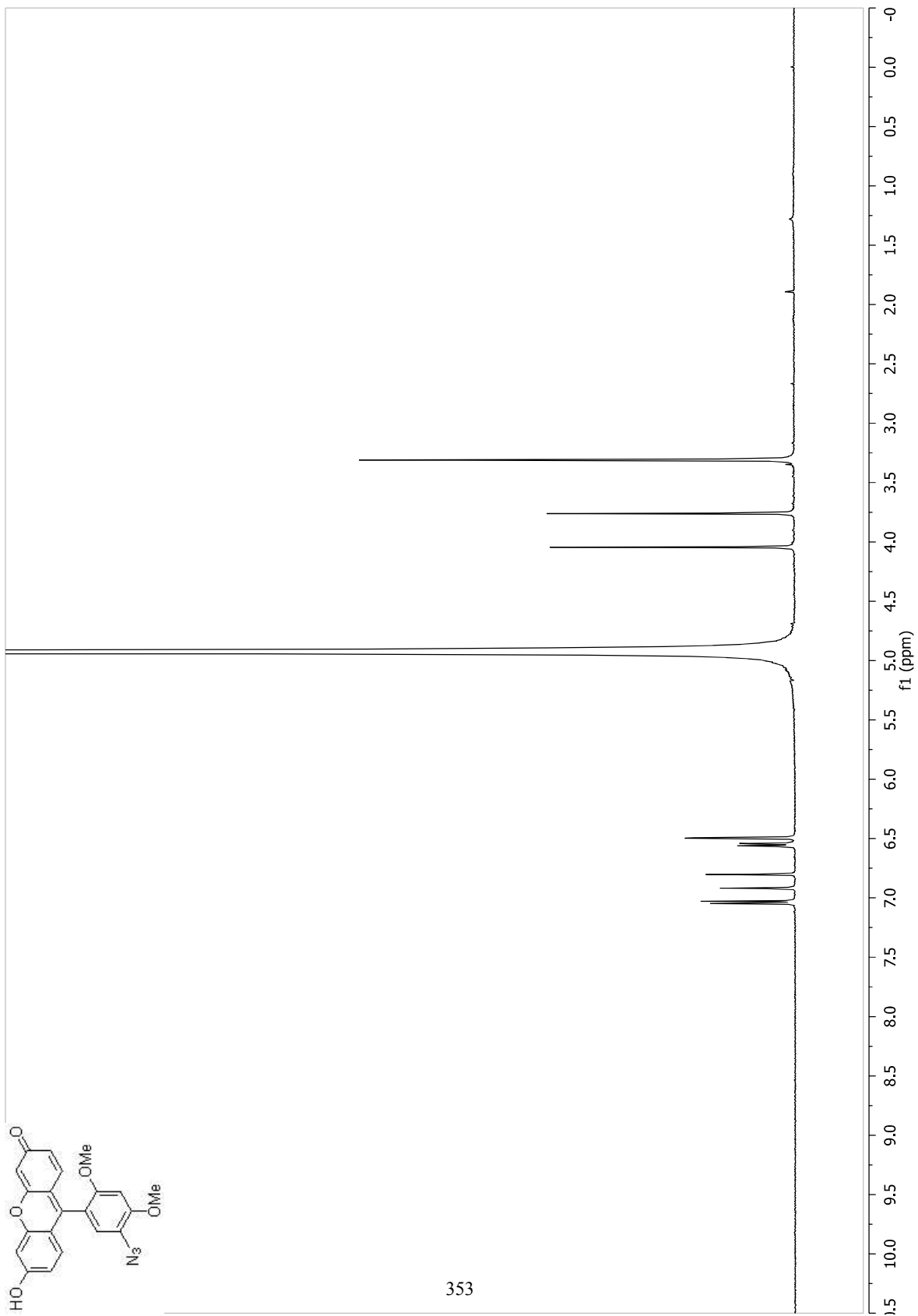


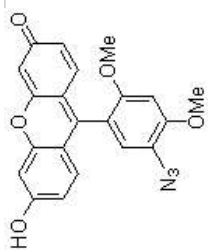
352



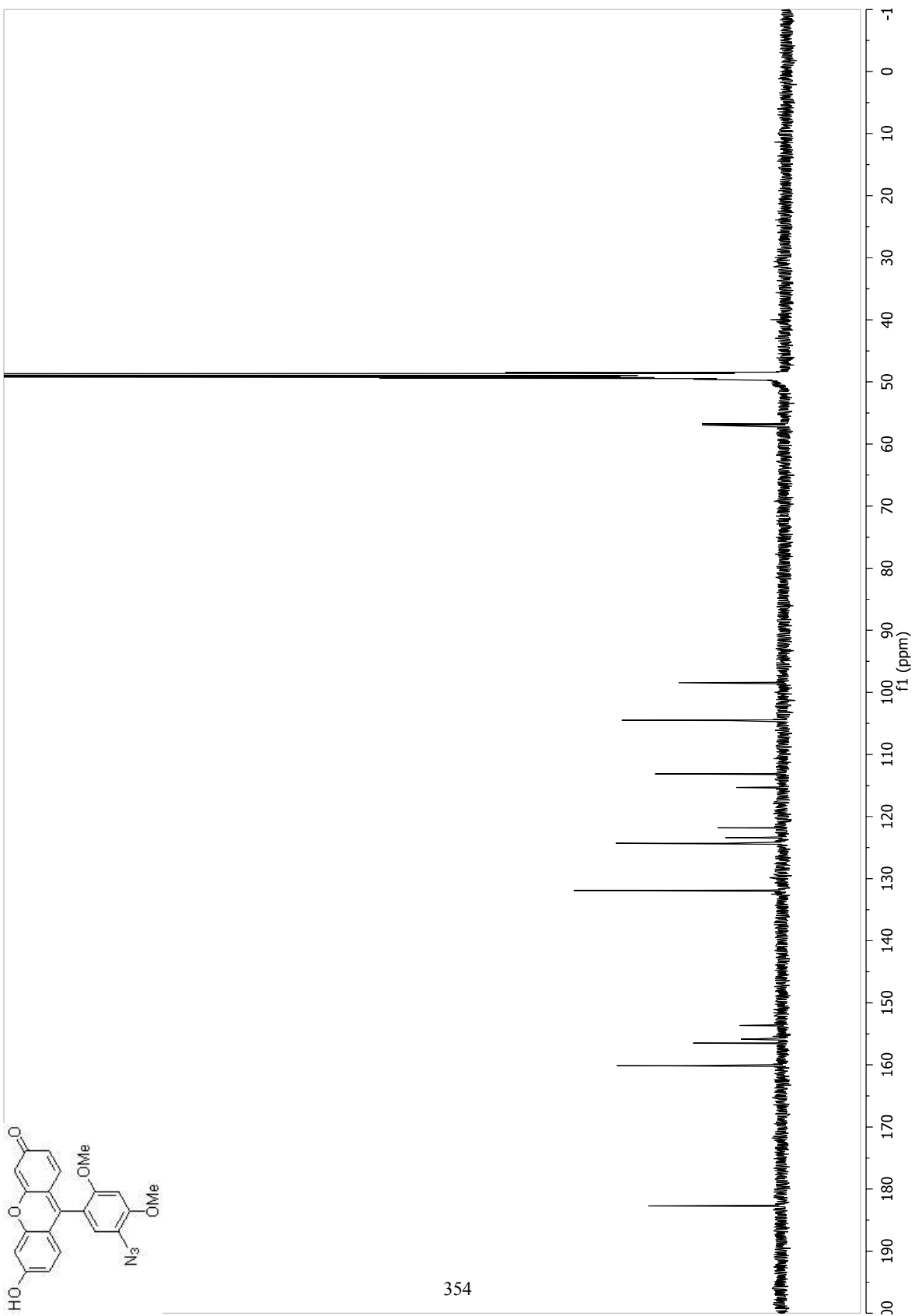


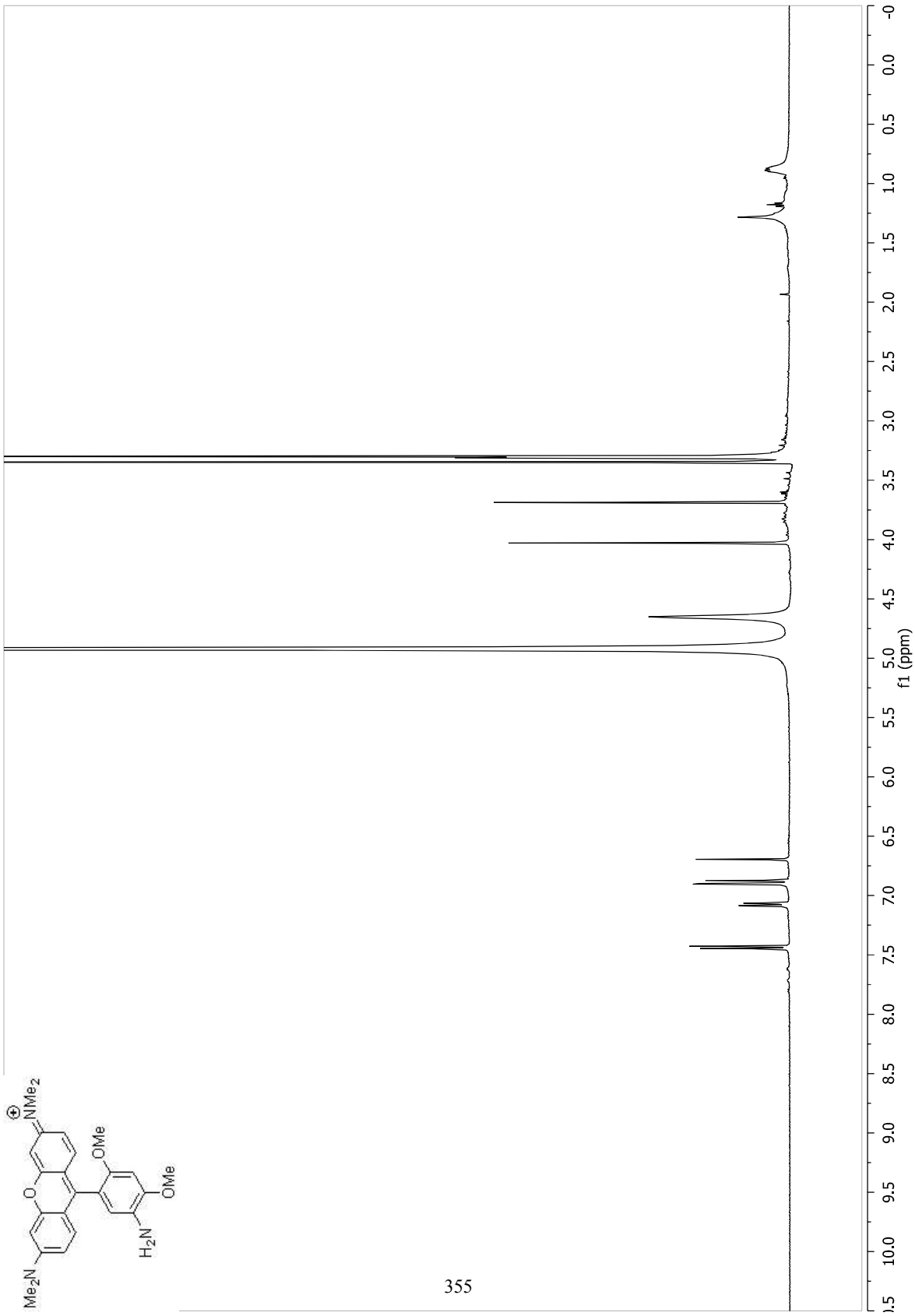
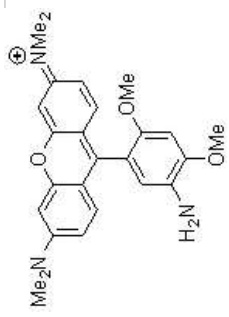
353

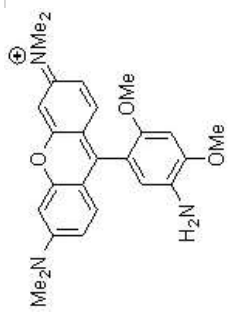




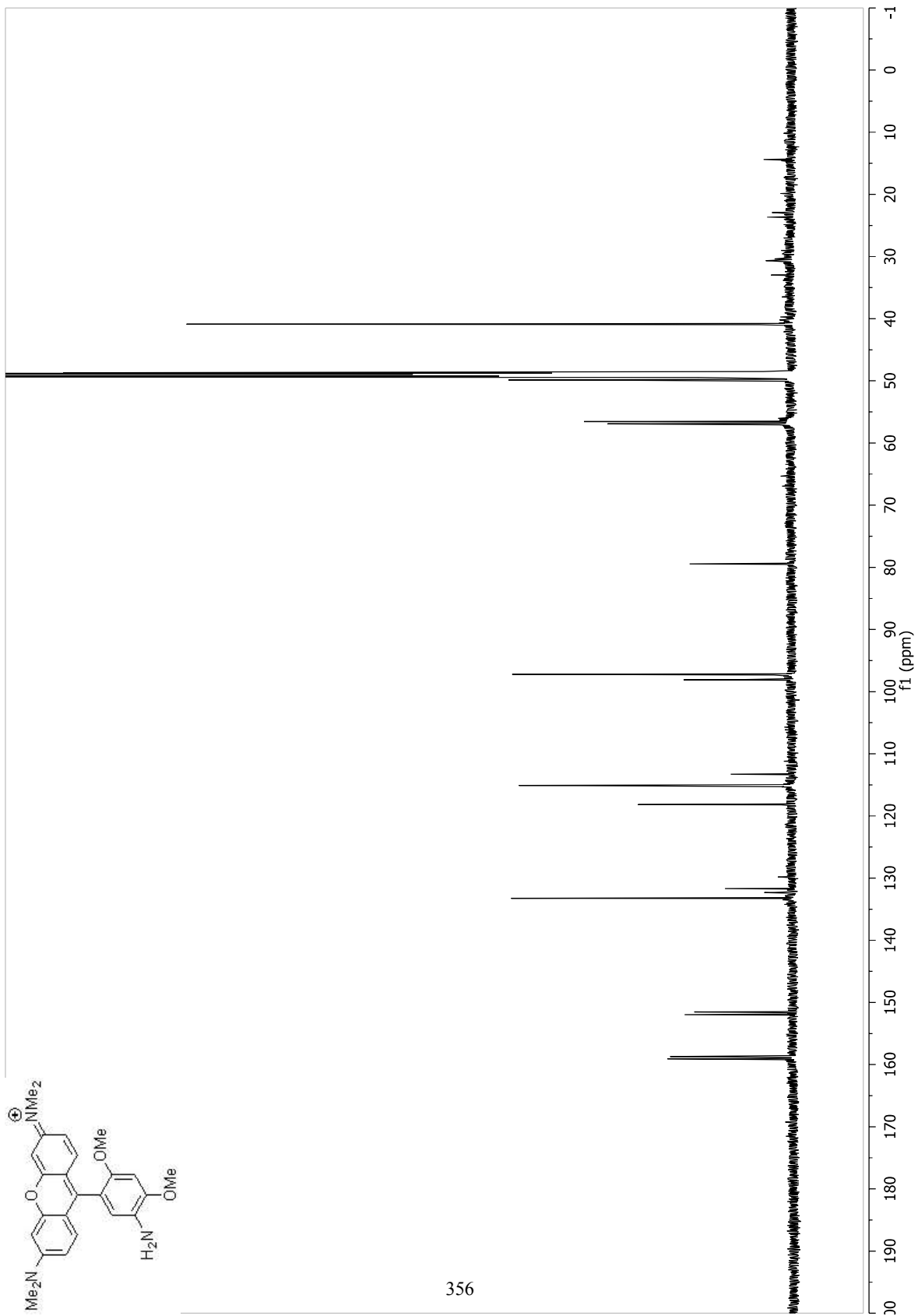
354

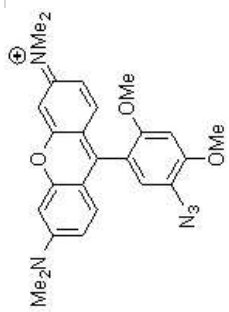




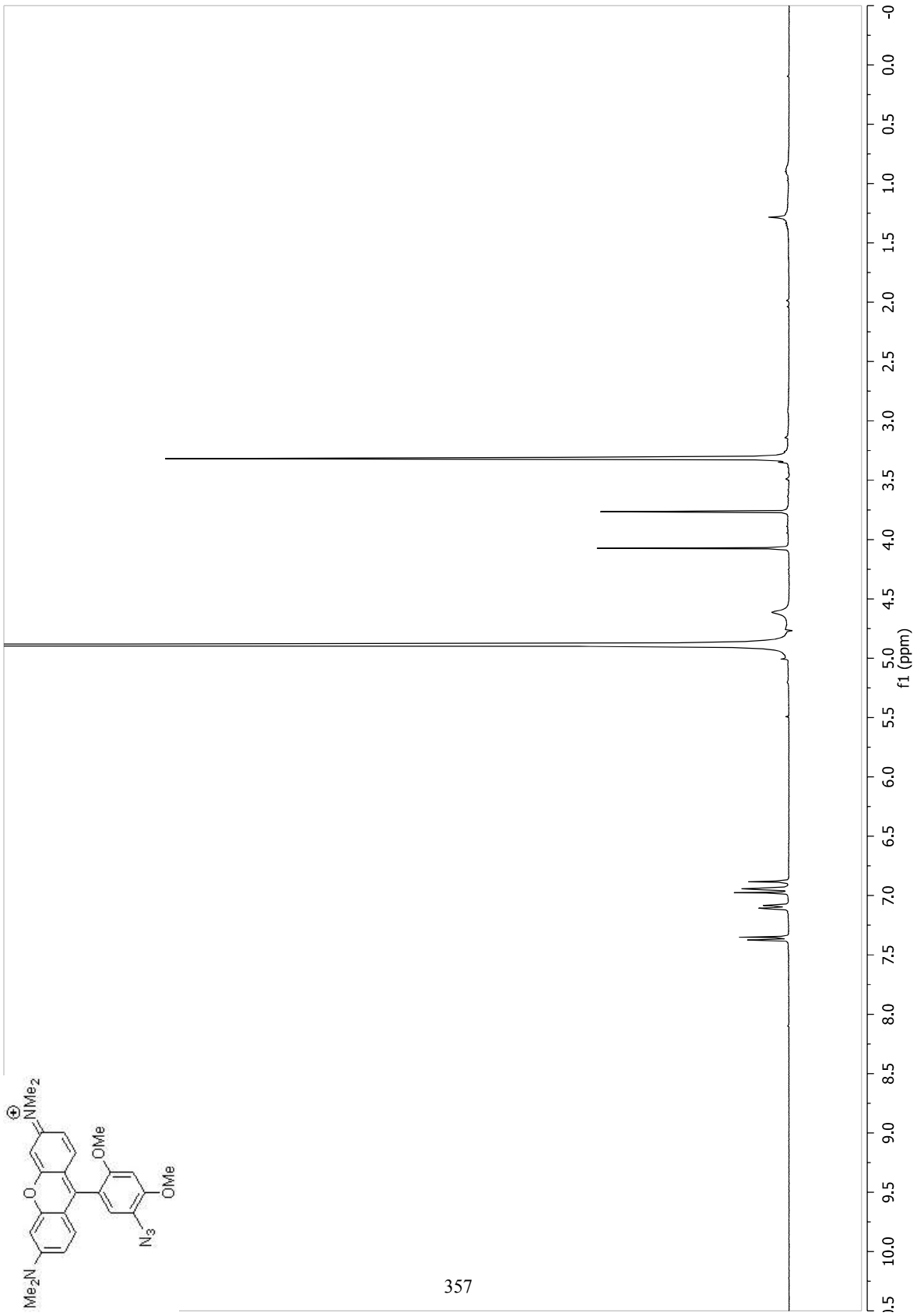


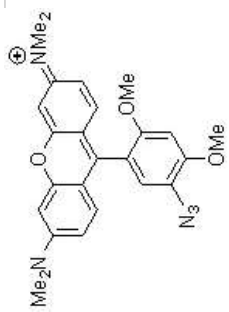
356



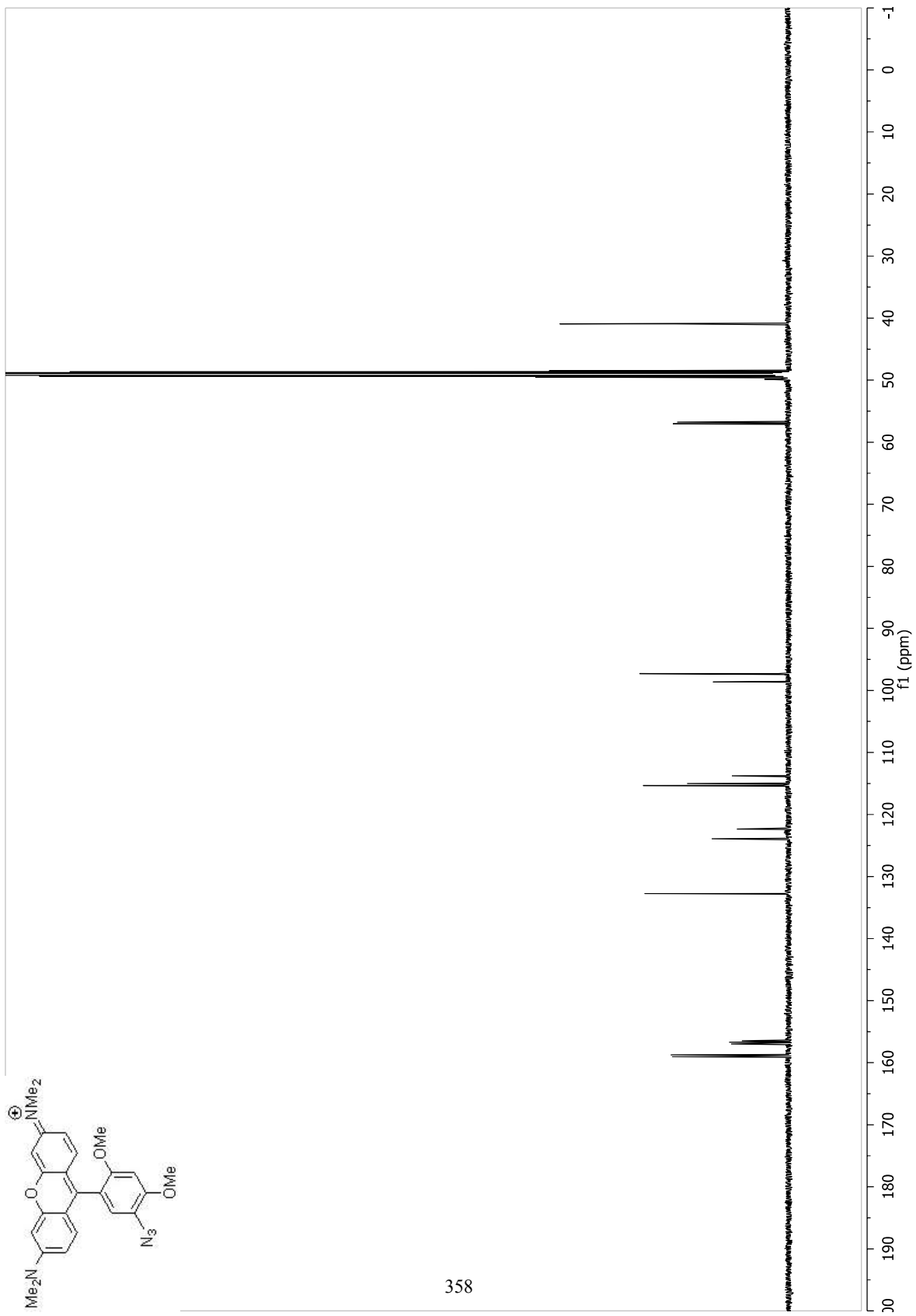


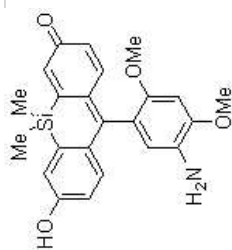
357



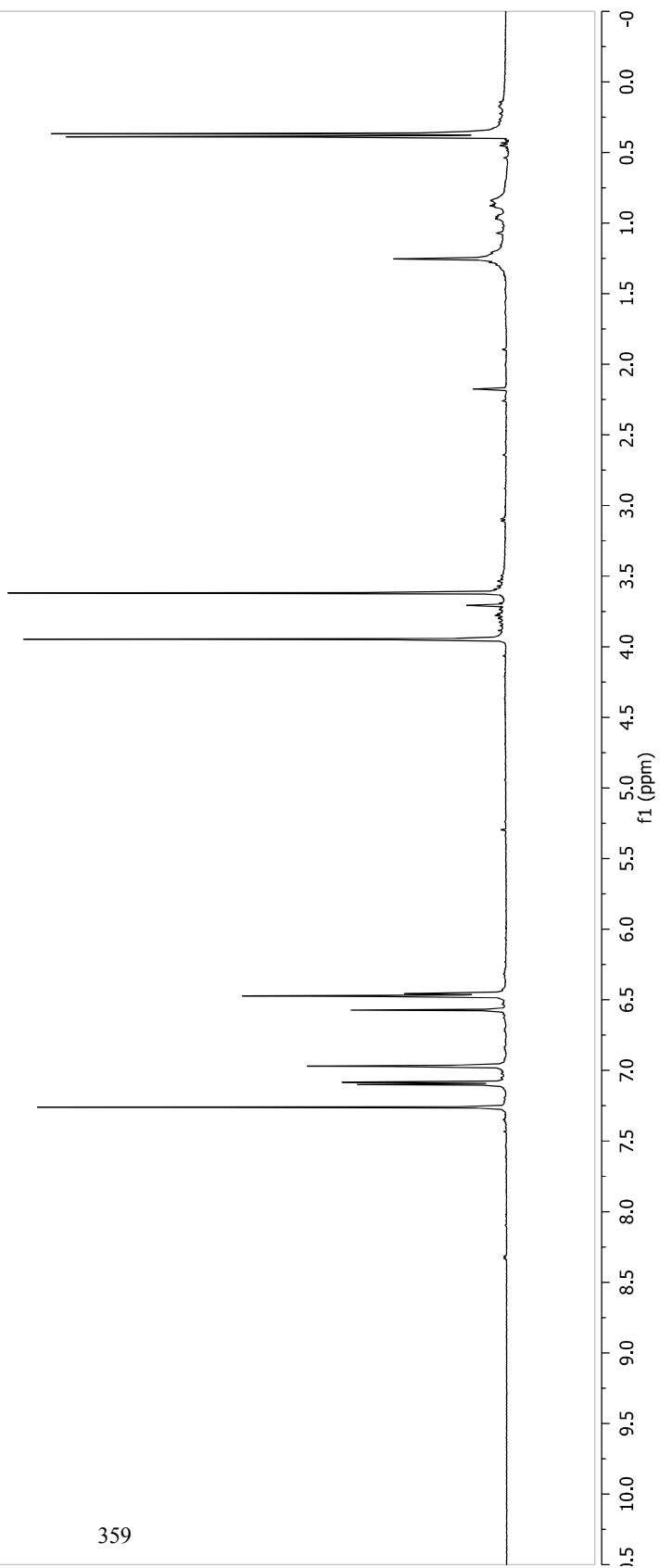


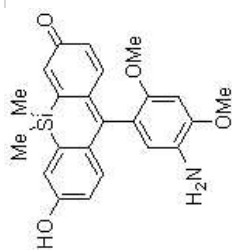
358



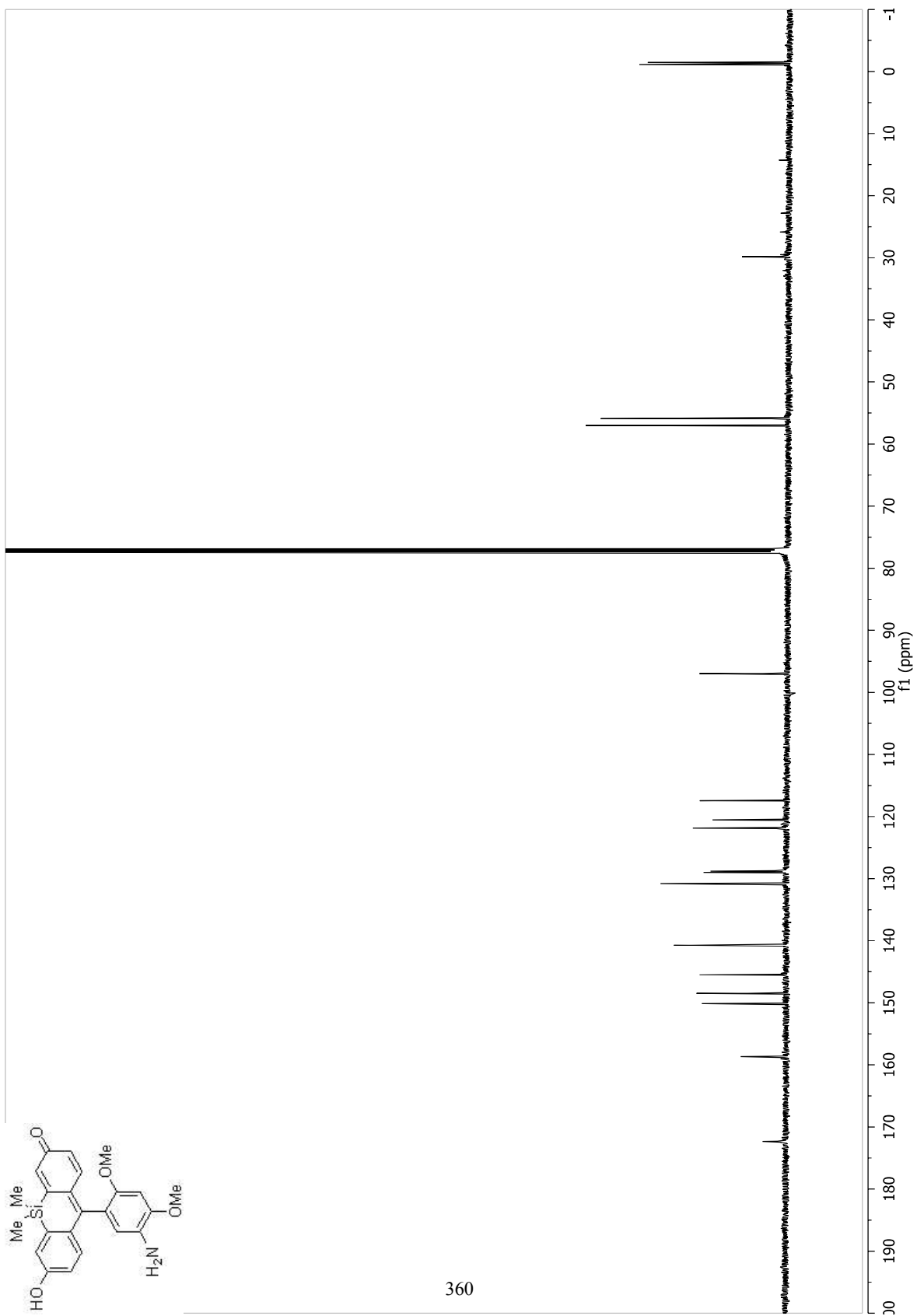


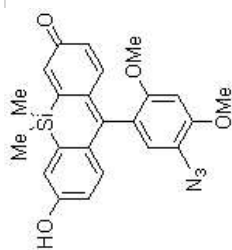
359



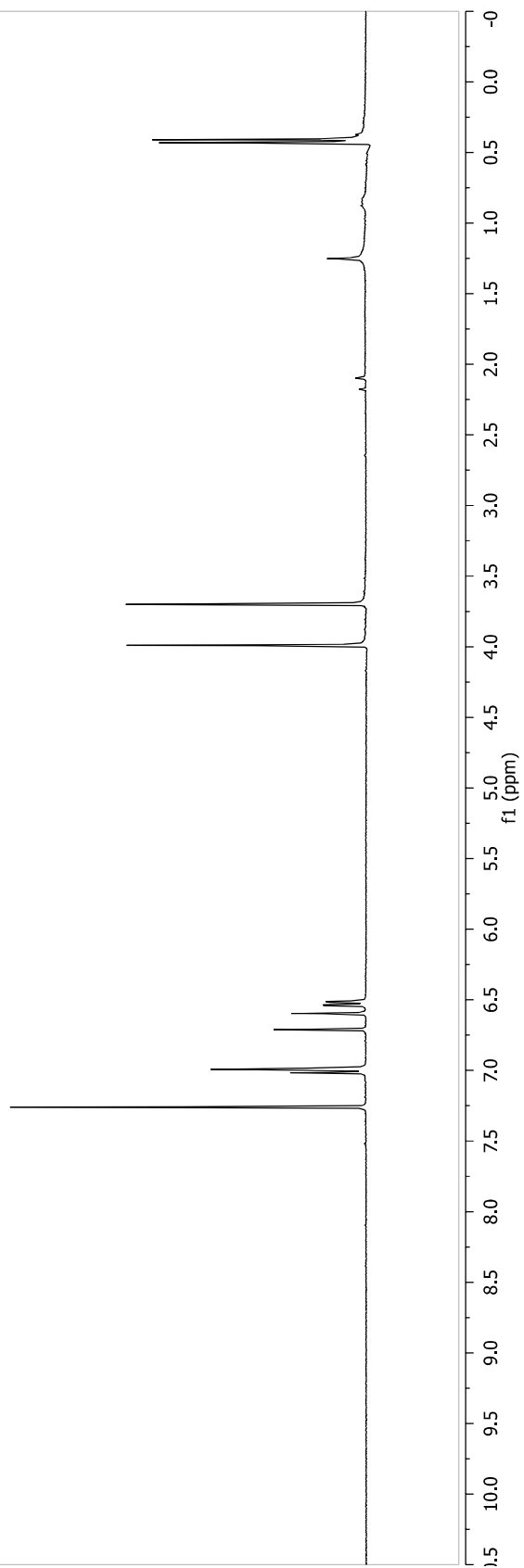


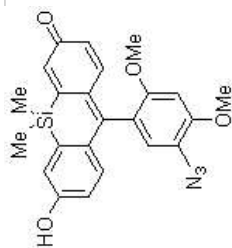
360



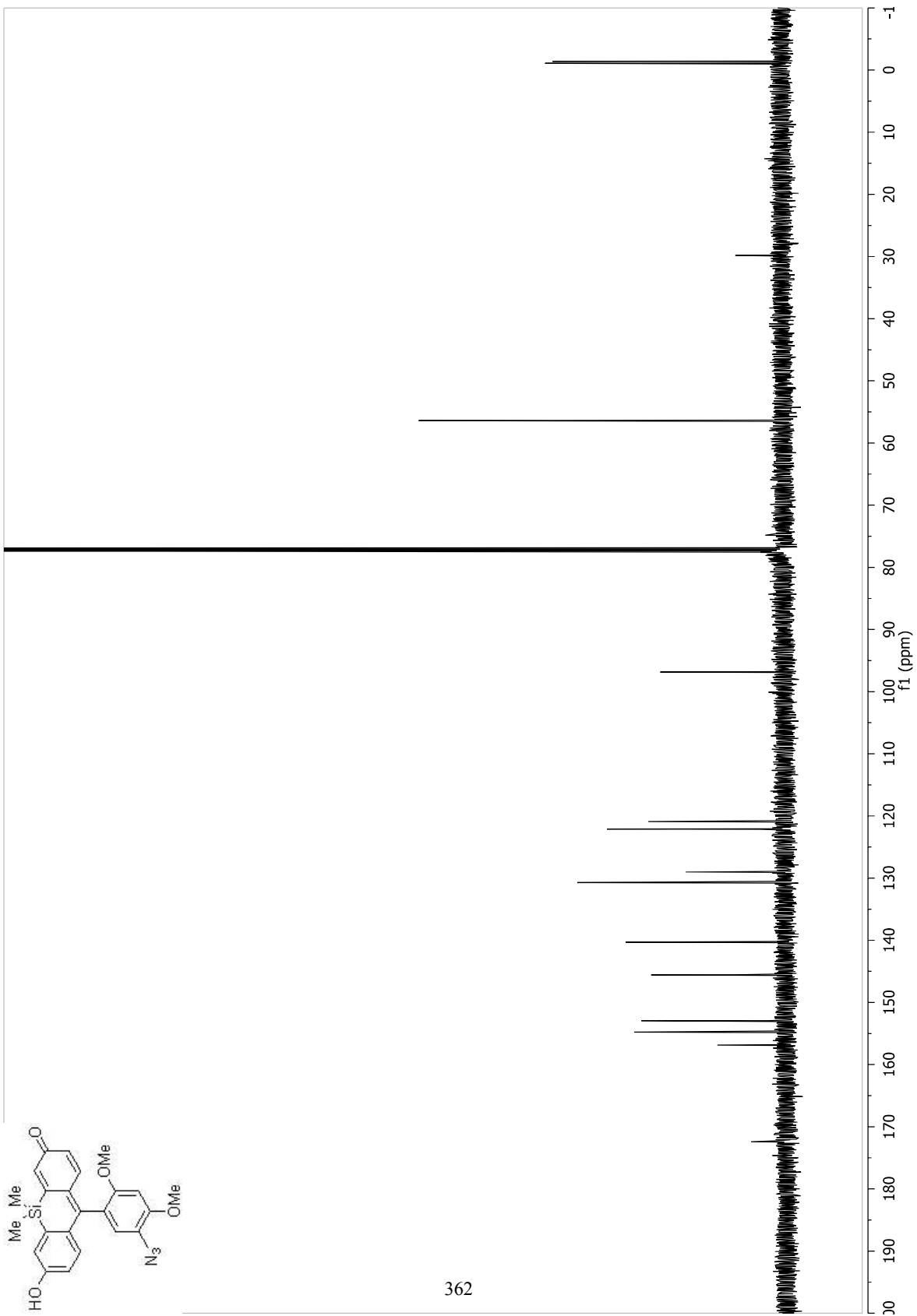


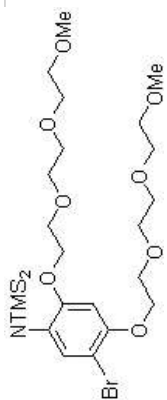
361



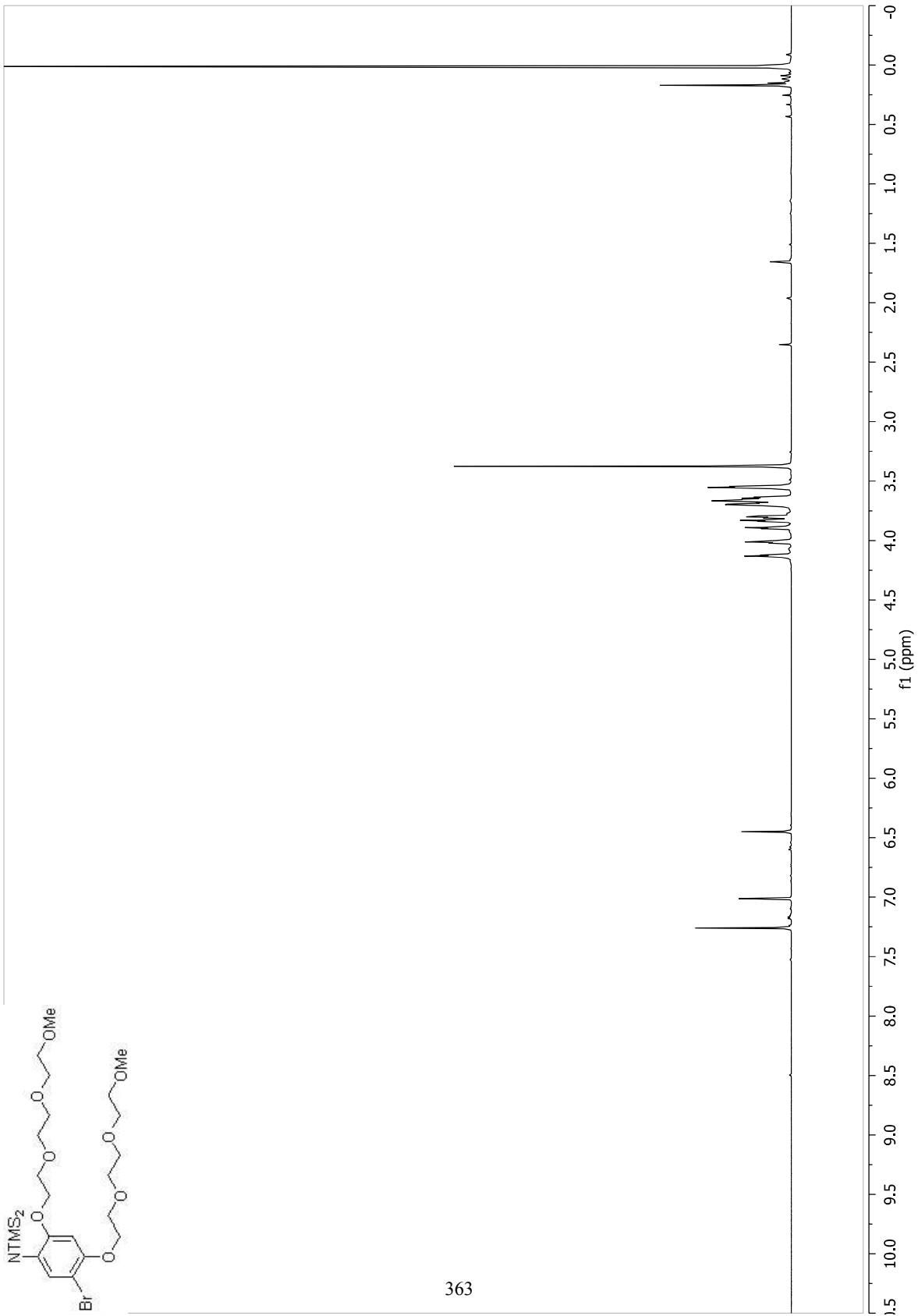


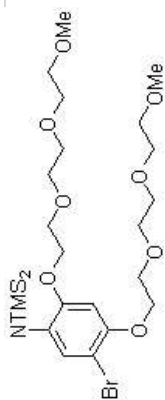
362



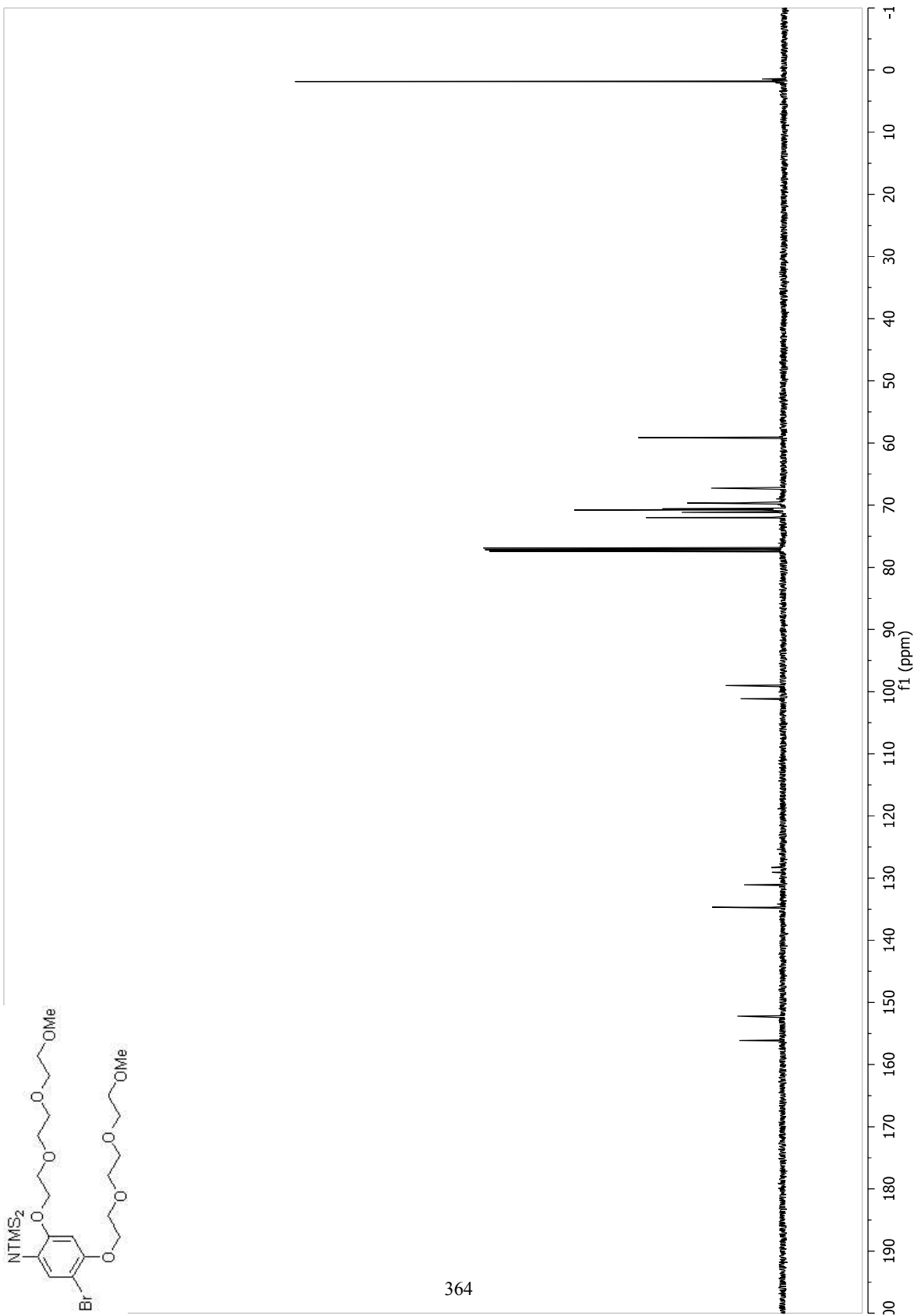


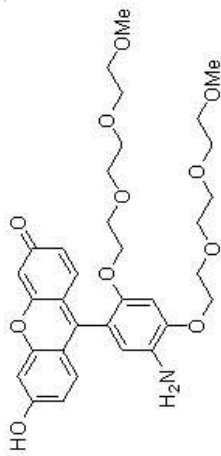
363



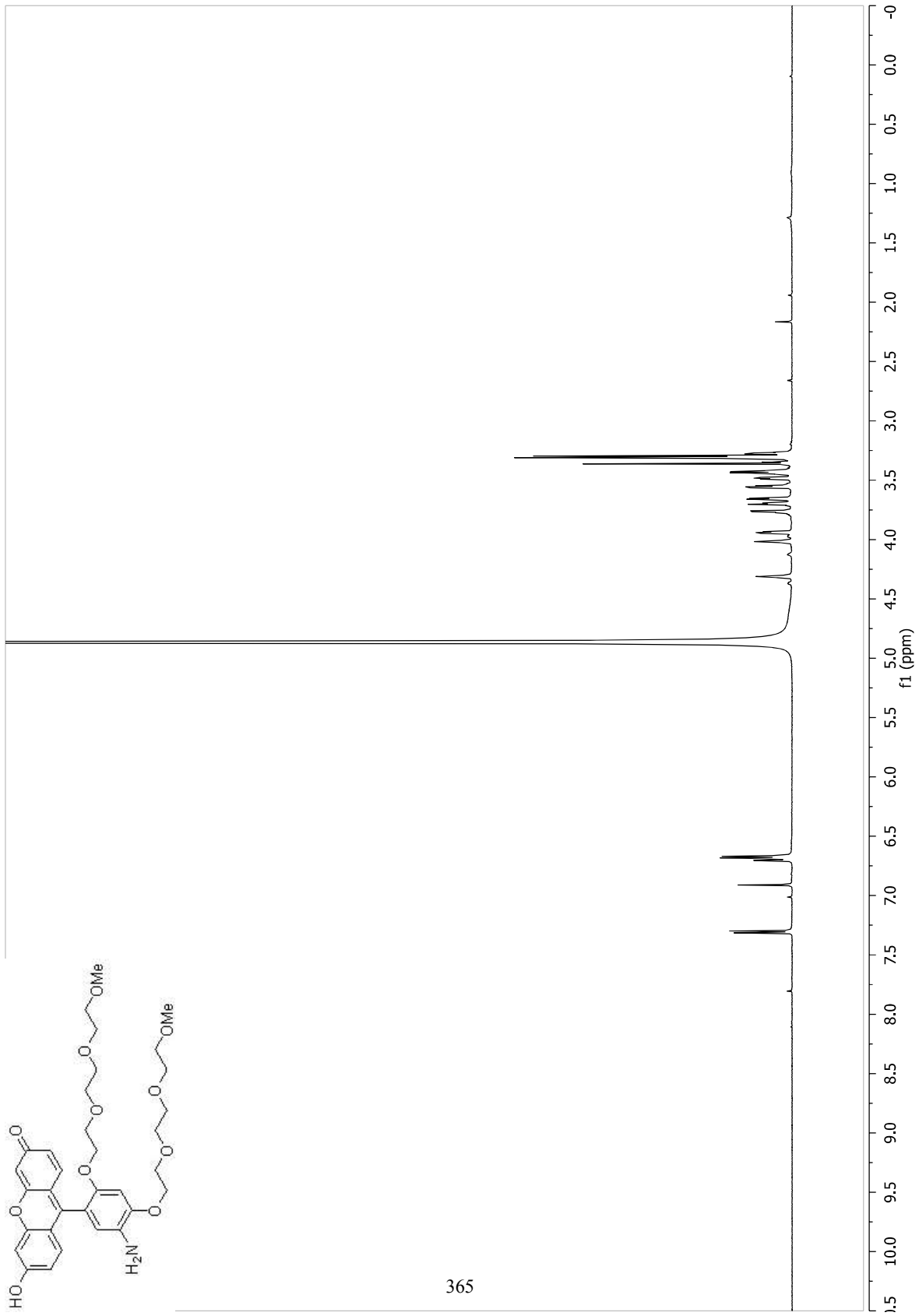


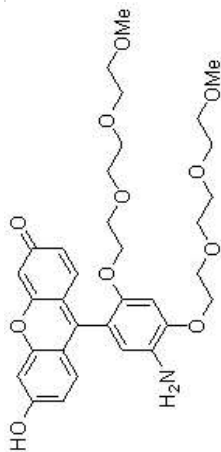
364



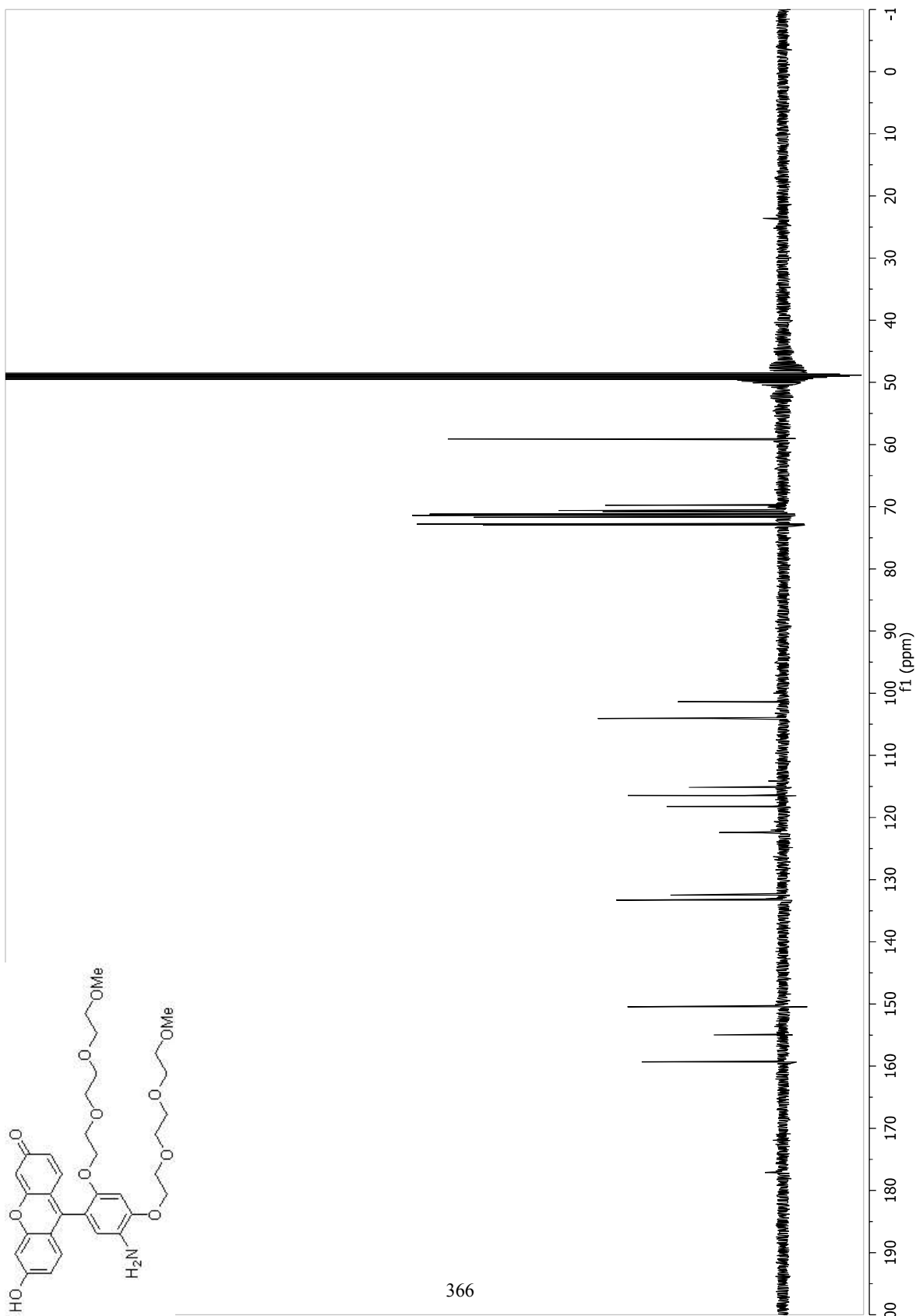


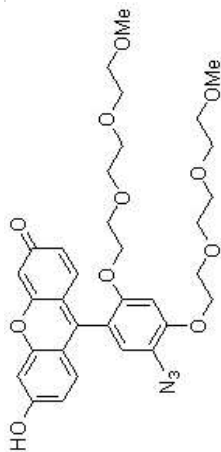
365



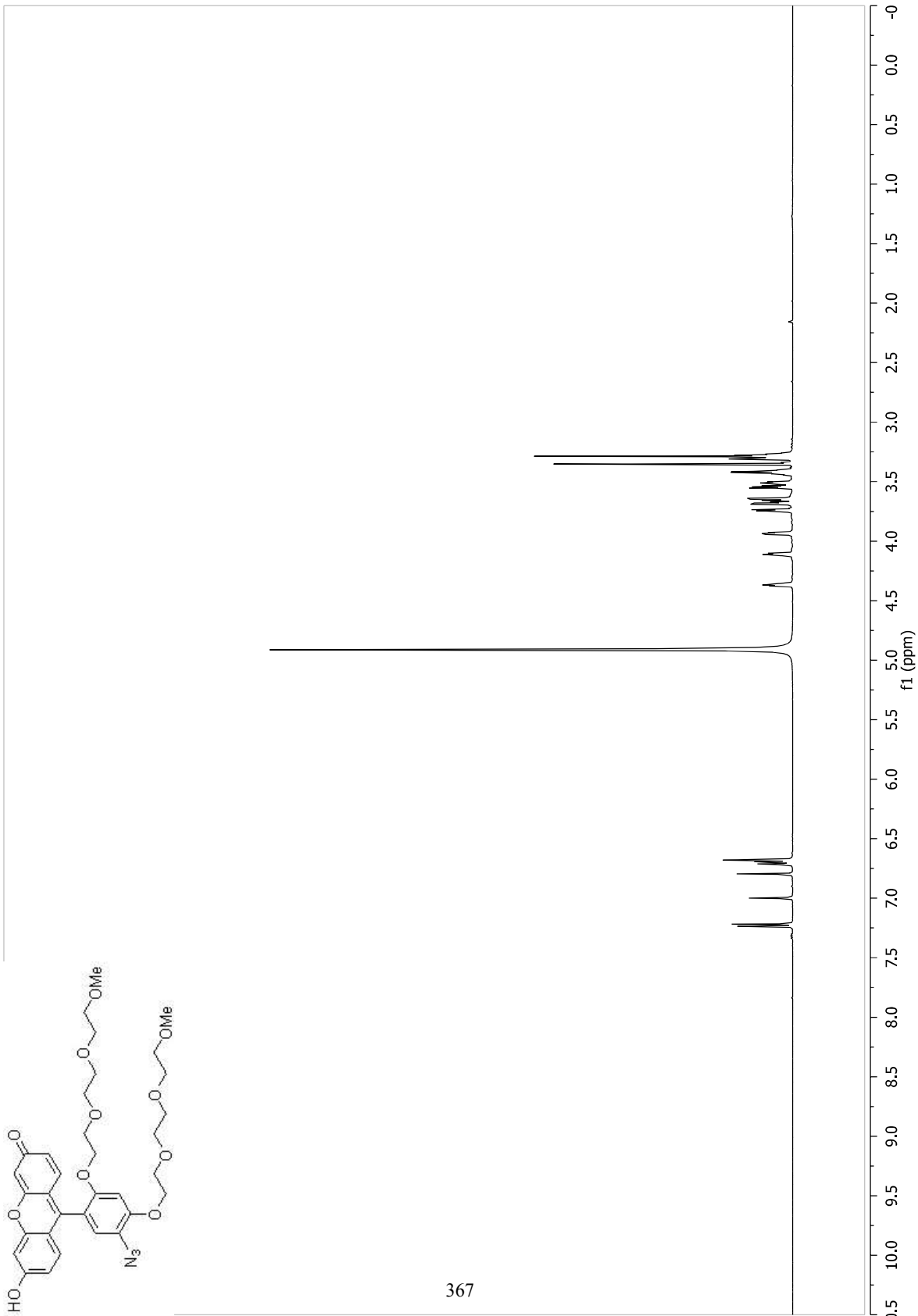


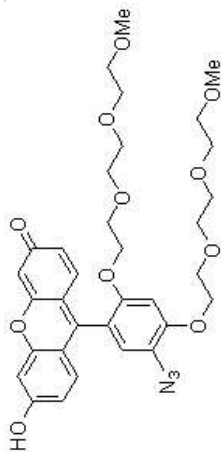
366



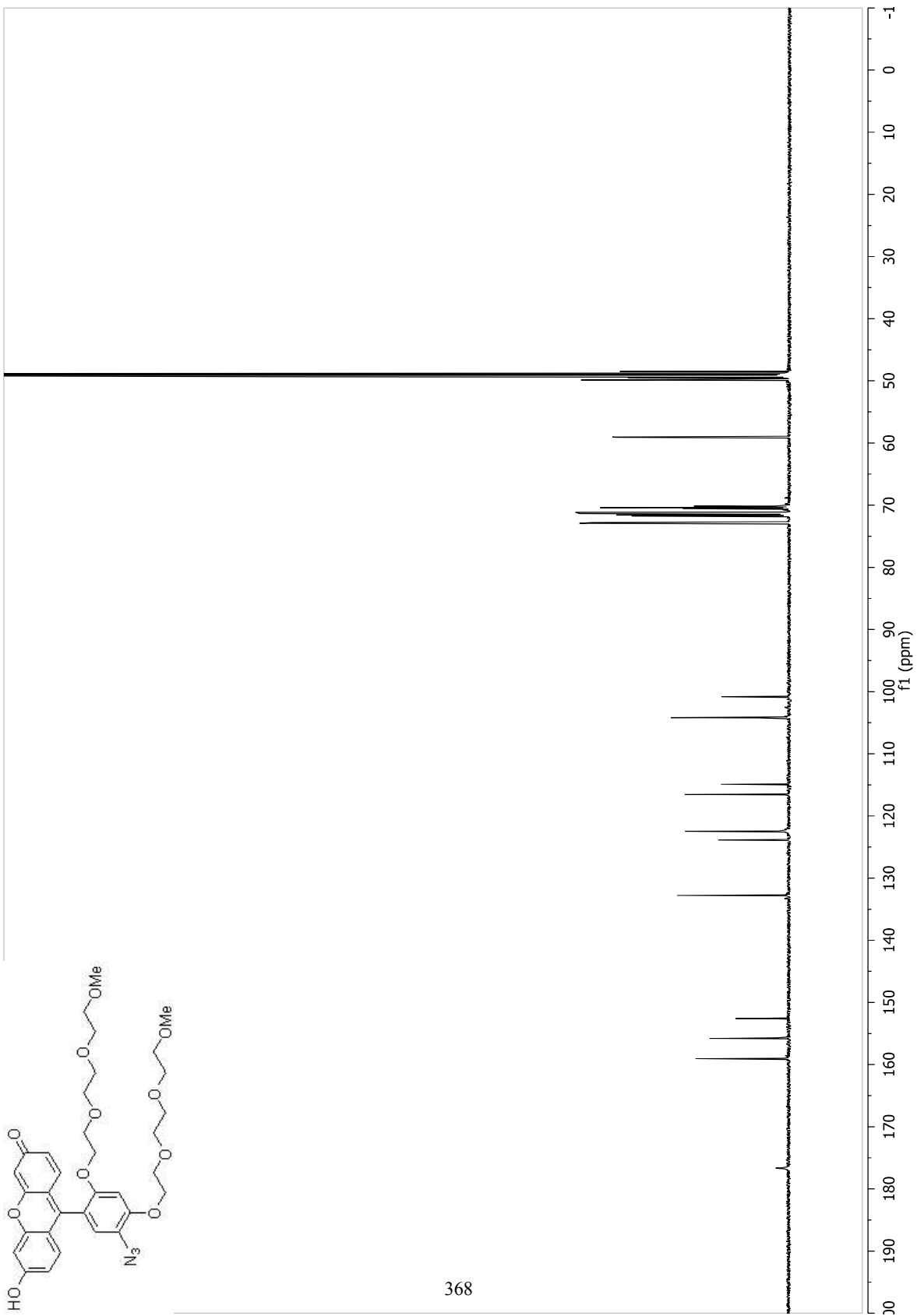


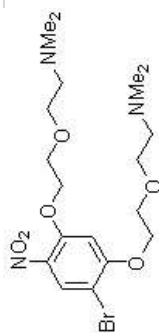
367



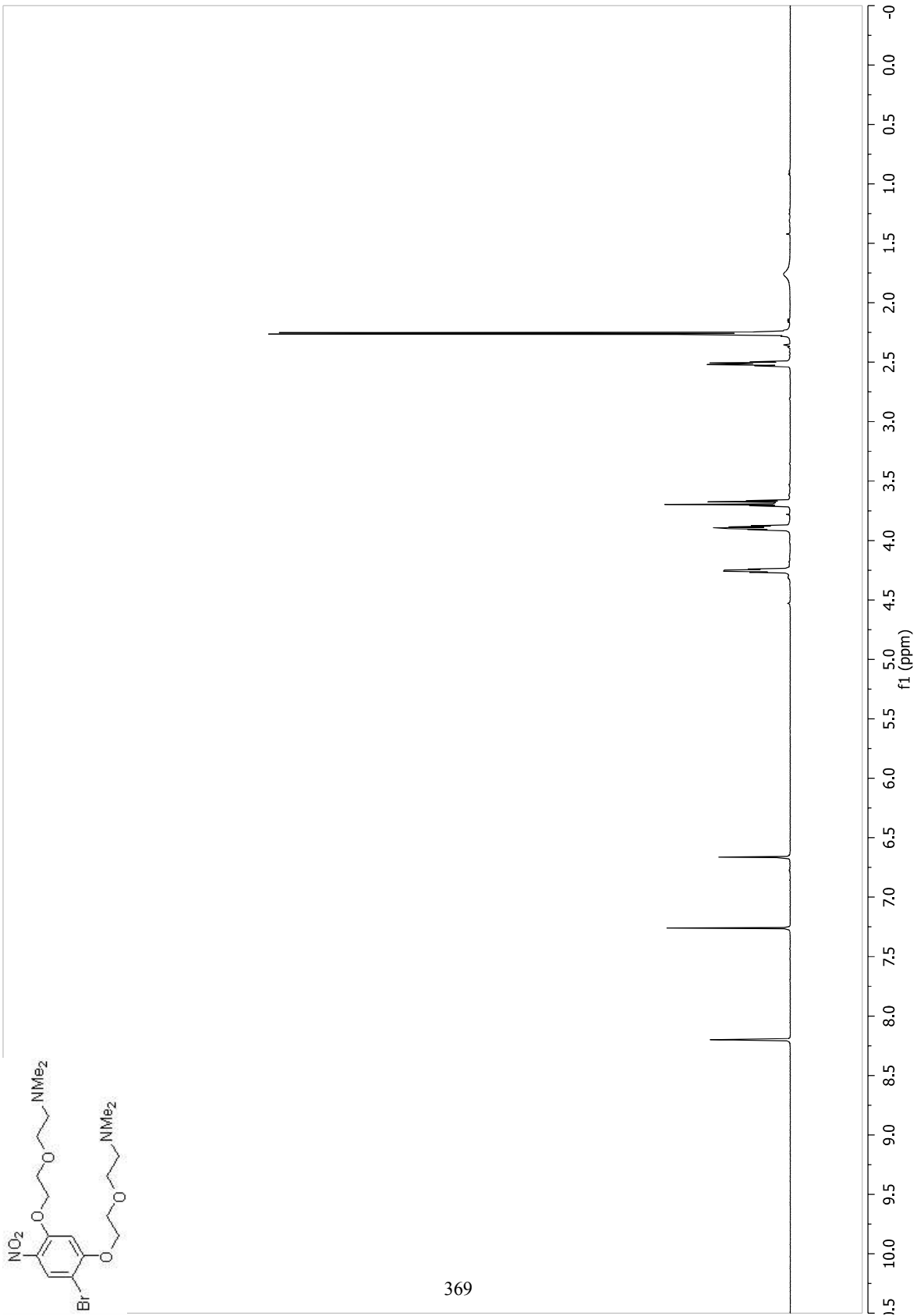


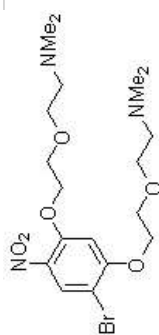
368



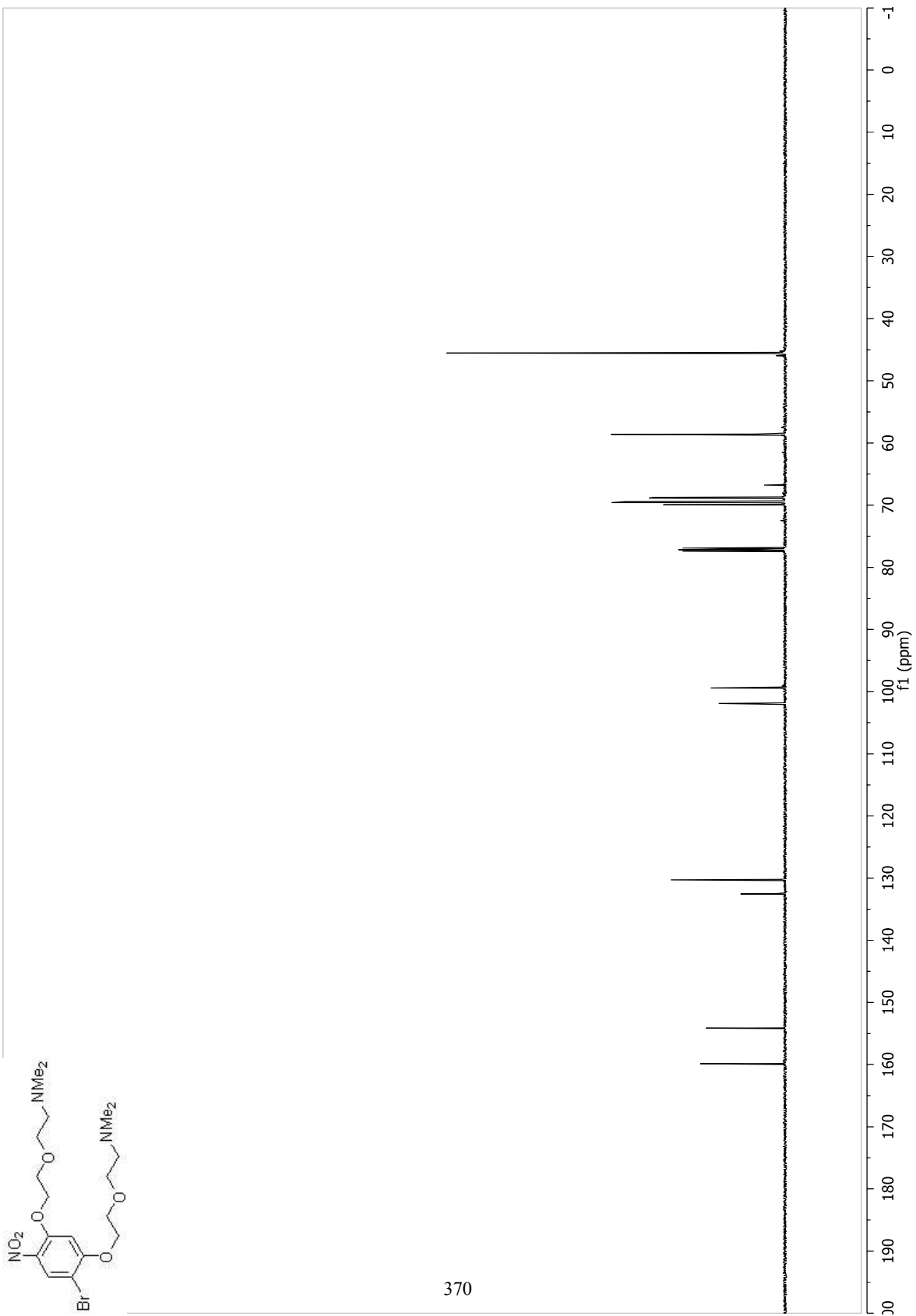


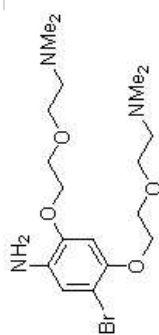
369



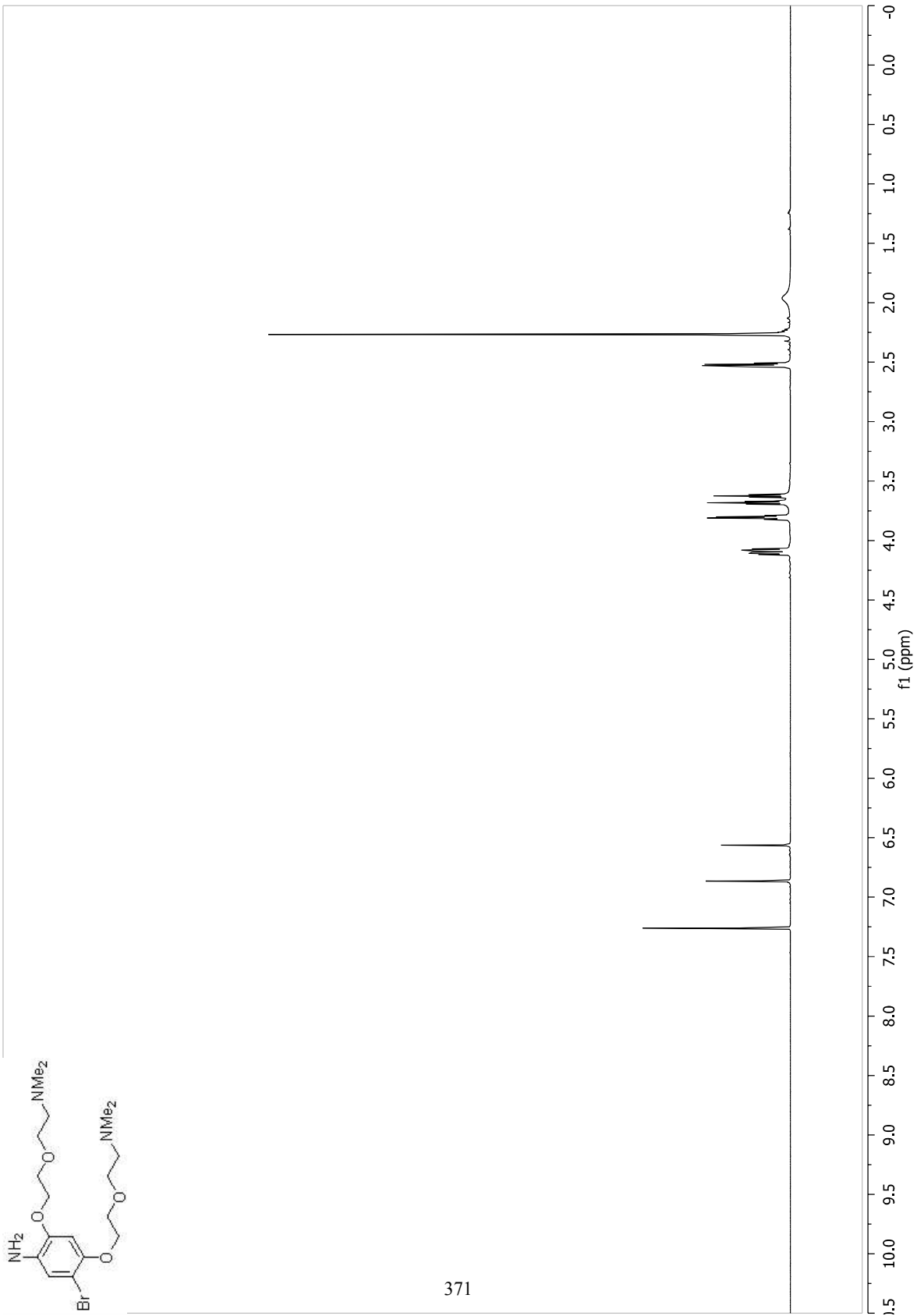


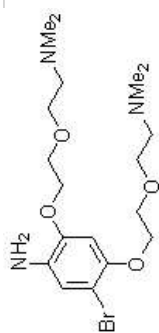
370



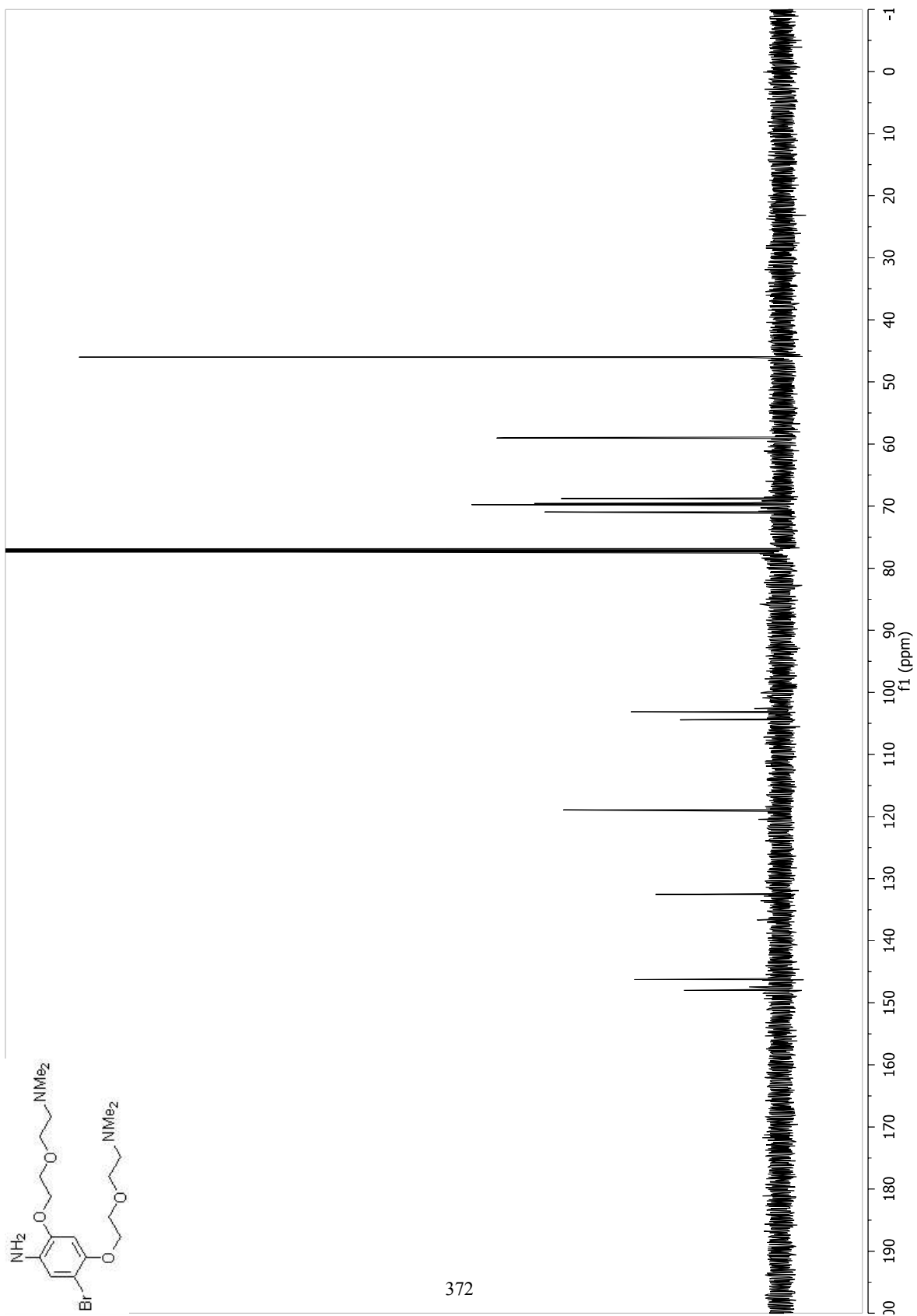


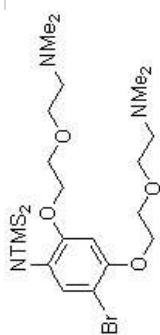
371



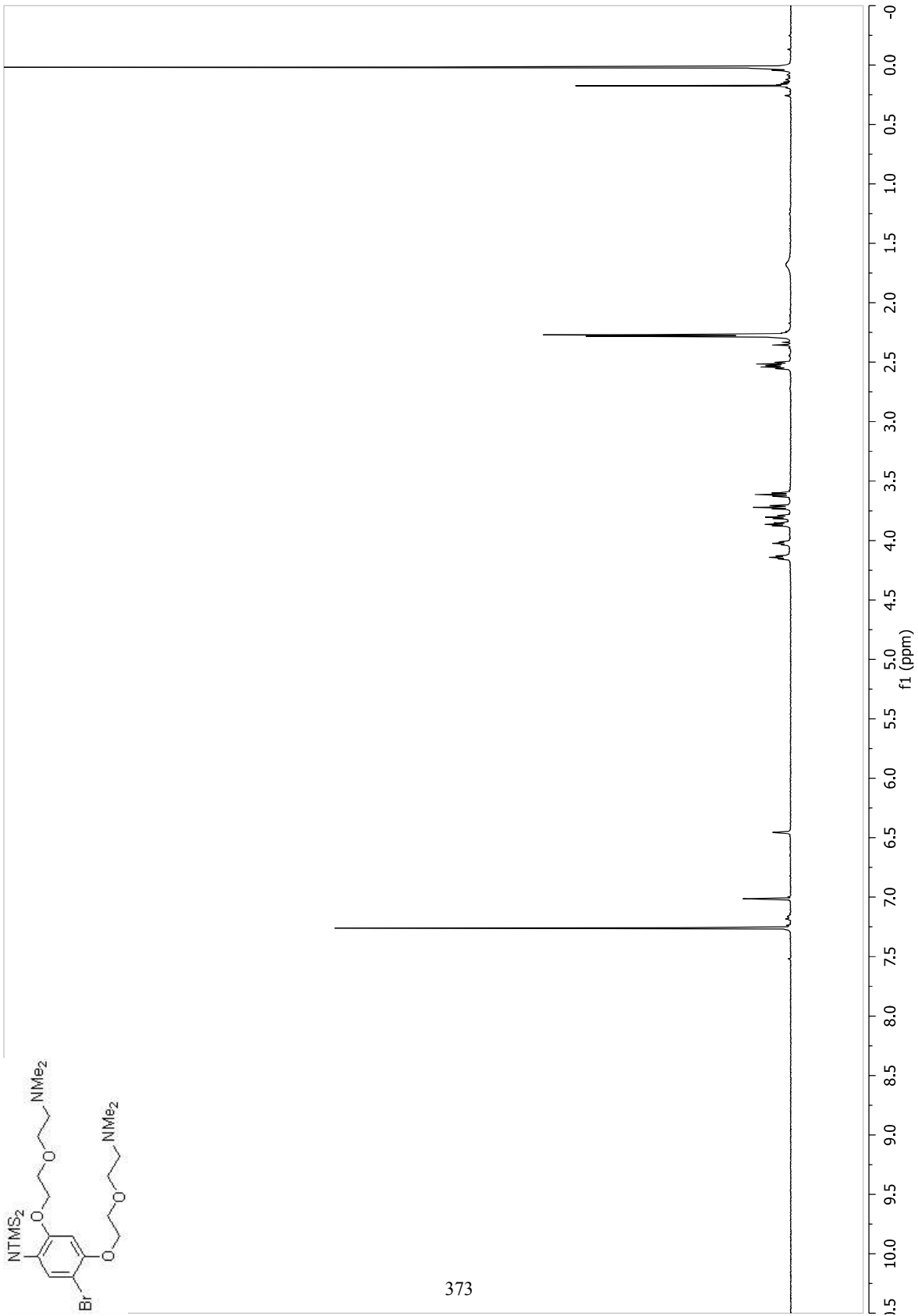


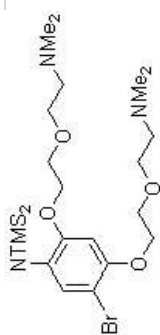
372



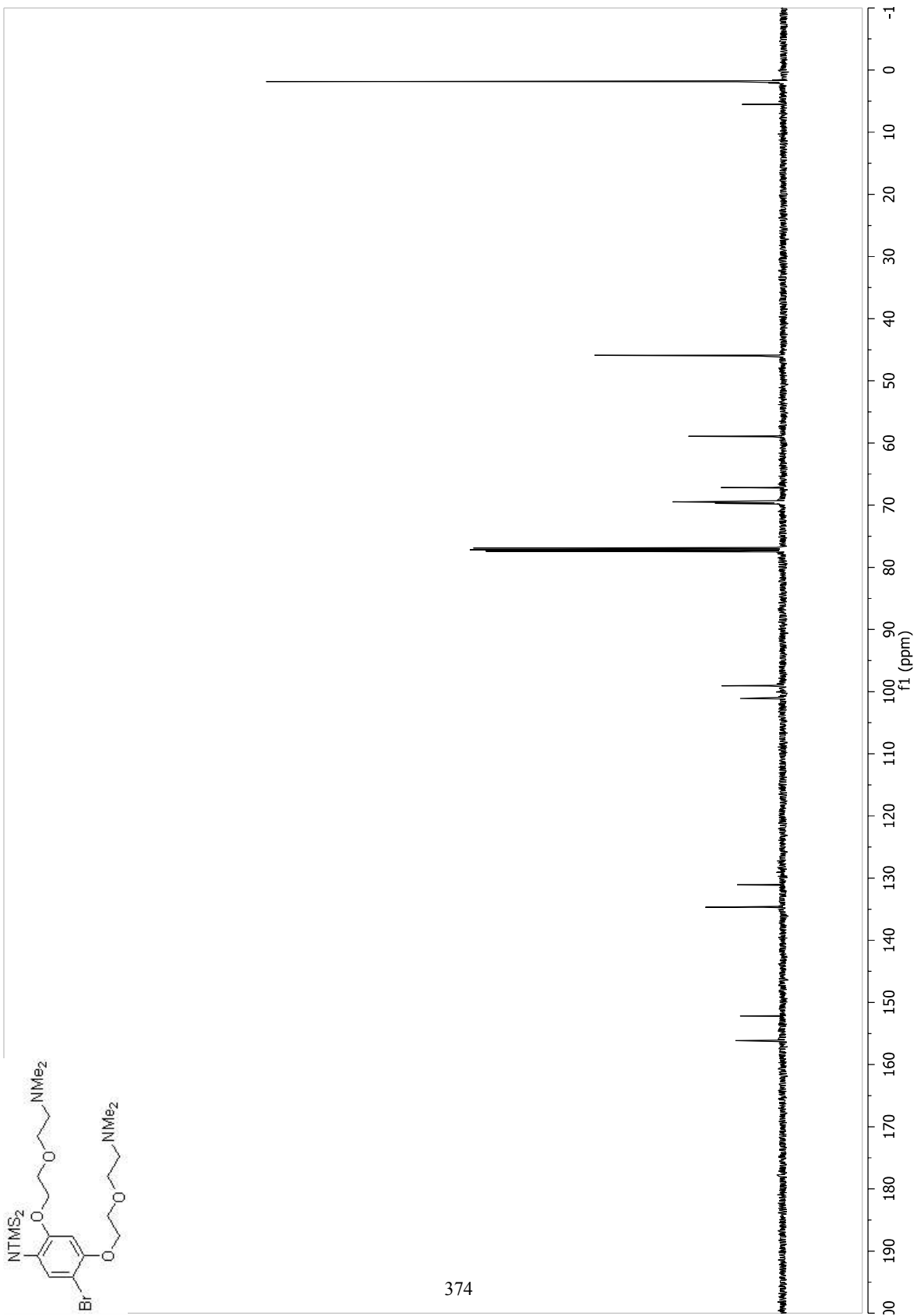


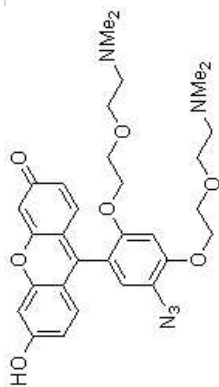
373



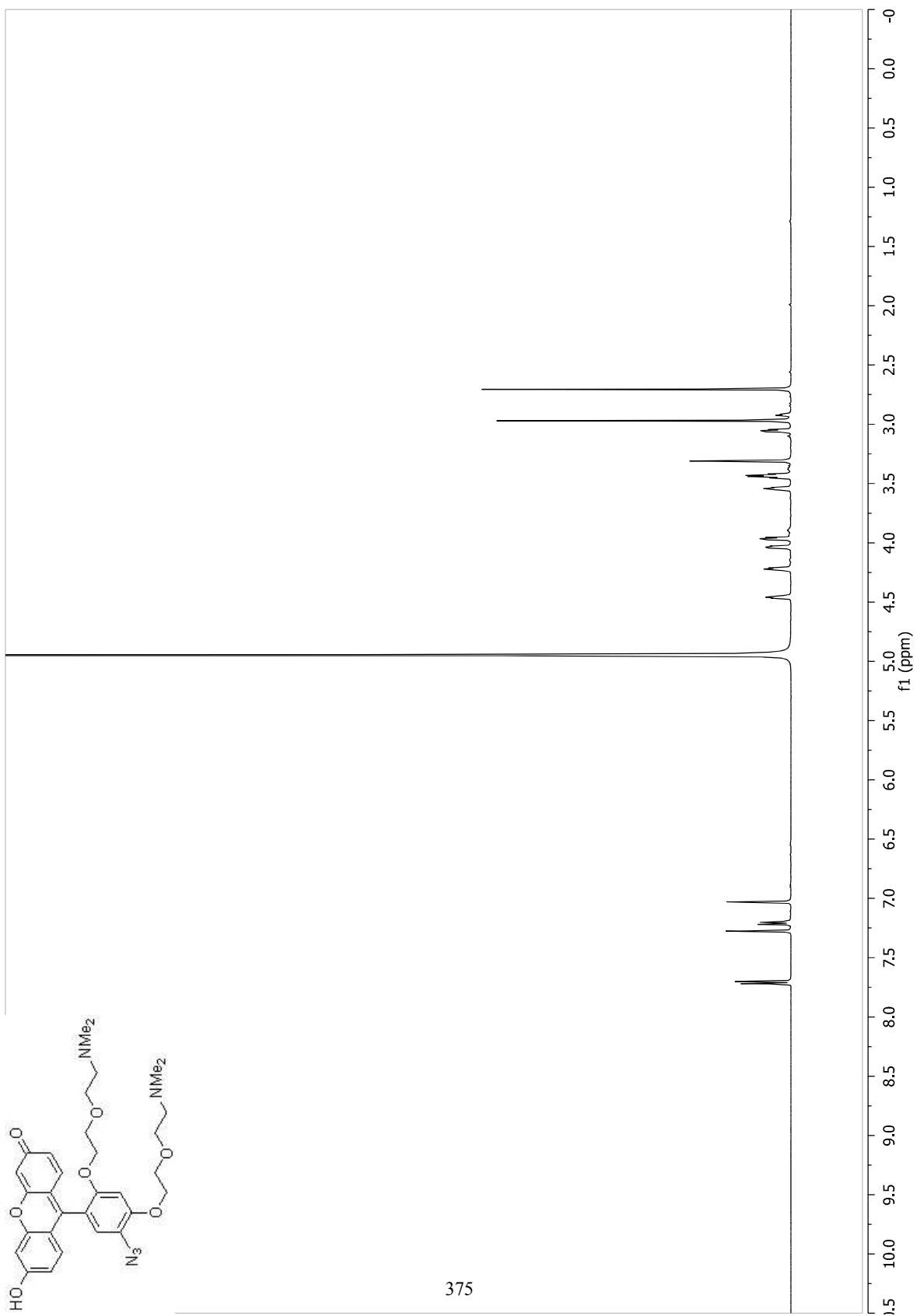


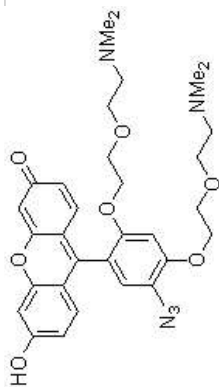
374



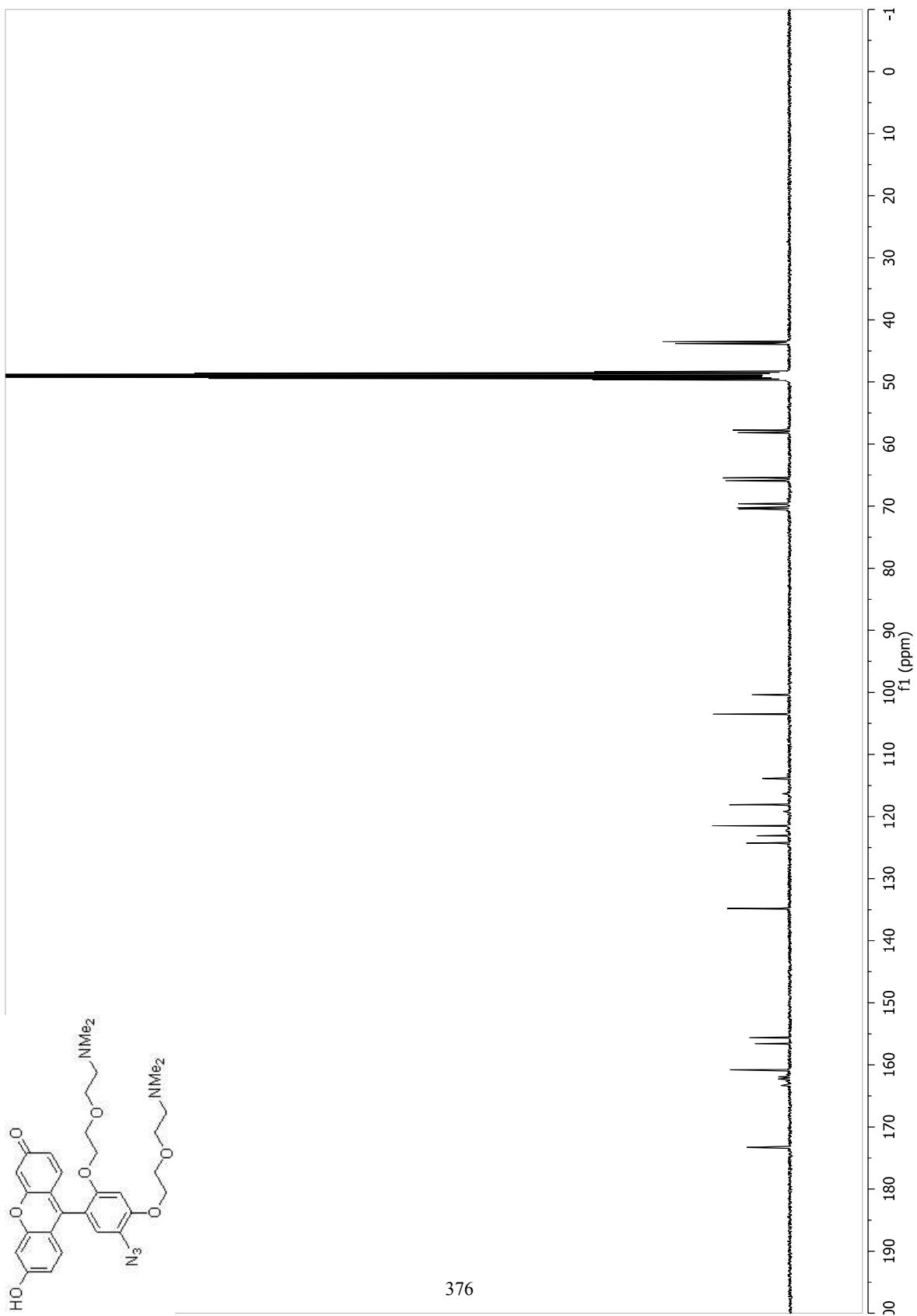


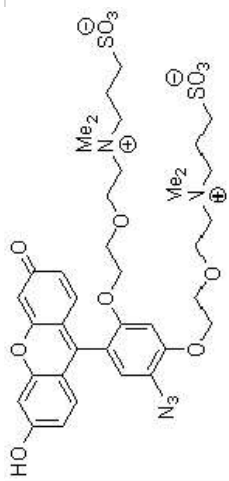
375



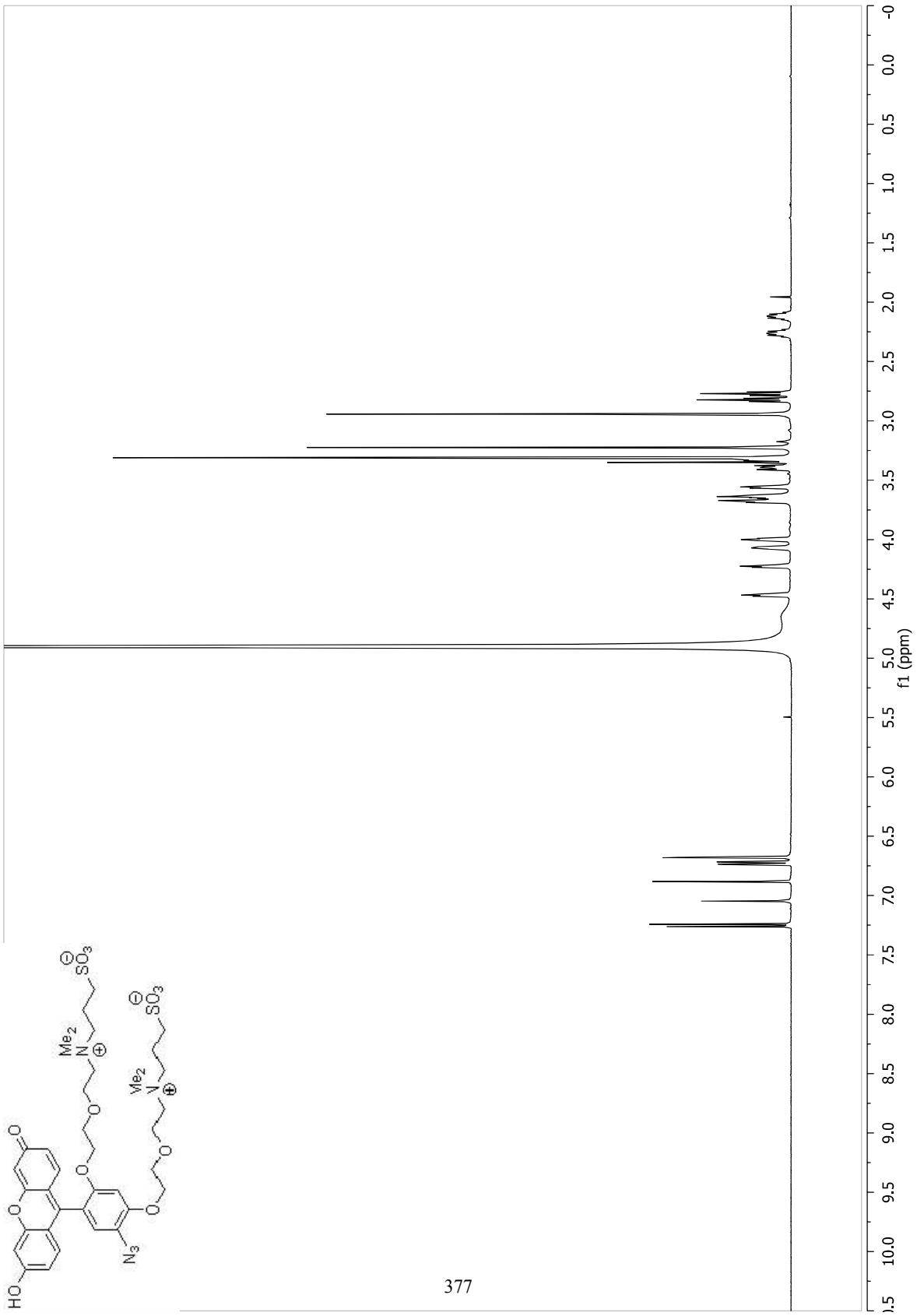


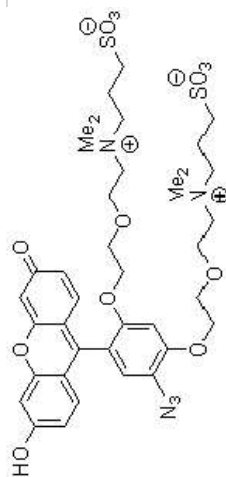
376



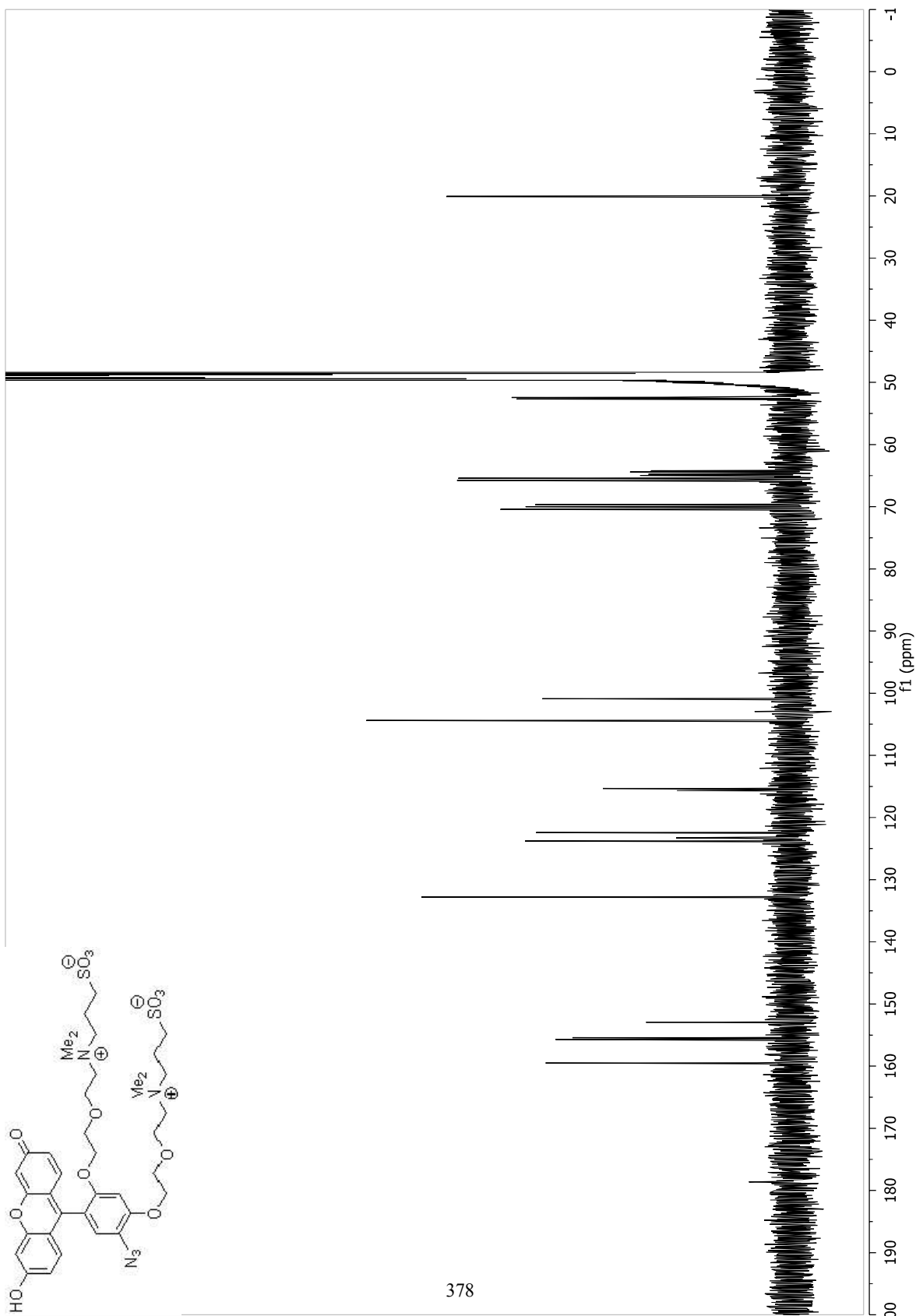


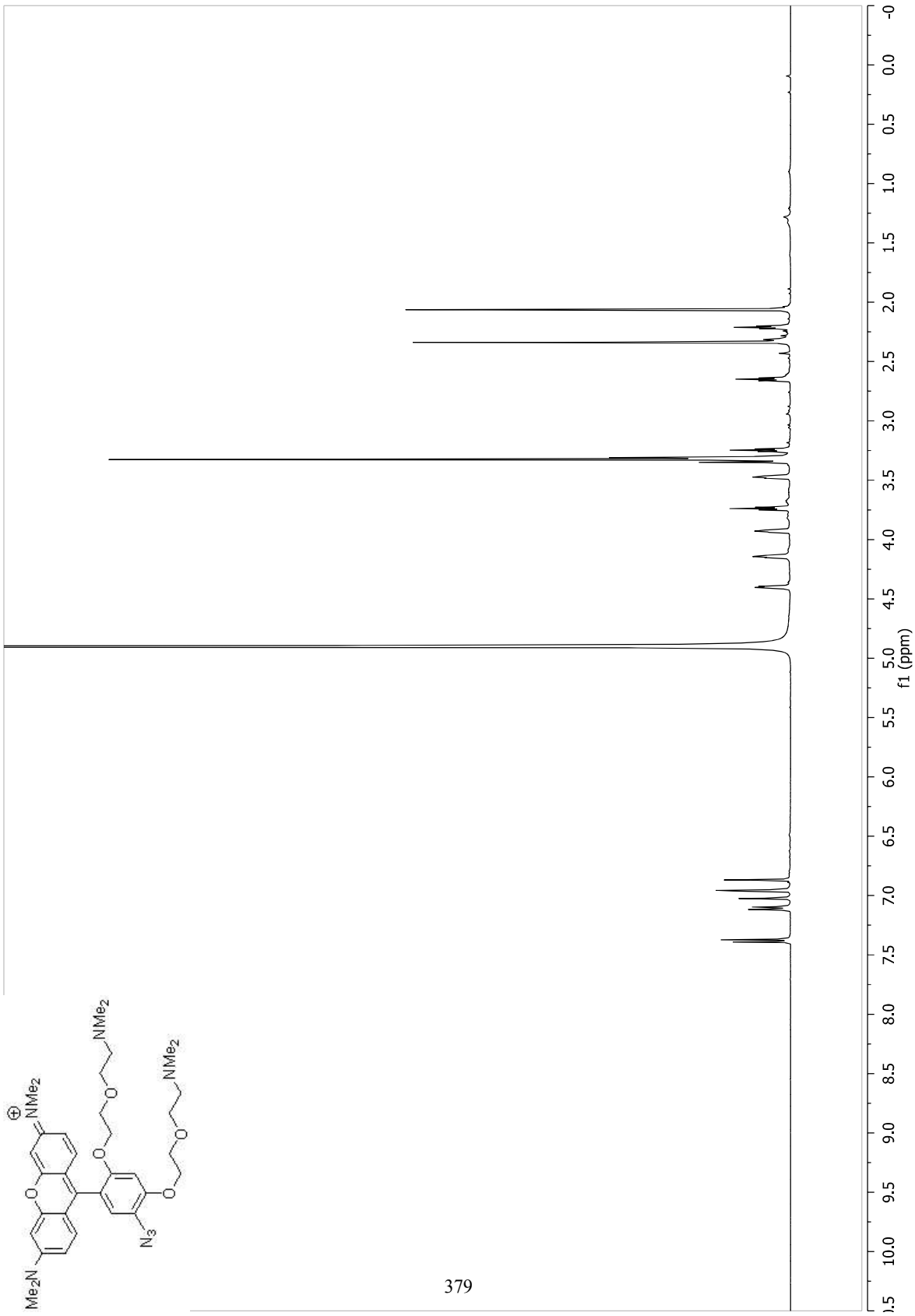
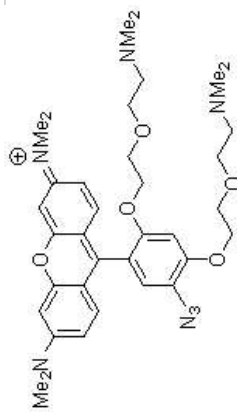
377

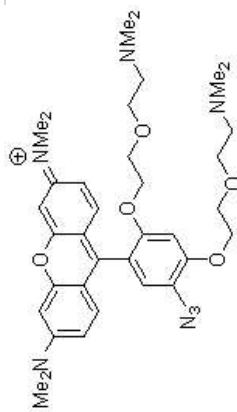




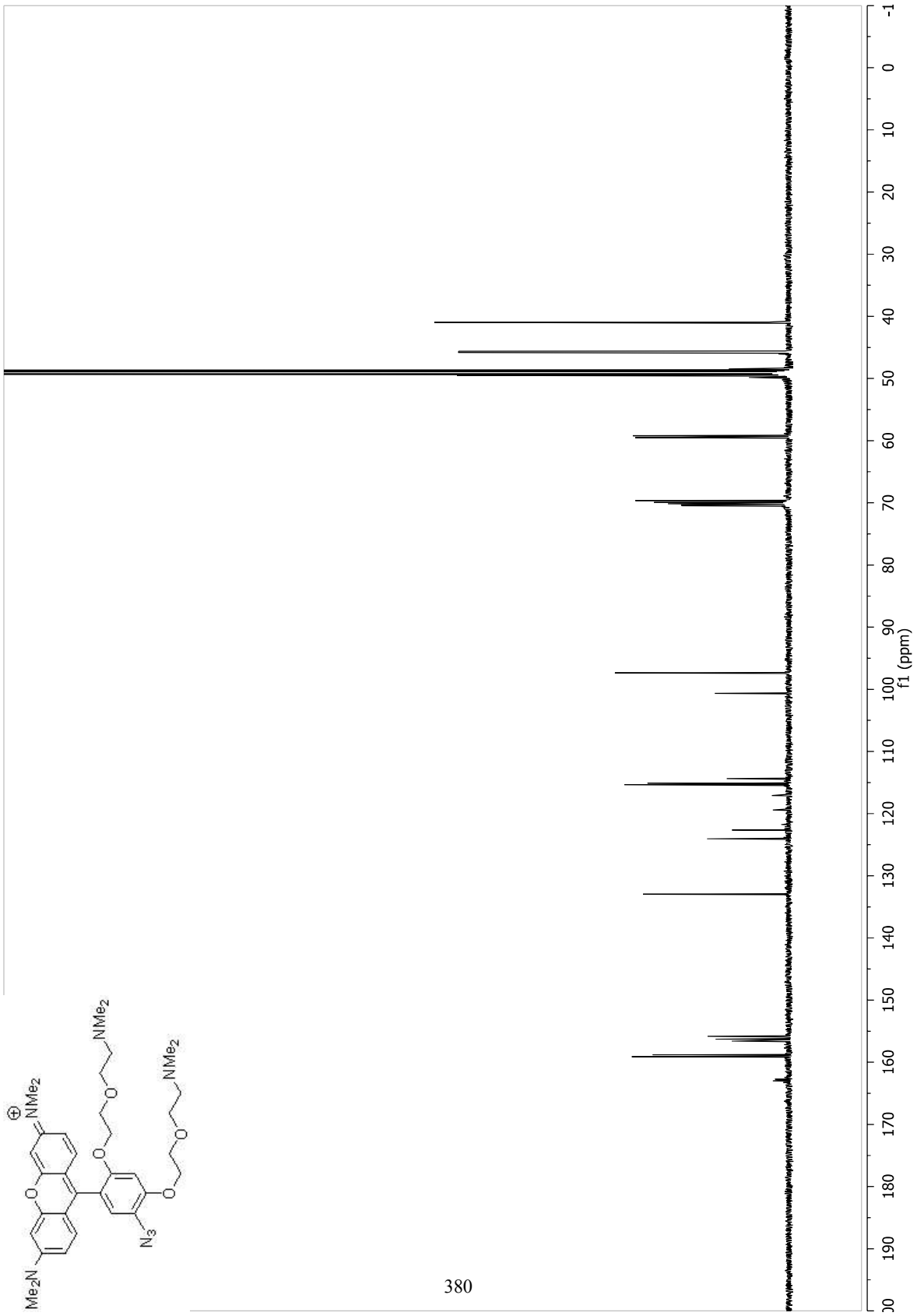
378

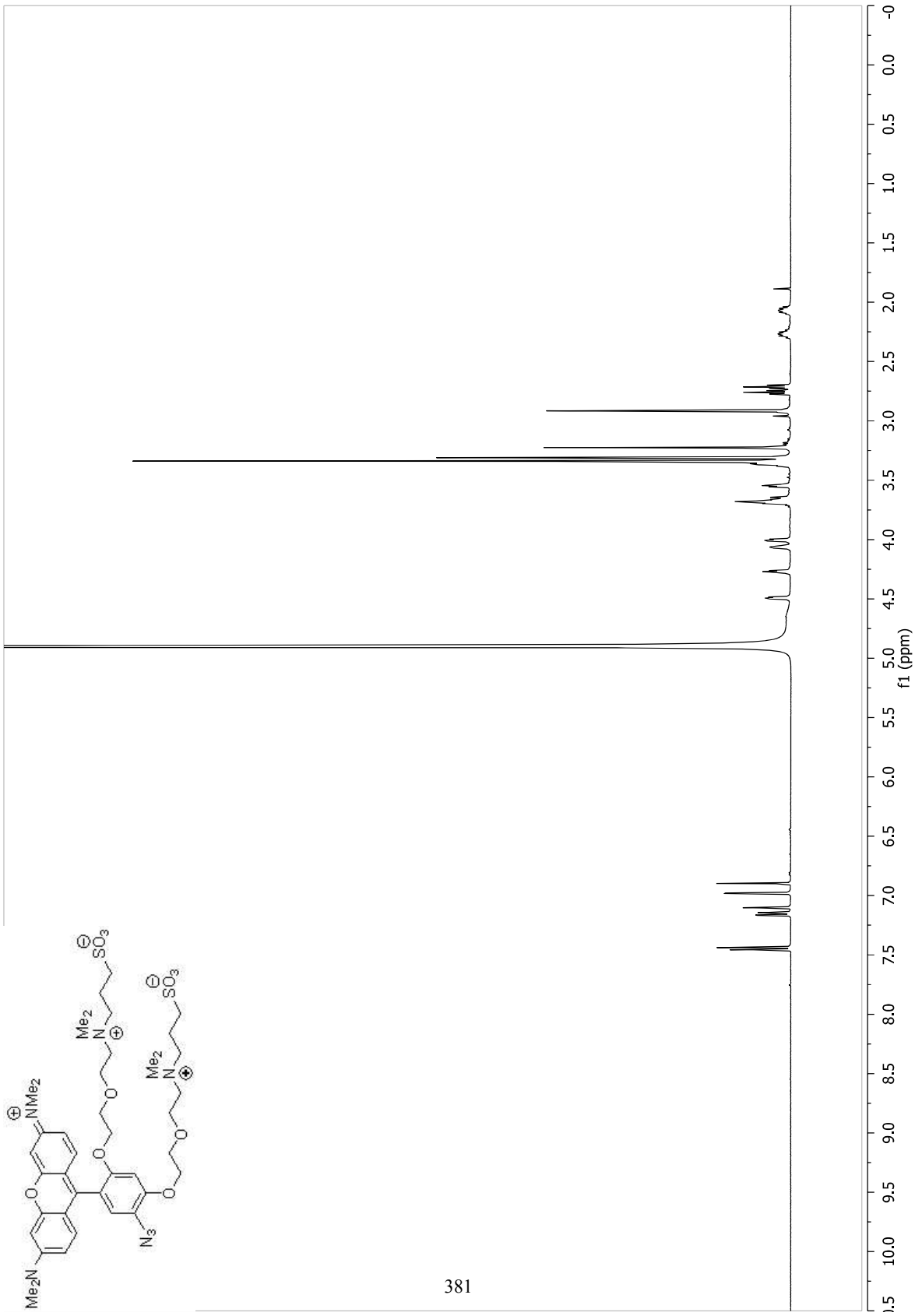


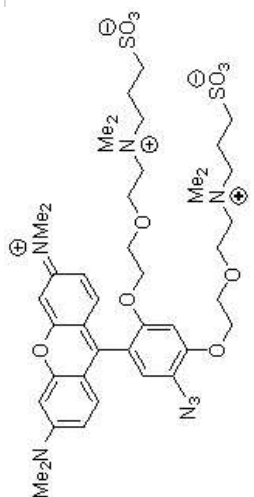




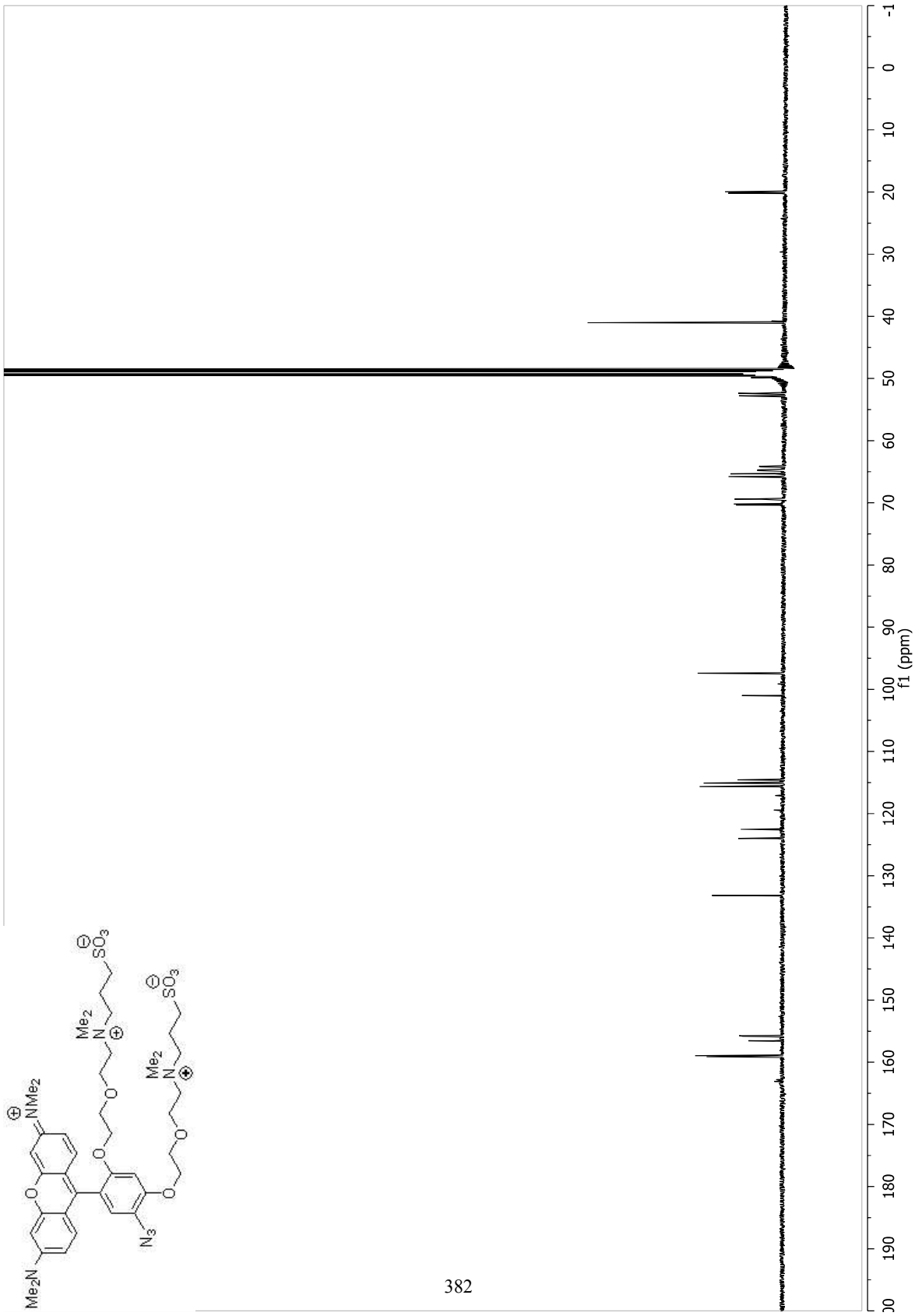
380

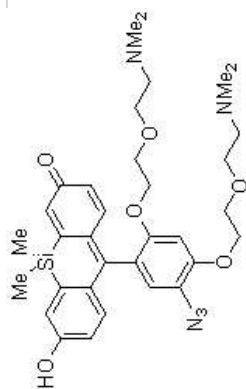




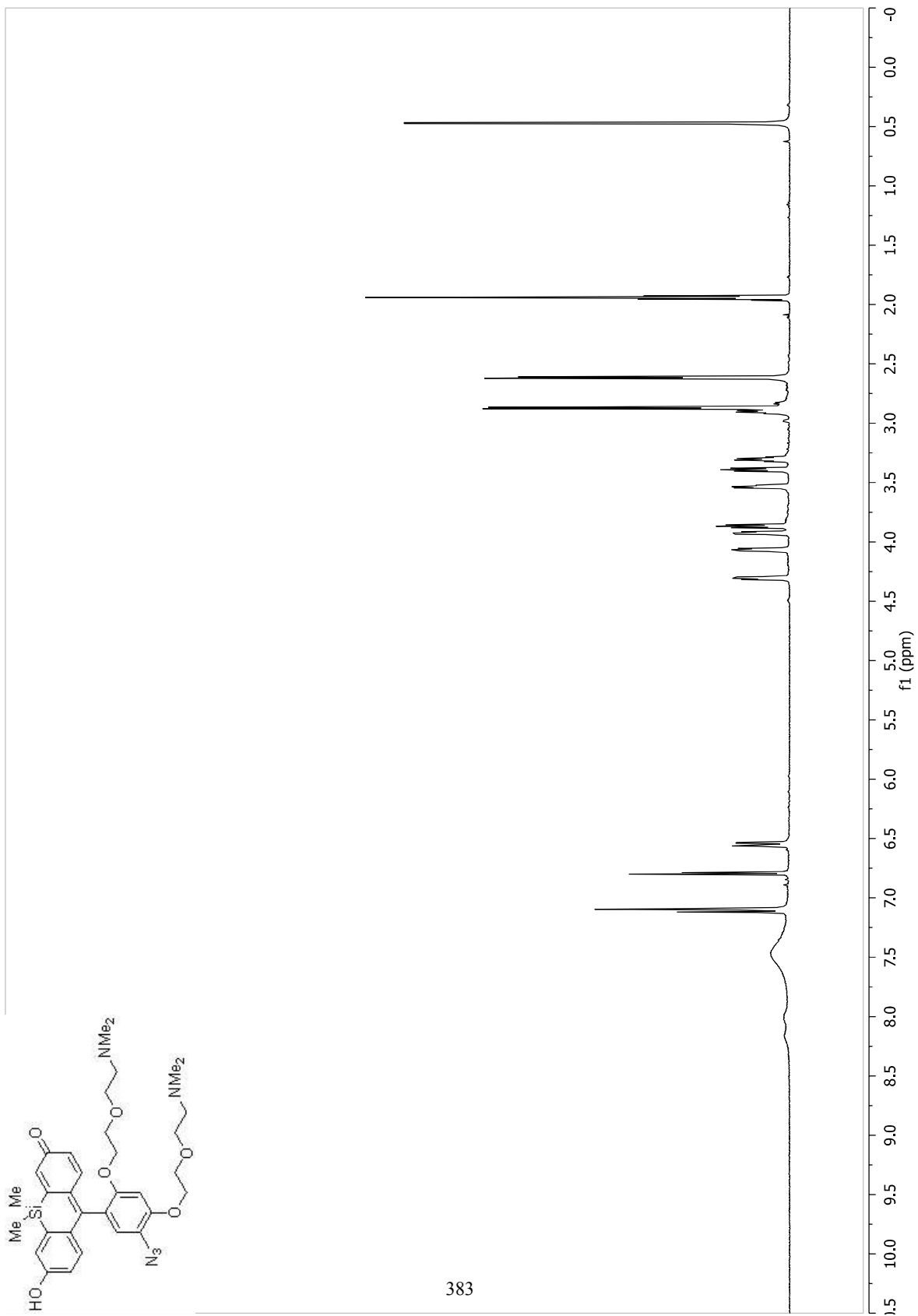


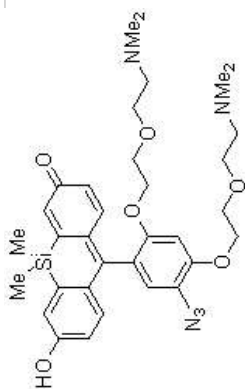
382



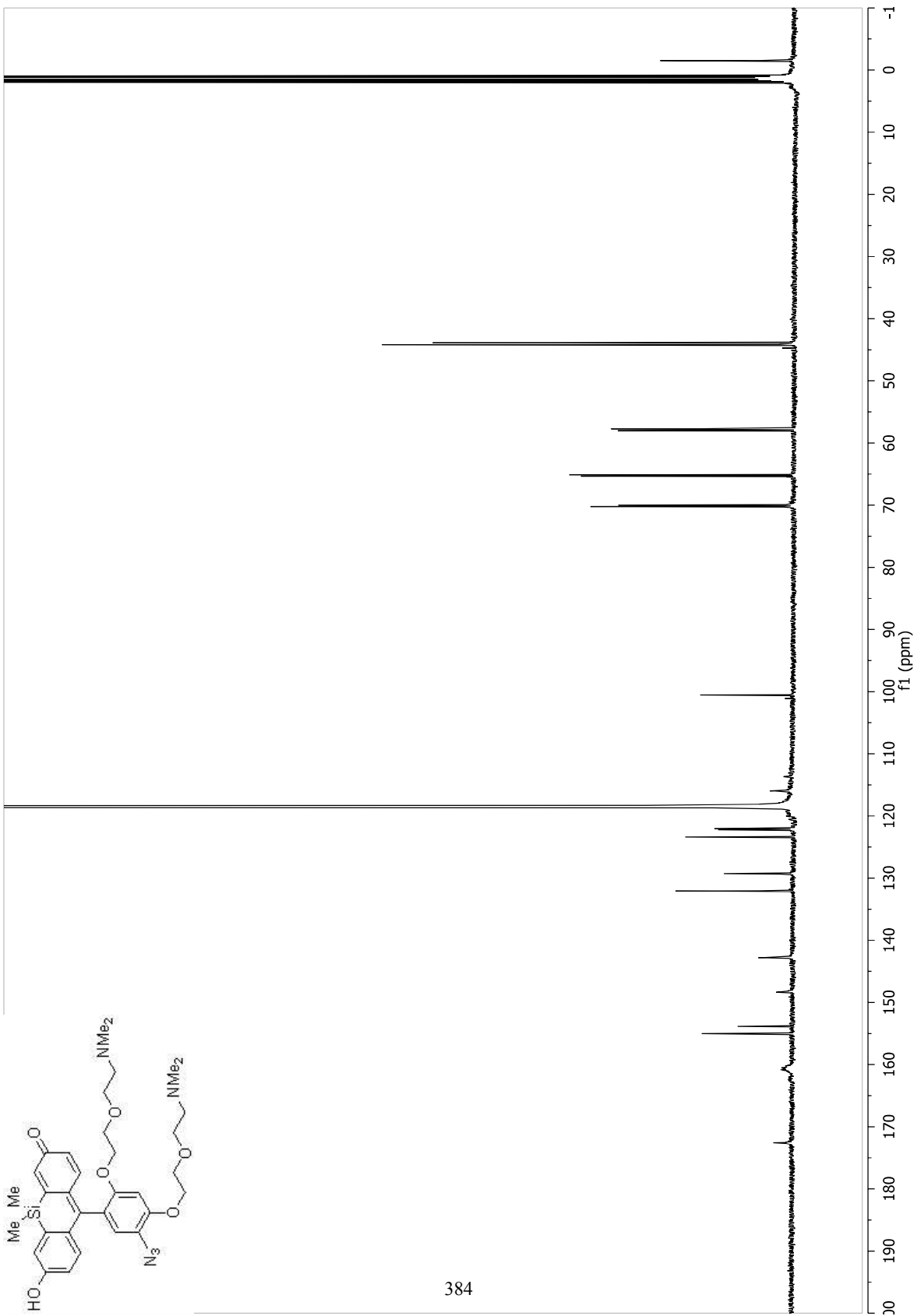


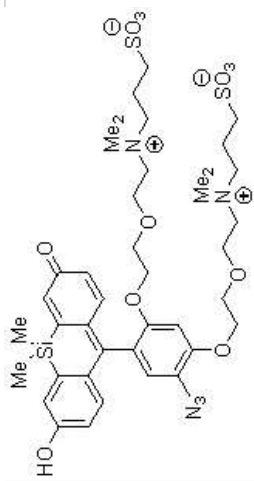
383



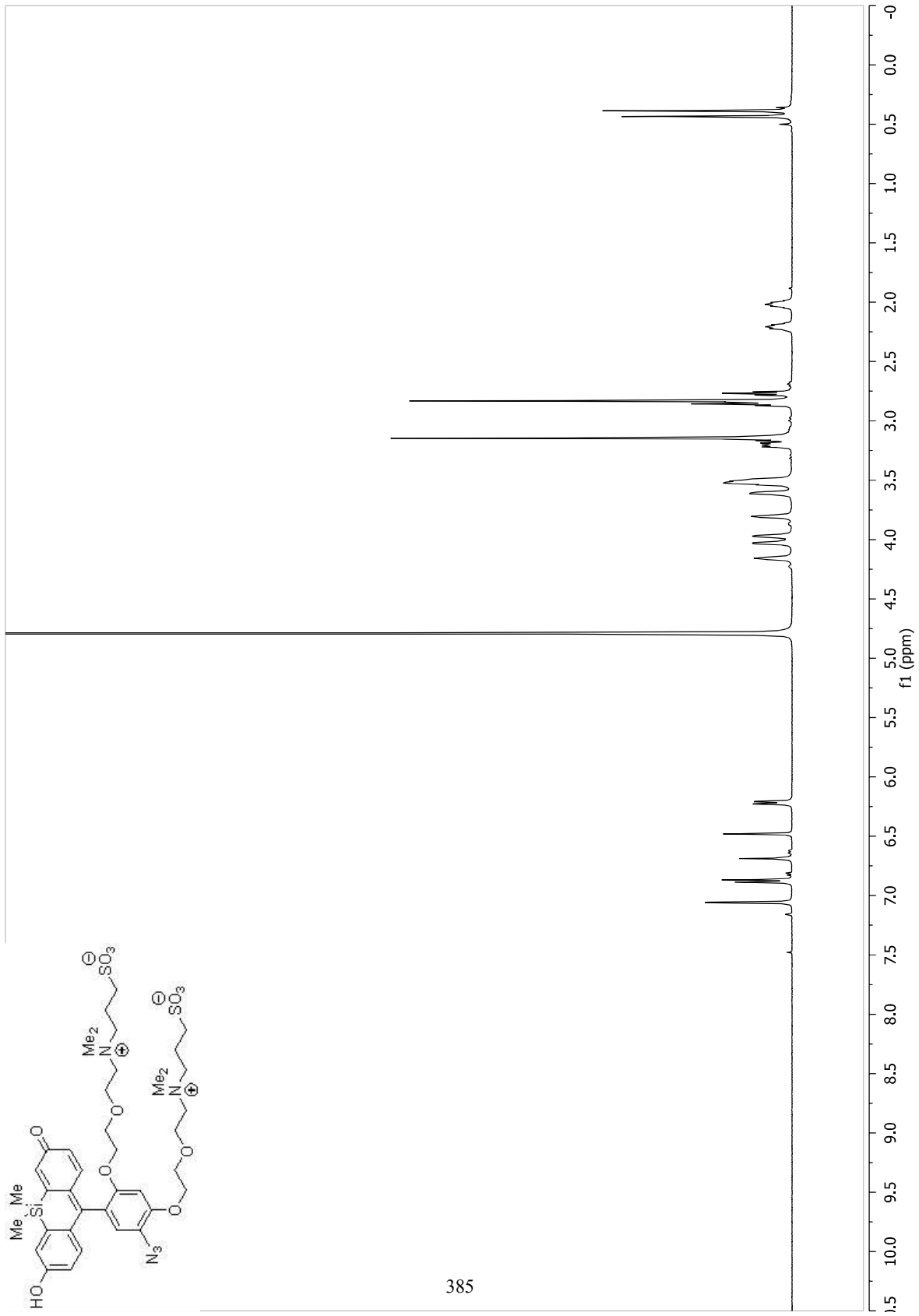


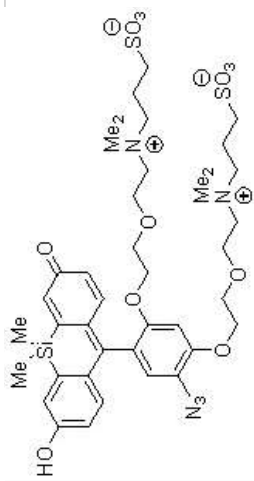
384



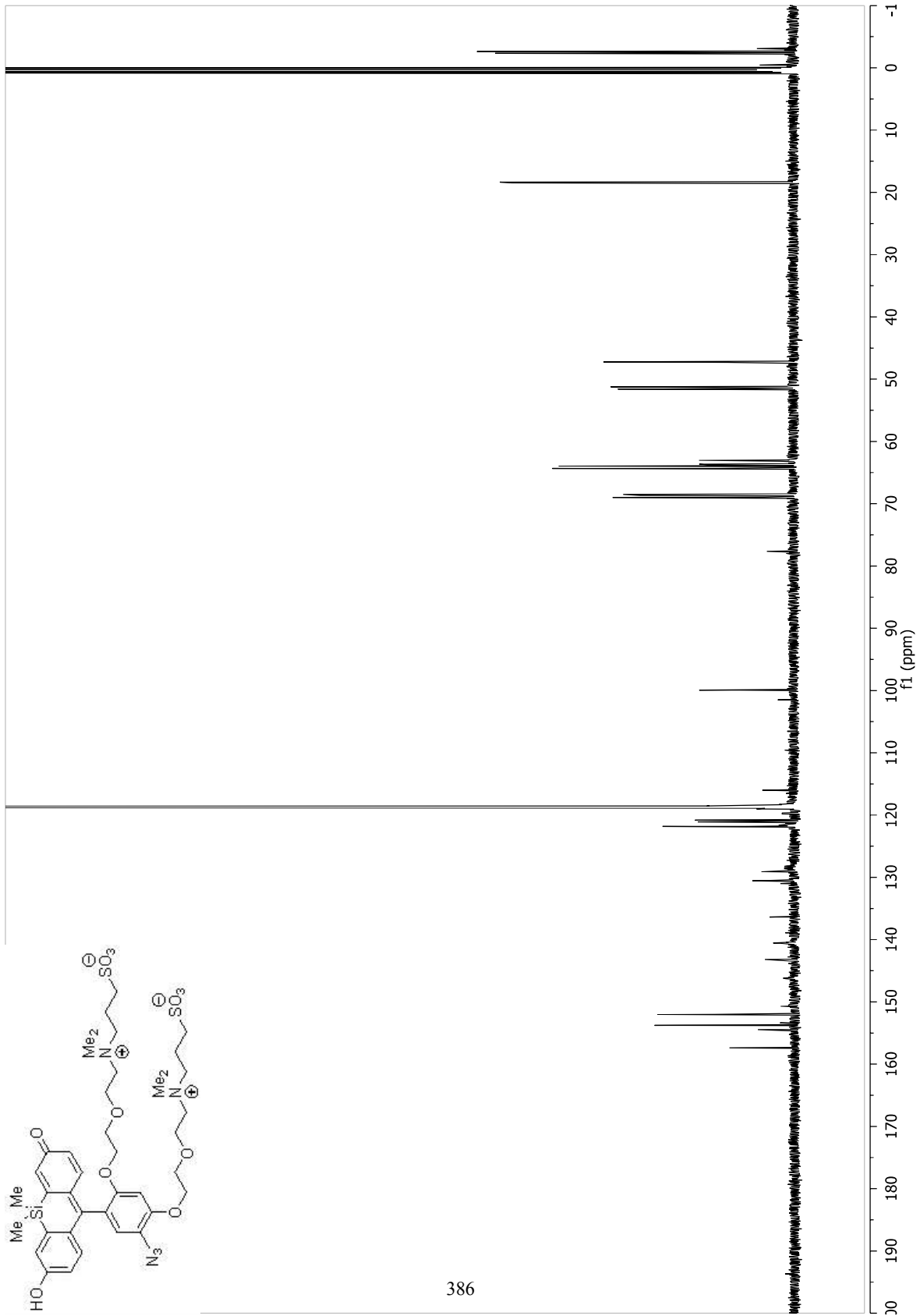


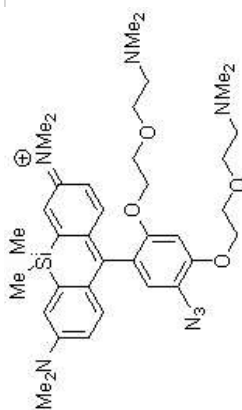
385



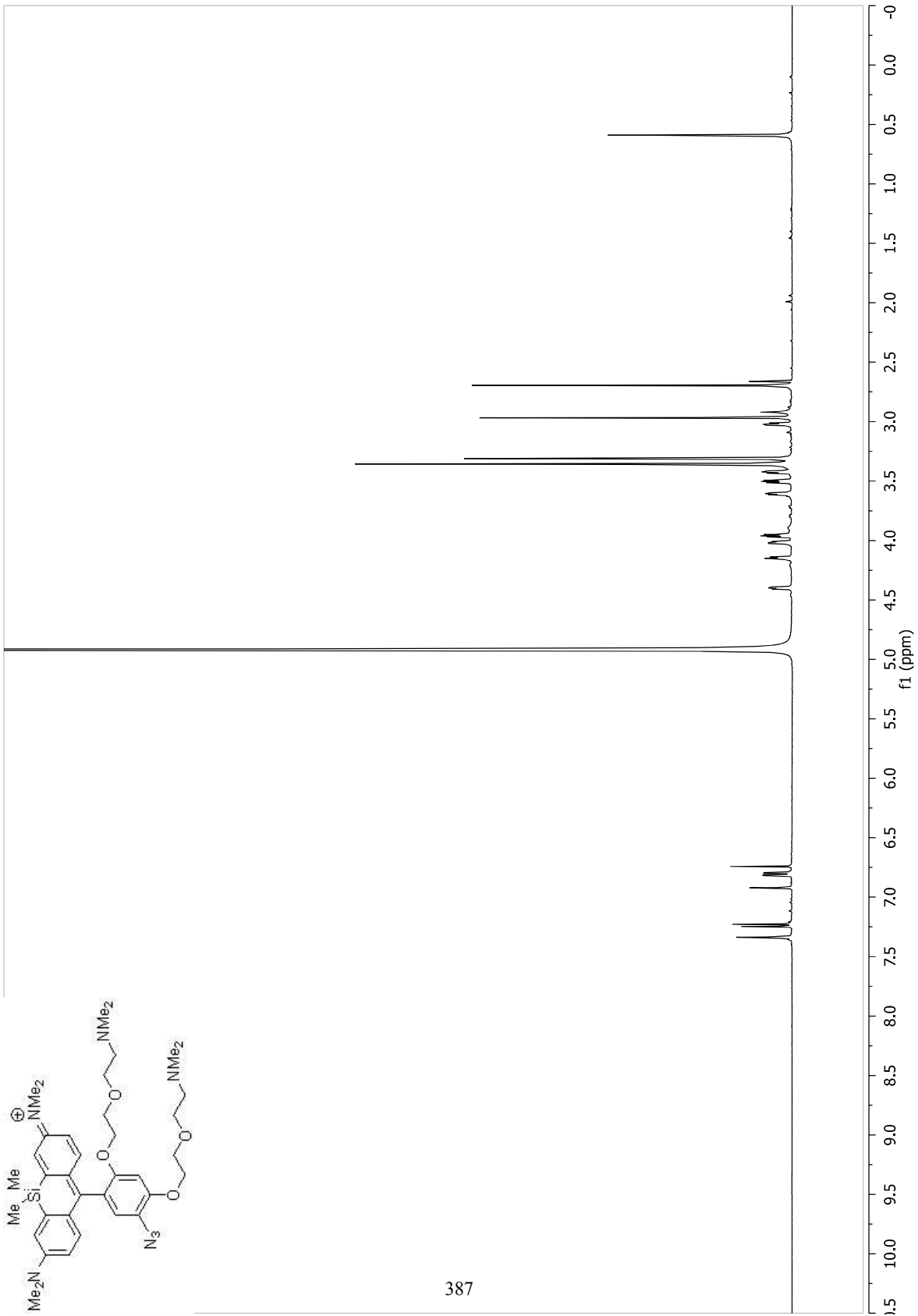


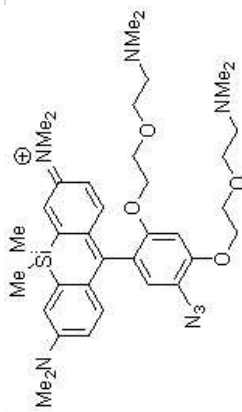
386



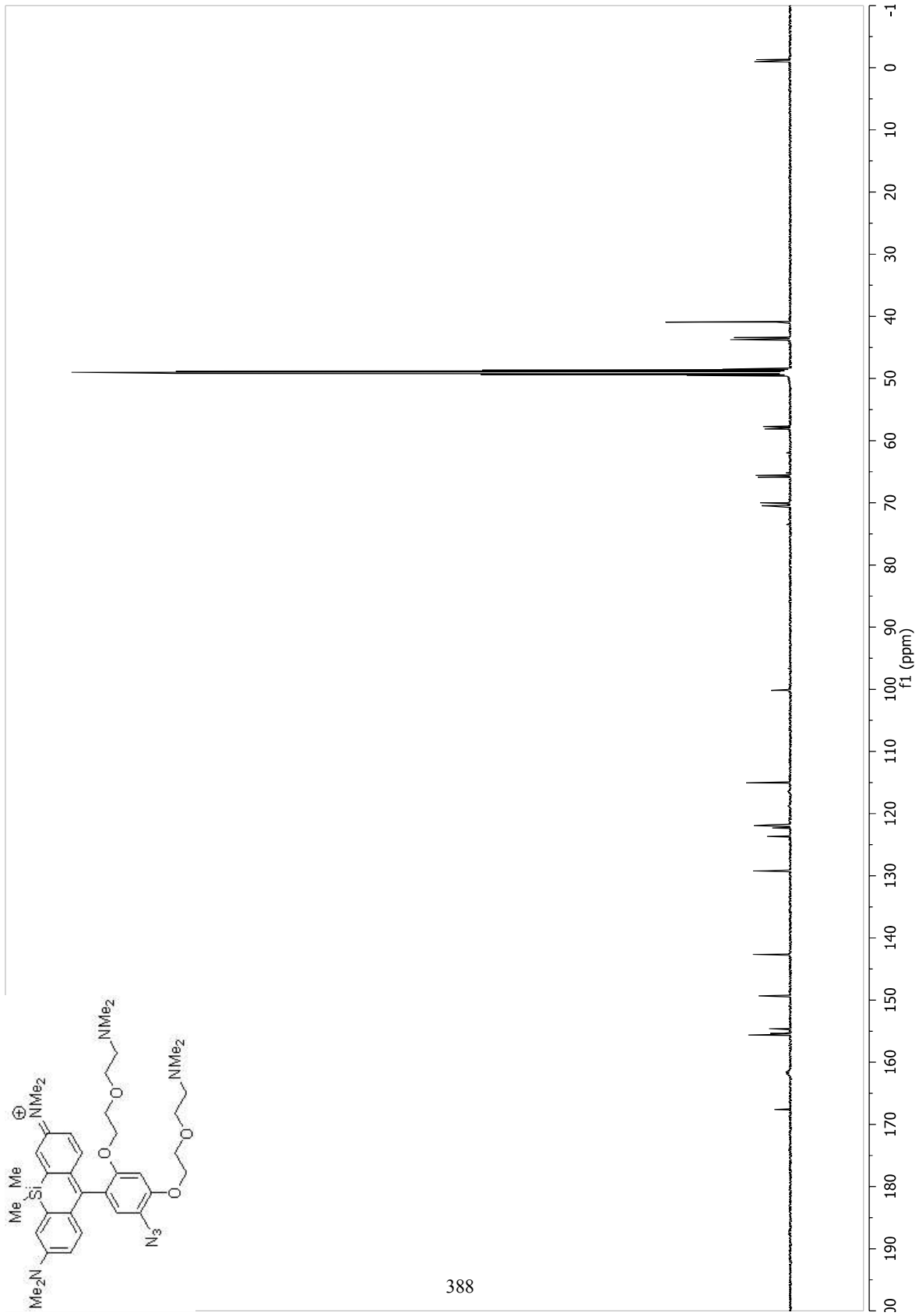


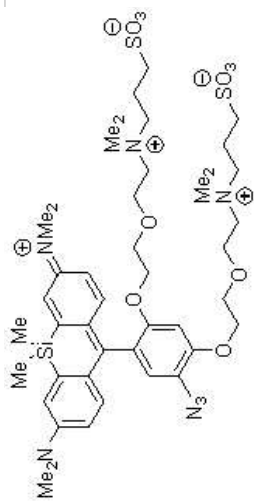
387



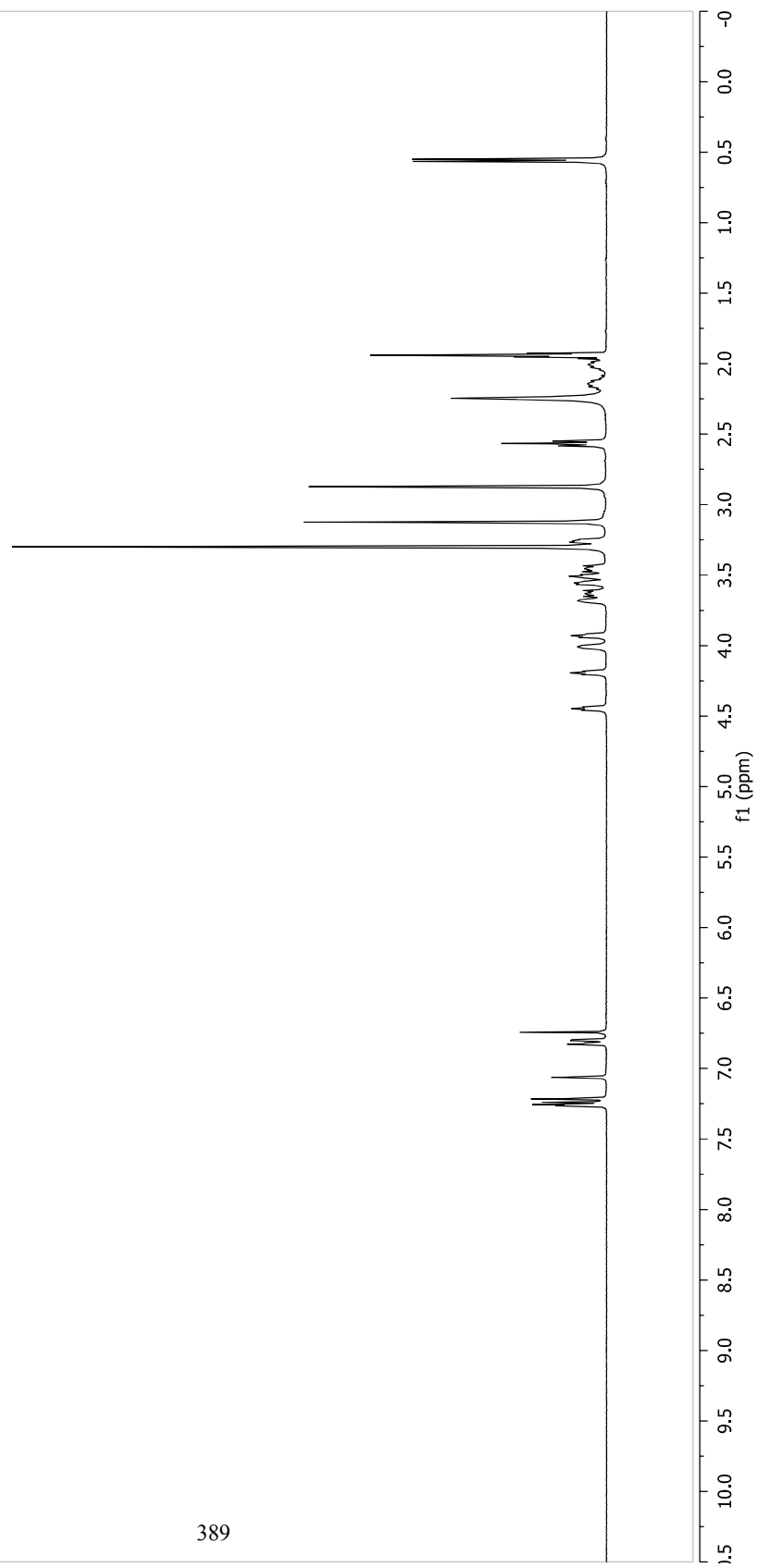


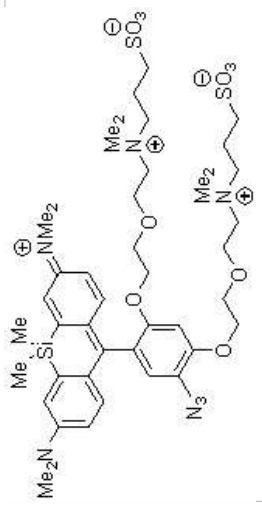
388



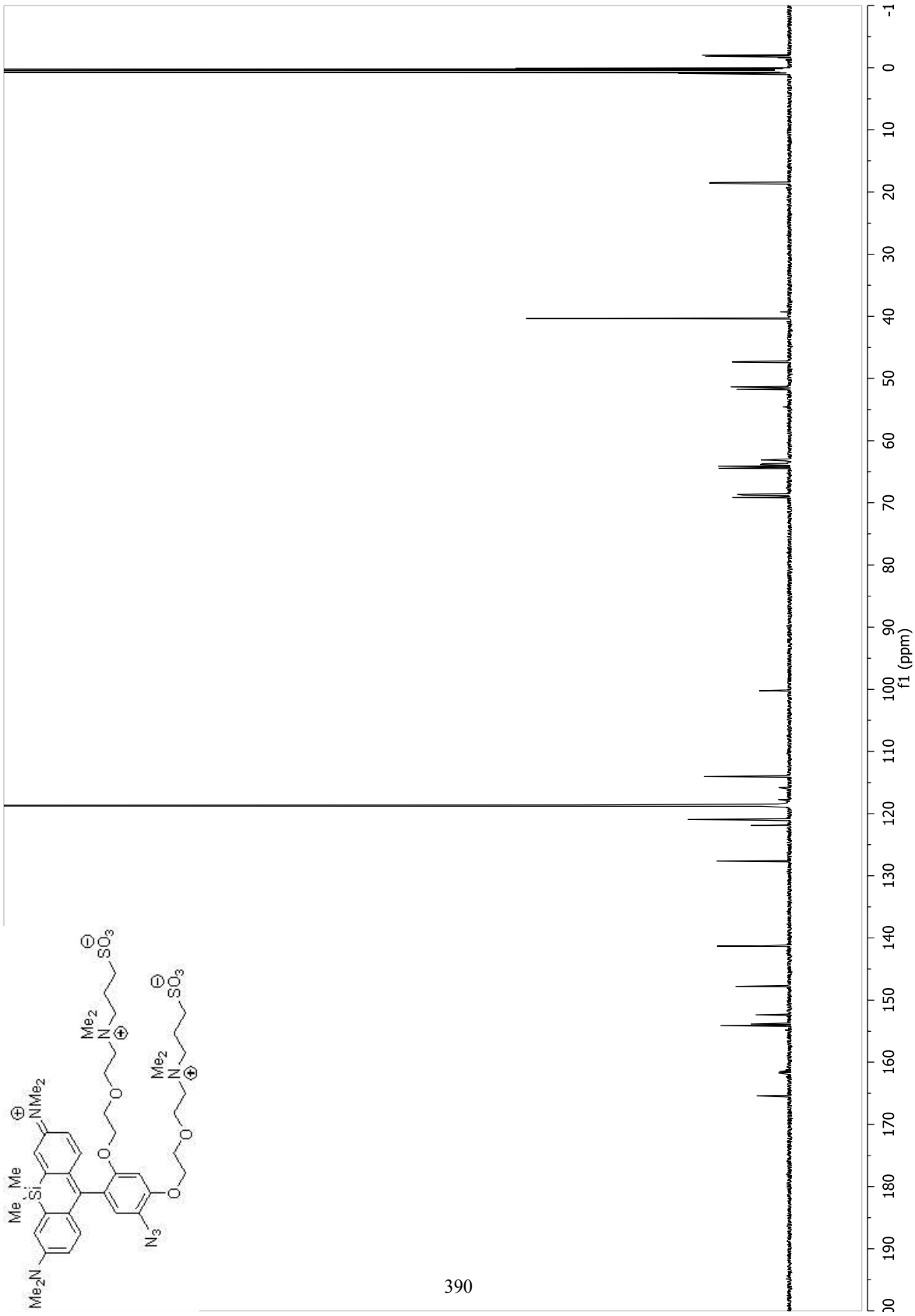


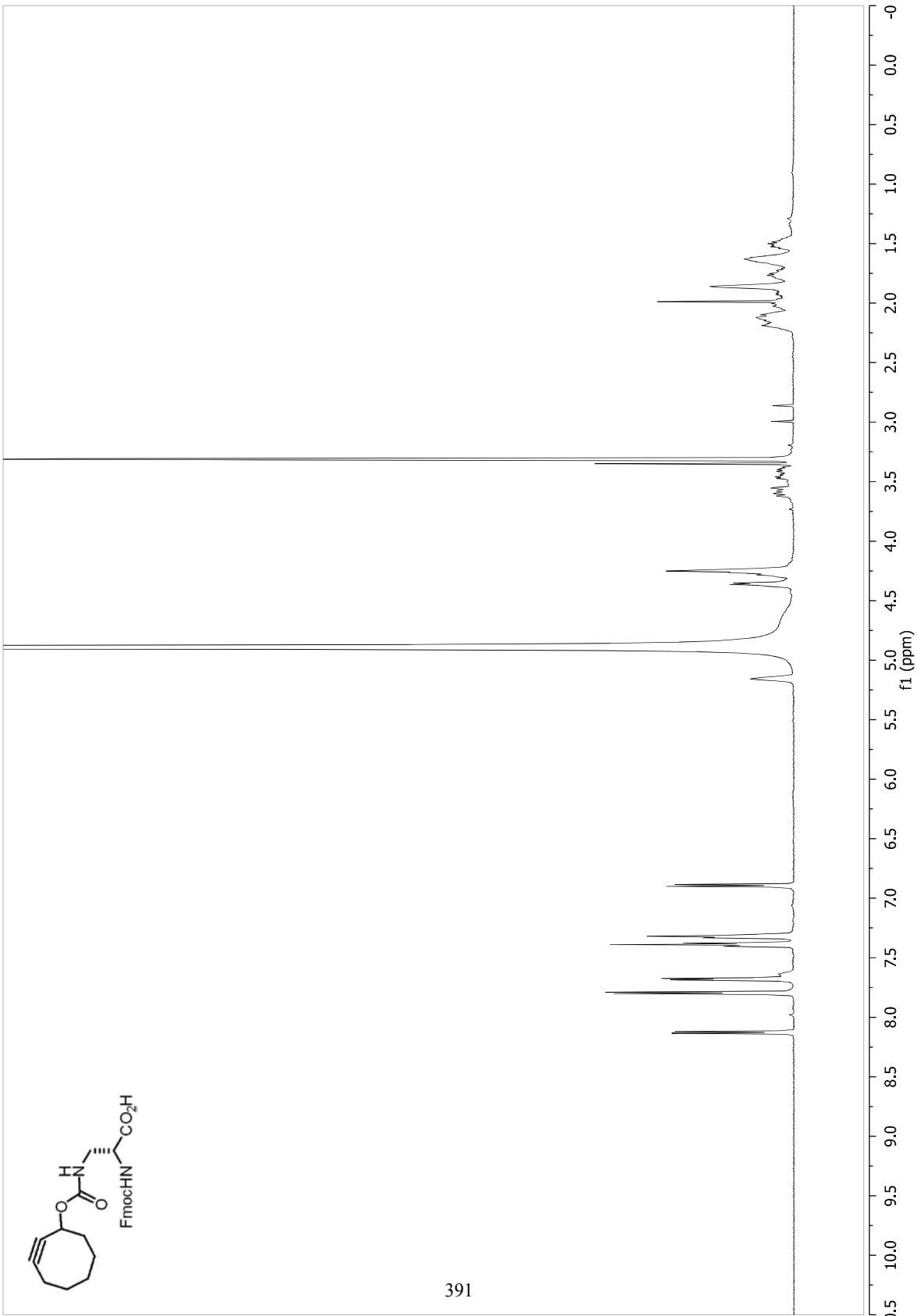
389

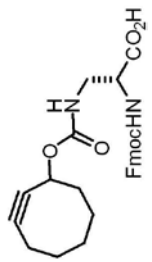




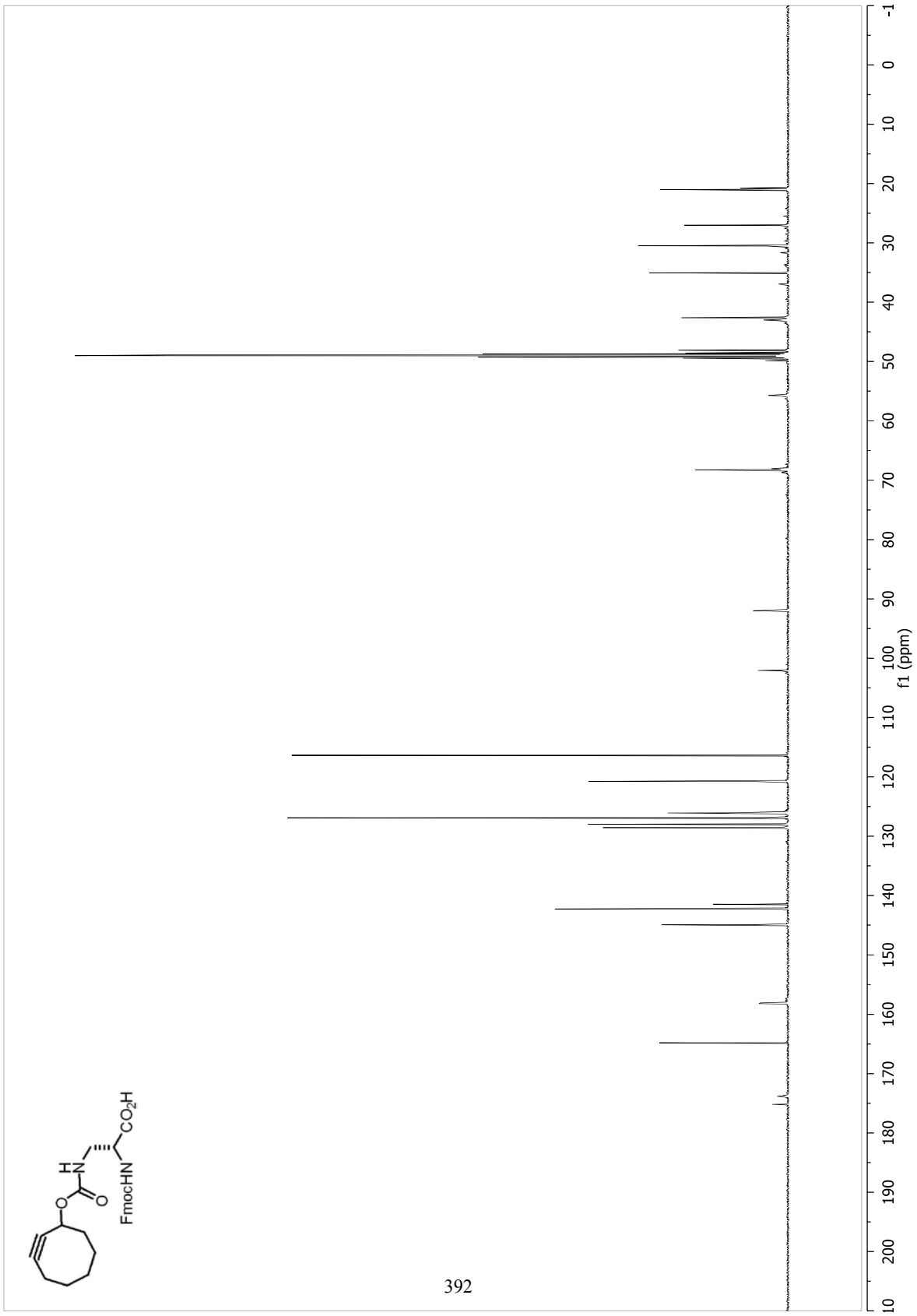
390

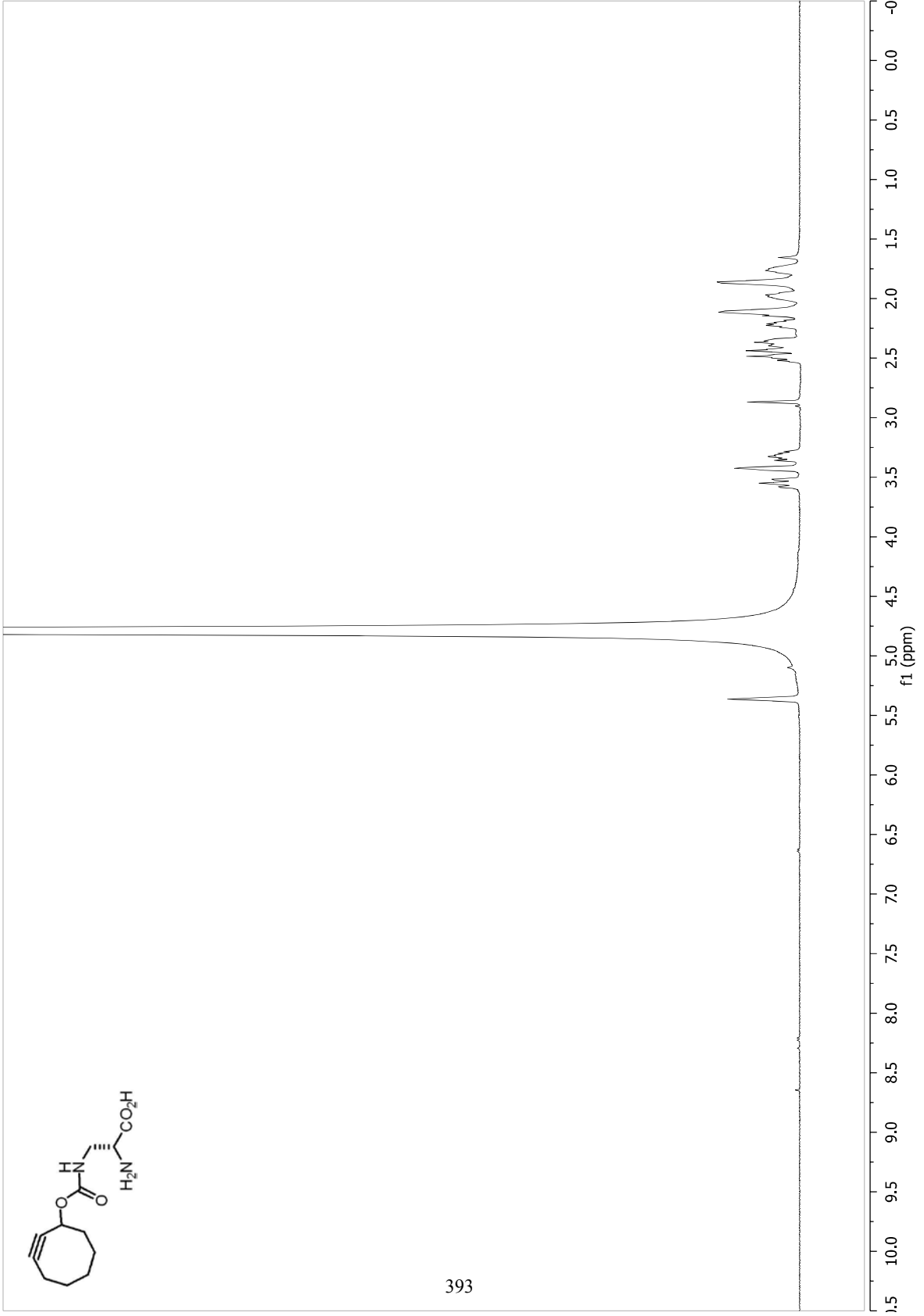


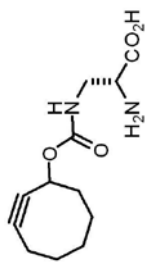




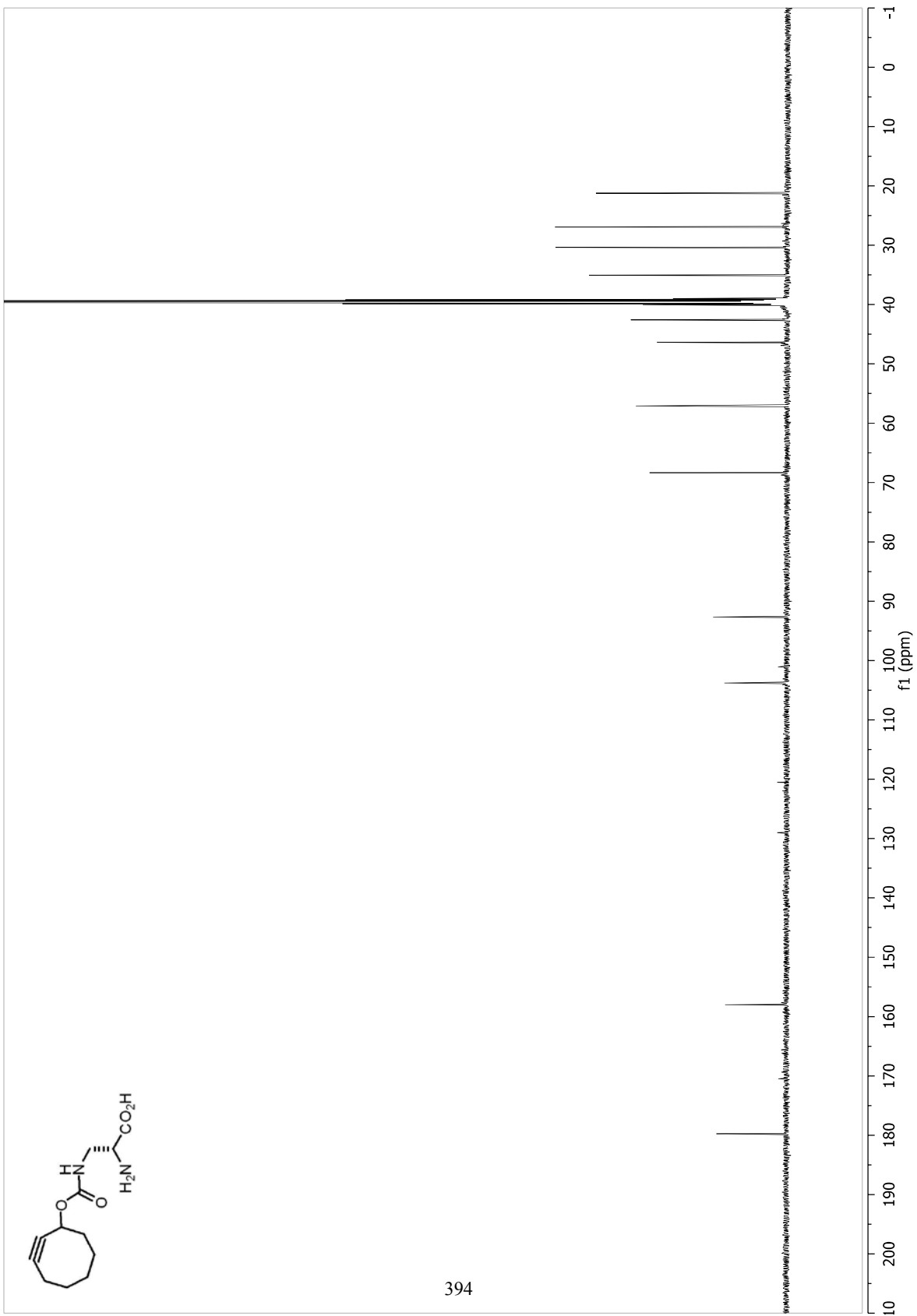
392

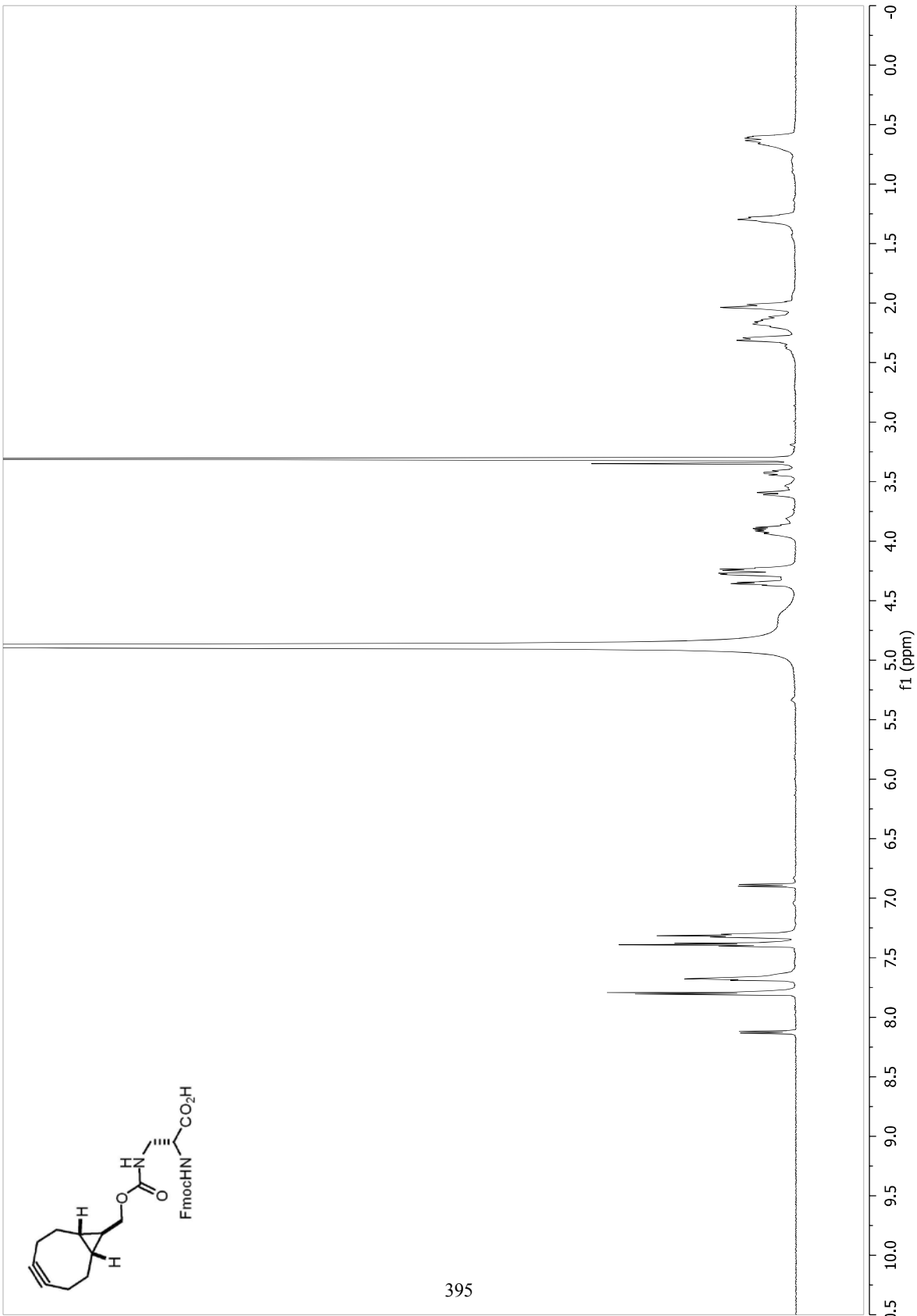


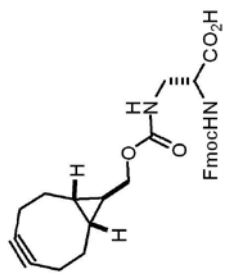




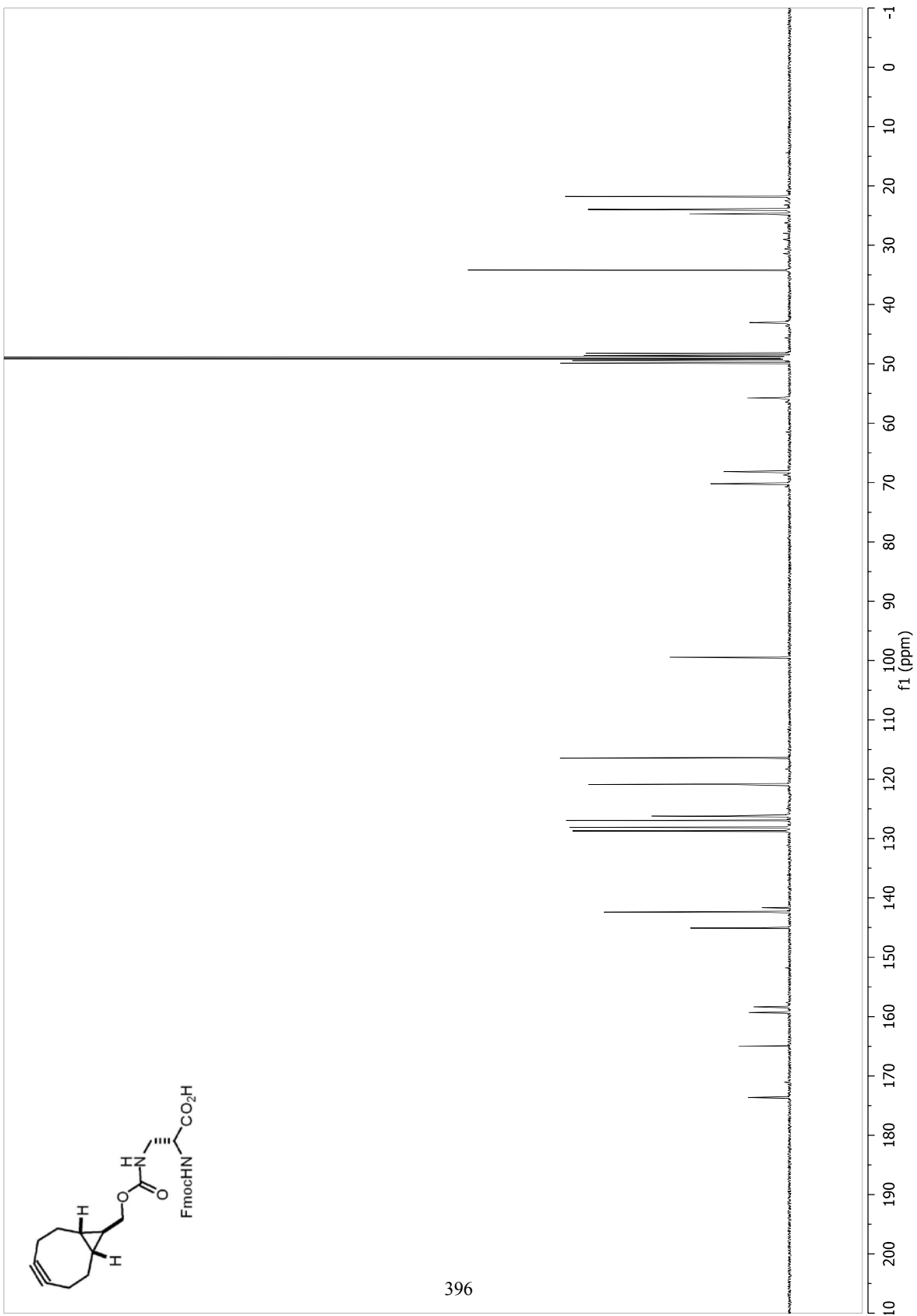
394

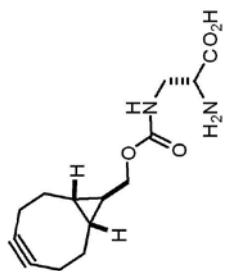




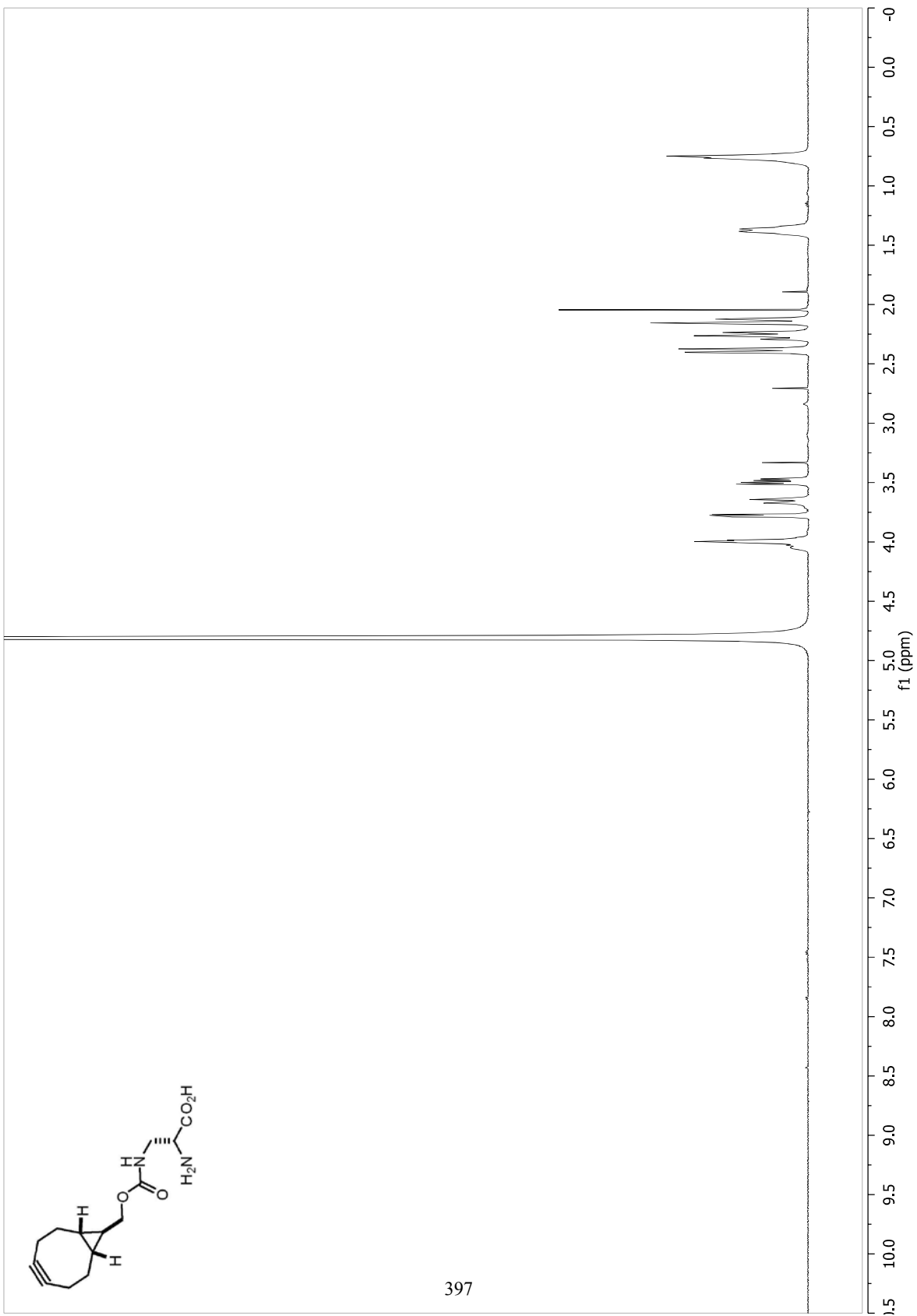


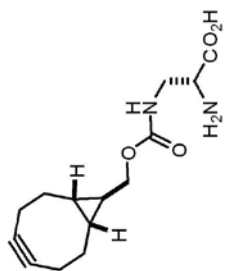
396



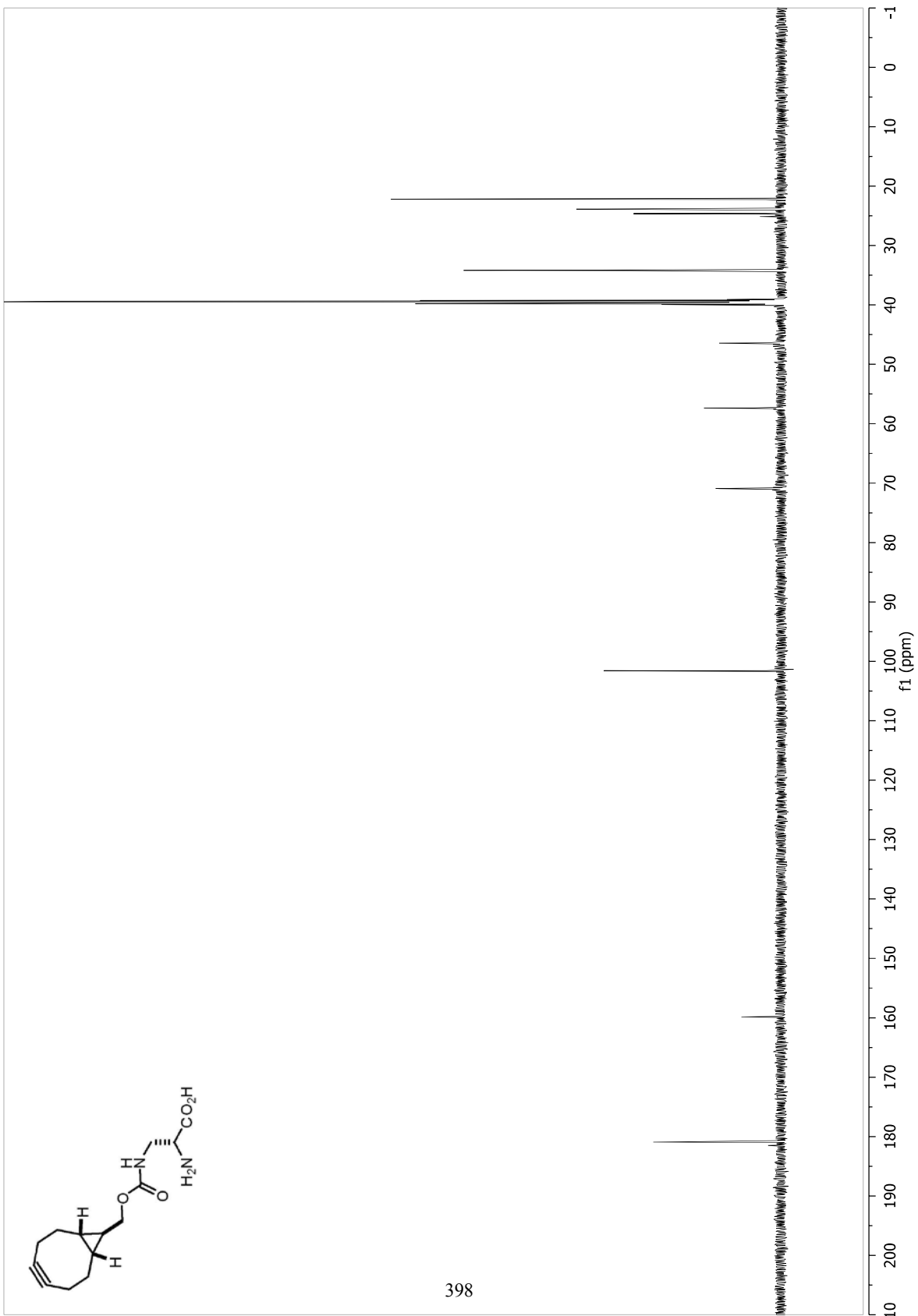


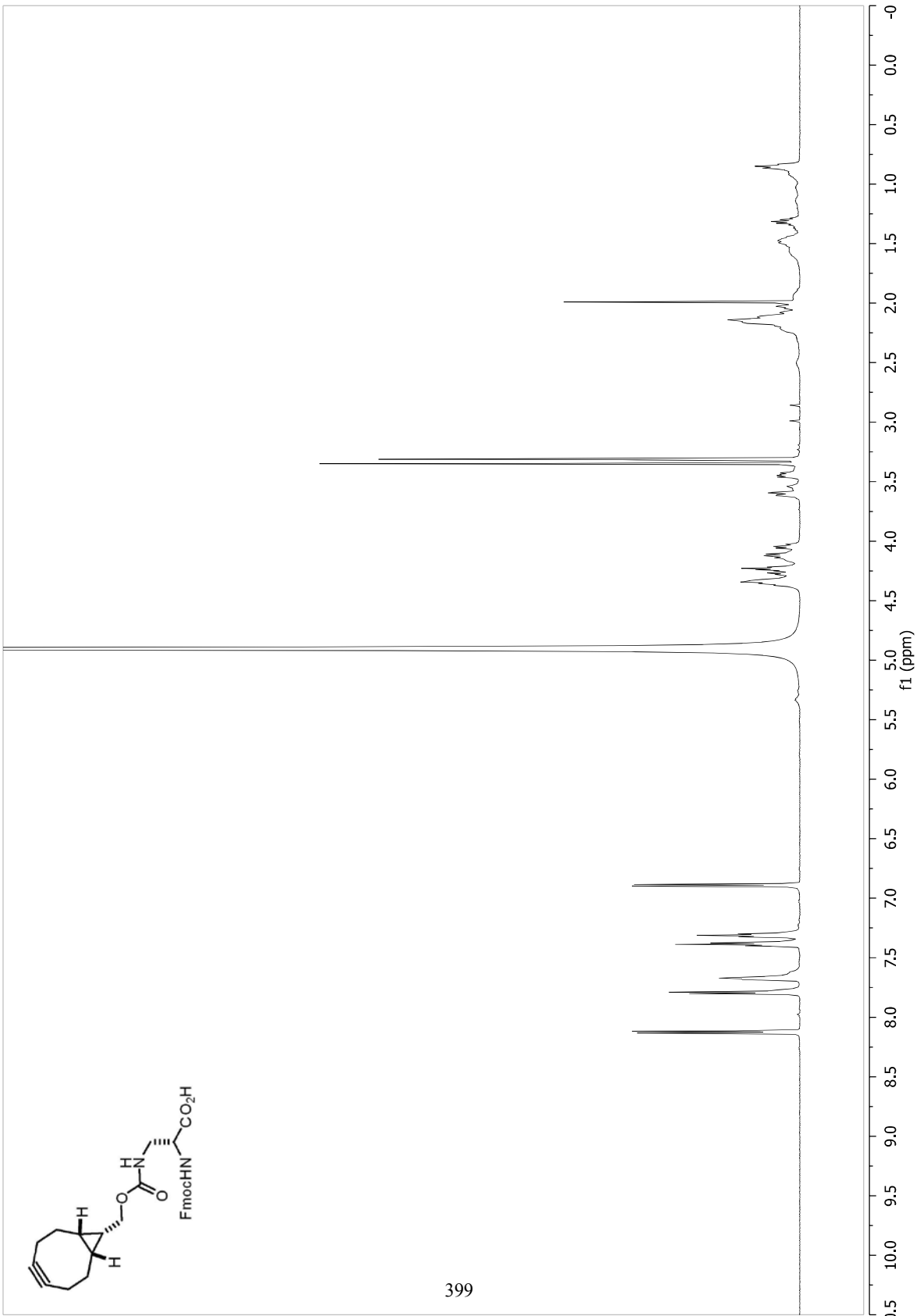
397

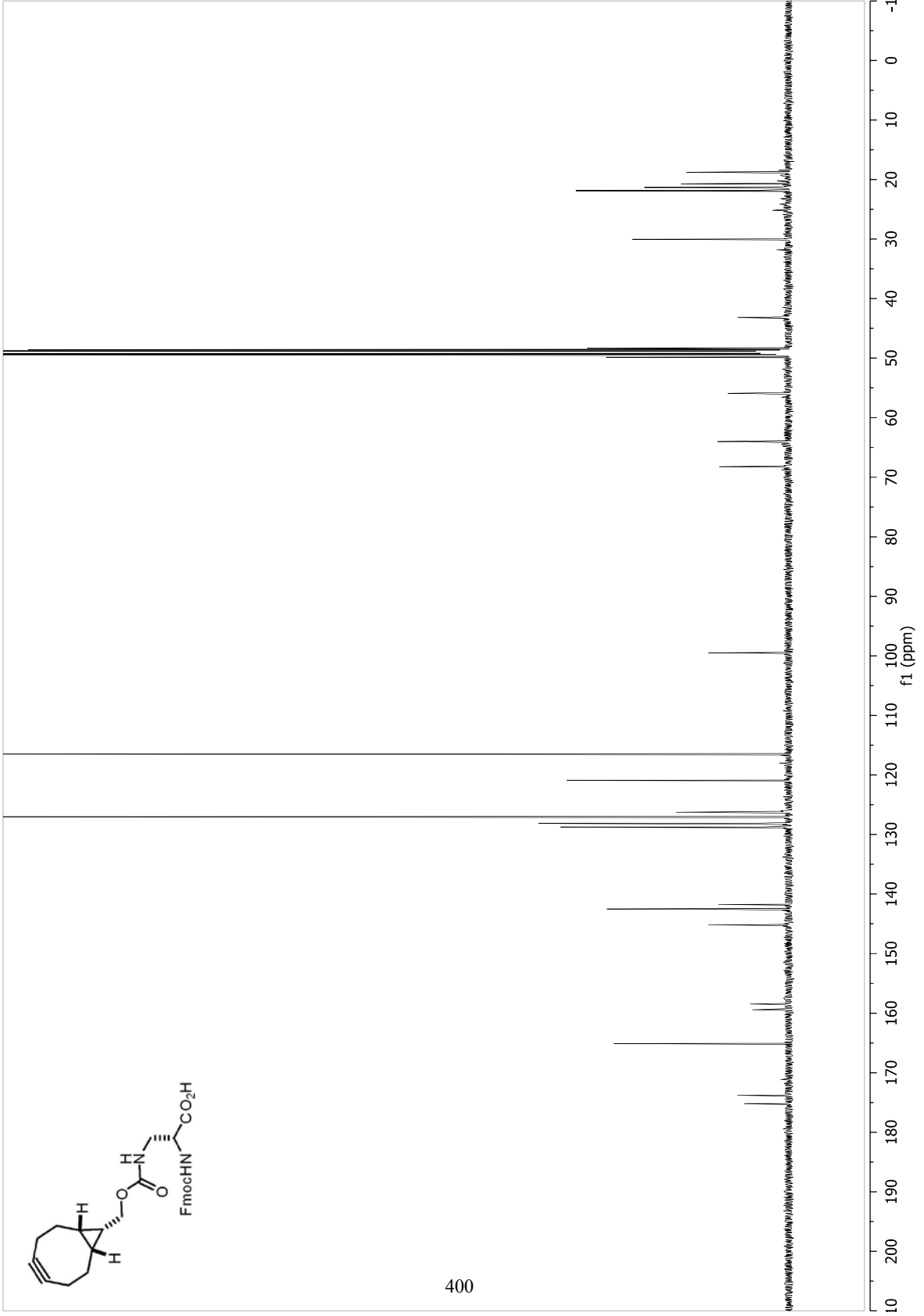


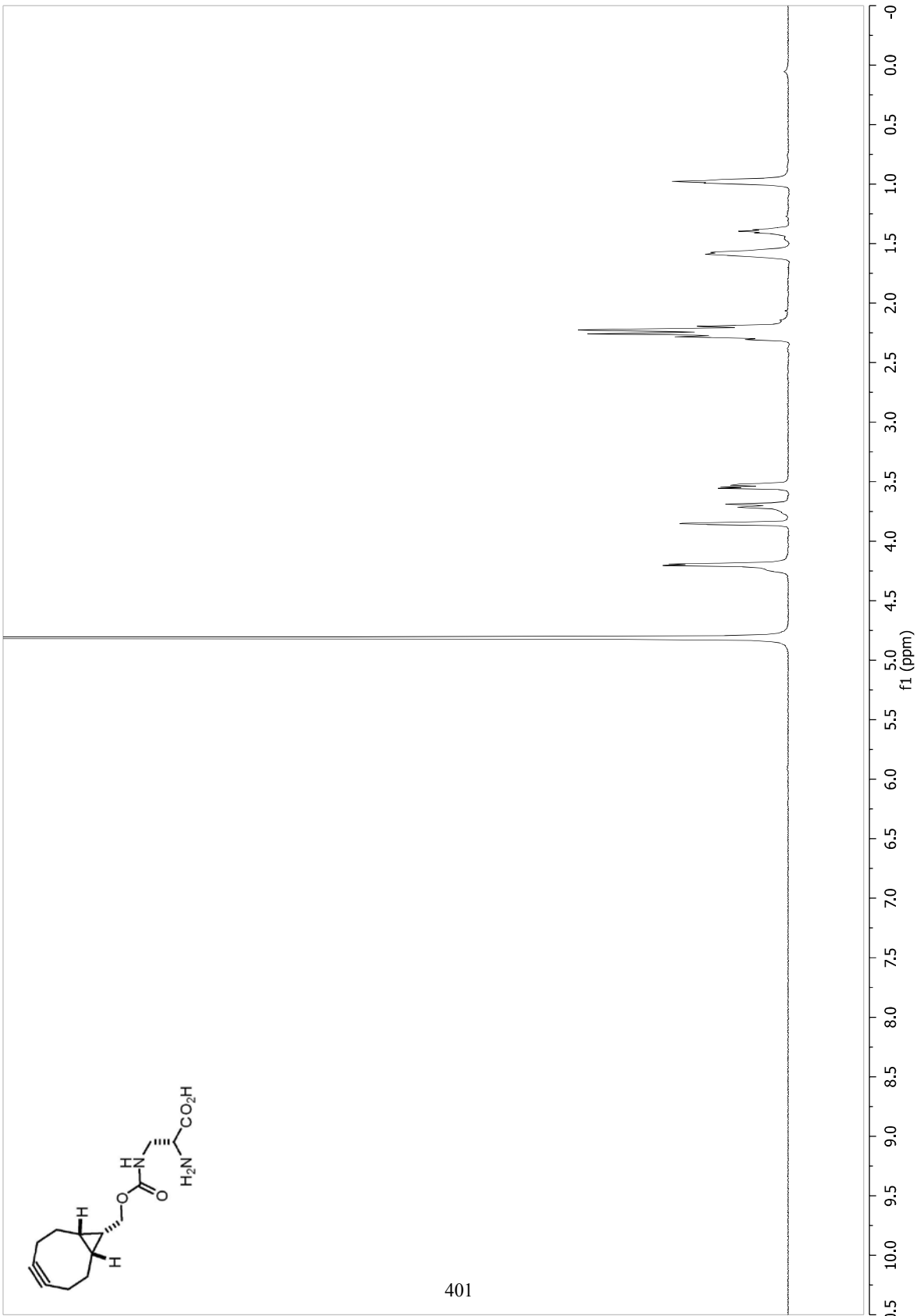


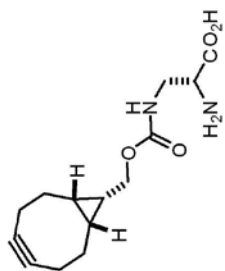
398











402

